

Sheffield Hallam University

Stationary shoulder friction stir welding of military aircraft sheet alloys

PUCKRIN, Emma Louise

Available from the Sheffield Hallam University Research Archive (SHURA) at:

<http://shura.shu.ac.uk/30615/>

A Sheffield Hallam University thesis

This thesis is protected by copyright which belongs to the author.

The content must not be changed in any way or sold commercially in any format or medium without the formal permission of the author.

When referring to this work, full bibliographic details including the author, title, awarding institution and date of the thesis must be given.

Please visit <http://shura.shu.ac.uk/30615/> and <http://shura.shu.ac.uk/information.html> for further details about copyright and re-use permissions.

Stationary Shoulder Friction Stir Welding of Military Aircraft Sheet Alloys

Emma Louise Puckrin

A thesis submitted in partial fulfilment of the requirements of

Sheffield Hallam University

for the degree of Doctor of Philosophy

In collaboration with

Royal Navy 1710 Naval Air Squadron

January 2022

Candidate Declaration

I hereby declare that:

1. I have not been enrolled for another award of the University, or other academic or professional organisation, whilst undertaking my research degree.
2. None of the material contained in the thesis has been used in any other submission for an academic award.
3. I am aware of and understand the University's policy on plagiarism and certify that this thesis is my own work. The use of all published or other sources of material consulted have been properly and fully acknowledged.
4. The work undertaken towards the thesis has been conducted in accordance with the SHU Principles of Integrity in Research and the SHU Research Ethics Policy.
5. The word count of the thesis is 90,756.

Name	Emma Louise Puckrin
Date	January 2022
Award	Doctor of Philosophy
Faculty	Materials and Engineering Research Institute
Director of Studies	Dr Stephen Magowan

Abstract

Stationary Shoulder Friction Stir Welding (SSFSW) allows joining of materials without the addition of mass and could be a potential solution to expedient helicopter repair in operational theatre. This research considers the suitability for SSFSW of two aluminium alloys commonly used within the Merlin helicopter airframe, AA8090 and BS L165.

Techniques including optical microscopy, hardness, tensile and fatigue testing were used to characterise the two alloys and to establish a baseline for comparison with the welded specimens. The welds were performed in four configurations, with each welded both parallel and perpendicularly to the material's rolling direction. This was in an effort to establish: the alloy's suitability for SSFSW in both similar and dissimilar welds; the effect of changing the alloy positioned on the advancing side; and the influence of the material rolling direction on the quality of the weld. Techniques similar to those used in the material characterisation were used to determine the quality of each configuration.

Encouraging tensile and fatigue strength results were achieved, especially for the similar materials welds with BS L165 welded parallel to the rolling direction achieving over 100% UTS weld efficiency. Inconsistent quality including the presence of kissing bonds was, however, observed. When welding parallel to the rolling direction, stronger welds were produced with BS L165 positioned on the advancing side. The presence of kissing bonds made analysis of those welded perpendicular to the rolling direction inconclusive. The material rolling direction also had an effect on the weld, as demonstrated through differences in weld appearance, degree of mixing of materials and tensile and fatigue test results.

Additionally, a relationship between hardness and tensile strength was determined which revealed close correlation between the governing equation and the test results, with only 7% scatter. This will allow for prediction of tensile strength, based on the measured hardness, when the materials are joined using SSFSW.

Acknowledgements

There are many people who have made this project possible, and I offer my sincere gratitude to all of them.

Firstly I would like to thank my supervisors. Dr Stephen Magowan, thank you for your support, advice and for setting me deadlines. I might not have reached the finish point without them! Dr Cheryl Pitt, I greatly appreciate your infinite patience, encouragement and support both throughout this research and during my 11+ years working for you. Your expertise on all things materials has been invaluable and I have learned a huge amount with you as a mentor and role-model. Professor Alan Smith, I am grateful for the project inspiration and support until your well-deserved retirement.

Key personnel at Sheffield Hallam University include Phil Stevenson and Tim O'Hara in Mechanical Testing. Thank you for the long hours spent assisting me with fatigue testing. Dr Francis Clegg offered helpful advice and guidance with the PhD process. I must also express my thanks to all of the MERI administrative staff who were always on hand to keep me on track with university processes.

I wish to acknowledge the expertise, guidance and support of Dr Jereon De Backer at TWI; your assistance with welding at the start of my project was vital.

Thank you to my colleagues at 1710 NAS for your support and ideas during my research, and for your patience when I was busy on this project.

I am grateful to Navy Command for the finance and trust to see the project to completion.

My family deserve a heartfelt round of applause for their support and encouragement for the past 8 years, and for their patience when I was grumpy! Special thanks to my mum and Paul, dad and Cathy, and brother Stuart who all bore the brunt of my frustration when things weren't going well. And thanks to my best boy (dog) Dexter, who gives the greatest cuddles and picks me up again.

Finally, to my partner Dan: thank you for your patience, support and for all the help with grain counting! Your never-ending encouragement and positive attitude kept me going; you could see the light at the end of the tunnel even when I couldn't! I think we deserve a holiday...

Contents

1	Introduction	1
1.1	Issue	1
1.2	Technique Selection	2
1.3	Materials Selection	3
1.4	Project Aim	4
1.5	Objectives	5
2	Literature Review	6
2.1	EH 101 (Merlin) Helicopter	6
2.1.1	UK Merlin Helicopter	6
2.1.2	AA8090 and BS L165 in Merlin airframes	8
2.2	Materials	9
2.2.1	Precipitation Hardening Aluminium Alloys	9
2.2.2	Recovery and Recrystallisation	11
2.2.2.1	Static Recovery	12
2.2.2.2	Static Recrystallisation	13
2.2.2.3	Dynamic Recovery	13
2.2.2.4	Dynamic Recrystallisation	14
2.2.3	Grain size and mechanical properties	14
2.2.4	AA8090 Characteristics	15
2.2.4.1	Metallurgy	15
2.2.4.2	Mechanical Properties	18
2.2.4.3	Weldability	21
2.2.5	BS L165	22
2.2.5.1	Metallurgy	22
2.2.5.2	Mechanical Properties	26
2.2.5.3	Weldability	28
2.3	Friction Stir Welding	29
2.3.1	Friction Stir Welding Process	29
2.3.2	Stationary Shoulder Friction Stir Welding (SSFSW)	33
2.3.3	FSW/ SSFSW of AA8090	37
2.3.4	FSW/ SSFSW of BS L165/ AA2014	38

2.3.5	FSW/SSFSW of Dissimilar Aluminium Alloys.....	42
2.3.5.1	Dissimilar FSW containing Al-Li.....	42
2.3.5.2	Dissimilar FSW containing BS L165/ AA2014	44
2.3.5.3	Dissimilar SSFSW of aluminium alloys.....	47
2.3.6	FSW/ SSFSW of Al-clad Material	48
2.3.7	FSW/ SSFSW of Thin Sheet Aluminium Alloy.....	50
2.3.8	FSW/ SSFSW Mechanisms	52
2.3.8.1	Material Flow	52
2.3.8.2	Temperature and Heat Generation	56
2.3.8.3	FSW microstructural evolution in the various zones	58
2.3.9	Parameters, Tools and Mechanical Properties.....	59
2.3.9.1	Parameters.....	59
2.3.9.1.1	<i>Rotational and traversing speeds.....</i>	59
2.3.9.1.2	<i>Tool tilt angle.....</i>	61
2.3.9.1.3	<i>Plunge depth</i>	61
2.3.9.1.4	<i>Tool offset.....</i>	62
2.3.9.2	Tools.....	62
2.3.9.2.1	<i>Tool material</i>	62
2.3.9.2.2	<i>Tool features.....</i>	63
2.3.9.3	Mechanical Properties	67
2.3.9.3.1	<i>Hardness.....</i>	67
2.3.9.3.2	<i>Tensile Strength and Ductility.....</i>	69
2.3.9.3.3	<i>Fatigue.....</i>	72
2.3.9.3.4	<i>Residual Stress (RS).....</i>	73
2.3.9.4	Summary of literature.....	76
2.3.10	FSW/ SSFSW Defects.....	83
2.3.11	Portability of FSW/ SSFSW	85
2.4	Summary.....	87
3	Methodology	89
3.1	Materials.....	89
3.1.1	Material Orientations	89
3.1.2	Material Condition	89
3.1.2.1	AA8090.....	89
3.1.2.2	BS L165.....	90
3.1.3	Elemental Analysis of Parent Materials.....	90
3.1.3.1	Inductively Coupled Plasma with Optical Emission Spectroscopy (ICP-OES).....	91

3.1.3.2	Energy Dispersive X-ray (EDX) Analysis.....	91
3.2	Welding.....	92
3.2.1	Procedure.....	92
3.2.2	Tool	93
3.2.3	Workpiece preparation.....	95
3.2.4	Process Parameters	96
3.3	As-Welded Examination	98
3.3.1	Optical Microscopy	98
3.3.1.1	Photography and Stereo Microscopy	98
3.3.1.2	Inverted Optical Microscopy.....	99
3.3.2	Optical and Contact Profilometry	99
3.4	Testing	100
3.4.1	Hardness	100
3.4.1.1	Sample preparation	100
3.4.1.2	Test procedure	100
3.4.2	Tensile Testing	101
3.4.3	Fatigue Testing.....	103
3.4.3.1	Procedure Overview	103
3.4.3.2	The Staircase Method	105
3.4.4	Residual Stress	106
3.4.4.1	Test Method.....	106
3.4.4.1.1	<i>Strain gauge</i>	<i>108</i>
3.4.4.1.2	<i>Positioning of gauges</i>	<i>108</i>
3.4.4.1.3	<i>Test set-up and parameters</i>	<i>110</i>
3.4.4.2	Analysis Method.....	114
3.4.4.2.1	<i>Integral Method</i>	<i>114</i>
3.4.4.3	Uncertainty Analysis	117
4	Characterisation of Parent Materials	119
4.1	AA8090	119
4.1.1	Elemental Composition.....	119
4.1.2	Material Microstructure	120
4.1.3	Mechanical Properties	124
4.1.3.1	Hardness	124
4.1.3.2	Tensile Strength	126
4.1.3.3	Fatigue Strength.....	129

4.1.3.4	Residual Stress	133
4.2	BS L165	133
4.2.1	Elemental Composition.....	133
4.2.2	Material Microstructure	134
4.2.3	Mechanical Properties	139
4.2.3.1	Hardness	141
4.2.3.2	Tensile Strength	141
4.2.3.3	Fatigue Strength.....	145
4.2.3.4	Residual Stress	147
5	Welding and Test Results	148
5.1	As-welded examination.....	148
5.1.1	Photography/ Stereo Microscopy.....	148
5.1.2	Optical and Contact Profilometry	149
5.1.3	Optical Microscopy	151
5.1.3.1	Weld Cross-sections.....	151
5.1.3.2	Grain Size	157
5.2	Testing and Analysis	159
5.2.1	Hardness	159
5.2.1.1	Comparison Values	159
5.2.1.2	Welded specimen test results.....	160
5.2.2	Tensile Testing	163
5.2.2.1	Test Results	163
5.2.2.2	Optical microscopy and SEM of fracture surfaces	165
5.2.3	Fatigue	168
5.2.3.1	Test Results	168
5.2.3.2	Optical microscopy and SEM of fracture surfaces	169
5.2.4	Residual Stress	170
5.2.4.1	Residual stress variance with depth	171
5.2.4.1.1	<i>Validation of residual stress results.....</i>	<i>172</i>
5.2.4.1.2	<i>Poor residual stress results.....</i>	<i>175</i>
5.2.4.2	Comparison of configurations.....	176
5.2.4.3	Residual stress distribution across weld	179
5.2.4.4	Residual stress as a % of yield strength	182
6	Discussion	184
6.1	Introduction	184

6.2	AA8090-AA8090.....	184
6.2.1	As-Welded Examination.....	184
6.2.1.1	Welded Sheets	184
6.2.1.2	Weld Surface	187
6.2.1.3	Weld Macro- and Micro-structures	194
6.2.1.3.1	<i>Nugget</i>	196
6.2.1.3.2	<i>TMAZ</i>	203
6.2.1.3.3	<i>HAZ</i>	207
6.2.2	Testing.....	210
6.2.2.1	Hardness	210
6.2.2.2	Tensile Testing.....	214
6.2.2.3	Fatigue Testing	229
6.2.2.4	Residual stress.....	239
6.2.2.4.1	<i>Residual Stress with Hole Depth</i>	239
6.2.2.4.2	<i>Residual Stress Across Weld</i>	242
6.2.3	Summary/ Conclusions for this Configuration.....	244
6.3	BS L165-BS L165	245
6.3.1	As-Welded Examination.....	245
6.3.1.1	Welded Sheets	245
6.3.1.2	Weld Surface	248
6.3.1.3	Weld Macro- and Micro-structures	255
6.3.1.3.1	<i>Nugget</i>	258
6.3.1.3.2	<i>TMAZ</i>	264
6.3.1.3.3	<i>HAZ</i>	268
6.3.1.3.4	<i>Alclad Mixing</i>	272
6.3.2	Testing.....	274
6.3.2.1	Hardness	274
6.3.2.2	Tensile Testing.....	277
6.3.2.3	Fatigue Testing	290
6.3.2.4	Residual Stress (RS)	302
6.3.2.4.1	<i>Residual Stress with Hole Depth</i>	302
6.3.2.4.2	<i>Residual Stress Across Weld</i>	304
6.3.3	Summary/ Conclusions for this Configuration.....	306
6.4	AA8090-BS L165	307
6.4.1	As-Welded Examination.....	307
6.4.1.1	Welded Sheets	307
6.4.1.2	Weld Surface	309

6.4.1.3	Weld Macro- and Micro-structures	316
6.4.1.3.1	<i>Nugget</i>	321
6.4.1.3.2	<i>TMAZ</i>	328
6.4.1.3.3	<i>HAZ</i>	332
6.4.2	Testing.....	337
6.4.2.1	Hardness	337
6.4.2.2	Tensile Testing.....	340
6.4.2.3	Fatigue Testing	358
6.4.2.4	Residual Stress	371
6.4.2.4.1	<i>Residual Stress with Hole Depth</i>	371
6.4.2.4.2	<i>Residual Stress Across Weld</i>	374
6.4.3	Summary/ Conclusions for this Configuration.....	377
6.5	BS L165-AA8090.....	378
6.5.1	As-Welded Examination.....	378
6.5.1.1	Welded Sheets	378
6.5.1.2	Weld Surface	378
6.5.1.2.1	<i>BS L165-AA8090 // welds</i>	378
6.5.1.2.2	<i>BS L165-AA8090 ⊥ welds</i>	381
6.5.1.3	Weld Macro- and Micro-structures	384
6.5.1.3.1	<i>Nugget</i>	386
6.5.1.3.2	<i>TMAZ</i>	396
6.5.1.3.3	<i>HAZ</i>	400
6.5.1.3.4	<i>Weld Surface Region</i>	407
6.5.2	Testing.....	412
6.5.2.1	Hardness	412
6.5.2.2	Tensile Testing.....	415
6.5.2.3	Fatigue Testing	435
6.5.2.4	Residual Stress	452
6.5.2.4.1	<i>Residual Stress with Hole Depth</i>	452
6.5.2.4.2	<i>Residual Stress Across Weld</i>	454
6.5.3	Summary/ Conclusions for this Configuration.....	457
6.6	Comparison of Weld Configurations	458
6.7	Property Relationships.....	463
6.7.1	Relationship Between Hardness and Tensile Strength.....	464
6.7.2	Regression Analysis.....	467
7	Conclusions and Further Work.....	476

7.1	Main Conclusions from Analysis.....	476
7.2	Further Work	478
8	References	481

List of Tables

Table 1: Showing temper designations of wrought aluminium alloy products. Modified from Benedyk (2010) and Kaufman (2000).....	11
Table 2: Showing elemental composition of AA8090 as per 1) EM 101 (Agusta Westland International Ltd, 2010) and 2) ASM Handbook Volume 2 (ASM International Handbook Committee, 1990). When only one value is given rather than a range, this constitutes a maximum value.	16
Table 3: Showing table of AA8090-T81 mechanical properties as per EM101 (Agusta Westland International Ltd, 2010), Certificate of Conformity (Dolgarrog Aluminium Limited, 2005) and ASM Handbook Volume 2 (ASM International Handbook Committee, 1990).	21
Table 4: Showing the elemental composition of 1) BS L165 as per BS L165 (The British Standards Institution, 1978a), and 2) AA2014 as per ASTM B209 (ASTM International, 2014). When only one value is given rather than a range, this constitutes a maximum value.	23
Table 5: Showing table of BS L165 and alclad AA2014-T6 mechanical properties as per material specification ^{1,2} and Certificate of Conformity ³ (BS L165).....	27
Table 6: Showing comparison of clad and unclad materials and the effect on mechanical properties. The table shows the mechanical properties for the thickness relevant to this research, i.e. 0.7 mm.	27
Table 7: Showing elemental compositions of AA2024 and AA2198 (Robe et al., 2015), all compositions in wt%.	42
Table 8: Characteristics and effects of different shoulder geometries on FSW. Reproduced from Verma et al. (2016).....	65
Table 9: Characteristics and effects of different pin geometries on FSW process. Reproduced from Verma et al. (2016).	66
Table 10: Showing a selection of the available literature regarding tool choice, process parameters and mechanical properties relevant to the current research.....	77
Table 11: Summary of flaws/ defects characteristic of FSW; contributions from Threadgill et al. (2009), The Welding Institute (2013) and Mishra et al. (2014).	83
Table 12: Showing wavelengths used for ICP-OES analysis.....	91

Table 13: Showing weld configurations, orientations and designations. refers to parallel orientation, ⊥ refers to perpendicular orientation.	95
Table 14: Showing weld parameters common to all material configurations.	97
Table 15: Showing process parameters which vary with material configuration.	98
Table 16: Showing fractional length of welds available for residual stress testing. ...	109
Table 17: Showing drilling parameters and materials properties used in residual stress hole-drilling.	112
Table 18: Showing ICP-OES results for AA8090.	119
Table 19: Showing measured grain sizes of AA8090-T81 material.	123
Table 20: Showing summary of AA8090 measured mechanical properties with specified minimum values where appropriate.	125
Table 21: Showing AA8090 fatigue test specimen data set.	130
Table 22: Showing analysis of data set for AA8090 fatigue testing.	130
Table 23: Showing summary of AA8090 fatigue testing results.	131
Table 24: Showing ICP-OES results for BS L165.	133
Table 25: Showing SEM-EDX results for BS L165.	134
Table 26: Showing measured grain sizes of BS L165.	139
Table 27: Showing summary of BS L165 measured mechanical properties with specified values where appropriate.	140
Table 28: Showing calculated average grain sizes for each section of welds.	158
Table 29: Showing tensile test results.	164
Table 30: Showing locations of tensile fractures on welded test specimens.	166
Table 31: Showing fatigue test analysis results.	169
Table 32: Showing results of fatigue test specimen examinations.	170
Table 33: Showing σ_{\max} as a percentage of yield strength.	182
Table 34: Showing AA8090 parent material and weld nugget grain size dimensions, showing Relative Accuracy (%RA) in brackets.	198
Table 35: Showing AA8090 parent material and weld HAZ grain size dimensions, showing Relative Accuracy (%RA) in brackets.	209
Table 36: Showing AA8090 tensile test results.	215
Table 37: Showing BS L165 parent material and weld nugget grain size dimensions, showing Relative Accuracy (%RA) in brackets.	260

Table 38: Showing BS L165 parent material and weld HAZ grain size dimensions, showing Relative Accuracy (%RA) in brackets.	272
Table 39: Showing BS L165 tensile test results.	278
Table 40: Showing AA8090-BS L165 weld nugget grain size dimensions with similar weld grain sizes for comparison, showing Relative Accuracy (%RA) in brackets.	323
Table 41: Showing AA8090-BS L165 weld HAZ grain size dimensions with parent material and similar weld grain sizes for comparison, showing Relative Accuracy (%RA) in brackets.	335
Table 42: Showing AA8090-BS L165 tensile test results with parent material and similar welds shown for comparison.	342
Table 43: Showing nugget width dimensions for all configurations.	386
Table 44: Showing BS L165-AA8090 weld nugget grain size dimensions with grain sizes of all other configurations shown for comparison, showing Relative Accuracy (%RA) in brackets.	394
Table 45: Table showing HAZ widths of all weld configurations.	401
Table 46: Showing BS L165-AA8090 weld HAZ grain size dimensions with parent material and grain sizes of all other configurations shown for comparison, showing Relative Accuracy (%RA) in brackets.	405
Table 47: Showing BS L165-AA8090 tensile test results with parent material with all other configurations shown for comparison.	418
Table 48: Showing summary of most salient features of welds, as discussed previously in Chapter 6.	458
Table 49: Showing results of residual stress regression analysis based on hardness and grain size.	471

List of Figures

Figure 1: Showing a Merlin Mk4 helicopter landing on HMS Queen Elizabeth with RFA Tideforce in support. Photo credit LPhot Kyle Heller, reproduced under the Open Government Licence (Heller, 2019).	7
Figure 2: Showing the effects on strength of time and temperature of typical precipitation hardening alloys, courtesy of Higgins (1993).	10
Figure 3: Showing an illustration of the basic steps during recovery, static recrystallisation and grain growth. From Raabe (2014).	12
Figure 4: Showing a typical age hardening curve (at 190 °C) for AA8090, courtesy of Prasad (1999), with additional labelling.	17
Figure 5: Showing microstructures of AA8090 sheet: (a) Recrystallised grain structure; (b) Unrecrystallised grain structure. From ASM Handbook Volume 2 (ASM International Handbook Committee, 1990).	19
Figure 6: Showing Saleh’s (2018) work depicting hardness with respect to aging time at 165 °C for AA2014 alloy.	24
Figure 7: Showing the microstructural changes due to solution and precipitation heat treatments of an Al-Cu alloy, courtesy of Higgins (1993).	25
Figure 8: Showing diagram of the FSW process: 1) plunge of the tool to the material; 2) dwell at the insertion point to generate heat in the material; 3) traverse of the tool along the workpiece; 4) retraction of the tool from the material.	30
Figure 9: Showing diagram of typical aluminium alloy FSW microstructural areas.	31
Figure 10: Showing FSW of an Al-Si casting. This image has been reproduced from Bhadeshia (no_date) who identifies Professor J. Fukii of JWRI Japan as the source (no reference provided).	32
Figure 11: Showing diagram of typical aluminium alloy SSFSW microstructural areas. Labels A, B, C and D have the same meanings as per Figure 9. The nugget depicted by the orange dashed line described the “spherical/ basin/ drum” shape, while the nugget depicted by the green dashed line describes the conical “V” shape.	34
Figure 12: Showing (a) SSFSW AA7075-T651; microstructure shape broadly follows that of the pin, courtesy of Patel et al. (2019), and (b) SSFSW AA7075-T651; microstructure is described as “drum” shaped, courtesy of Li et al. (2015).	35

Figure 13: Showing double S-shape on AA2198-AA2024 dissimilar weld, reproduced from Khalilabad et al. (2021): a) whole joint; b) retreating side transition between parent metal and nugget; c) 1st S-shape transition in nugget; d) 2nd S-shape transition in nugget; e) advancing side transition between nugget and parent material.	44
Figure 14: Showing the various zones of AA6061-AA2014 weld, produced from Ventakeswara Rao and Senthil Kumar (2020).	46
Figure 15: Showing schematic representation of material movement based on the roles of the shoulder (a and b) and the pin (c and d). Reproduced from Mishra et al. (2014).	53
Figure 16: Showing the forces around the (a) pin, and (b) shoulder during FSW. Reproduced from Mishra et al. (2014).....	55
Figure 17: Showing schematic of the microstructural evolution in different zones of FSW material. Note BM = base material and is equivalent to parent material. Reproduced from Mishra et al. (2014).....	58
Figure 18: Showing some features of FSW tool shoulders and pins. Reproduced from Mishra et al. (2014).	64
Figure 19: Showing plots of generic hardness profiles for non-heat treatable (top images) and heat treatable (bottom images) aluminium alloys in various temps. Reproduced from Threadgill et al. (2009).....	68
Figure 20: Showing distribution and shape of residual stresses across the width of a FSW. Reproduced from Mishra et al. (2014).	76
Figure 21: Showing conceptual design of a “portable” FSW machine, designed by Rohith Renish et al. (2018).....	86
Figure 22: Showing CTC’s portable FSW equipment in situ, reproduced from Concurrent Technologies Corporation (2021a).	87
Figure 23: Showing material orientation definitions.	89
Figure 24: Showing ABB IRB 7600-400 robot onsite at TWI, Rotherham.	93
Figure 25: Showing SSFSW tool: (a) assembled tool; (b) stationary shoulder; (c) pin; (d) diagram detailing shoulder and pin dimensions (not to scale).	94
Figure 26: Showing clamping arrangements for FSW workpieces, photographed during a parameter trial.....	96
Figure 27: Showing hardness specimen of an AA8090-BS L165 weld: (a) overview image; (b) individual indent.	101

Figure 28: Showing a tensile test sample. The example shown is manufactured from BS L165 only, with no weld. The approximate position of the weld line on other samples is indicated by the dotted line.	102
Figure 29: Showing fatigue test specimen design. The weld line is at the mid-way point indicated by the line.	104
Figure 30: Showing positioning of RS holes on welded specimen.....	110
Figure 31: Showing micrographs of AA8090-T81 material: (a) longitudinal face; (b) transverse face; (c) short-transverse face.	122
Figure 32: Showing extruded AA8090-T851 microstructure, courtesy of Srivatsan and Place (1989).	123
Figure 33: SEM images showing an AA8090-T81 parent material tensile test specimen fracture surface which was tested in the longitudinal direction. Both (a) and (b) are from the same tensile test specimen and are representative of all fracture surfaces tested in this orientation.....	127
Figure 34: SEM images showing an AA8090-T81 parent material tensile specimen fracture surface which was tested in the transverse direction. Both (a) and (b) are from the same tensile test specimen and are representative of all fracture surfaces tested in this orientation.....	128
Figure 35: SEM images showing an AA8090-T81 parent material fatigue specimen fracture surface. Both (a) and (b) are from the same fatigue test specimen and are representative of all fracture surfaces.....	132
Figure 36: Showing micrographs of BS L165 material: (a) longitudinal face; (b) transverse face; (c) short-transverse face.	138
Figure 37: Showing AA2014-T4 microstructure, courtesy of Babu et al. (2013).	138
Figure 38: SEM images showing an BS L165 parent material tensile test specimen fracture surface which was tested in the longitudinal direction. Both (a) and (b) are from the same tensile test specimen and are representative of all fracture surfaces tested in this orientation.....	143
Figure 39: SEM images showing an BS L165 parent material tensile test specimen fracture surface which was tested in the transverse direction. Both (a) and (b) are from the same tensile test specimen and are representative of all fracture surfaces tested in this orientation.....	144

Figure 40: SEM images showing BS L165 parent material fatigue specimen fracture surface. Both (a) and (b) are from the same fatigue test specimen and are representative of all fracture surfaces.	146
Figure 41: Showing macro image of upper surface of as-welded BS L165 \perp	148
Figure 42: Showing (a) output generated using an optical profilometer, and (b) contact profilometry plot of upper surface of as-welded AA8090 \perp joint.	150
Figure 43: Showing (a) output generated using an optical profilometer, and (b) contact profilometry plot of upper surface of as-welded AA8090-BS L165 \perp joint.....	151
Figure 44: Macrograph showing BS L165 \perp etched weld cross section.	154
Figure 45: Macrograph showing an AA8090-BS L165 \perp etch weld cross section....	154
Figure 46: Showing material mixing on dissimilar AA8090-BS L165 \parallel weld.	155
Figure 47: Showing advancing side HAZ, TMAZ and nugget of BS L165-AA8090 \perp weld. The dashed lines show the approximate boundary between the different zones.	155
Figure 48: Showing alclad layer within weld of a BS L165 \parallel weld.....	156
Figure 49: Showing joint line remnant on an AA8090-BS L165 \parallel dissimilar weld..	156
Figure 50: Showing the grain size at different areas of the weld for all configurations.	159
Figure 51: Showing the designated material face orientations relevant to the hardness assessment.	160
Figure 52: Graph showing hardness test results of all welded specimens and parent materials. Note: y-axis has been limited to starting at 90 HV1 for clarity.....	161
Figure 53: Showing AA8090 similar weld hardness results, with parent material values for comparison.....	161
Figure 54: Showing BS L165 similar weld hardness results, with parent material values for comparison.....	162
Figure 55: Showing dissimilar weld hardness results.	162
Figure 56: Showing mid-weld fracture of AA8090 \perp : (a) etched cross-section showing position of fracture falls on the joint line; (b) SEM image showing “stir” markings, remnants of the SSFSW process and indicating inadequate joining of the materials..	167
Figure 57: Plot of maximum principal stress against hole depth for BS L165 \perp at the five strain gauge positions.	171
Figure 58: Showing comparison of data from various tests conducted on the AA8090 \perp parent material.....	173

Figure 59: Showing comparison of 2 tests carried out on AA8090 \perp retreating side edge of weld.....	174
Figure 60: Showing comparison of 2 tests carried out on AA8090-BS L165 II in weld.	174
Figure 61: Showing results from AA8090 \perp . Note: the retreating side parent material was a failed test and has thus not been included.....	175
Figure 62: Showing comparisons of the 8 configurations at (a) the parent material advancing side, (b) edge of weld retreating side, and (c) in weld.	177
Figure 63: Showing weld profile at different hole depths across weld line for BS L165 \perp	181
Figure 64: Showing weld profile at different hole depths across weld line for AA8090 II.	181
Figure 65: Showing as-welded AA8090 sheets: a) AA8090 longitudinal distortion; b) AA8090 II transverse angular distortion; c) AA8090 \perp sheet lifting ahead of tool. .	186
Figure 66: Showing weld top surface of with profile of SSFSW tool superimposed, a) AA8090 II weld, and b) AA8090 \perp weld.	189
Figure 67: Showing AA8090 II weld surface topography, a) optical profilometer 3D model image, and b) contact profilometry surface plot.....	191
Figure 68: Showing AA8090 \perp weld surface topography, a) optical profilometer 3D model image, and b) contact profilometry surface plot.....	192
Figure 69: Showing macrographs of weld cross-sections: a) AA8090 II (advancing side on left); and b) AA8090 \perp (advancing side on right).	195
Figure 70: Showing micrographs of the advancing side of the nugget: a) AA8090 II; b) AA8090 \perp	199
Figure 71: Showing microstructure of FSW AA8090 (temper unknown), courtesy of Vigraman et al. (2021).....	201
Figure 72: SEM images of weld taken at weld root, a) AA8090 II and b) AA8090 \perp ;and mid-thickness, c) AA8090 II and d) AA8090 \perp	202
Figure 73: Showing micrographs of the TMAZ: a) AA8090 II advancing side and b) retreating side; c) AA8090 \perp advancing side and d) retreating side.	206
Figure 74: Showing microstructure of advancing HAZ of AA8090, a) II and b) \perp	208
Figure 75: Showing hardness and grain size plots of a) AA8090-AA8090 II, and b) AA8090-AA8090 \perp	211

Figure 76: Showing advancing edge of tensile fracture of AA8090 II weld; (a) micrograph showing fracture from top surface, (b) cross-section of weld showing crack path, and (c) and (d) SEM image showing details of mid-thickness fracture surface. .218

Figure 77: Showing mid-weld tensile fracture of AA8090 II weld; (a) micrograph showing fracture from top surface, (b) cross-section of weld showing crack path, and (c) and (d) SEM image showing details of fracture surface.221

Figure 78: Showing advancing edge of weld tensile fracture on AA8090 \perp weld; (a) micrograph showing fracture from top surface, (b) cross-section of weld showing crack path, and (c) and (d) SEM image showing details of fracture surface.....225

Figure 79: Showing mid-weld tensile fracture of AA8090 \perp weld; (a) micrograph showing fracture from top surface, (b) cross-section of weld showing crack path, (c) micrograph showing transition in fracture surfaces and (d) SEM image showing details of fracture surface.....228

Figure 80: Showing mid-weld fatigue fracture of AA8090 weld; (a) micrograph showing fracture from top surface, (b) micrograph of fracture surface, (c) cross-section of weld showing crack path, (d) and (e) SEM images showing details of fracture surface.233

Figure 81: Showing AA8090 II fatigue fracture occurring within the weld close to the advancing edge; (a) micrograph showing fracture from top surface, (c) cross-section of weld showing crack path, (c) and (d) SEM images showing details of fracture surface.....235

Figure 82: Showing AA8090 II fatigue fracture along the advancing edge; (a) micrograph showing fracture from top surface, (c) cross-section of weld showing crack path, (c) and (d) SEM images showing details of fracture surface.238

Figure 83: Showing residual stress results plotted against drilled hole depth; (a) AA8090 II, and (b) AA8090 \perp240

Figure 84: Showing residual stress across weld at varying hole depths: (a) AA8090 II and (b) AA8090 \perp243

Figure 85: Showing longitudinal distortion on two BS L165 II welds: (a) convex and (b) sinusoidal curving, and (c) angular distortion on a \perp weld.246

Figure 86: Showing warping and distortion to mid-point of BS L165 weld during parameter trials.....247

Figure 87: Showing L165 II weld surface with superimposed tool profile.....249

Figure 88: Images for comparison of differing quantities of additional material at side of weld along length of BS L165 II weld. Note, these images are taken from the same weld.	250
Figure 89: Showing BS L165 II weld surface topography, (a) optical profilometer 3D model image, and (b) contact profilometry surface plot.	251
Figure 90: Showing BS L165 (⊥) weld surface. Both are from the same weld, with (b) taken from slightly further along (approx. 100 mm) from (a).	253
Figure 91: Showing BS L165 ⊥ weld surface topography, (a) optical profilometer 3D model image, and (b) contact profilometry surface plot.	255
Figure 92: Showing macrograph of BS L165 weld cross-section; (a) II and (b) ⊥. The green dashed line indicates the extent of the SAZ, while the purple dashed box indicates the presence of the residual join line/ kissing bond. The HAZ extends beyond the limits of these images.	257
Figure 93: Showing Al-Cu phase diagram, courtesy of Liao (2006).	259
Figure 94: Showing micrographs of the advancing side of the nugget: a) BS L165 II; b) BS L165 ⊥.	261
Figure 95: Showing FSW AA2014-T6 nugget, courtesy of Rajendran et al. (2019)..	263
Figure 96: Showing alclad layer being drawn into the lazy S on a II weld.	264
Figure 97: Showing micrographs of the TMAZ: a) BS L165 II advancing side and b) retreating side; c) BS L165 ⊥ advancing side and d) retreating side.	267
Figure 98: Showing alclad layer being drawn into the weld at the nugget/ advancing side TMAZ interface of a ⊥ weld.....	268
Figure 99: Showing microstructure of advancing HAZ of BS L165, a) II and b) ⊥. ...	271
Figure 100: Showing the alclad layer response on the top surface within the nugget at (a) biased to the advancing side, (b) mid-weld, and (c) biased to the retreating side. All images are from II weld.....	274
Figure 101: Showing hardness and grain size plots of a) BS L165 II, and b) BS L165 ⊥. ...	276
Figure 102: Showing mid-weld tensile fracture of BS L165 II weld with a rough and ragged crack path; (a) micrograph showing fracture from top surface, (b) macrograph of fracture surface (c) cross-section of weld showing crack path, and (d) SEM image showing details of fracture surface.....	281

Figure 103: Showing mid-weld tensile fracture of BS L165 II weld with a smooth crack path; (a) micrograph showing fracture from top surface, (b) cross-section of weld showing crack path, and (c) SEM image showing details of fracture surface.	283
Figure 104: Showing retreating edge of weld tensile fracture of BS L165 II weld; (a) micrograph showing fracture from top surface, (b) cross-section of weld showing crack path, and (c) SEM image showing details of fracture surface.	285
Figure 105: Showing differing fracture paths of BS L165 \perp tensile tests; (a) ragged and (b) smooth.	287
Figure 106: Showing etched cross-sections of BS L165 \perp tensile specimens; (a) with a kissing bond shape, and (b) almost diagonally straight failure.	288
Figure 107: Showing SEM images of BS L165 \perp tensile specimens; (a) a fracture surface from a specimen with a kissing bond, and (b) a fracture surface from a specimen with no indication of a kissing bond.....	289
Figure 108: Showing an in-weld fatigue fracture biased towards the retreating side of a BS L165 weld; (a) micrograph showing fracture from top surface, (b) cross-section of weld showing crack path, (c) and (d) SEM images showing details of fracture surface.....	293
Figure 109: Showing an in-weld fatigue fracture biased to the advancing side of a BS L165 weld; (a) micrograph showing fracture from top surface, (b) cross-section of weld showing crack path, (c), (d) and (e) SEM images showing details of fracture surface.	296
Figure 110: Showing advancing EoW fatigue fracture of BS L165 weld; (a) micrograph showing fracture from top surface, (b) cross-section of weld showing crack path, (c) and (d) SEM images showing details of fracture surface.....	299
Figure 111: Showing retreating EoW fatigue fracture of BS L165 weld; (a) micrograph showing fracture from top surface, (b) cross-section of weld showing crack path.	301
Figure 112: Showing residual stress results plotted against drilled hole depth; (a) BS L165 II, and (b) BS L165 \perp	303
Figure 113: Showing residual stress across weld at varying hole depths: (a) BS L165 II and (b) BS L165 \perp	305
Figure 114: Showing longitudinal distortion on AA8090-BS L165 welds: (a) sinusoidal and (b) convex curving on II and \perp welds respectively, and (c) angular distortion on a \perp weld.	308

Figure 115: Showing AA8090-BS L165 II weld surface with superimposed tool profile: (a) shows area representative of the average weld, (b) shows how the surface appearance can change.	312
Figure 116: Showing AA8090-BS L165 II weld surface topography, (a) optical profilometer 3D model image, and (b) contact profilometry surface plot.....	313
Figure 117: Showing AA8090-BS L165 \perp weld surface with superimposed tool profile: (a) shows area representative of the average weld, (b) shows how the surface appearance can change.	315
Figure 118: Showing AA8090-BS L165 \perp weld surface topography, (a) optical profilometer 3D model image, and (b) contact profilometry surface plot.....	316
Figure 119: Showing macrograph of AA8090-BS L165 weld cross-section; (a) II and (b) \perp . The areas indicated by the blue boxes in (a) are shown in greater detail in Figure 120.	319
Figure 120: Showing cracks/ voids within the II weld nugget: (a) sub-surface; and (b) both sub-surface and surface breaking.	320
Figure 121: Showing micrographs of the II weld nugget: (a) advancing side AA8090 material and (b) retreating side BS L165 material.	325
Figure 122: Showing micrographs of the \perp weld nugget: (a) advancing side AA8090 material and (b) retreating side BS L165 material.	326
Figure 123: Showing alclad layer being drawn into the weld and kissing bond on a AA8090-BS L165 \perp weld.....	328
Figure 124: Showing micrographs of the TMAZ: a) AA8090-BS L165 II advancing side and b) retreating side; c) AA8090-BS L165 \perp advancing side and d) retreating side. ...	331
Figure 125: Showing micrographs of the HAZ: a) AA8090-BS L165 II advancing side and b) retreating side; c) AA8090-BS L165 \perp advancing side and d) retreating side	334
Figure 126: Showing hardness and grain size plots of a) AA8090-BS L165 II, and b) AA8090-BS L165 \perp	339
Figure 127: Showing tensile fracture of AA8090-BS L165 II weld occurring at the advancing side EoW; (a) macrograph showing fracture from top surface, (b) cross-section of weld showing crack path, (c) and (d) SEM image showing detail of fracture surface.	347

Figure 128: Showing tensile fracture of AA8090-BS L165 II weld occurring mid-weld; (a) macrograph showing fracture from top surface, (b) cross-section of weld showing crack path, (c), (d) and (e) SEM image showing detail of fracture surface.....351

Figure 129: Showing tensile fracture of AA8090-BS L165 \perp weld occurring mid-weld; (a) macrograph showing fracture from top surface, (b) cross-section of weld showing crack path, (c) low magnification SEM image showing fracture surface full-thickness, (d) SEM image showing predominantly AA8090 fracture surface (e) SEM image showing predominantly BS L165 fracture surface.355

Figure 130: Showing tensile fracture of AA8090-BS L165 \perp weld occurring at the advancing EoW; (a) macrograph showing fracture from top surface, (b) cross-section of weld showing crack path, (c) SEM image showing fracture surface detail.357

Figure 131: Showing fatigue fracture of AA8090-BS L165 II weld occurring close to the advancing edge of the weld; (a) macrograph showing fracture from top surface, (b) image showing fracture surface corresponding to ragged length of fracture, (c) image showing fracture surface corresponding to straight length of fracture, (d) cross-section of weld showing crack path, (e) SEM image showing detail of fracture surface.....363

Figure 132: Showing fatigue fracture of AA8090-BS L165 II weld occurring mid-weld; (a) macrograph showing fracture from top surface, (b) cross-section of weld showing crack path, (c) low magnification SEM image fracture surface full thickness, (d) and (e) SEM image showing detail of fracture surface.367

Figure 133: Showing fatigue fracture of AA8090-BS L165 II weld occurring close to the retreating edge of the weld; (a) macrograph showing fracture from top surface, (b) stereo microscope image showing fracture surface, (c), (d) and (e) cross-sections of weld showing crack path, (f) SEM image showing detail of fracture surface.371

Figure 134: Showing residual stress results plotted against drilled hole depth; (a) AA8090-BS L165 II, and (b) AA8090-BS L165 \perp373

Figure 135: Showing residual stress across weld at varying hole depths: (a) AA8090-BS L165 II and (b) AA8090-BS L165 \perp376

Figure 136: Showing BS L165-AA8090 II weld with superimposed tool profile.....380

Figure 137: Showing relatively large deposit of material on the advancing side edge of BS L165-AA8090 II weld.380

Figure 138: Showing BS L165-AA8090 II weld surface topography: (a) optical profilometry image, and (b) contact profilometry surface plot.381

Figure 139: Showing BS L165-AA8090 \perp weld with superimposed tool profile.....	382
Figure 140: Showing BS L165-AA8090 \perp weld surface topography: (a) optical profilometry image, and (b) contact profilometry surface plot.	383
Figure 141: Showing macrograph of BS L165-AA8090 weld cross-section; (a) II and (b) \perp . The areas indicated by the blue boxes in (a) highlight oxide chains and are discussed in section 6.5.1.3.1, as is the area indicated by the green box in (b) which highlights a large inclusion. The areas indicated by the purple boxes in (a) and (b) highlight the surface transition from the smooth ironed area to the rough and rippled area, and are discussed in section 6.5.1.3.4.	385
Figure 142: Showing micrographs of the II weld nugget: (a) advancing side BS L165 material and (b) retreating side AA8090 material.	388
Figure 143: Showing micrographs of the \perp weld nugget: (a) advancing side BS L165 material and (b) retreating side AA8090 material.	389
Figure 144: Showing areas highlighted by blue boxes in Figure 141(a).....	391
Figure 145: Showing oxide chains within BS L165 area of \perp weld nugget.	392
Figure 146: Showing large oxide inclusion in centre of weld, highlighted by green box in Figure 141(b), and oxide chains emanating from the joint line.....	392
Figure 147: Showing micrographs of the BS L165-AA8090 II TMAZ: (a) advancing side, and (b) retreating side.....	398
Figure 148: Showing micrographs of the BS L165-AA8090 \perp TMAZ: (a) advancing side, and (b) retreating side.....	399
Figure 149: Showing micrographs of the BS L165-AA8090 II HAZ: (a) advancing side, and (b) retreating side.....	402
Figure 150: Showing micrographs of the BS L165-AA8090 \perp HAZ: (a) advancing side, and (b) retreating side.....	403
Figure 151: Showing weld surface region on advancing side of the weld: (a) alclad mixing into weld at rippled area of the nugget (II weld); (b) alclad mixing with AA8090 along top surface of weld, and mixing with BS L165 sub-surface, showing oxide chains (II weld); (c) deposited alclad material adjacent to weld as previously shown in Figure 136 (\perp weld).	409
Figure 152: Showing the weld surface region within advancing and retreating side of nugget: (a) showing sharp step between rough, uneven, rippled area and ironed area of	

the weld top surface (\perp weld); (b) showing alclad mixing with AA8090 (II weld); (c) showing alclad mixing with AA8090 and sub-surface voids (\perp weld).	411
Figure 153: Showing hardness and grain size plots of a) BS L165-AA8090 II, and b) BS L165-AA8090 \perp	414
Figure 154: Showing tensile fracture of BS L165-AA8090 II weld which failed mid-weld with a ragged appearance: (a) macrograph showing fracture from top surface; (b) macrograph showing part of fracture surface; (c) cross-section of weld showing crack path; (d), (e), (f) and (g) SEM images showing detail of fracture surface.....	423
Figure 155: Showing tensile fracture of BS L165-AA8090 II weld which failed mid-weld with a straight appearance: (a) macrograph showing fracture from top surface; (b) stereo micrograph showing part of fracture surface; (c) cross-section of weld showing crack path; (d) and (e) SEM images showing detail of fracture surface.	426
Figure 156: Showing tensile fracture of BS L165-AA8090 II weld which failed at the retreating edge of weld: (a) macrograph showing fracture from top surface; (b) and (c) cross-sections of weld showing crack path; (d) and (e) SEM images showing detail of fracture surface.....	429
Figure 157: Showing tensile fracture of BS L165-AA8090 \perp weld which failed mid-weld: (a) macrograph showing fracture from top surface; (b) cross-section of weld showing crack path; (c), (d) and (e) SEM images showing detail of fracture surface.....	432
Figure 158: Showing tensile fracture of BS L165-AA8090 \perp weld which failed at the retreating side edge of weld: (a) macrograph showing fracture from top surface; (b) cross-section of weld showing crack path; (c) and (d) SEM images showing detail of fracture surface.....	434
Figure 159: Showing fatigue fracture of BS L165-AA8090 II weld which failed in-weld but biased towards the advancing side: (a) macrograph showing fracture from top surface; (b) cross-section of weld showing crack path; (c) and (d) SEM images showing detail of fracture surface.....	438
Figure 160: Showing fatigue fracture of BS L165-AA8090 II weld which failed mid-weld: (a) macrograph showing fracture from top surface; (b) cross-section of weld showing crack path; (c), (d), (e) and (f) SEM images showing detail of fracture surface.	442
Figure 161: Showing fatigue fracture of BS L165-AA8090 II weld which failed partially mid-weld and partially in-weld but biased towards the advancing edge: (a) macrograph showing fracture from top surface; (b) macrograph showing another multi-site failure;	

(c) and (d) cross-section of weld showing crack path at mid-weld position; (e) and (f) cross-section of weld showing crack path at in-weld towards advancing edge position; (g), (h) and (i) SEM images showing detail of fracture surface at mid-weld position; (j), (k), (l), (m) and (n) SEM images showing detail of fracture surface at advancing edge position.	451
Figure 162: Showing residual stress results plotted against drilled hole depth; (a) BS L165-AA8090 II, and (b) BS L165-AA8090 \perp	453
Figure 163: Showing residual stress across weld at varying hole depths: (a) BS L165-AA8090 II and (b) BS L165-AA8090 \perp	456
Figure 164: Showing relationship between hardness and UTS for AA8090 and BS L165 and their SSFSW configurations.....	466
Figure 165: Showing MS Excel summary output of AA8090 II regression analysis. As a MS Excel summary output each term is not defined here, rather those terms deemed most important are highlighted.....	469
Figure 166: Showing plots of measured vs. predicted RS for each configuration: (a) AA8090 II; (b) AA8090 \perp ; (c) BS L165 II; (d) BS L165 \perp ; (e) AA8090-BS L165 II; (f) AA8090-BS L165 \perp ; (g) BS L165-AA8090 II; (h) BS L165-AA8090 \perp	474

Nomenclature

Symbol or Abbreviation	Definition
A	Variable used in staircase method for fatigue analysis
$\hat{A}(H, h_i)$	Generalisation of the uniform stress calibration constants \hat{a}
\bar{a}_{ij}	The strain relaxation due to a unit P stress within increment j of a hole i-increments deep
ANOVO	Analysis of Variance
ARTIMS	Aircraft Repair Task Information Management Systems
ASD-STAN	Aerospace and Defence Industries Association of Europe Standardisation
ASM	American Society for Materials
ASTM	American Society for Testing and Materials
AW	Agusta Westland
B	Variable used in staircase method for fatigue analysis
BM	Base material
BS	British Standards
C	Variable used in staircase method for fatigue analysis
CHF	Commando Helicopter Force
CofC	Certificate of Conformity
CTC	Concurrent Technologies Corporation
d	Average diameter of grain (Hall-Petch)
d	Stress increment used in staircase method for fatigue analysis
D	Variable used in staircase method for fatigue analysis
E	Young's modulus
EBSD	Electron Backscatter Diffraction
EDX	Energy Dispersive X-ray
EoW	Edge of Weld
ERI	Engineering Repair Instructions
FCC	Face Centred Cubic
FCG	Fatigue Crack Growth

Symbol or Abbreviation	Definition
FEA	Finite Element Analysis
f_i	Number of events (staircase method)
FSP	Friction Stir Processing
FSW	Friction Stir Welding
GP	Guinier-Preston
GS ₁ , GS ₂	Grain Size 1, Grain Size 2
GTAW	Gas Tungsten Arc Welding
H	Nondimensional hole depth from surface (depth from surface/ strain gauge rosette mean radius)
H	Hardness
h	Nondimensional hole depth (hole depth/ strain gauge rosette mean radius)
HAZ	Heat Affected Zone
ICP-OES	Inductively coupled plasma with optical emission spectroscopy
	Symbol denoting that the material has been welded parallel to its rolling direction
IMC	Intermetallic Compound
k	Material constant relating to the capability of grain size hardening for an alloy (Hall-Petch)
k	One-sided tolerance limit for a normal distribution (staircase method)
L	Longitudinal
/	Number of stress levels (staircase method)
MERI	Materials and Engineering Research Institute
mm/min	millimetres per minute
mm/s	millimetres per second
MoD	Ministry of Defence
MPa	Mega Pascals
MS	Microsoft
MSLP	Merlin Life Sustainment Programme

Symbol or Abbreviation	Definition
N	Newtons
n	Number of partial hole depths achieved during drilling (Integral method)
N/A	Not Applicable
NAS	Naval Air Squadron
NC	Navy Command
NPL	National Physical Laboratory
OEM	Original Equipment Manufacturer
P	Probability of failure (staircase method)
P(H)	Isotropic stress combination that exists at depth H from the measured surface
p(h _i)	Isotropic strain combination which is relieved when the hole reaches a depth h at increment i
PFZ	Precipitate free Zones
p _i	Isotropic combination strain at increment i, corresponding to P _j
P _j	Isotropic combination stress at increment j
PM	Parent Material
Q(H)	45° shear strain combination that exists at depth H from the measured surface
q(h _i)	45° shear strain combination which is relieved when the hole reaches a depth h at increment i
Q', Q	Precipitates in BS L165 (Cu ₂ Mg ₈ Si ₆ Al ₅ , Al ₃ Cu ₂ Mg ₉ Si ₇ or Al ₄ Cu ₂ Mg ₈ Si ₇)
q _i	45° shear combination strain at increment i, corresponding to Q _j
Q _j	45° shear combination stress at increment j
r	Radius of tool pin
R	fatigue load ratio
RA	Relative Accuracy
rad/s	Radians per second
RAF	Royal Air Force

Symbol or Abbreviation	Definition
RN	Royal Navy
RPM	Rotations Per Minute
RS	Residual Stress
RTR	Room Temperature Rolled
S	Percentage scatter of results
s	Standard deviation (staircase method)
S', S''	Strengthening Precipitate in AA8090 and BS L165 (Al ₂ CuMg)
S ₀	Lowest stress value considered valid for the data set (staircase method for fatigue)
SAZ	Shoulder Affected Zone
SEM	Scanning Electron Microscope
SEM-EDX	Scanning Electron Microscope-Energy Dispersive X-ray
SHT	Solution Heat Treated
SHU	Sheffield Hallam University
S-N	Stress-strain
SSFSW	Stationary Shoulder Friction Stir Welding
SSS	Supersaturated solid solution
S-T	Short-Transverse
T	Transverse
T(H)	Axial strain combination that exists at depth H from the measured surface
t(h _i)	Axial strain combination which is relieved when the hole reaches a depth h at increment i
T ₁	Strengthening precipitate in AA8090 (Al ₂ CuLi)
TEM	Transmission Electron Microscope
t _i	Axial shear combination strain at increment i, corresponding to T _j
TIG	Tungsten Inert Gas
T _j	Axial shear combination stress at increment j
TMAO	Transverse Mechanical Arc Oscillation
TMAZ	Thermo-Mechanically Affected Zone

Symbol or Abbreviation	Definition
TWI	The Welding Institute
UK	United Kingdom
UTS	Ultimate Tensile Strength
UTS _{parent material}	Ultimate Tensile Strength of the Parent Material
UTS _{weld}	Ultimate Tensile Strength of the Welded Material
UV/IR	Ultraviolet/ Infrared
VP	Variable Pressure
VVIP	Very, Very Important Person
W/mK	Watts per meter Kelvin
WE	Weld efficiency
WHPS	Westland Helicopter Process Specification
WLI	White Light Interferometry
wt%	Weight percentage
\hat{y}	Estimated lower limit of fatigue strength (staircase method)
β	Principal stress direction – the clockwise angle from gauge 1 axial direction to the σ_{\max} direction
β'' , β' , β	Precipitates in BS L165 (Mg ₅ Al ₂ Si ₄ or Mg _{1.8} Si)
δ	Incoherent precipitate in AA8090 (AlLi)
δ'	Strengthening Precipitate in AA8090 (Al ₃ Li)
$\epsilon_1, \epsilon_2, \epsilon_3$	Measured strains from elements 1, 2 and 3 of the strain gauge
η_s	Coefficient of variation (staircase method)
θ' , θ	Precipitates in BS L165 (Al ₂ Cu)
λ , λ'	Precipitates in BS L165 (Cu ₂ Mg ₈ Si ₆ Al ₅ , Al ₃ Cu ₂ Mg ₉ Si ₇ or Al ₄ Cu ₂ Mg ₈ Si ₇)
ν	Population/ number of degrees of freedom (staircase method)
ν	Poisson ratio
ν	Linear speed
π	Pi (approximately 3.14)
σ_0	Material constant relating to frictional stress or the starting stress for dislocation movement (Hall-Petch)

Symbol or Abbreviation	Definition
σ_{UTS}^{est}	Estimated UTS
σ_{UTS}^{exp}	UTS obtained experimentally
σ_m	Mean fatigue strength
$\sigma_{max}, \sigma_{min}$	Maximum and minimum principle stress
σ_{pt}	The normal force exerted by the tool pin in the direction of travel
σ_{UTS}	UTS of the SSFSW material at the position of hardness minimum in the absence of any flaws
σ_y	Yield Strength
τ_s	Shear force exerted by tool pin
τ_{sh}	Shear force exerted by tool shoulder
ω	Angular velocity
\perp	Symbol denoting that the material has been welded perpendicular to its rolling direction

1 Introduction

1.1 Issue

1710 Naval Air Squadron (NAS) provides specialist scientific and engineering support to the UK Navy Command (NC) Fleet Air Arm and to other establishments (Ministry of Defence, no_datea). The Squadron's remit is to assess and repair damaged helicopters and unmanned air systems, design and fit modifications to enhance the capabilities of UK military aircraft, provide advice and support on the material integrity and health of aircraft and provide specialist support with in-depth investigations following equipment failures and accidents.

Within the scope of "repair to damaged helicopters", 1710 NAS may be required to conduct expedient repair and enduring structural repair of helicopters in an operational theatre, such that they may remain operationally active. Repairs are currently carried out in theatre (once the asset is recovered to the local base) using riveting techniques and structural adhesives. If the asset cannot be repaired in-situ or returned to base safely it may be destroyed at great expense to the Ministry of Defence (MoD) and UK taxpayer.

A repair using patches and riveting adds mass and expense to an aircraft as additional material is required to ensure a structurally sound joint, using sufficient material overlap with potentially numerous rows of rivets. Riveting is a process dependent on the skill of the maintainer through which poorly installed rivets may fail early, or damage to the aircraft caused by the process may lead to fatigue cracking of the structure. Further, the addition of rivet holes to a structure may weaken it. Finally, certain areas of an aircraft do not lend themselves to riveting as a repair technique making it complicated and time consuming to carry out.

With regards to bonded repairs there is a general lack of confidence both in the bond strength and in the method of providing quality assurance through adhesively bonded test samples that are not fully representative of the joint. Repair teams from 1710 NAS have experienced this and have been required to remove and replace the repair,

sometimes many times, before getting acceptable results from the shear test pieces (Hepplewhite, 2013).

This research aims to ascertain whether another cost-effective and reliable method of conducting both expedient and enduring helicopter repairs, which does not add weight to the aircraft and is not reliant on maintainer skill, is possible in operational theatre. While fusion welding is utilised extensively throughout the build and in-depth maintenance of helicopters, it is heavily reliant on the welder's skill, makes use of consumables and is not suitable for use with several commonly used aerospace aluminium alloys. As such, Friction Stir Welding (FSW) has been considered.

1.2 Technique Selection

FSW is a solid-state process which uses mechanical means to “stir” the subject materials together. As the materials never reach their melt temperature the process can be carried out in any orientation as there is no weld pool such as found in fusion welding (Threadgill, Leonard, Shercliff, & Withers, 2009). This process can be used to join materials considered to be difficult to fusion weld successfully e.g. 2000 and 7000 series aluminium alloys and can be used to join dissimilar materials. There are no consumables used and no exhaust system or UV/IR protection is required. Research (Threadgill et al., 2009; Zhang, T., He, Shao, Zhang, & Wu, 2013) indicates superior joint properties for many aluminium alloys over fusion welding and riveting, especially with respect to fatigue.

Stationary Shoulder FSW (SSFSW) uses the same general process of solid-state stirring of materials, however while conventional FSW utilises a tool with a rotating shoulder and pin (more detailed description provided in sections 2.3.1 and 2.3.2), SSFSW has a rotating pin but stationary shoulder. This was originally intended for welding materials with low thermal conductivity (Martin, 2013), such as titanium, in an effort to mitigate uneven temperature distribution (Li, Z., Yue, Ji, Chai, & Zhou, 2016). SSFSW can be used to control residual stress and distortion in thin sheet aluminium welds when compared with conventional FSW (He, Li, Song, Liu, & Hu, 2019) and can also mitigate against thinning of the workpiece (Liu, Li & Dunn, 2013). For these reasons, and due to thin sheet aluminium alloys being used extensively on helicopter airframes, SSFSW was selected for investigation in this research.

FSW is currently a permanently fitted workshop tool for manufacture of components in the aircraft, aerospace, marine, automotive and rail industries. In order to be seriously considered as a technique for repair in operational theatre, especially in the case of expedient repair, it would require development into a portable, ideally handheld apparatus. The development of portable equipment is not being considered within this research.

1.3 Materials Selection

For FSW to be a feasible and economical repair technique for in-service UK military helicopters it must be proven for repairs which are carried out regularly. A vast number of materials are used across the various types of aircraft used by the UK military and so, to narrow the field to a manageable level for this research, the decision was made to concentrate on the versatile Merlin aircraft, section 2.1. The 1710 NAS Aircraft Repair Task Information Management System (ARTIMS) (1710 Naval Air Squadron, 2014) documents all repairs carried out by the 1710 NAS Repair department on current Royal Navy (RN) aircraft. This was interrogated and cross-referenced with Technical Publications (Agusta Westland International Ltd, 2014) and Agusta Westland (now known under the parent company name of Leonardo Helicopters) Engineering Repair Instructions (ERI) (Agusta-Westland International Ltd, 2013). The interrogation concerned understanding the most common repair type, position on the aircraft and the alternative repair material used if applicable.

Hence, it was determined that the research would focus on damage to the lower forward aircraft skin which is manufactured from 0.7 mm thick AA8090-T81 (damage-tolerant, recrystallised) sheet aluminium alloy. The type of damage in this area was typically cracks and holes which patches using rivets or adhesive were used to repair. Instead of patches, SSFSW butt welding could be used to simulate both repairing a crack without the application of a patch, i.e. welding the crack faces together, or cutting a larger section from the airframe and using butt welding to apply the patch without any overlap. AA8090 is no longer in widespread use due to a perceived anisotropy of tensile properties dependent on the orthogonal direction in rolled material, particularly strength and fracture toughness in the Short-Transverse (S-T) direction. However, as the material was used extensively by the Original Equipment Manufacturer (OEM) on Merlin

aircraft which are still in use, it was necessary to investigate the suitability of this material with regards FSW in the event of damage in theatre. The now-cancelled Agusta Westland specification for AA8090-T81 (Agusta Westland International Ltd, 2010) specifies BS L167 (The British Standards Institution, 2016) as the repair replacement, however BS L167 was withdrawn by the British Standards Institution with no replacement upon commencement of this research. BS L165 (The British Standards Institution, 1978a) was selected to be used as the alternative repair material for the purposes of this research due to its similarities to BS L167 and its prevalence in aircraft repairs as revealed in ARTIMS. In 2016 BS L165 was withdrawn and BS L167 reinstated due to its continued and frequent use in aerospace applications. Due to work already completed, the decision was taken not to revert to the recommended repair material of BS L167 but to continue with the withdrawn alternative of BS L165.

In summary, 0.7 mm thick AA8090-T81 and BS L165 aluminium alloys were selected as the most suitable materials to determine if SSFWS would be a suitable method of expedient and enduring repair to the Merlin aircraft lower forward fuselage skin and other locations where these thin sheet aluminium alloys were employed within the airframe.

1.4 Project Aim

The aim of this research was to determine whether SSFSW is a suitable joining technique for AA8090 and BS L165 in various configurations, based on the quality of welds produced. The eventual goal is to ascertain whether SSFSW could be used as an expedient repair technique on UK military Merlin helicopters in operational theatre, however this would require significant advances in the portability of the equipment and is outside the scope of this research. This research instead focuses on the metallurgy of the welds produced.

1.5 Objectives

The objectives of this research were as follows:

1. Interrogation of data held by Ministry of Defence (MoD) Navy Command (NC) to characterise and identify the type of repair and material to focus research upon.
2. Characterisation of the material(s) to ensure they were consistent with the respective specifications and to establish a baseline prior to welding.
3. Determination of SSFSW tools and parameters to achieve defect free welds.
4. To carry out SSFSW, produce test specimens and conduct testing to characterise the microstructure and mechanical properties of the FSW materials. This was to consider similar and dissimilar welds and the influence of the material orientation, if any, to the weld quality.
5. Analysis of test results to determine suitability of SSFSW as a repair technique based on the materials examined.

2 Literature Review

2.1 EH 101 (Merlin) Helicopter

The EH 101, known in the UK as “Merlin” is a medium lift helicopter available in several variants utilised in a range of roles within the UK military today. The aircraft is also used by the militaries of numerous other nations under different guises and variants including Italy (EH 101), Canada (CH-149 Cormorant), Denmark (EH 101) and Japan (MCH101) among others (Pittman, 2017). A luxury variant was also developed primarily for the transport of Very, Very Important Persons (VVIP), utilised by several nations.

2.1.1 UK Merlin Helicopter

The Merlin is capable of lifting approximately 3.8 tonnes and is equipped with a variety of weaponry and surveillance equipment (Royal Navy, no_date); an example is shown in Figure 1. It was developed in the 1980s as a collaboration between the British company Westland and Italian company Agusta who formally amalgamated in 2000 to become AgustaWestland, now Leonardo Helicopters (Pittman, 2017).

Following the introduction of the original Merlin Mk1 in the 1990s, the modern Merlin fleet is primarily operated by the Royal Navy in the UK, with different variants employed for a diverse range of roles. These are summarised below:

- Mk2: This variant entered service in 2014 as an upgrade to the original Mk1; its primary roles are airborne anti-submarine warfare and maritime force protection. It is intended to replace the airborne surveillance and control role of the Sea King Mk7 (Royal Navy, no_date).
- Mk3: This variant was originally purchased for the Royal Air Force (RAF) with the formal rollout in 1998. These were used to support many operations worldwide before all aircraft were handed over to 845 NAS (Royal Navy) in 2015 (Pittman, 2017).
- Mk3A: The RAF acquired six additional Mk3A aircraft from Denmark in 2008 (Pittman, 2017). The Mk3A varies from the Mk3 with an altered nose, cabin and window layout. The Mk3A was not used in front line service, but as a training

aircraft. The fleet was handed over to the Royal Navy Commando Helicopter Force (CHF) in 2014. Both the Mk3 and Mk3A are currently undergoing a programme to be modified into the Mk4/ Mk4A variant (Ministry of Defence, no_dateb).

- Mk4/ Mk4A: The UK Merlin Life Sustainment Programme (MSLP) was introduced in 2014 to convert the Mk3/ Mk3A aircraft into an aircraft optimised for ship operations to be utilised by the RN CHF (Leonardo, 2016). CHF is the air wing of the UK Royal Marines, and the aircraft will be used for troop and supply transport and delivery and Search and Rescue operations, with the full fleet expected by 2023 (NavalToday.com, 2018).



Figure 1: Showing a Merlin Mk4 helicopter landing on HMS Queen Elizabeth with RFA Tideforce in support. Photo credit LPhot Kyle Heller, reproduced under the Open Government Licence (Heller, 2019).

2.1.2 AA8090 and BS L165 in Merlin airframes

The Merlin utilises significant amounts of the alloy AA8090 (see section 2.2.4 for more details of this alloy) in its design. This second-generation aluminium-lithium alloy was recently commercialised at the time of the Merlin development and the material was designed to be both light and damage resistant, with the result that approximately 90% of the original airframe was constructed from it (Pittman, 2017). It is now known that aluminium alloys with lithium content of >2 wt% suffer disadvantages in anisotropic properties, low short-transverse (S-T) ductility and fracture toughness and a loss of toughness due to thermal instability (Eswara Prasad, Gokhale, & Wanhill, 2014), although AA8090 is still present in modern Merlin structures.

The Merlin Mk4 Aircraft Documentation (Agusta Westland International Ltd, 2014) refers to AA8090 in various temper states for use on “structural parts where medium strength is required”, “repairs on dynamically loaded structural parts with low static loads” and “aircraft structures where medium strength is required”. Specific areas in which the alloy is used include skin, stringers and frame forgings. During development of the Merlin helicopter, designers were tasked to provide a target minimum weight saving of 55 kg. This was a major justification of using Al-Li over conventional aluminium alloys extrusions, sheet and forgings, as composite materials were considered too expensive at the time (Smith, 1988).

In 2004 a Merlin helicopter suffered a crash from only 4-5 metres in height which resulted in severe damage (disintegration) to the airframe. In 2006 a Canadian Cormorant helicopter crashed into the sea off Nova Scotia which resulted in extensive damage, including separation of the entire cockpit area. The investigations of both accidents highlighted that the damage to the airframes was more severe than might be expected (Wanhill, Symonds, Merati, Pasang, & Lynch, 2013). Although material deficiencies were not the primary cause of the afore-mentioned accidents, the extensive damage to the airframes was exacerbated by low-energy brittle fracture of AA8090 components (Wanhill et al., 2013).

AA8090 sheet was originally intended as a substitute for BS L165 (among other alloys) (Smith, 1988) due to the weight saving characteristics. Issue 5 of the Agusta Westland AA8090-T81 materials specification was released in 2010 with a cancellation statement

(Agusta Westland International Ltd, 2010) indicating the withdrawal of AA8090 from new use in Merlin helicopter manufacture. The recommended replacement was BS L167, however BS L167 was withdrawn with no replacement upon commencement of this research, as described in section 1.3. BS L165 (The British Standards Institution, 1978a) was selected to be used as the alternative repair material for this research as it has the same composition and temper as BS L167 with the addition of an alclad layer (a layer of commercially pure aluminium on the surface to improve corrosion resistance). Additionally, following an interrogation of the Aircraft Repair Task Information Management System (ARTIMS) (1710 Naval Air Squadron, 2014), it was found that BS L165 had been used regularly in repairs to the original AA8090 structure. The types of damage which this material had been used to repair were mainly impact or ordinance damage, or cracks.

Throughout this literature review, when discussing results of other researchers work, if a material is not specifically referred to as alclad it should be assumed to be bare, i.e. no layer of commercially pure aluminium on its surface.

2.2 Materials

2.2.1 Precipitation Hardening Aluminium Alloys

AA8090 and BS L165 are both precipitation-hardened aluminium alloys. In these alloys, a sequence of time and temperature dependent changes occur. In the first instance solute alloying elements are dissolved in aluminium. Fast cooling (quenching) results in an unstable supersaturated solid solution. At ambient temperature (i.e. no active external heating) and above, these solute atoms form clusters which are coherent with the matrix (Guinier-Preston (GP) zones), which produce distortions in the lattice planes causing local strain and hardening. As aging times or temperatures are increased, these zones are either converted or replaced by particles known as transition precipitates. These precipitates generally have a coherent or semi-coherent structure relationship with the solid solution. They have a strengthening effect due to dislocation-particle interactions which are dependent on the dislocation movement and volume fraction of precipitates. Dislocations either cut through the precipitates when coherent or semi-coherent, or loop around them as coherency is lost. The strength continues to increase

as the size of the precipitates increase while the dislocations are still able to cut the precipitates. As the precipitates grow they lose their coherency with the solid solution and change from transition to equilibrium form. The dislocations then loop around the precipitates and the strength drops. Precipitation hardening aluminium alloys must be aged at specific times and temperatures to achieve maximum strength without overaging. Figure 2 illustrates the influence of changing time and temperatures on the tensile strength of a typical precipitation hardening alloys, courtesy of Higgins, (1993). This shows the fine balance required to achieve optimal strength, without incoherent precipitates being formed.

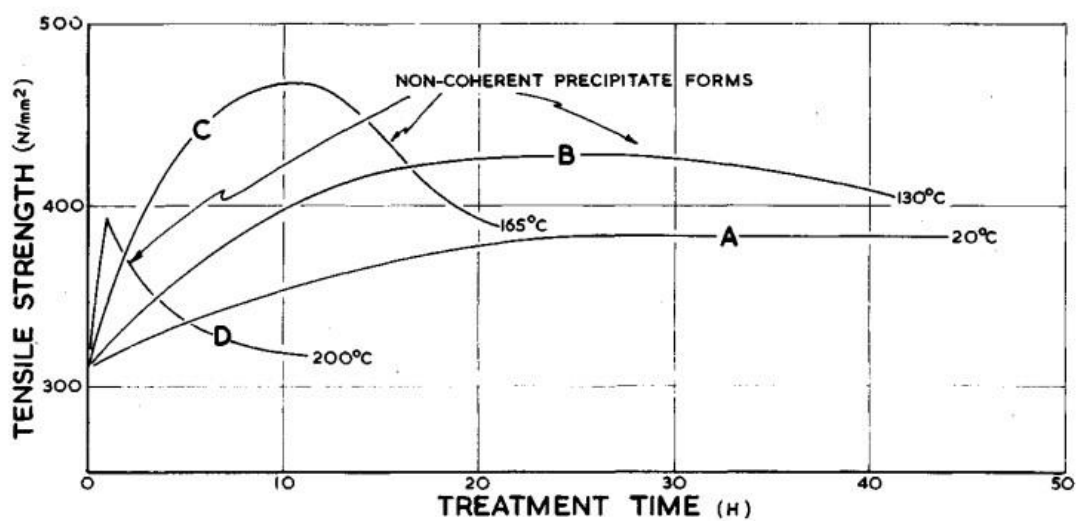


Figure 2: Showing the effects on strength of time and temperature of typical precipitation hardening alloys, courtesy of Higgins (1993).

Depending on the type of aging (e.g. natural or via precipitation heat treatment) and cold working, precipitation hardening aluminium alloys are used in various tempers, including T4, T6 and T8 (ASM International Handbook Committee, 1990). Table 1 provides a short description of the heat treatments required to achieve each specific temper for wrought aluminium products. Note, the temperatures and times (at each temperature) will differ for different alloys.

Table 1: Showing temper designations of wrought aluminium alloy products. Modified from Benedyk (2010) and Kaufman (2000).

Temper	Definition
T1	Cooled from an elevated temperature shaping process and naturally aged.
T2	Cooled from an elevated temperature shaping process, cold worked, and naturally aged.
T3	Solution heat treated, cold worked and naturally aged.
T4	Solution heat treated and naturally aged.
T5	Cooled from an elevated temperature shaping process and artificially aged (precipitation heat treatment).
T6	Solution heat treated and artificially aged.
T7	Solution heat treated and artificially overaged.
T8	Solution heat treated, cold worked and artificially aged.
T9	Solution heat treated, artificially aged and cold worked.
T10	Cooled from an elevated temperature shaping process, cold worked, and artificially aged.
Other	Where a "1" is added to the end of a temper designation (e.g. T81), this designates that the material has been quenched in boiling water or oil, rather than cold water. For example, T81 has been solution heat treated, quenched in boiling water/ oil, cold worked, and artificially aged.

2.2.2 Recovery and Recrystallisation

Raabe (2014) provides a detailed overview of recovery and recrystallisation; Figure 3 shows their schematic representation of the process. Recovery and recrystallisation can often be used to restore desirable mechanical properties following severe plastic deformation. Recovery can occur either statically (when previously deformed materials are subjected to suitable temperature) or dynamically (during cold-working) and both involve microstructural (sub-grain) changes to release internal stored energy. During both processes the defects/ dislocations created during cold-working (e.g. stretching or rolling) move or are absorbed which reduces the internal stresses. This movement leads to the formation of sub-grains within the original deformed grains. Recrystallisation can again occur either statically or dynamically. It concerns the nucleation and formation of new high-angle grain boundaries to replace the recovered cold-worked structure with strain-free and equiaxed grains.

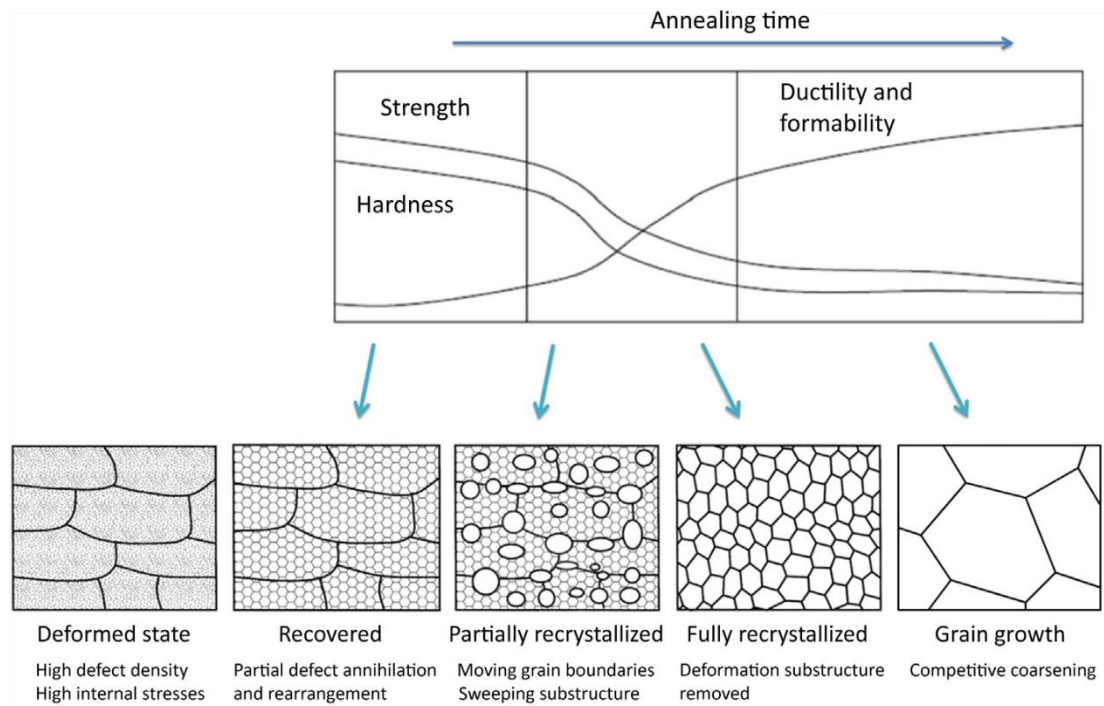


Figure 3: Showing an illustration of the basic steps during recovery, static recrystallisation and grain growth. From Raabe (2014).

FSW is both a thermal and mechanical process (see section 2.3 for a description of the process) and so a combination both static and dynamic recovery and recrystallisation is undertaken. Mishra, De and Kumar (2014) describe how static recovery and recrystallisation occurs both as the tool approaches and moves away from an area of material under consideration; dynamic recovery and recrystallisation occurs when the tool is traversing the area under consideration.

2.2.2.1 Static Recovery

When a metal is plastically deformed there is an increase in the dislocation and vacancy density. Applying sufficient heat to this deformed material allows reorganisation of the dislocations via slip/ climb movement; the point defects are absorbed at grain boundaries and dislocations with opposite Burgers vectors annihilate each other (Mishra et al., 2014; Raabe, 2014). Static recovery can occur at modest temperatures well below that required for recrystallisation (itself only approx. $\frac{1}{3}$ – $\frac{1}{2}$ of the absolute melting temperature) (Raabe, 2014). As recovery continues, sub-grains with boundaries are formed; these sub-grain boundaries are described as low-angle boundaries (normal grain boundaries are high-angle boundaries) and have lower surface energy than the

normal grain boundaries (Mishra et al., 2014). Second phase particles can influence recovery via their interactions with dislocations and sub-grain boundaries.

2.2.2.2 Static Recrystallisation

While the main grain structure does not change in recovery (only the formation of sub-grains), in static recrystallisation the dislocations in the deformed microstructure glide or climb to form new strain-free, approximately equiaxed grains separated by high-angle boundaries (Mishra et al., 2014; Raabe, 2014). In static recrystallisation, no additional deformation is introduced. As recrystallisation requires an incubation period, the material will already be in a recovered state (i.e. recovery having occurred) before the process begins. For recrystallisation to initiate, a suitable amount of preceding plastic cold working has to have occurred; for aluminium alloys this is approximately 40-50% cold reduction prior to heat treatment, however the process is thermally activated and generally the temperature required for activation varies depending on the amount of preceding cold work. The presence of second phase particles can slow recrystallisation by retarding the movement of dislocations, although if recrystallisation occurs at the same time as precipitation from solid solution it can accelerate the process (Raabe, 2014).

2.2.2.3 Dynamic Recovery

Dynamic recovery occurs during the deformation process itself rather than due to an externally applied heat treatment. Mishra et al. (2014) describe that although dynamic recovery results in a similar sub-grain structure as found with static recovery, little is known about the steps which lead to this structure with the dynamic process. Raabe (2014) states that dynamic recovery is a gradual mechanism occurring in almost all metals in a continuous manner and leads to gradual annihilation of dislocations by climbing and cross-slip. In aluminium, dynamic recovery can continuously remove and balance strain hardening introduced during hot working, leading to overall steady-state plastic flow when forming occurs above 50% of melting temperature.

2.2.2.4 *Dynamic Recrystallisation*

Dynamic recrystallisation occurs when the new high-angle grain boundaries are formed during deformation at elevated temperatures. A specific threshold measure of deformation is required (which depends on the material and previous thermal and mechanical history) and beyond that nucleation occurs and new grains form (Raabe, 2014). However, these new grains will only grow to a certain size as they are continuously being further deformed by the ongoing hot work. Mishra et al. (2014) describe how an initial input strain produces recrystallisation resulting in new strain-free grains. The continued input strain introduces new dislocations into the newly recrystallised grains, forming sub-grains which act as nucleation sites for more recrystallisation as the strain input continues. This series of recrystallisation events is known as discontinuous dynamic recrystallisation (Mishra et al., 2014).

2.2.3 Grain size and mechanical properties

It is well known that the grain size of aluminium alloys is influenced by a number of factors including heat treatment, cold/ hot working, aging, alloying elements etc. It is also known that the mechanical properties of alloys are strongly dependent on the grain size. Grain boundary strengthening occurs when dislocations pile-up at grain boundaries producing a local stress eventually allowing the plastic deformation to pass to an adjacent grain. In materials with larger grain sizes there is the ability for many dislocations to pile up at each boundary and so the local stress is greater and the material therefore has a lower resistance to yielding. In materials with smaller grain sizes, fewer dislocations can pile-up thus increasing the material's resistance to yielding. The grain boundaries act as barriers to deformation propagation, thus in materials with smaller grain size, grain boundaries are more abundant and the deformation has more resistance to its propagation.

The Hall-Petch relationship, reproduced by Schempp, Cross, Häcker, Pittner and Rethmeier (2013) describes the inverse relationship between the yield strength and grain size; this relationship is shown in Equation 1.

$$\sigma_y = \sigma_0 + \frac{k}{\sqrt{d}} \quad \text{Equation 1}$$

Where σ_y is the material's yield strength, σ_0 is a material constant relating to a frictional stress or the starting stress for dislocation movement, k is a material constant relating to the capability of grain size hardening for the alloy and d is the average diameter of the grains. The Hall-Petch relationship applies for grains above a certain size (for example Jeong et al. (2015) found that grains above 70 nm in diameter followed this relationship); below this size dislocation pile-up does not occur and the applied stress is relieved by the lattice via grain boundary sliding which actually reduces the material's resistance to yield.

2.2.4 AA8090 Characteristics

2.2.4.1 Metallurgy

In order to develop low density and therefore lighter alloys, researchers took the approach of using elements with low atomic weights as alloying elements. Lithium is the lightest metallic element in the periodic table and has the characteristic that the addition of 1 wt% of lithium resulted in an approximate 3% decrease in density and approximate 6% increase in Young's modulus (Kulkarni, Banerjee, & Ramachandran, 1989; Sohn, Lee, & Kim, 1993). AA8090 was one of the "second generation" of aluminium-lithium alloys developed in the 1980s; these alloys were once viewed as the possible future of aerospace materials.

The elemental composition of AA8090 is shown in Table 2 from two sources for comparison, as per EM 101 (Agusta Westland International Ltd, 2010) and ASM Handbook Volume 2 (ASM International Handbook Committee, 1990); it was noted that both compositions were identical.

Table 2: Showing elemental composition of AA8090 as per 1) EM 101 (Agusta Westland International Ltd, 2010) and 2) ASM Handbook Volume 2 (ASM International Handbook Committee, 1990). When only one value is given rather than a range, this constitutes a maximum value.

	Element (%wt)												
	Si	Fe	Cu	Mn	Mg	Cr	Zn	Li	Zr	Ti	Others		Al
											Each	Total	
1	0.2	0.3	1.0-1.6	0.1	0.6-1.3	0.1	0.25	2.2-2.7	0.04-0.16	0.1	0.05	0.15	Remainder
2	0.2	0.3	1.0-1.6	0.1	0.6-1.3	0.1	0.25	2.2-2.7	0.04-0.16	0.1	0.05	0.15	Remainder

AA8090 is an Al-Li-Cu-Mg-Zr precipitation-hardening alloy with the primary strengthening precipitates of δ' (Al_3Li), T_1 (Al_2CuLi) and S' (Al_2CuMg) although other precipitates are present. The metastable spherical δ' forms a coherent precipitate on aging following solution heat-treatment, which orients with the aluminium matrix (Eswara Prasad et al., 2014) due to its similar lattice parameter (Kostrivas & Lippold, 1999), i.e. there are geometrical similarities between the lattice of δ' precipitates and that of α -FCC solid solution (Kebriyaei, Mirdamadi, & Saghafian, 2017). This results in low misfit strain which leads them to be easily sheared by moving dislocation lines thus allowing for planar slip (Holmes, Chin, Huang, & Pasternak, 1992). Overaging results in the formation of incoherent δ (AlLi) precipitates which nucleate both at grain boundaries and within the grains (Eswara Prasad et al., 2014). The precipitation sequence for δ' is: $\text{SSS } \alpha \rightarrow \text{Al}_3\text{Li} (\delta') \rightarrow \text{AlLi} (\delta)$. The changes in precipitation are illustrated in Figure 4 with respect to aging time and the effects on hardness.

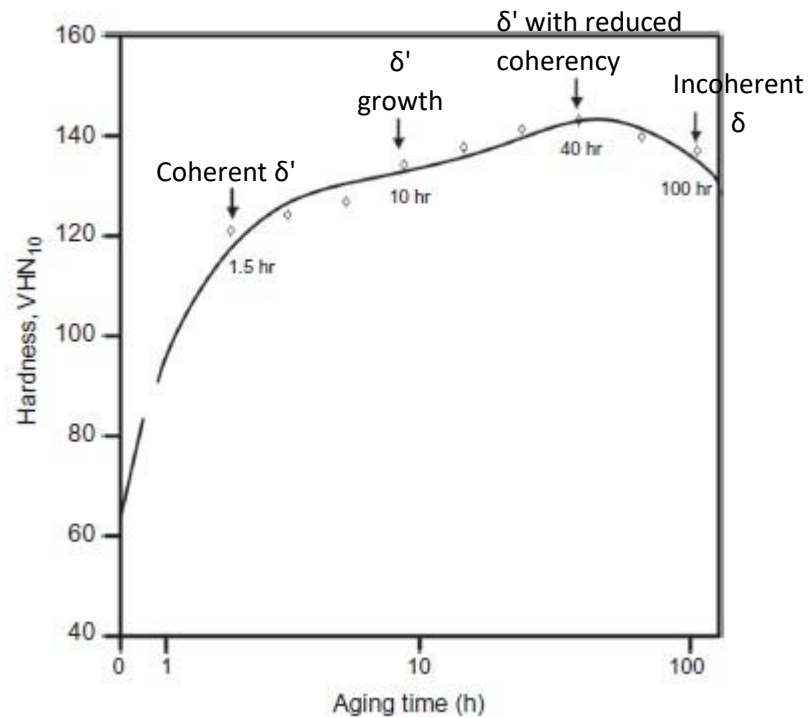


Figure 4: Showing a typical age hardening curve (at 190 °C) for AA8090, courtesy of Prasad (1999), with additional labelling.

The addition of copper produces the hexagonal, partially coherent T_1 phase in artificially aged conditions (Eswara Prasad et al., 2014; Kulkarni et al., 1989). This forms heterogeneously on dislocations and subgrain boundaries and, when in high concentration, this phase inhibits the growth of δ' . In the case of AA8090, S' phase dominates over T_1 (Kulkarni et al., 1989; Miller, White, & Lloyd, 1987) due to the ratio of Cu:Mg:Li in the alloy. S' is a semi-coherent orthorhombic structure which takes the form of laths. This precipitate promotes cross-slip, improves ductility and toughness by preventing the shearing of δ' (Kostrivas & Lippold, 1999) and this retards planar slip and crack nucleation. S' competes with T_1 for Cu atoms and heterogeneous nucleation sites which is the reason for stretching prior to aging; this provides new nucleation sites for S' within the matrix thus improving the mechanical properties (Kostrivas & Lippold, 1999; Sohn et al., 1993). The resultant material is of high strength but the ductility and fracture toughness are reduced (Kostrivas & Lippold, 1999).

In addition to precipitate phases, insoluble constituent particles generally occur within the matrix or at the grain boundaries of aluminium alloys. In the case of Al-Li alloys, these are mainly compounds of Al with Fe, Mn, Si and Cu.

2.2.4.2 *Mechanical Properties*

One of the primary concerns regarding Al-Li alloys is the perceived anisotropy of tensile properties dependent on the orthogonal direction in rolled material, particularly strength and fracture toughness in the S-T direction. This is more apparent in unrecrystallised products, e.g. extrusions, forgings and some sheet due to the crystallographic texture and strengthening precipitates. Recrystallised Al-Li damage-tolerant sheet (T81) shows far less anisotropy (ASM International Handbook Committee, 1990) and improved fracture toughness, comparable with AA2024-T3 sheet (Wanhill, 1994). Examples of the differences in these two grain structures (of recrystallised and unrecrystallised AA8090) are shown in Figure 5. Bregianos, Crosky, Munroe and Hellier (2010) describe the dispute within the literature as to the reason for low fracture toughness. It has been attributed to: slip planarity (Blankenship, Hornbogen, & Starke, 1993), i.e. shearing of δ' causing coarse inhomogenous slip with large dislocation groupings leading to a stress concentration and intergranular failure (low toughness); grain boundary precipitates or precipitate free zones (PFZ) (Vasudévan & Doherty, 1987). PFZ formation causes the accumulation of precipitates at grain boundaries which nucleate voids which join together and result in intergranular failure. This is accompanied by the presence of ductile microvoid coalescence resulting from the width of the PFZ; or to lithium segregation to the grain boundaries (Lynch, 1991; Lynch, Wilson, & Byrnes, 1993). Lithium segregation involves brittle intergranular failure when the lithium concentration at the grain boundaries is above a certain level, and ductile intergranular failure occurs below it. While Bregianos et al. (2010) found evidence to support aspects of each model in their experimental work, indicating that the dispute remains today.

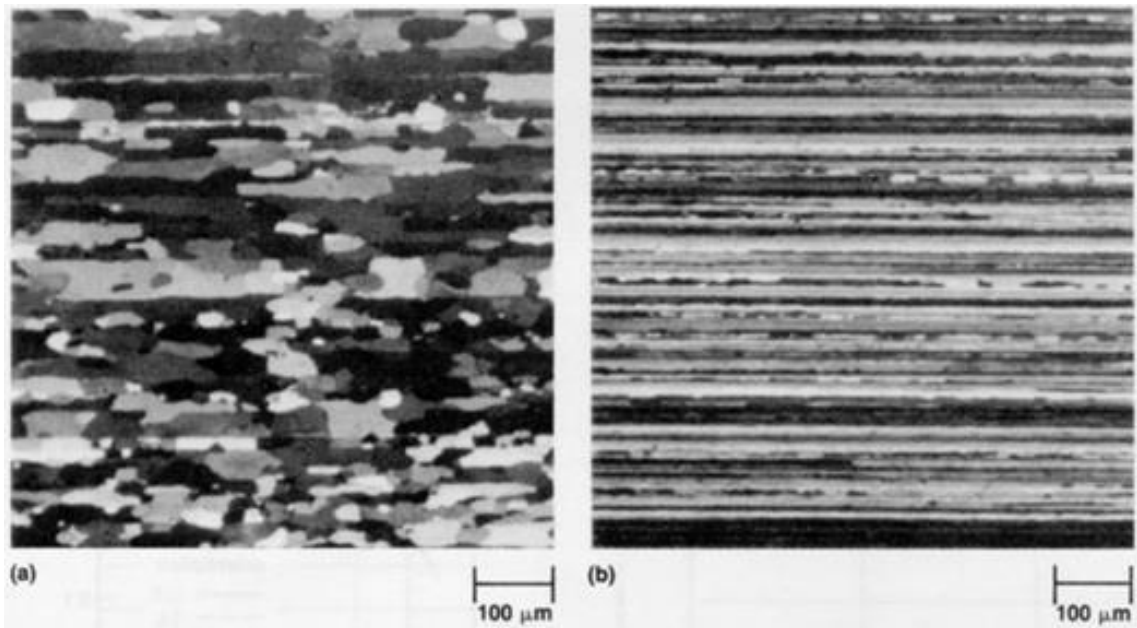


Figure 5: Showing microstructures of AA8090 sheet: (a) Recrystallised grain structure; (b) Unrecrystallised grain structure. From ASM Handbook Volume 2 (ASM International Handbook Committee, 1990).

Aside from the influence of the anisotropy involving the S-T direction, the failure mode of tensile overloaded AA8090 test specimens varies depending on the heat-treatment and cold-working applied. Burzić, Ćurović, Grahovac and Stefanović (1993) reported a vast range of failure and yield strengths and failure modes (ductile or brittle) depending on the heat treatment and degree of rolling applied. The experimental work by Panthri, Joshi and Pathak (2019) on ultrafine-grained AA8090 revealed a change in hardness, UTS, yield strength and ductility of products which were Room-Temperature Rolled (RTR) (post solution treatment) and then annealed at varying temperatures 100-350°C, compared with those with only a solution heat treatment. The following effects on mechanical properties are attributable to dynamic recrystallisation during RTR. The tensile and yield strengths of the former peaked at RTR+150°C and then fell to the minimum (beyond even the solution treated only samples) at RTR+350°C, while the ductility was highest in the solution treated only condition and fell sharply with RTR, but increased steadily with annealing temperature. The hardness increased from its minimum in the solution treated condition to a peak at RTR+150°C then fell with increasing annealing temperature. The fractography revealed mixed ductile-brittle (intergranular failure coupled with ductile microvoid coalescence) failure in those samples with annealing up to 200°C with only ductile failure modes present in the

solution treated samples and those annealed above 200°C. Although not specific to this alloy, Figure 2 in section 2.2.1 illustrates these changes. Srivatsan and Place (1989) found higher strength but lower ductility for tests carried out in the longitudinal direction over the transverse direction of AA8090-T851 (the heat treatment was a solution treatment, then 2% stretching, followed by artificial aging). The fractography revealed a mix of regions of transgranular shear fracture and regions of intergranular failure, with cracking along the sub-grain boundaries in the transgranular areas and micro-dimples on the intersubgranular fracture surface.

When Al-Li alloys are compared with conventional aluminium alloys in notched high-cycle fatigue testing, the results are generally favourable (Wanhill, 1994). Prasad, Gokhale and Rao (2003) report that Al-Li alloys are inferior to other aluminium alloys in low-cycle fatigue testing, however AA8090 in its partially-recrystallised form is far better. The presence of unrecrystallised grains improves the fatigue resistance, although there is a degree of anisotropy. The resistance to Fatigue Crack Growth (FCG) of Al-Li alloys is owing to a rough fracture surface topography which introduces increased roughness-induced crack closure, crack deflection and irregular crack fronts, although this is more prevalent in plate products than in sheet (Prasad et al., 2003; Wanhill, 1994).

However, results have been reported of AA8090-T81 (damage-tolerant, recrystallised) sheet achieving FCG resistance of an order of magnitude slower than AA2024-T3 (ASM International Handbook Committee, 1990). Contrary to this, Giglio, Manes, Fossati, Mariani and Giani (2010) compared the FCG of 0.8 mm sheet helicopter fuselage panels manufactured from AA8090-T81 and alclad AA2024-T3; they concluded that the two materials had similar damage tolerance. AA8090-T81 sheet and plate does however display macroscopic fatigue crack plane deviation and a change in fracture characteristics dependent on the speed of the crack growth; this may lead to unpredictable crack propagation (Gregson & Sinclair, 1996; Wanhill, 1994).

The mechanical properties of the AA8090-T81 material used in this research, as per the material specification (Agusta Westland International Ltd, 2010), certificate of conformity (Dolgarrog Aluminium Limited, 2005) and ASM Handbook Volume 2 (ASM International Handbook Committee, 1990) are shown in Table 3.

Table 3: Showing table of AA8090-T81 mechanical properties as per EM101 (Agusta Westland International Ltd, 2010), Certificate of Conformity (Dolgarrog Aluminium Limited, 2005) and ASM Handbook Volume 2 (ASM International Handbook Committee, 1990).

Source	UTS (MPa)	0.2% Proof Strength (MPa)	% Elongation	Hardness (HV)	Fatigue Strength at 50,000 Cycles
EM101	L = 400 T = 410 45° = 400	L = 280 T = 280 45° = 270	L = 6 T = 9 45° = 8	>120	150
Certificate of Conformity	423 ¹	287 ¹	15 ¹	Not provided	Not provided
ASM Handbook	L = 345-440 T = 385-450 45° = 380-435	L = 295-350 T = 290-325 45° = 265-340	L = 8-10 T = 10-12 45° = 14	Not provided	Not provided

Table 3 notes:

- 1 Orientation not specified

2.2.4.3 Weldability

FSW/ SSFSW of AA8090 will be discussed in section 2.3.3; this section focuses on fusion welding of AA8090 as a comparison and baseline.

Heat-treatable aluminium alloys are generally prone to solidification cracking due to their high coefficient of thermal expansion and tendency to form low melting point constituents. For this reason, these alloys are rarely, if ever, fusion welded for aerospace use. Vigraman, Vijay Krishna and Pavan Kumar (2021) state that difficulties in using Tungsten Inert Gas (TIG) welding on AA8090 arise due to the high oxidation potential of the material at elevated temperatures. The high temperatures generated during TIG welding causes lithium hydrate to form and evaporate; this depletion in Li leads to porosity, oxidation and brittleness.

Lippold (1989) compared Gas Tungsten Arc Welding (GTAW – known as Tungsten Inert Gas (TIG) welding in the UK) of AA8090-T3 and -T851 to other Al-Li alloys and reported a higher susceptibility to weld solidification cracking than other commercial alloys, including AA5083 and AA6061. The cracking was shown to occur along solidification grain boundaries with no evidence of eutectic crack healing. Griffee, Jenson and Reinhart (1989) achieved welds with no cracking in Variable Polarity Plasma Arc welded AA8090-T851. Kostrivas and Lippold (1999) summarise GTAW of AA8090 (temper

unknown) and show that improvements to joint efficiency ($UTS_{\text{weld}}/UTS_{\text{parent material}} \times 100$) can be made through post-weld heat treatments and choice of filler rod. Without these it is difficult, if not impossible, to achieve joint efficiencies higher than 60%. They did show that AA8090 solidification crack susceptibility reaches a maximum when the lithium content is ~2.5wt.% but it is less prone to HAZ liquitation cracking than AA2024.

Aluminium alloys are also prone to porosity in the nugget due to moisture absorption through the oxide layer forming hydrogen bubbles during solidification. Kostrivas and Lippold (1999) found that while AA8090 was susceptible to porosity, this could be greatly alleviated by careful surface preparation prior to welding.

Bonaccorsi, Costanza, Missori, Sili and Tata (2012) characterised the mechanical and metallurgical aspects of AA8090 GTAW joints; they produced sound welds, i.e. no cracking or macroscopic defects with full penetration. They showed that the weld metal was characterised by dendritic growth. The hardness varied across the weld with the minimum hardness close to the weld centreline. Tensile tests achieved joint efficiency of approximately 66% with a significant drop of approximately 75% in % elongation. Despite the lack of macroscopic defects or porosity, the weld quality was adversely affected due to coarsening of precipitates in the HAZ.

2.2.5 BS L165

2.2.5.1 Metallurgy

BS L165 is a British alloy designation which has a very similar American counterpart, alclad AA2014-T6. As the materials have extremely similar elemental compositions (apart from the composition of the alclad layer) and mechanical properties, for the purposes of this literature review the two materials shall be considered to be equivalent¹. BS L165 (and AA2014-T6) is a popular aerospace material owing to its high strength-to-weight ratio and corrosion resistance (the corrosion resistance is primarily owing to the alclad layer; unclad AA2014 may be susceptible to various corrosion mechanisms). The elemental compositions of BS L165 as per BS L165 (The British

¹ BS L165 specification (The British Standards Institution, 1978a) has a notation which states, "NOTE 2: The chemical compositions of the core and cladding of this material comply with those registered as International Designations 2014A and 1050A respectively." ASTM B209 (ASTM International, 2014) states that AA2014 is clad with AA6003.

Standards Institution, 1978a) and AA2014 as per ASTM B209 (ASTM International, 2014) are shown Table 4 below. BS L165 is an Al-Cu-Mg-Si-Mn precipitation-hardening alloy, i.e. solution heat treated, quenched and artificially aged, and is clad with AA1050 to an average thickness of approximately 4% thickness of the bulk material (The British Standards Institution, 1978a).

Table 4: Showing the elemental composition of 1) BS L165 as per BS L165 (The British Standards Institution, 1978a), and 2) AA2014 as per ASTM B209 (ASTM International, 2014). When only one value is given rather than a range, this constitutes a maximum value.

	Element (%wt)												
	Si	Fe	Cu	Mn	Mg	Cr	Ni	Zn	Ti	Ti + Zr	Others		Al
											Each	Total	
1	0.5-0.9	0.5	3.9-5.0	0.4-1.2	0.2-0.8	0.1	0.1	0.25	0.15	0.2	0.05	0.15	Remainder
2	0.5-1.2	0.7	3.9-5.0	0.4-1.2	0.2-0.8	0.1	-	0.25	0.15	-	0.05	0.15	Remainder

Differing designations for precipitates and descriptions for the precipitation sequence (during low temperature aging post solution treatment at a higher temperature and quenching) of AA2014 have been found in the literature (Bassani, Gariboldi, & Vimercati, 2007). Bassani et al. (2007) report on the work of several authors and give the following three potential sequences that may occur simultaneously: $SSS \rightarrow GP \text{ zones} \rightarrow \theta'' \rightarrow \theta' \rightarrow \theta$ where the θ particles comprise of Al_2Cu ; $SSS \rightarrow GP \text{ zones} \rightarrow (GP \text{ zone II or } S'') \rightarrow S' \rightarrow S$ where the S particles comprise of $CuMgAl_2$; and $SSS \rightarrow GP \text{ zones} \rightarrow Q' \rightarrow Q$ where the Q precipitates comprise of $Cu_2Mg_8Si_6Al_5$, $Al_3Cu_2Mg_9Si_7$ or $Al_4Cu_2Mg_8Si_7$ (the Q phase is referred to as λ by some authors, (Bassani et al., 2007; Dutta, Harper, & Dutta, 1994)).

Gazizov, Dubina, Zhemchuzhnikova and Kaibyshev (2015) report that the main strengthening particles are the coherent and semi-coherent configurations of θ phase (Al_2Cu). Both they, and Chand et al. (2016) assert that the precipitation sequence is independent of other phases and it is as follows: $SSS \rightarrow GP \text{ zones} \rightarrow \theta'' \rightarrow \theta' \rightarrow \theta$. Saleh (2018) agrees with this sequence and reports the precipitation sequence as a plot of hardness against aging time (Figure 6), showing that peak hardness is achieved at 12 hours of aging (at 165 °C). This plot begins at the solution heat treated position and attributes the hardening to the precipitation of 2nd phase θ'' and metastable θ' . Aging above 12 hours reduces the hardness due to the precipitation of equilibrium θ which is

incoherent with the matrix. A pictorial representation of the precipitation sequence is shown in Figure 7 with reference to the Al-rich end of the Al-Cu equilibrium diagram, courtesy of Higgins (1993). Cross-referencing of Figure 6 and Figure 7, shows that in the T6 condition (solution treated and precipitation hardened), the maximum volume fraction of θ' precipitates are present, with a resultant increase in the hardness. The T6 condition for AA2014 corresponds to the correct temper for BS L165. In the overaged condition (T7), non-coherent θ precipitates form, thus reducing the hardness of the material.

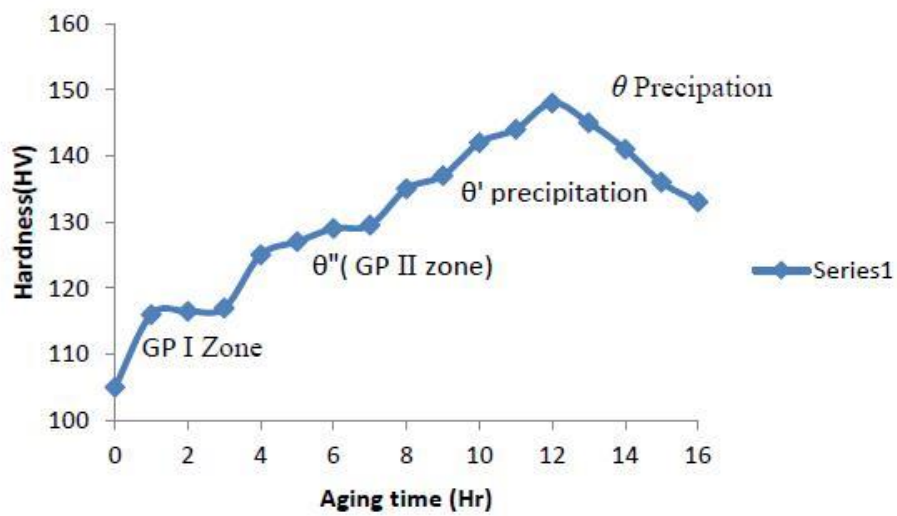


Figure 6: Showing Saleh's (2018) work depicting hardness with respect to aging time at 165 °C for AA2014 alloy.

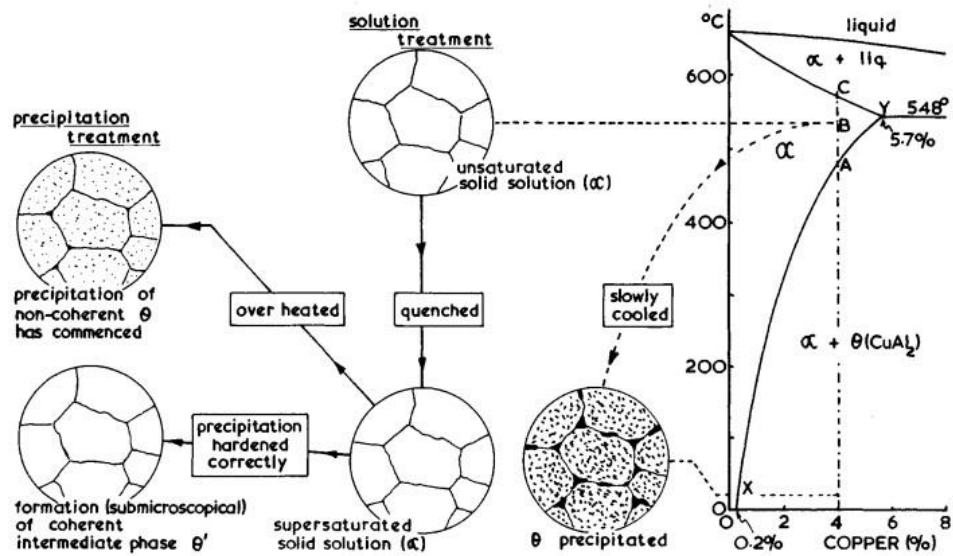


Figure 7: Showing the microstructural changes due to solution and precipitation heat treatments of an Al-Cu alloy, courtesy of Higgins (1993).

Gazizov et al. (2015) also report on secondary strengthening Mg-Si phases which occur in the sequence; SSS \rightarrow Mg-Si clusters \rightarrow GP-I zones \rightarrow β'' \rightarrow β' \rightarrow β . They report that β' and β'' differ in both structure and appearance such that particles of β'' ($Mg_5Al_2Si_4$) are needle shaped, and β' ($Mg_{1.8}Si$) are rod shaped. β phase is the equilibrium phase in the form of plates or cuboids. It is however noted elsewhere in the literature (Bassani et al., 2007) that the β phase precipitation sequence can only be found in alloys with a Mg/Si ratio greater than 1 which will not occur in all AA2014 alloys.

Gazizov et al. (2015) state that the precipitation sequence can change due to the Cu/Mg and Mg/Si composition ratios, and takes the form: SSS \rightarrow Mg-Si clusters \rightarrow GP zones \rightarrow β'' , Q' , $C \rightarrow Q' \rightarrow Q$. Dutta et al. (1994) report that precipitation begins with GP zones which nucleate either homogenously or at vacancy clusters. Dissolution of the GP zones act as nucleations sites for λ' (Q') precipitates which are evenly distributed throughout the matrix, while θ' nucleates independently on matrix dislocations.

Styles et al. (2015) comments that from the Al-Cu-Mg ternary phase diagram, alloys with Cu:Mg ratios of 2:1 (wt%) will produce $\alpha+S$ phase. Due to its specified composition AA2014 cannot achieve this ratio. Grenchnikov and Nosova (2017) base their experimental work on a similar alloy (AA2024) despite the misleading title, and indeed, none of the literature reviewed (including that referenced by (Bassani et al., 2007))

relate to the S phase in AA2014, rather to other alloys in the same family with different compositions.

2.2.5.2 Mechanical Properties

Throughout this literature review, whenever reference to AA2014 is made, it is assumed to be bare unless specifically stated as being alclad. Narender, Ramjee and Eswara Prasad (2019) studied the effects of aging on the anisotropy previously reported for AA2014. Carrying out testing on solution heat treated (SHT), underaged, peak aged (T6) and overaged specimens in the L, T and 45° orientations, they found that the in-plane anisotropy was highest in the T6 condition although it was described as moderate (no definition of “moderate” provided) overall. Examination of the fracture surfaces of the T6 specimens revealed microvoid coalescence typical of ductile failure, however there was a change in the size and shape of the dimples depending on the orientation examined (spherical and larger for L direction, progressively smaller and elongated for T and then L+45° directions).

Ashok, Maruthupandian, Ganesh Kumar and Vishal (2015) carried out tensile testing of L and T orientated AA2014 T651 specimens at both room temperature and increasingly elevated temperatures up to 300 °C. They found that the UTS and proof stress decreased with increasing temperature while the % elongation increased and attributed this to the coarsening of second phase particles.

Singh and Goel (2005) examined combinations of thermal and mechanical processes in an effort to improve the fatigue properties of AA2014. They found that the peak artificially aged condition (T6) produced the poorest fatigue results of all the treatments (including naturally aged T4) and that the inclusion of warm rolling markedly improved the results. TEM analysis indicated that the T6 condition produced the coarsest θ' precipitates, with the addition of warm rolling producing finer precipitates. These thermo-mechanical treatments also changed the nature (fine and uniform or coarse and non-uniform) of the dislocation-precipitate tangles, and the size and dispersion of intermetallic particles.

The UTS, yield strength and % elongation of BS L165 and alclad AA2014-T6 as per the material specification ((The British Standards Institution, 1978a) and (ASTM

International, 2014) respectively) and BS L165 as per the certificate of conformity (used in this research) (Wilson's Aero Metals Alliance, 2016) are shown in Table 5.

Table 5: Showing table of BS L165 and alclad AA2014-T6 mechanical properties as per material specification^{1,2} and Certificate of Conformity³ (BS L165).

Source	UTS (MPa)	0.2% Proof Strength (MPa)	% Elongation
BS L165 ¹	415	345	7
AA2014-T6 alclad ²	435	380	7
Certificate of conformity (BS L165) ³	455	407	8

Table 5 notes:

- 1 BS L165 (The British Standards Institution, 1978a)
- 2 ASTM B209 (ASTM International, 2014)
- 3 CofC (Wilson's Aero Metals Alliance, 2016)

The introduction of an alclad layer has the effect of reducing the UTS and yield strength of AA2014 when the same overall thickness of material is considered, due to part of that thickness being occupied by a material with lower strength. Table 6 shows a comparison of the UTS, 0.2% proof strength and % elongation of BS L165 with BS L157; these materials have the same elemental composition but the latter has no alclad layer. Also shown in Table 6 are both clad and unclad AA2014-T6 for comparison.

Table 6: Showing comparison of clad and unclad materials and the effect on mechanical properties. The table shows the mechanical properties for the thickness relevant to this research, i.e. 0.7 mm.

Material	UTS (MPa)	0.2% Proof Strength (MPa)	% Elongation
BS L165 ¹	415	345	7
BS L157 ²	430	370	6
AA2014-T6 alclad ³	435	380	7
AA2014-T6 bare ³	440	395	6

Table 6 notes:

- 1 BS L165 (The British Standards Institution, 1978a)
- 2 BS L157 (The British Standards Institution, 1978b)
- 3 ASTM B209 (ASTM International, 2014)

2.2.5.3 Weldability

BS EN 4632-002:2008 (Aerospace and Defence Industries Association of Europe - Standardization (ASD-STAN), 2008b), with reference to BS EN 4632-001:2008 (Aerospace and Defence Industries Association of Europe - Standardization (ASD-STAN), 2008a) recommends that AA2014 has a degree of weldability for TIG welding rated as 4. This is defined as “material with very bad weldability. To be avoided”.

Sivaprasad, Muthupandi Shankar and Sokkalingam (2019) carried out GTA welding of annealed AA2014, examining the microstructure and tensile properties. They reported on coarse equiaxed dendrites within the nugget with dispersed 2nd phase precipitates identified as coarse Al₂Cu around which dislocation looping accompanied by a drop in strength occurs. Testing revealed the hardness values to be lowest at the centre of the weld, rising above the parent metal’s values at the fusion boundary (boundary between the nugget and the HAZ) before dropping to parent material’s values throughout the HAZ. UTS was lower than the parent material values in the nugget and HAZ, although the yield strength in the nugget was similar. Ductility was lowest in the nugget.

Kramer, Heubaun and Pickens (1989) compared hot-cracking resistance of Weldalite 049 (Al-Li alloy) to GTA welded AA2014-T8 and other Al-Li alloys (not AA8090) and found AA2014 to be the least “weldable” of those tested based on comparison of the total length of cracking within the weld. In addition to hot cracking, cracks were also observed in the HAZ of AA2014, although the authors did concede that AA2014 can be successfully welded under well-controlled conditions with a suitable filler.

Biradar (2016) carried out studies using different filler materials and Transverse Mechanical Arc Oscillation (TMAO) to attempt to improve the resistance to solidification and liquidation cracking of AA2014 T6 TIG welds. Improved resistance to solidification cracking was observed through use of TMAO (although all welds still exhibited some), which was attributed to the mechanical disturbance of the TMAO breaking up the solidification structure and reducing dendritic growth resulting in a refined structure.

Limited research was found which compared alclad and bare aluminium fusion welds and the resultant effect of the alclad layer on weld properties. Hess, Wyant and Winsor (1947) found that when spot-welding alclad and bare materials (with the same core parent material), the fusion penetrated deeper into the bare material than the alclad

one. This was due to the higher melting temperature of the alclad layer when compared with the core parent material. Brungraber and Nelson (1973) found that the same size of HAZ was produced when alclad and bare AA3004-H14 were (separately) Gas Metal Arc Welded (GMAW) using the same weld equipment settings, although no data was provided on the weld strength of those materials.

2.3 Friction Stir Welding

FSW was invented and patented by The Welding Institute (TWI) in 1991 (Thomas et al., 1991), although this and subsequent patents have since expired. A plethora of additional patents from many different companies and individuals have since, and continue to be, submitted and approved as the technology progresses.

2.3.1 Friction Stir Welding Process

The FSW process for butt welding is described pictorially in Figure 8. A non-consumable rotating tool comprised of a shoulder and probe (also known as a pin) is inserted and traversed along the join-line of abutting sheets of material, mechanically stirring the material to form a joint. Figure 8 shows an advancing and retreating side of the weld. The advancing side is defined as that in which the tool's rotational direction matches that of the traversing direction, and the retreating side where the rotational direction opposes the traversing direction.

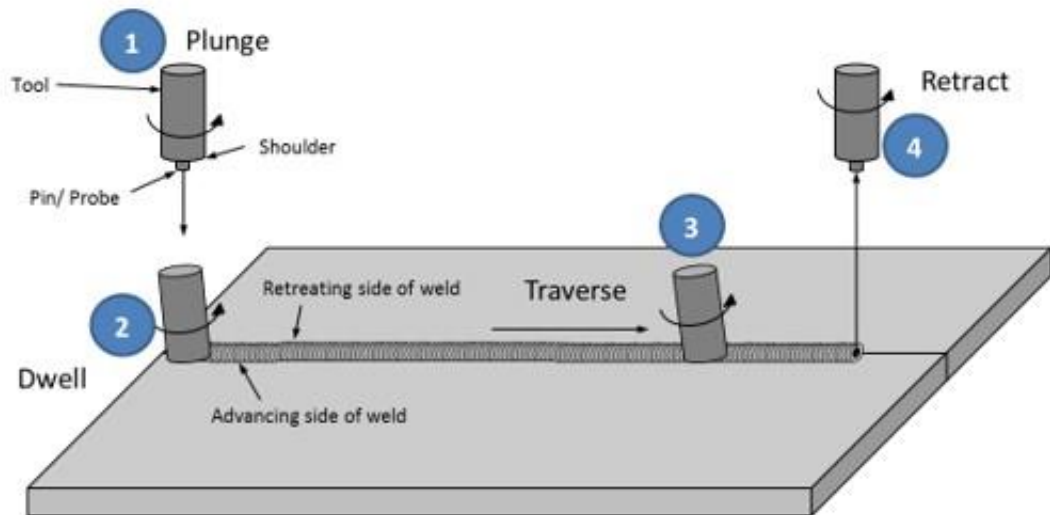


Figure 8: Showing diagram of the FSW process: 1) plunge of the tool to the material; 2) dwell at the insertion point to generate heat in the material; 3) traverse of the tool along the workpiece; 4) retraction of the tool from the material.

The process is solid-state, i.e. the material never reaches melting temperature, however heat is generated (the temperature of which depends on the materials and welding parameters used) during FSW to allow stirring of the material. There are several stages to FSW which Mishra, De and Kumar (2014) define as: a) plunge and dwell (shown as stage 1 and 2 in Figure 8); b) traverse (stage 3) and c) retract (stage 4). Plunge refers to insertion of the rotating tool into the workpiece. Prior to this stage both the tool and the material are at ambient temperature; as the tool is inserted the temperature of the surrounding material and tool rise, the rate of which depends on the rate of insertion. The temperature rises owing to frictional contact and from adiabatic frictional deformation within the material, until the workpiece reaches the critical temperature for plastic flow. This is dependent on the properties of the material and may require the tool to remain in this position for a short time (dwell). The tool then traverses along the material forming the joint. Threadgill, Leonard, Shercliff and Withers (2009) compare the FSW process to “constrained extrusion under the action of the tool”. The shoulder constrains the softened material and, as the tool traverses, material is gathered from the advancing side, swept around the pin and deposited between the retreating side and the surrounding cooler material.

There are several advantages and disadvantages of FSW in comparison with conventional fusion welding (Threadgill et al., 2009). Advantages include: the ability to weld alloys considered difficult to fusion weld e.g. 2XXX or 7XXX series due to their susceptibility to hot cracking; no consumables are used in conventional FSW; dissimilar materials can be joined. Disadvantages include: the current automated process makes it suitable for high volume, uniform welding, but less suitable for complex weld configurations or where access is limited as a fully portable assembly is required; an exit-hole is left following FSW; the requirement for adequate clamping to compensate for the forces applied during the process.

The thermo-mechanical process inherent in FSW produces a highly characteristic microstructure in aluminium alloys as described in Figure 9 below. Threadgill and Leonard (1999) proposed the terms defined below; these have been overwhelmingly adopted.

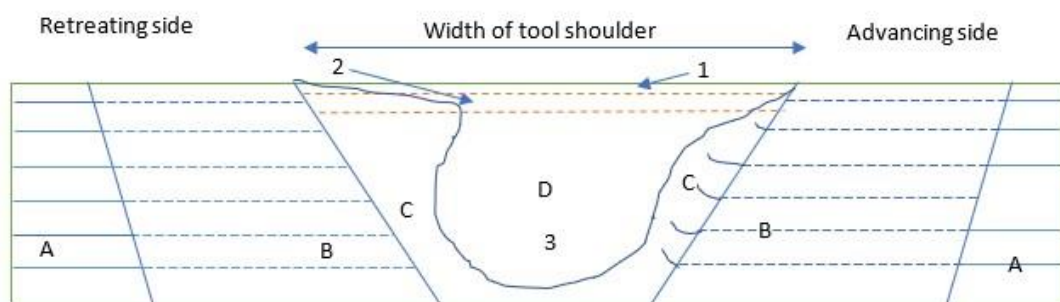


Figure 9: Showing diagram of typical aluminium alloy FSW microstructural areas.

Parent material (PM), indicated by “A” in Figure 9. Material is sufficiently distant from the nugget to remain unaffected in both microstructure and mechanical properties.

Heat Affected Zone (HAZ), indicated by “B” in Figure 9. Area is thermally affected with consequences to the microstructure and mechanical properties. It is not significantly plastically deformed.

Thermo-Mechanically Affected Zone (TMAZ), indicated by “C” in Figure 9. Area is thermally affected and plastically deformed with consequences to the microstructure and mechanical properties. The microstructural change in this area is primarily through recovery (The Welding Institute, 2013).

Nugget, indicated by “D” in Figure 9. For aluminium alloys the nugget lies within the TMAZ and is formed at the hottest part of the weld where the material has undergone dynamic recrystallization. The nugget is off-set from the centre of the weld due to the asymmetry in FSW.

These areas are also shown in an actual weld in Figure 10. In this weld “SN” references the “stir nugget” or nugget, and the defects identified were owing to the original parent material being cast.

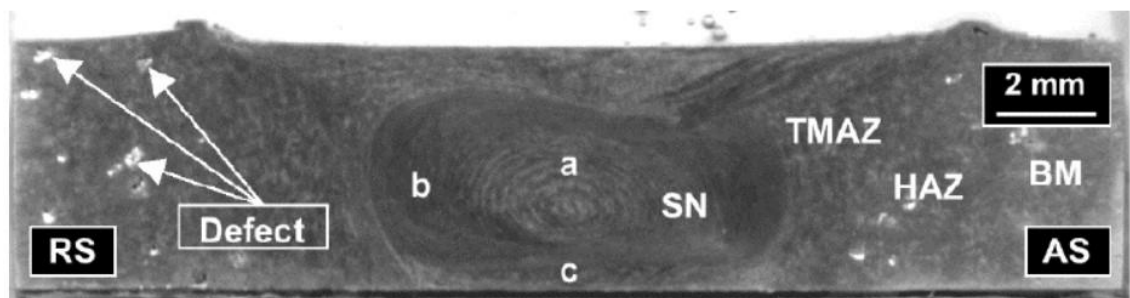


Figure 10: Showing FSW of an Al-Si casting. This image has been reproduced from Bhadeshia (no_date) who identifies Professor J. Fukii of JWRI Japan as the source (no reference provided).

The “onion ring” effect can often be observed in this area (not shown in Figure 9) and is characterised by metallurgical banding, the origin of which is alternatively attributed to: periodical deposition of layers of material behind the tool; differences in grains sizes in the deposited layers; and variations in particle density in the layers (Mishra et al., 2014; The Welding Institute, 2013; Threadgill et al., 2009; Threadgill & Leonard, 1999). Additionally, several areas can often be observed in the nugget, as indicated by numbers 1-3 in Figure 9: 1) a Shoulder Affected Zone (SAZ); 2) a pin and shoulder influenced region; and 3) a pin influenced region (Ahmed, M., Wynne, Rainforth, & Threadgill, 2008).

2.3.2 Stationary Shoulder Friction Stir Welding (SSFSW)

Stationary Shoulder FSW (SSFSW) was developed at TWI (Gibson et al., 2014) in 2004 and was intended for welding materials with low thermal conductivity (Martin, 2013), such as titanium, in an effort to mitigate an uneven temperature distribution (Li, Z. et al., 2016). SSFSW differs from conventional FSW in that the shoulder does not rotate; the pin rotates and provides the majority of frictional heat generation while the shoulder slides over the surface providing forging pressure only (Gibson et al., 2014). According to Neto and Neto (2013) approximately 60-80% of the heat in conventional FSW is generated by the rotating shoulder due to the tool/workpiece relative velocity. This leads to a significant temperature gradient between the top and bottom surfaces of the workpiece. Using SSFSW, a narrower, more focused HAZ may be produced. The reduced temperature gradient can be used to control residual stress and distortion in thin sheet aluminium welds when compared with conventional FSW (He et al., 2019).

A diagram showing the microstructural areas of a typical SSFSW is shown in Figure 11. This shows the smaller HAZ area associated with SSFSW when compared with conventional FSW. Two shapes of nugget have been observed in the literature, depicted by the green and orange dashed lines. The green line describes a V-shaped/conical morphology which reasonably follows the shape of the tool pin. This shape was achieved by Ji, Li, Zhou and Zhang (2017), Ahmed, Wynne, Rainforth and Threadgill (2011), Zhang et al. (2015) and Patel, Li, Liu, Wen and Su (2019). Ahmed et al. (2011) attribute the increased width at the top of the weld to an increase in the tangential velocity of the tapered pin as its diameter increased, coupled with the stationary shoulder acting as a heat sink on the top surface. The second shape, depicted by the orange dashed line has been described in the literature as “spherical” (Liu et al., 2013), “basin-like” (Dong et al., 2019) and “drum-shaped” (Li, D., Yang, Cui, He, & Zhang, 2015). It generally forms a bulbous shape and can have the maximum width either at the weld mid-thickness or close to the weld bottom. Examples of these shaped from literature are shown in Figure 12. There is little in the literature to explain the difference in shape, however Liu et al. (2013) suggest that at faster traversing speeds the high tangential velocity on the surface of the pin cuts material rather than allowing it to stick. In this way slower traversing speeds achieve the orange dashed line shape, gradually changing to the green dashed line shape at higher traversing speeds. A review of the weld parameters used by other

researchers shows some support for this; the images provided by Zhang et al. (2015) (Figure 5 of their work) show a changing morphology towards a more well-defined V-shape/conical as the traversing speed is increased. However, some researchers achieved the V/conical shape at relatively slow traversing speeds (Ji et al. (2017) at 50 mm/min and Patel et al. (2019) at 100 mm/min). It should however be noted that while Liu et al. (2013) used a stationary shoulder in their research, the pin encompassed a sub-sized rotating (with the pin) shoulder which they acknowledge would also be a contributory factor together with the increasing traversing speed to the difference in weld morphology.

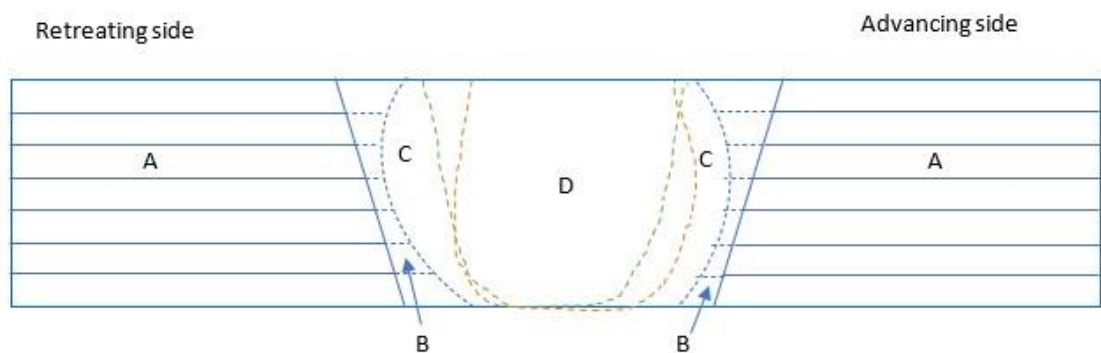
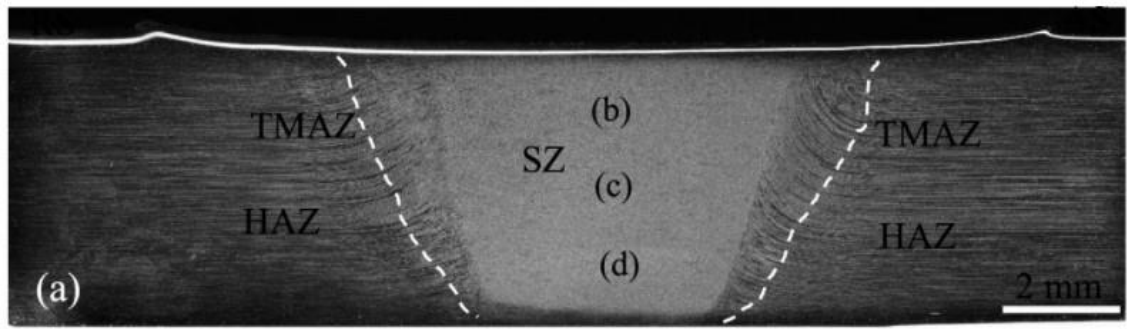
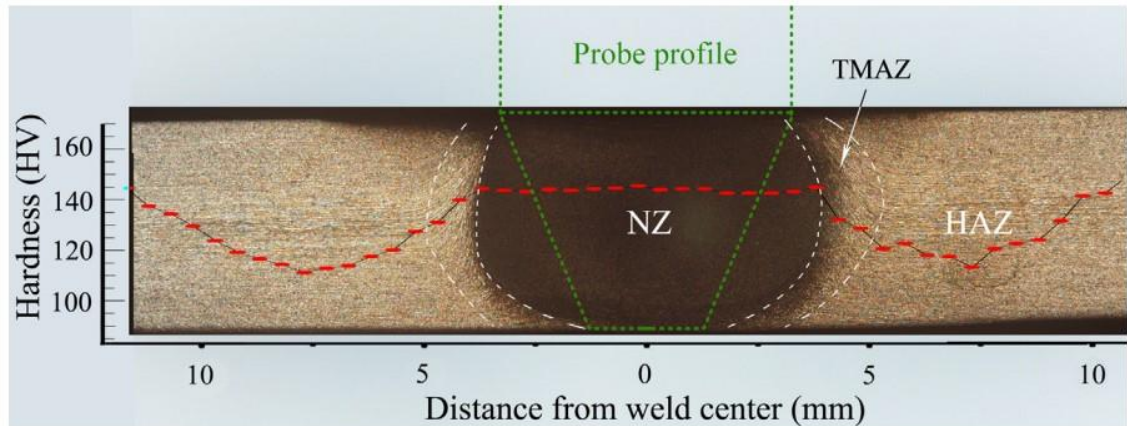


Figure 11: Showing diagram of typical aluminium alloy SSFSW microstructural areas. Labels A, B, C and D have the same meanings as per Figure 9. The nugget depicted by the orange dashed line described the “spherical/ basin/ drum” shape, while the nugget depicted by the green dashed line describes the conical “V” shape.



(a)



(b)

Figure 12: Showing (a) SSFSW AA7075-T651; microstructure shape broadly follows that of the pin, courtesy of Patel et al. (2019), and (b) SSFSW AA7075-T651; microstructure is described as “drum” shaped, courtesy of Li et al. (2015).

SSFSW can also be used to mitigate against thinning of the workpiece (Liu et al., 2013). TWI (Martin, 2013) had success using SSFSW on titanium and aluminium alloys and produced smooth weld surfaces with no thinning of the workpiece at the centreline, an issue for conventional FSW especially in thin sheet, and small HAZ areas. Li et al. (2016) incorporated both a conventional FSW tool and an external stationary shoulder to weld 3 mm thick Alclad AA2024-T4 and observed negligible weld thinning, little flash, a smooth surface. They concluded that using the external stationary shoulder produced fewer defects at a wider range of parameters than conventional FSW. Wu, Chen, Strong and Prangnell (2015) found that when they compared conventional FSW of AA7050 with SSFSW, the weld thinned <0.2 mm on the SSFSW compared with ~1 mm on the FSW specimens. This reduction in thinning was a result of the far reduced heat generation from the stationary shoulder meaning that the colder material could support the

shoulder's downforce without sinking into the material. Additionally, they found that the surface finish was greatly improved on the SSFSW welds, with a surface roughness parameter (R_a) over an order of magnitude lower than for conventional FSW. This was attributed to the "ironing" effect of the stationary shoulder sliding over the weld surface during traverse.

SSFSW has also been used effectively for joint geometries which do not lend themselves to conventional FSW, such as fillet joints. Martin (2013) describes the procedure in which a rotating pin inside a non-rotating shoulder is shaped to the internal corner of the plates to be welded and can be used to create corner joints.

Chehreh, Grätzel, Bergmann and Walther (2020) carried out studies comparing fatigue and corrosion resistance of AA5754 when welded using conventional FSW, SSFSW and dual FSW (the shoulder rotates in the opposite direction from that of the pin). The fatigue resistance of SSFSW welds was found to exceed both that of the conventional FSW and the dual FSW, and was comparable with that of the unwelded parent material. This was attributed to the lower heat generated by the tool for SSFSW, and to the introduction of beneficial compressive residual stresses introduced to the weld by the stationary shoulder. The SSFSW specimens also performed best in the corrosion tests, second only to the unwelded parent material specimens.

Although no reference to the "ideal" SSFSW surface appearance was found, a large amount of the literature praise smooth, ironed surfaces. Li, Yang, Cui, He and Shen (2014) created smooth weld surfaces which did not require subsequent machining and which, they considered, would be beneficial to the fatigue resistance of the finished weld. They found that the weld top surface width was equivalent to the diameter of the stationary shoulder. Sejani, Li and Patel (2021) found that the stationary shoulder produced an ironing effect whereby the sliding motion of the shoulder over the joint removes markings on the top surface. They did however find that the contact friction between the stationary shoulder and the weld surface causes material adhesion and removal which created a duller appearance at the edges of the weld surface, in comparison to the centre area of the weld surface which was more reflective; they termed this change in appearance to be "scraping traces".

There are some known issues with SSFSW in that the tool design leads to large forces being applied to the pin in the welding direction which can lead to failure, and material has been found to flow into the space between the shoulder and the pin resulting in the requirement for regular cleaning (Barbini, Carstensen, & dos Santos, 2018). Sinhmar and Dwivedi (2020b) developed a tool which essentially self-cleans due to its innovative design, however the volume of research available on SSFSW is still far smaller than that of conventional FSW.

The parameters used when welding using either FSW or SSFSW are of great importance and have a significant effect on the quality of the weld; see section 2.3.9 for further details.

2.3.3 FSW/ SSFSW of AA8090

There is little documented in the literature specifically targeting FSW of AA8090 and no research could be found on SSFSW of this alloy, perhaps due to the use of AA8090 falling out of popularity as FSW and latterly SSFSW gained momentum.

Lertora and Gambaro (2010) investigated optimal parameters for defect free joints in 5 mm thick AA8090-T8 using conventional FSW perpendicular to the material's rolling direction. They used a tool tilt angle (see section 2.3.9.1.2) of 2° and a modest range of rotational (230, 330 and 460 rpm) and traversing speeds (115 and 170 mm/min) in their comparison. The results of their hardness, tensile and fatigue tests are reported in the relevant sections of this chapter, however they did report zero distortion during welding attributed to low thermal load and radiographic tests found no defects in any of the weld parameter combinations used. They achieved a fine equiaxed grain structure in the nugget, in which the grain size grew as the weld ratio (rotational speed/ traversing speed) increased due to change in heat input to the weld. The nugget contained large precipitates concentrated at the grain boundaries with the concentration much greater in the nugget than in the parent material (no analysis on the type of precipitates was provided).

Pedemonte, Gambaro, Lertora and Mandolino (2013) studied conventional FSW on 5 mm thick AA8090-T8. They used welding parameters of 2° tool tilt angle, rotational speed 330 rpm and traversing speed 175 mm/min. The parameters were sourced from

elsewhere (Ponte, 2007)² and stated to be the optimal parameters for this material, although a “kissing bond” defect (see section 2.3.10) was observed on one weld.

Vigraman et al. (2021) studied FSW of 10 mm thick AA8090 (temper not provided) using a range of rotational speeds (800, 1000 and 1200 rpm) with constant traversing speed (2.5 mm/s). Optical microscopy and SEM revealed the presence of fine grains and intermetallic compounds likely to have been Al₂Cu, AlCuLi, β-phase, FeAl₂, Mn₃Si₂Al₁₂ and oxides throughout the nugget. It was observed that Li containing precipitates were concentrated more at the weld nugget than at the interface between the weld and the parent material (presumed by this author to refer to the HAZ/ TMAZ). They postulated that this was a result of centrifugal action of the thermo-mechanical process, segregating the heavier elements and compounds to the interface.

Panwar and Chandan (2021) investigated FSW of 5 mm thick AA8090 (temper not provided), although the measured composition of the material was outside the tolerances given in the specifications in Table 2 (Li 3.07 %wt and other discrepancies). They used the Taguchi design process to reduce the number of experiments required to predict and achieve optimal weld parameters; these parameters were found to be rotational speed 1400rpm, traverse speed 25 mm/min, 7 s dwell time with 0° tool tilt based on the mechanical testing (discussed later in the relevant sections). Note, the parameters tested used different weld ratios throughout the experiments.

2.3.4 FSW/ SSFSW of BS L165/ AA2014

A significant amount of work has been carried out on FSW of AA2014; this is discussed throughout the subsequent sections where appropriate, e.g. with respect to tool design, weld parameters etc. Where not specifically stated as being alclad, the author has assumed the material to be bare, i.e. with no alclad layer.

BS EN 4632-002:2008 (Aerospace and Defence Industries Association of Europe - Standardization (ASD-STAN), 2008b), with reference to BS EN 4632-001:2008 (Aerospace and Defence Industries Association of Europe - Standardization (ASD-STAN), 2008a) recommends that AA2014 has a degree of weldability for FSW welding rated as

² Note: the author did not have access to this original source.

2. This is defined as “material with good weldability but which may require special precautions when welding (for example preheating, low advance speed, etc)”.

Rajendran, alongside various other researchers, has carried out substantial research into FSW of AA2014. Rajendran, Srinivasan, Balasubramanian, Balaji and Selvaraj (2018) carried out FSW of 2 mm thick AA2014-T6 (believed not to be alclad) and found fine and equiaxed grains in the nugget, with fewer (presumably than pre-weld) but uniformly distributed and fine 2nd phase precipitates (Al₂Cu). The large precipitates found in the parent material (Al₂Cu and Fe-Mn-Al) were fractured within the nugget due to the extensive plastic deformation involved. The TMAZ showed severely deformed non-recrystallised grains, and no significant grain boundary coarsening was observed in the HAZ. Rajendran, Parthiban, Pranav and Nithi Balaji (2021) and Rajendran, Srinivasan, Balasubramanian, Balaji and Selvaraj (2016) investigated the effect of post-weld heat treatments (PWHT) on the properties of FSW AA2014-T6. They found that the previously identified soft region in the HAZ/ TMAZ was reduced in width and shifted towards the centre of the weld/ nugget due to the dissolution of coarse precipitates in the aluminium matrix and precipitation of fine θ' particles. Rajendran, Srinivasan, Balasubramanian, Balaji and Selvaraj (2019a) compared the peak load obtained from tensile tested TIG welded, FSW and riveted sheets of AA2014-T6. They found that the TIG welded specimens gave a peak load approximately 50% that of the FSW samples with comparable results to single cover riveted butt joint and a riveted lap joint, with the double cover riveted butt joint having almost double the load carrying capability of the TIG welded butt joint and approximately 40% stronger than the TIG welded lap joint.

Lin, Zhao and Wu (2006) conducted testing on 8 mm thick AA2014 and considered that the welded joint could be regarded as finite thin layers throughout the thickness and carried out their testing accordingly by sectioning it into 3 layers. They found that the mechanical properties varied throughout the thickness with the weakest being the middle layer. This was attributed to the influence of the shoulder on the top layer which inputted more heat into this part of the weld and allowed material to flow more freely with less variation in microstructure between the different zones of the weld (eg. HAZ, nugget etc.). The middle and lower layers were influenced only by the pin and experienced a lower heat input as a result. The middle layer also absorbed more heat and had reduced heat output than the lower layer experienced (due to heat dissipation

from the lower layer to the backing plate), resulting in it softening more than the other layers.

In the work conducted by Ramanjaneyulu, Madhusudhan Reddy, Venugopal Rao and Markandeya (2013) on 5 mm thick AA2014-T6 it was found that although the lowest hardness value was measured on the advancing side TMAZ/ HAZ, the softened region was wider on the retreating side than the advancing side due to the material flow (relatively higher velocity difference between the tool and the material) on the advancing side, and therefore tensile failure always occurred on the retreating side.

Das, Robi and Sankar (2020) examined the microstructure of their most successful (judged on mechanical properties) FSW AA2014 (temper not provided). They found that the grains at the top of the nugget were finer compared with the bottom due to the influence of the shoulder, although they do not quantify the difference in size. They measured (via the Heyn line intercept method) that the average grain diameter at the top of the nugget was 84% smaller than that of the parent material. The grains at the advancing TMAZ were slightly smaller than those at the retreating side (advancing 66% smaller than parent material and retreating side 64% smaller). They state that the material is extracted from the advancing side, moved around the tool and deposited on the retreating side and then the advancing side undergoes dynamic recrystallisation resulting in finer grains. They postulate that this is the reason that their tensile tests failed at the retreating side TMAZ. The grain size in the HAZ (no distinction between retreating and advancing) was 35% smaller than the parent material.

Muhammad et al (2021) compared FSW 2.5 mm thick AA2014 sheets in the T0 and T6 tempers. They observed partial onion rings in both, although they were more dominant in the T6 temper. They stated that the onion ring feature demonstrated sufficient plastic flow in the weld with the plasticised material deposited in layers and owing to an uneven distribution of hard particles. For T6 the majority of precipitates were metastable of which many were dissolved in the aluminium matrix during FSW. The fraction of stable precipitates was unaffected by FSW and became segregated into high strain regions resulting in high and low particle density bands within the nugget. In the T0 condition there were far fewer metastable precipitates to dissolve as the majority existed in the stable state, thus the banding effect was less prominent. They also observed a transition area between the nugget and TMAZ on both sides of the T6 weld, however this was

more distinct on the advancing side. This was due to the advancing side producing greater shear forces and plastic strains because of the direction of travel and material flow, producing a distinct “line” between the nugget and the TMAZ. There was no distinguishable boundary between the HAZ and the parent material due to no recrystallisation occurring in that area. The did note that in some cases the grain size may be slightly larger in the HAZ than in the parent material and precipitates can dissolve or coarsen which results in a reduction in hardness.

A novel “self-cleaning” (does not allow build-up of material on the shoulder) stationary shoulder tool was used (Sinhmar & Dwivedi, 2020b) to weld 6mm thick AA2014 and compared with conventional FSW. They observed a more uniform nugget, a smaller shoulder-affected region and a narrower HAZ on the SSFSW. The interface between the nugget and TMAZ on the SSFSW was less distinct with some mixing between the two and the grain size in the nugget was smaller. The size of the strengthening precipitates was also found to be smaller in the nugget and HAZ of the SSFSW, in the range of 35 nm-65 nm and 61 nm-124 nm respectively, compared with 60 nm-83 nm and 94 nm-197 nm in the conventional FSW. Precipitate density was measured as 122 precipitates/ μm^2 and 67 precipitates/ μm^2 in the SSFSW nugget and HAZ respectively, compared with 89 precipitates/ μm^2 and 40 precipitates/ μm^2 in the FSW. Further work (Sinhmar & Dwivedi, 2020a) was carried out on the same material to compare the width of HAZ and corrosion properties between FSW and SSFSW using the same novel tool. They measured the width of the HAZ at mid-thickness (advancing or retreating side not specified) and found the FSW to be 2.69 mm and the SSFSW to be 1.18 mm, with the precipitates in the nugget and HAZ of FSW measuring 0.55-0.69 μm and 0.53-0.83 μm respectively, and in the SSFSW 0.44-0.58 μm and 0.43-0.53 μm . The precipitates at grain boundaries of the HAZ of the FSW were continuous, while those at the grain boundaries in the HAZ of the SSFSW were unconnected.

2.3.5 FSW/SSFSW of Dissimilar Aluminium Alloys

As BS L165 is used as a repair material for the original AA8090 used on the aircraft it is necessary to consider joining the two materials together. This is currently achieved through riveting, however it is possible to FSW dissimilar materials; both different aluminium alloys and different types of metal. Mishra et al. (2014) explain how consideration of the different melting points of the materials to be welded and thus the ease of material flow at different temperatures must be considered and how the positioning of each, i.e. which is situated on the advancing side and which on the retreating side, is of great importance. They also note that there is conflicting data within the literature regarding this positioning.

There is a plethora of research on dissimilar FSW within the literature. For brevity, this review was intended to be limited to those most relevant for this research, i.e. dissimilar FSW/ SSFSW involving AA8090 or BS L165/ AA2014. No research was found on FSW of AA8090-BS L165/AA2014, and indeed none regarding any dissimilar welds incorporating AA8090, therefore other Al-Li alloys shall be included. Joining of aluminium alloys to other metals (e.g. steel, copper) is not considered in this review.

2.3.5.1 Dissimilar FSW containing Al-Li

A significant number of studies concerned FSW of the Al-Li alloy AA2198 to dissimilar aluminium alloys, particularly AA2024 (although there are others). The compositions of these materials are shown in Table 7.

Table 7: Showing elemental compositions of AA2024 and AA2198 (Robe et al., 2015), all compositions in wt%.

Alloy	Cu	Li	Mg	Ag	Mn	Fe	Zn	Si	Ti	Al
AA2024	3.8-4.9	-	1.2-1.8	-	0.3-0.9	0.5	0.2	0.5	0.15	Remainder
AA2198	2.9-3.5	0.8-1.1	0.25-0.8	0.1-0.5	0.5	0.1	0.35	0.08	-	Remainder

Robe et al (2015) examined FSW 3.2 mm thick AA2198-T3 – AA2024-T3, with AA2198 positioned on the advancing side and the weld perpendicular to the rolling direction of AA2198 and parallel to the rolling direction of AA2024. This configuration was selected to overcome the anisotropic mechanical behaviour present in both, with the

longitudinal tensile properties of AA2198 similar to the transverse tensile properties of AA2024. They found that the advancing HAZ/ TMAZ region was narrower than the retreating as previously discussed regarding similar metal FSW, however it was not possible to distinguish between the HAZ and TMAZ using optical microscopy alone. Two distinct areas were observed in the etched nugget, showing the two materials separated by an S-shaped boundary, and Energy Dispersive X-ray (EDX) analysis mapping confirmed the lack of mixing of the two materials based on the Mg content on each side of the S. A banded onion ring structure was observed within the AA2198 part of the nugget, however the SEM analysis confirmed that this was not due to mixing of the materials, rather a difference in grain orientation. Macroscopic and microscopic analysis, together with Electron Backscatter Diffraction (EBSD) suggested that the joining mechanism was due to mechanical impingement and micro-joining of the grains, rather than actual mixing of the materials.

Khalilabad, Zedan, Texier, Jahazi and Bocher (2021) welded the same materials in the same orientations and referenced the reasons given by Robe et al. (2015) for welding using those orientations. They produced welds which had nuggets with 3 areas, rather than 2, with each area separated by 2 S-shaped borders which was attributed to the variant flow rate of the material at the centre and around the pin, shown in Figure 13. The first S shape separated AA2024 and AA2198, with the second separating two areas of AA2198 with a variation in Mg between all three areas. This microstructure was not explained fully but it was suggested that different recrystallisation mechanisms may be at play.

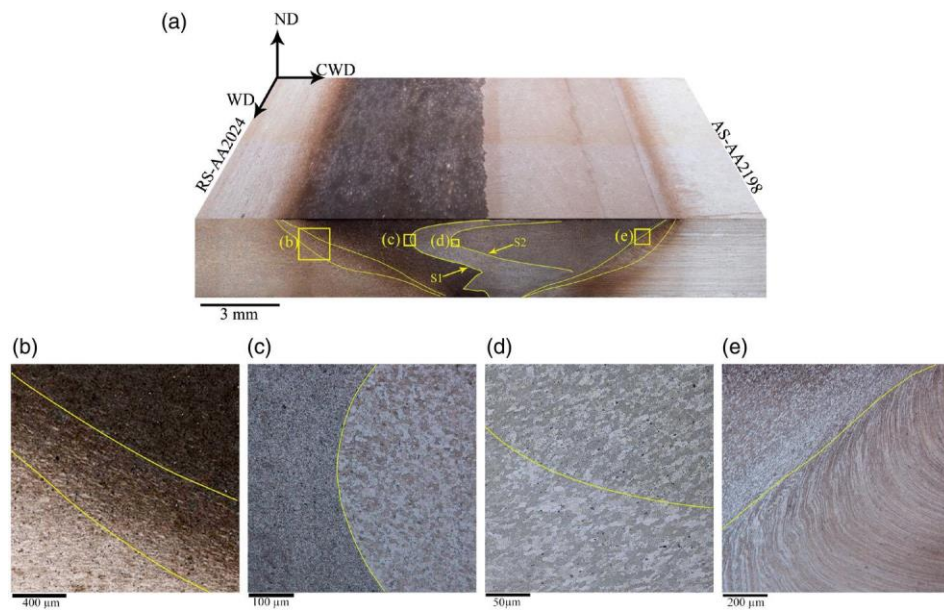


Figure 13: Showing double S-shape on AA2198-AA2024 dissimilar weld, reproduced from Khalilabad et al. (2021): a) whole joint; b) retreating side transition between parent metal and nugget; c) 1st S-shape transition in nugget; d) 2nd S-shape transition in nugget; e) advancing side transition between nugget and parent material.

Wu, Deng, Fan, Ji and Zhang (2018) studied dissimilar 10 mm thick Al-Li-Cu and Al-Zn-Mg-Cu FSW alloys (actual alloy designation not provided) in the T6 condition, with the welding direction parallel to the rolling direction of both plates and the Al-Zn-Mg-Cu alloy on the advancing side. Microscopy showed that the S-shape previously described in the nugget was not present, however there were clear areas consisting of each alloy and the two alloys were “metallurgically integrated” via an interface. When analysed it was shown that Mg had diffused from the Al-Zn-Mg-Cu alloy to the Al-Li-Cu alloy.

2.3.5.2 Dissimilar FSW containing BS L165/ AA2014

A significant volume of work exists on dissimilar FSW of AA2014 and AA6061. The composition of AA6061 is 0.4-0.8 Si, 0.7 Fe, 0.15-0.4 Cu, 0.15 Mn, 0.8-1.2 Mg, 0.04-0.35 Cr, 0.25 Zn, 0.15 Ti with the remainder as Al (Hema, Sai Kumar Naik, & Ravindranath, 2017). Raturi, Garg and Bhattacharya (2019) conducted dissimilar FWS of the two materials (6.1 mm thick) in T6 condition, with AA6061 on the advancing side (no information on the material orientations was provided). Using a selection of pin types (see section 2.3.9.2) they reported thorough mixing and “heterogeneous interlocking”

(not defined in the study but presumed to refer to uneven intimate mechanical joining) of the materials in the nugget. The tensile tests failed in the advancing HAZ and this was attributed to the softened zone (due to thermal influences and the accumulation and coarsening of Mg_2Si precipitates) and inherently weaker properties of AA6061-T6 compared with AA2024-T6.

Venkateswara Rao and Senthil Kumar (2020) joined 10 mm thick plates of the same materials (temper unknown) with AA2014 on the advancing side. Clear onion rings were apparent in the nugget, with no S-shape, shown in Figure 14. They reported alternate layers of the two alloys formed in the nugget (Figure 14c and d), due to the stirring action of the tool, and the presence of 2nd phase particles from both materials within these onion rings. The authors of the two studies based on AA2014-AA6061 dissimilar welds discussed so far used different process parameters and tools so a direct comparison cannot be made between the two for judging which configuration is superior, i.e. which side the AA2014 is positioned in based on only this. It was however noted that the most successful tests achieved 74% joint efficiency (based on the lower AA6061 UTS) for AA2014 on the retreating side (Raturi et al., 2019), and 70% with AA2014 on the advancing side (Venkateswara Rao & Senthil Kumar, 2020). In other studies, AA2014 was positioned on the retreating side with the most successful weld achieving 65% joint efficiency (Nadikudi, 2021), and 68% joint efficiency (Raturi & Bhattacharya, 2020).

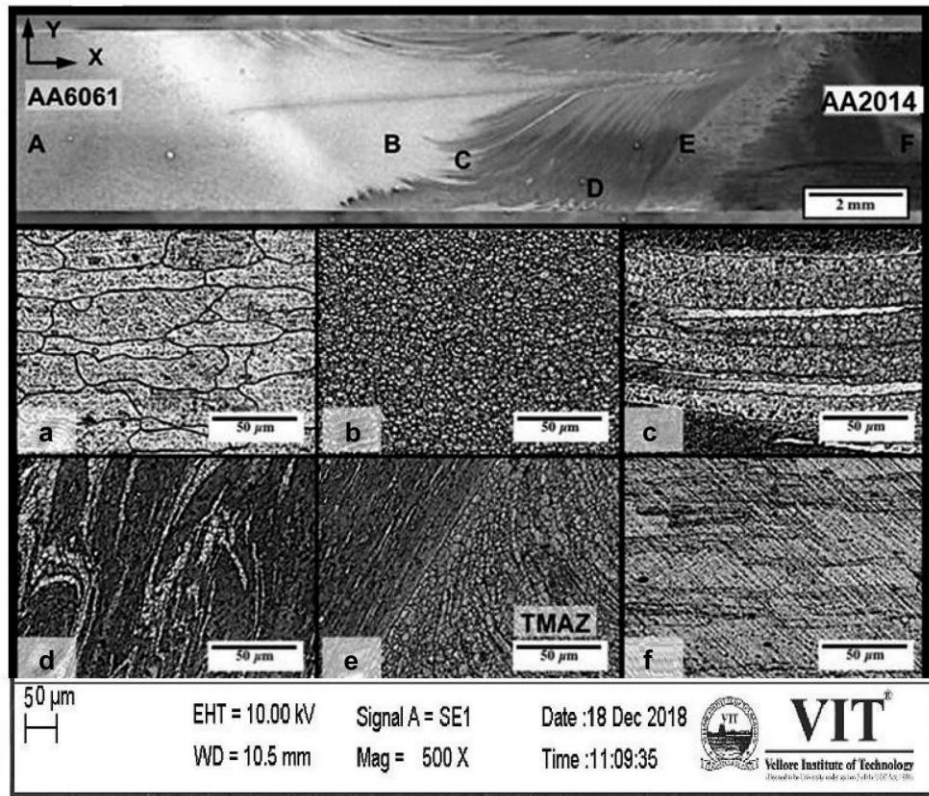


Figure 14: Showing the various zones of AA6061-AA2014 weld, produced from Ventakeswara Rao and Senthil Kumar (2020).

Raturi and Bhattacharya (2020) also carried out testing on AA2014 welded with AA7075 (AA2014 on the retreating side). They found that although the tensile strength of these welds exceeded that of AA6061-AA2014 (due to the higher initial strength of AA7075), the ductility was severely reduced to only 2.3% elongation. The joint efficiency was not included in the study but these have been calculated as 64% for AA7075-AA2014 and 63% for AA6061-AA2014 (based on UTS values in ASTM B209M-14 (ASTM International, 2014)). Saravanan, Banerjee, Amuthakkannan and Rajakumar (2015) positioned AA2014 on the advancing side of their AA2014-AA7075 joints and achieved 76% joint efficiency for their most successful weld. They found that an appropriate welding speed and diameter of shoulder/ diameter of pin ratio (D/d) was required to achieve proper mixing of the two materials without resulting in turbulent flow, i.e. sufficient heat input was required to properly plasticise the materials and achieve sufficient movement from the advancing side to the retreating side.

2.3.5.3 *Dissimilar SSFSW of aluminium alloys*

Very few studies could be found regarding SSFSW of dissimilar aluminium alloys (most concern dissimilar aluminium to another metal, e.g. steel, copper), with none on the materials under investigation in this research.

Barbini, Carstensen and dos Santos (2018) carried out comparisons of FSW and SSFSW of 2 mm thick sheet AA2024 T3-AA7050 T7651 with AA2024 positioned on the advancing side. That decision was taken based on previous work indicating that the best results are achieved when the weaker material is on the advancing side (previous work is not referenced). It was necessary to use different parameters for the FSW and SSFSW to achieve defect-free welds due to the different amounts of heat input from the rotating or stationary tool influence, i.e. the SSFSW had a rotational speed of 1200 rpm, compared with only 600 for the FSW. The same pin was used for both welds. They noted a lack of shoulder affected zone in the SSFSW with the nugget profile strongly resembling the pin profile. There was a resultant reduction in the width of the TMAZ in SSFSW, especially in the upper half of the weld thickness due to the far reduced influence of the shoulder, i.e. it was not stirring the material to cause deformation. The authors used EDX to analyse the degree of interdiffusion between the two materials by measuring across an onion ring. To find the amount of diffusion they measured the Zn content, as there is a significant difference in content between the two materials (AA7075 6.2wt% and AA2024 0.25 wt%). Both welds had a sharp interface between the alloys, with a thin zone of interdiffusion; this level of interdiffusion decreased with increasing traversing speed (due to lower heat input). FSW had a slightly larger interdiffusion thickness of 17-20 μm (SSFSW 13-16 μm), which was attributed to the lower heat input in the SSFSW process. The tensile test results (for the most successful welds) were reported as 86.4% for FSW and 94% for SSFSW.

2.3.6 FSW/ SSFSW of Al-clad Material

In their literature survey, Zhang, Xiao, Wang and Ma (2011) describe the work of Talwar et al (2003)³ where it was found that the alclad layer on AA2024 FSW was drawn into the weld at the advancing side at the boundary of the nugget and the TMAZ, causing deterioration of the mechanical properties. The solution was to remove the alclad layer on the root side via machining; Zhang et al. (2011) assert that this is not a best practice solution, hence their work into the effect of the alclad layer in AA2024 FSW. They compared 6.5 mm thick alclad AA2024-T351 with 5.0 mm thick unclad AA2024-T351 using varying weld parameters to monitor the change in material flow, especially with respect to the alclad layer. Regions of residual alclad were observed on the top and bottoms of the welds. Using a small plunge depth and low traversing speed, the bottom surface alclad layer was drawn into the weld at the boundaries of the nugget on both the advancing and retreating sides. A build-up of alclad material was observed beneath the tool shoulder region (the thickness was noted as 0.5 mm while the original layer was only 0.2 mm) as the material in close proximity to the pin was severely deformed and flowed to the shoulder. There was found to be a distinct difference in material flow around the tool between the alclad and unclad FSW, and the top layer was found to play an important part in this difference in flow. They noted that the soft alclad layer between the shoulder and the parent material created a “lubricating” effect during FSW, reducing the friction coefficient which in turn reduced the plastic deformation of the parent material in the SAZ, with the size of the SAZ being smaller than that for unclad FSW. This made the pin-affected region much more important, and the parameters used critical to the quality of the weld. Slow rotational speed or fast traversing speeds caused the alclad material from the bottom surface to extend into the weld along the nugget boundaries.

In addition to studying the effect of tools, process parameters and initial temper on 3 mm thick AA2014 FSW lap welds and Friction Stir Spot Welds (FSSW), Babu et al. (2012; 2013) examined the effect of the alclad layer. They found the presence of alclad made little difference to the microstructure or mechanical properties of the finished FSSW or

³ Cited as R. Talwar, D. Bolser, R. Lederich and J. Baumann: 4th Int. Symp. Friction Stir Welding, Park City, UT, 2003. Based on the authors listed, it is considered that this actually refers to a paper in the 2th International Symposium on Friction Stir Welding in 2000, however neither paper could be obtained by the author to review.

lap welds. They did however note that as the alclad is removed from the top surface during welding, the finished weld may be more susceptible to corrosion.

Rajendran, Srinivasan, Balasubramanian, Balaji and Selvaraj (2019) tested a variety of parameters when carrying out FSW of 2 mm thick alclad AA2014-T6, however could not achieve a joint efficiency of greater than 83% which was attributed to the redistribution of the alclad layer providing a preferred path for crack propagation. They also found that 90% of the tensile failures occurred at the advancing side TMAZ which was attributed to thermal softening and grain coarsening, and the differing velocity gradient of plasticised materials between the advancing and retreating sides.

Aoh, Huang and Lin (2013) found that during FS lap welding of 1.6 mm AA2024-T3, the alclad layer between the two sheets appeared as a continuous layer throughout the nugget, despite the pin penetrating through this area (they acknowledged that no other authors had reported this outcome). As a result they carried out work to find a tool which could better break or deform the alclad layer in this area. They concluded that a cylindrical or sector-shaped threaded tool best achieved this, however the mechanical properties for the welds created by the cylindrical tool were not improved by disruption of the alclad layer, although those of the sector-shaped tool were. This was attributed to the formation of onion rings in those welds made by the sector-shaped tool.

When conducting FSW of 0.8 mm alclad AA2024-T4 sheets, Yue, Wang, Yang, Wu and Yan (2018) found that different parameters resulted in differing amounts of redistribution of the alclad layer. At 100 mm/ min traversing speed an unbroken layer of alclad was observed in the nugget drawn from the top surface; at 150 mm/min alclad was observed flowing upward into the nugget from the bottom surface. This was attributed to the plasticisation of the weld and uneven material flow between the advancing and retreating sides of the weld.

2.3.7 FSW/ SSFSW of Thin Sheet Aluminium Alloy

FSW of thin or ultra-thin (< 1 mm, sometimes referred to as micro-FSW (μ FSW), (Scialpi, De Giorgi, De Filippis, Nobile, & Panella, 2008) sheet creates additional complications over the more comprehensively studied thicker sheet. These complications include the issue that most FSW results in a small reduction in thickness over the stirred area due to the forging effect of the shoulder. This is generally acceptable for thicker materials as the percentage reduction is negligible. For thin or ultra-thin sheet however, this could result in a significant reduction in mechanical properties of the weld (Scialpi et al., 2008). Huang, Meng, Zhang, Cao and Feng (2017) stated that generally the thickness reduction always reduces the tensile properties and that the thickness reduction should not exceed 10% of the parent material thickness to avoid tensile property reductions, however this statement was not elaborated on nor its origin cited. Scialpi et al. (2008) examined FSW 0.8 mm AA2024-T3 and AA6082-T6 in both similar and dissimilar configurations. The welds suffered approximately 15-25% thickness reduction (calculated from the reported images) which was blamed in part for a reduction in mechanical properties and location of tensile failure. Scialpi et al. (2008) also caution against micro defects which, again, may be acceptable in thicker sheet welds but could be highly detrimental to thin or ultra-thin sheet welds.

Dong et al. (2019) joined 0.8 mm thick AA2024 sheets using SSFSW for lap welds and compared with conventional FSW of the same material. They found that the surface roughness of the SSFSW was improved by almost 50% compared with the FSW and noted that material loss was reduced, achieving 96% of the original thickness when the traversing speed was 200 mm/min and 85% and 91% at lower traversing speeds. This was attributed to the stationary shoulder acting as a sealed barrier to block plasticised material escaping as flash, and faster traversing speeds allowing for reduced plasticisation of the material than at slower speeds; at slower (and thus hotter) speeds the shoulder penetrated further into the material due to the softer material and thinned the weld. The authors found that the lap shear failure loads of the SSFSW were generally higher than the FSW which they attributed to lower heat input from the stationary shoulder.

Fourier's law of heat conduction shows that the rate of heat conduction is inversely proportional to the thickness of the material (Çengal & Turner, 2001), thus thinner

materials conduct greater amounts of heat in a fixed period of time. Additionally, the surface to volume ratio of the plasticised zone increases with decreasing zone radius, i.e. as the thickness decreases, the surrounding parent material provides a means for more rapid heat dissipation (Teh, Goddin, & Whitaker, no_date). A challenge of μ FSW is compensating for the heat loss (sufficient heat is required to form a weld) resulting from the reduced thickness, without introducing weld parameters which would cause deleterious effects on the weld, for example higher rotational speeds with relatively large tool shoulders can cause tearing of thin sheet materials (Teh et al., no_date). To compensate for the substantial heat loss, Park, Joo and Kang (2020) studied the effects of backing plates with different thermal conductivities (ceramic, titanium alloy and copper alloy) on the weldability and mechanical properties of dissimilar 1 mm FSW AA6061-T6 and AA5052-H32. The copper alloy plate (with a higher thermal conductivity) caused poor stirring at the bottom of the weld interface resulting in defects and poor mechanical properties while the ceramic plate produced welds with the maximum tensile strength of the three due to a reduction in heat loss from the weld.

Separation of the sheets whilst welding is also an issue for thin sheet, for which Sattari, Bisadi and Sajed (2012) employed clamps (always used in FSW) and a roller forward of the tool to hold the sheets in place when FSW 0.8 mm thick AA5083-H323. The problem arose that as the tool rotated it could lift the thin sheet as it traversed due to motion and the thermal gradient; this is not typically an issue for thicker sheet or plate due to the increased stiffness. The roller in front of the tool stopped this lifting effect and thus prevented sheet separation. In addition to sheet separation, the introduction of distortion to the sheet material can arise due to the high thermal gradient. Ahmed and Saha (2018) developed a fixture to secure 0.5 mm thick AA6061-T6 and then compared various weld parameters. The fixture involved a 35 mm thick stainless steel backing plate, asbestos cover plates, a top clamp which reached close to the weld area and lateral clamps to minimise movement and distortion. Despite these precautions a degree of distortion was observed in all welds; concave bending was observed in the longitudinal direction and convex distortion in the transverse direction.

The rigid clamping, necessary to hold the workpiece in place and mitigate distortion, impede the thermal contraction in both the longitudinal and transverse direction and therefore lead to the introduction of residual stresses in the weld. This is discussed in

greater detail in section 2.3.9.3.4, however it is intuitive that due to the higher distortions inherent to thin sheet FSW that this may be more of a concern than with thicker materials.

2.3.8 FSW/ SSFSW Mechanisms

2.3.8.1 *Material Flow*

FSW is a thermo-mechanical process, i.e. it relies on both heat and material flow to stir the workpiece material to create a weld. There are various studies throughout the literature documenting how the material flows in a complex pattern in the locality of the tool and that the pin and shoulder have differing influences on the flow. Based on marker experiments, Mishra et al. (2014) schematically describe the role of the shoulder and pin in moving material, as shown in Figure 15. The shoulder (represented by images a and b in Figure 15) transfers the marker from the advancing to the retreating side, while the marker on the retreating side is moved to the advancing side. The difference between the two is that the rotational movement from the advancing side pushes the material vertically downward into the weld, while the rotational movement from the retreating side pushes the material vertically upwards towards the surface which can result in flash. The pin (represented by images c and d in Figure 15) transfers the material from the advancing side by almost a full pin circumference to return to approximately its original lateral position. The marker on the retreating side is pushed behind the tool by the pin. There is a similar vertical movement of the material as to that described for the shoulder. The interface between the bottom surface of the pin and the material works in a similar manner to that of the shoulder. It was however noted that other authors have described more complex movement of material.

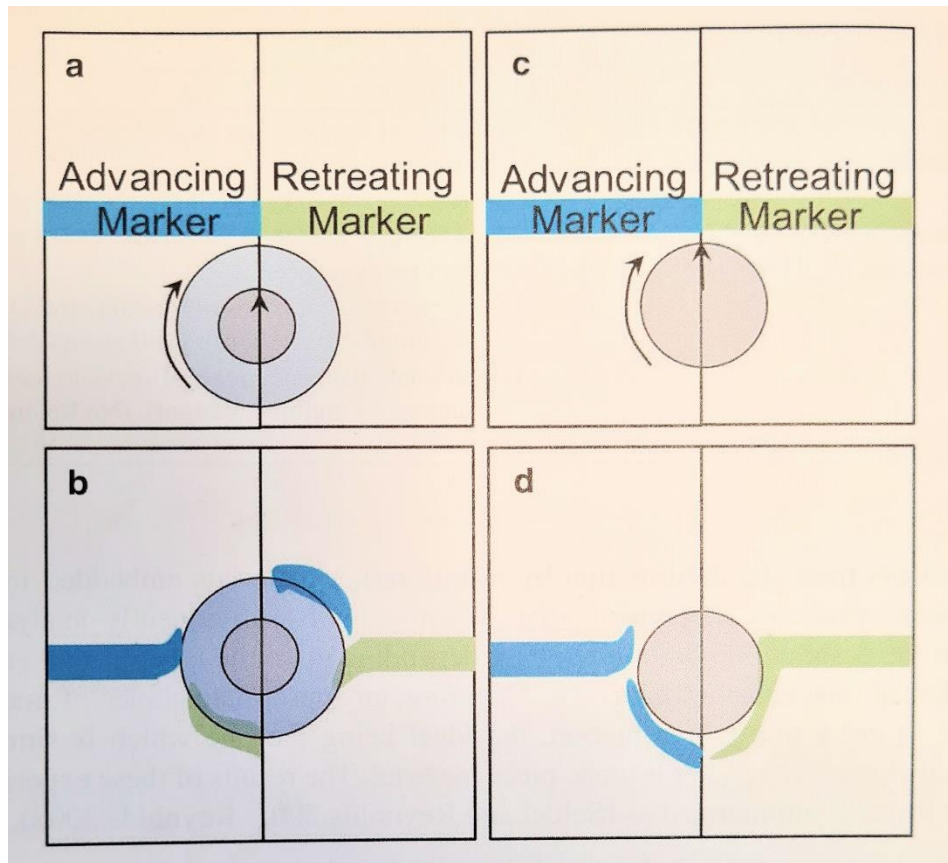
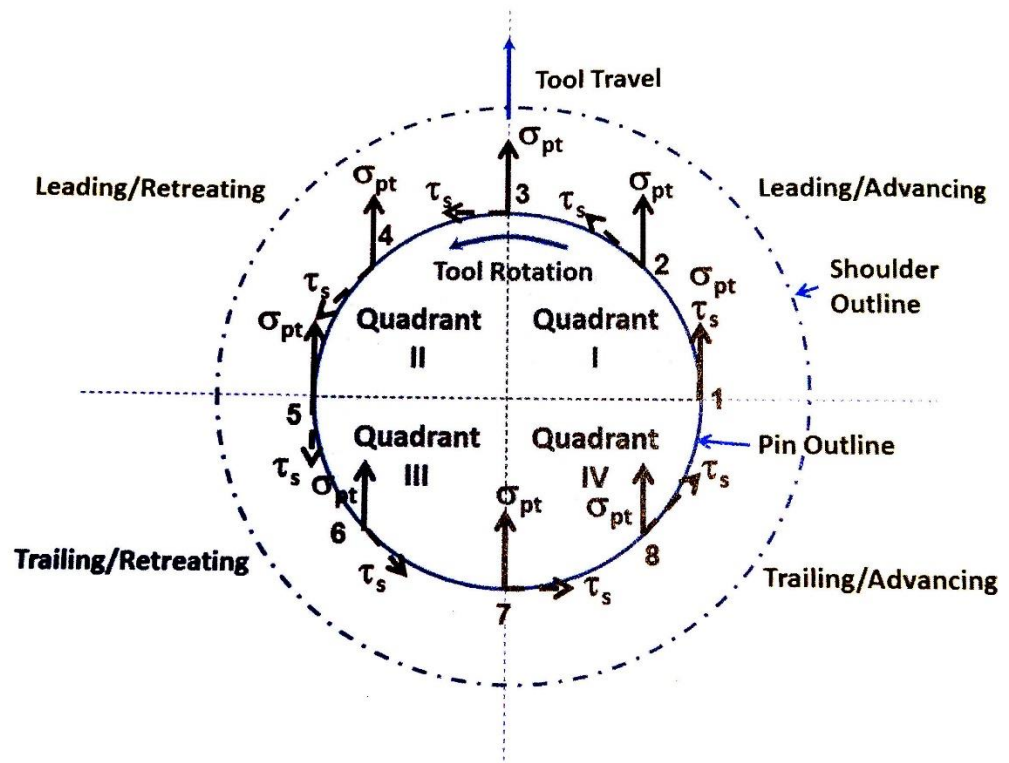


Figure 15: Showing schematic representation of material movement based on the roles of the shoulder (a and b) and the pin (c and d). Reproduced from Mishra et al. (2014).

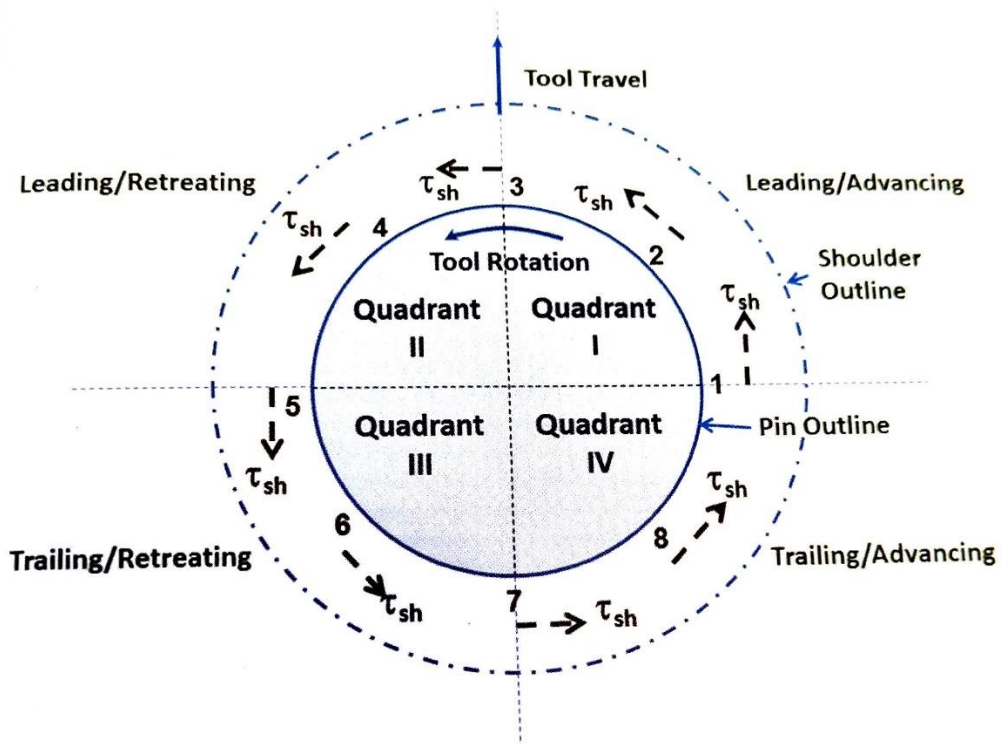
The deformation, i.e. material movement, is closely related to the thermal cycle which determines the degree of material flow. Mishra et al. (2014) state that due to the dynamic recovery experienced during the process, in FSW the material strain becomes independent of the stress due to plastic flow and deformation follows a flow based on the premise that the material behaves like an incompressible fluid. They assert that based on experimentation and modelling, material flow close to the pin occurs mainly via shear and can be split into different zones. The rotational zone is positioned immediately adjacent to the pin and the material movement is a mix of transverse, longitudinal and angular displacement. The transition zone is a sheared layer situated between the rotational zone and the undeformed material border. These areas (rotational and transition) comprise the shear zone. Mishra et al. (2014) report on equations developed by Long, Wang and Reynolds (2007) calculating the strain at different points of the FSW shear zone. The estimated strain distribution showed that the strain on the retreating side was approximately zero, reaching a maximum on the

advancing side; Mishra et al. (2014) postulated that this corresponds to experimental findings where the shear zone has a sharp transition at the advancing side (between the nugget and TMAZ) while there is a far more gradual transition on the retreating side.

In order to understand the forces in play during FSW, Mishra et al. (2014) developed simplified schematics of forces around the pin and shoulder, shown in Figure 16.



(a)



(b)

Figure 16: Showing the forces around the (a) pin, and (b) shoulder during FSW. Reproduced from Mishra et al. (2014).

Referring to the pin forces, Mishra et al. (2014) describe the shear force (Figure 16a) as always tangential and represented by τ_s ; for a cylindrical pin with no features (rare, see section 2.3.9) the force interacts with the material in a uniform manner. The normal force exerted by the pin in the direction of travel, i.e. as it traverses, is represented by σ_{pt} . The images have been split into 4 quadrants to describe the region of interest. On the leading side (quadrant 1 (QI) and quadrant 2 (QII)) the σ_{pt} pushes the material to the pin surface while the σ_{pt} on the trailing side (QIII and QIV) exert no pressure on the material behind; this leads to lack of consolidation behind the pin. If the pin shape is changed from cylindrical to conical a downward component of σ_{pt} will be introduced which enhances material flow and consolidation. This can also be resolved with a tool tilt (discussed in section 2.3.9) which again introduces a downward element to σ_{pt} .

In their examination of FSW alclad AA2024, Zhang et al. (2011) described the material flow during the process through use of “stop-action” where they used a brittle tool which would break at various stages during the process and allow the material flow to be observed. They found that the material moved closely with the pin, and it could be observed that the material flowed vertically downward on both the advancing and retreating sides of the pin, with a vertical swirl occurring beneath the pin, and the bottom alclad layer being mixed into the parent material with no extension of the alclad layer into the weld at the high traversing speed used. At the trailing side the shear layer detached leaving a temporary “hole” behind the pin. At a cross-section close to the edge of the pin, the previously detached shear layers were deposited and formed the onion ring structure described previously. These detached layers moved upwards to fill the temporary hole being pushed by incoming material. They noted that the parent material around that hole was pushed into the hole at the retreating side, suggesting that the hole was displaced by the upward sheared material attributed to the pin and downward sheared material attributed to the shoulder.

2.3.8.2 Temperature and Heat Generation

Mishra et al. (2014) state that the heat generation in FSW results from two sources: friction between the tool and the workpiece surface (predominantly in the case of conventional FSW rather than SSFSW); and heat generated during plastic deformation/ adiabatic shear within the weld/ workpiece. The frictional force is dependent on both

the physical and chemical properties of the tool and material (e.g. macro/microscopic asperities on the surfaces), plus the loading and velocity of the process. Heat is generated at different areas of the tool; the shoulder, pin shaft and pin bottom/ tip. There are several models for the frictional heat generation at each of these areas however these are not discussed further here. The heat generation from plastic deformation within the material is demonstrated by Mishra et al. (2014) in that when a tensile test is performed, part of the total energy expended in the process is converted to heat (the test-piece will feel warm/ hot to the touch depending on the material after failure), while the rest is stored in the material microstructure. It is generally acknowledged in the literature that the majority of heat generation arises from the frictional contact between the shoulder and the workpiece (Barbini et al., 2018; Mishra et al., 2014).

When comparing FSW and SSFSW of dissimilar 2 mm thick AA2024-T3 and AA7050-T7651, Barbini et al. (2018) found that different welding parameters were required for the different processes due to the severe reduction of heat generation from the stationary shoulder when compared with the conventional tool; the SSFSW required higher rotational speeds and slower traversing speeds to achieve sufficient heat generation to produce material flow which would result in defect free welds. The higher rotational speed allows for greater material flow around the pin, however the lack of heat generated by the shoulder results in less overall material being affected. This can result in higher loading on the pin, especially at higher traversing speeds as the material directly in front of the pin has less time to heat and soften due to the more localised thermal field. He et al. (2019) used an external stationary shoulder in addition to the smaller rotating shoulder and pin. They found that the external stationary shoulder absorbed a significant amount of the heat generated, resulting in a slower heating rate and increased cooling rate of the material, and uniform temperature distribution throughout the thickness of the workpiece.

2.3.8.3 FSW microstructural evolution in the various zones

As previously alluded to there are several microstructural evolutions that occur during FSW due to the thermo-mechanical process involved, resulting in different distinct zones within the weld. Mishra et al. (2014) summarised these evolutions schematically, as shown in Figure 17.

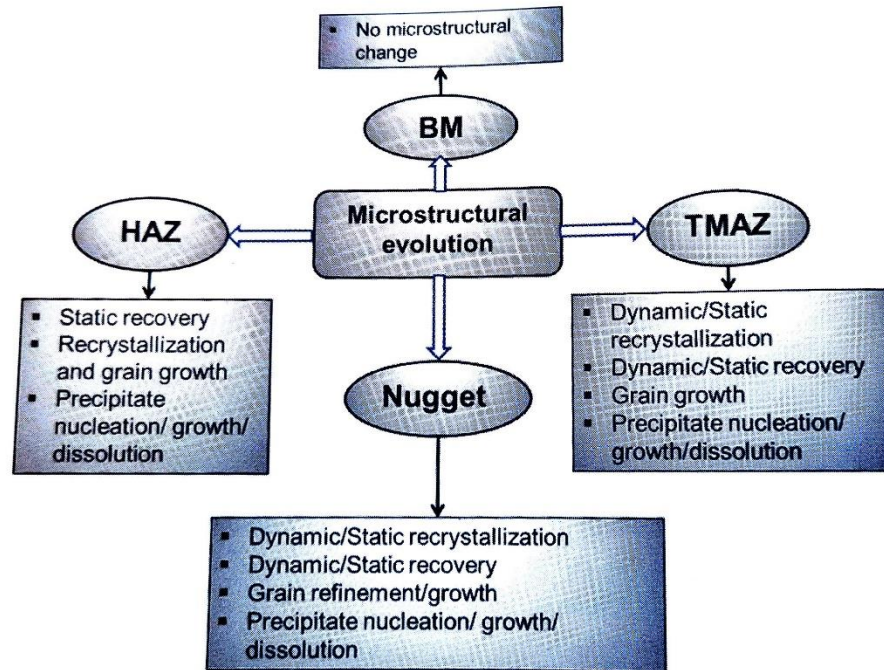


Figure 17: Showing schematic of the microstructural evolution in different zones of FSW material. Note BM = base material and is equivalent to parent material. Reproduced from Mishra et al. (2014).

The parent material (or base material as is shown in Figure 17) remains unchanged by the process; this material is sufficiently removed from the tool as to not be affected by either the thermal or mechanical aspects of the process. The HAZ is only affected by the thermal aspects of the process therefore depending on the parent material microstructure and processing history it is possible for static recovery, recrystallisation and grain growth and precipitation to occur, although most authors do not report recrystallisation as having occurred. The TMAZ is plastically deformed under a thermal cycle therefore its microstructural evolution is comparable to hot-working. In this zone dynamic recovery and recrystallisation will be followed by static recovery and recrystallisation, grain growth and precipitation, dependent on the original parent material, with the development of dislocations.

In the nugget there are three stages to the microstructural evolution. Stage I refers to the material being moved within the shear layer to the trailing side of the tool. In stage II there is a combination of stress and thermal activity in which the microstructure undergoes repeated grain growth, dynamic recovery and dynamic recrystallisation (similar to TMAZ). Once the pin has moved and the material is no longer within its deformation zone, stage III occurs involving static recovery, static recrystallisation and grain growth (similar to the HAZ).

2.3.9 Parameters, Tools and Mechanical Properties

This section shall comprise of a description of various elements of parameters, tools and mechanical properties relevant to the current research and their influence on the finished weld. A summary of the literature which relates parameters, tools and the mechanical properties of the weld shall then be provided in section 2.3.9.4, Table 10. There is a plethora of literature available documenting research on FSW of aluminium alloys and one cannot hope to capture it in its entirety, therefore only the literature deemed particularly relevant to the current research due to the materials, process, thickness, cladding or configuration used will be included.

2.3.9.1 *Parameters*

Several variables influence material flow and temperature distribution in FSW/ SSFSW. Because of this, the resulting quality of weld is dependent on these variables including rotational and traversing speeds, plunge depth and tilt angle.

2.3.9.1.1 *Rotational and traversing speeds*

Rotational and traversing speeds are two of the most important parameters in FSW due to their role in frictional heat generation within the material and therefore the influence they exert over the finished weld quality (Sidhy & Chatha, 2012). As suggested by the name, rotational speed refers to the rate at which the tool rotates and is usually measured in rotations per minute (RPM). The traversing speed is the rate at which the tool travels along the weld line and is usually measured in mm/min. In general, as the rate of rotation increases so too does the amount of heat generated and thus the amount of plasticisation, until a point where the material is over-softened and the frictional influence is no longer valid (The Welding Institute, 2013). Referring to the

traversing speed, if the tool travels slowly heat generated via friction and plastic deformation has time to conduct ahead of the tool and thus the tool will move into pre-heated and softened material. This also applies to the dwell time discussed in section 2.3.1. Conversely if the tool travels quickly, the heat generation and conduction and therefore plasticisation ahead of the tool is reduced. “Cold welds” (low rotational speed, high traverse speed) can produce higher strength welds due to less thermal damage having occurred (The Welding Institute, 2013) but can lead to wormhole defects or insufficient penetration (Mishra et al., 2014). “Hot welds” (high rotational speed, low traverse speed) enhance material flow and reduce the transverse force on the tool, reducing the likelihood of tool breakages (The Welding Institute, 2013). However, this can cause surface lack-of-fill as the shoulder struggles to contain the material (Mishra et al., 2014) and material strength may be reduced due to an increased HAZ. Defects associated with FSW are discussed in further detail in section 2.3.10. The rotation of the tool also provides the means of stirring the material – very important in friction “stir” welding. However, this is closely related to the heat generation allowing material flow discussed previously.

As stated previously, rotational speed is usually measured and reported in RPM; indeed, this appears to be the industry standard unit and the vast majority of literature report it in this manner. This, however, presents a difficulty in comparison of process parameters between researchers and studies. If tools of different diameters are used at the same RPM, the actual linear speed of the tool (or a point on the tool surface) would be different for the different tools. This in turn affects the amount of heat generated in the weld, and thus studies using the same RPM but different tool diameters are not directly comparable.

An example could be a comparison of two studies, both of which use a rotational speed of 1000 RPM, but one uses a tool with a 5 mm pin diameter (at its widest point), and another which uses an 8 mm pin diameter. The RPM is converted to angular velocity using Equation 2, and has units of radians per second (rad/s):

$$\omega = \frac{RPM}{60} 2\pi \quad \text{Equation 2}$$

And so in this example, the angular velocity for both would be 104.72 rad/s

And the linear speed is then calculated from Equation 3, with units of meters per second (mm/s).

$$v = \omega r \quad \text{Equation 3}$$

Where r is the radius of the tool pin.

In this example, the linear speeds are 261.8 mm/s and 418.88 mm/s for the 5 mm and 8 mm diameter tool pins respectively. It is thus clear that more heat would be generated using the larger tool.

As RPM appears to be the industry standard in terms of reporting rotational speed, this is the format which has been reported in this research when describing work in literature. However, the reader should keep in mind this issue when considering these studies.

2.3.9.1.2 Tool tilt angle

The tool is often tilted, typically 0-3° (He et al., 2019; Mishra et al., 2014; The Welding Institute, 2013), so that the rear (heel) of the tool is slightly lower than the front and exerts a downward force on the plasticised material behind the pin, helping to consolidate the weld (the “hole” discussed in section 2.3.8.1). This tilt also has the benefit of “riding” up and over the material ahead of it rather than trying to gouge its way through (The Welding Institute, 2013). This tilt is usually used on tools with flat or concave shoulders, however it can sometimes be used effectively on those tools with scrolled shoulders (The Welding Institute, 2013), see section 2.3.9.2.2.

2.3.9.1.3 Plunge depth

The plunge depth refers to the measurement from the pin bottom/ tip to the top surface of the workpiece during welding (Mishra et al., 2014) and has a strong influence on weld penetration. In general, a pin length which is approximately 95% of the material thickness should be sufficient to successfully FSW most aluminium alloys as mixing occurs below the tip of the pin (The Welding Institute, 2013), however if the pin is too short this mixing would not be sufficient thus the plunge depth can be altered. If a short pin is used, plunge depth can be increased to generate more heat within the material to promote material flow (The Welding Institute, 2013) by increasing the shoulder contact

with the workpiece, although care must be taken not to impart shoulder grooves in the top surface. Increasing the plunge depth also reduces the distance between the pin tip and the bottom of the workpiece and can apply a larger downforce on the surface of the material improving consolidation (The Welding Institute, 2013).

2.3.9.1.4 Tool offset

The entire tool, or just the pin, position can be offset from the weld centreline; this is mainly used in dissimilar metal welds, i.e. aluminium alloys with ferrous alloys to compensate for the difference in material melt temperatures by primarily concentrating the heat generation on the side with the lower melt temperature to promote thorough material mixing or to avoid excessive tool wear by reducing contact with the harder material (Ahmad Shah, Midawi, Walbridge, & Gerlich, 2020; Mishra et al., 2014). It was suggested (de Backer, 2015) that an offset may also be used when joining very thin material as it may be sensible to separate the pin from the centreline to ensure maximum material mixing across the faying surfaces, however no evidence of this can be found in the literature.

2.3.9.2 Tools

The tool selection is of vital importance to the success of the weld; the tool must physically survive the welding process and the pin and shoulder must promote sufficient mixing within the workpiece to produce a sound weld.

2.3.9.2.1 Tool material

The tool material must be able to withstand the loads imposed during welding as it plunges, rotates and traverses, especially at the start of the weld when both the tool and workpiece are cold, and it must be able to withstand the welding temperatures generated during the process without melting or deterioration, i.e. the tool material must be both stronger than the workpiece parent material and have a significantly higher melt temperature. Mishra et al. (2014) list 6 characteristics that a suitable tool material should possess: 1) sufficient strength at both ambient and welding temperatures; 2) adequate fatigue strength at weld temperature; 3) satisfactory fracture toughness; 4) suitably resistant wear characteristics; 5) long term thermal stability; and 6) chemical stability, i.e. it will not react with the workpiece parent

material. When considering aluminium alloys as the workpiece parent material, two popular choices are H13 tool steel and MP159 cobalt base super-alloy (Mishra et al., 2014; The Welding Institute, 2013). H13 is easily available, relatively low cost and is suitable for FSW lower strength aluminium alloys, while MP159 has high strength and moderate ductility and is readily machinable in its as-received state; both materials require hardening heat treatments for use in FSW (The Welding Institute, 2013). There are however drawbacks of both materials in the form of wear susceptibility; a weaker material (i.e. the aluminium workpiece) can induce wear on the tool material in certain circumstances, e.g. an aluminium containing hard intermetallic particles over a long weld(s). Additionally, in an industrial environment where long, continuous (potentially miles, e.g. ship building) of runs are required, fatigue life at elevated temperatures becomes an issue (Mishra et al., 2014).

2.3.9.2.2 Tool features

The tool geometry plays an important part in controlling material flow during FSW. According to The Welding Institute (2013) the role of the shoulder is to generate heat both via friction on the surface indirectly via material shear below the shoulder, exerting a down force to hold in material and consolidate the weld and to feed material towards the pin. They show that the role of the pin is to break up and disperse oxide layers and contaminants, generate heat via friction in order to plasticise the material and to mechanically mix the separate plates/ sheets of material. There are a wide range of tools available; Mishra et al. (2014) pictorially summarise some of the common features of FSW, shown in Figure 18.

A FSW shoulder can be flat, concave or convex (Mishra et al., 2014), however flat or concave tools typically require a suitable tool tilt angle to achieve a sound weld (Mishra et al., 2014; The Welding Institute, 2013) and convex shoulders require a scroll (Mishra et al., 2014), although scrolls can be used on flat and concave shoulders also. The scroll acts to sweep material in from the edge of the nugget towards the centre which aids in weld consolidation.

With regards to the pin, The Welding Institute (2013) asserts that cylindrical and plain tapered tools can struggle to effectively mix the material vertically which can lead to wormhole defects (see section 2.3.10). Threads on pins generate more heat and can

improve material flow due to the introduced down force. Mishra et al. (2014) show that a stepped spiral pin will displace more material per rotation than a threaded pin and have a larger down force. Flutes and flats are used on a tool pin where it is important that the remnant oxide film is fully broken up; these features disrupt material flow in both the horizontal and vertical directions, so that instead of continuous flow (as with a threaded or spiral tool) the material is displaced discontinuously and the oxide film is successfully broken up (Mishra et al., 2014).

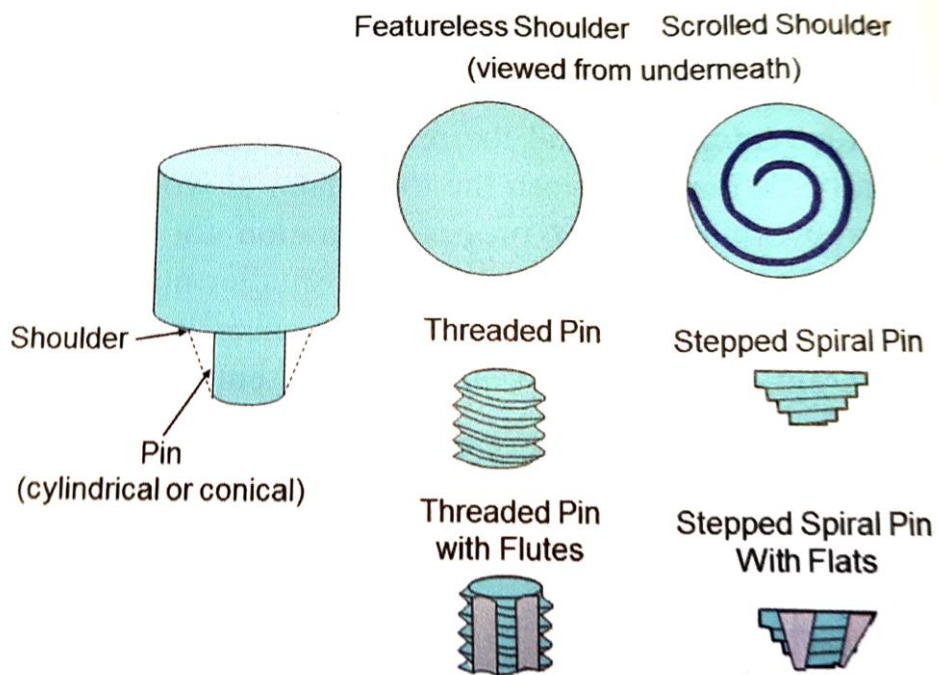


Figure 18: Showing some features of FSW tool shoulders and pins. Reproduced from Mishra et al. (2014).

Verma, Gupta and Mishra (2016) provide illustrative tables detailing the characteristics of shoulder and pin designs; these have been reproduced here in Table 8 and Table 9.

Table 8: Characteristics and effects of different shoulder geometries on FSW.
 Reproduced from Verma et al. (2016)

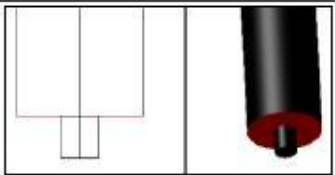
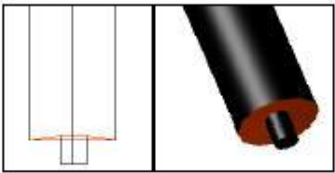
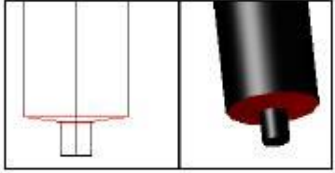
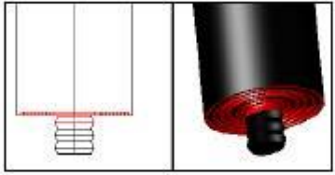
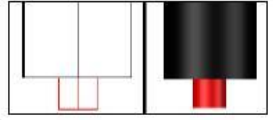
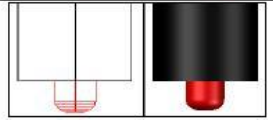
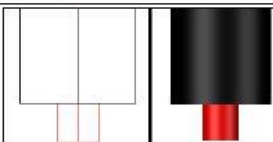
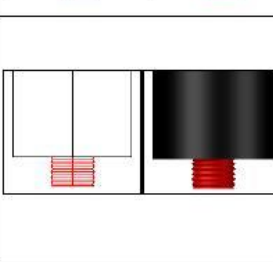
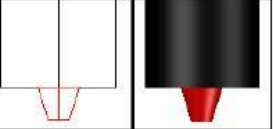
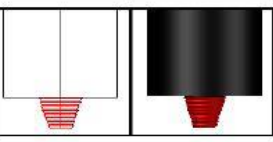
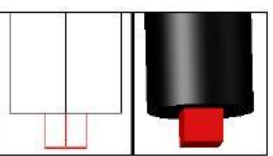
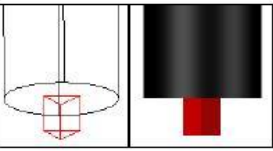
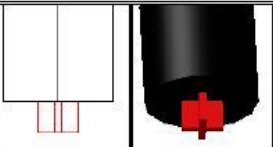
Geometry	Characteristics and effects	Example
Flat Shoulder	<ul style="list-style-type: none"> • Simple in design • Fails to entrap flowing metal beneath shoulder surface during process due to this flash increases. 	
Concave Shoulder	<ul style="list-style-type: none"> ✓ Most commonly used shoulder which is simple in design and easily machined. ✓ It is easy to control the flowing metal beneath the surface and it reduces flashes. ✓ It requires tilt angle (1° to 3°). ✓ Improves surface integrity and Stirring 	
Convex Shoulder	<ul style="list-style-type: none"> • It is worst design of shoulder which pushes the flowing material away from the probe due to this strength decreases. • It may be used for material having thickness below 1mm. 	
Scroll Shoulder	<ul style="list-style-type: none"> ✓ Features geometry used on shoulder surface. ✓ Complex in design and difficult to machine. ✓ It avoids tilt angle and produces same amount of weld quality as compared with concave shoulder. ✓ Shoulder surface increases friction during process which increases stirring phenomena and improve weld and surface quality. ✓ Containment of soften material ✓ Enables higher welding speed 	

Table 9: Characteristics and effects of different pin geometries on FSW process.
 Reproduced from Verma et al. (2016).

Geometry	Characteristics and their effects	Example
Flat Surface Pin	<ul style="list-style-type: none"> • High plunge force requirement 	
Domed Surface Pin	<ul style="list-style-type: none"> ✓ Requires less plunge force ✓ Improve quality of weld and tool life. 	
Cylindrical Pin without Thread	<ul style="list-style-type: none"> • Simple in Design • No pulsating stirring. 	
Threaded Cylindrical	<ul style="list-style-type: none"> ✓ Ratio of plasticized material from static volume to dynamic volume (ratio of swept volume) is 1.01. ✓ No pulsating stirring. ✓ Compression of weld zone. ✓ The stirring material moves from the top to bottom of the pin via threads and deposited in the stir zone. 	
Geometry	Characteristics and their effects	Example
Tapered Cylindrical	<ul style="list-style-type: none"> • Ratio of plasticized material from static volume to dynamic volume (ratio of swept volume) is 1.09. • No pulsating stirring. 	
Threaded Taper	<ul style="list-style-type: none"> ✓ Extremely uniform particle distribution. ✓ Hardness of the joint has good correlation with the grain size 	
Square Pin	<ul style="list-style-type: none"> • Incompressible material flow • Ratio of plasticized material from static volume to dynamic volume (ratio of swept volume) is 1.56. • Pulsating stirring. • Higher mechanical strength 	
Triangular Pin	<ul style="list-style-type: none"> ✓ It is associated with eccentricity ✓ Incompressible material flow during the process. ✓ Ratio of plasticized material from static volume to dynamic volume (ratio of swept volume) is 2.35. ✓ Pulsating stirring. ✓ Higher mechanical strength. 	
Four Flute Square	<ul style="list-style-type: none"> • Large Cluster formation in nugget zone. • Hardness of the joint has good correlation with the grain size. 	

2.3.9.3 Mechanical Properties

Several of the most common mechanical properties examined in FSW research are considered below, with the main trends for each discussed and the literature summarised in Table 10 of section 2.3.9.4.

2.3.9.3.1 Hardness

A hardness profile is an illustrative means of indicating a change in mechanical properties across the cross section of a weld. Threadgill et al. (2009) summarise the generic hardness profiles for heat treatable and non-heat treatable aluminium alloys graphically, which are shown in Figure 19. Of greatest interest to this research is the heat treatable alloys in T6 and overaged conditions which typically take the form of a “W”. It is cautioned by Threadgill et al. (2009) that care should be taken during interpretation of hardness results from literature due to: natural aging occurring post weld as the elapsed time between welding and measurement is not always provided; the load used for hardness testing, as low loads can introduce higher uncertainty and scatter; some researchers may choose to mount their samples in a hot press which can further age the material; and most researchers take the hardness measurements through the mid-point of the cross section, however this is not always stated and there is a variation in hardness throughout the thickness of the specimen.

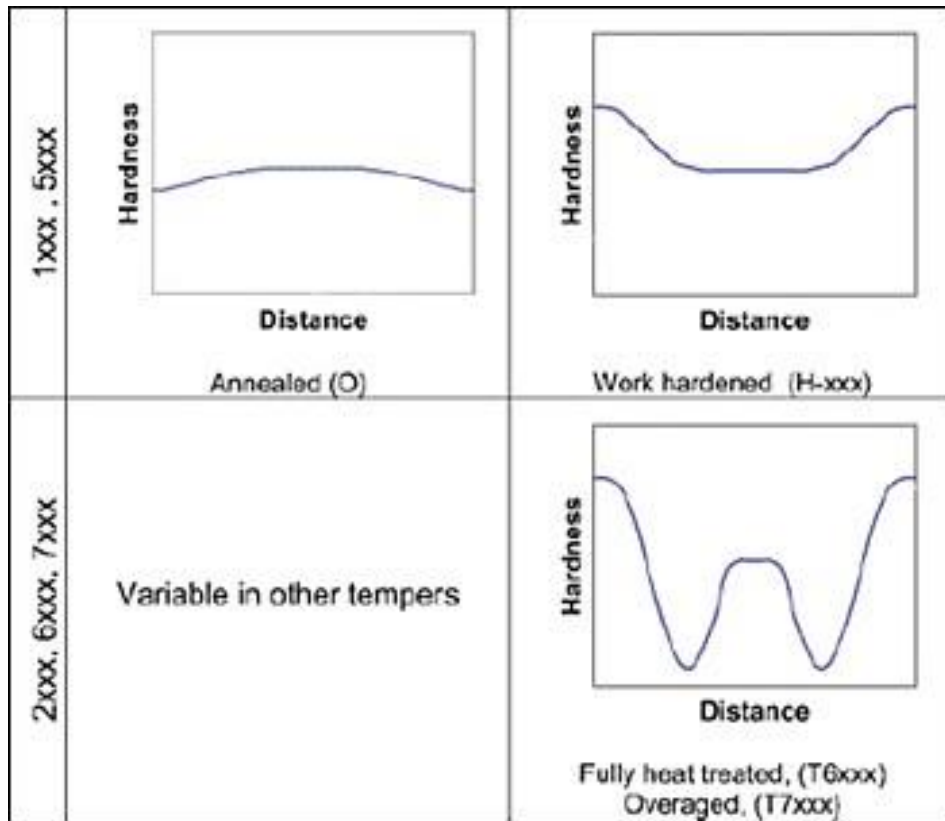


Figure 19: Showing plots of generic hardness profiles for non-heat treatable (top images) and heat treatable (bottom images) aluminium alloys in various tempers. Reproduced from Threadgill et al. (2009).

The “W” shaped hardness profile shown in Figure 19 is formed due to the thermal inputs and microstructural evolutions in the different zones of the weld, as described previously. Threadgill et al. (2009) describe the hardness as being at a peak in the parent material, then a softening in the HAZ with sharp reduction as the TMAZ is approached with the minimum hardness values typically being observed at the HAZ/ TMAZ boundary. Some of the hardness is regained in the nugget, in part to the Hall-Petch relationship previously described, and may or may not achieve the original parent material value. The literature available regarding FSW of AA8090 indicates that the hardness in the nugget should recover to and even beyond that of the parent material (Lertora & Gambaro, 2010; Pedemonte et al., 2013; Vigraman et al., 2021). Mixed results were reported for AA2014-T6 with Rajendran et al. (2019) achieving parent material hardness within the nugget, but others (John, Shanmuganatan, Kiran, Senthil Kumar, & Krishnamurthy, 2019; Satyanarayana & Kumar, 2019) only achieving limited hardness recovery. Muhammad et al. (2021) attribute the lack of hardness recovery in the nugget to high temperature and severe plastic deformation causing dissolution of the hardening

precipitates into the aluminium matrix, with the partial limited hardness recovery due to grain refinement and re-precipitation of hardening phases during cooling. Some authors place the point of minimum hardness at the TMAZ/ nugget boundary (Barbini et al., 2018) and some specify that the hardness is lower on the advancing side for a narrow region than on the retreating side due to relatively greater velocity difference between the tool and workpiece producing a higher rate of heat generation in that area (Ramanjaneyulu et al., 2013), although the width of the softened zone was larger on the retreating side.

In the case of dissimilar welds, Threadgill et al. (2009) explain that the behaviour of the HAZ/ TMAZ is typically of that described for similar welds, however differing behaviour is often observed in the nugget where it can either oscillate between hardness levels expected for the two alloys or a relatively flat level (in the nugget) attained through combination of the two hardness levels involved. Mishra et al. (2014) describe research in which the degree of variation in hardness within the nugget was dependent upon which side the AA6061 and AA5052 alloys were positioned; in this study the hardness minimum was located within the HAZ and it was at this point that tensile fracture occurred. Robe et al. (2015) reported hardness maps of AA2024 and Al-Li AA2198 dissimilar welds which showed variation within each “half” of the nugget with higher values reported close to the weld centreline. They also state that for precipitation hardening aluminium alloys the grain size is not a reliable indication of hardness. Saravanan et al. (2015) used AA2014-T6 within a dissimilar weld and found that the hardness minima occurred within the HAZ. They assert that the hardness within the nugget depends greatly on the amount of material mixing which occurs within the weld. In their research on AA2198-AA2024, Khalilabad et al. (2018) found that the hardness minima occurred in the TMAZ/ HAZ area but did not specify exactly which area.

2.3.9.3.2 Tensile Strength and Ductility

In their review of FSW, Threadgill et al. (2009) state that, due to the different weld zones, the tensile strength and ductility may vary significantly across the weld, and may vary dependent on whether the sample is tested longitudinally or transversely with respect to the weld. They also point out that although there are many reports of low elongation in FSW tensile tests, this may not be due to low ductility as a reduction in area is also

noted; instead the strain may be concentrated in a small, locally softer region of the weld. Thus, overall elongation measurements are generally not considered to be representative of any particular region of the weld and instead show the likely failure location. In respect to this, they report that for heat-treatable aluminium alloys, tensile tests usually fail at the side of the nugget, on or close to the HAZ/ TMAZ boundary (either advancing or retreating side), with a ductile shear failure mechanism and 45° facets. The elongation is always less than that of the parent material due to the reasons already given. They report that for these alloys, the tensile strength is generally approximately equal to that of the parent material's annealed condition, although significant improvements can be made by optimising weld parameters to change the thermal cycle to avoid overaging.

In their FSW AA8090-T8 Lertora and Gambaro (2010) achieved tensile weld efficiencies (tensile strength of weld divided by tensile strength of parent material (x100)) of 56.34-71.53% depending on the weld parameters used and the amount of natural aging which had occurred. Vigraman et al. (2021) achieved 88.9% weld efficiency on their FSW AA8090 (no temper stated). The position of failure was reported as within the parent material. This was attributed to fine grains and dispersion of fine intermetallic compounds and secondary particles which acted to increase the weld's strength and hardness. However, as the reported tensile strength of the welded specimen was below that of the parent material, this author considers it more likely that the specimens failed within the HAZ.

With regards to AA2014-T6, most researchers report weld efficiencies in the approximate range of 80-90% (Das et al., 2020; Rajendran, C., Anudeep, & Ajith, 2019). Some researchers (Devaraju, 2017; Ramanjaneyulu et al., 2013) actually report weld efficiencies of over 100%, i.e. the weld was stronger than the original parent material, however it was not clear whether the efficiency was measured against the parent material specification or a measured UTS. Rajendran, Srinivasan, Balasubramanian, Balaji and Selvaraj (2019) reported that all of their specimens failed at the advancing side of the weld, however the exact position varied from within the nugget, to TMAZ, to HAZ depending on the weld parameters used. Changing the weld parameters also had a strong effect on the fractography; those welds produced with low heat input parameters failed in a brittle manner where layered ridges were observed. Conversely, those

produced with high heat input parameters failed in a ductile manner with large and elongated microvoid dimples observed.

Dissimilar weld efficiency is typically measured against the weaker of the two parent materials (Bandhu, Kumar, Nishant, & Thakur, 2017; Barbini et al., 2018; Park et al., 2020; Venkateswara Rao & Senthil Kumar, 2020). When considering 6 relevant⁴ studies in the literature it was found that the weld efficiency of germane dissimilar materials varied between 42.9% and 94% for the most successful welds produced, with an average (of the 6 results considered) of 71.5%. Rao and Kumar (2020) attribute the lower tensile strength of dissimilar joints to a different microstructure being formed within the nugget, creating a non-uniform stress distribution within the weld. They state that dissimilar joint strength is generally attributed to mechanical interlocking of the materials rather than metallurgical bonding, thus the lower tensile strength. Rao and Kumar (2020) state that a general “rule of thumb” for weld qualification in dissimilar welding is that the joint should fail in the HAZ of the weaker material rather than within the nugget. They assert that joints which failed within the nugget generally experienced inadequate mixing of plasticised material or suffered excessive heat input. Other research is in agreement with this rule (Bandhu et al., 2017; Barbini et al., 2018; Masoumi et al., 2016; Sivaraman et al., 2021).

There is debate within the literature as to which side the stronger material should be positioned in dissimilar FSW. Verma and Misra (2021) found that the stronger material should be positioned on the advancing side due to the increased heat generation at this location, which allows greater plasticisation of the stronger material and subsequently superior mixing. However, Barbini et al. (2018) found that positioning the stronger material on the advancing side resulted in lower torque and thus lower heat input due to the material’s higher strength and lower ductility, producing poorer results. They found that increasing the heat input by lowering the traversing speed cause intolerable coarsening of precipitates in the other material, but reducing the heat input by

⁴ Relevance was judged based on the materials used. The studies examined were (Bandhu et al., 2017) regarding AA2014-AA6061 welds, (Barbini et al., 2018) regarding AA2024-AA7050 welds, (Venkateswara Rao & Senthil Kumar, 2020) regarding AA6061-AA2014 welds, (Masoumi Khalilabad et al., 2021) regarding AA2198-AA2024 welds, (Masoumi, Zedan, Texier, Jahazi, & Bocher, 2016) regarding AA2024-AA2198 welds and (Sivaraman et al., 2021) regarding AA2014-AA2075 welds.

increasing the traversing speed did not allow for adequate mixing between the two materials.

There is little research within the literature on the effect of the rolling direction on the weld quality, however Barbini et al. (2018) did study it. They found that for AA2024 the yield strength was strongly affected by the weld orientation but that UTS was only affected at low traversing speeds with the specimens welded perpendicularly to the rolling direction achieving significantly lower results.

2.3.9.3.3 Fatigue

Threadgill et al. (2009) conducted a review of the literature and concluded that: fatigue results of FSW butt welds are typically poorer than that of the parent material under the same test conditions, this could be improved for some alloys by milling the top surface to remove stress concentrations; the fatigue performance of FSW exceeds that of comparable fusion welds; the initiation point tended to be located at a stress concentration at the side (advancing or retreating not specified) of the weld on the top surface and where those stress concentrations were removed (e.g. by mechanical removal of the top surface of the weld), the failure usually occurred in the region with lowest strength, e.g. HAZ/ TMAZ, although this was often very close to the original stress concentration. They also highlight that the three most important factors in determining fatigue strength were residual stress, microstructure, and defects; as all three factors are rarely reported together (according to Threadgill et al. (2009)) it is difficult to determine trends for fatigue of aluminium alloys as much of the data appears contradictory.

Besharati-Givi and Asadi (2014) indicate that the surface quality of FSW has more influence on fatigue performance than the rotational/ traverse speed ratio, and work by Vidal, Infante and Vilaça (2010) on AA2024-T351 and Pedemonte et al. (2013) on AA8090-T8 revealed definite improvement on fatigue properties with surface finishing techniques employed. With regards to fatigue testing of AA8090 in the literature, Pedemonte et al. (2013) found that AA8090-T8 specimens tested with a maximum stress of 155 MPa achieved up to approximately 50,000 cycles before failure. Lertora and Gambaro's (2010) results are presented as the stress range plotted against number of cycles; at 50,000 cycles the stress range achieved was 110 MPa, and the authors advised

using a weld ratio (tool rotational speed (RPM) divided by tool traversing speed (mm/minute) of 4.

With regards to fatigue testing of AA2014, Aydin et al. (2012) found that the FSW fatigue strength was always lower than that achieved by the parent material as stated previously, regardless of the weld parameters used. They attributed this difference to the reduced ductility inherent in the welded specimens and the presence of different microstructural zones, e.g. TMAZ, HAZ etc., which introduce areas of stress concentration and promote fatigue crack growth. They also found that almost all welded fatigue specimens failed within the weld, with high stress fractures occurring around the nugget and TMAZ on the advancing side, and low stress fractures occurring in the HAZ with no preference between advancing and retreating sides.

As with similar FSW, the literature states that generally dissimilar aluminium FSW have lower fatigue strength than the base materials (Wang, Pan, & Lados, 2018). Cavaliere, De Santis, Panella and Squillace (2009) found that the positioning of the materials, i.e. what parent material is positioned on the advancing side, has a significant effect on the fatigue strength, with best results for AA2024-AA6082 being produced with the stronger material (AA2024) on the retreating side. Cavaliere and Panella (2008) also found that even if the stronger material is positioned on the advancing side, fatigue results can be improved if an advancing side tool offset is utilised. However, Sillapasa, Mutoh, Miyashita and Seo (2017) positioned the harder 7N01 material on the advancing side of a 7N01-6N01 weld and reported a fatigue strength of 83.7% of the weaker material. They also found that the lowest fatigue strength occurs within the HAZ, followed by the nugget (TMAZ was not considered). Sillapasa et al. (2017) cut small round bar test specimens to test the fatigue strength of different weld locations and found that the HAZ was the weakest area with regards to fatigue. This suggests that the failure location in these welds should be the HAZ.

2.3.9.3.4 Residual Stress (RS)

Internal stresses which remain in an elastic body following the removal of any external mechanical or thermal forces or loads are termed as residual stresses (Mishra et al., 2014). Residual stresses can be either beneficial or detrimental depending upon the conditions, i.e. when they are tensile in nature they can accelerate fatigue crack growth,

and when they are compressive they can impede fatigue crack growth. Mishra et al. (2014) explain that when FSW was first introduced it was assumed that residual stresses in these welds would be insignificant due to FSW being a solid-state process, however subsequent research has proven this to be incorrect and that they can approximate the yield strength of the parent material. Residual stresses are formed in FSW due to the non-uniform heat distribution and plastic deformation which occur, leading to the formation of different zones, and the choice of process parameters strongly influences the extent of residual stress within the weld. RS generation in FSW is also partially generated due to the large forces and resultant rigid clamping required which prohibits material contraction during cooling and thus introduces RS (Casavola, 2018).

There are various methods available for measuring residual stress which are compared by Kandil, Lord, Fry and Grant (2001) and some of which are briefly described below:

- Hole drilling: a small hole is drilled into a component where a strain gauge rosette is attached, and the locally relieved strain measured. This strain is then used to calculate the residual stress using experimentally and Finite Element Analysis (FEA) determined formulae.
- X-ray Diffraction (XRD): using the elastic deformation within a material, the internal stresses are measured due to the changes in the spacing of their lattice planes from the stress-free value to that applicable when stressed.
- Synchrotron: these are very intense beams of high energy X-rays which have increased depth penetration beyond that of normal X-rays, which allows them to produce 3D maps of the strain distribution within a component.
- Neutron Diffraction: measurements are conducted in a similar manner to XRD but have significantly higher penetration depths.
- Curvature and layer removal: when layers are removed from one side of a flat plate containing residual stresses the stresses become unbalanced and the plate bends. This curvature can be measured and the distribution of stress in the original plate deduced.

The choice of technique will depend on a number of factors including the component and materials from which it is composed, cost, availability, operator skill and degree of accuracy required.

Mishra et al. (2014) summarised residual stress profile trends from literature in a diagram which is shown in Figure 20. This summary led to several general conclusions: longitudinal (parallel to the weld line) residual stresses are tensile within the welded region. The constraints on the welding zone which prohibit contraction result in the welded zone (nugget, TMAZ and HAZ) being in tension as it cannot contract. While outside the welded zones they are compressive, moving to approximately zero in the parent material at a distance removed from the weld. Transverse residual stresses are also tensile, with these typically being smaller in magnitude than the longitudinal residual stresses. The maximum values tend to occur in the HAZ or TMAZ, although in some cases the maximum is found in the nugget at the weld centre. These conclusions produce a residual stress profile across the weld which can typically either resemble an inverted V or U shape (represented by the broken line in Figure 20) or a M shape (represented by the solid line). When a M shape is produced, Delijaicov, de Oliverira Silva, Resende and Batalha (2018) attribute the reduction in RS within the nugget when compared to the TMAZ to significant mechanical work but reduced thermal input in the TMAZ and HAZ, and to the pressure from the tool shoulder.

Studies using relevant dissimilar aluminium alloys (e.g. AA2024-AA7075, AA2024-AA6061, AA7075-AA6062) were examined and all produced results with a double peak, i.e. an asymmetric “M” shape (Guo, Ma, Zhang, Qian, & Li, 2020; Hadji, Badji, Gaceb, Kherrouba, & Rabahi, 2018; Jamshidi Aval, 2015; Zapata, Toro, & López, 2016) with the peaks at the edges of the weld and a dip in RS within the nugget. There are conflicting reports in the literature as to where the maximum residual stress is measured within the weld. Guo et al. (2020) and Jamshidi Aval (2015) both reported that the maximum RS occurred at the edge of the weld at the side corresponding to the stronger material, with Guo attributing this to the higher heat input at the advancing side combined with the elevated mechanical properties of AA7075 compared with AA2024. However, Zapata et al. (2016) reported the maximum RS at the side corresponding to the weaker material, which was attributed to the properties, chemical composition and heat treatments of the materials used as the weaker material had higher RS when similar welding was conducted. Hadji et al. (2018) reported that the RS was at a maximum on the retreating side regardless of material positioning of AA2024 and AA7075, however when the weaker AA2024 was positioned on the advancing side, the RS increased

overall. These results were attributed to the local mechanical properties and inhomogeneous temperature distributions before and after welding.

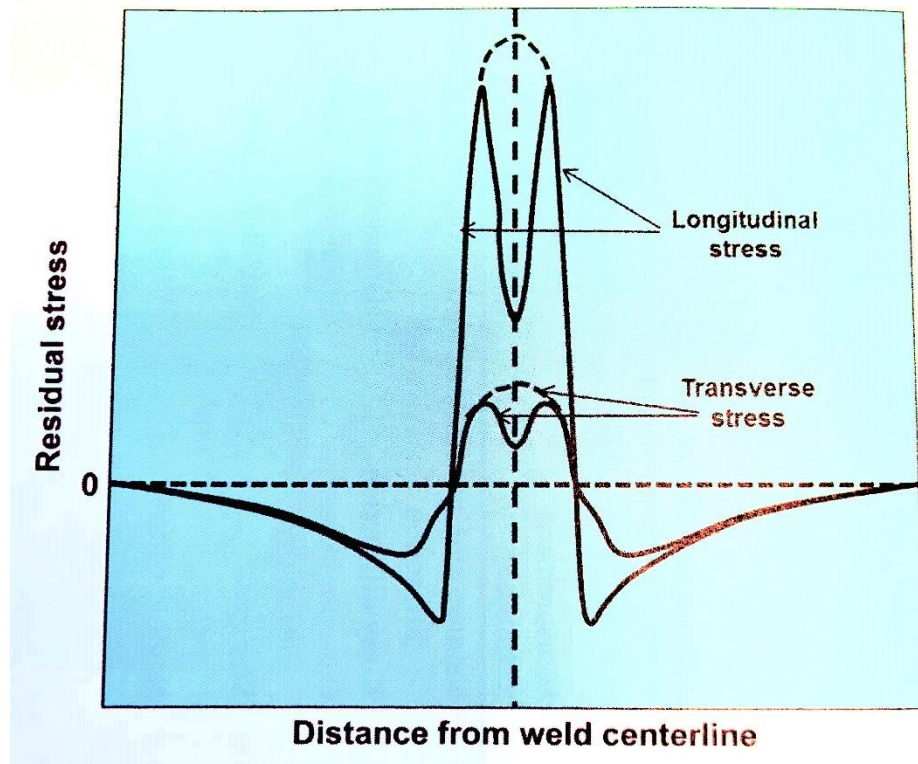


Figure 20: Showing distribution and shape of residual stresses across the width of a FSW. Reproduced from Mishra et al. (2014).

2.3.9.4 Summary of literature

Table 10 summarises a selection of literature relevant to the current research with respect to the material, tool, weld parameters and mechanical properties. It is acknowledged that there is a wealth of information not covered by this table. Where multiple tools or parameters have been used, only the results considered by the authors to be the “best” are reported here; the “best” results are usually determined by the mechanical properties produced.

Table 10: Showing a selection of the available literature regarding tool choice, process parameters and mechanical properties relevant to the current research.

Material and thickness	Tool description	Orientation of welding	Process Parameters					Measured mechanical properties				Reference
			Rotational speed (RPM)	Traversing speed (mm/min)	Tool tilt angle (°)	Dwell time (s)	Plunge depth (mm)	Weld efficiency ¹ (%)	Position of tensile failure	Hardness (description of hardness profile)	Fatigue strength	
5.0 mm AA2014-T6	Hexagonal 4.7 mm long tapered pin. Rotating 12 mm shoulder	Perpendicular to rolling direction	1000	600	2	N/A ²	N/A	91	Retreating side, 45° shear mode at nugget/TMAZ boundary.	Vaguely W shaped but oscillates significantly in nugget. Min hardness in TMAZ, max hardness in nugget although significant reduction at weld centreline	N/A	(Ramanjaneyulu et al., 2013)
6.0 mm AA2014	Square, non-threaded 5.6 mm long pin, rotating 24 mm shoulder	Parallel to rolling direction	815	63	N/A	N/A	0.06	86	Retreating side HAZ. Mix of ductile and brittle failure	Inverted V shape with max value in nugget and lowest value in HAZ.	N/A	(Das et al., 2020)
8.0 mm AA2014	Taper screw thread 7.6 mm long pin, rotating 24 mm shoulder	N/A	400	100	2	N/A	N/A	75	Middle of weld	N/A	N/A	(Zhao, Lin, Wu, & Qu, 2005)
2.5 mm AA2014-T6	5 x 5 mm square pin, pin length 2.3 mm rotating 20 mm shoulder	N/A	1000	105	2.5	N/A	N/A	75.6	N/A	N/A	N/A	(Khan, Bhatti, Iqbal, Zaigham, & Salam, 2016)

Material and thickness	Tool description	Orientation of welding	Process Parameters					Measured mechanical properties				Reference
			Rotational speed (RPM)	Traversing speed (mm/min)	Tool tilt angle (°)	Dwell time (s)	Plunge depth (mm)	Weld efficiency ¹ (%)	Position of tensile failure	Hardness (description of hardness profile)	Fatigue strength	
2.0 mm AA2014-T6	Tapered cylindrical pin with left hand thread and plain concave 6 mm rotating shoulder	Parallel to rolling direction	1500	40	1.5	N/A	N/A	83	N/A	W shaped, max in nugget, min in TMAZ	N/A	(Rajendran, C., Anudeep, & Ajith, 2019)
5.0 mm AA2014	Cylindrical pin tool, rotating shoulder	N/A	1200	20	N/A	N/A	0.1	26	N/A	Inverted U shape, hardness in nugget (max), TMAZ and HAZ higher than base material	N/A	(ABHISHEK & SANJEEV, 2019)
3 mm AA2014-T6	Cylindrical, conical, left-hand screw threaded 2.9 mm long pin and flat rotating 17 mm shoulder	Parallel to rolling direction	2140	80	2.5	30	N/A	95	HAZ/ TMAZ on advancing side	W shape, nugget max, HAZ/ TMAZ minimum	130 MPa at 6x10 ⁶ cycles	(Aydin, Tutar, Durmuş, Bayram, & Sayaca, 2012)
5.0 mm AA8090-T8	Tapered, threaded 4.8 mm long pin, 19 mm rotating shoulder.	Perpendicular to rolling direction	330	175	2	N/A	N/A	N/A	N/A	Overall inverted U shape (may resemble W if extended to parent material) with significant oscillation. Max hardness in nugget, min hardness appears to be retreating HAZ	As welded approx. 100 MPa at 2x10 ⁶ cycles	(Pedemonte et al., 2013)

Material and thickness	Tool description	Orientation of welding	Process Parameters					Measured mechanical properties				Reference
			Rotational speed (RPM)	Traversing speed (mm/min)	Tool tilt angle (°)	Dwell time (s)	Plunge depth (mm)	Weld efficiency ¹ (%)	Position of tensile failure	Hardness (description of hardness profile)	Fatigue strength	
5.0 mm AA8090	Cylindrical threaded pin and 16 mm concave rotating shoulder.	N/A	1400	25	0	7	N/A	51.5	N/A	Not plotted. Max in nugget	N/A	(Panwar & Chandna, 2021)
10 mm AA8090	6 mm diameter pin, 18 mm rotating shoulder	N/A	1200	2.5	0	N/A	N/A	89	HAZ/ TMAZ (close to parent material, side not specified)	W shape if extended to parent material. Max hardness in nugget. Min value HAZ/ TMAZ (side not specified)	N/A	(Vigraman et al., 2021)
5.0 mm AA8090-T8	Conical threaded pin and 19 mm rotating shoulder	Perpendicular to rolling direction	460	115	2	N/A	N/A	68.6	TMAZ immediately following welding, nugget after natural aging	As welded: U shaped, i.e. min hardness in nugget. After natural aging, slight elongated W shape, max in nugget, min HAZ	66.6% of yield strength	(Lertora & Gambaro, 2010)
3.2 mm AA2198-T3 (Al-Li) and AA2024-T3 Dissimilar ³	Tapered cylindrical pin and raised fan rotating shoulder	AA2198 perpendicular to rolling direction, AA2024 parallel to rolling direction	750	50	0	N/A	0.2	~77	Advancing side (AA2198) TMAZ. Ductile and shear fracture with no dimples.	Rough W shape which oscillates in nugget due to difference in parent materials. Max in nugget, min at HAZ/ TMAZ on AA2198 side (AA2198 also drops in the nugget)	N/A	(Masoumi Khalilabad et al., 2018)

Material and thickness	Tool description	Orientation of welding	Process Parameters					Measured mechanical properties				Reference
			Rotational speed (RPM)	Traversing speed (mm/min)	Tool tilt angle (°)	Dwell time (s)	Plunge depth (mm)	Weld efficiency ¹ (%)	Position of tensile failure	Hardness (description of hardness profile)	Fatigue strength	
5.0 mm AA2014-T6 and AA7075-T6 Dissimilar	Cylindrical pin with rotating shoulder. Shoulder to pin diameter ratio of 3	N/A	1200	20	N/A	N/A	N/A	76	Advancing side (AA2014) HAZ. Fine dimples and large population of microvoids in varying sizes	Asymmetric W shape due to differences in parent materials. Lowest at HAZ on advancing side. Max in nugget biased towards the retreating side	N/A	(Saravanan et al., 2015)
10.0 mm AA2014-T6 and AA6061-T6 Dissimilar	Polygonal hybrid square 9.8 mm long pin, with 30 mm rotating shoulder	N/A	900	20	1	N/A	N/A	70	HAZ/TMAZ on retreating (AA6061) side. Mainly ductile failure	Asymmetric W shape with min hardness at retreating TMAZ/HAZ.	N/A	(Venkateswara Rao & Senthil Kumar, 2020) Note: uses 1.5 mm tool offset
2.0 mm AA2024-T3 and AA7050-T7651 Dissimilar	Conical threaded 1.9 mm long pin with 3 flat surfaces. Convex 48 mm diameter <u>stationary</u> shoulder (contact area 8 mm)	N/A	1200	3	1	N/A	N/A	94	Advancing side HAZ	Asymmetric W shape, min at TMAZ/ HAZ boundary on advancing side, nugget hardness lower than retreating HAZ	N/A	(Barbini et al., 2018)
6.0 mm AA2014	5.8 mm long pin and 16 mm diameter <u>stationary</u> shoulder	N/A	931	13	0	90	0	68.5	TMAZ/ nugget interface, small sized dimples.	Shallow W shape, nugget hardness much reduced from parent material, min hardness at TMAZ/ nugget interface	N/A	(Sinhmar & Dwivedi, 2020a)

Material and thickness	Tool description	Orientation of welding	Process Parameters					Measured mechanical properties				Reference
			Rotational speed (RPM)	Traversing speed (mm/min)	Tool tilt angle (°)	Dwell time (s)	Plunge depth (mm)	Weld efficiency ¹ (%)	Position of tensile failure	Hardness (description of hardness profile)	Fatigue strength	
5.0 mm AA2219-T6	Conical threaded 4.8 mm long pin, concave rotating 9.8 mm diameter shoulder and stationary 14 mm diameter shoulder.	Parallel to rolling direction	800	100	2.5	N/A	N/A	69	Mid weld/nugget (kissing bond)	Shallow W shape, significant drop in hardness at all areas of the weld. Min hardness at TMAZ/nugget interface on advancing side	N/A	(Liu et al., 2013)
6.3 mm AA7050-T7651	Conical threaded 5.9 mm long pin with 3 flats, convex 18 mm diameter stationary shoulder	N/A	1500	400	0	N/A	0	91.5	HAZ/TMAZ boundary	W shape with nugget values close to that of the parent material. Min at HAZ/ TMAZ boundary	N/A	(Wu, H. et al., 2015)
0.5 mm commercial pure Al alloy	Tapered pin 0.35 mm long, with 6.4 mm rotating shoulder	N/A	1070	78	1	N/A	N/A	107	N/A	Inverted U shape, hardness highest at the nugget (significantly in excess of the parent material)	N/A	(Panchal, Patel, Vyas, & Mehta, 2020)
0.8 mm AA6082-T6 and AA2024-T3 Dissimilar	Cylindrical non-threaded 0.6 long pin and rotating 6 mm diameter shoulder	Parallel to rolling direction	2085	762	N/A	N/A	N/A	69	Retreating side HAZ	Asymmetric W shape, min hardness at retreating HAZ	57.7 MPa at 2x10 ⁶	(Scialpi et al., 2008)

Material and thickness	Tool description	Orientation of welding	Process Parameters					Measured mechanical properties				Reference
			Rotational speed (RPM)	Traversing speed (mm/min)	Tool tilt angle (°)	Dwell time (s)	Plunge depth (mm)	Weld efficiency ¹ (%)	Position of tensile failure	Hardness (description of hardness profile)	Fatigue strength	
0.8 mm Alclad AA2024-T4	Tapered threaded 0.6 mm long pin and concentric circle rotating 15 mm diameter shoulder	N/A	1000	150	2.5	N/A	0.08	85	N/A	W shape, minimum hardness at HAZ on advancing side, nugget approx. 6% softer than parent material	N/A	(Yue et al., 2018)

Table 10 notes:

- 1 Weld UTS/ parent material UTS, expressed as a percentage.
- 2 Where N/A is reported, the information was not provided in the literature.
- 3 For dissimilar welds, the material on the advancing side is listed first.

2.3.10 FSW/ SSFSW Defects

Although not typically susceptible to defects frequently found in fusion welding, such as porosity or hot cracking, there are flaws and defects detrimental to quality in FSW which must be mitigated by appropriate choice of tooling and weld parameters. According to The Welding Institute (2013), a flaw is an imperfection which one would prefer not to have and may or may not affect the integrity of the weld, and a defect is an imperfection which cannot be tolerated due to its deleterious effect on the weld. If, after an evaluation, a flaw is deemed to be intolerable then it becomes a defect; if it does not compromise the integrity of the weld it is a tolerable flaw. A number of characteristic flaws (becoming defects if they exceed an acceptance criteria) are described in Table 11, with descriptions gathered from Threadgill et al. (2009), The Welding Institute (2013) and Mishra et al. (2014).

Table 11: Summary of flaws/ defects characteristic of FSW; contributions from Threadgill et al. (2009), The Welding Institute (2013) and Mishra et al. (2014).

Flaw Type	Description	Location	Cause
Void	A void is a cavity within the weld, sometimes incorrectly identified as porosity. Sufficient plastic flow is required to produce a successful FSW, but if the material cannot flow it can break up	Advancing side at edge of nugget or any part of the weld, but often found in the transition between the shoulder and pin dominated regions	Low forging pressure. Welding speed too high. Plates not clamped close enough together. Joint gap too wide. Temperature too low.
Wormhole	Long, continuous, tunnel-like void occurring sub-surface.	Sub-surface, often at the advancing side of the nugget/ TMAZ boundary or beneath the pin tip. If this occurs on the surface (due to increasing traversing speed or reducing down force) it is then known as a groove defect.	Insufficient temperature resulting from rotational speed too slow, or traversing speed too fast – this leads to insufficient plasticisation and material flow.

Flaw Type	Description	Location	Cause
Joint line remnant (Lazy S)	A curving line visible within the weld cross-section, comprising of oxide particles from the original material surfaces which have been drawn into the weld.	Weld nugget, extending from the root of the weld at the point where the original plates butted together.	Inadequate removal of oxide from plate edges. Inadequate disruption and dispersal of oxide by tool. Inappropriately designed pin.
Lack of penetration/ root flaw	Incomplete welding at the root. This can appear as a clear visible discontinuity between the plates, or as a weak bond where the material is in intimate contact but not completely joined (kissing bond).	Weld nugget, extending from the root of the weld at the point where the original plates butted together.	Tool pin too short. Incorrect tool plunge depth. Poor joint to tool alignment. Weld too "cold" resulting in poor material flow under pin. Tool offset from weld centre.
Surface flash/ lack of surface fill	Excess material which is extruded from under the tool shoulder. The material released as flash results in thinning of the weld.	Top surface of the weld	Lack of constraint from tool shoulder; hot material can flow out rather than be constrained within the weld.
Surface galling	Rough surface on the top of the weld which can act as an initiation source from cracking during service.	Top surface of the weld.	High rotational speeds causing high shear rates and pick up and redistribution of soft material by the tool.
Undercutting	The weld surface is depressed below the surrounding parent material. This can act as a stress concentration, especially if the transition between weld and parent material is severe.	Top surface of the weld.	Excessive down force applied, particularly when combined with high rotational speed and low traverse speed (hot weld), allows for excessive plasticisation and for the weld to be compressed.

2.3.11 Portability of FSW/ SSFSW

For FSW to become a feasible repair technique for military helicopters it must become portable with the ideal equipment comprising a lightweight, handheld device which could be operated by a single person to produce high quality welds. At present, FSW uses fixed equipment within workshops or factories, however some advances have been made in developing portable equipment. The difficulties stem from the requirement to control process parameters: rotational speed; traverse speed; position and loads which are currently controlled automatically. Another issue is the rigid clamping essential to secure the workpieces and ensure sufficient contact between the tool and workpiece, and the requirement for a heat sink, a role currently performed by the backing plate.

Longhurst et al. (2017) presented two technologies which may overcome the difficulties and lead to the eventual development of a portable product: one which utilises a fixed shoulder-to-shoulder bobbin tool (this tool has two shoulders, one on either side of the workpiece, joined by the pin, which constrain the material between them) with convex shoulders and a free flowing motion capability allowing for self-adjustment and alignment; and another technology which allows for in-process monitoring for void detection. They found that although the tool and monitoring showed promise, the forces experienced during plunge and traverse were challenging when compared to that which a handheld operator would be expected to manage.

Rohith Renish, Pranesh and Logesh (2018) designed a portable FSW machine which they analysed for a 2-tonne load, welding plates of 2 mm thickness. They reported success for this analysis based on the final design meeting their conditions of joining, compression and release of parts, rotation and friction under pressure, braking and adjustment. However this author questions the actual “portability” of the machine; it appears to be a smaller version of a typical workshop machine, which could in theory be moved to work on site, however it is not a “handheld” solution. Their conceptual design is shown in Figure 21.

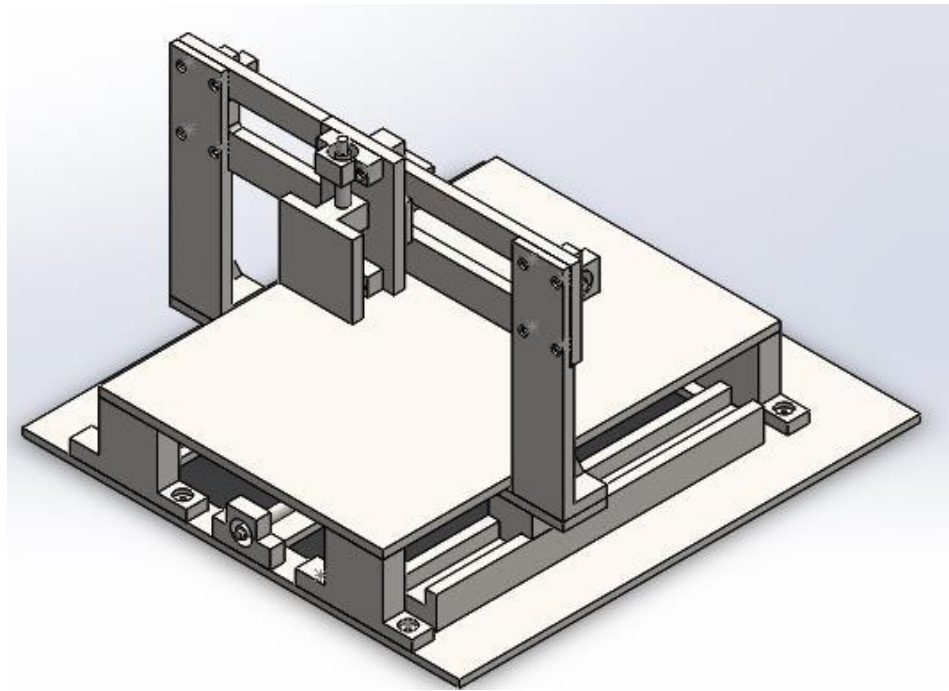


Figure 21: Showing conceptual design of a “portable” FSW machine, designed by Rohith Renish et al. (2018).

Concurrent Technologies Corporation (CTC) have developed a portable FSW machine specifically aimed at welding inserts into $\frac{1}{4}$ inch thick sensitised 5000 series aluminium panels used in shipbuilding (Concurrent Technologies Corporation, 2021b). As a proprietary technology little information is available publicly, however they state that the equipment consists of a weld head, track, control hardware and data acquisition to record and display process parameters; these components are hand carried and assembled on the ship with air motors used to drive the weld head and power the spindle. The equipment is shown in situ and resembles an arc welding set-up, Figure 22. This equipment has been reported (Concurrent Technologies Corporation, 2021a) as having been used to repair a section of bulkhead on the USS Vicksburg (CG 69) through insertion of an insert.



Figure 22: Showing CTC's portable FSW equipment in situ, reproduced from Concurrent Technologies Corporation (2021a).

2.4 Summary

This literature review has covered a wide range of areas, as such a short summary of the most salient information is provided below.

- BS L165 (AA2014-T6) and AA8090 are both precipitation-hardening aluminium alloys and are typically difficult to weld via fusion methods.
- FSW is a solid-state joining process which plasticises the material to form welds.
- Different areas are formed in the weld: the HAZ, TMAZ and nugget and others of less significance have been described.
- SSFSW is a more recent development in FSW and makes use of a stationary shoulder which typically produces cooler welds and results in reduced thinning of the weld.
- The identification of appropriate process parameters is vital in producing successful welds.
- Dissimilar, thin sheet and alclad coatings all present additional complications in achieving sound welds.
- FSW depends on appropriate heat generation, material flow and microstructural evolution to achieve good quality welds. The mechanisms of static recovery and

recrystallisation, dynamic recovery and recrystallisation and grain growth occur within the welds.

- To the best of the author's knowledge, BS L165 (or alclad AA2014-T6) and AA8090 have never been documented as having been dissimilarly SSFSW at this thickness (0.7 mm).

3 Methodology

3.1 Materials

3.1.1 Material Orientations

The material orientation, i.e. direction with respect to rolling direction, is important due to the anisotropy inherent in AA8090 and the significance that orientation can have in FSW/ SSFSW. For the purposes of this research the material orientations are as shown in Figure 23 below.

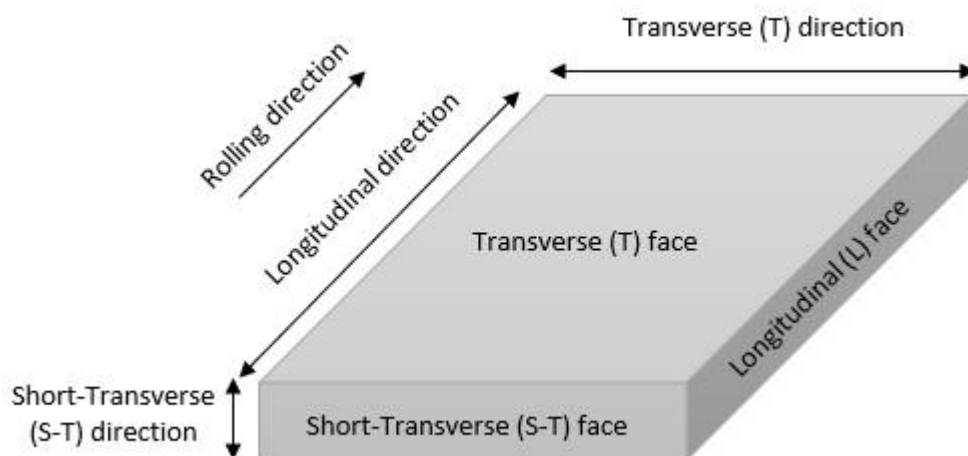


Figure 23: Showing material orientation definitions.

3.1.2 Material Condition

3.1.2.1 AA8090

It was necessary to source the AA8090 material from the original aircraft manufacturer, Agusta Westland International Ltd (now Leonardo Helicopters), as 0.7 mm thick AA8090 sheet could not be obtained commercially, despite ten suppliers being approached (Hendry et al., 2014). In one respect this was advantageous; as the material was from holding stock it was likely to be of the same age and quality as that used on the

helicopters currently in service, albeit it will not have been subjected to different environmental conditions as experienced by the helicopters.

AA8090 was delivered in the T3 condition, which denotes solution heat-treatment at 525-535 °C followed by water quench and then controlled stretching of 2-2.5 % (cold working). Once received, the material was artificially aged in-house at 1710 NAS in a calibrated furnace at 142-148 °C for 24 hours to reach the T81 temper state, in accordance with the AW standard EM 101 (Agusta Westland International Ltd, 2010).

3.1.2.2 BS L165

At the time of commencement of the research BS L165 (similar to AA2014-T6 alclad) was a specification of material used extensively in aerospace applications, and as such was easily commercially available. As a popular material used for repairs, the advantage of AA8090 coming from holding stock did not apply as different batches of BS L165 would have been used at various points throughout the life of the helicopter.

BS L165 was delivered in the required condition, T6. As per the specification (The British Standards Institution, 1978a), the material had been solution heat-treated at 505 ± 5 °C for up to 60 min and water quenched, prior to artificial aging at 175 ± 5 °C for 7-12 hours. The specification stated that the alclad layer should constitute an average of 4% of the material thickness on each side (28 µm for 0.7 mm thickness). Cross sections were measured using an inverted binocular microscope and the alclad material present on the delivered material was consistent with this specification.

3.1.3 Elemental Analysis of Parent Materials

A common and repeatable method of ascertaining the elemental composition of solid conductive specimens is via Scanning Electron Microscopy with semi-quantitative Energy Dispersive X-ray (SEM-EDX) analysis. This, however, could not be used in the identification and quantification of the elemental composition of AA8090 as lithium (a major alloying element in AA8090) has low-energy characteristic radiation which is difficult to detect using this method. Because of this, and for consistency between the results, the elemental composition of both BS L165 and AA8090 was determined by Inductively Coupled Plasma with Optical Emission Spectroscopy (ICP-OES) with SEM-EDX used as a comparator for the BS L165 analysis.

3.1.3.1 Inductively Coupled Plasma with Optical Emission Spectroscopy (ICP-OES)

ICP-OES was used to determine the elemental composition of both parent materials, BS L165 and AA8090, using a Perkin Elmer Optima 7300V ICP Spectrometer and autosampler. ICP-OES is a trace-level, elemental analytical technique that uses the emission spectra of a sample to identify and quantify the elements present. Samples are vapourised to form a plasma at temperatures that cause dissociation into atoms with significant atomic collisional excitation and ionisation. The elements can be identified by measurement of the intensity of light emitted by each element due to the excitation at the relevant wavelengths (Boss & Fredeen, 1999).

A standard containing all required elements for analysis of both materials was acquired from MBH Analytical Ltd and analysis quality nitric and hydrochloric acids were procured. Samples of AA8090 and BS L165 each weighing approximately 0.5 g were dissolved in aqua regia and processed. The BS L165 alclad layer was removed via mechanical grinding prior to sample dissolution. Each element was analysed using two wavelengths as shown in Table 12 below.

The ICP-OES uncertainty was calculated via the “Nordtest single lab validation” technique described by Padmasubashini, Sunilkumar, Krishnakumar and George (2020).

Table 12: Showing wavelengths used for ICP-OES analysis

Element	Wavelength 1 (nm)	Wavelength 2 (nm)
Al	396.153	308.215
Cu	327.393	324.752
Fe	238.204	239.562
Li	670.784	610.362
Mg	328.213	279.077
Mn	257.610	259.372
Si	251.611	212.412
Zr	343.823	339.197

3.1.3.2 Energy Dispersive X-ray (EDX) Analysis

The SEM-EDX used for comparison of the BS L165 ICP-OES results was carried out through use of a Zeiss Sigma VP SEM with semi-quantitative Oxford Instruments X-max EDX with Inca software. SEM-EDX uses a high-energy beam of electrons focused on the sample to excite the electrons in the atomic shells leading to the release of X-rays as the electrons drop back to orbits closer to the nucleus. The characteristic energy and

intensity of the X-rays released by each element is analysed by the spectrometer to ascertain the composition of the sample.

The SEM-EDX was locally calibrated (gain calibration) using a cobalt validation standard. Polished BS L165 cross sections were analysed using a 60 μm aperture at 20 kV and 8.5 mm working distance at x1000 magnification, as recommended by the manufacturer (Oxford Instruments, 2010). The “point and analyse” tool was used to analyse four selected areas (each representative of the bulk material) and average values for each element were obtained.

3.2 Welding

3.2.1 Procedure

As the welding was intended to be representative of a repair to aircraft skin, both lap welding (to model application of a patch repair proud of the surface) and butt welding (application of a patch repair flush to the aircraft surface or modelling of removal of a crack via Friction Stir Processing (FSP)) were considered. It was determined that a repair which did not add to the aircraft weight and which disrupted the structure to the minimum extent would be of the greatest benefit and so butt welding was selected to represent removal of a crack via FSP, i.e. the discrete faying surfaces represented the open crack sides.

SSFSW was carried out at The Welding Institute (TWI) in Rotherham, UK. An ABB IRB 7600-400 robot (ABB Robotics, 2015a), Figure 24, operated via ABB RobotStudio 6.02 software (ABB Robotics, 2015b) was used with a SSFSW tool mounted on a FSW head. A 6-axis force/ moment sensor system (JR3 Inc. model 75E20S4-M125AS-E 6000N1150) was also part of the configuration, however this was not fully operational at the time of testing and so reliable force/ moment readings were not taken.

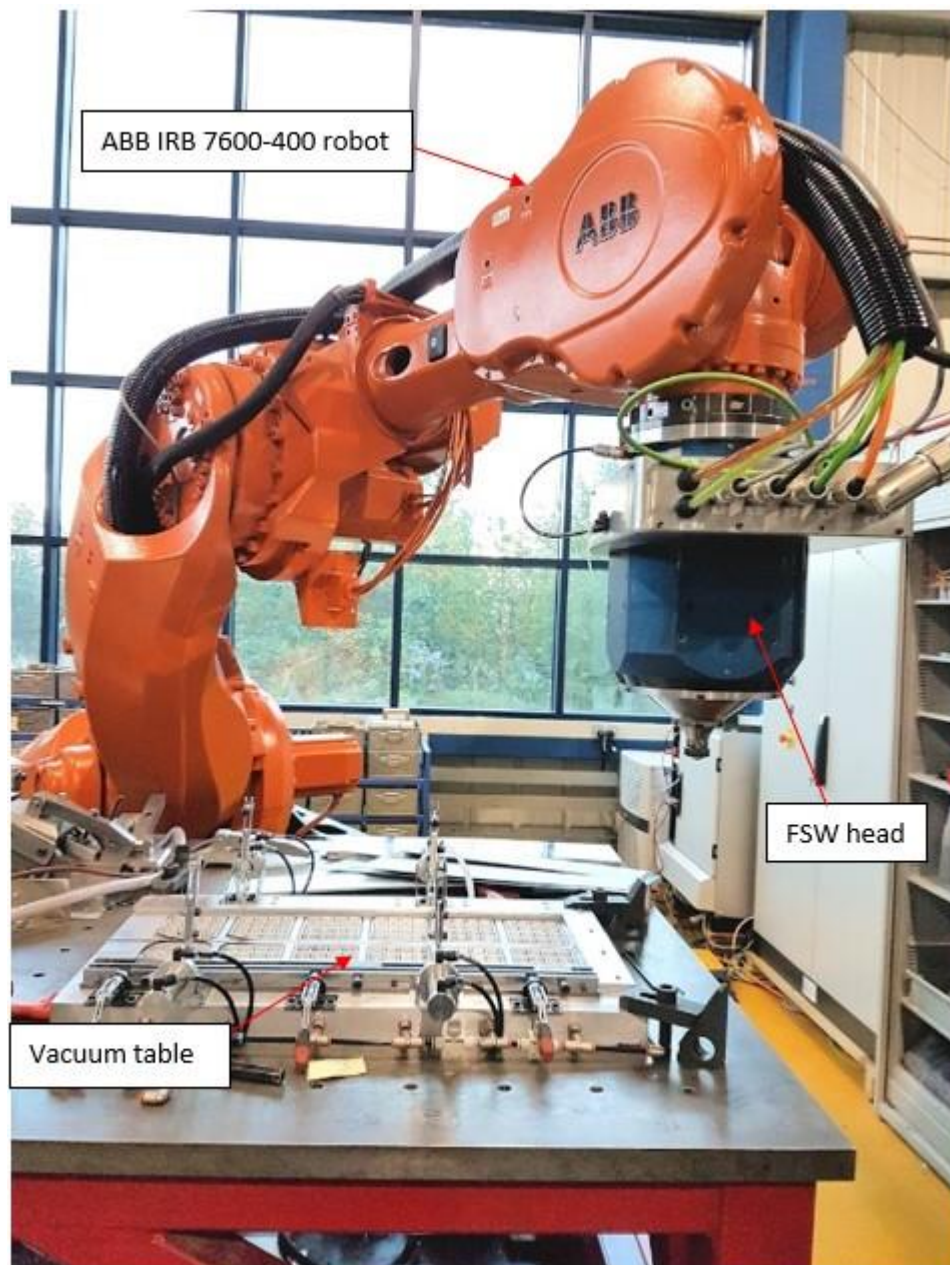


Figure 24: Showing ABB IRB 7600-400 robot onsite at TWI, Rotherham.

3.2.2 Tool

Finance was not available to source or manufacture a bespoke designed tool for the purposes of the research and so the tool was selected from those already available at TWI. The tool chosen was judged most appropriate for the application based on its dimensions. The tool was manufactured from MP159 NiCoCr alloy. It was comprised of a stationary shoulder component which was flat with an internal diameter of 5 mm and outer diameter of 8 mm, Figure 25(a) and (b), and a rotating pin component, Figure 25(c). The pin had a 0.4 mm height stepped spiral design with an approximate 4.95 mm

diameter at its widest step, and was extended by an additional 0.2 mm, effectively protruding 0.6 mm from the shoulder surface to obtain full penetration welds in 0.7 mm material, Figure 25(c) and (d). There was 0.05 mm clearance nominally between the probe and the shoulder. All tool measurements were conducted using calibrated digital callipers although the taper height and spiral step height (Figure 25(d)) required the additional use of a shadowgraph for measurement. The tool was provided by and used with permission of TWI and remains the property of TWI. The author was not granted permission to reproduce the formal tool drawings.

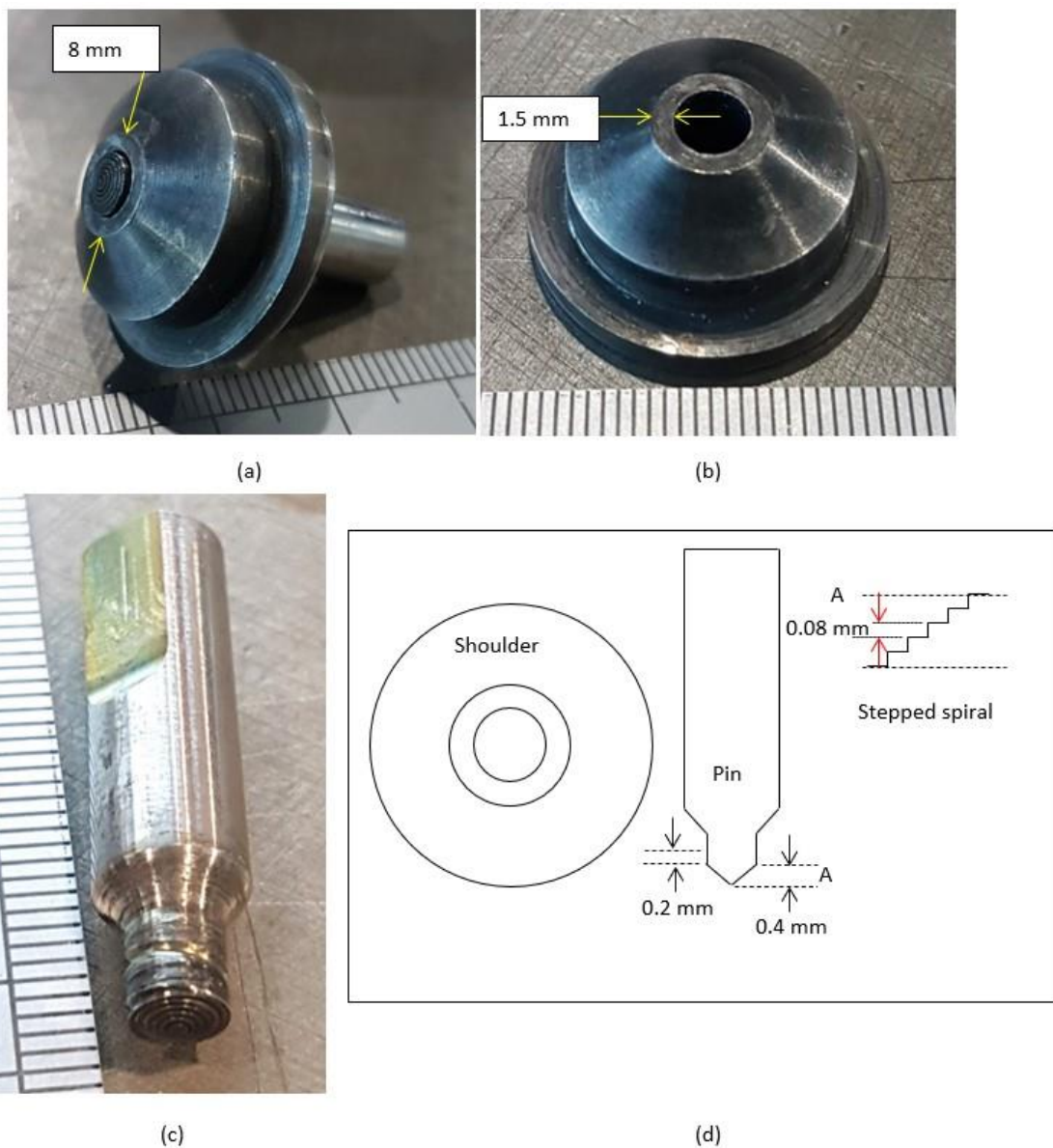


Figure 25: Showing SSFSW tool: (a) assembled tool; (b) stationary shoulder; (c) pin; (d) diagram detailing shoulder and pin dimensions (not to scale).

3.2.3 Workpiece preparation

The materials to be welded were 0.7 mm thick sheet measuring 600 x 125 mm in the configurations shown in Table 13 below. The sheets were cut to size using an industrial bandsaw in 1710 NAS workshops. In Table 13 “parallel” refers to the weld line as parallel to the material’s direction of rolling and is depicted by the symbol “||”, and “perpendicular” refers to the weld line as perpendicular to the material’s direction of rolling and is depicted by the symbol “⊥”. For dissimilar welds, the material positioned on the advancing side (see section 2.3.1 for description of advancing and retreating sides) is listed first in the configuration. The different configurations and orientations will henceforth be referred to by the designations shown in Table 13.

Table 13: Showing weld configurations, orientations and designations. || refers to parallel orientation, ⊥ refers to perpendicular orientation.

Weld Material Configuration and Orientation	Weld Designation
AA8090-AA8090 Parallel	AA8090
AA8090-AA8090 Perpendicular	AA8090 ⊥
BS L165-BS L165 Parallel	BS L165
BS L165-BS L165 Perpendicular	BS L165 ⊥
AA8090-BS L165 Parallel (AA8090 advancing side)	AA8090-BS L165
AA8090-BS L165 Perpendicular (AA8090 advancing side)	AA8090-BS L165 ⊥
BS L165-AA8090 Parallel (BS L165 advancing side)	BS L165-AA8090
BS L165-AA8090 Perpendicular (BS L165 advancing side)	BS L165-AA8090 ⊥

The material surfaces were prepared by cleaning along faying edges with fine wire cloth and acetone. The sheets were secured in place using a vacuum table, fixed clamps, locally produced clamps and additional material, Figure 26. The additional material was required to spread the load of the clamps across the whole workpiece as close to the weld area as possible as it was found that BS L165 tended to distort significantly as the weld progressed.

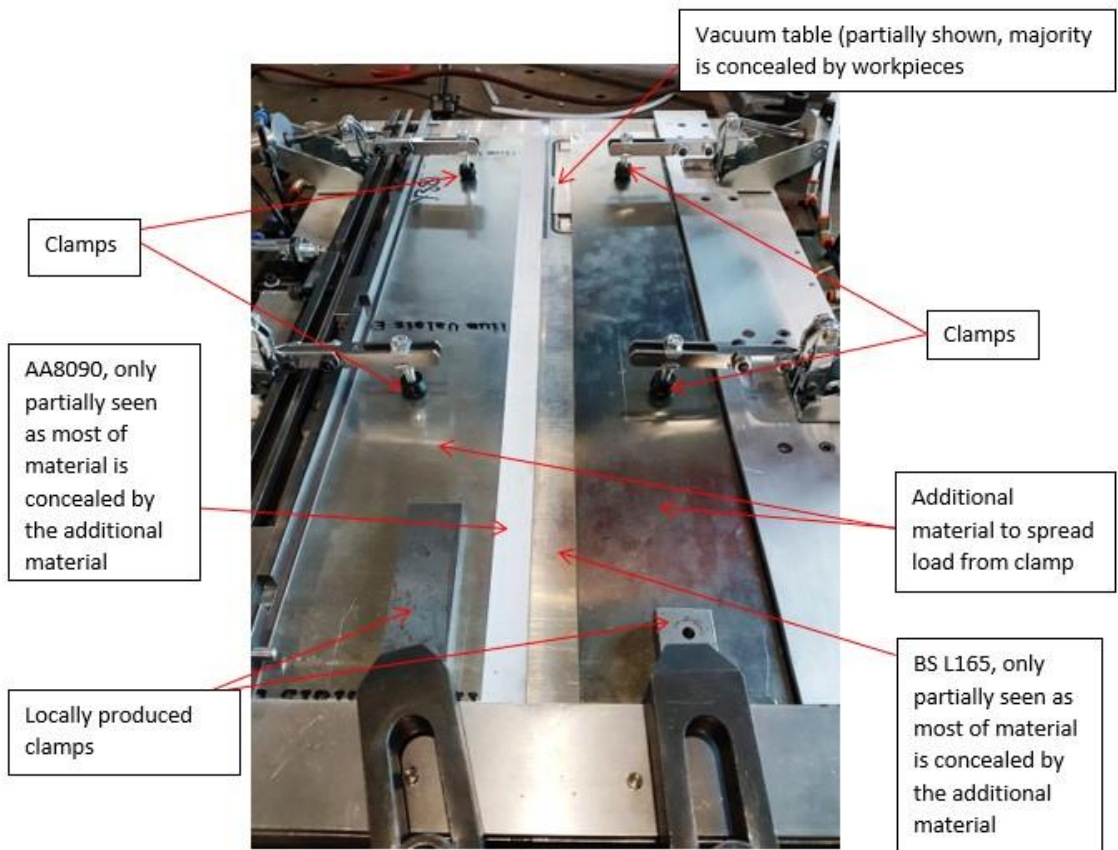


Figure 26: Showing clamping arrangements for FSW workpieces, photographed during a parameter trial.

3.2.4 Process Parameters

Due to the complications in acquiring AA8090 previously described, and the costs associated with purchasing both materials, additional material outside of that required for final welding was restricted and therefore process parameter testing and trials were consequently limited.

A starting point for parameter trials was chosen based on the experience of the TWI Principal Project Leader and optimised within the limitations of material availability, cost and time constraints until successful welds were achieved for each material configuration. A weld was determined to be successful if it achieved the following criteria. One, it was visually acceptable, i.e. it showed little to no distortion over the whole length (an example of a visually unacceptable weld is provided in Figure 86 in section 6.3.1.1). Two, it successfully passed both root and crown bend tests. These tests consisted of cutting approximate 20 mm thick sections 50 mm from each end of the weld, cut with the weld at the centre using a sheet metal shear cutter, and bent in a

table mounted, hand operated device. The bend test was deemed to be successful if the material/ weld did not crack. Three, the weld quality was visually repeatable using the same parameters. There was insufficient time, budget and material available to optimise the weld parameters beyond these criteria and so further work may include optimisation to achieve the best possible weld in these materials.

All material configurations used the parameters shown in Table 14. The parameters which were varied for the different material configurations are shown in Table 15. The least amount of stirring occurs directly underneath the pin tip, thus this was offset so that it did not coincide with the join line by the introduction of a transverse offset of 0.2 mm to the advancing side. Significant distortion was observed when the weld parameters produced “hot” welds, i.e. using a long dwell time, high rotational speed and low traverse speed. Conversely, when the parameters produced excessively “cold” welds the bend tests were unsuccessful due to insufficient mixing at the root. BS L165 was particularly susceptible to distortion due to the thermal variations caused by the alclad layer. Therefore weld parameters that would produce colder welds were used (slower rotational speed) in welds containing this material. AA8090 required a slightly hotter weld to achieve full penetration. A compromise was required for dissimilar material configurations to mitigate the distortion of BS L165 while achieving full penetration of AA8090. By conducting welds with varying parameters, successful welds (as defined above) were achieved using the parameters shown in Table 15.

Table 14: Showing weld parameters common to all material configurations.

Parameter	Value
Plunge axial force	2500 N
Plunge rotational speed	2000 RPM (1036.7 mm/s)
Penetration speed	0.5 mm/s
Dwell time	0 s
Tilt angle	1.5°
Initial rotational speed	2500 RPM (1295.9 mm/s)
Initial weld speed	2 mm/s
Transverse offset	0.2 mm (towards advancing side)

Table 15: Showing process parameters which vary with material configuration.

Weld configuration and orientation	Steady state weld force (N)	Steady state weld rotational speed		Steady state traversing speed (mm/s)
		RPM	mm/s	
AA8090 II	3000	3000	1555.1	10
AA8090 ⊥	3000	3000	1555.1	10
BS L165 II	3000	2700	1399.6	10
BS L165 ⊥	3000	2700	1399.6	10
AA8090-BS L165 II	3300	2700	1399.6	8
AA8090-BS L165 ⊥	3300	2700	1399.6	8
BS L165-AA8090 II	3300	2700	1399.6	8
BS L165-AA8090 ⊥	3300	2700	1399.6	8

In each configuration with the weld parallel to the rolling direction, 7 welds (measuring approximately 90-95% of 600 mm material length) were produced for testing and analysis, and for those with the weld perpendicular to the rolling direction 4 welds were produced. Fatigue testing was only conducted for those welds parallel to the rolling direction due to the deficit of material and the large number of specimens required for fatigue testing, hence the reduction in welds in the perpendicular direction. Insufficient material was available to weld combinations of parallel and perpendicular materials together.

3.3 As-Welded Examination

3.3.1 Optical Microscopy

3.3.1.1 Photography and Stereo Microscopy

The as-welded sheets were photographed using a Canon 6D SLR camera with a Canon EF 24-70 f/4L IS USM lens in a photographic studio setting at 1710 NAS. This was used to capture the overall appearance of the welds and to document any distortion.

A Zeiss Discovery.V12 stereo microscope using ZEN Core v2.6 software was used to examine the weld surface appearance for comparison between the configurations. The as-welded specimens were examined in order to view the topography at higher magnification to reveal any differences between the weld configurations and any flaws or surface-breaking defects.

3.3.1.2 Inverted Optical Microscopy

A Zeiss Observer.Z1m inverted optical microscope was used to examine metallographically prepared weld cross-sections and parent material in order to analyse the microstructure (see section 3.4.1.1 for details of preparation). The grain size of all areas of the weld was determined using the intercept method (with intercept line at 0° and 90° to assess directionality implications) detailed in specification ASTM E112 (ASTM International, 2013a). The intercept method counts the number of times that a randomly positioned line intercepts a grain boundary and then the ratio of grain boundary line intercepts to line length is calculated. In the case of the parent materials, grain size was calculated on all three orientations, i.e. longitudinal face, transverse face and short-transverse face. For welded samples the grain size was calculated using a cross-section transverse to the weld and calculated at different areas of the weld, i.e. HAZ and TMAZ. The Relative Accuracy (RA) of each measurement was calculated according to the method details in section 15 of ASTM E112 (ASTM International, 2013a).

Inverted microscopy was also used to examine the metallographically prepared cross-sections, following etching with Keller's reagent (1% hydrofluoric acid, 1.5% hydrochloric acid, 2.5% nitric acid, remainder water). This examination was carried out to analyse the microstructure, determine if any defects were present in the weld, examine the alclad layer interaction within the weld and assess the quality of the weld in general.

3.3.2 Optical and Contact Profilometry

A Bruker NPFLEX optical profilometer utilising non-contact White Light Interferometry (WLI) technology was used to generate profiles of the weld surfaces. The purpose of this was to examine the surface topography and associated depth measurements and make comparisons based on the different configurations of materials and orientation. It was necessary to vary the light intensity and scan length for each weld to achieve suitable scans due to the differences in reflectivity of the materials.

Additionally, a Taylor Hobson Form Talysurf 50, which utilises contact of a stylus along the specimen surface to measure surface roughness, was used to graphically show the roughness of the weld surfaces, and to indicate positions of underfill or overfill of the welds.

3.4 Testing

3.4.1 Hardness

3.4.1.1 Sample preparation

Hardness testing was carried out in accordance with BS EN ISO 6507-1 (The British Standards Institution, 2018). Sections were taken from the steady-state section of the weld, i.e. the standard addressing FSW for aluminium (The British Standards Institution, 2020a) considers that the initial and final 50 mm of the weld should be disregarded until the steady-state parameters are operational. Three samples of each weld configuration were cold-mounted using Struers EpoFix and vacuum impregnation, then metallographically prepared using a Struers recommended method (Bjerregaard, Geels, Ottesen, & Rückert, 2000). This method consisted of plane grinding to achieve a flat surface using Piano 120 (comparable to SiC paper grit 120) and Primo 220 (comparable to SiC paper grit 220) grinding discs with water cooling, then progressively finer polishing starting with the Largo polishing disc and associated diamond suspension to achieve a 9 µm abrasive finish, then Mol disc (and diamond suspension) to achieve 3 µm finish, and finally Dac with OP-S suspension to produce a 1 µm mirror finish.

Sections were also taken of the parent material and prepared in the same manner as part of the material characterisation. These sections were taken from all three orientations; L, T and S-T to account for any effects of anisotropy.

3.4.1.2 Test procedure

Hardness testing was carried out using a calibrated Struers DuraScan Vickers hardness tester using a 1 kg load for 10 seconds. Vickers indents were made along the centreline of the weld starting well within the parent material on the advancing side and traversed along the section at 0.5 mm intervals, Figure 27, through the TMAZ, HAZ and nugget zones before emerging well into the parent material on the retreating side. For parent material characterisation 5 single measurements were taken of each section and averaged. Measurements were made automatically by the DuraScan software where appropriate, and manually otherwise. Suitable machine verification using a calibrated hardness block was carried out prior to use in accordance with BS EN ISO 6507-1 (The

British Standards Institution, 2018). The expanded uncertainty of the measurement was calculated using a locally authored procedure and spreadsheet (Slater, 2018b; Slater, 2019) which was developed in accordance with the standard (The British Standards Institution, 2018). This was calculated to be ± 7.6 HV.

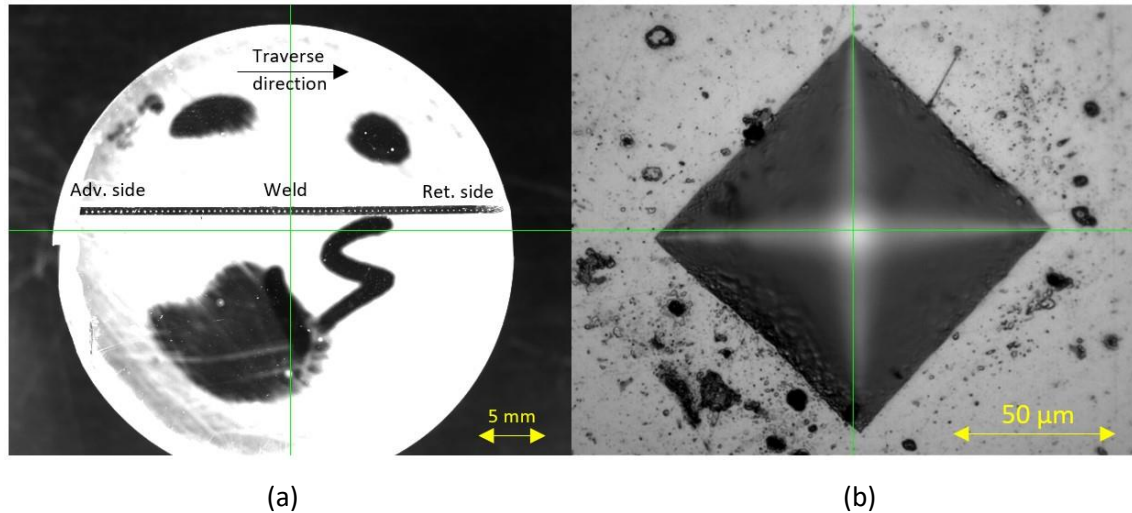


Figure 27: Showing hardness specimen of an AA8090-BS L165 weld: (a) overview image; (b) individual indent.

3.4.2 Tensile Testing

Components used on Royal Navy aircraft which require quality assurance via tensile testing are tested according to British Standard BS EN 2002-1:2005 (The British Standards Institution, 2006) in order to be compliant with the United Kingdom Accreditation System (UKAS), by whom the laboratory is accredited to BS EN ISO 17025 (The British Standards Institution, 2017) specification. A gauge length of 50 mm and 12.5 mm gauge width were used in accordance with BS EN ISO 6892-1 (The British Standards Institution, 2020b) as shown in Figure 28 below.

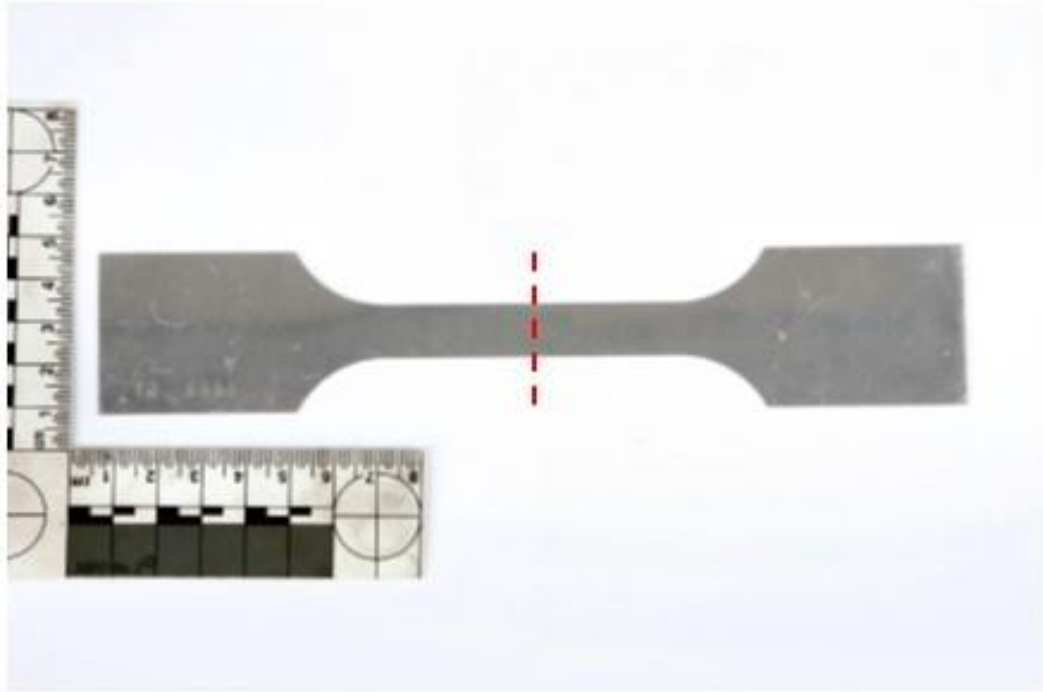


Figure 28: Showing a tensile test sample. The example shown is manufactured from BS L165 only, with no weld. The approximate position of the weld line on other samples is indicated by the dotted line.

Ten specimens were tested of each parent material and 20 specimens of the welded sheets (two batches of 10, each batch taken from a separate weld to indicate weld quality and repeatability) in each configuration. The testing was carried out using a calibrated Zwick 1474 Universal Tester with 100 kN load cell and calibrated Zwick Axial automatic 50 mm mechanical contact extensometers, using a strain rate of 0.005 min^{-1} . The expanded uncertainty of the measurement was calculated using a locally authored procedure and spreadsheet (Slater, 2018a; Slater, 2019). This was calculated to be $\pm 4.6 \text{ MPa}$ for UTS. It was acknowledged that the tests were operating at the low end of the load cells capability which may have an impact on the results. The annual calibration (performed by ZwickRoell Ltd., a UKAS accredited calibration laboratory) involved calibration steps at many low values. The relative uncertainty recorded at 2000 N and 4000 N (the closest values to the lowest and highest force exerted for these tests) was 0.24 % which has been incorporated into the expanded uncertainty.

The British Standard associated with qualification of FSW, BS EN ISO 25239-4:2020 (The British Standards Institution, 2020a) states that tensile test specimens should be taken at least 50 mm from either end of the weld, however due to limited material it was not

possible to comply with this and the first specimen from each weld was taken from within the first 50 mm.

It should be noted that comparison with fusion welding is difficult. Due to the challenges associated with fusion welding of the alloys employed within this research, non-uniform results for tensile strength are generally found. Additionally, as fusion welding of BS L165 or AA8090 would not be used on a UK military aircraft comparison of the two techniques is not appropriate.

Upon completion of testing, optical stereo microscopy (section 3.3.1.1) and SEM were used to examine the fracture surfaces of the welds. Scanning Electron Microscopy (SEM) uses a beam of electrons focused upon the sample of interest to create an image from the backscattered (deflected original) electrons or secondary (generated from within the sample) electrons. The former's efficiency relies on the atomic mass of the atoms within the parent material. Therefore this technique provides information relevant to the composition of the sample. The latter technique gives topographical information. A high-quality image of the sample topography which can reach magnifications allowing features measuring 10+ nm to be viewed can be achieved. A Zeiss Sigma VP SEM was used with a 30 µm aperture at 20 kV in this examination.

3.4.3 Fatigue Testing

3.4.3.1 Procedure Overview

The "staircase method" (Section 7 of BS ISO 12107 (The British Standards Institution, 2003)) was used to find the mean fatigue strength at a predetermined number of cycles, as this method allows realistic results to be achieved with a modest number of samples. This was important as materials and access to welding facilities were limited.

The test specimen design is shown in Figure 29. It was intended that the test specimen design comply fully with ASTM E466 (ASTM International, 2015), however due to the thin nature of the test material the resultant design would have been impractically large using excessive material. The criteria on which the design differs from the specification are the width to thickness ratio at the narrowest point due to the small thickness of the material, and the test section length exceeds the recommended value in order to achieve the minimum radius of curvature.

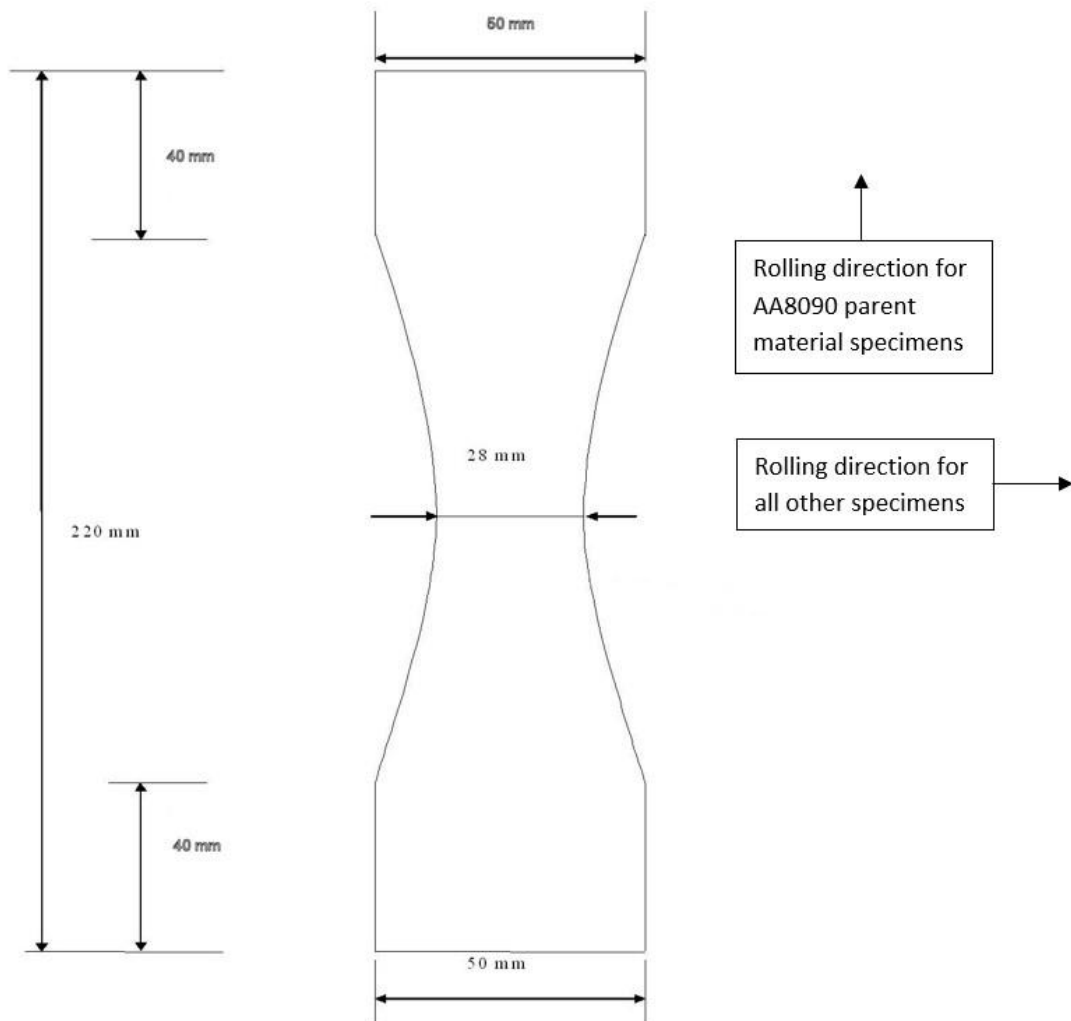


Figure 29: Showing fatigue test specimen design. The weld line is at the mid-way point indicated by the line.

A load ratio (R) of 0.1 was used. This ratio was stipulated in the AA8090 material specification, EM101 (Agusta Westland International Ltd, 2010), and is used frequently in aerospace fatigue testing (Roylance, 2001). A frequency of 6.5 Hz was used as it was determined (during laboratory testing at Sheffield Hallam University) to be the highest rate possible without degrading the stress amplitude or it coinciding with the resonant frequency of the hydraulic ring-main. Testing was carried out on 30 specimens (subsequent to initial trials) of each configuration in the parallel orientation only. The parallel orientation is specified in EM101 (Agusta Westland International Ltd, 2010); due to material availability and time restrictions additional testing was not carried out on the perpendicular orientation.

An initial value was estimated using available fatigue results in literature, from the results of tensile testing and from the limited initial fatigue trials. For AA8090 this value was minimum 150 MPa (Agusta Westland International Ltd, 2010), and for BS L165 the initial value was 300 MPa, (Henry, 1995). Fatigue testing was conducted by shifting up one stress increment when the pre-assigned number of cycles was reached and down one stress increment when the specimen failed prior to reaching this number. This was in accordance with the procedure described in BS ISO 12107:2003 (The British Standards Institution, 2003), adapted from the original procedure proposed by Dixon and Mood (1948). Pollak, Palazotto and Nicholas (2006) advocates a stress increment (d) of $0.5s \leq d \leq 2s$ (s is the standard deviation). A stress increment of 10 MPa was selected for convenience during testing; this was later found not to comply with the recommended stress increment (above) in all cases (see Section 5.2.3). The predetermined cycle count was 50,000 cycles; ideally testing would have been carried out over a larger number of cycles, however 50,000 was considered an acceptable compromise as the intention was not to produce reference S-N curves but to compare mean fatigue strengths of the parent materials and welded configurations, using the process described in section 3.4.3.2. Additionally, testing to 50,000 cycles was documented within the literature (Cavaliere & Panella, 2008).

3.4.3.2 The Staircase Method

The method was carried out as per BS ISO 12107:2003 (The British Standards Institution, 2003) and uses the following equations. The mean fatigue strength was calculated using the equation:

$$\sigma_m = S_0 + d \left(\frac{A}{C} \pm \frac{1}{2} \right) \quad (\text{Equation 4})$$

Where S_0 is the lowest stress value considered valid for the data set (see worked example in section 5.2.3.1), A and C are described below, s and d were defined previously. In the bracketed section of Equation 4, addition was used when there was a greater number of non-failed specimens in testing and subtraction used when there was the greater number of failed specimens. The standard deviation was calculated using:

$$s = 1.62d(D + 0.029) \quad (\text{Equation 5})$$

The variables used in these equations are given below.

$$A = \sum_{i=1}^l i f_i \quad (\text{Equation 6})$$

$$B = \sum_{i=1}^l i^2 f_i \quad (\text{Equation 7})$$

$$C = \sum_{i=1}^l f_i \quad (\text{Equation 8})$$

$$D = \frac{BC - A^2}{C^2} \quad (\text{Equation 9})$$

Where l is the number of stress levels, i is each individual stress level (numbered 0, 1, 2 etc) and f_i the number of events (number of failures or non-failures) at each level. Equation 5 is only valid when $D > 0.3$.

The coefficient of variation (η_s) was calculated using:

$$\eta_s = \frac{s}{\sigma_m} \quad (\text{Equation 10})$$

The estimated lower limit of fatigue strength (\hat{y}) at a probability of failure, P (for example 10%, 0.1) for population v at a confidence level of $1 - \alpha$ (e.g. 95%, 0.95), was calculated from:

$$\hat{y}_{(P,1-\alpha)} = \sigma_m - k_{(P,1-\alpha,v)} s \quad (\text{Equation 11})$$

Where: σ_m is defined in Equation 4, $k_{(P,1-\alpha,v)}$ is the one-sided tolerance limit for a normal distribution, as given in Table B.1 of BS ISO 12107:2003 (The British Standards Institution, 2003); v is the number of degrees of freedom (number of tests used in estimating the standard deviation).

Upon completion of testing, optical stereo microscopy and SEM were used to examine the fracture surfaces of the welds.

3.4.4 Residual Stress

3.4.4.1 Test Method

The incremental hole drilling method was used to measure residual stress in the parent materials and welds via a calibrated SINT Technology RESTAN MTS3000 hole drilling system with HBM Spider 8.30 digital strain gauge amplifier and SINT RSM v6.43 software. SINT Technology EVAL Back Calculation software (v7.14) was used for the analysis of strain gauge readings using the Integral method of analysis.

Hole drilling was selected due to the availability of equipment which 1710 NAS have in-house, and cost as the only additional expense was consumables such as strain gauges and drill bits. X-ray Diffraction was considered as an alternative, however it is suitable for only very near surface stresses (material must be incrementally removed to measure at depth) and as it was suspected that the residual stress would vary with depth this method was disregarded.

The hole-drilling method involves drilling a small hole through a strain gauge rosette into the surface of a component. This hole relieves any strains present which are measured via the strain gauges and software. These strains are then analysed according to the most appropriate method and the residual stress calculated.

There are several methods available for calculation of the residual stress from the relieved strains obtained by hole drilling, some of these are:

- Uniform (thin, intermediate or thick workpieces): covered by ASTM E837-20 (ASTM International, 2020). This is only appropriate where the stresses do not vary throughout the thickness of the material under investigation.
- Non-uniform: covered by ASTM E837-13 (ASTM International, 2013b). This superseded standard is included as the evaluation software (EVAL v7.14) available is based on this standard. However, it does not account for thin sheet non-uniform stresses and the appropriate calibration matrices are not therefore included in the software. For this reason this method could not be used.
- Integral method, first proposed by Schajer (1988) provides a separate residual stress analysis at every hole-drilling depth increment, i.e. the contributions to the total measured relaxation at all depths are considered. The integral method is considered to be most accurate when stresses vary significantly with depth, however it also has a high sensitivity to error. The Good Practice Guide No. 53 (Grant, Lord, & Whitehead, 2006) states that the Integral Method is the preferred technique. It should however be noted that the Good Practice Guide No. 53 (now in its second issue) was last updated in 2006 and therefore refers to a far earlier version of ASTM E837 (2001 version) in its analysis. The Integral Method is included as an analysis technique within the EVAL v7.14 software, with the calibration coefficients calculated by SINT using FEA for many strain gauges

available on the market. For these reasons, the Integral Method was selected as the analysis technique in this research.

3.4.4.1.1 Strain gauge

The strain gauge model selected for the research was Type B HBM 1-RY61-1.5/120R3 rosettes. ASTM E837-20 (ASTM International, 2020) recommends Type B rosettes as “useful where measurements need to be made near an obstacle”. This feature was important in this research as it was intended that measurements be made both at the edge of the weld and on the weld. Additionally, the author had used these gauges previously with limited experience and they were available pre-wired which reduced the potential additional uncertainty in non-expert soldering of wires to the gauges.

Due to procurement limitations it was not possible to source pre-wired Type B strain gauges with a temperature compensation factor tailored to aluminium; the strain gauges used had a temperature compensation relating to steel. The testing was carried out at room temperature (not at elevated temperature), however as with all mechanical drilling processes some localised heat is generated which may have had an influence on the results. To counteract this, the drill delay and acquisition delay were increased (see section 3.4.4.1.3) so that a steady gauge output could be achieved.

3.4.4.1.2 Positioning of gauges

The literature indicated several factors which should be considered when the positioning the strain gauges. These were stress relaxation due to sectioning of welds, potential changes to the RS along the length of the weld and distance between drilled holes.

Only one weld per configuration was available for residual stress testing and in some cases the weld was not a full one, i.e. it had been sectioned to accommodate other testing earlier in the research. Kumar, Mishra and Baumann (2014) discuss the research carried out by Altenkirch et al. (2009) in which it was noted that upon sectioning AA7449 FSW there was significant longitudinal residual stress relaxation and that a suitable specimen size must be used to mitigate against underestimation of the residual stress due to stress relaxation from sectioning. This suitable specimen size was found to be 40% of the original length of the weld (Altenkirch, Steuwer, Peel, Richards, & Withers,

2008). At this fractional length little unexpected relaxation of residual stress was noted. Altenkirch et al. (2009) also stated that the minimum length of test-piece required to retain approximately 90% of the unrelaxed residual stress value was 8 times the stress peak width. No literature on this subject was found for the materials under investigation here, however it was deemed prudent to consider the possibility of stress relaxation due to sectioning. The fractional lengths of the material available for the research are shown in Table 16 below. It can be seen that the minimum length stated for AA7449 was met in all cases and thus the relaxed stress due to cutting the weld is considered to have negligible significance on the results.

Table 16: Showing fractional length of welds available for residual stress testing.

Configuration	Fractional length of weld available for RS research
AA8090 II	0.40
AA8090 I	1.00
BS L165 II	0.53
BS L165 I	0.53
AA8090-BS L165 II	1.00
AA8090-BS L165 I	1.00
BS L165-AA8090 II	0.49
BS L165-AA8090 I	0.52

In addition to potential stress relaxation due to sectioning, Kumar et al. (2014) also briefly allude to limited experimental work showing that the nature and magnitude of RS distribution may significantly change from one end of a FSW plate to the other. They do not state what materials this experimental work was carried out on, nor do they give any further detail or references. There was insufficient time and resources to carry out this experimental work for the welds under consideration here, however as a result of Kumar et al.'s statement, it was considered sensible to position the strain gauges at the same location on each configuration rather than at different arbitrary locations along the lengths of the welds.

Finally, and similarly to stress relaxation due to sectioning, the act of drilling the hole releases stress locally and as such must be considered when positioning subsequent strain gauges. The National Physical Laboratory (NPL) Good Practice Guide No. 53 (Grant et al., 2006) make the recommendation of a minimum distance between holes of at least 6 hole diameters, based on the literature. As the nominal hole diameter in this testing was approximately 1.8 mm, this gives a minimum distance between holes of 10.8 mm.

As a result of the factors discussed, the initial holes were drilled at the positions shown in Figure 30. The first hole was to be drilled 100 mm from the exit hole which allowed sufficient distance from both the exit hole and the edge of the sectioned weld in all cases. This also ensured that the holes were located at the same position along the length of the weld for all configurations. A distance of 25 mm comfortably exceeded the NPL recommendation for minimum distance between holes.

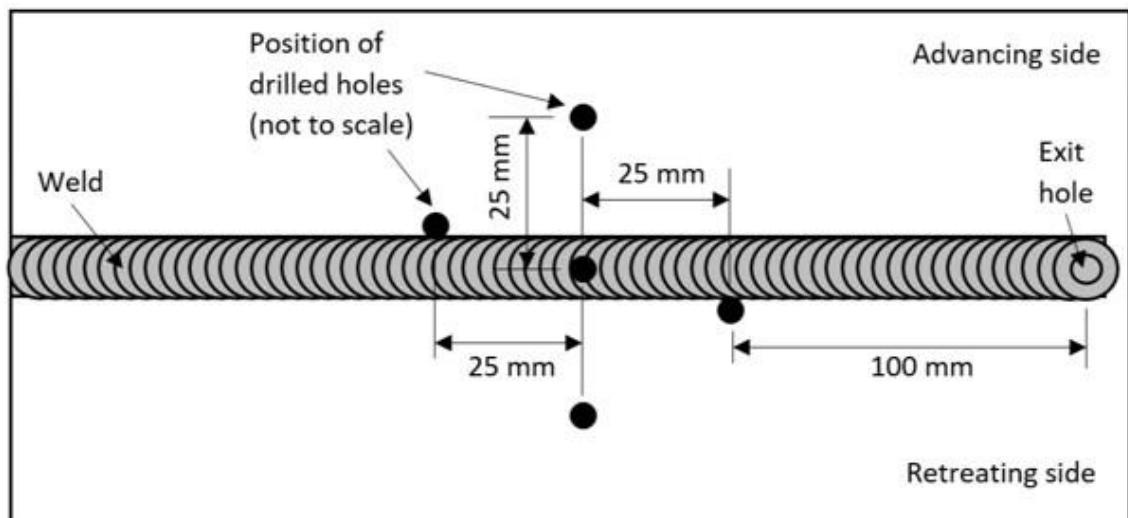


Figure 30: Showing positioning of RS holes on welded specimen.

3.4.4.1.3 Test set-up and parameters

The material surfaces were prepared for strain gauge application by gently abrading with 320 and 400 grit paper to achieve a surface suitable for adhesion, in accordance with the local 1710 NAS procedure. The potentially undesirable effects of this abrasion described in the Good Practice Guide No. 53 (Grant et al., 2006) were acknowledged by the author and the results from the first few incremental steps were treated with caution. RMS1 solvent was used to clean and degrease the surfaces before adhering the strain gauges with M-Bond cyanoacrylate adhesive.

Following checks that the drill system was set at 90° to the target material, the drill was set to the zero height (just touching the material surface) using the built-in software. A TiAlN coated inverted cone carbide drill bit with 1.6 mm diameter specifically designed for the drill system was used. The Good Practice Guide No. 53 (Grant et al., 2006) states that it is essential that the drill bit is changed after every hole drilled; this was not possible due to the volume of testing to be carried out and number of drill bits available.

Each drill bit was used for 4 holes and the impact of potentially non-parallel sides and flat hole bottom have been considered. The TiAlN coated drill bit was used in an effort to alleviate the consequences of reusing them as they were designed for use on materials harder than aluminium.

The drilling parameters and material properties used are shown in Table 17.

Table 17: Showing drilling parameters and materials properties used in residual stress hole-drilling.

Parameter/ Property	Value		Justification/ Source
Depth Interval	28 steps at 0.025 mm		The drilling apparatus offers a minimum depth increment of 0.005 mm and ASTM E837-20 (ASTM International, 2020) recommends a practical depth step of 0.05 mm for non-uniform stresses. The Good Practice Guide No.53 suggests a smaller number of larger depth increments is more reliable, especially remote from the surface, however based on a recommendation from SINT Technology a depth increment of 0.025 mm was selected which required 28 steps to reach through-thickness.
Drill Speed	0.2 mm/min		This is the default drill speed on the software. Following initial trials, this speed produced a suitable compromise between test duration and drill bit wear. SINT Technology recommends drill speeds of between 0.1 and 0.25 mm/min with low speeds intended for hard materials and higher speeds for ductile materials (SINT Technology, Nonea).
Acquisition Delay	5 s		This is the delay time where the software automatically reads the strains before resuming drilling the next step; it allows for a stable reading to be taken. The software recommends 3-5 seconds for this delay; 5 seconds were selected to allow for maximum stability (SINT Technology, Nonea).
Drill Delay	3 s		This setting allows the drill to turn without increasing the depth at the end of each step to produce a cleaner and flatter hole. The default setting of the software is 2 seconds; this was increased to 3 seconds to offer further reassurance (SINT Technology, Nonea).
Young's Modulus	AA8090-T81	77 GPa	There was insufficient confidence in the Young's modulus results obtained during the tensile testing. As a result, Young's Modulus for AA8090-T81 was obtained from the Elsevier Knovel database (Elsevier, 2021). BS L165 was also obtained from this source using that for AA2014-T6 data. The Young's Modulus for dissimilar welds was taken as the mean of both.
	BS L165	72.4 GPa	
	Dissimilar	74.7 GPa	
Poisson's Ratio	AA8090-T81	0.33	The data for Poisson's Ratio was obtained in the same manner as for Young's Modulus.
	BS L165	0.33	
	Dissimilar	0.33	

Parameter/ Property	Value		Justification/ Source
Yield Strength (MPa)	AA8090 parent (longitudinal)	343	The Yield Strength data was taken from the tensile testing results. Parent materials: yield strength used was that for the unwelded material as the strain gauge site was remote from the weld. Edge of weld and in weld: yield strength used from tensile test of relevant configuration.
	AA8090 parent (transverse)	307	
	BS L165 parent (longitudinal)	400	
	BS L165 parent (transverse)	393	
	8090-8090 edge of weld and in weld (longitudinal)	253	
	AA8090-8090 edge of weld and in weld (transverse)	262	
	BS L165-L165 edge of weld and in weld (longitudinal)	320	
	BS L165-L165 edge of weld and in weld (transverse)	341	
	8090-L165 edge of weld and in weld (longitudinal)	282	
	8090-L165 edge of weld and in weld (transverse)	271	
	L165-8090 edge of weld and in weld (longitudinal)	284	
	L165-8090 edge of weld and in weld (transverse)	286	

Upon completion of drilling, the hole diameter was measured using the optical scope and the results input to the software in order to measure eccentricity angle and radius. The data was then transferred to the SINT Technology EVAL Back Calculation software (v7.14) for analysis.

3.4.4.2 Analysis Method

3.4.4.2.1 Integral Method

As with most modern analyses, the residual stress calculation was carried out by the software (EVAL v7.14 used for this research) due to the requirement of FEM in the evaluation of the calibration coefficients. ASTM E837-20 is the most up-to-date international standard on the calculation of residual stress using the hole drilling method, and the non-uniform calculations are based on the Integral method. However, the software used in this analysis (EVAL v7.14) is based on earlier versions of the standard and the Integral method is based on the analysis originally proposed by G.S. Schajer in 1988 (Schajer, G. S., 1988). For this reason, the methodology is taken from the SINT Technology literature (SINT Technology, None) unless otherwise stated, with an abbreviated version highlighting the steps involved in an analysis shown below.

The evaluation of residual stresses in a non-uniform case can be obtained through the resolution of the integral equations below:

$$p(h_i) = \frac{1+\nu}{E} \cdot \int_0^{h_i} \hat{A}(H, h_i) \cdot P(H) dH \quad \text{Equation 12}$$

$$q(h_i) = \frac{1}{E} \cdot \int_0^{h_i} \hat{B}(H, h_i) \cdot Q(H) dH \quad \text{Equation 13}$$

$$t(h_i) = \frac{1}{E} \cdot \int_0^{h_i} \hat{B}(H, h_i) \cdot T(H) dH \quad \text{Equation 14}$$

Where:

$p(h_i)$ = isotropic strain combination which is relieved when the hole reaches a depth h at increment i

$q(h_i)$ = 45° shear strain combination which is relieved when the hole reaches a depth h at increment i

$t(h_i)$ = axial strain combination which is relieved when the hole reaches a depth h at increment i

ν = Poisson ratio

E = Young's modulus

$\hat{A}(H, h_i)$ and $\hat{B}(H, h_i)$ = generalisations of the uniform stress calibration constants \hat{a} and \hat{b}

h = nondimensional hole depth (hole depth/ strain gauge rosette mean radius)

H = nondimensional hole depth from surface (depth from surface/ strain gauge rosette mean radius)

P(H) = isotropic stress combination that exists at depth H from the measured surface

Q(H) = 45° shear strain combination that exists at depth H from the measured surface

T(H) = axial strain combination that exists at depth H from the measured surface

\hat{A} and \hat{B} are functions for equibiaxial and shear stress to account for the effect of the stress relieved at depth H of a h-depth hole on the strain gauge measurements (SINT Technology, None).

Using the integral method, the contributions to the total measured strain relaxations of the stresses at all depths are considered simultaneously. Schajer (1988) proposed that if the influence function integrals could be calculated for each drill step then the stress field could be described by means of step-wise functions whose value is constant through the partial hole depth. By such means, the calibration constants \bar{a} and \bar{b} (used to define the strain/ stress sensitivity of the measurement within the calculations (Schajer, Gary & Whitehead, 2013) can be expressed as:

$$\bar{a}_{ij} = \int_{h_{j-1}}^{h_j} \hat{A}(H, h_i) dH \quad \text{Equation 15}$$

$$\bar{b}_{ij} = \int_{h_{j-1}}^{h_j} \hat{B}(H, h_i) dH \quad \text{Equation 16}$$

Where:

\bar{a}_{ij} = the strain relaxation due to a unit P stress within increment j of a hole i-increments deep

\bar{b}_{ij} = the strain relaxation due to a unit P stress within increment j of a hole i-increments deep

$1 \leq j \leq i \leq n$, where n is the number of partial hole depths achieved during drilling.

Equations 12, 13 and 14 then become:

$$\frac{E}{1+\nu} \cdot p_i = \sum_{j=1}^i \bar{a}_{ij} P_j \quad \text{Equation 17}$$

$$E \cdot q_i = \sum_{j=1}^i \bar{b}_{ij} Q_j \quad \text{Equation 18}$$

$$E \cdot t_i = \sum_{j=1}^i \bar{b}_{ij} T_j \quad \text{Equation 19}$$

The calibration coefficients are typically calculated using FEA. Schajer (1988) provided computed calibration coefficients for a specific strain gauge, and SINT Technology have evaluated coefficients for many types of strain gauge available on the market (SINT Technology, None) including the Type B HBM 1-RY61-1.5/120R3 used in this research. By selecting the strain gauge as one of the parameters in the software, the correct calibration coefficients are used in the residual stress evaluation.

The residual principal stresses and angle are then calculated from:

$$\sigma_{max}, \sigma_{min} = P_j \pm \sqrt{Q_j^2 + T_j^2} \quad \text{Equation 20}$$

$$\beta = \frac{1}{2} \arctan\left(\frac{-T_j}{-Q_j}\right) \quad \text{Equation 21}$$

Where: $P_j = \frac{E}{(1+\nu)\bar{a}_{ij}} p_i$ $Q_j = \frac{E}{\bar{b}_{ij}} q_i$ and $T_j = \frac{E}{\bar{b}_{ij}} t_i$ Equation 22

And: $p_i = \frac{\varepsilon_3 + \varepsilon_1}{2}$ $q_i = \frac{\varepsilon_3 - \varepsilon_1}{2}$ and $t_i = \frac{\varepsilon_3 - 2\varepsilon_2 + \varepsilon_1}{2}$ Equation 23

Where:

σ_{max} = maximum principal stress at increment j

σ_{min} = minimum principal stress at increment j

P_j = isotropic combination stress at increment j

Q_j = 45° shear combination stress at increment j

T_j = axial shear combination stress at increment j

β = principal stress direction – the clockwise angle from gauge 1 axial direction to the σ_{max} direction

p_i = isotropic combination strain at increment i, corresponding to P_j

q_i = 45° shear combination strain at increment i, corresponding to Q_j

t_i = axial shear combination strain at increment i, corresponding to T_j

$\varepsilon_1, \varepsilon_2$ and ε_3 = measured strains from elements 1, 2 and 3 of the strain gauge.

3.4.4.3 Uncertainty Analysis

Calculation of the uncertainty in hole-drilling residual stress measurement has been explored within the literature. The Good Practice Guide No.53 (Grant et al., 2006) describes a project conducted by the UNCERT consortium (Oettel, 2000) in which a number of potential sources of uncertainty are identified and then a worked example of the uncertainty calculation is provided. Unfortunately, this example and analysis are only valid for uniform stress distribution throughout the depth and where there are no measurement points close to significant geometry changes. As this research regards measurement on and close to welds and the stress varies significantly with depth, it is not valid for use here.

Peral et al. (2017) produced a paper giving clear guidance on the calculation of uncertainty for non-uniform residual stresses using the integral method. The paper demonstrates that the sources of uncertainty can be grouped into three areas: material properties, matrices \bar{a}_{ij} and \bar{b}_{ij} , and measured strains and estimates the uncertainty using the Monte Carlo method. Regrettably, as the calibration coefficients calculated by SINT Technology are proprietary information, they cannot be extracted from the software with the package being used for this research. As such it has not been possible to follow this method of uncertainty calculation.

Schajer and Altus (1996) considered four main sources of potential error: strain errors, hole depth errors, uniform hole diameter errors and material constant elimination errors. They showed that the uncertainty increased with hole depth. Similarly to that noted for Peral et al. (2017), this method of uncertainty analysis could not be utilised for this research.

Magnier et al. (2017) calculated the calibration coefficients for thin sheet (0.7, 1.0 and 1.6 mm) using FEM and validated the results experimentally. They showed that the correct thickness of material must be considered in the calculation of the calibration constants or errors of up to 100% could be experienced. This work also suggested that viable results could only be achieved in thin material for depths between 0.06 mm and 0.4 mm (for 0.7 mm sheet thickness) due to errors involved in the zero-depth setting and increased measurement errors at depths greater than 0.4 mm. This limitation in depth is described at length in literature. Based on this, only residual stress evaluated

between 0.05 mm (second increment to overcome zero depth errors or surface roughness characteristics) and 0.4 mm will be considered in this research.

It is not clear what data is considered within the EVAL v7.14 software when computing the calibration coefficients and subsequent residual stresses. The user is instructed to enter data for sheet thickness and material properties and then take measurements of the hole dimensions to produce hole eccentricity data, however it is not clear if this data is then used to produce correction factors in the calculation of the residual stresses, thus partially alleviating some of the potential sources of uncertainty. Additionally, as proprietary information calculated by SINT Technology, the calibration coefficients cannot be extracted from the software with the package being used for this research. As a result of these issues, a numerical uncertainty has not been calculated for this research and the results have been treated as qualitative rather than quantitative and are used for comparison between the different materials and configurations. This approach is further validated by the ASTM E837-20 criteria which states that “if several computed stresses significantly exceed 80% of the material yield stress, then the results are not quantitative, and shall be reported as “indicative only”, which may be the case here.

4 Characterisation of Parent Materials

This section presents the characterisation work conducted and analysis of both parent materials, including material microstructure, measured elemental composition and measured mechanical properties relevant to this research.

4.1 AA8090

4.1.1 Elemental Composition

The averaged and normalised ICP-OES results are shown in Table 18 with the uncertainty shown in brackets. The table shows only the main alloying elements for which the standard was obtained; the additional trace elements detailed on the specifications are not listed in Table 18. Also shown in the table is the specification according to the applicable standard, and the results from laboratory testing from the suppliers (certificate of conformity). With regards to the ICP-OES results, it was observed that the alloying element's average normalised values were all within the tolerable range on the specification, although there were disparities between that measured via ICP-OES and the results provided by the material suppliers, which was assumed to be a discrete measured value rather than a maximum or minimum.

Table 18: Showing ICP-OES results for AA8090

	Average normalised elemental concentration (%)				
	Al	Cu	Li	Mg	Zr
AA8090 ¹ specification	remainder	1.0-1.6	2.2-2.7	0.6-1.3	0.04-0.16
As per certificate of conformity ²	remainder	1.19	2.316	0.78	0.06
ICP-OES average normalised results	95.9 (8.1%)	1.2 (15.1%)	2.2 (10.7%)	0.6 (14.2%)	0.05 (9.3%)

Table 18 notes:

- 1 As per EM101 (Agusta Westland International Ltd, 2010)
- 2 As per Leonardo Certificate of Conformity (Dolgarrog Aluminium Limited, 2005)

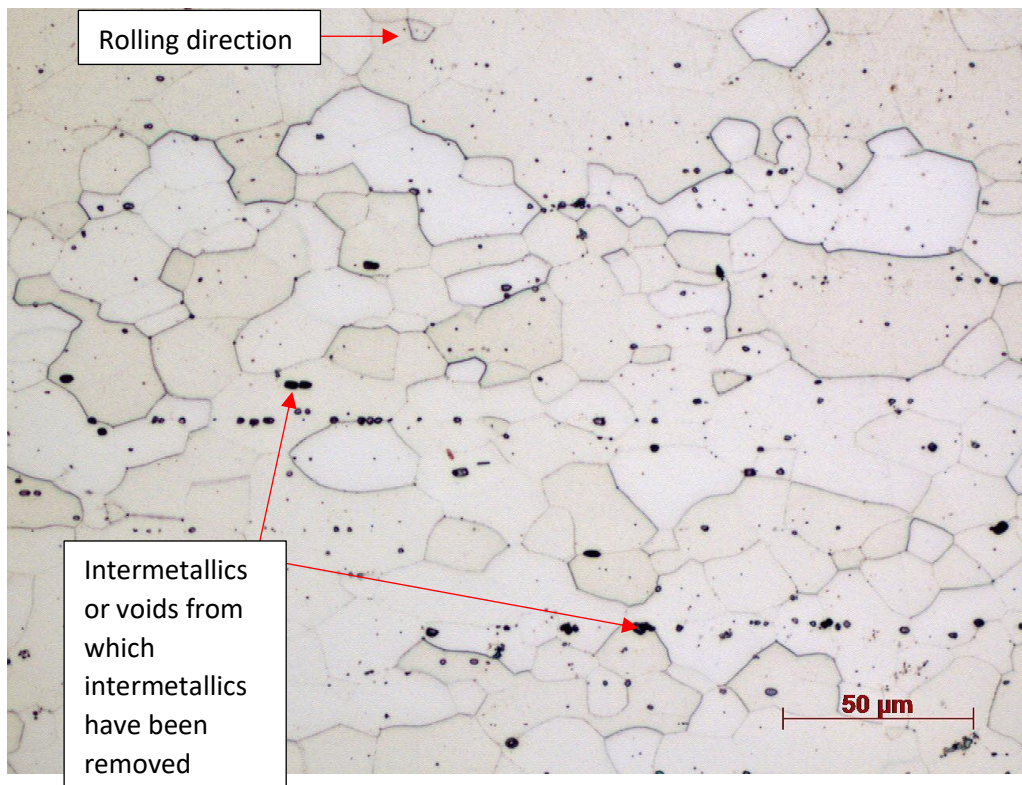
4.1.2 Material Microstructure

Micrographs detailing the microstructure of AA8090-T81 (after heat treatment to achieve T81 temper, see section 3.1.2.1 for details) are shown in Figure 31 with measured grain sizes shown in Table 19. These micrographs show areas representative of the overall microstructure. With regards to the grain size, the relative accuracy (%RA) is shown in brackets in Table 19 for each measurement, given to the nearest whole percentage. ASTM E112-13 (ASTM International, 2013a) states that a 10% RA (or lower) is generally considered to be acceptable precision for most purposes; it can be seen that while most of the %RA lie below or close to 10% the short-transverse direction 2 measurement is greater than this value. As a result, additional work is required in this area to improve the relative accuracy and confidence in the results, however there was insufficient time available for this.

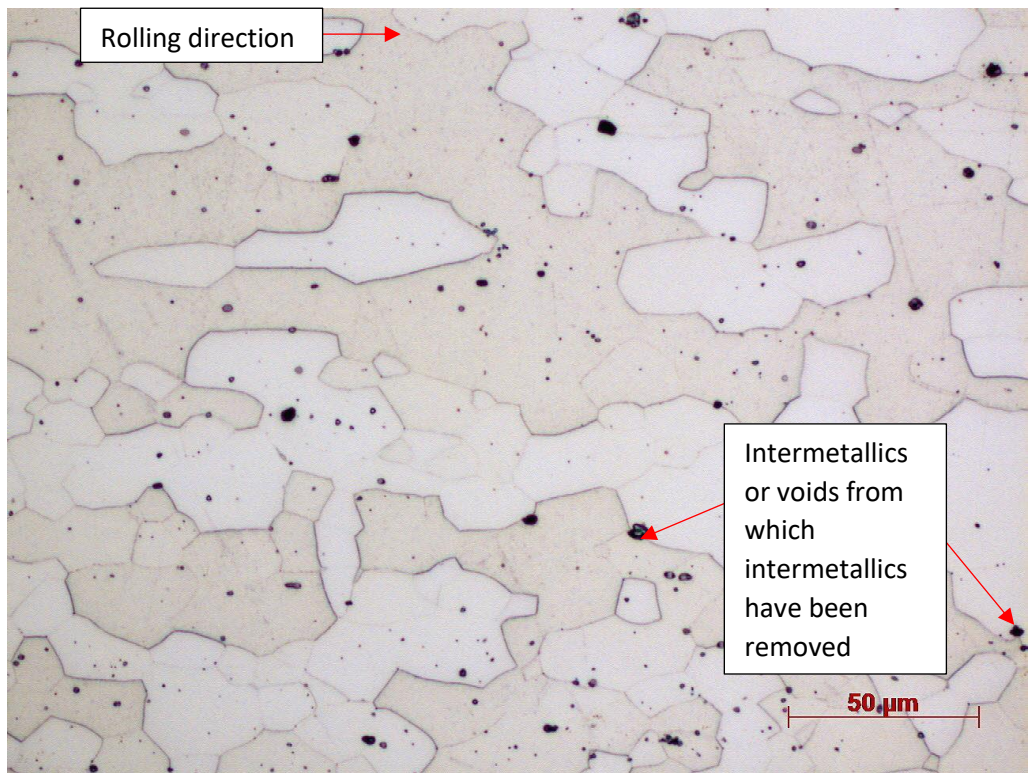
AA8090 had similar sized grains on both the longitudinal and transverse face. The grains on the short transverse face were slightly larger and far more equiaxed. The only quantified grain size found for AA8090 parent material in literature was reported by Vigraman, Vijay Krishna and Pavan Kumar (2021) with a value of 4-5 μm , however no details of the material temper or heat treatment were provided. The disparity between the results obtained here and that found in literature is attributed to potential differences in heat treatment as grain size is highly dependent on thermal history, and the results from this research are considered valid.

The micrographs revealed fine black spherical particles distributed homogeneously throughout the matrix, both on the grain boundaries and within the grains, with coarser particles were also observed in Figure 31. The microstructures were compared with literature (Srivatsan & Place, 1989), Figure 32 Although the microstructure shown in Figure 32 originates from an extruded specimen, and the size and volume fraction of the particles is significantly larger than that found in this research, they are considered to be comparable due to the material compositions and base tempers (Srivatsan & Place (1989) used AA8090-T851, and AA8090-T81 was used in this research). As such, based on the bromine-etching and SEM carried out by Srivatsan and Place, these particles are considered to be iron-rich and manganese-rich insoluble intermetallics such as FeAl_2 , $\text{Mn}_3\text{Si}_2\text{Al}_{12}$ (Srivatsan & Place, 1989). SEM-EDX was not conducted to analyse these particles as it was considered that the excitation of X-rays arising from the bulk material,

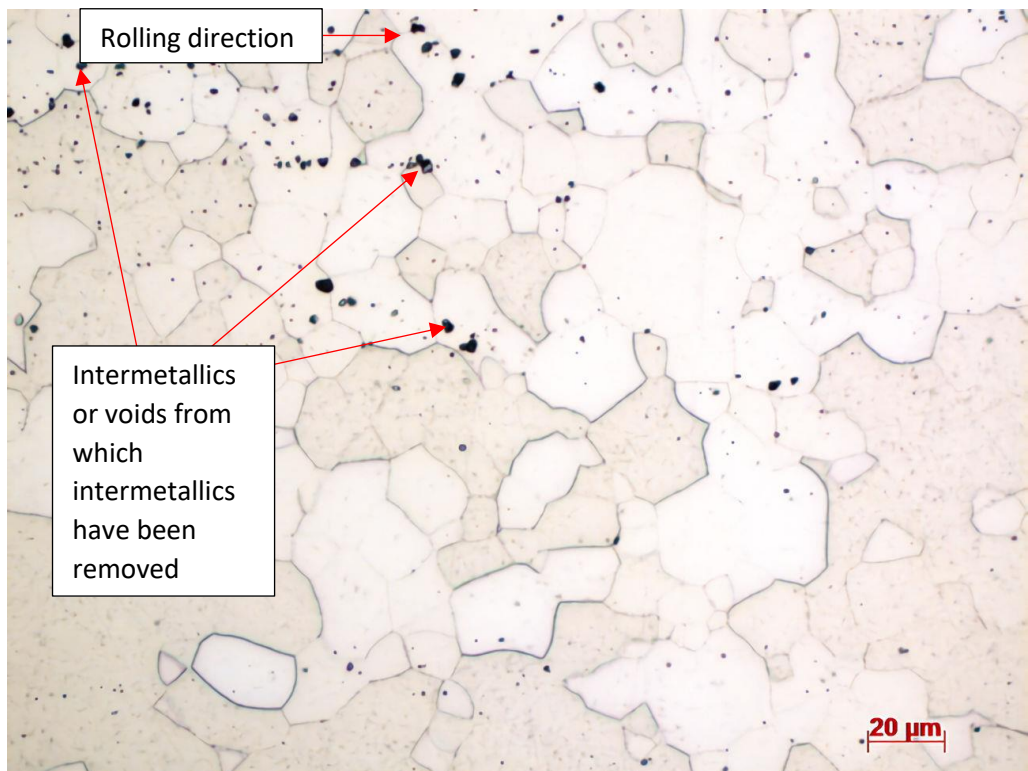
which would have been within the excitation volume, would produce low accuracy of results. These are distributed fairly evenly on the transverse face (Figure 31(b)), located mainly at the grain boundaries, but are more numerous and distributed more heterogeneously on both the longitudinal (Figure 31(a)) and short-transverse (Figure 31(c)) faces with clusters and chains formed. Transmission Electron Microscopy (TEM) was not carried out during this research and therefore strengthening precipitates such as δ' , T_1 or S' could not be characterised. However based on the heat treatment, hardness properties and literature (see section 2.2.4.1), these precipitates were present in the material.



(a)



(b)



(c)

Figure 31: Showing micrographs of AA8090-T81 material: (a) longitudinal face; (b) transverse face; (c) short-transverse face.

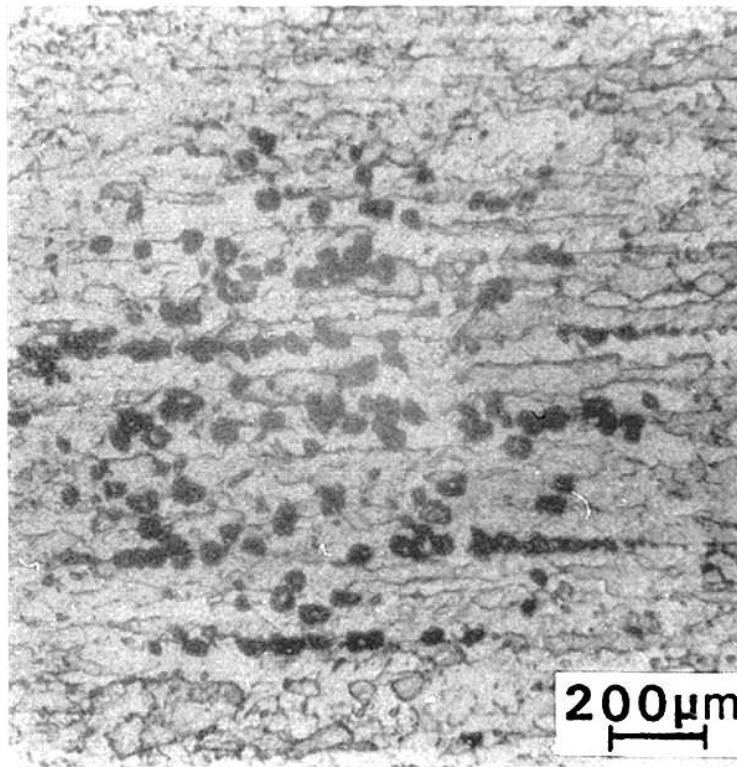


Figure 32: Showing extruded AA8090-T851 microstructure, courtesy of Srivatsan and Place (1989).

Table 19: Showing measured grain sizes of AA8090-T81 material.

AA8090-T81 material	Grain size (μm)	
	Direction 1	Direction 2
Longitudinal	21.2 (9%)	16.2 (6%)
Transverse	19.5 (6%)	14.0 (3%)
Short-Transverse	28.0 (4%)	25.4 (16%)

4.1.3 Mechanical Properties

The measured mechanical properties are summarised in Table 20 with a brief analysis of the results of each property in the following sub-sections.

4.1.3.1 *Hardness*

Despite the perceived anisotropy in AA8090 mechanical properties, this was not observed to a great extent with regards to the hardness tests as there was only approximately 2% difference between the lowest (longitudinal) value and highest (short-transverse) value. Note, for this property the orientations refer to the faces, rather than the directions (Figure 23). All results were well in excess of the minimum required value as specified (Agusta Westland International Ltd, 2010). Only the longitudinal and short-transverse results were used in the analysis during comparison with the welded joints, see 5.2.1.1.

Table 20: Showing summary of AA8090 measured mechanical properties with specified minimum values where appropriate.

Material		Hardness (HV1)	Tensile			Fatigue			
			UTS (MPa)	0.2% Proof Strength (MPa)	% Elongation	Mean Fatigue Strength (σ_m) (MPa)	Standard Deviation (s) (MPa)	Coefficient of Variation (η_s)	Lower Limit of Fatigue Strength ($\hat{Y}_{(0.1,0.95)}$) (MPa)
Specified ¹	Longitudinal	120	400	280	6	150	N/A	N/A	N/A
	Transverse	120	410	280	9	N/A	N/A	N/A	N/A
	Short-Transverse	120	N/A	N/A	N/A	N/A	N/A	N/A	N/A
As Measured	Longitudinal	138.8 (± 7.1)	443	343	9.5	322.1	17.66	0.055	285.6
	Transverse	140.0 (± 7.4)	438	307	11.1	N/A	N/A	N/A	N/A
	Short-Transverse	141.6 (± 6.6)	N/A	N/A	N/A	N/A	N/A	N/A	N/A

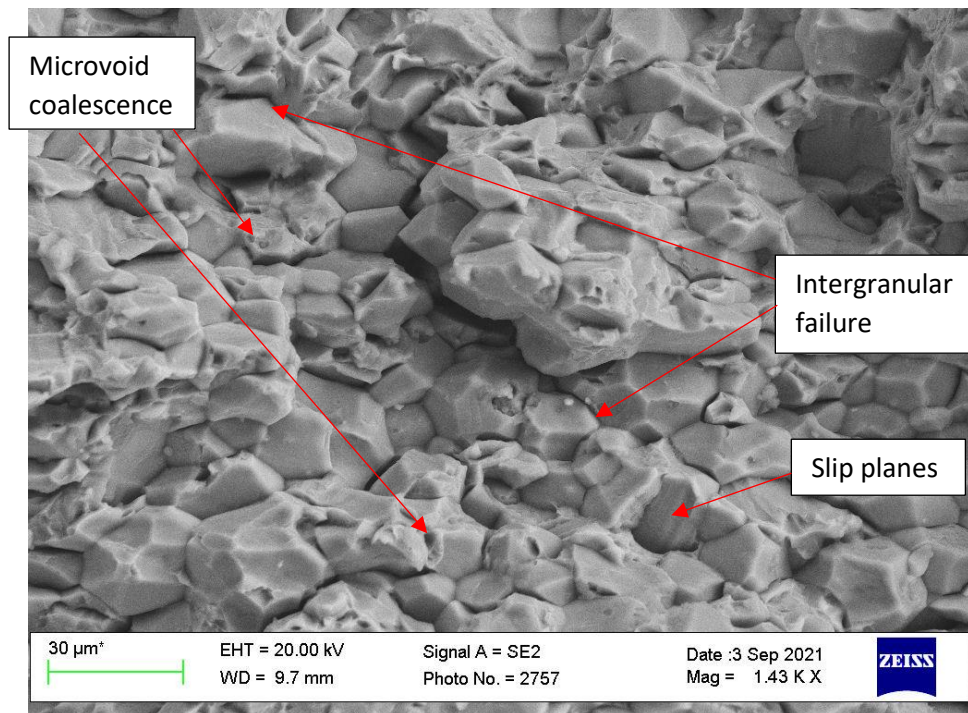
Table 20 notes:

- 1 Specification EM 101 (Agusta Westland International Ltd, 2010)

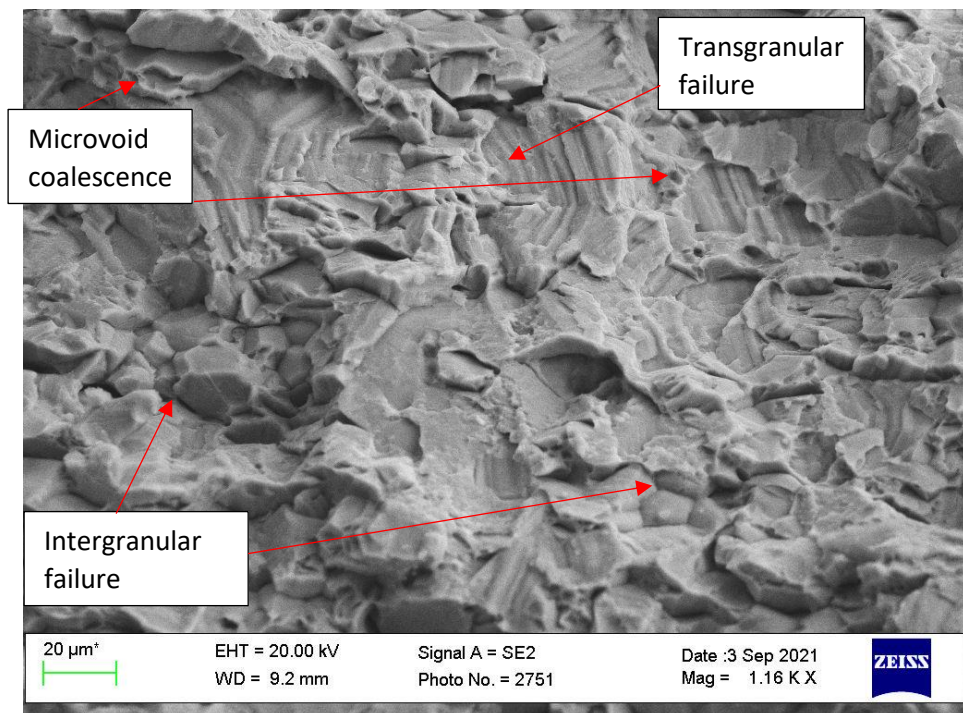
4.1.3.2 Tensile Strength

Table 20 reveals that the parent material exceeded the minimum requirements for tensile strength in both the longitudinal and transverse directions; note, for this property the orientations refer to the directions rather than the faces, see Figure 23. The measured UTS of both orientations was similar, with only approximately 1% difference. A more significant difference exists between the measured values of 0.2% proof strength and % elongation for each orientation of approximately 10% and approximately 14% respectively, which is revealing of the anisotropy inherent with this alloy. Not shown on Table 20 is the standard deviation of the UTS, which is a measure of the spread of results between various test specimens and is thus an indication of the reliability of the result. The standard deviation was calculated to be 3.17 MPa for the longitudinal test specimens and 2.52 MPa for the transverse test specimens, meaning that there was little spread and thus high confidence in the results.

With regards to the fractography of the tensile test specimens, all (both orientations) failed normal to the direction of loading. The fracture surfaces all featured either 45° slopes to the loading direction or took the form of a “V”, i.e. two 45° slopes reflected about the centre, and were bright in appearance with a rough topography. Where 45° slopes are revealed throughout this research, this is indicative of plane stress failure. SEM analysis revealed that the specimens tested in the longitudinal direction failed in a predominantly intergranular manner, although some areas of transgranular failure were present elsewhere on the same test specimens, Figure 33. Very limited microvoid coalescence was present on some grain boundaries, indicative of localised ductile failure, however the overall fracture surface indicated brittle failure, with slip planes visible on several grain boundaries. The presence of the slip planes indicates that a limited number of slip systems were operative. SEM analysis of the transversely tested fracture surfaces revealed mixed intergranular and transgranular failure, similar to the longitudinally tested specimens, although the degree of transgranular failure was significantly higher, Figure 34. Again, localised microvoid coalescence and slip planes were present.

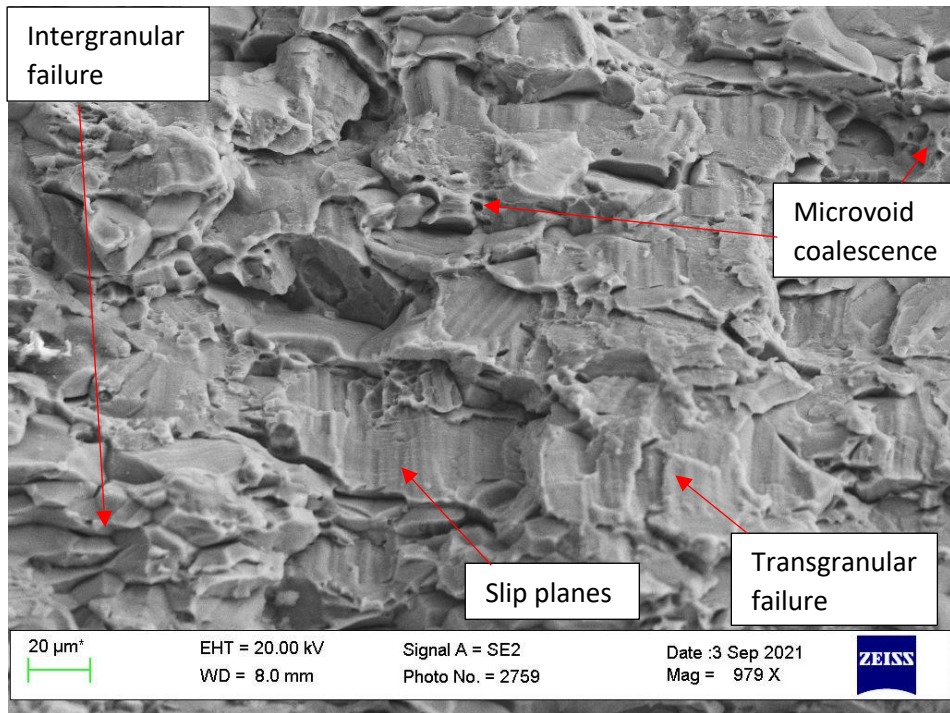


(a)

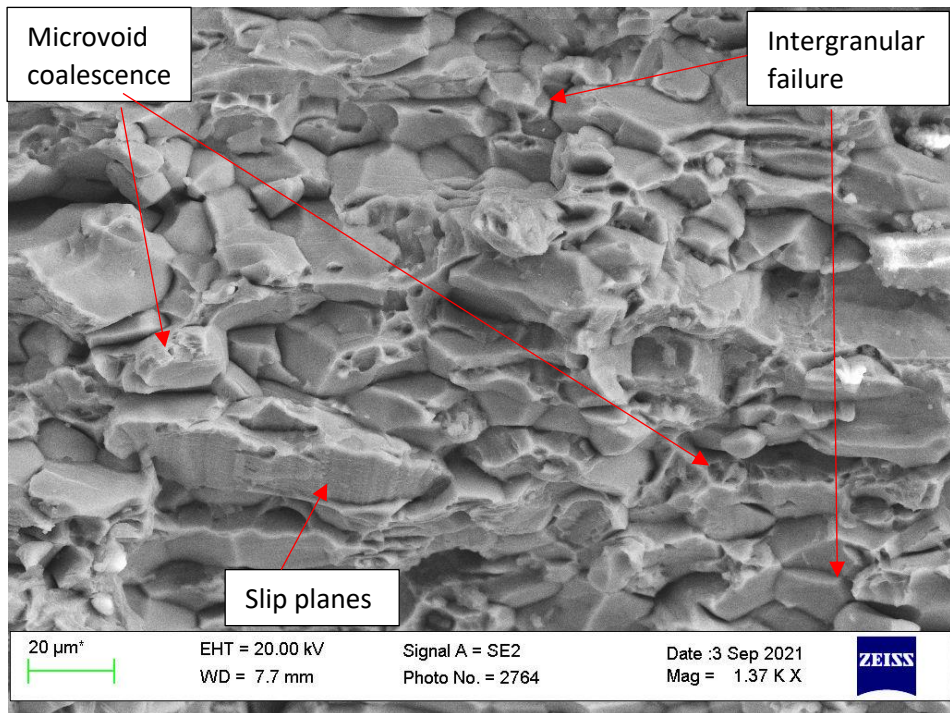


(b)

Figure 33: SEM images showing an AA8090-T81 parent material tensile test specimen fracture surface which was tested in the longitudinal direction. Both (a) and (b) are from the same tensile test specimen and are representative of all fracture surfaces tested in this orientation.



(a)



(b)

Figure 34: SEM images showing an AA8090-T81 parent material tensile specimen fracture surface which was tested in the transverse direction. Both (a) and (b) are from the same tensile test specimen and are representative of all fracture surfaces tested in this orientation.

4.1.3.3 Fatigue Strength

The following shows a brief worked example of the staircase method as detailed in section 3.4.3.2.

Table 21 shows the data set created through testing of the AA8090 specimens. The last non-failure is the first valid specimen for analysis (The British Standards Institution, 2003), and so in this case the data is analysed from specimen number 2 onwards. Therefore, discounting specimen number 1, there are 15 “failures” and 14 “non-failures”. Substituting into Equation 4:

$$\sigma_m = S_0 + d \left(\frac{A}{C} + \frac{1}{2} \right)$$

From the data set (Table 21), $S_0 = 300$ MPa, as it is the lowest stress level considered. The stress increment, d , was 10 MPa as described in section 3.4.3.1.

Table 21: Showing AA8090 fatigue test specimen data set.

Stress S_i (MPa)	Test Specimen Number																														
	1	2	3	4	5	6	7	8	9	10	11	12	13	14	15	16	17	18	19	20	21	22	23	24	25	26	27	28	29	30	
340			X		X																				X				X		
330		0		0		X		X			X												0		X		0		X		
320	0						0		X		0		X		X						X		0					0			
310										0				0		X		X		0		0									
300																	0		0												
X	Failed before 50000 cycles, a record of number of cycles to failure is available																														
0	Unbroken at 50000 cycles																														

Table 22: Showing analysis of data set for AA8090 fatigue testing.

Stress, S_i (MPa)	Level (i)	Frequency (f_i)	if_i	i^2f_i
340	4	0	0	0
330	3	4	12	36
320	2	4	8	16
310	1	4	4	4
300	0	2	0	0
Sum	N/A	14 (Equation 8)	24 (Equation 6)	56 (Equation 7)

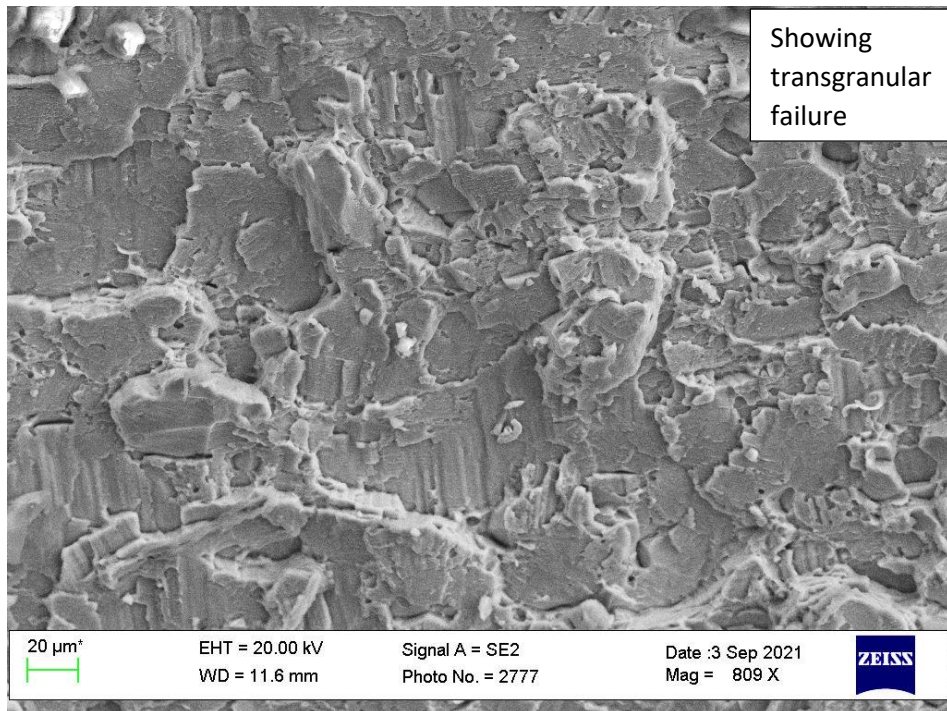
The data set was analysed in terms of the non-failures as there were fewer of these than failures, as per BS ISO 12107:2003 (The British Standards Institution, 2003), and as shown in Table 22. The values of Equation 6, Equation 7 and Equation 8 were revealed by the “Sum” row of Table 22, and thus the values of A, B and C were 24, 56 and 14 respectively, and D (calculated using Equation 9) was 1.06122. The mean fatigue strength (σ_m) was calculated as 322.1 MPa using Equation 4.

The standard deviation (s) was then calculated using Equation 5 and was 17.66 MPa. As $D > 0.3$, the standard deviation was considered to be valid (The British Standards Institution, 2003). The coefficient of variation (η_s) was calculated using Equation 10 (0.055). The lower limit of fatigue strength (\hat{y}) was found using Equation 11 (with $k_{(p,1-\alpha,v)}$ taken from Table B.1 of BS ISO 12107:2003 (The British Standards Institution, 2003) and was 2.068), and was found to be 285.62 MPa. The salient results are therefore summarised in Table 23, and comparison with Table 20 shows that the mean fatigue strength (and lower limit of fatigue strength) is well in excess of the specified minimum requirement.

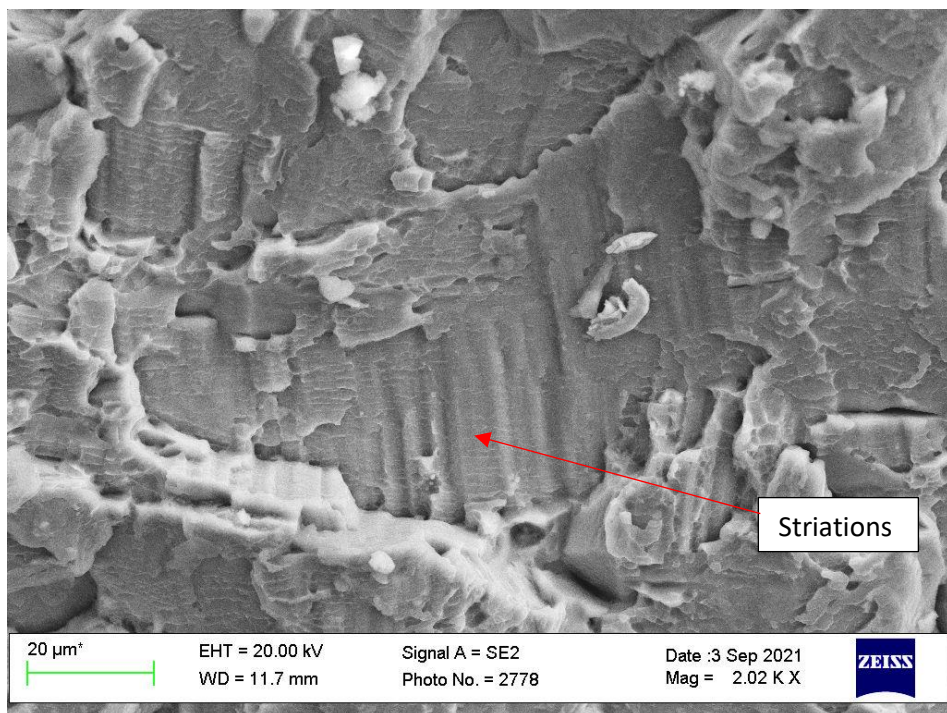
Table 23: Showing summary of AA8090 fatigue testing results.

Material	Mean fatigue strength (σ_m) (MPa)	Standard deviation (s) (MPa)	Coefficient of variation (η_s)	Lower limit of fatigue strength $\hat{y}_{(0.1,0.95)}$ (MPa)
AA8090-T81	322.1	17.66	0.055	285.6

With regards to the fractography of the fatigue specimens, all 15 failed normal to the direction of loading. The fracture surface was macroscopically sloped at approximately 45° to the loading direction, although the direction of the slope changed along the length of the fracture. The fracture surfaces were matt but bright in appearance and macroscopically smooth. SEM analysis, Figure 35, revealed the fracture surfaces to be predominantly transgranular with striations typically indicative of fatigue failure as expected.



(a)



(b)

Figure 35: SEM images showing an AA8090-T81 parent material fatigue specimen fracture surface. Both (a) and (b) are from the same fatigue test specimen and are representative of all fracture surfaces.

4.1.3.4 Residual Stress

The residual stress results of the parent material have little significance in isolation; they are intended merely as a baseline for analysing how the RS varies across the weld. As such, these results are not presented here and are instead presented alongside results from various parts of the weld in later sections (see section 5.2.4).

4.2 BS L165

4.2.1 Elemental Composition

The averaged and normalised ICP-OES results are shown in Table 24 similar to that shown for AA8090. Again, similar to AA8090, the alloying element's average normalised values were all within the tolerable range in the specification, but with some disparities between that measured via ICP-OES and the results provided by the material suppliers, again assumed to be a discrete measured value rather than a maximum or minimum.

Table 24: Showing ICP-OES results for BS L165

	Average normalised elemental concentration (%)				
	Al	Cu	Mg	Mn	Si
BS L165 ¹	remainder	3.9-5.0	0.2-0.8	0.4-1.2	0.5-0.9
As per certificate of conformity ²	remainder	4.29	0.62	0.70	0.72
ICP-OES average normalised results	93.9 (8.8%)	4.5 (9.1%)	0.4 (14.7%)	0.7 (15.6%)	0.5 (17.0%)

Table 24 notes:

- 1 As per BS L165 (The British Standards Institution, 1978a)
- 2 As per Wilsons Certificate of Conformity (Wilson's Aero Metals Alliance, 2016)

Results of the SEM-EDX analysis for BS L165 are shown in Table 25 below. The results show all elements detailed in the specification, not limited to those included in the ICP standard. Table 25 also shows the specification according to BS L165 (The British Standards Institution, 1978a) and the results of laboratory testing by the supplier.

Table 25: Showing SEM-EDX results for BS L165.

	% by weight												Al
	Cr	Cu	Fe	Mg	Mn	Ni	Si	Ti	Ti + Zr	Zn	Others		
											Each	Total	
BS L165 ¹	0.1	3.9-5.0	0.5	0.2-0.8	0.4-1.2	0.1	0.5-0.9	0.15	0.2	0.25	0.05	0.15	Remainder
As per certificate of conformity ²	0.02	4.29	0.28	0.62	0.7	-	0.72	0.02	-	0.01	0.01	0.01	Remainder
SEM-EDX	-	4.4	0.3	0.6	0.7	-	0.8	-	-	0.2	-	-	93.0

Table 25 notes:

- 1 As per (The British Standards Institution, 1978a). All elements in specification included.
- 2 As per Wilsons Certificate of Conformity (Wilsons Aero Metals Alliance, 2016)

The results indicated that all elements were within the specified range and a close correlation between these results and those obtained using ICP-OES was obtained for all elements with the exception of Mg and Si. The results also closely conform to those provided by the supplier. The difference of 0.2%wt and 0.3%wt for Mg and Si respectively between the two techniques is ascribed to a known artefact of quantitative EDX analysis at 1710 NAS using the stated SEM. Upon investigation, Oxford Instruments (manufacturer of the equipment) was not able to determine the cause. Upon advice from the manufacturer, it was not possible to calculate a reliable uncertainty for the EDX process (Latuta, 2021).

4.2.2 Material Microstructure

Micrographs detailing the microstructure of BS L165 (as-received from the manufacturer) are shown in Figure 36 with measured grain sizes shown in Table 26. These micrographs show areas representative of the overall microstructure of the material. Similar sized grains were observed on the longitudinal and transverse faces, with slightly larger grains observed on the S-T face. The RA was within the recommended tolerance for both the L and T faces, however it exceeded this recommendation for the S-T face indicating that additional work is required to find a more reliable value.

No quantified grain size values were found in the literature for BS L165 parent material, although reference was made to the grain size of a close comparison material AA2014-

T6. Several authors (Babu et al., 2013; Rajendran, C., Srinivasan, Balasubramanian, Balaji, & Selvaraj, 2019b; Rajendran, Chinnasamy et al., 2019) report the average parent material grain size as 30 μ m (presumed to be the measurement of the elongated orientation of the grain). While BS L165 and AA2014-T6 are considered to be close “equivalent” specifications, they are not exact and there is opportunity for differences to occur during heat treatment, hot/ cold working etc. The disparity between the results obtained here and that found in literature is attributed to these opportunities, and the results from this research are considered valid. The calculated parent material grain sizes were compared with micrographs of the materials as a secondary confirmation. It was observed that the calculated value was broadly consistent with the appearance of the micrographs, taking account of the differing sizes shown due to the random orientations of the grains through the cross-section.

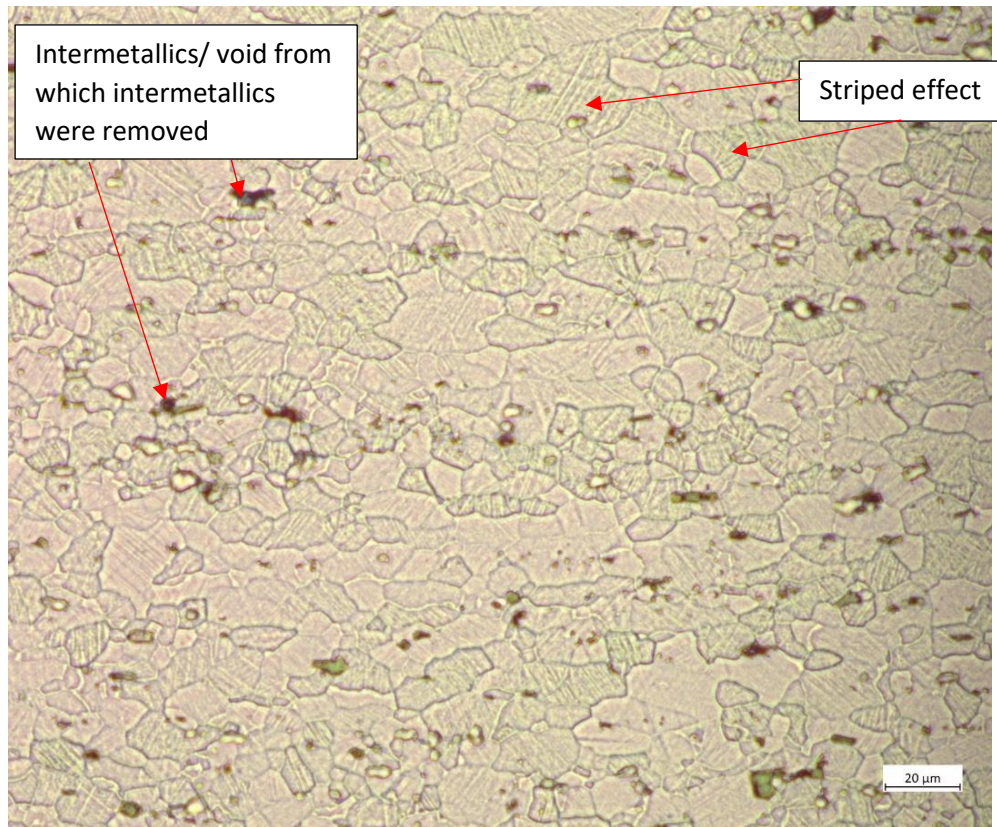
On comparison with AA8090 it was found that BS L165 grains were significantly smaller than AA8090, by approximately 50-60%.

Analysis of the micrographs show a significant number of large (especially in the case of the S-T face) particles, likely to be intermetallics. Babu et al. (2013) carried out EDX analysis of the intermetallics present on AA2014-T4 (Figure 37) and T6 and found them to comprise of Fe-Mn-Al (this was later confirmed by Rajendran et al. (2019)). Based on the similarities in microstructure (acknowledging that the image shown in Figure 37 is that of the T4 condition) and parallels with material composition and heat treatment, it is considered that the intermetallics found in this research are also comprised of Fe-Mn-Al.

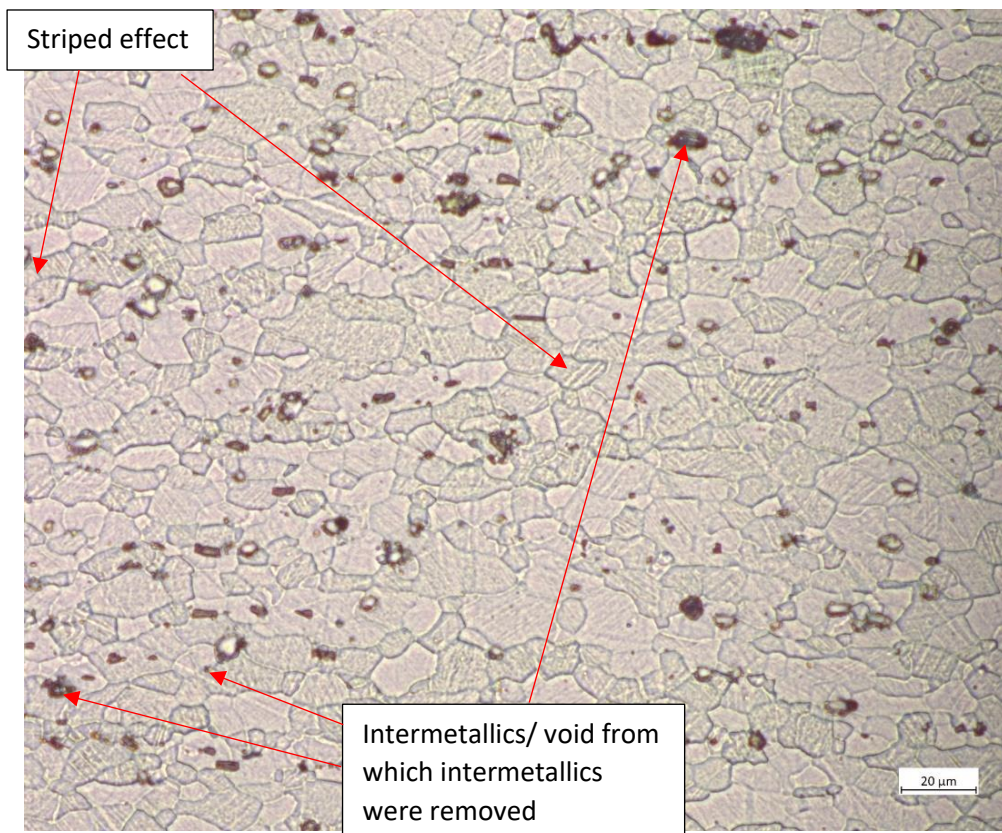
The strengthening precipitate θ' should also be present, based on the work of Gazizov et al. (2015) and Saleh (2018), but was not identified in this research due to the lack of TEM work. Saleh’s work, shown in Figure 6, shows that peak strengthening is achieved with precipitation of θ' ; as this BS L165 is in the T6 temper, this corresponds to the peak aged condition and thus θ' should be present. However, the hardness (shown in section 4.2.3) achieved by this material is approximately mid-range of that expected in the literature (see Table 27 footnotes), indicating that this material has passed peak strength in the aging sequence. This in turn indicates that some over-aging may have occurred and thus the strengthening precipitates may in fact have coarsened or dissolved. This

has likely resulted in the presence of equilibrium (incoherent) θ phase (Figure 6) which causes a reduction in hardness due to its incoherency with the matrix.

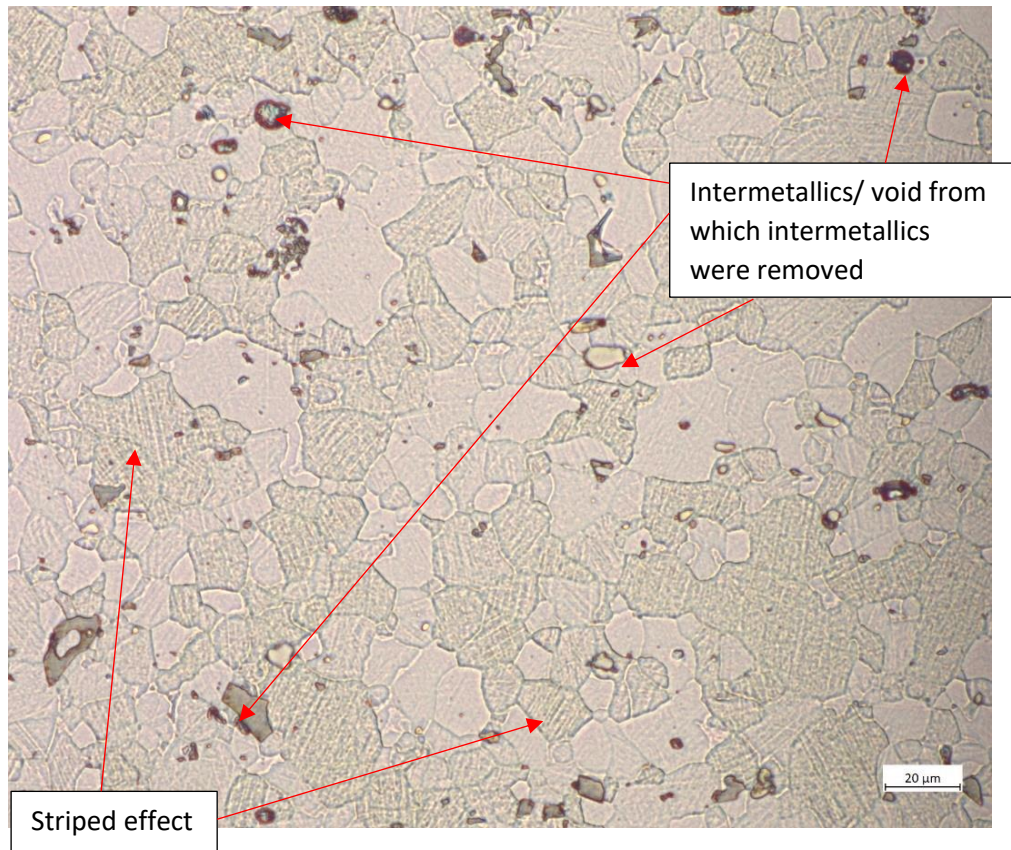
Figure 36 also shows orientated “stripes” within a significant number of the grains. This striped effect is considered to be an etching effect. It is likely that the etch has attacked specific planes within the grain structure which has resulted in these stripes or bands. As etching depends upon the orientation of the grain, and some orientations are more prone to a strong etch reaction, this explains why some grains show this reaction and some do not.



(a)



(b)



(c)

Figure 36: Showing micrographs of BS L165 material: (a) longitudinal face; (b) transverse face; (c) short-transverse face.

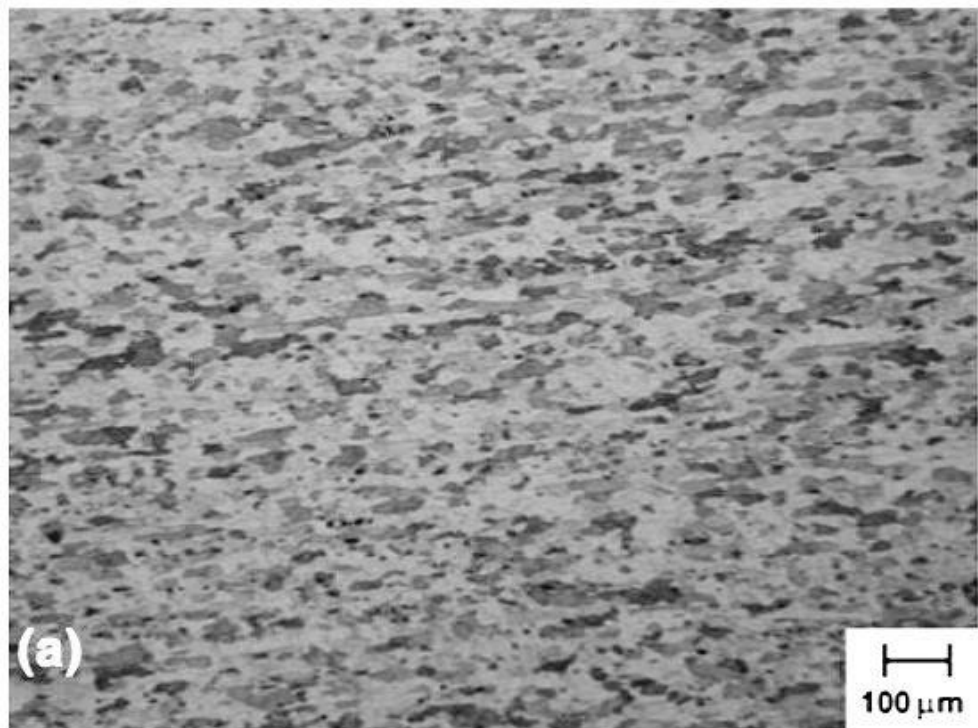


Figure 37: Showing AA2014-T4 microstructure, courtesy of Babu et al. (2013).

Table 26: Showing measured grain sizes of BS L165.

AA8090-T81 material	Grain size (μm)	
	Direction 1	Direction 2
Longitudinal	12.2 (4%)	7.5 (6%)
Transverse	12.0 (4%)	7.2 (4%)
Short-Transverse	14.4 (15%)	13.0 (13%)

4.2.3 Mechanical Properties

As with AA8090 the measured mechanical properties are summarised, in the case of BS L165 this summary is provided in Table 27. The results relevant to each property are then briefly analysed in subsequent sub-sections.

Table 27: Showing summary of BS L165 measured mechanical properties with specified values where appropriate.

Material		Hardness (HV1)	Tensile			Fatigue			
			UTS (MPa)	0.2% Proof Strength (MPa)	% Elongation	Mean Fatigue Strength (σ_m) (MPa)	Standard Deviation (s) (MPa)	Coefficient of Variation (η_s)	Lower Limit of Fatigue Strength ($\hat{Y}_{(0.1,0.95)}$) (MPa)
Specified ¹	Longitudinal	140-180 ²	415	345	7	N/A	N/A	N/A	N/A
	Transverse	140-180 ²	415	345	7	N/A	N/A	N/A	N/A
	Short-Transverse	140-180 ²	N/A	N/A	N/A	N/A	N/A	N/A	N/A
As Measured	Longitudinal	156.3 (± 7.6)	442	397	8.7	N/A	N/A	N/A	N/A
	Transverse	153.3 (± 7.4)	436	393	8.4	306.4	11.71	0.038	282.2
	Short-Transverse	159.3 (± 8.4)	N/A	N/A	N/A	N/A	N/A	N/A	N/A

Table 27 notes:

- 1 BS L165 (The British Standards Institution, 1978a)
- 2 No hardness value was detailed within the specification BS L165 (The British Standards Institution, 1978a), therefore the specified hardness values were taken from W.H.P.S. 439 (Westland, 2018)

4.2.3.1 *Hardness*

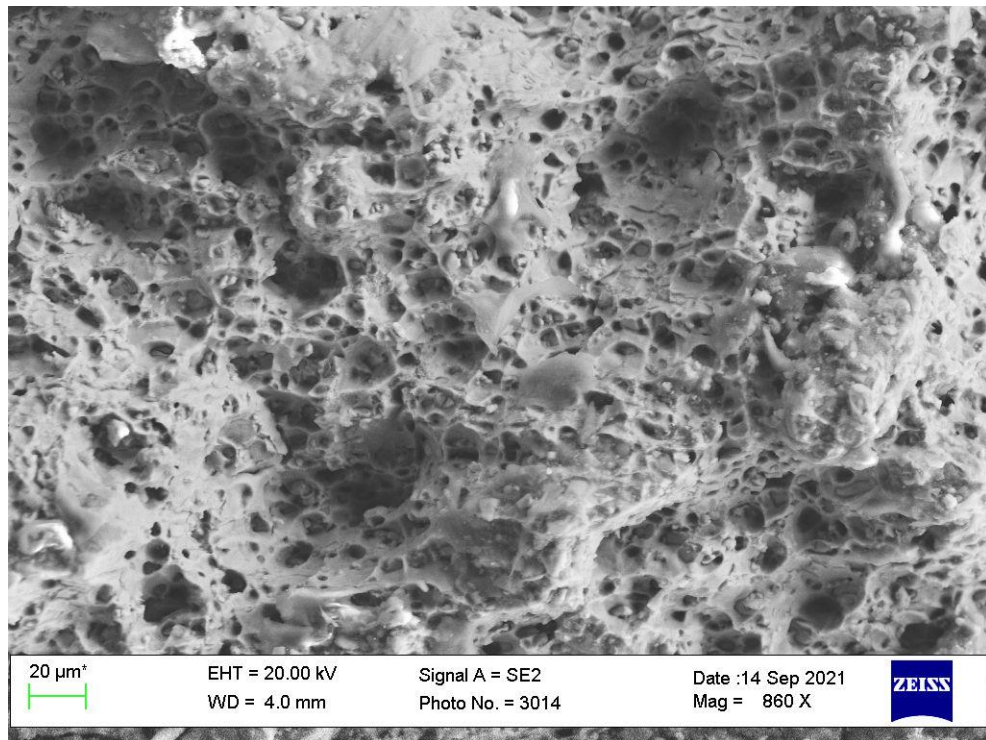
A hardness range was specified for BS L165; the minimum value (140 HV) was used in all comparisons and analyses throughout the research. For BS L165 the measured hardness values were similar in all orientations, i.e. there was only an approximate 4% difference between the extremes. As with AA8090, for this property the orientations refer to faces rather than directions (Figure 23). No hardness value is specified within the BS L165 specification (The British Standards Institution, 1978a) therefore the specification values were taken from Agusta Westland (now Leonardo Helicopters) Westland Helicopter Process Specification (WHPS) 439 (Westland, 2018). This specification was produced by the manufacturer and used for materials utilised on the aircraft under strict protocols used in aerospace engineering. All results were well in excess of the minimum required value specified, although as previously described, the results did not reach the peak within the range. Only the longitudinal and short-transverse results were used in the analysis during comparison with the welded joints, see 5.2.1.1.

4.2.3.2 *Tensile Strength*

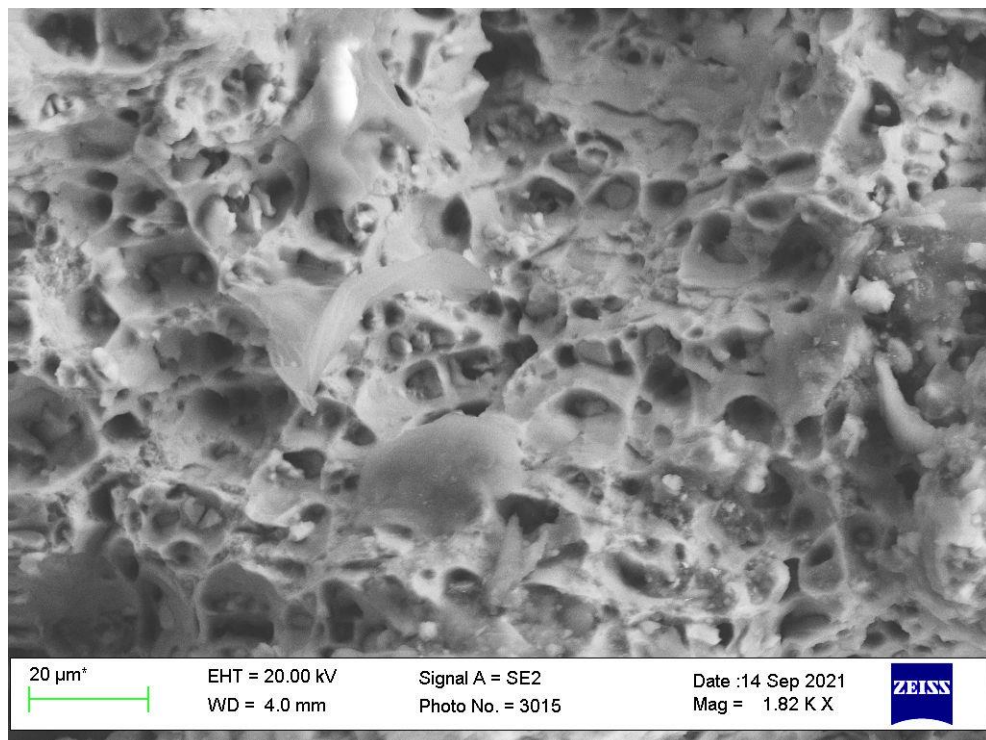
Table 27 reveals that the BS L165 material exceeded the minimum requirements for tensile strength in both the longitudinal and transverse directions; note, for this property the orientations refer to the directions rather than the faces, see Figure 23. The measured UTS of both orientations was similar, with only approximately 1% difference. This was also true to the 0.2% proof strength and elongation, with only approximately 1% and approximately 3% difference respectively. This indicates a lack of anisotropy in this alloy. The standard deviation was calculated to be 2.82 MPa for the longitudinal test specimens and 2.20 MPa for the transverse test specimens, meaning that there was little spread and thus high confidence in the results.

With regards to the fractography of the tensile test specimens, all (both orientations) failed normal to the direction of loading. The fracture surfaces all featured either 45° slopes to the loading direction (indicative of a plane stress failure) or took the form of a “V” (see section 4.1.3.2). The fracture surfaces were macroscopically bright in appearance with a slightly rough topography, although not as rough as AA8090. SEM analysis revealed that the specimens tested in both orientations failed in a

predominantly ductile manner, Figure 38 and Figure 39, with microvoid coalescence featuring across the fracture surface originating from large particles.

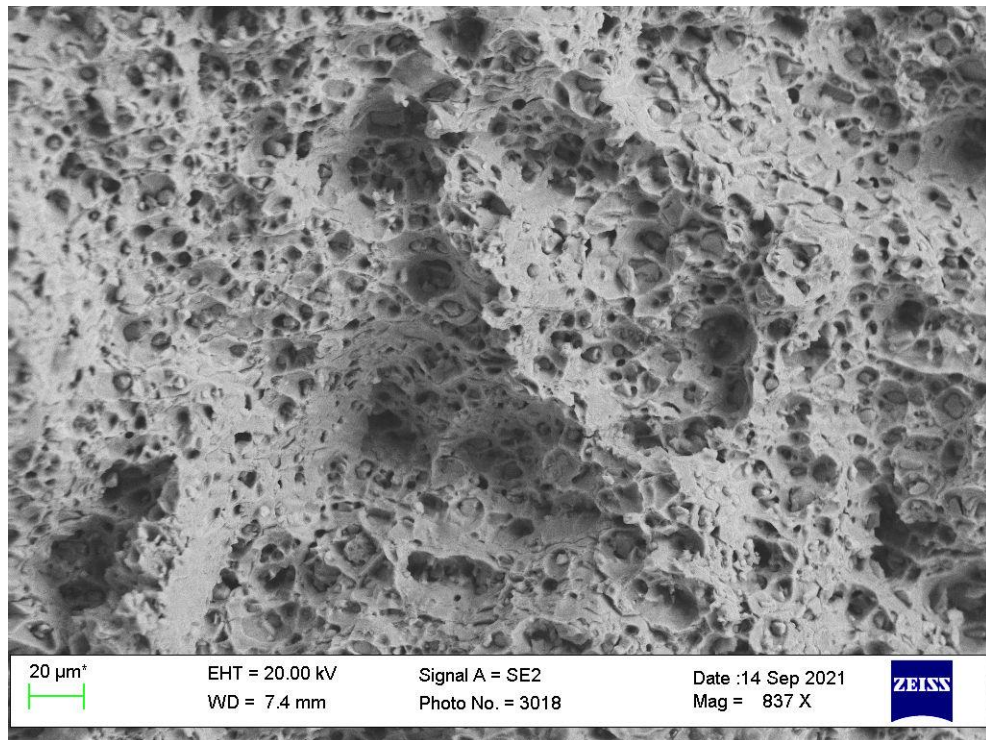


(a)

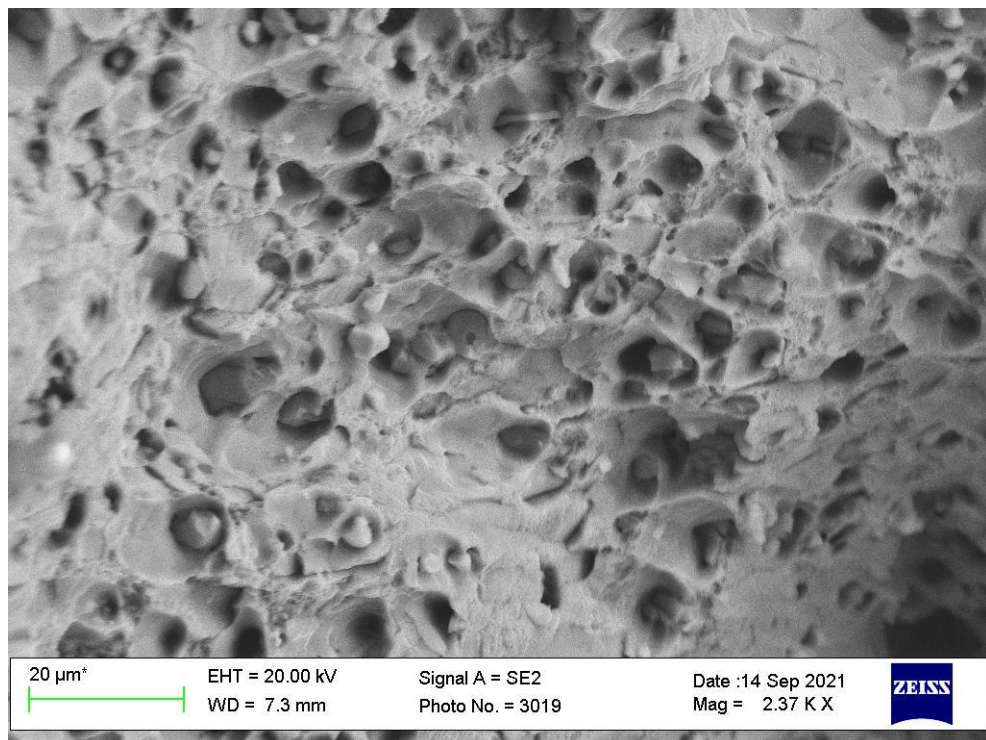


(b)

Figure 38: SEM images showing an BS L165 parent material tensile test specimen fracture surface which was tested in the longitudinal direction. Both (a) and (b) are from the same tensile test specimen and are representative of all fracture surfaces tested in this orientation.



(a)



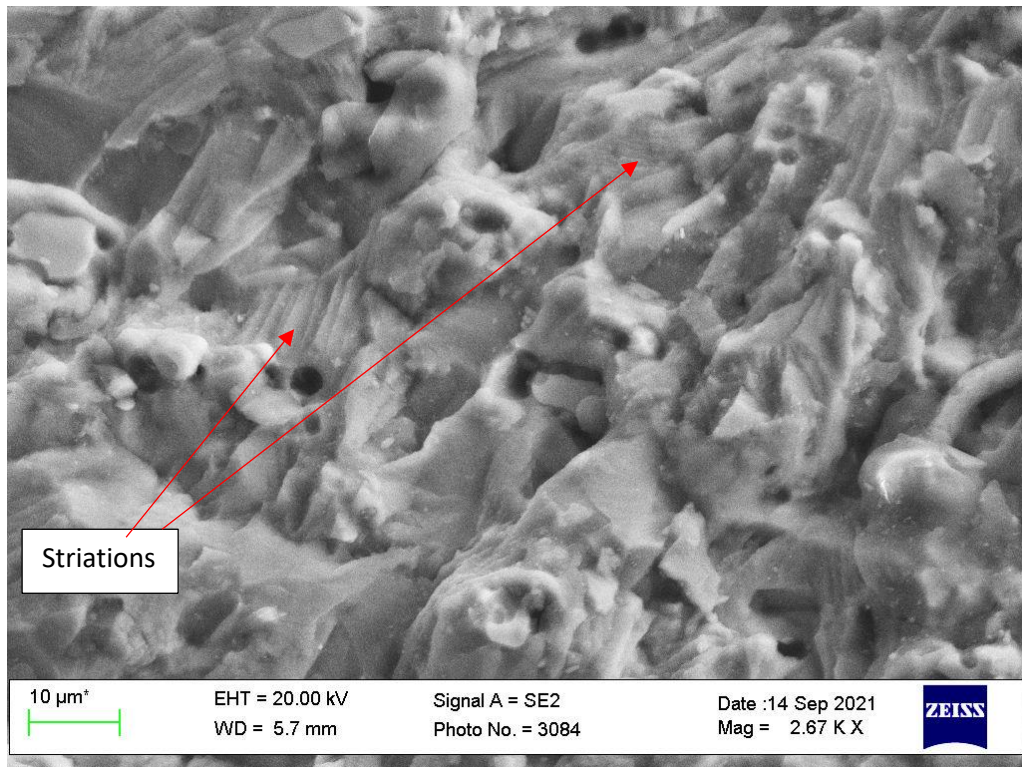
(b)

Figure 39: SEM images showing an BS L165 parent material tensile test specimen fracture surface which was tested in the transverse direction. Both (a) and (b) are from the same tensile test specimen and are representative of all fracture surfaces tested in this orientation.

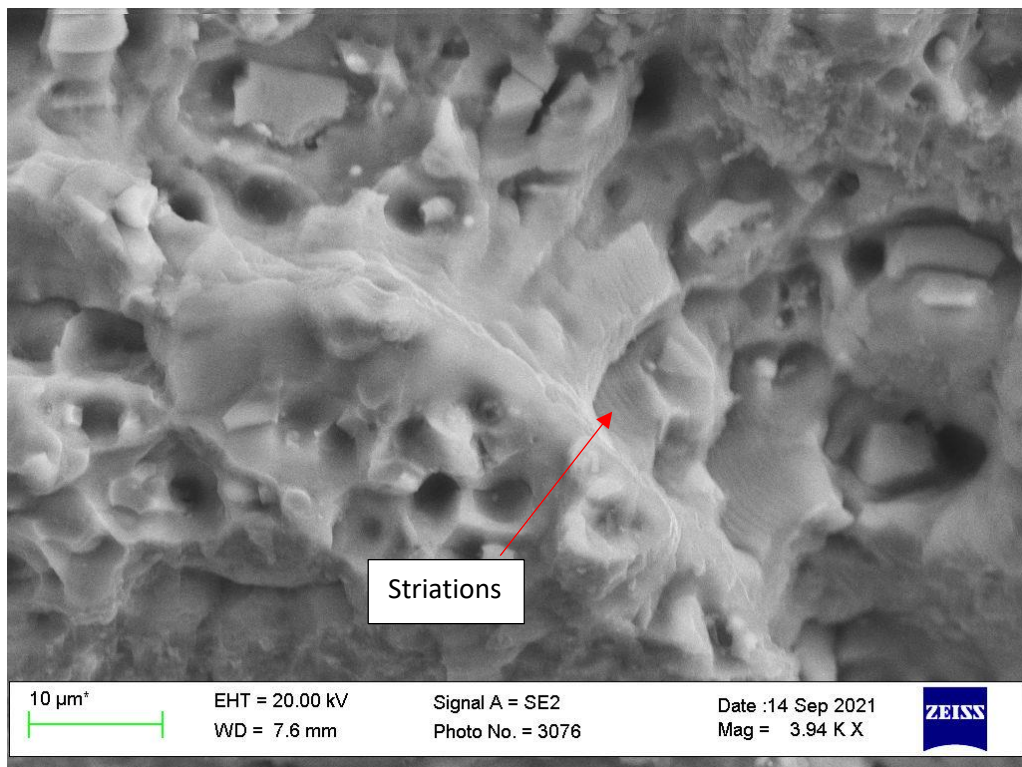
4.2.3.3 *Fatigue Strength*

There is no fatigue strength specified within the official specification (The British Standards Institution, 1978a), however the Aluminum Alloys Database, found using a Knovel search (Aluminum Alloy Database, 2021), quotes the room temperature fatigue strength of AA2014-T6 (non-clad) to be 269 MPa at 10^5 cycles, 207 MPa at 10^6 , 166 MPa at 10^7 and 131 MPa at 10^8 (no value provided for 10^4). As this testing was conducted on BS L165 which is alclad and the cycle limit was 50,000, an order of magnitude lower, the two are not directly comparable. This material achieved 306.4 MPa as the mean fatigue strength; rough extrapolation suggests that this could be a reasonable value for the material to achieve, especially due to the presence of the alclad layer which reduces overall material strength slightly (Table 5). The testing on this material achieved a lower standard deviation and coefficient of variation (comparison of fatigue data in Table 21 and Table 27) than AA8090 indicating less scatter in the results, and the lower limits of fatigue strength of the two materials were similar, despite AA8090 having an overall larger mean fatigue strength.

With regards to the fractography of the fatigue test specimens, all 18 failed specimens fractured normal to the direction of loading. The fracture surfaces were sloped at 45° to the direction of loading, although the direction of slope altered along the fracture of some specimens. The fracture surfaces were macroscopically smooth and had a matt but bright appearance. SEM analysis revealed that significant areas of the fracture surface had undergone ductile overload, with only relatively small areas failing via fatigue. The ductile overload manifested in a similar manner to that already observed in tensile testing (section 4.2.3.2). Those areas which failed via fatigue exhibited predominantly transgranular failure, with striations typically associated with fatigue observed, Figure 40.



(a)



(b)

Figure 40: SEM images showing BS L165 parent material fatigue specimen fracture surface. Both (a) and (b) are from the same fatigue test specimen and are representative of all fracture surfaces.

4.2.3.4 Residual Stress

The residual stress results of the parent material have little significance in isolation; they are intended merely as a baseline for analysing how the RS varies across the weld. As such, these results are not presented here and are instead presented alongside results from various parts of the weld in later sections (see section 5.2.4).

5 Welding and Test Results

5.1 As-welded examination

5.1.1 Photography/ Stereo Microscopy

The weld surface appearance is discussed in depth in the section relevant to each configuration in Chapter 6. An example of a BS L165 \perp weld is shown in Figure 41. While there were features which were common to most of the eight weld configurations, all weld surfaces varied to a degree and many varied in appearance between welds of the same configuration and even along the length of one weld. Features common to many of the welds were: partial surface ripples, galling⁵, grooves, smooth “ironed” material and material deposited adjacent to the weld. Not shown on Figure 41 but also common to many welds were areas of underfill in the rippled area. In this context underfill is defined as the condition where cross-sectionally part of the weld does not sit flush with or above the parent material, i.e. the weld area is underfilled.

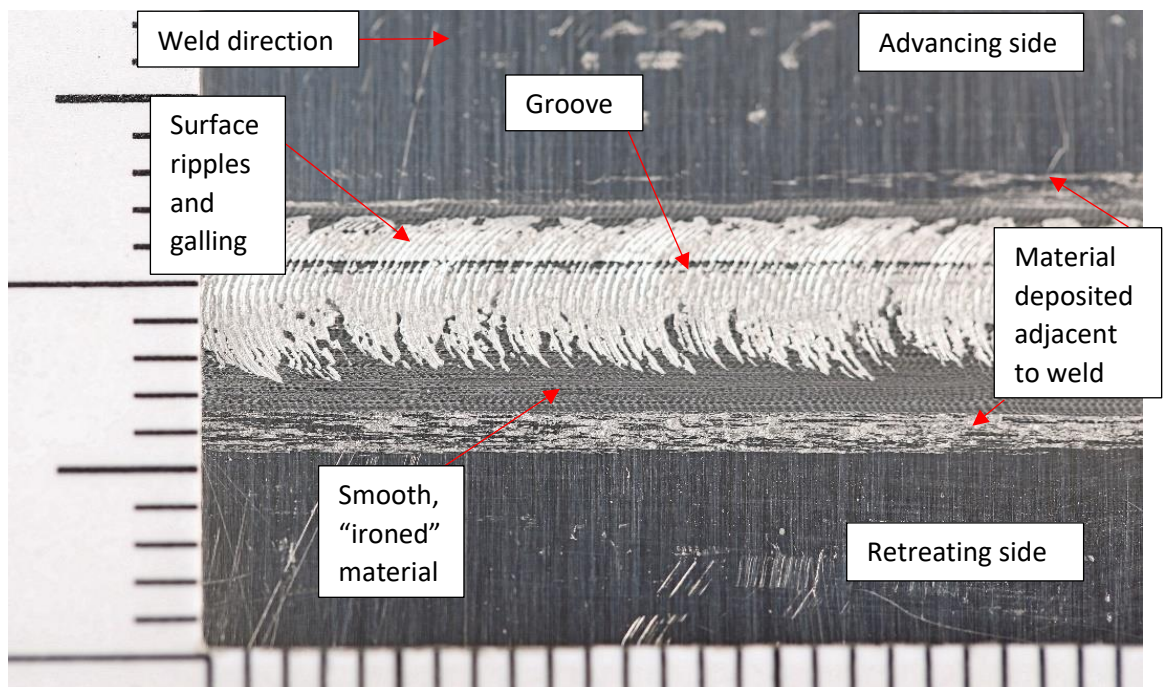


Figure 41: Showing macro image of upper surface of as-welded BS L165 \perp .

⁵ In FSW, galling refers to a poor surface finish with soft material deposited in a uneven and rough manner on the surface of the weld (The Welding Institute, 2013).

5.1.2 Optical and Contact Profilometry

Images generated using optical profilometry, together with contact profilometry plots are shown in Figure 42 and Figure 43. While there were differences between all configurations (including differences between \parallel and \perp welds of the same materials), two examples are provided to illustrate the main features. Optical profilometer images and contact profilometry plots are shown for all configurations in the relevant section of Chapter 6.

Some welds appeared quite smooth overall, Figure 42 with few material deposits on the upper surface but with a clearly defined trench along the weld line off-set from the centre towards the advancing side. Partial ripples were present on the advancing side of the weld although these are not clearly visible in the optical profilometry image (Figure 42(a)) and ridges on both the advancing and retreating edges were observed. Others were rougher with significant material deposited unevenly on the top surface, Figure 43. Where the top surface material was uneven, the markings from the shoulder could be observed underneath. Ridges were observed at the weld line edges and only partial weld thinning where the material had not sufficiently refilled the top surface as it traversed.

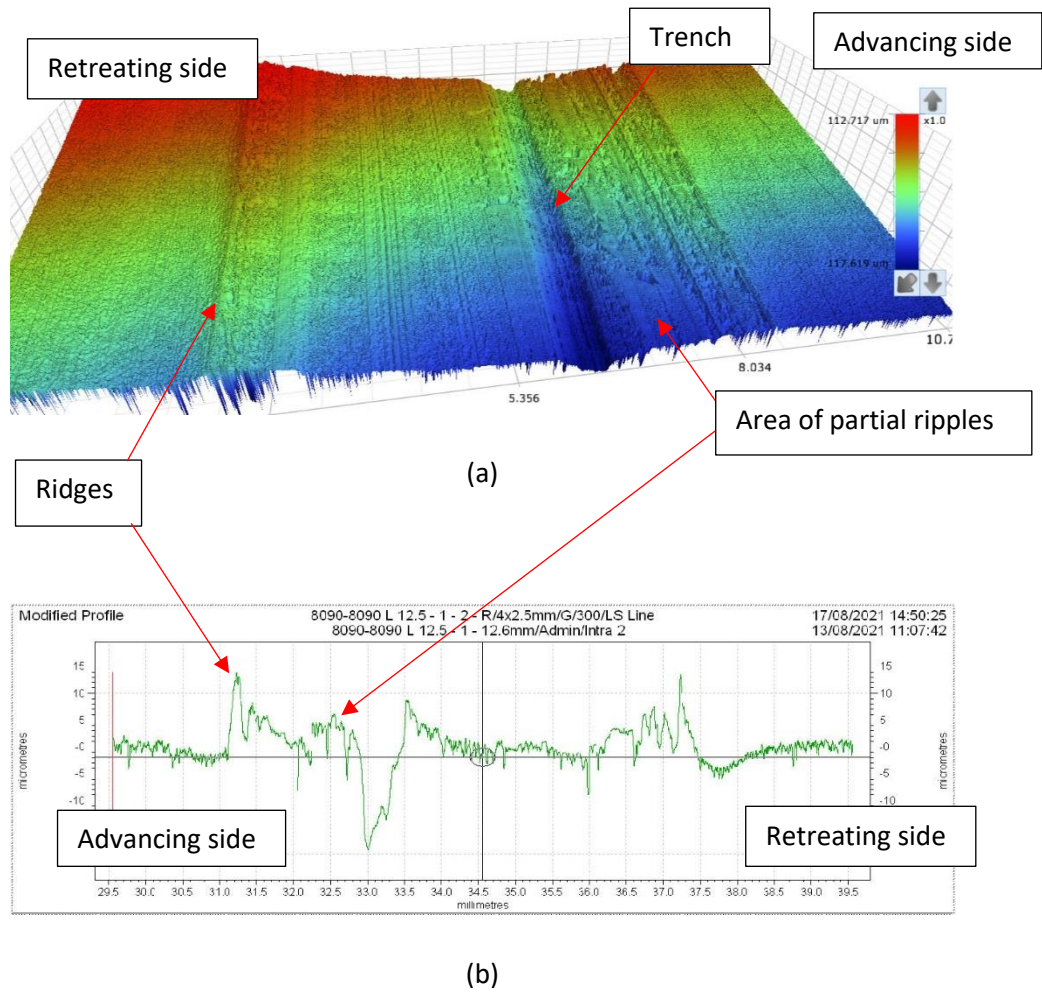


Figure 42: Showing (a) output generated using an optical profilometer, and (b) contact profilometry plot of upper surface of as-welded AA8090 II joint.

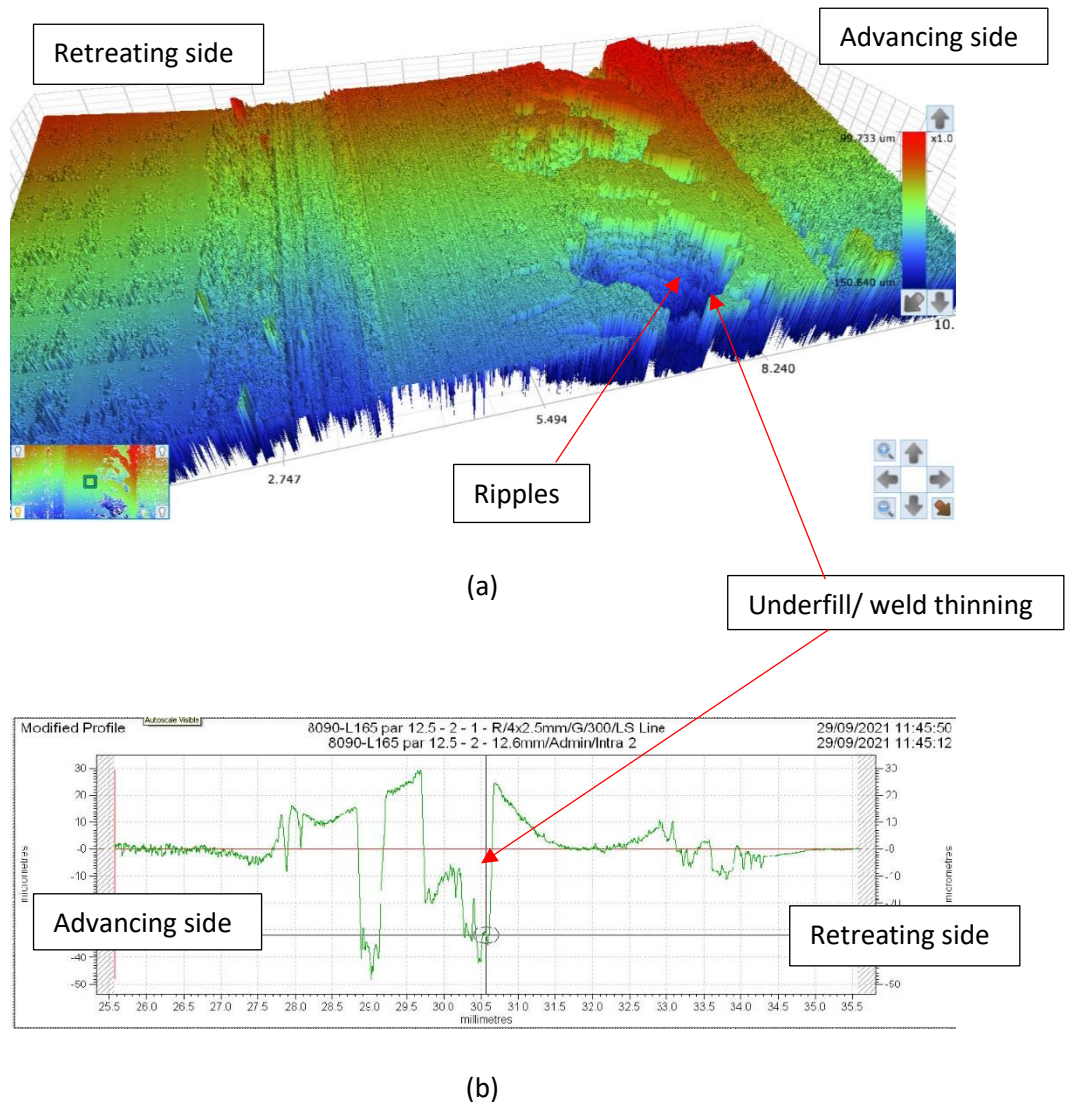


Figure 43: Showing (a) output generated using an optical profilometer, and (b) contact profilometry plot of upper surface of as-welded AA8090-BS L165 II joint.

5.1.3 Optical Microscopy

5.1.3.1 Weld Cross-sections

Cross-sections of each configuration are discussed in detail in Chapter 6, with general findings presented here. Throughout this chapter, and in Chapter 6, where a micrograph is shown, the area described is representative of the overall microstructure of the area of the weld under discussion.

A macrograph of an etched weld cross-section of BS L165 I is shown in Figure 44. The macrograph differentiates the different areas of the weld (HAZ, TMAZ and nugget) and

shows the “cup” shape typical of a stationary shoulder friction stir weld. It was noted that most welds had a larger retreating side TMAZ than that on the advancing side, as shown in Figure 44. A second etched cross-section is shown in Figure 45; this is a dissimilar weld of AA8090-BS L165 \perp . This shows the same features as described for the BS L165 \perp cross-section, however due to the differing etch response of the two materials, the degree of mixing between the two is clearly seen. It should be noted that this degree of mixing varied between different weld configurations; this is discussed further in Chapter 6. This mixing is shown in greater detail in Figure 46.

The advancing side (BS L165) HAZ, TMAZ and nugget of an BS L165-AA8090 \perp weld are shown in greater detail in Figure 47. Highly refined recrystallised grains were observed in the nugget, while deformed and elongated grains were observed in the TMAZ and grains typically resembling the parent material (although not identical to) were observed in the HAZ. A well-defined boundary was observed between the nugget and the TMAZ on the advancing side, while the boundary on the retreating side was more subtle. This feature was also noted by Ramanjaneyulu, Madhusudhan Reddy, Venugopal Rao and Markandeya (2013).

With the exception of AA8090 II and \perp welds, all welds include alclad material originating from the BS L165 material. This can mix within the weld in various places, for example along the top surface which can be faintly seen on Figure 44 and Figure 45. Additionally, the alclad material can be deposited sub-surface, i.e. during the stirring process core material is deposited on the surface with alclad trapped within, as shown in Figure 48.

Figure 49 shows the joint line at the weld root on an AA8090-BS L165 II. Within several of the welds insufficient mixing at the weld root as indicated by a continuous joint line remnant was revealed. This was attributed to oxides from the original material surfaces being drawn in during material flow around the tool pin. This was observed in a significant number of the welds to varying degrees. In the case shown in Figure 49, as the oxide line connects with the weld root, the joint line remnant is known as a “kissing bond”(Jolu, Morgeneyer, & Gourgues-Lorenzon, 2010). Kissing bonds were present despite successful bend tests being performed as a quality assurance measure during weld production. In this case the alclad layer can also be observed being drawn into the joint line, alongside the oxides. The alclad layer was also drawn across to the advancing AA8090 (non-alclad) side for a limited distance as a result of the stirring process. Even

when a suitable weld without the “kissing bond” defect was achieved, and mixing observed as shown in Figure 46, it was clear that the material from the advancing and retreating sides each dominate particular parts of the nugget, as shown in Figure 45.

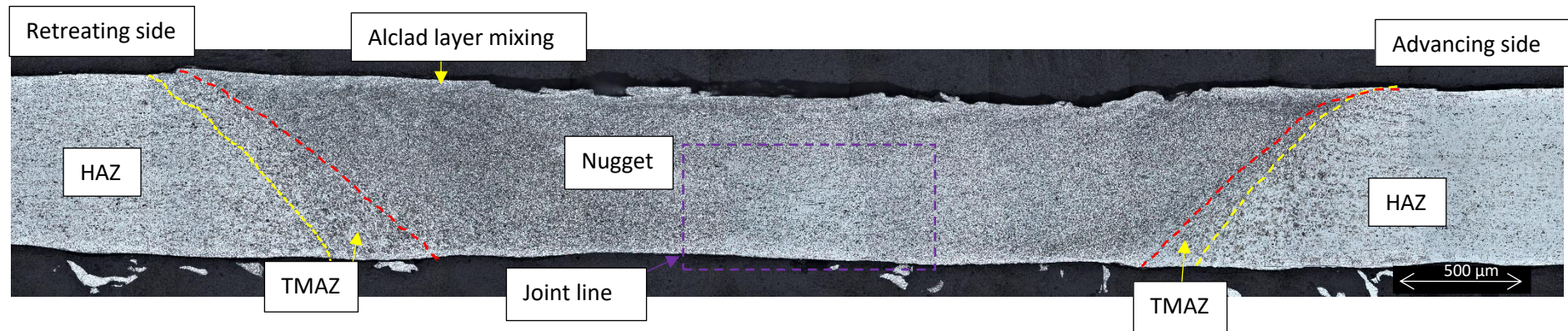


Figure 44: Macrograph showing BS L165 \perp etched weld cross section.

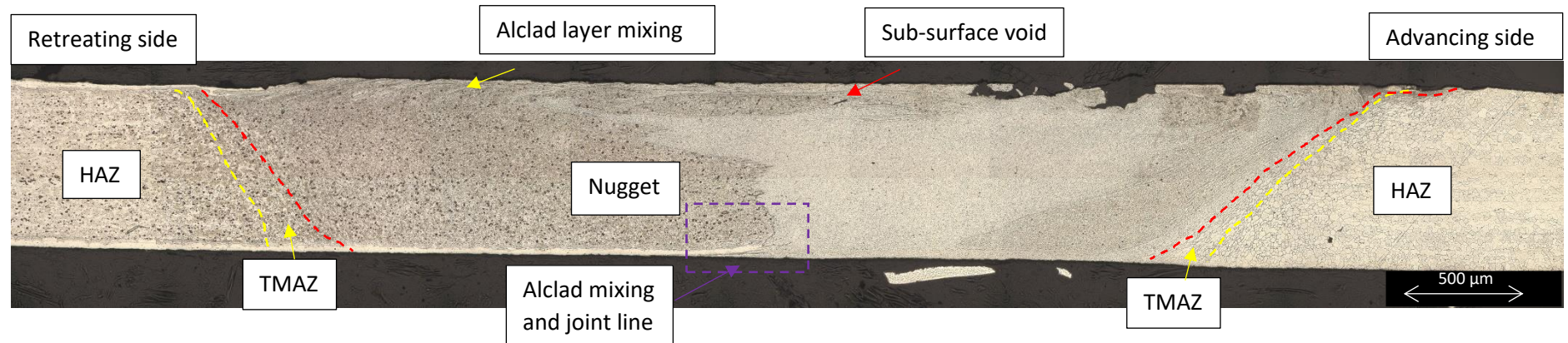


Figure 45: Macrograph showing an AA8090-BS L165 \perp etch weld cross section.

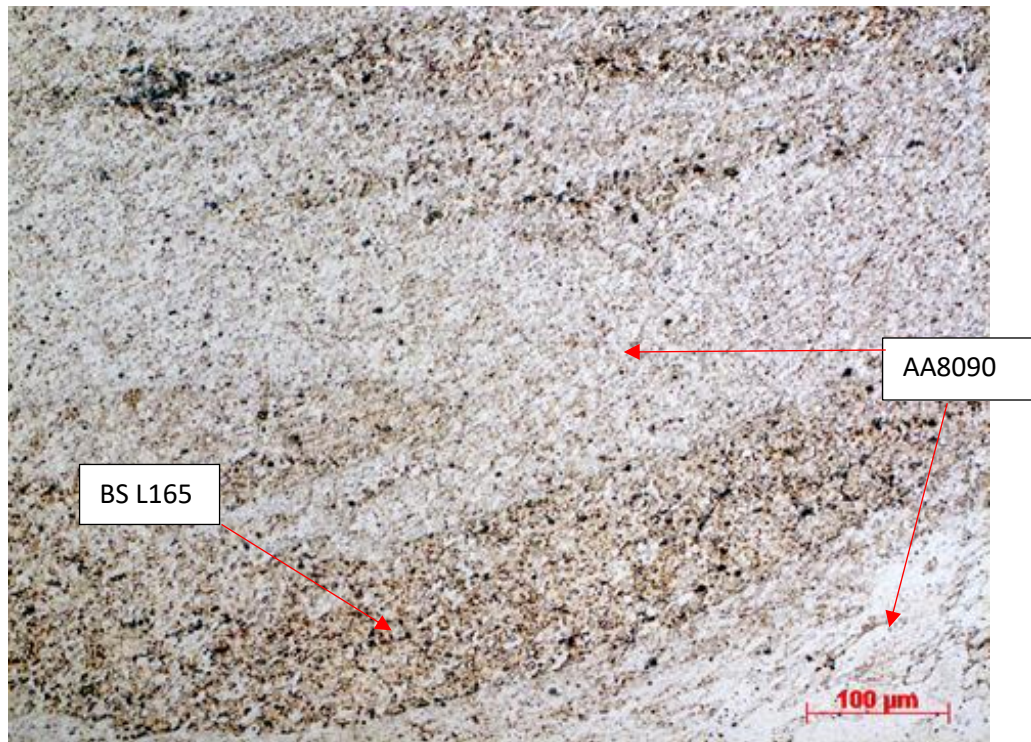


Figure 46: Showing material mixing on dissimilar AA8090-BS L165 || weld.

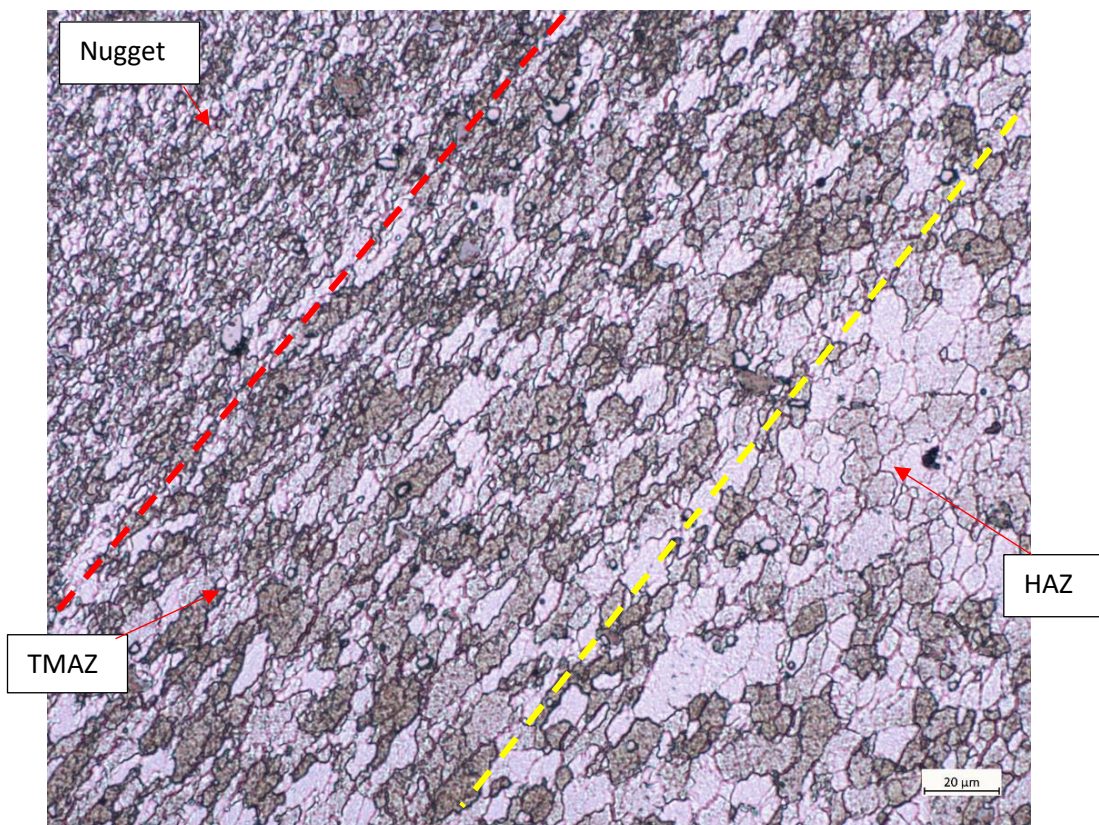


Figure 47: Showing advancing side HAZ, TMAZ and nugget of BS L165-AA8090 \perp weld. The dashed lines show the approximate boundary between the different zones.

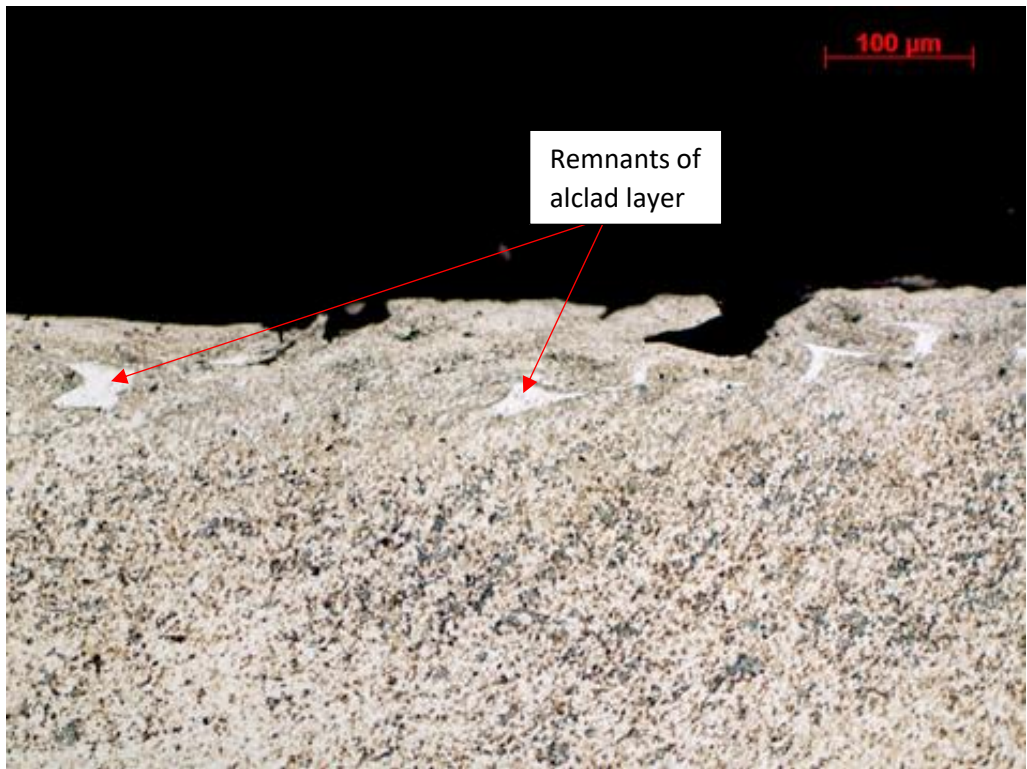


Figure 48: Showing alclad layer within weld of a BS L165 || weld.

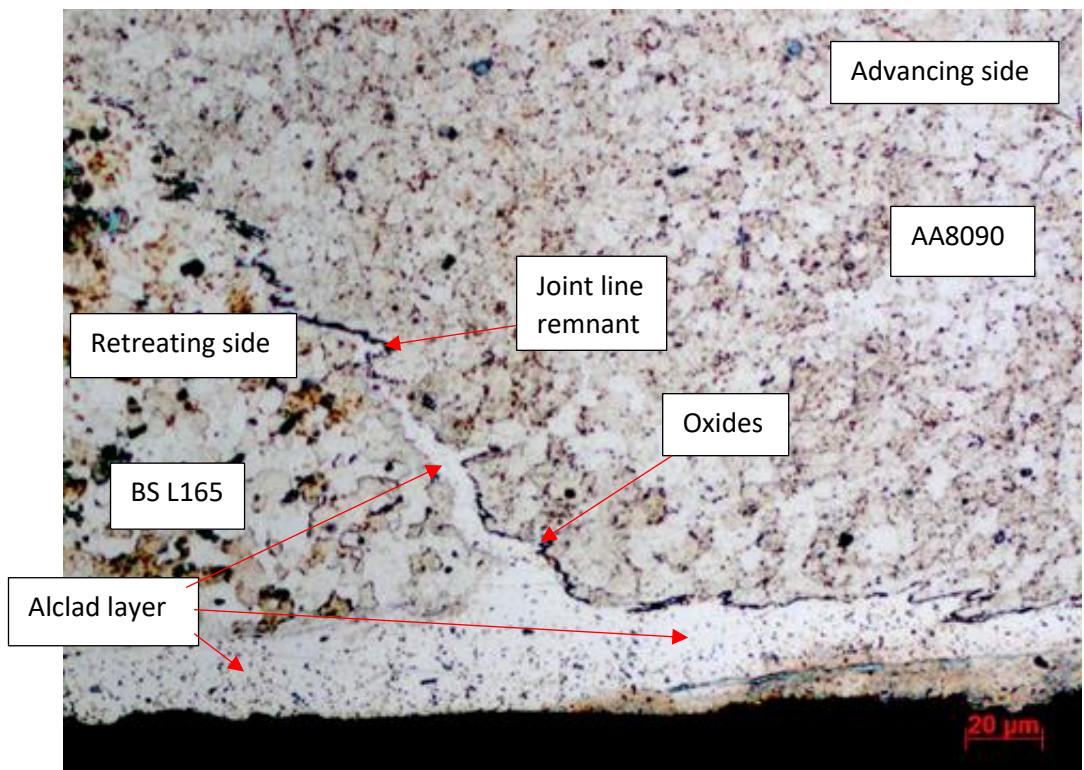


Figure 49: Showing joint line remnant on an AA8090-BS L165 || dissimilar weld.

5.1.3.2 Grain Size

Table 28 shows the calculated grain sizes for different areas of the weld, with the RA (see section 3.3.1.2) shown in brackets. Two areas of the nugget are reported in the table, advancing and retreating; these refer to the areas of the nugget dominated by the material from the advancing or retreating side respectively. All similar welds, i.e. AA8090-AA8090 or BS L165-BS L165, show slightly smaller grains on the advancing side of the nugget than the retreating, although in some cases this difference is very slight. The results for dissimilar welds were compared with the results for similar welds. In most cases it was found that the grain size of AA8090 in the nugget was reduced and the grain size of BS L165 in the nugget was increased. This was for the same position (advancing or retreating) and same orientation. The BS L165-AA8090 \perp retreating nugget did not follow this trend.

Several of the values listed in Table 28 have associated RAs far in excess of the recommended tolerance of 10%, in one case reaching 35%. This strongly implies that some results are not entirely reliable and further work may be required to achieve sufficient confidence in the results.

Table 28: Showing calculated average grain sizes for each section of welds.

Weld Configuration	Area of Weld	Average grain diameter (μm)		Weld Configuration	Area of Weld	Average grain diameter (μm)	
		Direction 1	Direction 2			Direction 1	Direction 2
AA8090	Advancing HAZ	25.3 (19%)	18.9 (13%)	AA8090-BS L165	Advancing HAZ	15.3 (11%)	12.4 (7%)
	Advancing TMAZ	21.9 (17%)	12.5 (14%)		Advancing TMAZ	18.1 (16%)	7.8 (15%)
	Advancing nugget	7.9 (8%)	7.8 (10%)		Advancing nugget	6.8 (7%)	6.6 (5%)
	Retreating nugget	10.6 (19%)	8.8 (13%)		Retreating nugget	7.4 (15%)	5.4 (9%)
	Retreating TMAZ	16.9 (17%)	9.5 (8%)		Retreating TMAZ	13.3 (20%)	7.5 (13%)
	Retreating HAZ	17.2 (14%)	15.3 (11%)		Retreating HAZ	10.0 (12%)	8.2 (6%)
AA8090 ⊥	Advancing HAZ	15.3 (6%)	12.2 (6%)	AA8090-BS L165 ⊥	Advancing HAZ	17.5 (11%)	13.2 (9%)
	Advancing TMAZ	20.3 (32%)	8.6 (16%)		Advancing TMAZ	21.9 (25%)	10.4 (16%)
	Advancing nugget	8.8 (9%)	7.4 (8%)		Advancing nugget	8.5 (12%)	6.8 (11%)
	Retreating nugget	9.4 (14%)	8.3 (10%)		Retreating nugget	7.8 (10%)	6.1 (12%)
	Retreating TMAZ	18.0 (22%)	9.5 (22%)		Retreating TMAZ	12.9 (35%)	8.0 (19%)
	Retreating HAZ	17.0 (11%)	13.4 (8%)		Retreating HAZ	13.0 (5%)	8.2 (11%)
BS L165	Advancing HAZ	11.3 (14%)	7.6 (10%)	BS L165-AA8090	Advancing HAZ	12.7 (10%)	7.4 (11%)
	Advancing TMAZ	12.6 (17%)	6.3 (10%)		Advancing TMAZ	13.7 (20%)	8.7 (12%)
	Advancing nugget	5.6 (16%)	4.8 (11%)		Advancing nugget	7.2 (10%)	5.8 (6%)
	Retreating nugget	6.6 (10%)	4.9 (14%)		Retreating nugget	10.4 (10%)	8.8 (9%)
	Retreating TMAZ	12.1 (22%)	7.6 (14%)		Retreating TMAZ	16.8 (17%)	11.6 (9%)
	Retreating HAZ	12.5 (8%)	7.5 (12%)		Retreating HAZ	17.2 (14%)	14.1 (9%)
BS L165 ⊥	Advancing HAZ	11.0 (8%)	7.9 (9%)	BS L165-AA8090 ⊥	Advancing HAZ	12.7 (14%)	7.9 (20%)
	Advancing TMAZ	14.3 (12%)	6.5 (7%)		Advancing TMAZ	14.2 (21%)	7.2 (11%)
	Advancing nugget	5.5 (10%)	4.8 (12%)		Advancing nugget	6.9 (12%)	5.0 (11%)
	Retreating nugget	6.3 (13%)	4.9 (5%)		Retreating nugget	10.9 (10%)	7.7 (11%)
	Retreating TMAZ	13.1 (12%)	7.6 (14%)		Retreating TMAZ	17.4 (22%)	9.4 (10%)
	Retreating HAZ	11.3 (11%)	7.8 (8%)		Retreating HAZ	16.3 (7%)	13.5 (7%)

The longer (direction 1) grain sizes from Table 28 have been plotted against the area of the weld in Figure 50. A strong correlation in graph plot shape is shown for all

configurations with the two exceptions being the advancing HAZ of AA8090 ||, and the overall shape of AA8090-BS L165 ⊥ is slightly different to the others.

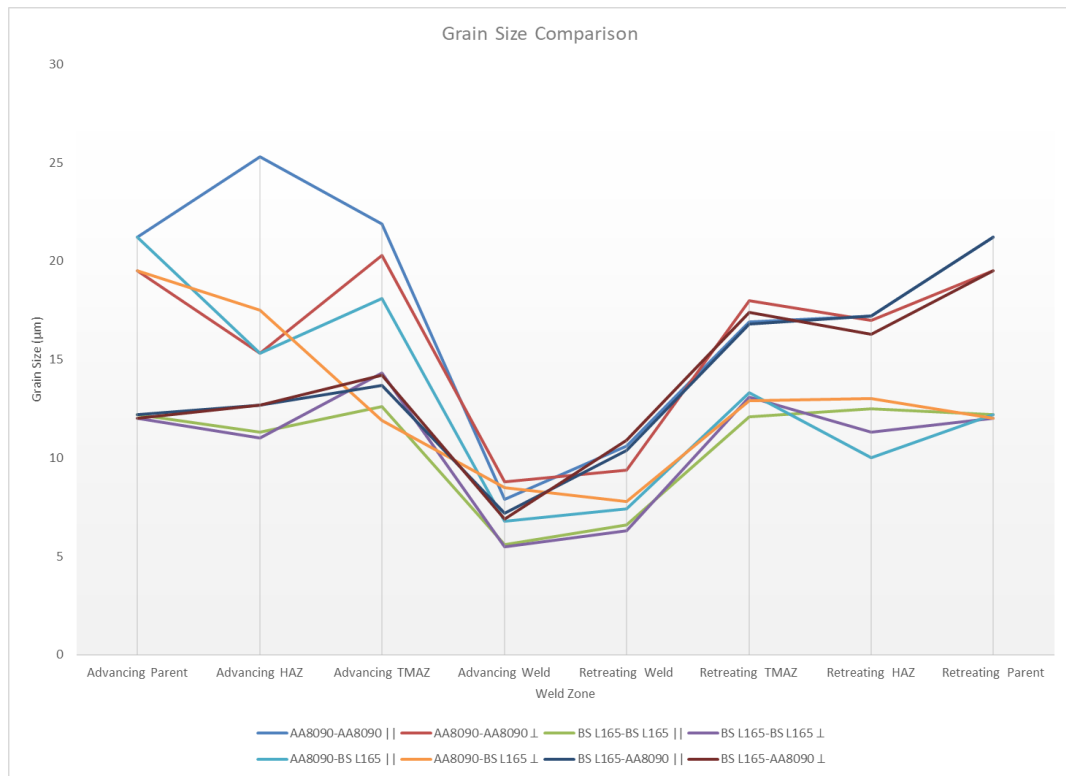


Figure 50: Showing the grain size at different areas of the weld for all configurations.

5.2 Testing and Analysis

5.2.1 Hardness

5.2.1.1 Comparison Values

For comparison of the welded specimen hardness values, relevant parent material hardness specifications and measured hardness values were used, section 4.1.3.1. The values used for comparison were dependent on the orientation of the weld configuration in question. Figure 51 demonstrates the manner in which the short-transverse and longitudinal faces change according to the rolling direction with respect to the weld line. It can be seen that when the weld orientation was parallel to the rolling direction (||) the corresponding comparison parent material hardness measurement and specification were from the short-transverse, and where the weld orientation was perpendicular to the rolling direction (⊥) the corresponding comparison parent material

hardness measurement and specification were from the longitudinal. For dissimilar welds the weaker parent material specification and measurement in the appropriate orientation was used.

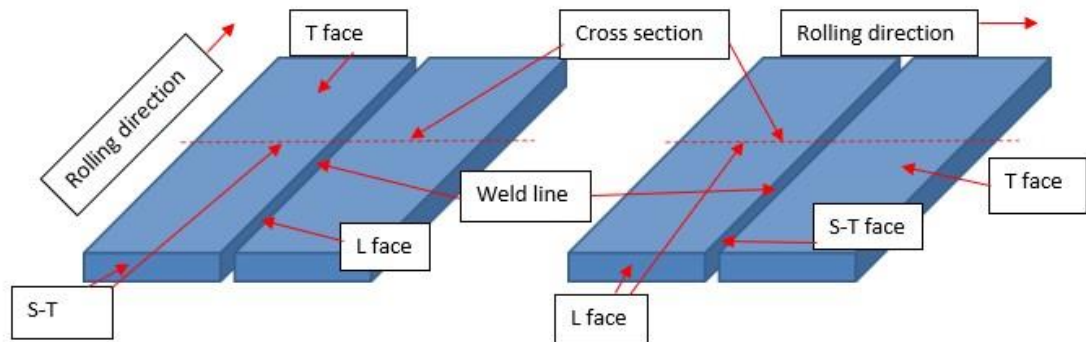


Figure 51: Showing the designated material face orientations relevant to the hardness assessment.

5.2.1.2 *Welded specimen test results*

The averaged test results for all specimens are shown in graphical format in Figure 52. This is provided as an overall comparison of all welds, and allows for evaluation of each configuration against any other. Also shown in Figure 53, Figure 54 and Figure 55 are comparison hardness results of the AA8090 similar welds (with parent materials shown), BS L165 (with parent materials shown) and the dissimilar materials respectively. The different weld configurations are depicted by the same colour in Figure 52 and the other chart in which they appear (either Figure 53, Figure 54 or Figure 55). Individual test results are presented and discussed in Chapter 6 (sections 6.2.2.1, 6.3.2.1, 6.4.2.1 and 6.5.2.1).

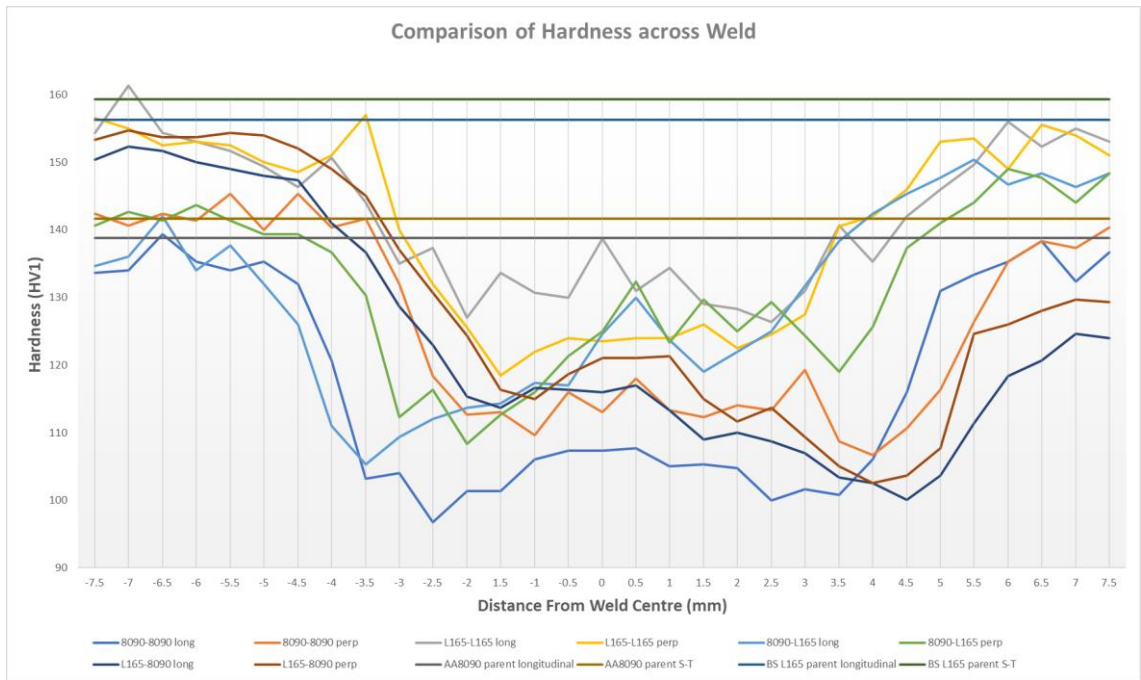


Figure 52: Graph showing hardness test results of all welded specimens and parent materials. Note: y-axis has been limited to starting at 90 HV1 for clarity.

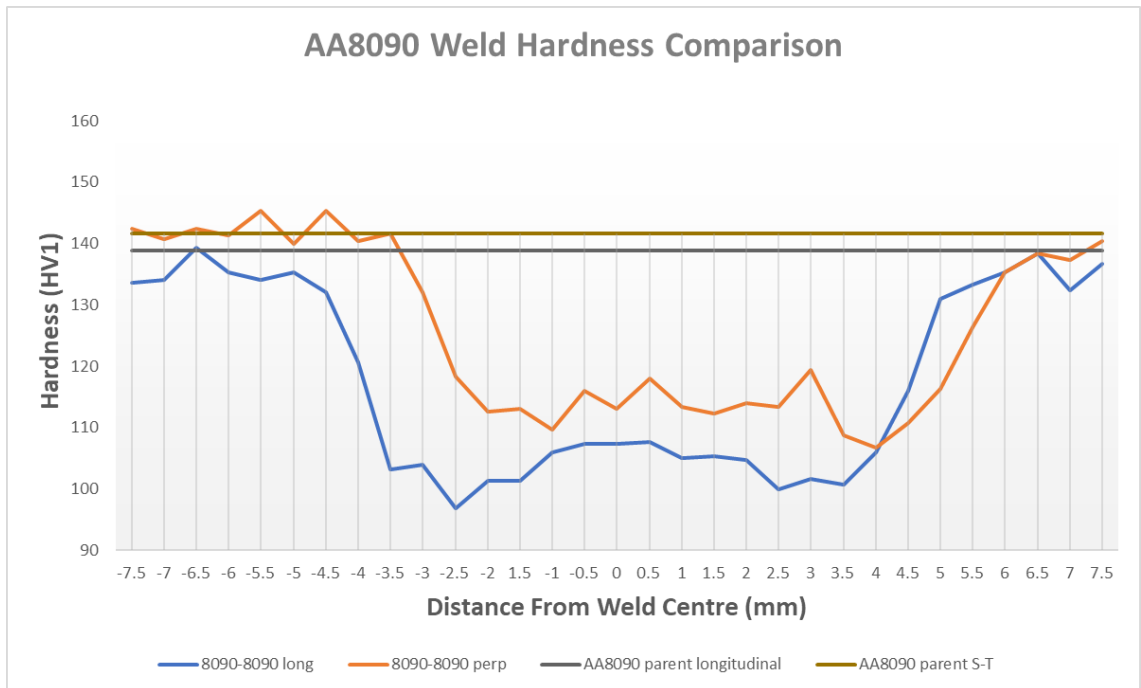


Figure 53: Showing AA8090 similar weld hardness results, with parent material values for comparison.

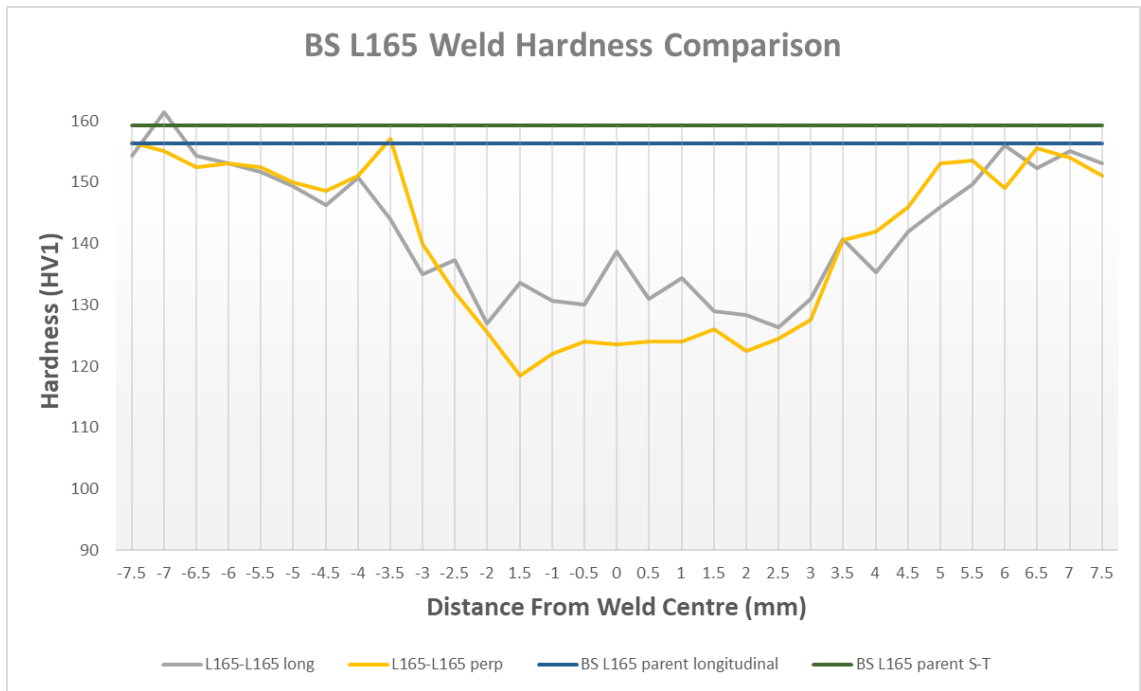


Figure 54: Showing BS L165 similar weld hardness results, with parent material values for comparison.

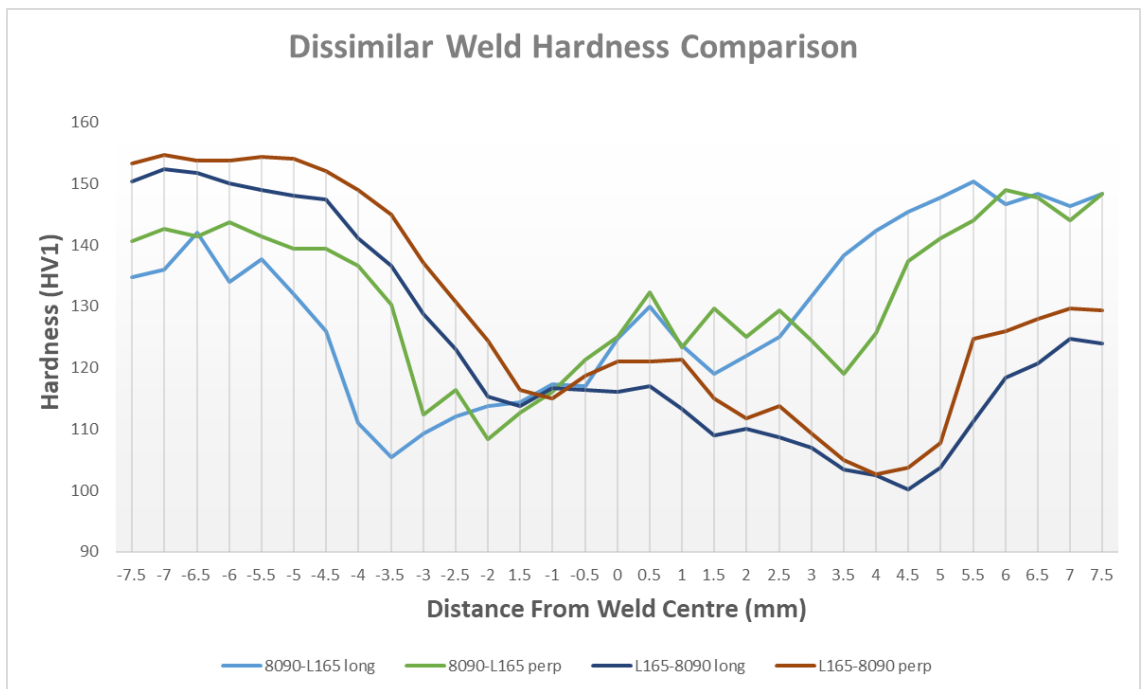


Figure 55: Showing dissimilar weld hardness results.

The hardness measurements taken from the parent material areas of the welded specimens were all broadly consistent with the related reference (non-welded parent material, section 4.2.3.1). However there were variations along the length and some of the parent materials in the welded specimens have hardness values slightly harder or softer than the references.

All welded specimen's hardness profile formed the typical "W" shape associated with precipitation hardening aluminium alloy FSW, although this was less clear on the dissimilar welds due to the difference in hardness between the materials. The lowest hardness values were found in the HAZ or TMAZ area of the welds; the hardness value in the TMAZ was below the associated minimum hardness specification in all cases.

5.2.2 Tensile Testing

5.2.2.1 Test Results

The averaged results of tensile testing for each configuration are shown in Table 29. The non-welded parent materials were tested first in both orientations; longitudinally with the rolling direction parallel to the pulling direction, and transversely with the rolling direction perpendicular to the pulling direction, section 4.2.3.2. However, when welded these directions were reversed, i.e. when the materials were welded with the joint line parallel to the rolling direction, this meant that the rolling direction would be perpendicular to the pulling direction and vice versa. For this reason, the longitudinal tensile specification and parent material measured results have been used to compare with transversely (\perp) welded specimens and vice versa.

The results were interrogated to ascertain whether there were any instances of the first test using material from the first 50 mm of the welds deviating significantly from the rest due to non-compliance with the FSW standard BS EN ISO 25239-4:2020 (The British Standards Institution, 2020a) (the specification states that the first 50 mm of the weld should be discarded). It was found that this happened in two cases only (BS L165 \perp and BS L165-AA8090 \parallel). Henceforward the first result from each set was disregarded so that the tensile test results reflected the steady state welds only. The results were also examined to check for repeatability; it was found that the weld strength did vary between the different welded sheets, suggesting that the parameters had not produced

welds of repeatable quality in all cases, or that flaws were present. This is illustrated by the high standard deviations in comparison with the unwelded test specimens, indicating a significant spread in results. The results have been compared to both the specification values and the measured values for the parent materials. For the dissimilar welds the results were compared to the material with the lowest UTS specification, i.e. AA8090, although there was little difference in both the specifications and measured results (for unwelded parent materials) between AA8090 and BS L165 for UTS. The uncertainty was calculated from a local procedure used to certify aircraft testing; for the thickness of these samples (0.7 mm) this was calculated to be ± 4.6 MPa for UTS, ± 2.9 MPa for 0.2% proof stress and $\pm 0.3\%$ elongation.

Table 29: Showing tensile test results.

	UTS (MPa)		0.2% Proof Strength (MPa)		% Elongation		UTS Standard Deviation (MPa)	% UTS Parent Material Specification	% UTS Measured Parent Material Specification
	Specification	Measured	Specification	Measured	Specification	Measured			
AA8090 Parent (L)	400	443	280	343	6	9.5	3.17	110.8	-
AA8090 Parent (T)	410	438	280	307	9	11.1	2.52	106.8	-
BS L165 Parent (L)	415	442	345	397	7	8.7	2.82	106.5	-
BS L165 Parent (T)	415	436	345	393	7	8.4	2.20	105.1	-
AA8090 II	410	357	280	256	9	3.3	8.39	87.1	81.5
AA8090 I	400	359	280	266	6	2.0	23.57	89.8	81.0
BS L165 II	415	437	345	340	7	3.3	38.9	105.3	100.2
BS L165 I	415	430	345	343	7	2.4	22.06	103.6	97.3
AA8090-BS L165 II	410	345	280	284	9	1.4	21.08	84.1	78.8
AA8090-BS L165 I	400	320	280	Note 1	6	Note 1	31.35	80.0	72.2
BS L165-AA8090 II	410	326	280	Note 1	9	Note 1	14.64	79.5	74.4
BS L165-AA8090 I	400	284	280	Note 1	6	Note 1	26.96	71.0	64.1

Table 29 Notes:

- 1 The 0.2% proof strength and elongation was inconclusive for this configuration owing to elongation being below the tolerance measurable by the equipment, i.e. the material did not achieve 0.2% strain before failure.

It can be seen from Table 29 that excellent results were achieved for both BS L165 welds, attaining approximately 100% of the measured parent material UTS. A reduction of approximately 20% of the measured parent material UTS was found for both AA8090 welds with further reductions in UTS for the dissimilar welds. The poorest result was from BS L165-AA8090 \perp , with a significant drop of approximately 36% from the measured parent UTS.

A considerable reduction in ductility was revealed for all welds with percentage elongation ranging from 47% of the parent material specification for BS L165 \parallel , to less than 10% for the two dissimilar welds orientated perpendicular to the rolling direction.

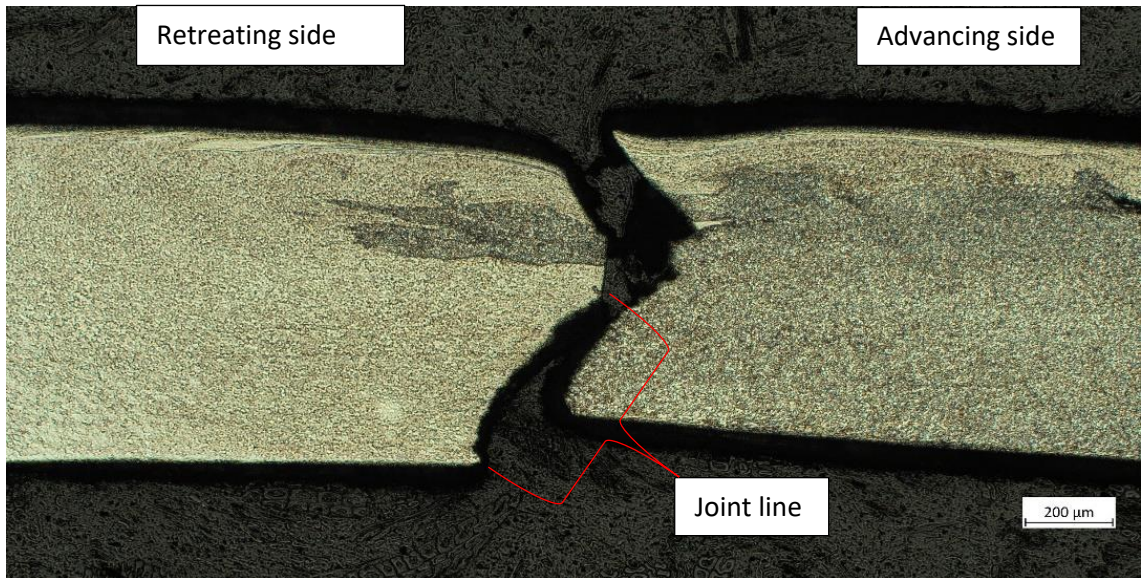
5.2.2.2 Optical microscopy and SEM of fracture surfaces

The fractography of the tensile test specimens, including the position of fracture with respect to the weld, the shape of the fracture, i.e. straight or ragged, the macroscopic appearance of the fracture surface and SEM analysis are all discussed in detail in Chapter 6. Table 30 provides a summary of the fracture locations for ease of comparison of the different weld configurations. Where a fracture position is listed as “mid-weld” this refers to the fracture being clearly within the visible weld judged by the naked eye. “Edge of weld” (EoW) (advancing or retreating) refers to the fracture being positioned directly on or close to the edge of the visible weld. At this stage it was not possible to define what weld zone (HAZ or TMAZ) the fracture fell within which was why the term “edge of weld” was used; the specific weld zone was clarified following metallographic preparation and is described within the relevant section of Chapter 6.

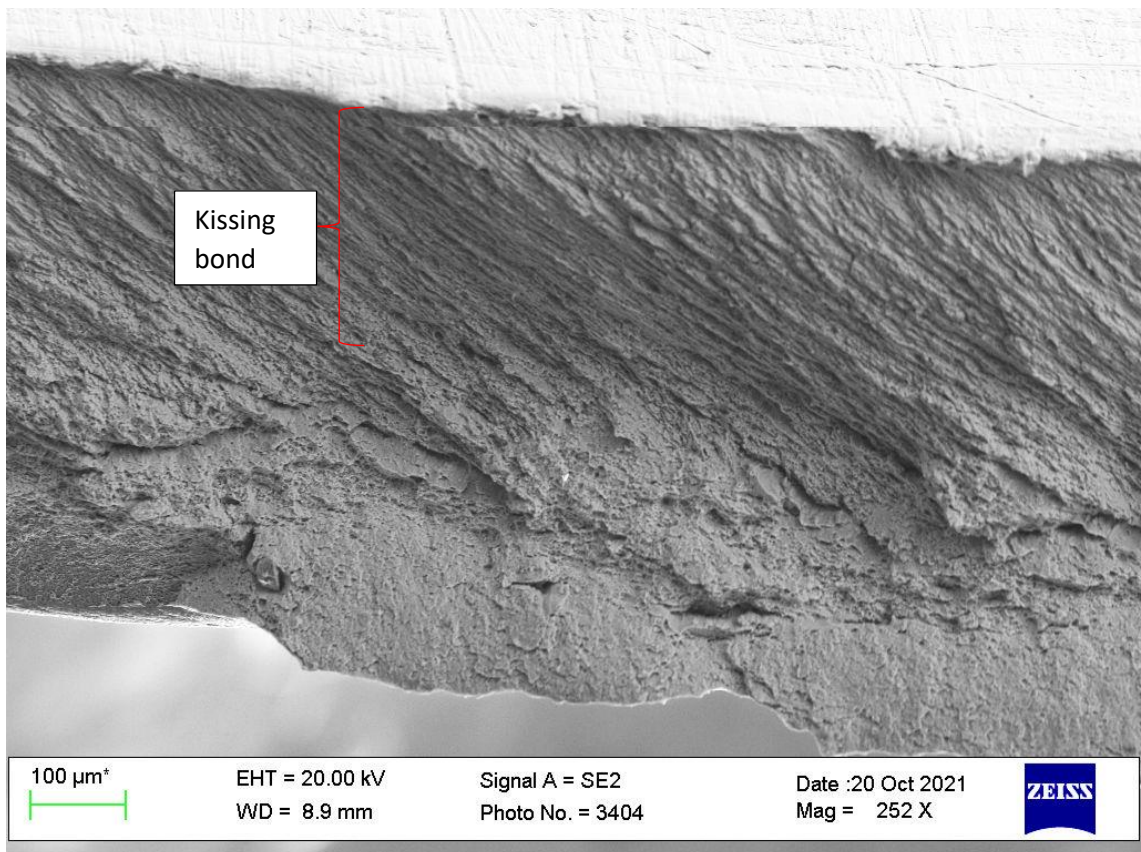
Table 30: Showing locations of tensile fractures on welded test specimens.

Configuration	Description of Fracture Position
AA8090 II	16 x Advancing Edge of Weld 3 x Retreating Edge of Weld 1 x Mid-Weld
AA8090 I	11 x Mid-Weld 6 x Advancing Edge of Weld 3 x Retreating Edge of Weld
BS L165 II	19 x Mid-Weld 1 x Retreating Edge of Weld
BS L165 I	20 x Mid-Weld
AA8090-BS L165 II	12 x Advancing Edge of Weld 8 x Mid-Weld
AA8090-BS L165 I	17 x Mid-Weld 3 x Advancing Edge of Weld
BS L165-AA8090 II	18 x Mid-Weld 2 x Retreating Edge of Weld
BS L165-AA8090 I	17 x Mid-Weld 3 x Retreating Edge of Weld

A large number of the specimens failed mid-weld. Optical microscopy and SEM analysis revealed that this was, at least partially, owing to the presence of kissing bonds which weakened the weld. An example of this on a BS L165-AA8090 I weld is shown in Figure 56.



(a)



(b)

Figure 56: Showing mid-weld fracture of AA8090 \perp : (a) etched cross-section showing position of fracture falls on the joint line; (b) SEM image showing “stir” markings, remnants of the SSFSW process and indicating inadequate joining of the materials.

5.2.3 Fatigue

5.2.3.1 Test Results

The fatigue specimens were tested early in the research and when analysed it was observed that while the AA8090 parent materials had been tested with the rolling direction parallel with the cycling load direction, the welded specimens were welded, cut and tested with the weld parallel to the rolling direction and the cyclic load therefore perpendicular to the rolling direction; as described in 3.4.3.1 only one orientation for each material configuration was tested in fatigue. This was an oversight by the researcher, however it is likely that this would reflect in conservative values of fatigue strength being obtained from the welded samples by comparison to the unwelded samples as clear crack paths would be available. The results will be presented and analysed here and in Chapter 6 with the caveat that had the parent material testing been truly representative of the welded material for comparison, that the results may be different. Unlike the AA8090 parent material, BS L165 parent material (unwelded) fatigue specimens were tested with the material rolling direction perpendicular to the direction of loading. This meant that the rolling direction was consistent with the welded specimens which were welded parallel with the rolling direction, and therefore tested with the rolling direction perpendicular to the loading direction.

The results for each material configuration are shown in Table 31 below. These results show that the similar welds, i.e. AA8090-AA8090 and BS L165-BS L165, achieve approximately 85% of the relevant base material fatigue strength, although the standard deviations and coefficients of variation were significantly higher, indicative of a larger spread of results. The dissimilar welds were less successful, with AA8090-BS L165 achieving approximately 70% of the weaker base material and BS L165-AA8090 approximately 60%. The dissimilar welds having lower fatigue strength than parent materials is consistent with literature (Wang et al., 2018), and it has been identified that several of the welds have flaws/ defects including kissing bonds which would further reduce both the tensile and fatigue strength of the welds. The AA8090-BS L165 results show the lowest standard deviation and coefficient of variation of all testing, indicating a low spread of results and therefore reasonably high confidence in the values achieved.

BS L165-AA8090 welds had a significantly higher standard deviation and coefficient of variation than all other results, indicating a large spread of results.

Table 31: Showing fatigue test analysis results.

Material configuration and orientation	Mean fatigue strength (σ_m) (MPa)	Standard deviation (s) (MPa)	Coefficient of variation (Standard deviation/ step increment) (η_s)	Lower limit of fatigue strength $\hat{y}_{(0.1,0.95)}$ (MPa)
AA8090 parent material	322.1	17.66	0.055	285.6
BS L165 parent material	306.4	11.71	0.038	282.2
AA8090	270.7	27.58	0.102	213.7
BS L165	259.4	28.76	0.111	201.8
AA8090-BS L165	217.0	7.38	0.034	202.0
BS L165-AA8090	185.7	77.08	0.415	29.04

5.2.3.2 Optical microscopy and SEM of fracture surfaces

The fractography of the fatigue test specimens, including the position of fracture with respect to the weld, the shape of the fracture, i.e. straight or ragged, the macroscopic appearance of the fracture surface and SEM analysis are all discussed in detail in Chapter 6. Table 32 provides a summary of the fracture locations for ease of comparison of the different weld configurations. The same conventions are used to describe the position of fracture as previously described for tensile testing in section 5.2.2.2 unless otherwise stated, although where a specimen has failed mid-weld but close to an edge, this has been noted.

Table 32: Showing results of fatigue test specimen examinations.

Configuration	Number of Failures Before 50,000 Cycles	Position of Fracture
AA8090 II	14	8 x Mid-Weld 4 x Mid-Weld Close to the Advancing Edge 2 x Advancing Edge of Weld
BS L165 II	16	13 x Within Weld; None (0) at Mid-Point. Of the 13, 10 were biased towards the Advancing Side and 3 biased towards the Retreating Side 2 x Advancing Edge of Weld 1 x Retreating Edge of Weld
AA8090-BS L165 II	17	All Within Weld. Of these: 9 x biased towards the Advancing Edge 5 x Mid-Weld 3 x biased towards the Retreating Edge
BS L165-AA8090	18	All Within Weld. Of these: 7 x biased towards the Advancing Edge 1 x Mid-Weld 10 x Multiple Fractures. These occurred both at the approximate Mid-Position, and simultaneously In-Weld but biased towards the Advancing Edge

For many of the specimens failing mid-weld, similar fractographies with respect to kissing bonds were observed as for the tensile tests, as shown in Figure 56 in section 5.2.2.2. This is not repeated here but is discussed in detail in the relevant sections of Chapter 6, along with the fractography of the fatigued (non-kissing bond) areas of the fracture surfaces.

5.2.4 Residual Stress

The maximum principal stress (σ_{max}) was plotted for various analyses. As described in the Methodology chapter (section 3.4.4.1), there is a limitation in the analysis of data with respect to hole depth; as such, although the full measurement has been plotted, only the data between 0.05 and 0.4 mm will be considered in the analysis. Tests were conducted in the parent material, at the mid-weld point and at the edge of the weld (advancing and retreating). In this case, edge of weld refers to immediately adjacent to the visible weld, as shown in Figure 30, section 3.4.4.1.2.

5.2.4.1 Residual stress variance with depth

Although the residual stress results are discussed for each configuration individually in Chapter 6, Figure 57 shows σ_{\max} plotted against the hole depth for BS L165 II at the five strain gauge positions as an example. This shows low levels of residual stress in the parent material as expected, with the maximum stress recorded at the edge of the weld on the retreating side at approximately 0.1 mm depth. Analysis of each of the eight configurations showed that the maximum stress was predominantly recorded at the edge of the weld (this varied between the advancing and retreating sides). In two cases (AA8090 \perp and AA8090-BS L165 \perp) the maximum stress was recorded in the weld, however for AA8090 \perp the data was considered to be poor for the edge of weld advancing side (discussed further in section 5.2.4.1.2), and the edge of weld retreating side maximum stress was very close to the result found in weld. For AA8090-BS L165 \perp both the results for the edge of weld were considered to be poor. When all configurations were considered and disregarding the measurements before 0.05 mm depth and after 0.4 mm depth, the maximum stresses were recorded between approximately 0.06 mm and 0.16 mm, see section 5.2.4.4.

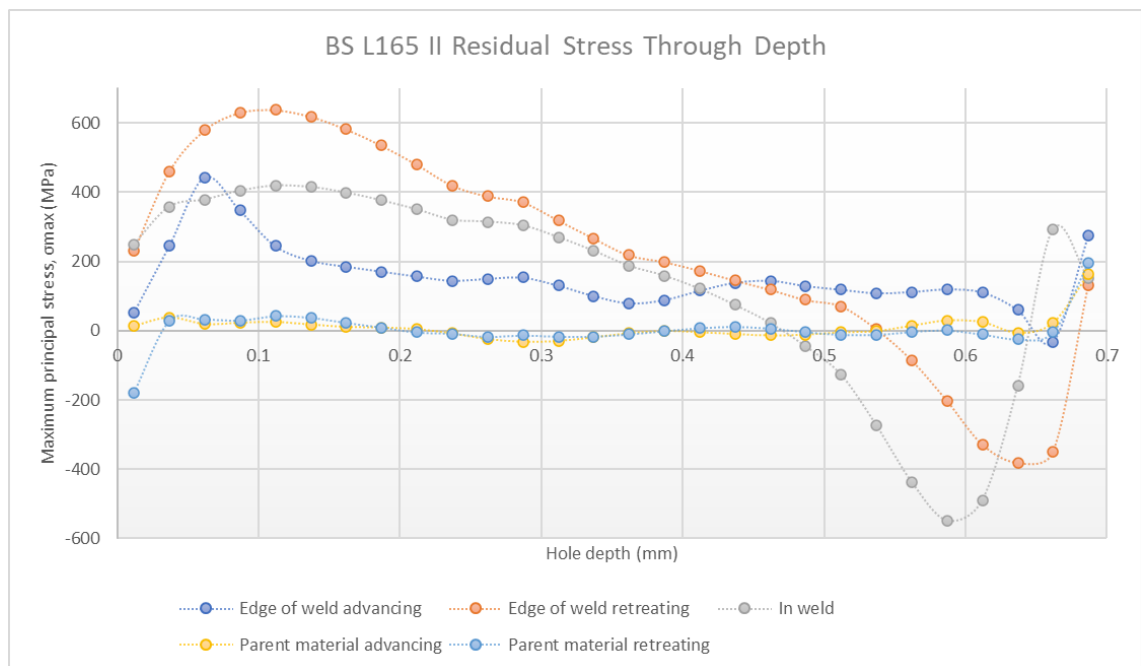


Figure 57: Plot of maximum principal stress against hole depth for BS L165 II at the five strain gauge positions.

5.2.4.1.1 *Validation of residual stress results*

It was not possible to carry out multiple tests for every test position in every configuration due to time constraints and cost of consumables (strain gauges, drill bits, air turbines). Consequently, the results of the strain gauge data gathered and subsequent residual stress calculation results could not be verified statistically via mass testing. In an effort to validate the results and provide more confidence in the data gathered, a limited number of tests were repeated. Additionally, multiple data-sets were gathered for the parent materials; as these positions were remote from the weld it was considered that the data from several tests could be used. As an example, it was hoped that the result for AA8090 \perp advancing side parent material could be validated by the results for AA8090-BS L165 \perp advancing side parent material and BS L165-AA8090 \perp retreating side parent material (as the test for AA8090 \perp retreating side parent material failed). This is shown graphically in Figure 58.

It can be seen that significant scatter exists in the results until the depth reaches approximately 0.2 mm. This scatter may be due to different sheets being used in the different datasets or the location of the strain gauge not being sufficiently remote from the weld. Similar outcomes were found on other comparisons of parent materials with the consequence that different data sets could not be used for validation.

In a limited number of cases, the same test was repeated on the same sheet/ weld (with the potential issues with change of residual stress along the length of a FSW alluded to by Kumar, Mishra and Baumann (2014) described in the Methodology chapter being acknowledged). The repeated tests were carried out on AA8090 \perp retreating side of weld and AA8090-BS L165 II in weld; the results are shown in Figure 59 and Figure 60. Strong correlation of results was observed in the tests carried out on AA8090 \perp and, while the stress magnitude was reduced in the second test carried out on AA8090-BS L165 II, the residual stress profiles of the two tests were very similar. These tests have validated the residual stress profile (to a limited extent) although the magnitude of the residual stresses must be treated with caution. Indeed, the magnitude of the maximum stresses is required to be treated with caution and shown as “indicative” rather than quantitative, due to the requirement and limitations described in ASTM E837-20 (ASTM International, 2020), i.e. the results are only quantitatively valid until 80% of the yield

strength is achieved; the maximum stresses far exceed this value in all cases (discussed further in Chapter 6).

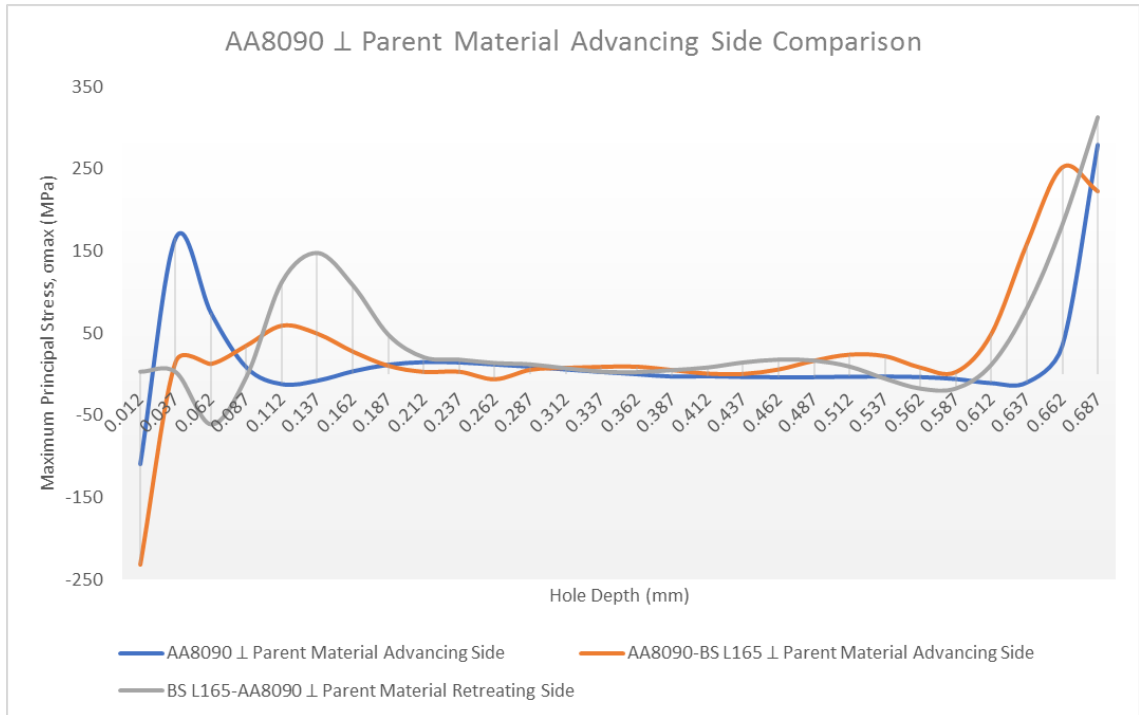


Figure 58: Showing comparison of data from various tests conducted on the AA8090 \perp parent material.

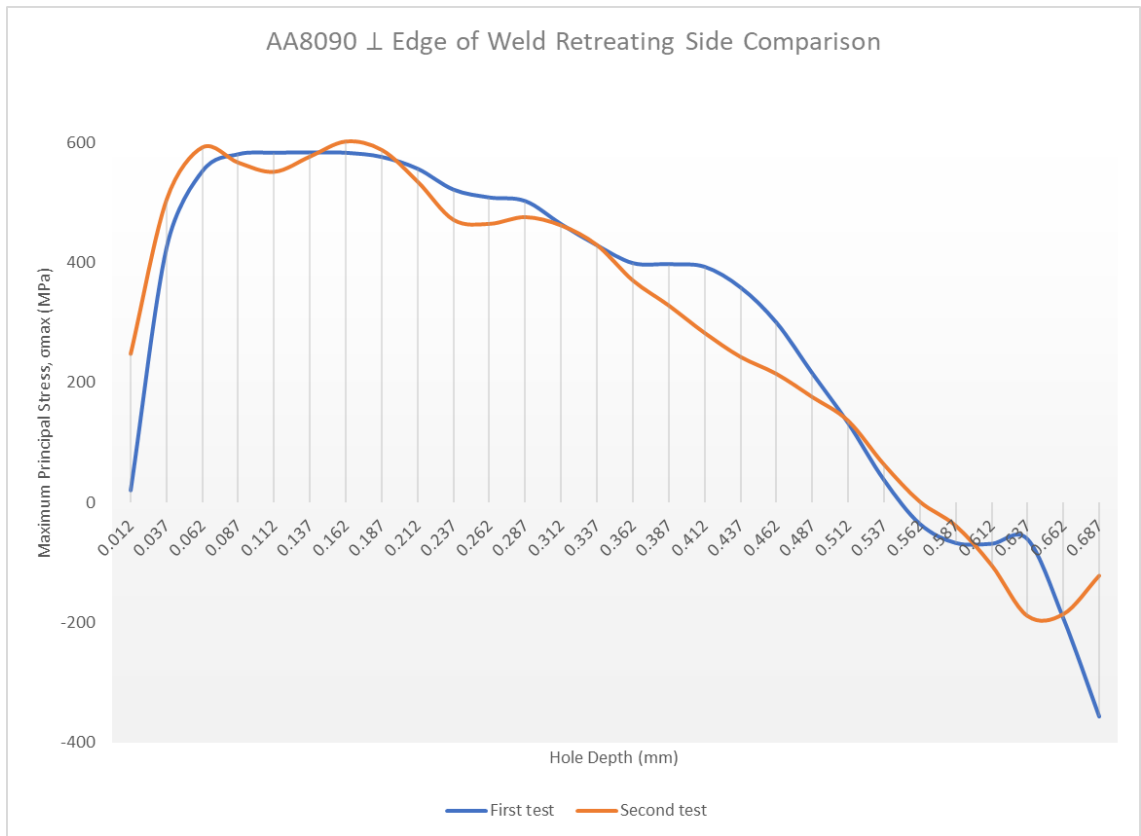


Figure 59: Showing comparison of 2 tests carried out on AA8090 ⊥ retreating side edge of weld.

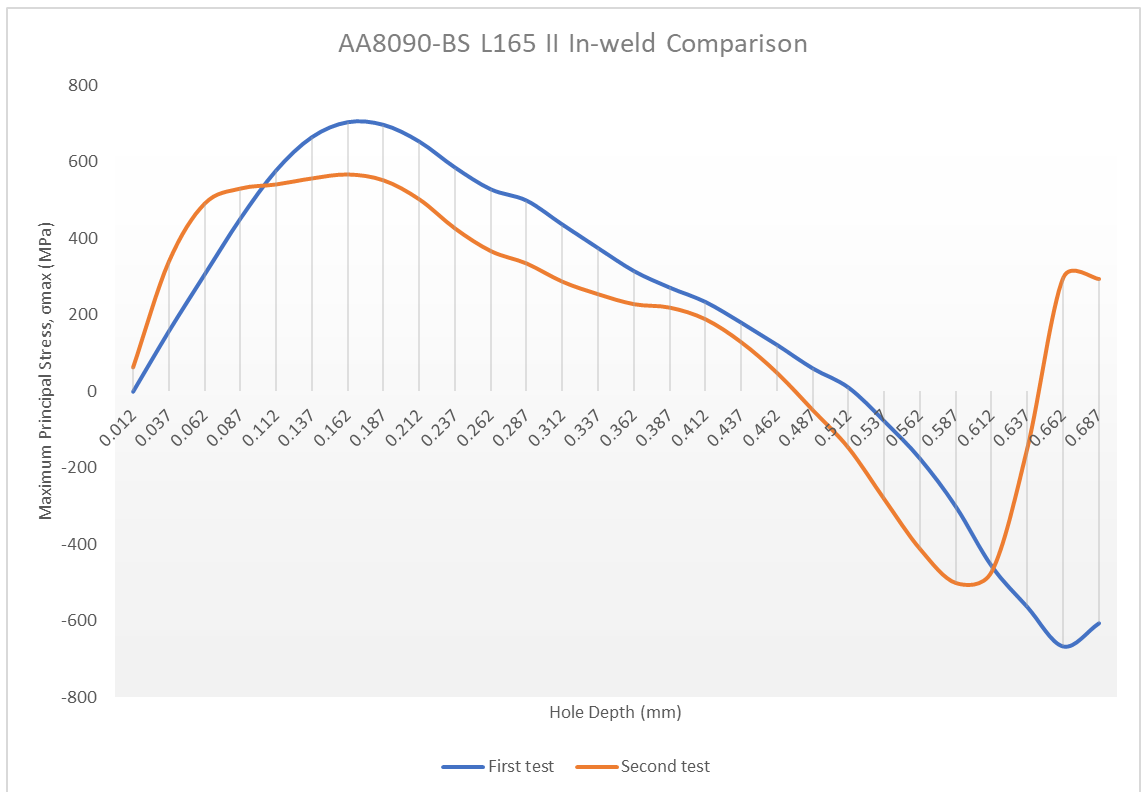


Figure 60: Showing comparison of 2 tests carried out on AA8090-BS L165 II in weld.

5.2.4.1.2 Poor residual stress results

As alluded to in section 5.2.4.1, several of the results obtained were considered to be “poor”. An example of this is shown in Figure 61 for AA8090 \perp . It is clear that the calculated residual stress profile for the advancing side edge of weld is significantly different for that of the retreating side and in weld. When other configurations are compared with this, the general trend is for the edge of weld and in weld results to follow similar profiles. This suggests that the oscillating nature of the edge of weld advancing side test profile is the result of a spurious test. Insufficient resources were available to conduct retesting where these results were observed.

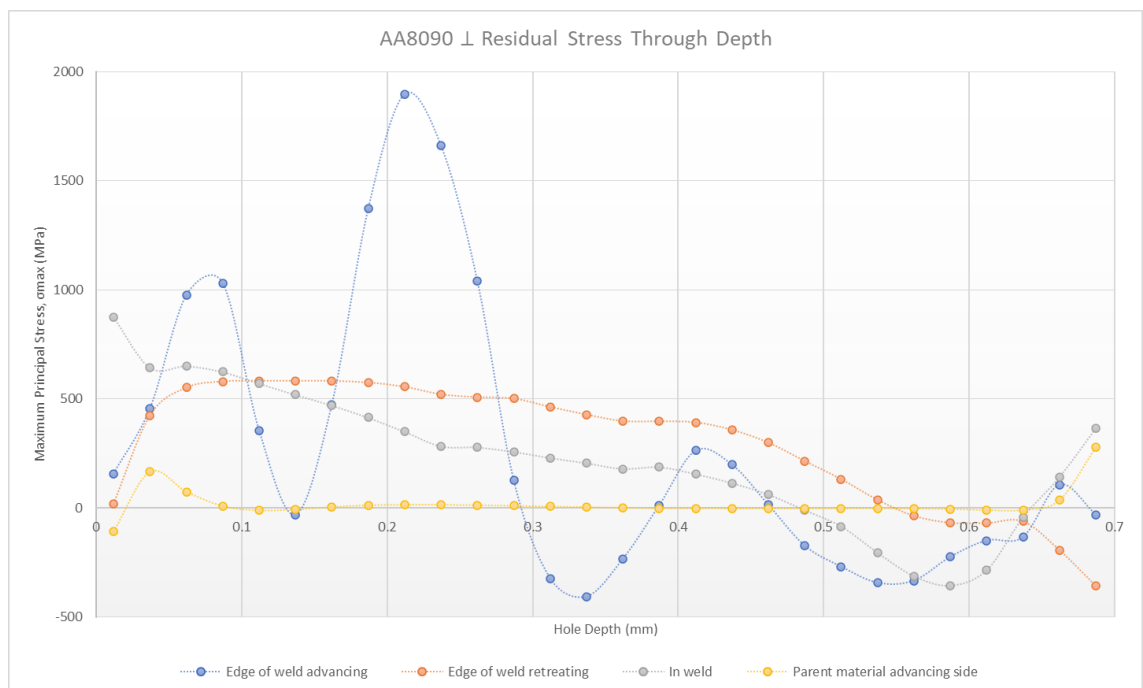
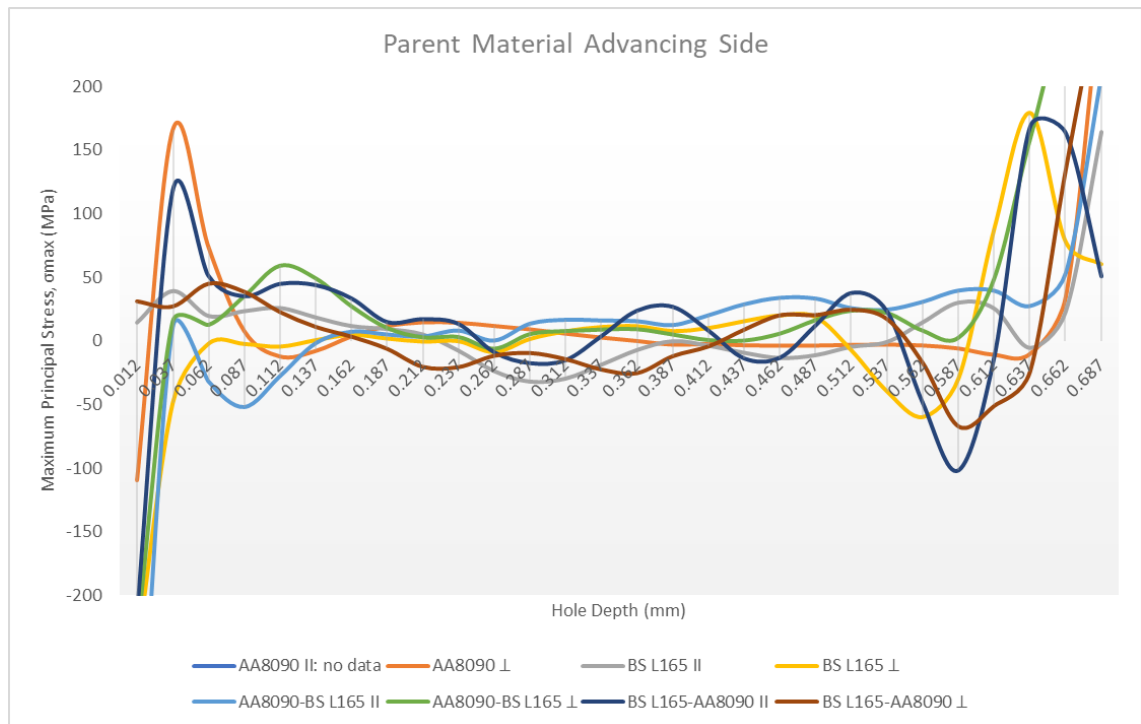


Figure 61: Showing results from AA8090 \perp . Note: the retreating side parent material was a failed test and has thus not been included.

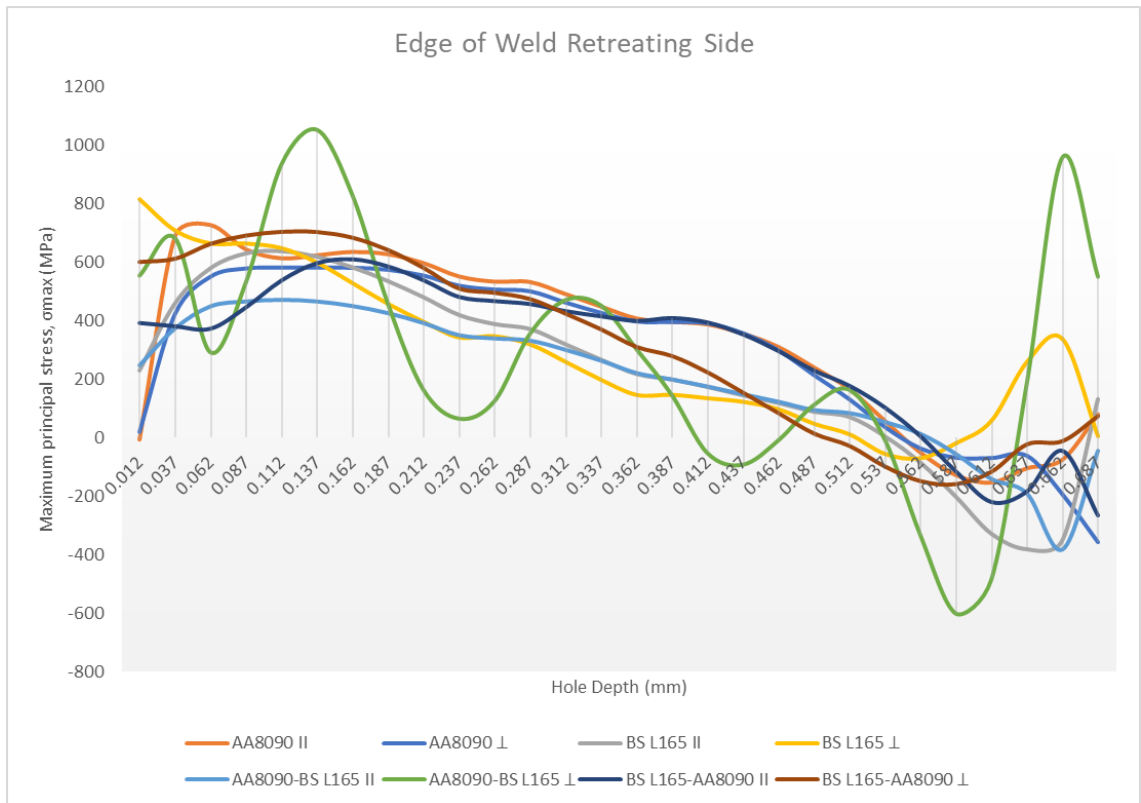
There are several potential causes of these poor results which would not affect the other results, including a faulty strain gauge or the strain gauge being damaged during installation, incorrect wiring or drilling and the measurement equipment disturbed during use. The most likely cause is considered to be damage to the strain gauges either during installation or test set-up.

5.2.4.2 Comparison of configurations

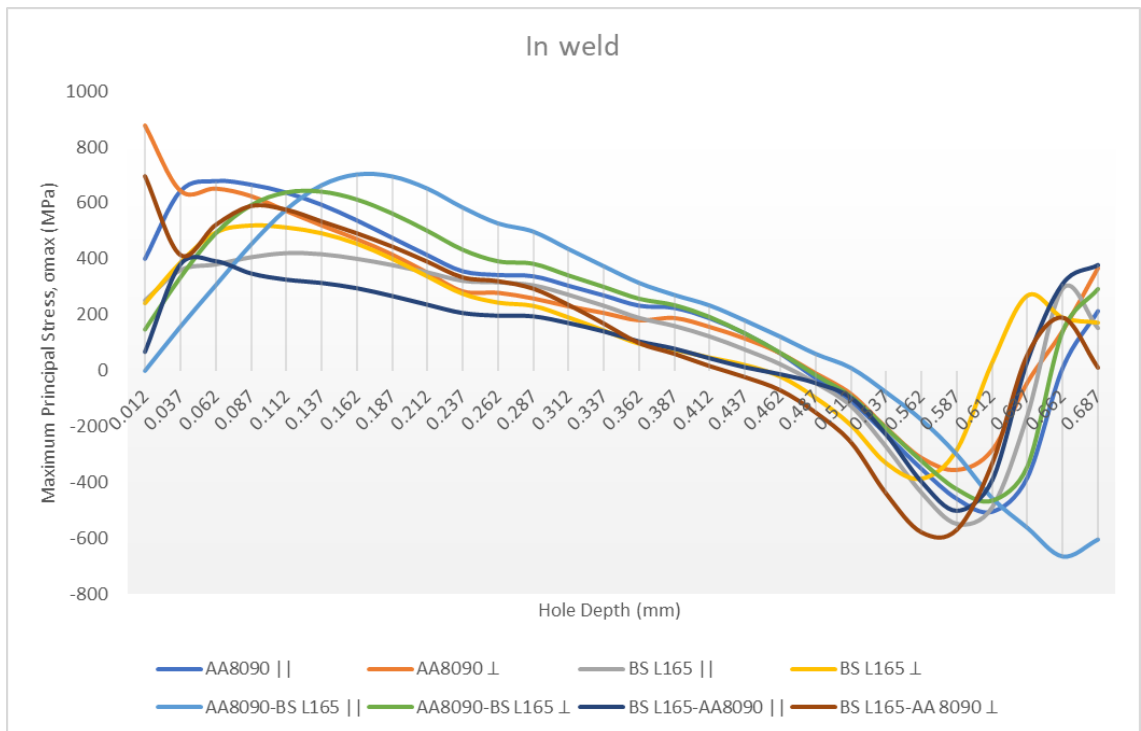
The 8 configurations were compared at each strain gauge position in an effort to assess if the different materials and orientations had an effect on σ_{\max} . These are shown graphically in Figure 62 for the parent material advancing side, edge of weld retreating side and in weld. Some of these comparisons (for example AA8090-BS L165 \perp in Figure 62(b)) are influenced to an extent by the poor results described in section 5.2.4.1.2 and by missing data from failed tests.



(a)



(b)



(c)

Figure 62: Showing comparisons of the 8 configurations at (a) the parent material advancing side, (b) edge of weld retreating side, and (c) in weld.

Analysis of the graphical data shows that:

- Note: as discussed previously, only data falling between 0.06 and 0.4 mm has been included in the analysis. Those occurring at 0.06 mm may be affected by the surface abrading during strain gauge installation and those values have therefore been treated with caution.
- Parent materials (Figure 62(a)):
 - The residual stress generally oscillates between tensile and compressive with peaks and troughs rarely exceeding ± 45 MPa and in many cases well below this value throughout most of the depth. This modest value of residual stress (approx. 11-15% of parent material yield strength or 13-18% of welded sheet yield strength) is considered to be as a result of the material sheet rolling process.
 - The different configurations are all broadly consistent in terms of residual stress values although the oscillations between tensile and compressive stress occur at different hole depths.
- Edge of weld:
 - The residual stresses were tensile in both the advancing side and retreating side edge of weld for all configurations throughout the hole depth.
 - The predominant profile (ignoring the spurious results) was one which started initially high and rose smoothly to a peak (the depth at which the peak occurred varied from 0.06 mm to 0.16 mm), before reducing gradually with depth. In most cases a small plateau of residual stress value against depth occurred at approximately 0.225-0.275 mm hole depth). The reason for this plateau requires further investigation.
 - Ignoring the spurious results, the configurations are ranked in the orders below in terms of broadly consistently higher to lower tensile σ_{\max} throughout hole depth:
 - Advancing side (not shown in Figure 62): AA8090-BS L165 II, BS L165 \perp , BS L165-AA8090 \perp , BS L165-AA8090 II, BS L165 II, AA8090 II. There is a difference of approximately 230 MPa in peak stress between AA8090-BS L165 II and AA8090 II.

- Retreating side (Figure 62(b)): BS L165-AA8090 \perp , AA8090 II, AA8090 \perp , BS L165-AA8090 II, BS L165 II, BS L165 \perp , AA8090-BS L165 II. There is a difference of approximately 445 MPa between BS L165-AA8090 \perp and AA8090-BS L165 II, however the result for AA8090-BS L165 II is considered potentially spurious. The difference between BS L165-AA8090 \perp and the second lowest overall σ_{\max} (BS L165 \perp) is approximately 250 MPa which is more consistent with that of the advancing side. Again, there is no clear trend regarding material type or orientation, and there is no coherence between the advancing and retreating sides for the configurations.
 - In weld (Figure 62(c)):
 - This is shown in Figure 62c and shows a broadly similar profile to that observed for the edge of the weld. This profile includes the initial rise and peak (peak occurring 0.06-0.16) the gradual reduction with small plateau at the approximate same depth of 0.225-0.275 mm.
 - The configurations are ranked in order in terms of broadly consistently higher to lower tensile σ_{\max} throughout hole depth:
 - AA8090-BS L165 II, AA8090-BS L165 \perp , AA8090 II, BS L165-AA8090 \perp , AA8090 \perp , BS L165 II, BS L165 \perp , BS L165-AA8090 II. Again, no clear trend can be observed from the rank order. There is a difference of approximately 310 MPa in peak stress between AA8090-BS L165 II and BS L165-AA8090 II.

5.2.4.3 Residual stress distribution across weld

The residual stress was plotted against hole depth for various depths of hole in order to show the residual stress profile across the weld. It would be preferable to have many more data points to show this profile in more detail, for example if the measurement was conducted using XRD, however due to quantities of strain gauges and other consumables required and the requirements for distance between drilled holes, this was not possible.

Kumar, Mishra and Baumann (2014) report that the majority of work on residual stresses in FSW show “M” shaped distributions across the weld. In this research, the “M” shape was achieved for 3 of the configurations; BS L165 ⊥ (Figure 63), BS L165-AA8090 II and BS L165-AA8090 ⊥ with the “evenness” of the “M” legs varying between the configurations and depth. Figure 63 shows that for L165-L165 ⊥ the highest residual stress for all depths occurred at the advancing side of the weld, with the exception of 0.062 mm (the shallowest depth) where the highest residual stress was at the retreating side, however the difference was very slight.

A second profile shape with a pronounced slope in σ_{\max} was observed on AA8090 II (Figure 64) and predominantly on BS L165 II and AA8090-BS L165 II. Both AA8090 II and BS L165 II had maximum stresses on the retreating edge of weld and AA8090-BS L165 II on the advancing edge of weld. BS L165 II and AA8090-BS L165 II are described as “predominantly” sloped as the shallowest increment analysed (0.062 mm) was “M” shaped.

Two of the plots (AA8090 ⊥ and AA8090-BS L165 ⊥) were invalid due to spurious data produced in the advancing side edge of weld measurement (AA8090 ⊥) and for both edge of weld measurements (AA8090-BS L165 ⊥) as described in section 5.2.4.1.2.

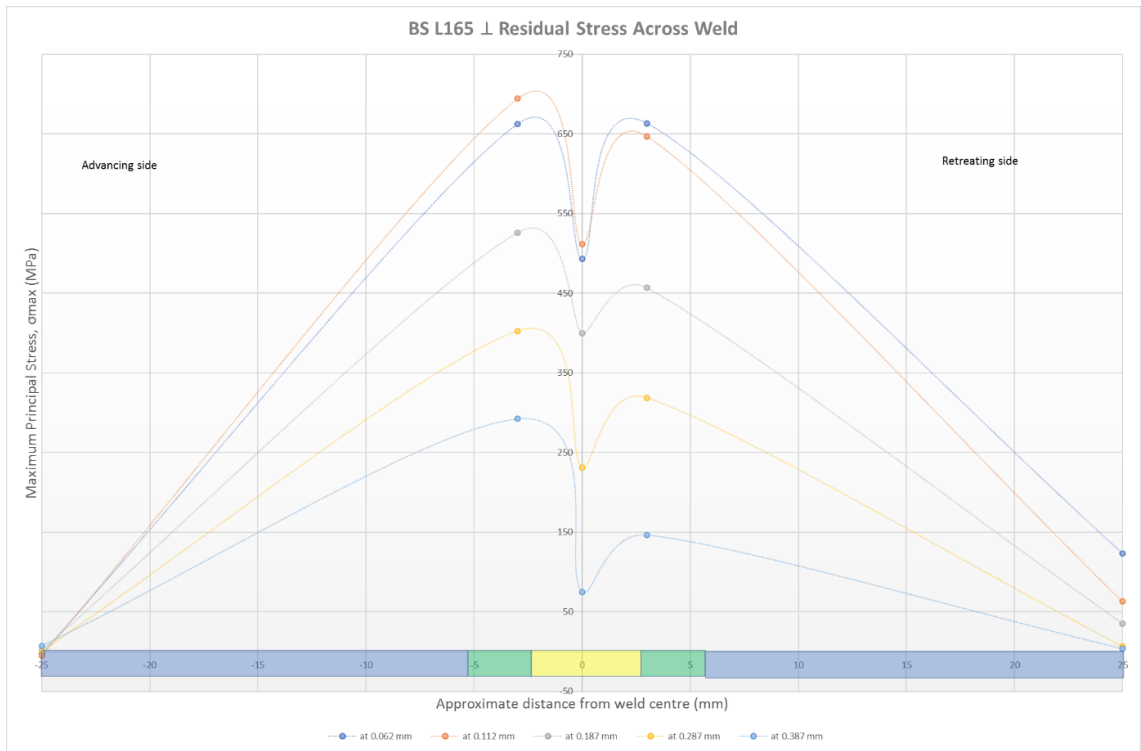


Figure 63: Showing weld profile at different hole depths across weld line for BS L165
I.

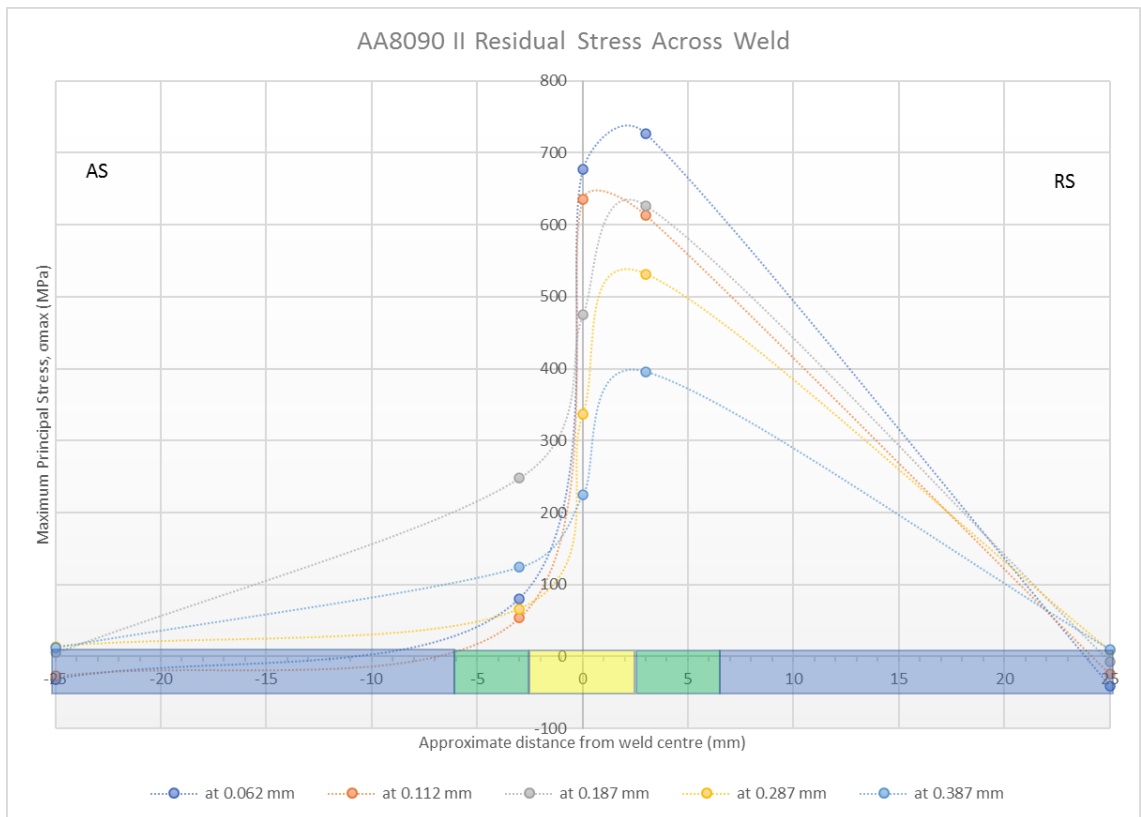


Figure 64: Showing weld profile at different hole depths across weld line for AA8090
II.

5.2.4.4 Residual stress as a % of yield strength

σ_{\max} as a percentage of yield strength has been calculated for each weld with the value and position, i.e. edge of weld retreating, and the depth at which it occurred and is shown in Table 33. Where spurious results were encountered, this has been indicated. Where a spurious result has been identified, this has been disregarded in favour of a more confident result. Kumar, Mishra and Baumann (2014) point out that although FSW often changes the yield strength of the overall welded sheet from the original material's yield strength, most researchers either show the σ_{\max} as a percentage of the parent material's yield strength or do not specify which yield strength has been used in the analysis. In this research the σ_{\max} has been calculated as a percentage of both the parent material's yield strength and as a percentage of the welded sheet for that configuration.

Table 33: Showing σ_{\max} as a percentage of yield strength.

Configuration	Location of σ_{\max}	Approx. hole depth of σ_{\max} (mm)	σ_{\max} (MPa)	Yield strength of parent material (MPa)	Yield strength of welded sheet (MPa)	σ_{\max} as a % of parent material yield strength	σ_{\max} as a percentage of welded sheet yield strength	Spurious result?
AA8090 II	EoW R	0.06	726	343	253	212%	287%	Yes – EoW A and no result for parent A
AA8090 I	In weld	0.06	651	307	262	212%	248%	Yes – EoW A and no result for parent R
BS L165 II	EoW R	0.09	630	400	320	158%	197%	No
BS L165 I	EoW A	0.11	694	393	341	177%	204%	No result for parent R
AA8090-BS L165 II	EoW A	0.16	722	343	282	210%	256%	Yes - parent R
AA8090-BS L165 I	In weld	0.14	639	N/A	371	N/A	236%	Yes – EoW R and EoW A
BS L165-AA8090 II	EoW A	0.06	636	400	284	159%	224%	No
BS L165-AA8090 I	EoW R	0.11	705	307	286	230%	247%	No

It can be seen that the maximum stresses are all well in excess of the yield strength, although as stated previously (3.4.4.3) the uncertainty in the calculation is unknown and

is likely to be considerable. As a result, these findings are only indicative of significant tensile residual stresses within the weld, and at which position.

6 Discussion

6.1 Introduction

In this chapter the results specific to each configuration will be presented and discussed. By analysing the weld appearance, macro and microstructure, and test results, the suitability of the configuration (AA8090-AA8090, BS L165-BS L165, AA8090-BS L165 and BS L165-AA8090 in both the \parallel and \perp orientations) for SSFSW can be determined. A summary of the most salient findings from each configuration is provided for comparison in Table 48 of section 6.6.

6.2 AA8090-AA8090

6.2.1 As-Welded Examination

6.2.1.1 *Welded Sheets*

Following SSFSW it was observed that all AA8090 welds (\parallel and \perp) showed distortion longitudinally, such that the sheets did not lay flat post-welding. Transversely, all welds showed a degree of angular distortion in the form of one or more sheets raising towards the edge, at one or both ends. These two distortions were due to thermal contraction as the welds cooled and are shown in Figure 65(a) and (b). In the opinion of this author, some distortion, particularly longitudinally, and although undesirable, should not necessarily be considered as a flaw or defect. The increased flexibility inherent in thin sheet (compared with thicker plate) material means that the process envelope for the material which produced a sound weld without any kind of distortion would be extremely narrow and would therefore necessitate extensive process parameter studies to find it. There are potentially heat treatments which may alleviate this distortion, however investigation into this is outside the scope of this research.

Additionally, in some welds one of the abutting sheets had risen above the other ahead of the tool as observed in the free ends at weld completion after the exit hole (Figure 65(c)). Vertical lifting is an issue which has been observed by other researchers (Sattari et al., 2012) due to the reduced stiffness when FSW is applied to thin sheet and occurred

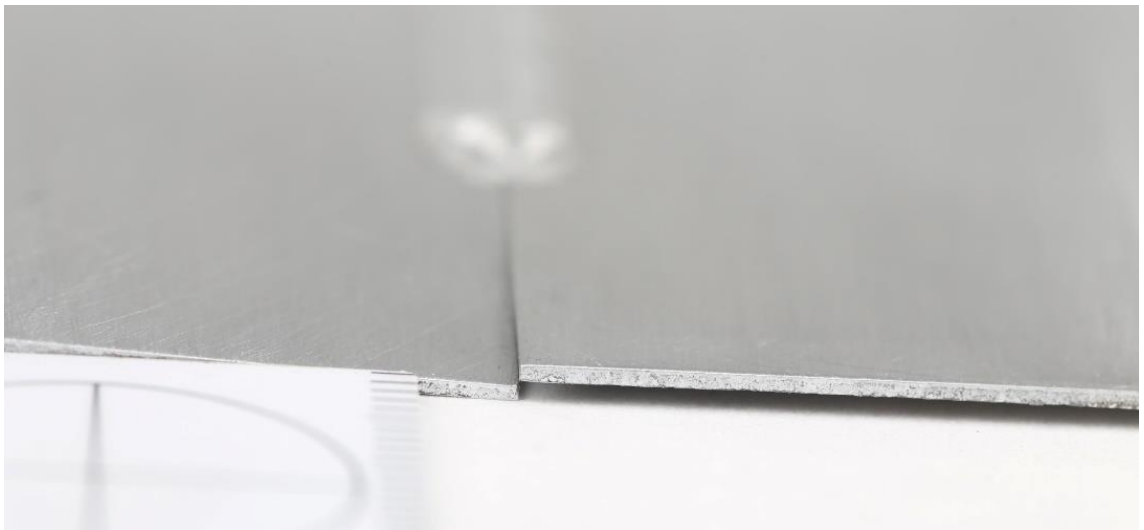
despite the rigid clamping in place. Zettler, Vugrin and Schmücker (2010) suggest that FSW of thin sheet (<2 mm) can benefit from a gap between the faying edges, especially towards the end of the weld run. This is due to rigid clamping combined with thermal expansion creating an unequal thermal gradient as material is moved from the front to behind the tool. This leads to the edges moving towards each other in front of the tool (the weld prevents it occurring elsewhere) as the sheets expand and where there is no gap, one sheet is forced to move vertically. The width of any gap would be dependent on the material thickness and thermal conductivity; in this case a suitable gap would likely be small and could be difficult to maintain accuracy during clamping.



(a)



(b)



(c)

Figure 65: Showing as-welded AA8090 sheets: a) AA8090 || longitudinal distortion; b) AA8090 \perp transverse angular distortion; c) AA8090 \perp sheet lifting ahead of tool.

6.2.1.2 *Weld Surface*

An area of the weld top surface representative of the steady state welding conditions of AA8090 II and \perp is shown in Figure 66 with a diagram showing the scaled dimensions of the tool shoulder inner and outer diameters and pin step diameters (spiral not shown) superimposed. The appearance of the weld top surface was not consistently identical for both configurations. For AA8090 II, the visible width of the weld measured approximately 6 mm, which did not correspond to either the shoulder (8 mm) or pin (maximum) diameter (4.95 mm). For some of the AA8090 \perp welds, it was observed that the visible width of the weld was smaller, at approximately 5.2-5.4 mm, however others of the AA8090 \perp welds were broadly consistent with II.

It was observed that both weld surfaces differed from the “ideal” SSFWS surface (described in Section 2.3.2) in several respects which require clarification.

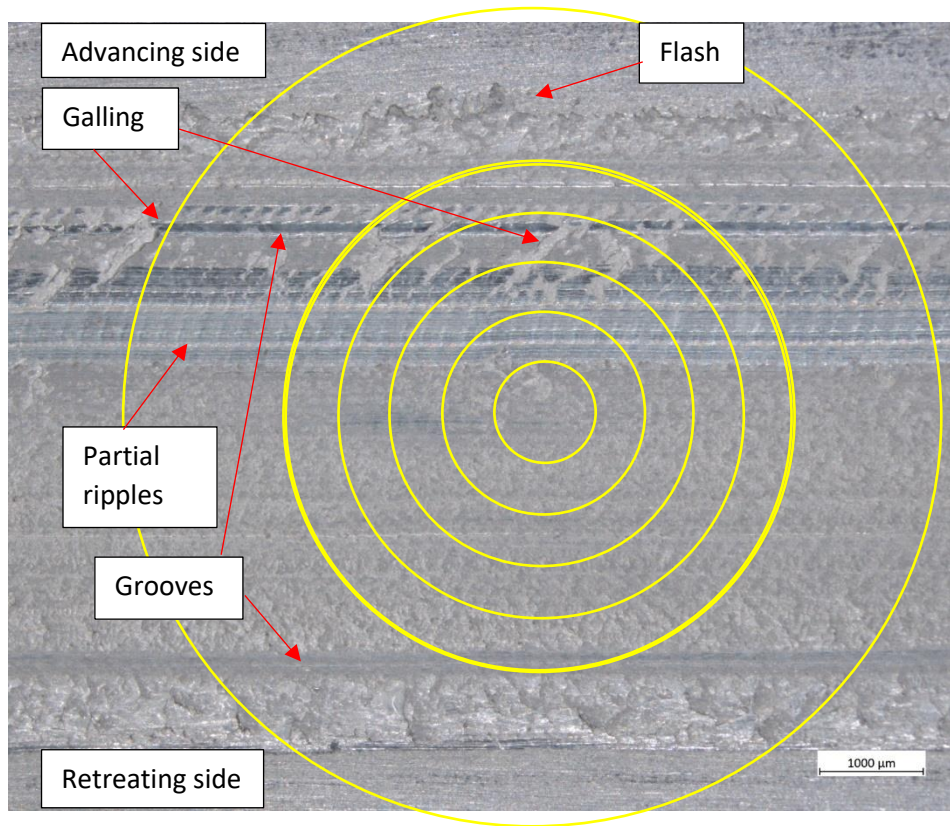
Regular partial circular “ripples” were observed, Figure 66; these are common particularly in traditional FSW. Many researchers consider these ripples to be formed by the cycloidal motion made by the final sweep of the trailing circumferential edge of the shoulder during traverse (Serio, Palumbo, De Filippis, Galietti, & Ludovico, 2016; Thomas, 1998). Of course, in SSFSW the shoulder does not rotate, therefore in this research the material could not be deposited in the final sweep of the shoulder trailing circumferential edge. Schneider, Brooke and Nunes (2016) postulate that the surface ripples and internal onion ring feature often seen in FSW are related, due to the rotating pin producing an up-and-down flow of material around said pin. These displacements result in both the onion ring effect and the surface ripples. For both AA8090 II and \perp welds, the circumference of the partial ripples closely matched that of the maximum pin diameter, as shown in Figure 66. This is suggestive of the ripples being formed as per Schneider et al.’s (2016) postulation. This is supported by Zhang et al.’s (2011) work previously described (section 2.3.8.1) in which they showed that the shear layers around the pin detached and were pushed upwards by incoming material, thus forming (partial) ripples.

Only partial ripples were observed on the surface of both AA8090 configurations, although they were visible to a far greater extent on AA8090 \perp , Figure 66(b). Additional material covered the majority of the potentially rippled surface on AA8090 II. The retreating side of the AA8090 \perp weld shown was rough, with material disrupting the

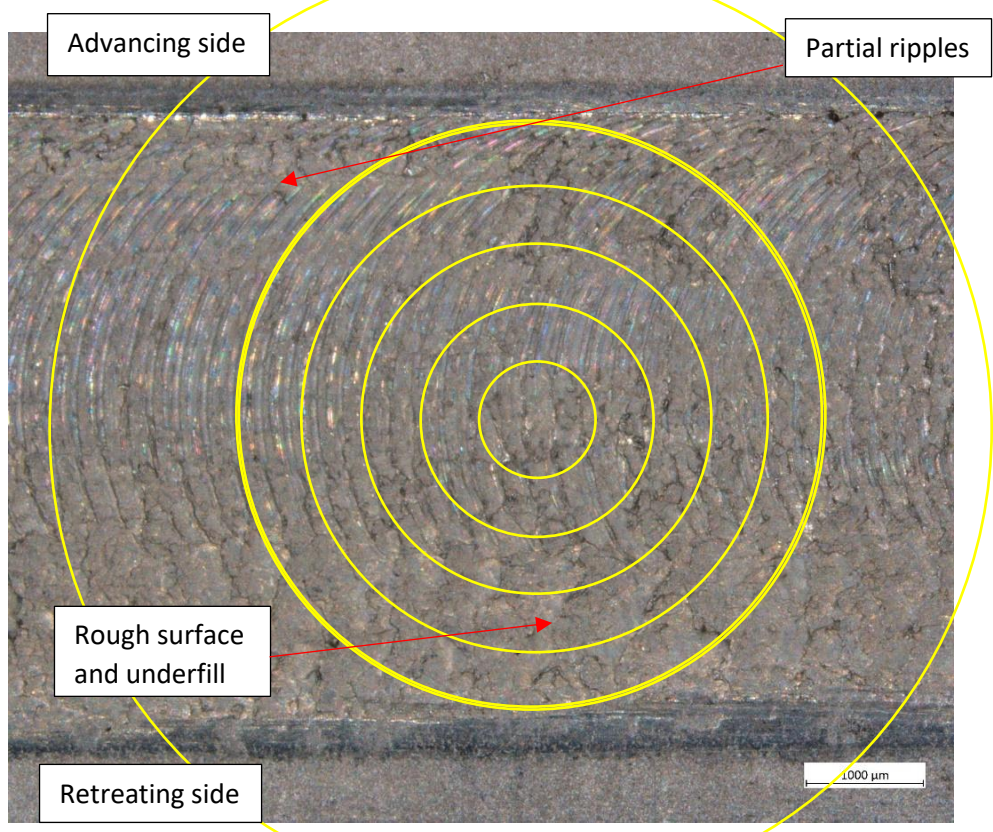
ripples and significant but variable underfill being observed. On AA8090 II a much smaller rough area was present on the retreating side (and a very limited area at the advancing side edge), however this did not include underfill, i.e. all of the roughness was above or very close to the parent material surface.

It is considered that the ripples were formed due to the shear layer detachment from the pin. The remainder of the surface weld width was comprised of material extruded from the weld as flash and galling. The stationary shoulder in SSFSW can have an “ironing” effect, smoothing the weld surface, and the ripples are generally reduced (You et al., 2020) or non-existent (Patel et al., 2019). This has happened to a limited extent, with some material deposited on the weld surface (above the ripples) being smoothed.

Both configurations were formed using a 1.5° tool tilt angle and 3000 N constant down force (at steady state conditions). It is likely that the partial smoothing described above occurred as a result of the tool tilt allowing the heel of the tool shoulder to contact the material. It is highly unlikely that the rest of the tool contacted the surface of the material as this would have resulted in frictional markings and additional heat being input to the weld. As the weld width did not extend to 8 mm, it is clear that this contact did not occur, with the exception of the trailing heel of the tool shoulder. This partial contact was also inconsistent, as shown by the particularly rough retreating side surface of the 8090 I weld (Figure 66(b)).



(a)



(b)

Figure 66: Showing weld top surface of with profile of SSFSW tool superimposed, a) AA8090 II weld, and b) AA8090 ⊥ weld.

The measured material properties showed approximately 1.3% reduction in the % elongation of AA8090 \perp from AA8090 II (see section 6.2.2.2, Table 36). This is not evidence of a severe reduction in material properties, but it does warrant consideration when designing a weld and shows a degree of anisotropy between the material orientations.

As the tool traversed through the \perp material it is likely that a greater traversing force was required than for the parallel weld, due to the requirement to traverse through a greater number of high energy grain boundaries. However the specific value of this traversing force is unknown due to the force/ moment sensor being non-operational at the time (see section 3.2.1). Barbini, Carstensen and dos Santos (2018) FSW AA2024-T3 in both the longitudinal and transverse directions. They found at lower traversing speeds that the anisotropy of the material resulted in an increase in force as the material had reduced deformability in the transverse direction (presumably due to traversing through an increased number of grain boundaries, as discussed above). It also resulted in a decrease in torque due to the lower strength in the transverse orientation. As a result, in this current research, as the II weld required less traversing force there was a consequential increase in the amount of flash extruded from the weld due a stronger response to the heat generation within the material.

The pitch (distance between each ripple) is dependent on both the rotational and traversing speeds, with the pitch increasing with increasing traversing speed (Thomas, 1998), i.e. as the traversing speed increases the distance between each ripple increases. The pitch is equal to the lateral distance travelled by the tool per revolution (Mishra et al., 2014). This is approximately equal to the ratio of traversing speed (mm/min)/ rotational speed (RPM) which approximately equals the forward distance per revolution of the tool (Li, Y., Sun, & Gong, 2019). In this case the ratio of traversing speed/ rotational speed was 0.2 mm/rev for both orientations and the measured pitch approximately 220 μm for both AA8090 orientations, showing good correlation.

Another way in which the surface appearance of the two configurations differ is that two “grooves” are visible on the AA8090 II surface, indicated in Figure 66(a) while no grooves are apparent on some of the AA8090 \perp surfaces, Figure 66(b). The topographies of the welds are shown more clearly via optical profilometry models and surface profilometer roughness plots in Figure 67 (AA8090 II) and Figure 68 (AA8090 \perp). Note

the advancing side of the optical profilometry model is on the right-hand side while the advancing side of the surface profilometry roughness plot is on the left. The model and roughness plot also show that the weld edges of AA8090 II have a steep gradient with sharp peaks which then roughly level out with the exception of the recessed ripples and two “grooves”. They also show that the edges of AA8090 \perp have shallower gradients and thicker peaks. No overall weld thinning was observed, but material was deposited above the surface level of the parent material (located on the weld surface rather than weld adjacent as would be the case of flash) and underfill.

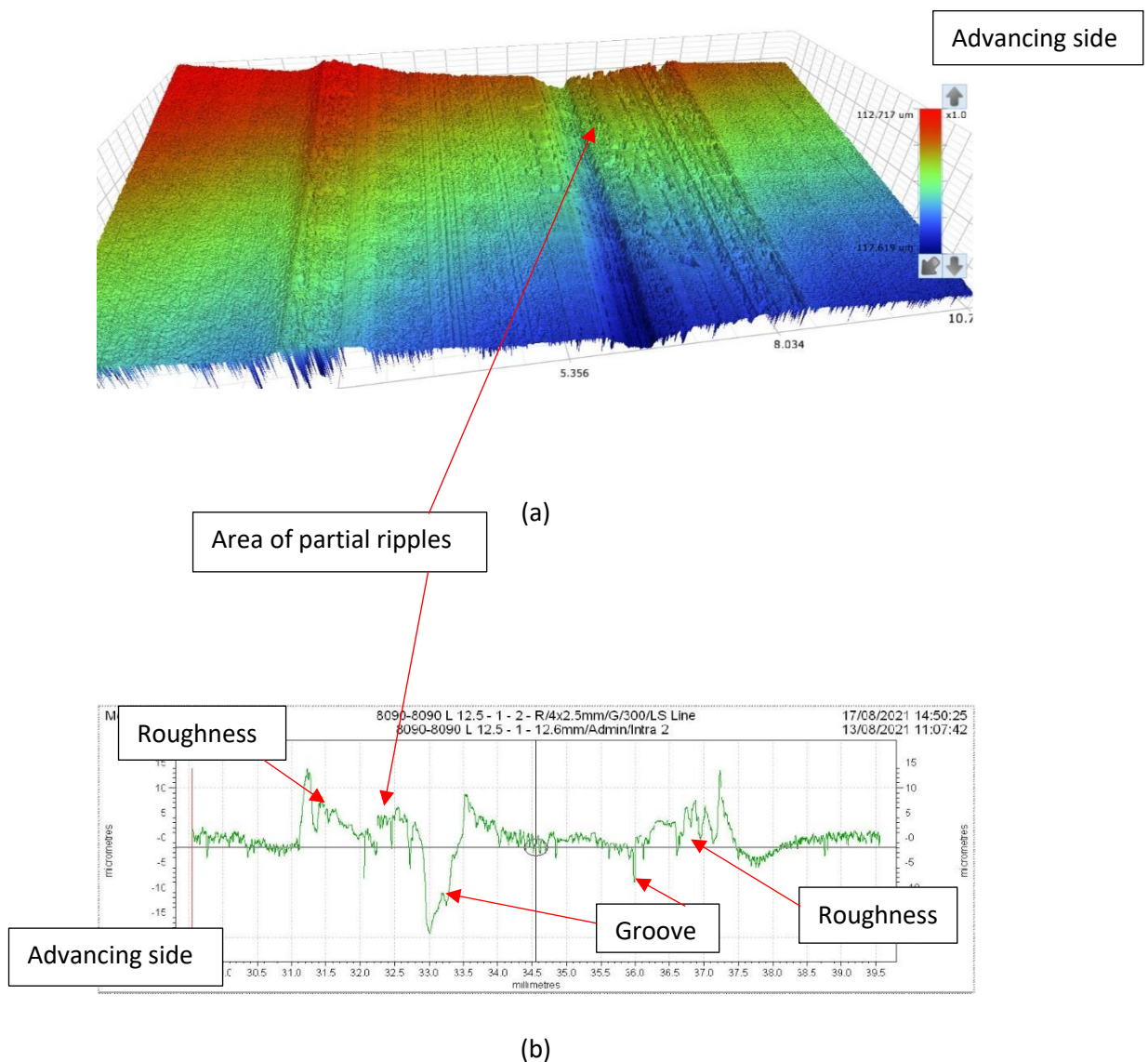


Figure 67: Showing AA8090 II weld surface topography, a) optical profilometer 3D model image, and b) contact profilometry surface plot.

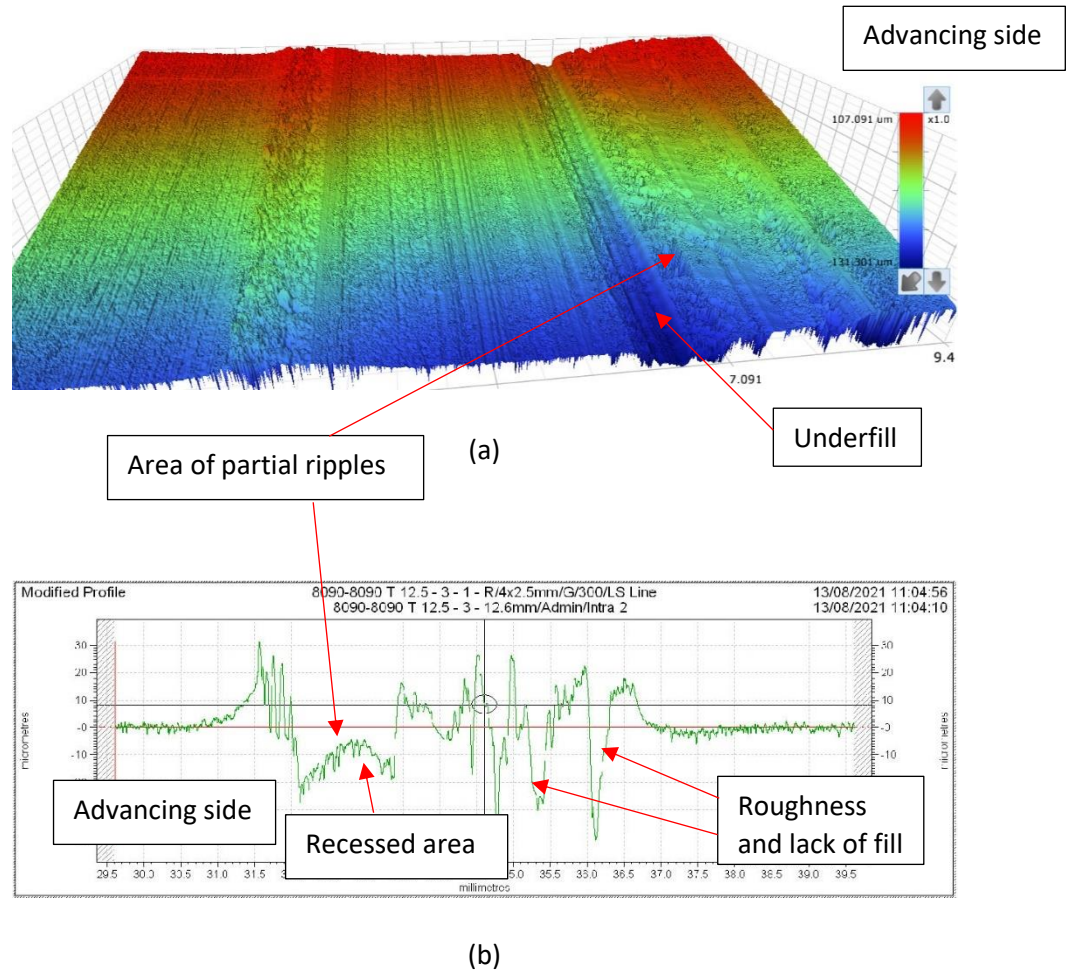


Figure 68: Showing AA8090 \perp weld surface topography, a) optical profilometer 3D model image, and b) contact profilometry surface plot.

According to Hoda, Arab, Gollo and Nami (2021), grooves are formed by two means: the first due to excessive heat and insufficient forging pressure, and the second due to a lack of mixing from insufficient heat.

1. If these grooves were formed due to the first cause (excessive heat and insufficient forging pressure), the excessive heat may be caused by low traverse speeds and high rotational speeds. A comparison with the literature (although direct read-across cannot be made between materials) shown in Table 10 (section 2.3.9.4), indicates that a traversing speed of 10 mm/s (600 mm/min) is not a low speed. However a rotational speed of 3000 RPM could be considered high. Therefore, it is plausible that the heat generation may have been excessive. Flash formation occurs if the heat generation was excessive, causing over-plasticisation and failure of the shoulder to hold and join the material behind the tool; flash can also be caused by excessive shoulder pressure in cooler welds. As

previously described, the shoulder played had little influence across the width of the weld and flash has gathered at both edges.

2. The second means of groove formation is caused by insufficient stirring. Hoda et al. (2021) describe material flow in FSW as flowing vertically and asymmetrically, i.e. the material is pushed up on the retreating side and downwards on the advancing side. The material on the advancing side flows in front of the tool and that on the retreating side flows behind. As the tool causes softening, mixing and forging of the material sufficient heat must be generated to allow complete stirring. As the tool moves material downwards from the advancing side, if adequate heat and therefore plasticisation are not present, sufficient material may not flow upwards on the retreating side to replace it when forged by the shoulder pressure. If insufficient stirring was the cause of these grooves, one would expect to see further evidence, i.e. internal tunnel defects or incomplete penetration. These additional defects were not observed, section 6.2.1.3.

The appearance of the grooves formed on AA8090 II differ from those shown in the literature. Here, they are smooth, straight, narrow and shallow; the literature indicates rough edges, meandering progression and significant depth. It is considered that the “grooves” in this research may have been caused by material adhering to the surface of the shoulder and essentially ploughing a furrow into the weld surface as it traversed. Additionally, the “groove” on the retreating side of the AA8090 II weld coincides fairly well with the position of the edge of the pin/ small (0.05 mm) gap between the pin and shoulder. This may be a position where material could gather, and thus produce the furrow in the weld surface. Regular cleaning or tool redesign would be required to mitigate against this occurring in future welds.

The underfill shown where the partial ripples were observed (not to be confused with grooves) is likely to have been caused by excessive heat generation allowing material to escape at the edges and to be deposited on the retreating side above the surface level of the parent material, rather than moving around the tool to be deposited on the advancing side to produce a smooth and flat weld. This is also shown on the AA8090 \perp weld, where the ripples are shown in a recessed area (Figure 68(b)) and the retreating side has rough, uneven deposits. Underfill as a result of excessive heat generation is further supported by the presence of surface galling. There is limited galling on AA8090

II (Figure 66(a)), however the excessive roughness over the retreating side of AA8090 \perp indicates fairly severe galling (Figure 66(b)). Galling is caused by high shear rates experienced with high rotational speeds in addition to the pick-up and redistribution of very soft materials (when excessive heat causes over-plasticisation) by the weld tool (The Welding Institute, 2013).

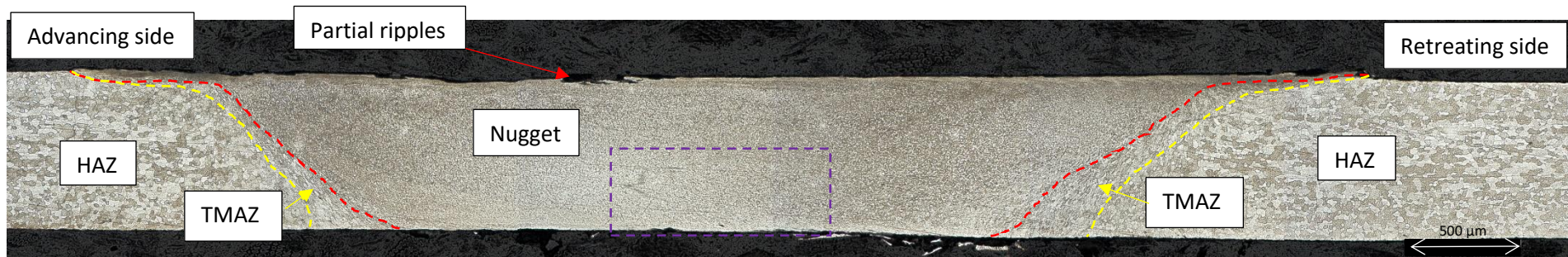
6.2.1.3 *Weld Macro- and Micro-structures*

The weld cross-section of AA8090 II is shown in Figure 69(a) and AA8090 \perp shown in Figure 69(b) with the HAZ, TMAZ and nugget indicated on both; based on hardness testing, none of the parent material is shown in the cross-sections. Note that in Figure 69(a) the advancing side is shown on the left while in Figure 69(b) the advancing side is on the right.

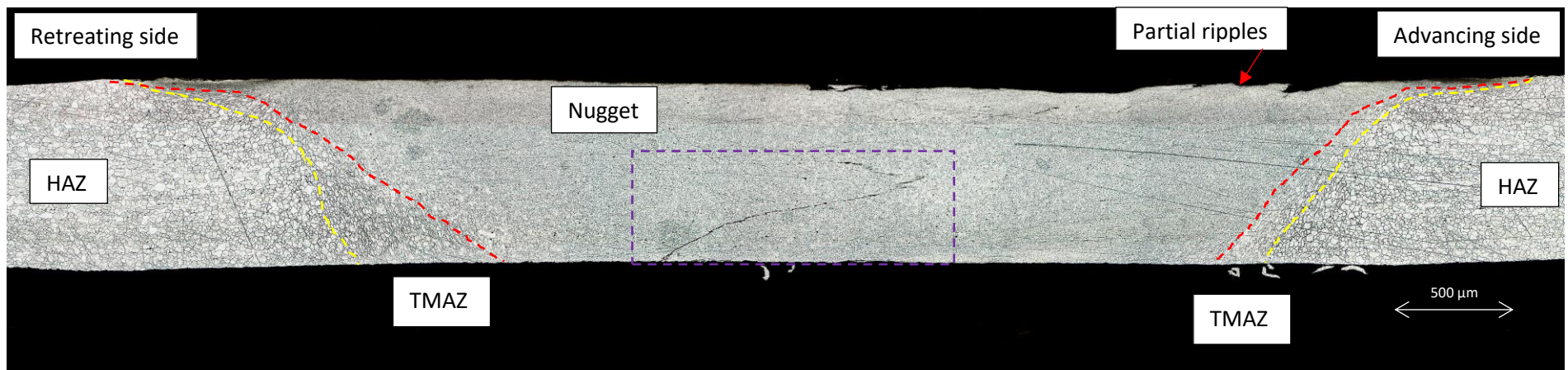
Negligible thinning of the weld was observed which is in keeping with SSFSW research in literature (Ji et al., 2017; Zhang, H. et al., 2015). The welds were predominantly influenced by the rotating pin, rather than the stationary shoulder as would be expected. A shallow area influenced by the maximum pin diameter extends to each side of the weld. This is indicative of surface friction from the widest part of the pin as it traversed, however, as previously shown in section 6.3.1.2, flash was extruded which will account for some of this width. Some roughness to the weld surface can be observed on the macrographs, from the advancing side to the mid-point. The roughness and lack of fill on the retreating side of AA8090 \perp is not apparent on the macrograph (Figure 69(b)), however the recessed areas of partial ripples can be seen on the surface.

The nugget followed the approximate shape of the pin (tapered) but was wider than the pin diameter, and the gradient of the boundary slope was steeper at the advancing side for both configurations. Both weld configurations achieved full penetration, although “kissing” bonds were observed on both. No other internal defects were observed on either configuration.

The TMAZ was narrower on the advancing side than the retreating for both weld configurations, although it was considerably larger on the retreating side of AA8090 \perp weld, especially towards the bottom of the weld where its shaped differed significantly from that of the AA8090 II weld. This is likely due to a differing reaction to SSFSW of the materials due to the change in orientations, see section 6.2.1.3.2.



(a)



(b)

Figure 69: Showing macrographs of weld cross-sections: a) AA8090 II (advancing side on left); and b) AA8090 L (advancing side on right).

6.2.1.3.1 Nugget

As noted, although the shape of the nugget approximates that of the pin, Figure 69, the nugget size exceeds that of the pin. The pin has 4.95 mm diameter at the surface, measures approximately 3.0 mm at the mid-point and reduces to approximately 1.0 mm at its tip. Disregarding the nugget width at the top surface (as this may include flash), the nugget width of AA8090 II measured approximately 3.7 mm and 2.6 mm at the mid-point and root respectively. The measurements for AA8090 \perp were 3.8 mm and 2.9 mm. This indicates that the influence of the pin significantly exceeds the immediate area in which it operates, especially at the root. The literature is split in this respect; some researchers observed nuggets significantly exceeding their pin dimensions (Ahmed, M. M. Z. et al., 2011; Li, D. et al., 2015) while others observed close correlation between the nugget and pin measurements (He et al., 2019; You et al., 2020). He et al. (2019) did however find that the nugget dimensions increased with an increase in rotational speed, which they attributed to an increased thermal input and greater plastic material flow. A comparison with literature indicates that 3000 RPM would be considered to be a high rotational speed therefore allowing pronounced plastic flow and an extended stir zone. Vigraman et al. (2021) state that the recrystallisation temperature of AA8090 is 300°C (no source is provided). Yang, Zhao, Xu, Zhou, Zhao and Liu (2021) carried out work on SSFSW of 2A14-T4 alloy and found that peak temperatures in the nugget exceeded 500°C and varied between approximately 250-350°C in the TMAZ. It should be noted that these temperatures varied according to weld parameters used and direct read across from work on another aluminium alloy is not possible due to differing thermal and mechanical properties. However it is certainly feasible that the temperature within the nugget in this research exceeded the 300°C recrystallisation temperature of AA8090. Therefore, dynamic recovery and recrystallisation occurred within the nugget.

As hardness measurements were taken at the weld mid-thickness, mid-thickness was also where the analysis of the grain size was focussed across all weld zones. Analysis of the grain sizes within the nugget (Table 34) indicated a considerable reduction in size from the parent material of approximately 46-72%⁶. There was a small difference in

⁶ Note: when the weld orientation was parallel to the rolling direction (II), the comparison parent material grain size was short-transverse. Similarly, where the weld orientation was perpendicular to the rolling

grain size between the advancing and retreating sides within the nugget and between the two configurations. The AA8090 II advancing side nugget grains were equiaxed and the AA8090 \perp advancing side nugget grains were significantly more equiaxed when compared with the original longitudinal parent material. Although the difference in grain size directions (the two measurements which show asymmetry in grain size, see Table 34) may exist, the Relative Accuracy (RA) associated with the weld grain size measurements indicate that the directions may not be as uneven as suggested.

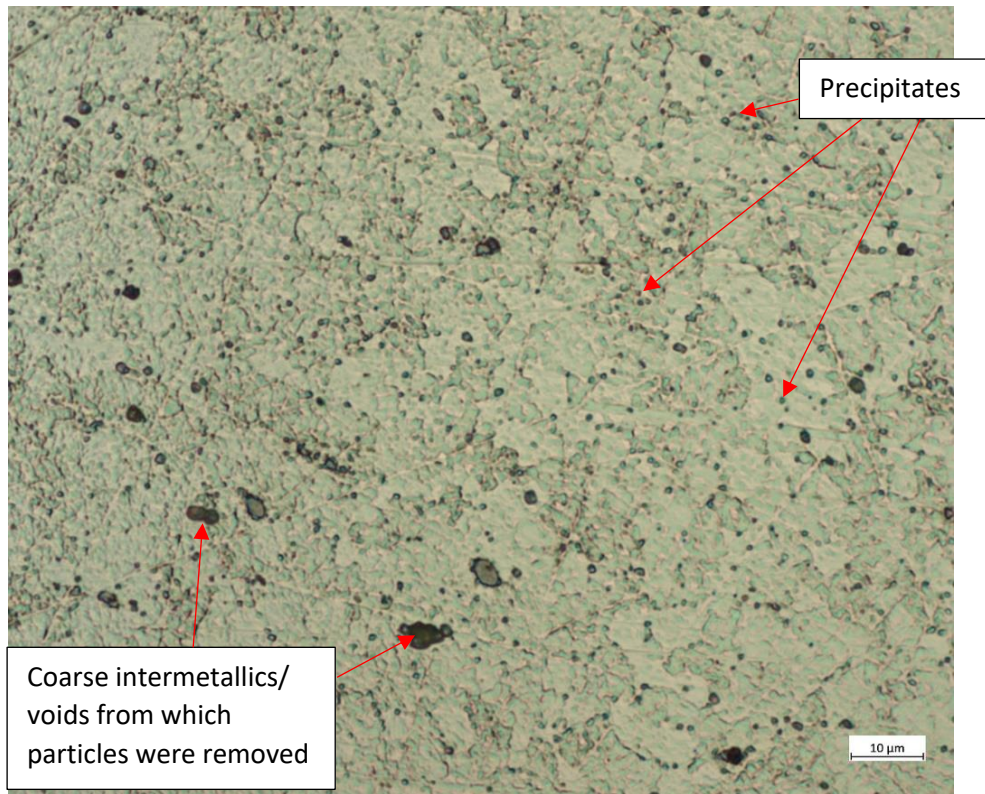
The grain size was larger with greater asymmetry on the retreating side of the nugget, in comparison with the advancing side, for both configurations. As described by Hamilton, Kopyściański, Senkov and Dymek (2013), the advancing side experiences temperatures at least slightly elevated from the retreating side. This is due to cooler material in front of the tool being swept to the retreating side as the tool traverses, while material which has been rotated around the tool and therefore heated, is deposited behind the tool at the advancing side. Others disagree, stating that the retreating side experiences higher temperature (Zhang, L. & Wang, 2018). Wu et al. (2019) attribute the temperature difference (higher on the advancing side) to the effective shear and strain being increased on the advancing side as opposed to the retreating side, with an associated increase in material flow and therefore temperature. Literature has reported larger grain sizes on the advancing side of the nugget due to the additional deformation experienced (Lee, Lee, & Min, 2016). In this research, as the retreating side of the nugget grain size was larger, this would indicate agreement with Zhang and Wang (2018), i.e. that higher temperatures were experienced on the retreating side. However, this author tends to agree with the other side of the argument (advancing side experiencing higher temperatures) due to the strength of arguments provided above. It is expected that the disparity here is related to inaccuracies in the grain counting process, as shown by the RAs which reach 19% in one instance (Table 34).

direction (\perp), the comparison parent material grain size was longitudinal. This was in keeping with the hardness measurements, as described in section 5.2.1.1.

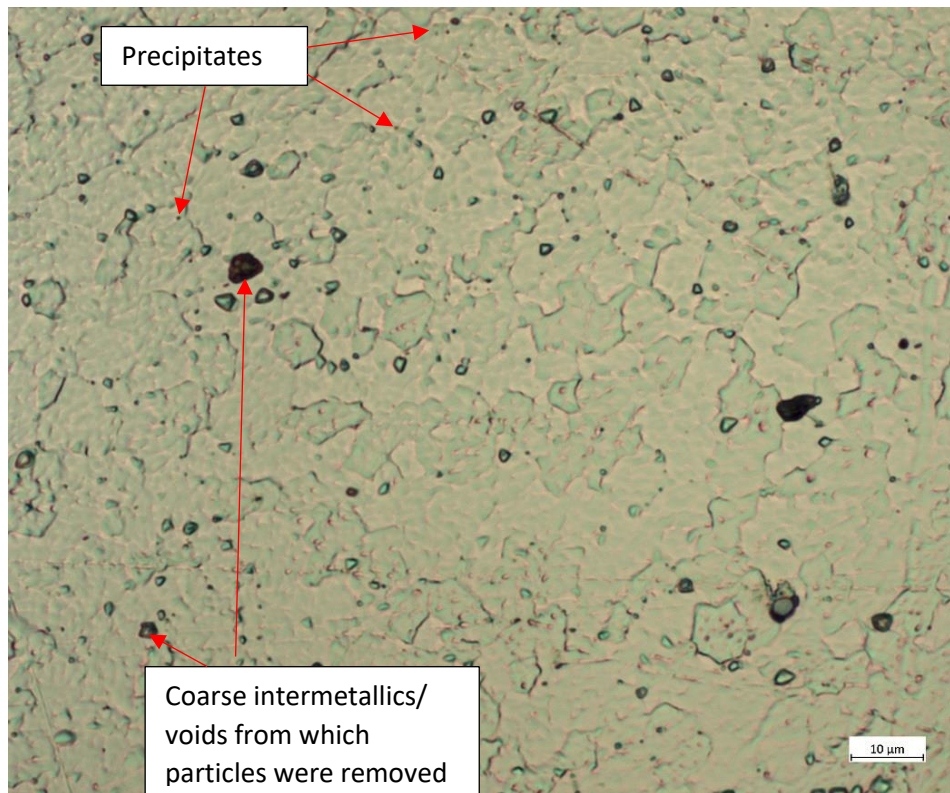
Table 34: Showing AA8090 parent material and weld nugget grain size dimensions, showing Relative Accuracy (%RA) in brackets.

Configuration	Average grain diameter (μm) in two directions			
	Advancing side		Retreating side	
	Direction 1	Direction 2	Direction 1	Direction 2
Parent material longitudinal	21.2 (9%)	16.2 (6%)	N/A	
Parent material short-transverse	28.0 (4%)	25.4 (16%)	N/A	
AA8090 II	7.9 (8%)	7.8 (10%)	10.6 (19%)	8.8 (13%)
AA8090 I	8.8 (9%)	7.4 (8%)	9.4 (14%)	8.3 (10%)

Focusing on the advancing side of the nugget, micrographs of the two configurations are shown in Figure 70.



(a)



(b)

Figure 70: Showing micrographs of the advancing side of the nugget: a) AA8090 II; b) AA8090 L

Analysis of the nugget microstructure reveals a significant volume of fine black approximately spherical particles clustered around the grain boundaries on the AA8090 II weld; these are considered to be a coalescence of coarsened incoherent δ precipitates. While the density of precipitates visible at the grain boundaries in the nuggets of both configurations far exceeds that of the parent material (these are not visible in Figure 31, section 4.1.2), they are more numerous on the II weld than on the weld \perp . The reason for an increase in the II weld relates to the heat generation and plastic deformation within the weld; AA8090 II may have experienced more deformation indicated by the slightly smaller grain size. Through consideration of the literature (TEM work was not undertaken in this research), and upon comparison with the parent material (Figure 31, section 4.1.2) and hardness testing (see section 6.2.2.1) it is considered that the heat input and tool rotation has caused dissolution and coarsening of the strengthening phases, as noted by Akhtar, Jin and Wu (2018). The material in the nugget has a high probability of being overaged (see section 6.2.2.1) thus some finer δ' precipitates likely dissolved into the matrix enabling coarsening of the grain boundary precipitates upon cooling. The spherical precipitates (annotated on Figure 70) are considered to be heterogeneously nucleated incoherent δ (AlLi). The strengthening phases T1 and S' cannot generally be observed without use of a TEM, however Akhtar et al. (2018) postulated that these may be broken down by the heat input and plastic deformation, which, together with the coarsened δ precipitates, may account for the resultant reduction in hardness within the nugget when compared with the parent material (section 4.1.3.1 and section 6.2.2.1).

Coarse intermetallic compounds were also present, generally located around grain boundaries, Figure 70. Vigraman et al. (2021) report (Figure 71) aluminium lithium precipitates and intermetallic compounds including Al_2Cu , Al_2Fe , AlCu , $\text{Mn}_3\text{Si}_2\text{Al}_{12}$ and Al-Fe-Cu (confirmed with EDX and XRD), along with oxides and fine porosity (although the "porosity" is more likely to be small voids as porosity is not inherent to FSW). The intermetallics indicated on Figure 70 are considered to be iron-rich and manganese rich insoluble phases such as FeAl_2 and $\text{Mn}_3\text{Si}_2\text{Al}_{12}$ based on the work of Vigraman et al. (2021) and Srivatsan and Place (1989). Conversely to the differing density of precipitates noted between the two configurations, there are similar volumes of coarse intermetallics in the II and \perp welds. The density and size of the intermetallics are

comparable with the parent material, however within the nugget they have pinned the grain boundaries during recrystallisation.

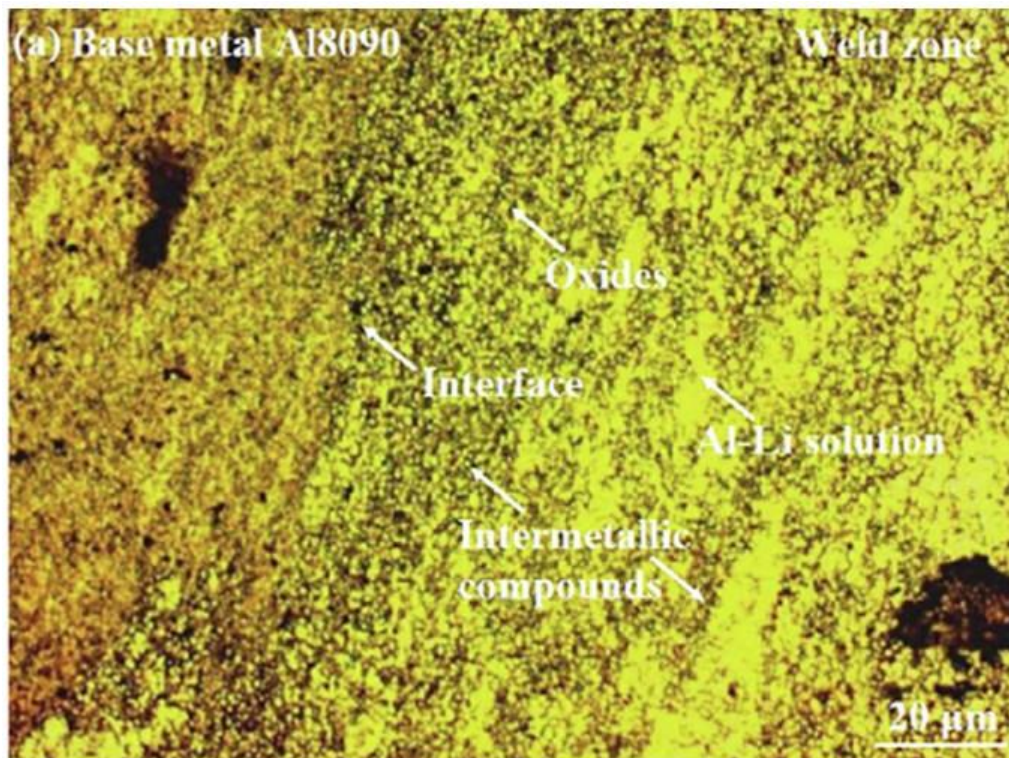
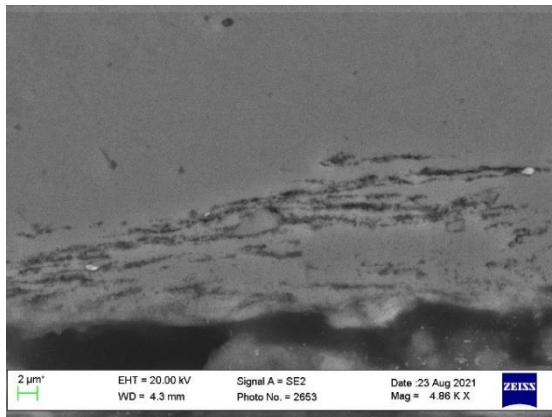


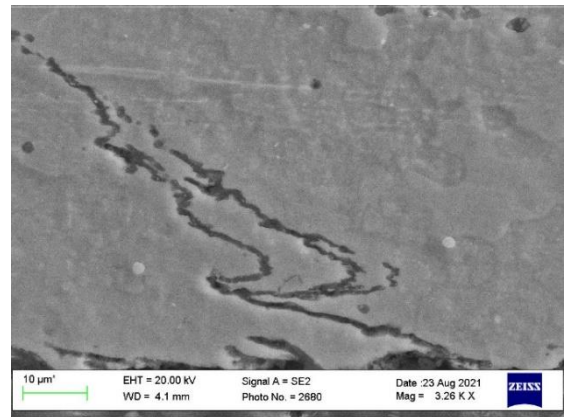
Figure 71: Showing microstructure of FSW AA8090 (temper unknown), courtesy of Vigraman et al. (2021).

Kissing bonds were observed in both configurations. These featured throughout most of the weld thickness, with the most discernible part highlighted by the purple dashed boxes in Figure 69. As previously noted, these may be caused by oxides originally present on the material faying surfaces (Tao et al., 2014; Zhou et al., 2018) or generated during the welding process itself (Schneider et al., 2016). The effect of a kissing bond on the mechanical properties of a weld is debated in the literature, as summarised by Zhou et al. (2018). Tao et al. (2014) made a distinction between a lazy S and a kissing bond by specifying the lazy S as high density clusters of aluminium oxide (Al_2O_3) particles, while the kissing bond was comprised of a continuous oxide film. SEM images of the “kissing bond” on the weld, taken at the weld root and mid thickness are shown in Figure 72. It can be seen that the feature takes the form of a kissing bond at the root, although the feature on the \perp weld is more defined than on the \parallel weld, before transiting to a lazy S further into the weld. This was similar on the \parallel weld. Several researchers (Schneider et al., 2016; Tao et al., 2014; Zhou et al., 2018) found that variations in weld process

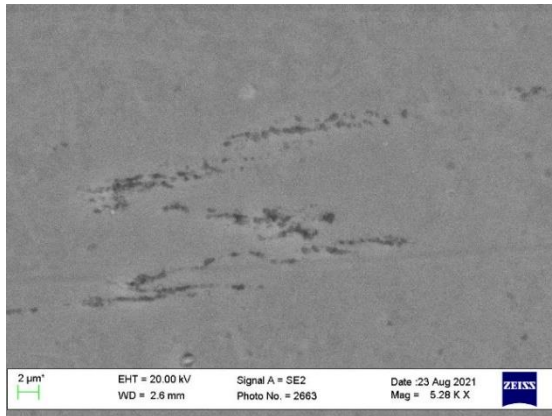
parameters affected the “waviness” and the extent that the kissing bond/ lazy S progressed throughout the thickness of the weld, if at all. Generally, an increase in rotational speed may mitigate against kissing bond formation, however the additional heat generation can have deleterious effects elsewhere and so a compromise is required. The effect of the kissing bond on the mechanical properties is discussed in sections 6.2.2.2 and 6.2.2.3.



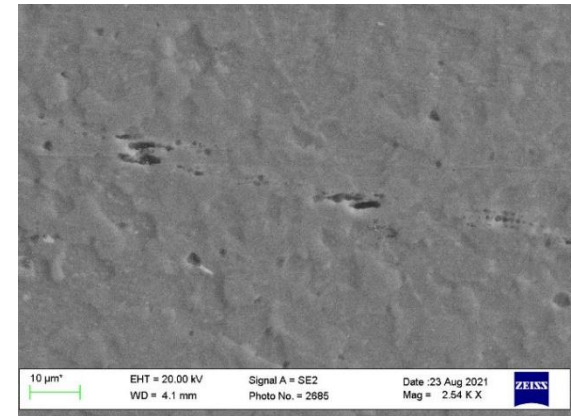
(a)



(b)



(c)



(d)

Figure 72: SEM images of weld taken at weld root, a) AA8090 II and b) AA8090 ⊥; and mid-thickness, c) AA8090 II and d) AA8090 ⊥.

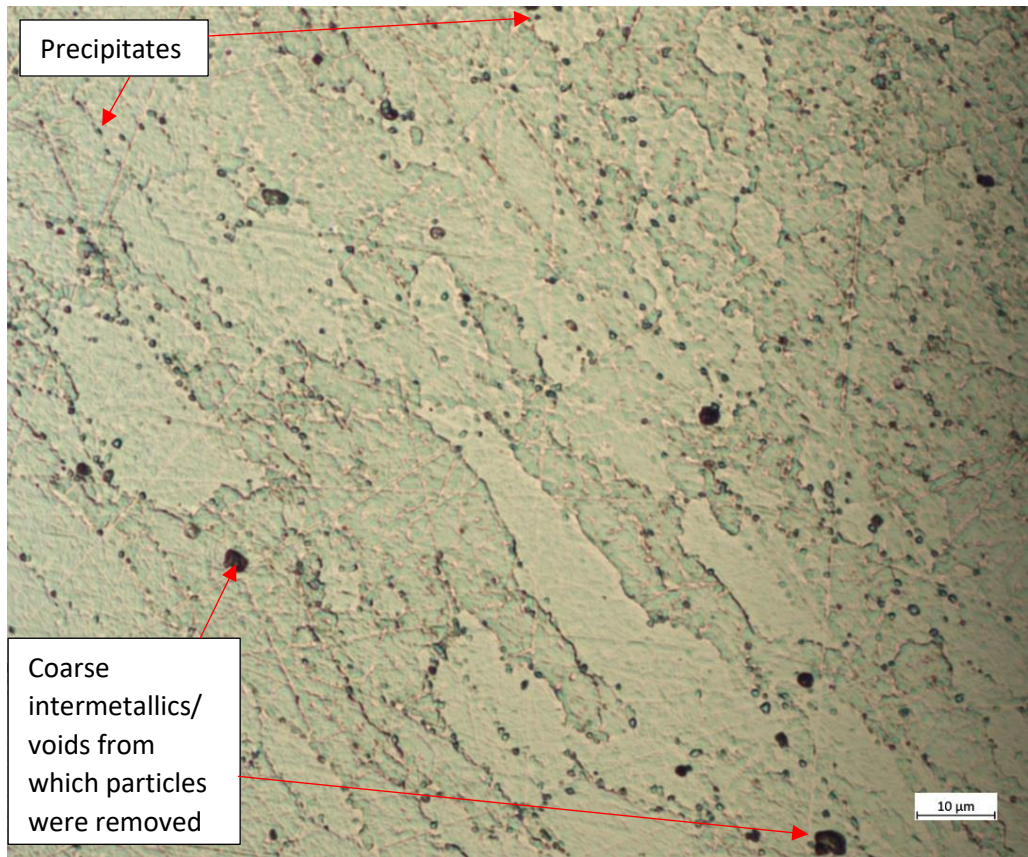
6.2.1.3.2 TMAZ

The TMAZ region is identified by elongated grains alongside the boundary of the nugget, aligned at an angle inconsistent with the other areas of the weld and the parent material. The boundary between the nugget and the TMAZ on the advancing side has a sharp interface, while the boundary transition on the retreating side is significantly more gradual, Figure 69. This is in keeping with the literature (Zhou et al., 2018) and can be attributed to the strain rates and temperature gradients being much steeper on the advancing side (Moradi, Jamshidi Aval, Jamaati, Amir Khanlou, & Ji, 2018). Additionally, it can be seen that in both configurations the TMAZ is narrower on the advancing side than on the retreating side. At the midpoint, the AA8090 II advancing TMAZ width is approximately 160 μm while the retreating side is 250 μm , and the AA8090 \perp advancing TMAZ width is approximately 175 μm while the retreating side is 350 μm . As described by Zolghadr, Akbari and Asadi (2019) on the advancing side the coincidence of rotational direction with traversing direction has a resultant increase in relative velocity and increase in shear. This results in higher heat generation through plastic deformation (Al-moussawi, Smith, Young, Cater, & Faraji, 2017). One would expect then for the advancing side TMAZ to be wider than the retreating side, but this is not experimentally true. Zolghadr et al. (2019) suggest that the higher strain and temperature force the material to recrystallise and enter into the nugget; on the retreating side the strain has changed the microstructure over a wider area but the combination of strain and temperature was not sufficient for recrystallisation. This does not however explain the hard boundary on the advancing side. According to Bhattacharyya et al. (2021) as the flow on the advancing side is clockwise and the flow currents do not mix, a sharper interface is observed than on the retreating side, where upward and downward currents flow across the TMAZ resulting in a diffused appearance.

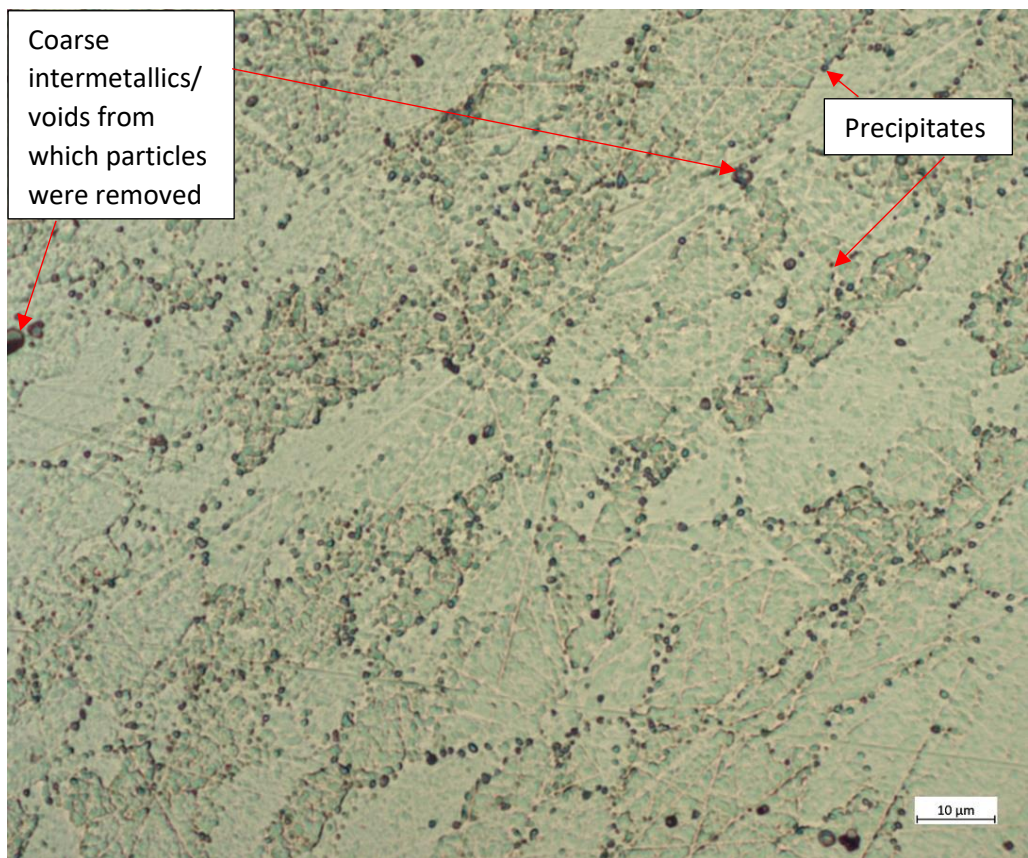
It is clear from Figure 69 that the width of the TMAZ increases with depth on both sides of the weld and for both configurations. Zolghadr et al. (2019) also observed this but gave no explanation as to the cause. The reason may be due to material flow in FSW as described by Zhao, Lin, Qu and Wu (2005); plasticised material is driven from top to bottom of the weld on the advancing side and then driven upwards on the retreating side, however the heel of the inclined shoulder may impede this upward motion. It is however considered more likely that the widening of the TMAZ with depth is due to the

forging pressure of the backing plate generating heat and thus increasing the width of this zone. The retreating side TMAZ of AA8090 \perp far exceeds its advancing side and both side of the AA8090 II weld, with the notable change in width starting at approximately one third thickness. This specific result has not been observed in the literature, however Barbini et al. (2018) observed a difference in weld cross-sectional shape between AA2024 welded both perpendicularly and parallel to the rolling direction, although little explanation was provided. They did note decreased deformability in the transverse direction of the material in front of the tool leading to a decrease in torque for that weld. It is likely that the difference in shape observed here is related to the decreased deformability in front of the tool, combined with the forging pressure from the backing plate leading to a more diffuse retreating edge.

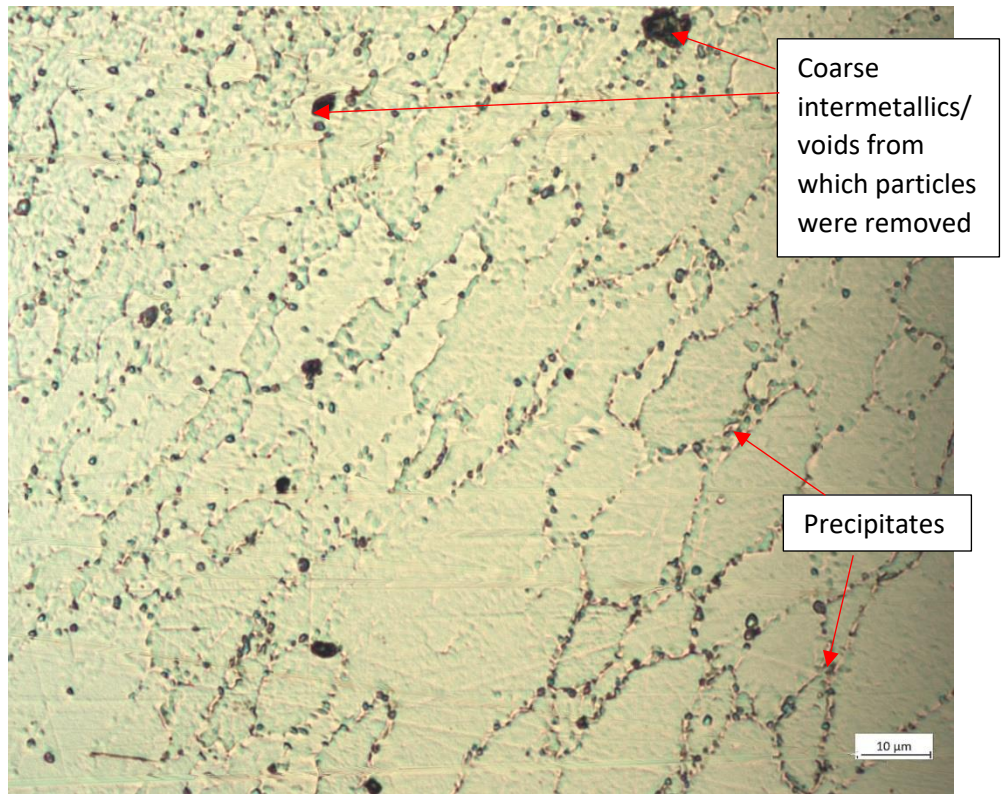
Figure 73(a) and (b) show a significant number of coarse precipitates, assumed to be incoherent δ (see section 6.2.1.3.1), present on AA8090 II TMAZ and located at grain boundaries, with some intermetallics (see section 6.2.1.3.1) also present. Figure 73(c) and (d) indicate a reduced volume fraction of precipitates present in AA8090 \perp TMAZ when compared with the II weld. There are, however, a larger number of coarse intermetallics present in the \perp TMAZ. It is considered that the II weld may have experienced higher heat input in this area resulting in the increased volume fraction of precipitates following overaging and subsequent cooling.



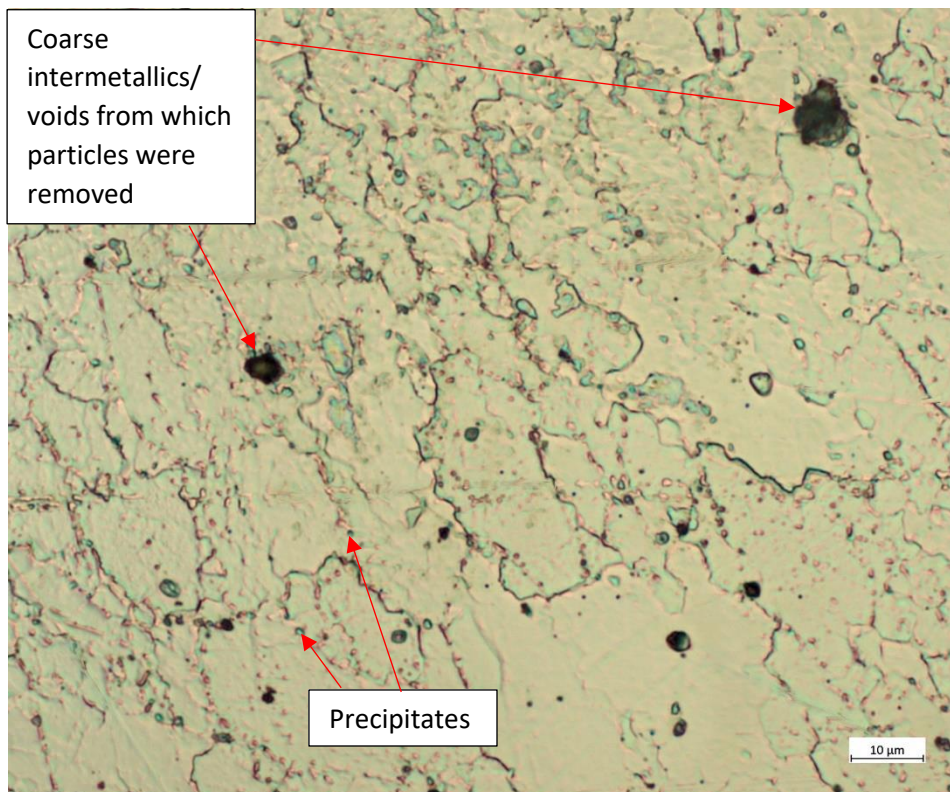
(a)



(b)



(c)



(d)

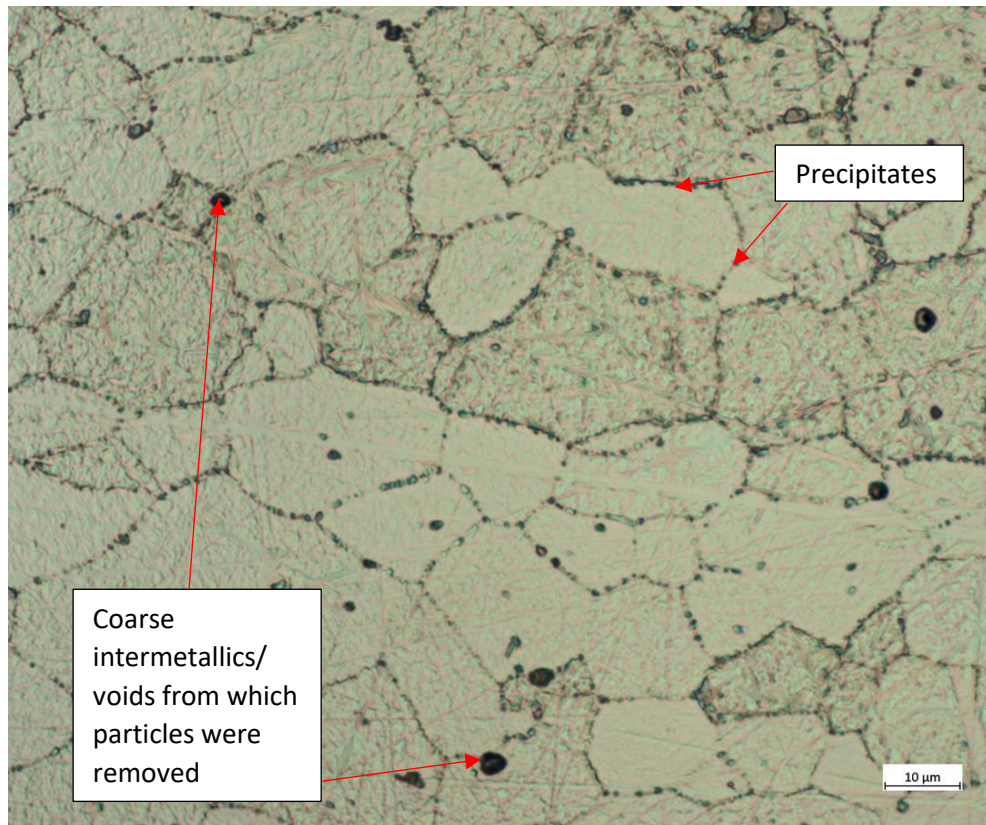
Figure 73: Showing micrographs of the TMAZ: a) AA8090 II advancing side and b) retreating side; c) AA8090 L advancing side and d) retreating side.

6.2.1.3.3 HAZ

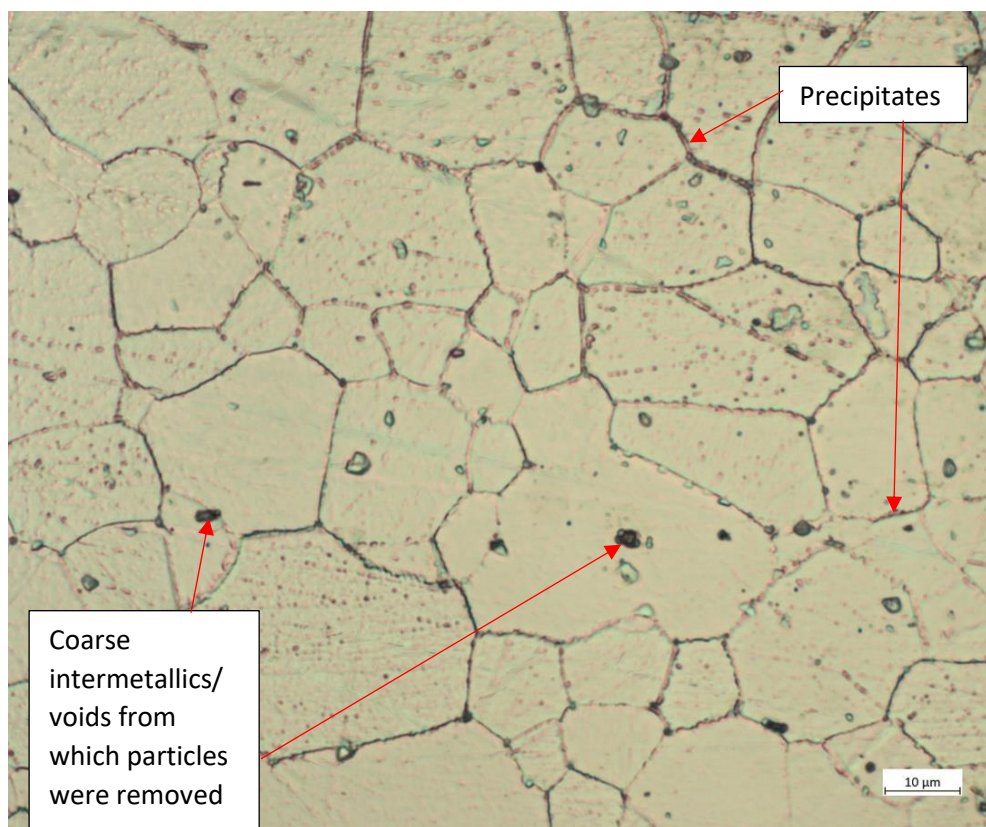
The transition from HAZ to parent material is not visually obvious on micrographs due to the grains being of a similar size (see changes described later and in Table 35) and shape. In order to ascertain the width of the HAZ it was necessary to consider the results from hardness testing; the HAZ was taken as the area in which the hardness value was below the steady value of the parent material, and outside of the TMAZ as indicated by etching post hardness test. The measurement was thus limited by the 0.5 mm increments of the hardness testing. The width was found to measure approximately 2.0 mm (advancing) and 2.5 mm (retreating) for both AA8090 II and \perp . The difference in HAZ widths is likely to be related to material flow; as cooler material is swept from in front of the tool around the retreating side to be heated (Hamilton et al., 2013) it is reasonable that this would thermally affect a wider area than that at the advancing side where the material is deposited.

The literature, for example Ji et al. (2017) and Wu (2017), reports that SSFSW generally has a smaller HAZ and TMAZ than conventional FSW owing to the reduced heat input as the shoulder does not rotate. Conventional FSW has not been carried out in this research for comparison, however the HAZ implied here due to the hardness data seems significantly larger than observed elsewhere. It is considered that this extended width of the HAZ is a function of the thin material used, the thermal conductivity of the material, the high rotational speed of the pin and the frictional influence of the pin on the material surface extending the HAZ beyond where may be expected.

Figure 74(a) and (b) show the microstructure of the advancing HAZ of both weld configurations. There is a clear and significant increase in coarsened precipitates at grain boundaries in comparison with the parent material (Figure 31 in 4.1.2). These number fewer than in the nugget but are comparable with the TMAZ in terms of volume fraction at grain boundaries, however the TMAZ features a greater number of grain boundaries and thus more precipitates. It should be noted that the images shown in Figure 74 are located close to the TMAZ and these coarsened precipitates gradually decrease in number as the parent material is approached. The intermetallics are of comparable size and number to that observed in the parent material and are considered to be of the same composition as observed in the parent material and nugget.



(a)



(b)

Figure 74: Showing microstructure of advancing HAZ of AA8090, a) II and b) \perp .

The grain sizes of the two configurations are shown in Table 35 with the parent materials for comparison (longitudinal for comparison with AA8090 \perp and S-T for comparison with AA8090 II). It can be seen that the HAZ grain sizes on the welded specimens have universally reduced in size in comparison with the parent material, by as much as approximately 40% in the case of AA8090 II retreating side direction 2. The AA8090 II weld grains are no longer equiaxed (in comparison with the parent material S-T), while the AA8090 \perp weld grains retained approximately the same ratio between the two directions as the longitudinal parent material.

The grain size was measured at only one point across the HAZ, close to the TMAZ; considering the change in hardness and precipitate coarsening throughout the HAZ, a methodical analysis of grain size variation across the HAZ would be beneficial further work. As the measurement was taken at the same point on each configuration and side (close to the HAZ/ TMAZ boundary) an explanation is required as to why such a difference in grain size response has occurred. Although not referred to in the text, Dawood, Mohammed and Rajab (2014) show images which indicate that a difference in grain size between the HAZ and parent material was experienced, however generally the literature indicates that recrystallisation should not occur in the HAZ (section 2.3.8.3) as deformation does not occur in this area. In this research it is unclear as to why a reduction in grain size has occurred over part of the HAZ.

Table 35: Showing AA8090 parent material and weld HAZ grain size dimensions, showing Relative Accuracy (%RA) in brackets.

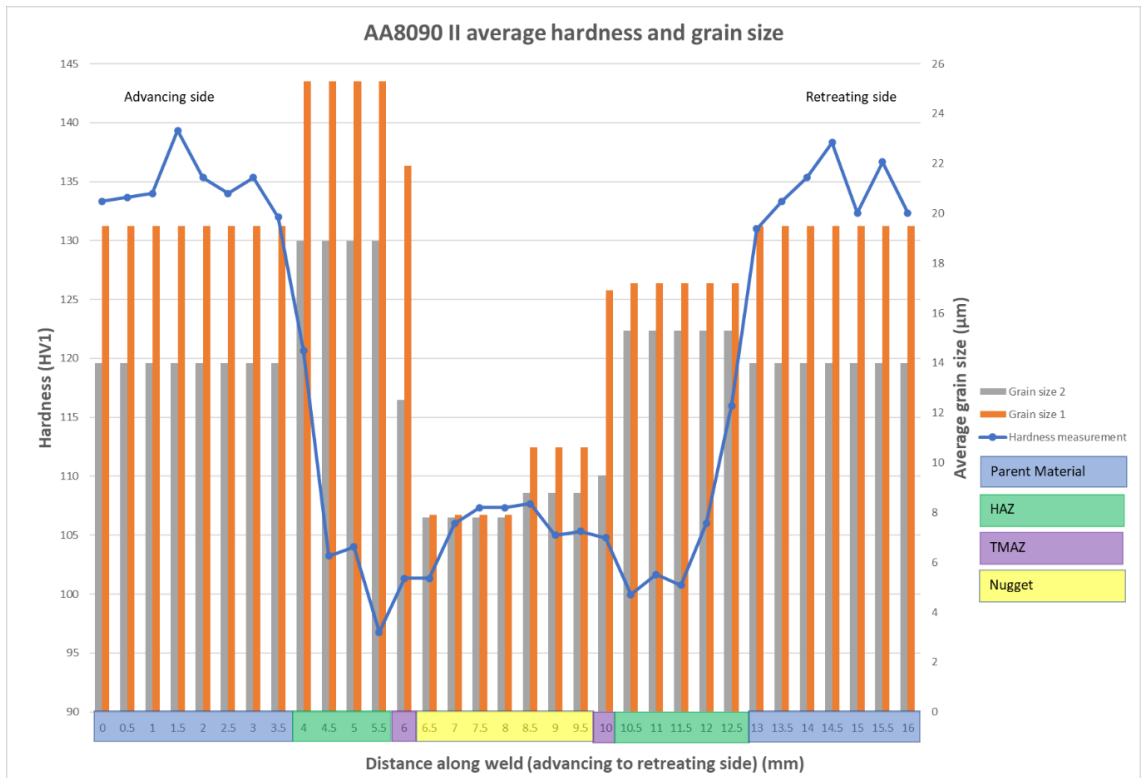
Configuration	Average grain diameter (μm) in two directions							
	Advancing side				Retreating side			
	Direction 1	% difference from parent material	Direction 2	% difference from parent material	Direction 1	% difference from parent material	Direction 2	% difference from parent material
Parent material longitudinal	21.2 (9%)	N/A	16.2 (6%)	N/A	N/A			
Parent material short-transverse	28.0 (4%)	N/A	25.4 (16%)	N/A	N/A			
AA8090 II	25.3 (19%)	-9.6	18.9 (13%)	-25.6	17.2 (14%)	-38.6	15.3 (11%)	-39.8
AA8090 \perp	15.3 (6%)	-27.8	12.2 (6%)	-24.7	17.0 (11%)	-19.8	13.4 (8%)	-17.3

6.2.2 Testing

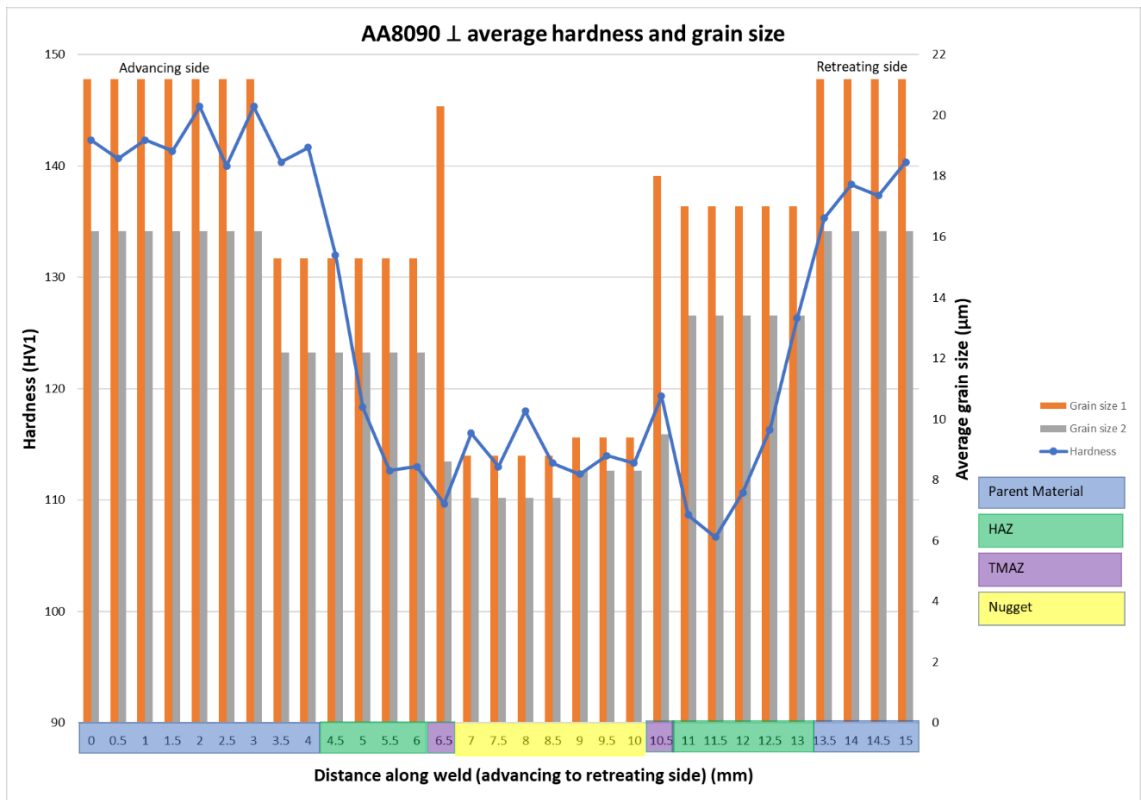
6.2.2.1 Hardness

The hardness values along the approximate centreline of the weld cross-section have been plotted together with the grain size corresponding to the relevant area of the weld, shown in Figure 75. Note, the grain size was not individually measured for each hardness test location, rather the grain sizes of parent material, advancing and retreating HAZ and TMAZ, and nugget were measured at one position each and these values plotted. As observed in section 6.2.1.3.3, the grain size changed along the length of the HAZ and increased to eventually match the original parent material size, and the distribution and refinement of precipitates in this zone change as it approaches the parent material. This changing distribution and refinement of precipitates along the length of the HAZ accounts for the changing hardness values.

In Figure 75 the areas of the weld, i.e. HAZ, TMAZ etc. are indicated by the coloured bars along the x-axis; these are an approximate indication of the location of each area. Analysis of the plots reveal some inconsistencies between the material orientations with regards to the positions of the HAZ and hardness minima, although that may be expected due to the anisotropy inherent in this material and measured via the parent material hardness testing (section 4.1.3.1), in addition to the difference in heat input between the two configurations previously discussed.



(a)



(b)

Figure 75: Showing hardness and grain size plots of a) AA8090-AA8090 II, and b) AA8090-AA8090 I.

Analysis of the hardness plots indicate that both configurations suffered reductions in hardness in the HAZ and TMAZ, with only limited hardness increase in the nugget. This is at odds with the, albeit limited for this alloy, research in the literature. Vigraman, Krishna and Kumar (2021), Pedemonte, Gambaro, Lertora and Mandolino (2013) and Lertora and Gambaro (2010) all report an increase in the nugget hardness greater than of the parent material post-aging, indicative of significant hardness recovery.

Research carried out on other precipitation hardening aluminium alloys has produced similar hardness profiles to that observed here, in fact it is relatively common (Mishra et al., 2014). Dada (2020) describes that the peak temperature and quenching rate experienced by the nugget determines its final state, and that it may finish as: overaged where the hardness is reduced; partially solution heat treated where some hardness can be recovered; or in a single phase solid solution where post-weld aging enables the hardness properties to be recovered to that of the parent material. In this case it is considered that the nugget has been overaged, with most strengthening precipitates first dissolving into the matrix and then causing coarsening and coalescing of previously homogeneously nucleated strengthening precipitates and grain boundary incoherent δ precipitates resulting in a reduction in hardness. This explains why the fine grain size in the nugget does not follow the Hall-Petch relationship. Fewer coarsened precipitates were observed on the \perp weld, explaining the overall increase in hardness over that of the II weld.

The position of hardness minima in the II weld was with the HAZ on the advancing side, and within the HAZ on the retreating side on the \perp weld. In their research on SSFSW of AA2219, Liu et al. (2013) found that the position of hardness minima changed from the advancing side nugget/ TMAZ interface to the retreating side nugget/ TMAZ interface when the welding parameters used (fast traversing speed) produced a cooler weld. It is considered that when the traversing speed is of sufficient value (thus producing a sufficiently cool weld), the fact that the higher relative velocity between the tool and workpiece on the advancing side produces higher heat input at that position is less significant. For the \perp weld it is considered that the position of minimum hardness transferred from the more common advancing side position due to the tool producing additional frictional conducted heat ahead of the traverse. This meant that the flow of material on the retreating side which should have been relatively cool, was heated prior

to passing the tool. This surpassed the heat generated on the advancing side and thus changed the position of hardness minima.

In both configurations the softened HAZ is wider on the retreating side than on the advancing. This is common throughout the literature although few explanations are provided. As described earlier, the reason is likely due to the material flow; material swept from in front of the tool around the retreating side has an affect over a wider area than that on the advancing side where the material is deposited. In the II weld, the parent material, i.e. that material outside of that affected by the welding process, did not achieve its previously measured value of 141.6 HV₁. On the advancing side, the average hardness of what was thought to be the parent material of the welded specimen was approximately 1.7-8.3 HV₁ (1.2-5.9%) lower than the original measured value. Some of these values were outside the uncertainty of the measurement (6.6 HV₁). This likely indicates that the HAZ extended for a wider distance than expected, despite the apparent levelling of measurement on the plot.

The hardness at the TMAZ is higher than at the HAZ for the II weld at both sides, however on the ⊥ weld the hardness is lower in the TMAZ at the advancing side but considerably higher on the retreating side. Again, this is considered to be due to the differing thermal cycle of each weld. In the II TMAZ the grains are elongated with smaller overall measurement in both directions than that of the grains in the HAZ (Table 28, section 5.1.3.2). Interpretation of the Hall-Petch relationship suggests that the hardness may be expected to be higher in the TMAZ due to the smaller grain size. In the ⊥ weld the direction 1 grain size of the advancing TMAZ is significantly larger than both HAZ (advancing and retreating) measurements, (although the direction 2 grain size measurement is significantly smaller) and this large measurement explains the reduction in hardness in the TMAZ over the HAZ. The TMAZ grain size at the retreating side is only slightly larger than the HAZ in one direction but considerably smaller in the other direction, thus explaining the significant increase in hardness in the TMAZ over the HAZ due to the higher concentration of grain boundaries.

6.2.2.2 Tensile Testing

The results of tensile testing have been reproduced in Table 36. As described previously, II welds are compared with transverse test results and \perp compared with longitudinal results. Comparison with the parent material measured result was considered to be more indicative of the weld quality than comparison with the minimum specification. In this case, the AA8090 II weld achieved 81.5% weld efficiency (WE) (see section 2.3.9.3.2 for weld efficiency calculation) and the AA8090 \perp weld 81%; these appear to be moderate values when compared with FSW of aluminium alloys overall (Table 10, section 2.3.9.4). When compared with research specific to this alloy (Lertora & Gambaro, 2010; Vigraman et al., 2021) these results are at the upper end of weld efficiencies where provided.

While there was a decrease in UTS (81.5% and 81% WE) and proof strength (83.4% and 77.6% WE) from parent material to welded, the most dramatic reduction was in the % elongation, Table 36, with % elongation WE of 29.7% and 21%, indicating a significant reduction in ductility. Table 30 (section 5.2.2.2) shows the position of failure for the tensile specimens. Where the specimens have failed within the nugget, the reduction in ductility is attributed to the presence of internal flaws, e.g. kissing bonds or embrittlement through introduction of oxides within the weld. In terms of the debate referred to in section 6.2.1.3.1 regarding the influence of kissing bonds on mechanical properties, this research indicates that when sufficiently defined, i.e. kissing bonds rather than lazy S, these flaws are in fact detrimental to the mechanical properties of a weld. Where fracture occurred in the HAZ or TMAZ, this is attributed to the heterogeneous nucleation of coarsened grain boundary precipitates, embrittling the grain boundaries as found by Ku, Hung and Lui (2019).

The UTS standard deviation for the AA8090 II welds is increased beyond that of the parent material testing, and there is a significant standard deviation increase in the UTS for the \perp weld. Concentrating on the \perp weld, on examination of the test results it was observed that one of the welds (from which 10 tensile test specimens were cut) showed significant scatter with a difference of 67 MPa between the highest and lowest result. The other \perp weld results featured a difference of 34 MPa between the highest and lowest result, however there was considerably less scatter in them. This suggests that the weld parameters do not produce welds of repeatable quality and that the quality of

the weld changes throughout the weld run. There are several potential sources of this issue with quality: it may be related to the clamping apparatus used, i.e. the material may have had more opportunity to distort in differing positions along its length; the force control used may have generated inconsistent heat input if there was fluctuation in material thickness or robot arm stability, thereby changing the material properties throughout the weld; inconsistencies in material preparation, i.e. cleaning and oxide removal prior to welding could allow ingress of oxides to the weld to varying degrees producing more and less severe kissing bonds along the length of the weld.

Table 36: Showing AA8090 tensile test results.

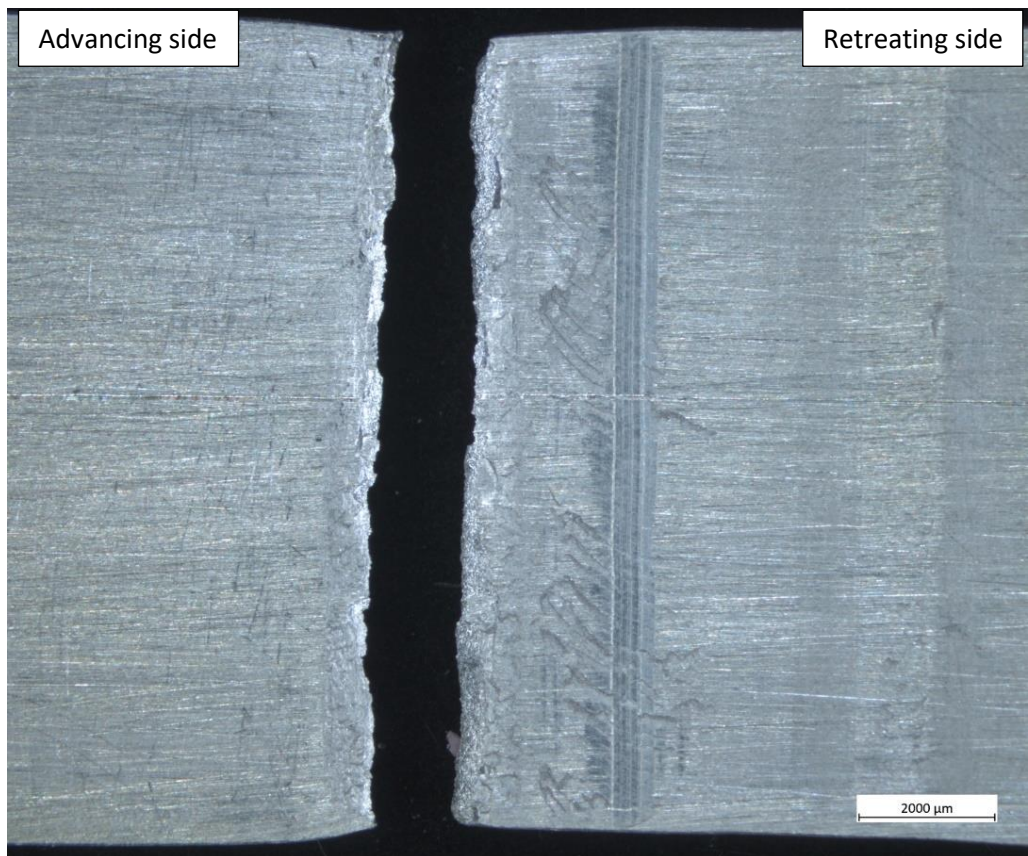
	UTS (MPa)		0.2% Proof strength (MPa)		Elongation (%)		UTS Standard Deviation	% UTS Parent Material Spec	% UTS measured Parent Material
	Spec	Measured	Spec	Measured	Spec	Measured			
AA8090 parent L	400	443	280	343	6	9.5	3.17	110.8%	-
AA8090 parent T	410	438	280	307	9	11.1	2.52	106.8%	-
AA8090 II	410	357	280	256	9	3.3	8.39	87.1%	81.5%
AA8090 L	400	359	280	266	6	2.0	23.57	89.8%	81.0%

Of the 20 AA8090 II tensile tests (10 each from two welds), 16 failed at the advancing side at the edge of the visible part of the weld surface, 3 failed at the retreating side of the weld and one failed mid-weld. Examples of each failure type, showing position of fracture from the top surface, as a cross section and showing detailed SEM images of the fracture surface are shown in Figure 76 (advancing edge of weld) and Figure 77 (mid weld). All fracture surfaces featured either a “V” shape or were sloped at approximately 45°, both orientated transversely to the longitudinal axes of the samples. Those which ruptured at the advancing and retreating edges featured a bright, shiny and granular fracture surface appearance while the mid-weld fracture surface had a dull appearance.

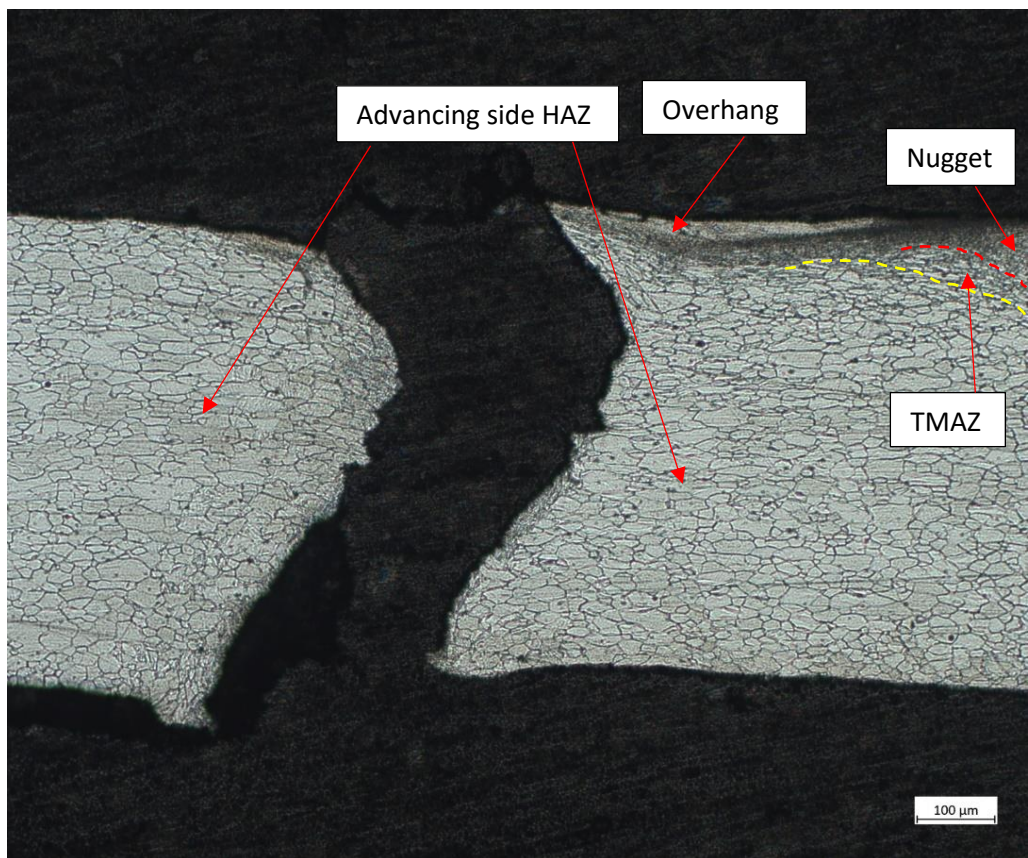
With reference to Figure 76, those tensile tests which fractured at the advancing edge did so along the edge of the visible weld as viewed from the surface. When the etched cross-section of the fracture surfaces was examined, it was observed that the fracture occurred within the HAZ a clear distance from the TMAZ and propagated from an initiation site within the overhang (previously described in 6.2.1.3) on the advancing

side. This overhang was comprised of an area which had suffered heat input through the frictional contact of the maximum pin diameter on the material surface, and included flash. This created a region with most likely altered mechanical properties (although the hardness was not tested along the surface) from the surrounding HAZ, and thus introduced a stress concentration.

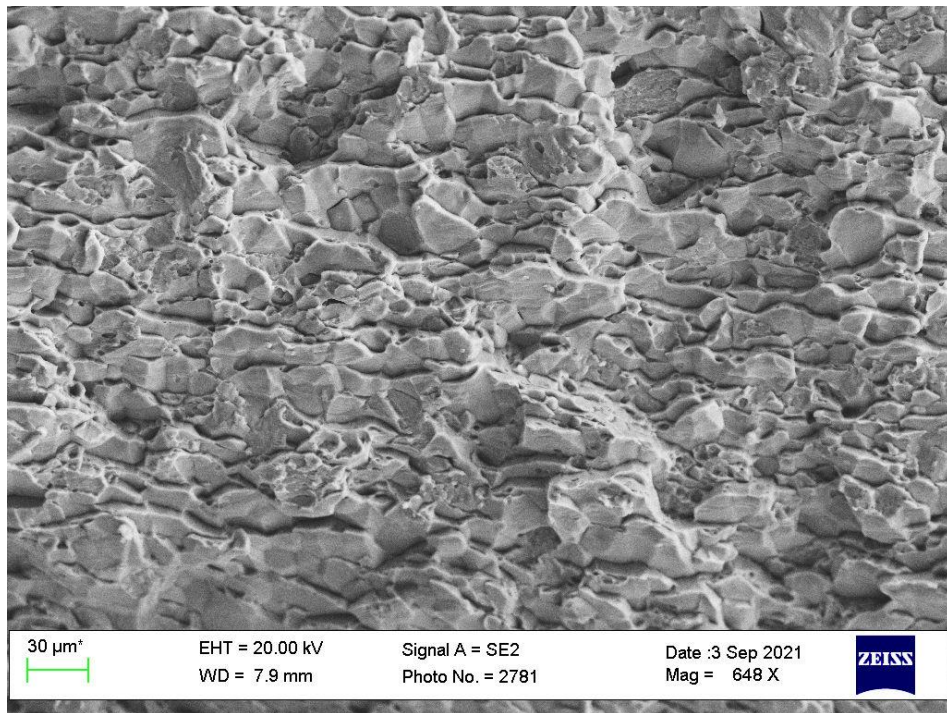
The fracture surfaces were macroscopically bright, shiny and granular. The fracture surfaces showed a mix of inter and transgranular failure featuring slip planes on the grain boundaries. This differed from the predominantly transgranular failure of the unwelded specimens which were pulled perpendicularly to the rolling direction, for comparison with these welded parallel to the rolling direction (Figure 34, section 4.1.3.2). Small pockets of localised microvoid coalescence were occasionally observed between grains, which was similar to the parent material. The welded specimen appeared “cleaner” along the grain boundaries, indicating reduced local plastic deformation in comparison with the parent material.



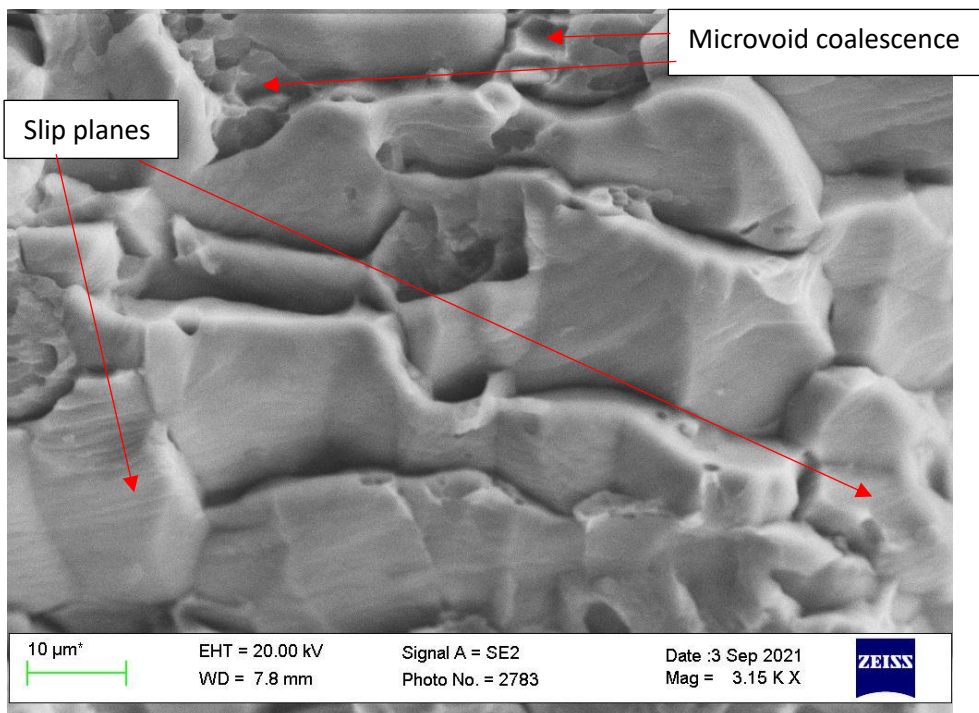
(a)



(b)



(c)



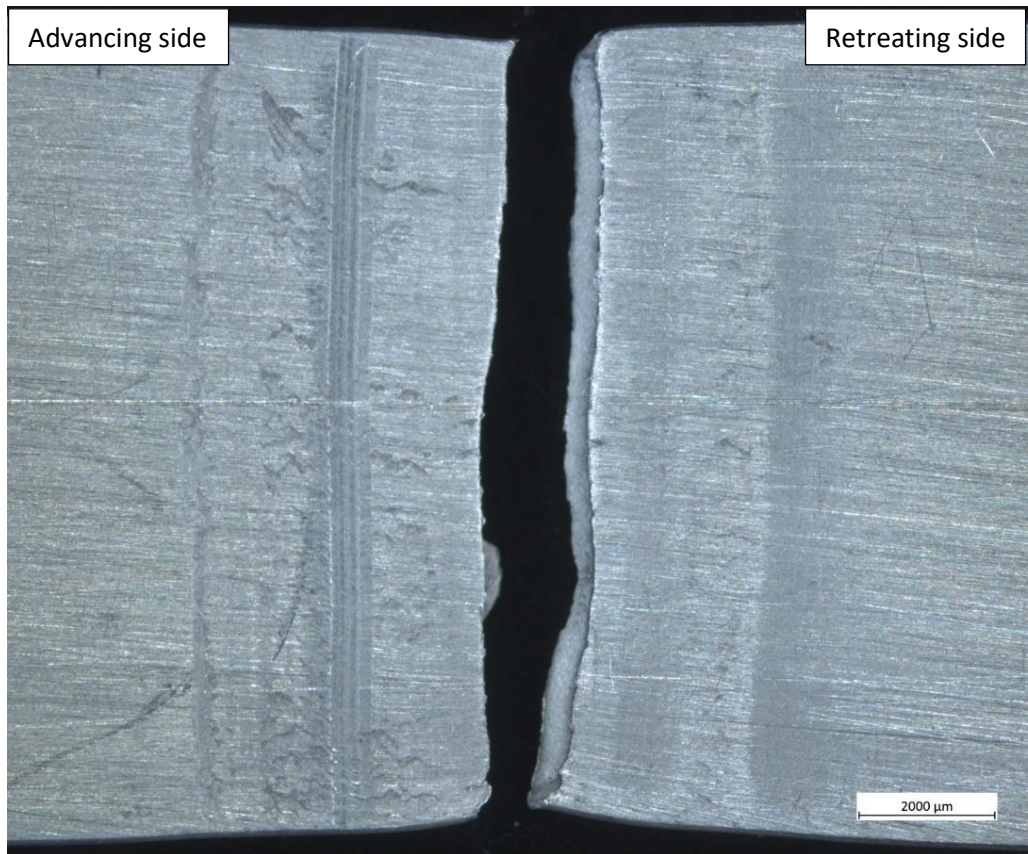
(d)

Figure 76: Showing advancing edge of tensile fracture of AA8090 II weld; (a) micrograph showing fracture from top surface, (b) cross-section of weld showing crack path, and (c) and (d) SEM image showing details of mid-thickness fracture surface.

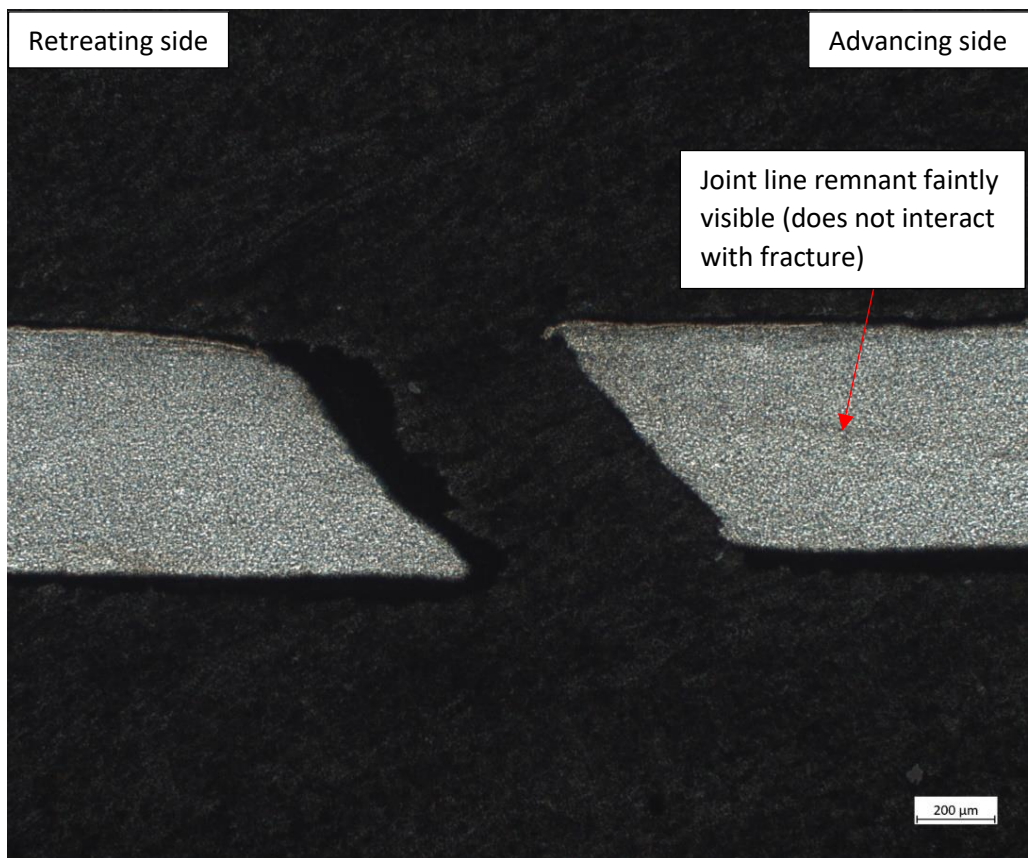
Those failures (3 of) occurring at the retreating side of the weld did so in a manner similar to those failing at the advancing side previously described, with regards to position (except they did not initiate within the overhang) and fracture surface macro and microscopic appearance. The reason for these three specimens failing at the retreating side is unknown but may be due to small flaws caused by the process when cutting the tensile specimens.

The numerical values obtained in the II tensile tests showed little correlation between UTS value and failure position of the samples, although those which achieved the two highest test values (362 MPa and 361 MPa) were for tensile test specimens which failed at the retreating side and advancing side of the weld respectively. As most of the tensile specimens failed at the advancing side of the weld, this is considered to be the “typical failure” for this configuration and is consistent with the hardness minima occurring in this region.

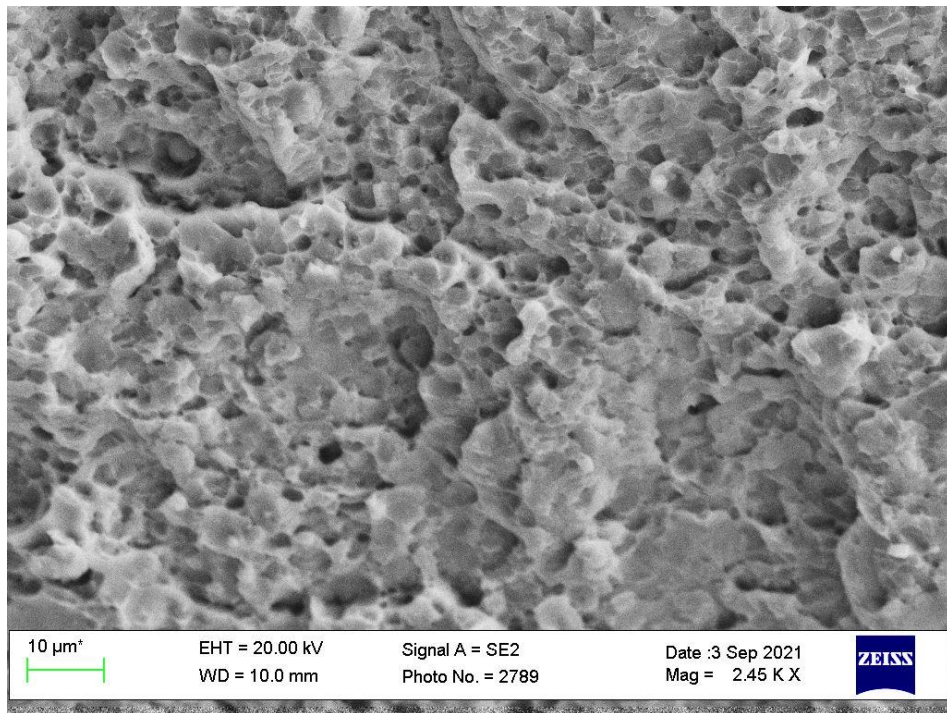
With reference to Figure 77, the one II tensile specimen which failed mid-weld did so along the approximate mid-line and did not coincide with any of the surface “grooves” described previously. The etched cross-section revealed a clean, relatively straight 45° fracture which was not coincident with a faint lazy S flaw present; the fracture occurred slightly towards the retreating side with reference to the lazy S position. Macroscopically the fracture surface was dull with a fairly smooth appearance. SEM analysis revealed non-uniformity across the fracture surface; a mix of microvoid coalescence indicative of ductile failure and transgranular failure. This tensile specimen achieved the lowest UTS and % elongation for any of this weld configuration, indicating that the fracture occurred in this location due to the non-uniformity in precipitate coarsening and coalescing within the nugget causing a stress raiser at that location. As this is the only specimen to fail mid-weld it is considered that the heat input at that position during welding may have fluctuated for reasons unknown, indicating that the process was not steady-state. As only one specimen failed mid-weld this is considered to be an outlier.



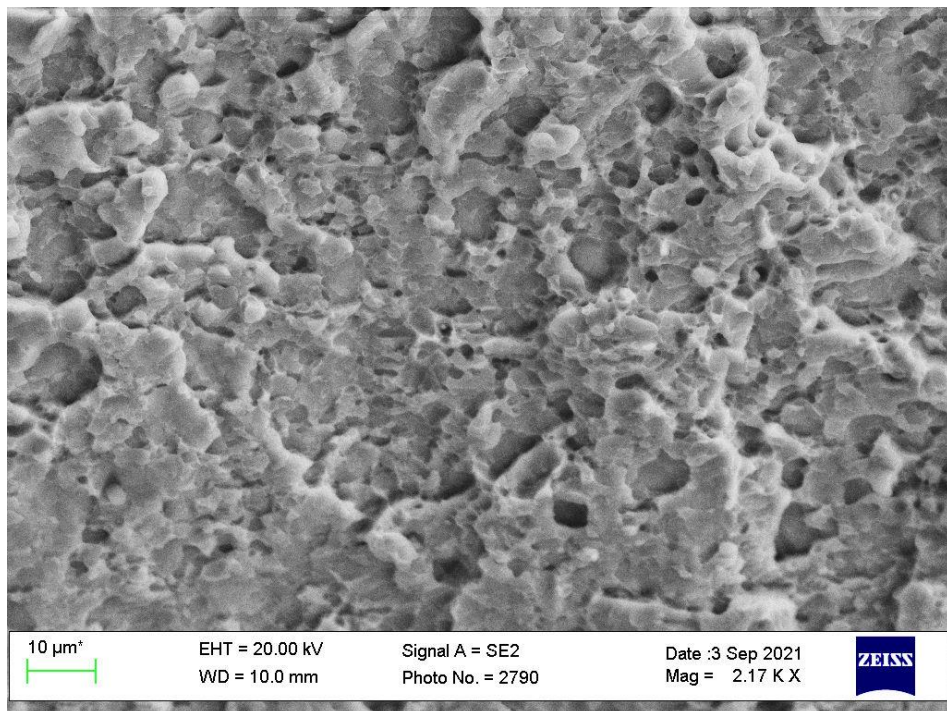
(a)



(b)



(c)



(d)

Figure 77: Showing mid-weld tensile fracture of AA8090 II weld; (a) micrograph showing fracture from top surface, (b) cross-section of weld showing crack path, and (c) and (d) SEM image showing details of fracture surface.

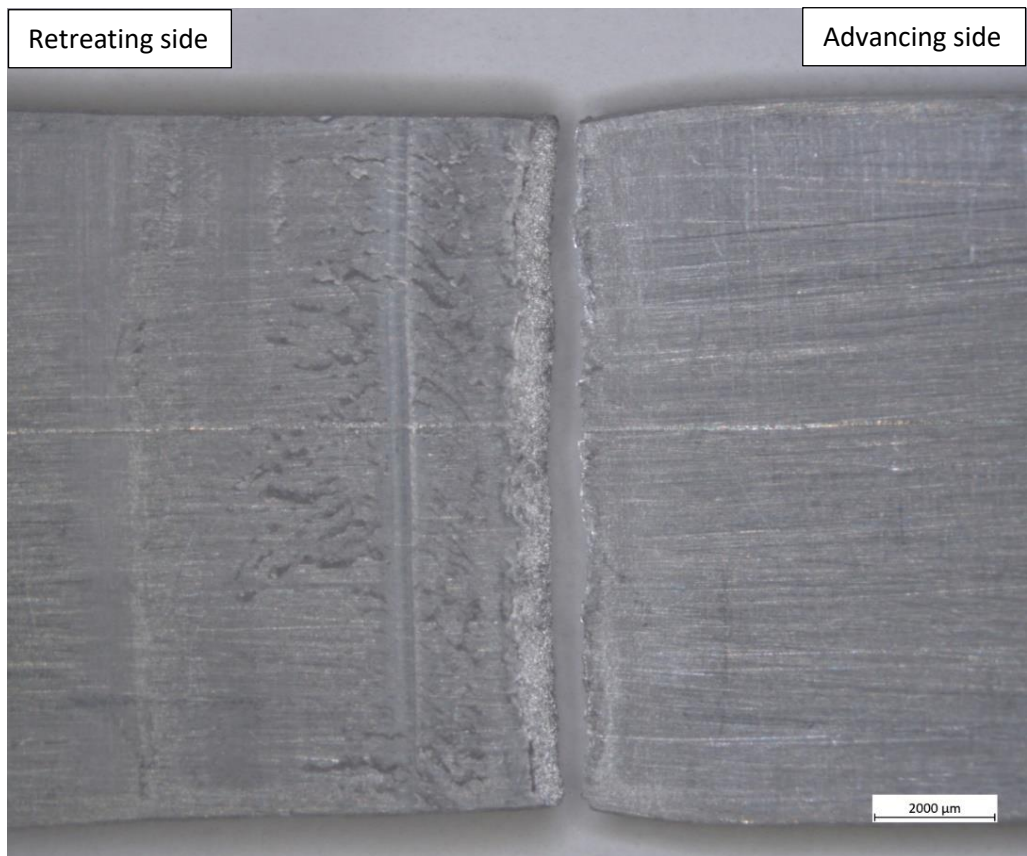
Of the 20 AA8090 \perp tensile tests (10 each from two welds), 11 failed mid-weld, 6 failed at the advancing side at the edge of the visible part of the weld surface and 3 failed at the retreating side of the weld. Examples of each failure type, showing position of fracture from the top surface, as a cross section and showing detailed SEM images of the fracture surface are shown in Figure 78 (advancing edge of weld) and Figure 79 (mid weld). All fracture surfaces were sloped at approximately 45° , although those which failed at mid-weld featured an approximate 45° slope which then transitioned into a separate slope close to the bottom surface of the weld. Those which ruptured at the advancing and retreating edges featured bright, shiny and granular fracture surfaces while the mid-weld fracture surfaces had a light coloured but dull (not shiny) appearance in the area close to the top of the weld, and had a dark, dull appearance with directional markings close to the bottom surface of the welds.

With reference to Figure 78, those failures occurring on the advancing side of the weld did so along the visible edge of the weld as viewed from the top surface. The fracture surface was bright, granular and sloped at approximately 45° . The etched cross-section showed that the fracture propagated through the HAZ, a clear distance from the TMAZ, but likely initiating within the overhang. A slight reduction in cross-sectional area was noted. SEM analysis revealed a mix of trans and intergranular failure, with slip planes on the grain boundaries and localised microvoid coalescence. The parent material which was tested by pulling parallel to the rolling direction (for comparison with those welded perpendicularly to the rolling direction) also showed a mix of trans and intergranular failure (Figure 33, section 4.1.3.2). In both cases (parent material and welds) there were significant areas with each failure type, rather than them being more evenly mixed together.

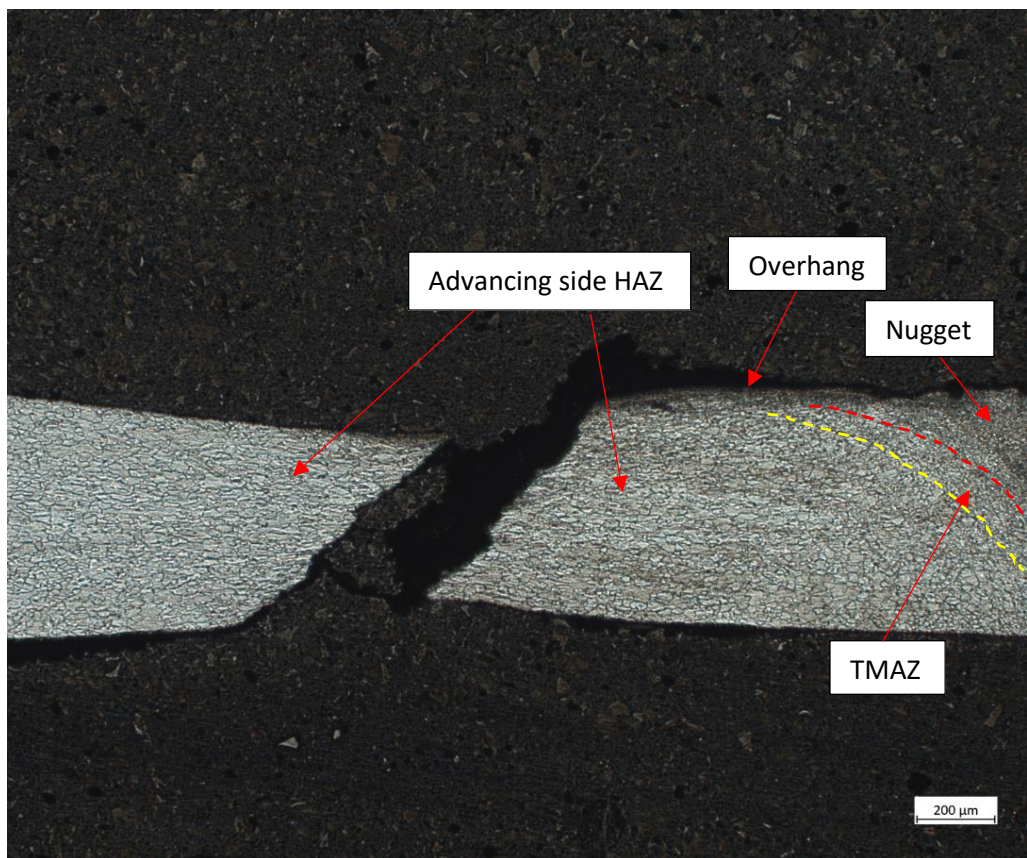
Similar to the II welds, the tensile specimens which failed at the retreating edge were consistent in terms of fracture surface appearance and morphology to those which failed at the advancing side.

With regards to the numerical values achieved during the tensile testing, there was significant spread in the results for the \perp welds. Those failing at the advancing and retreating sides all achieved varying results, however all results were lower than those which failed mid-weld.

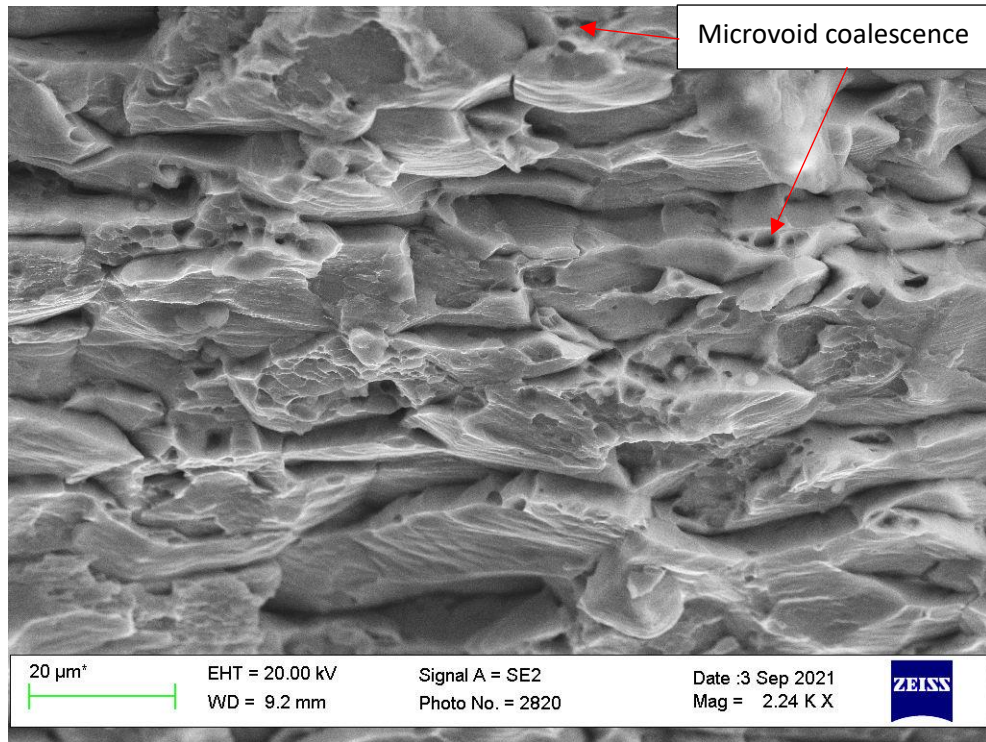
The hardness minimum for the \perp welds was within the HAZ on the retreating side; this does not marry with the tensile test results. This suggests that the weld parameters and set-up did not allow for consistent welding across all welds or maintain the quality throughout the weld run.



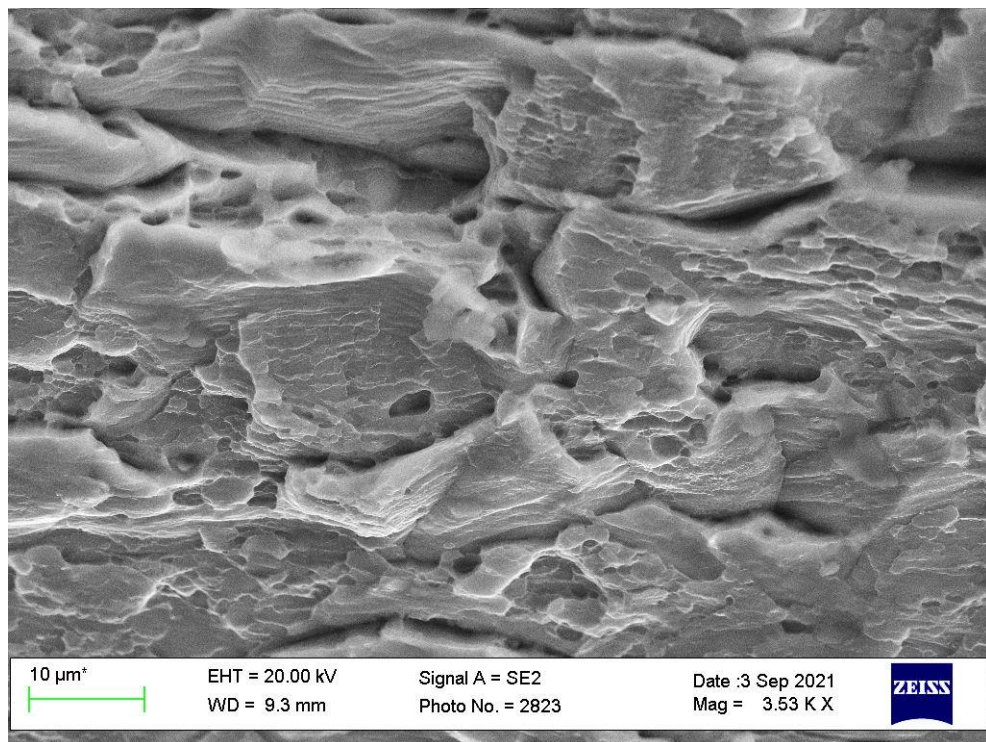
(a)



(b)



(c)

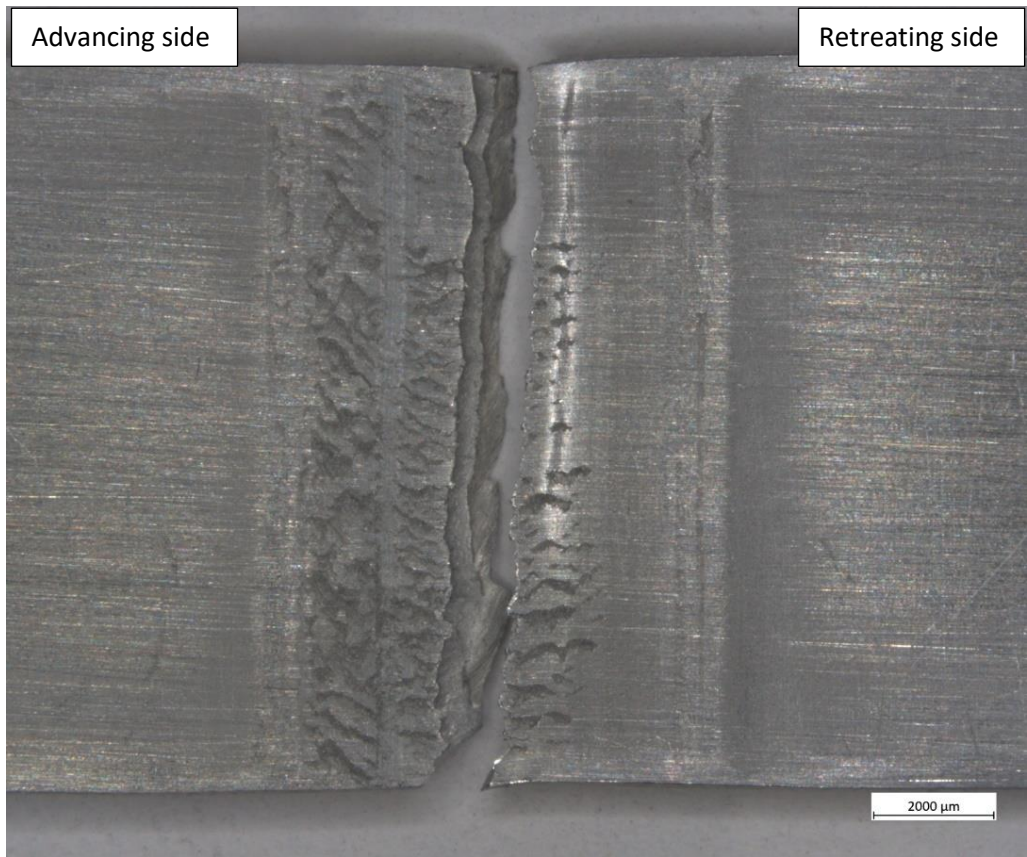


(d)

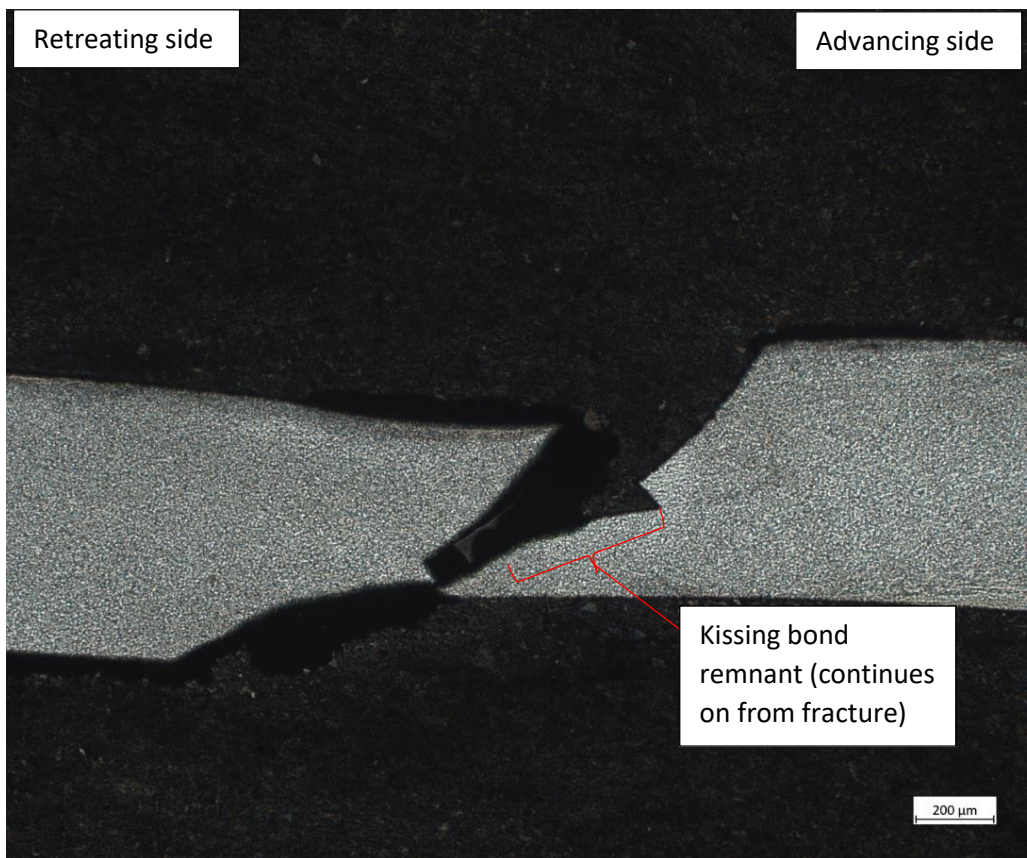
Figure 78: Showing advancing edge of weld tensile fracture on AA8090 \perp weld; (a) micrograph showing fracture from top surface, (b) cross-section of weld showing crack path, and (c) and (d) SEM image showing details of fracture surface.

With reference to Figure 79, those which failed mid-weld did so within the rough rippled surface when viewed from the top, but not within any of the grooves previously described. None of the welds which did not feature grooves were tensile tested. The fracture surface was in two halves, the first closest to the weld surface was bright but not shiny, while the second, closest to the weld bottom was dark, dull and featured directional markings. When the etched cross-section was examined, it was clear that the bottom half of the fracture had followed the kissing bond present within the weld which was more distinct at the bottom surface than elsewhere in the weld. It is suspected that when it changed from a kissing bond to a lazy S, that the fracture stopped following this path and was then influenced by the nugget microstructure as it propagated through-thickness. The directional markings on the bottom half of the fracture surface are considered to be “stir” marks indicating the material flow during welding. SEM analysis indicated a similar fracture surface to that of the II welds which failed mid-weld; a mix of microvoid coalescence and transgranular failure.

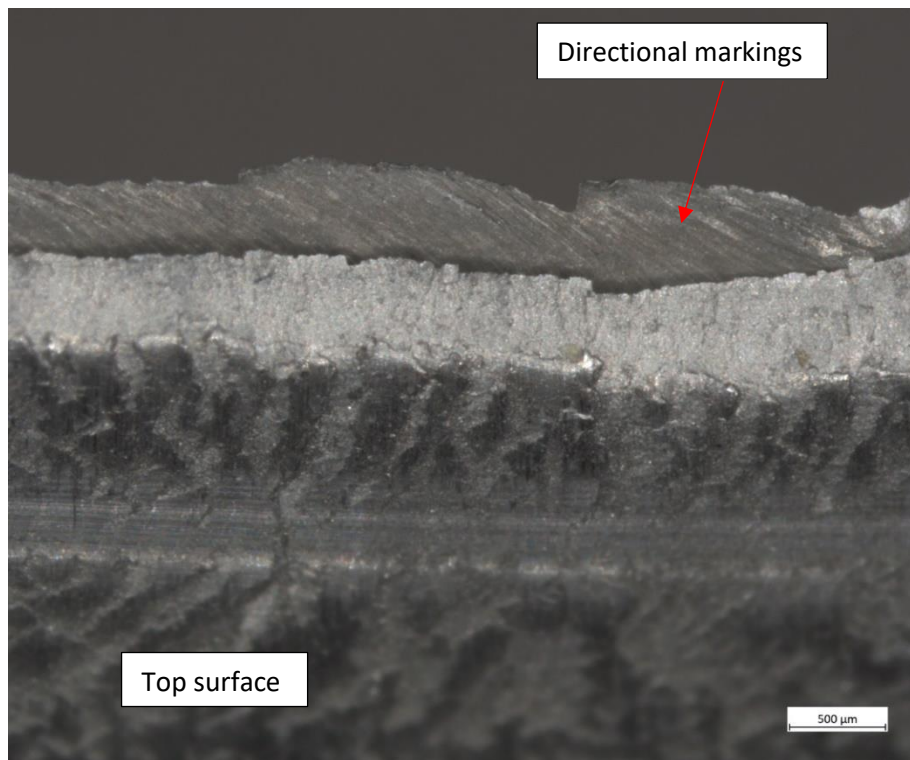
The mid-weld failures achieved the largest values of UTS of those tested, and while there was considerable scatter in these results overall, those which failed mid-weld all achieved similar UTS values, although it should be noted that most of these occurred in one weld run. This suggests that although the tensile strength was influenced by the kissing bond, a greater UTS may have been achieved had the kissing bond not been present. This scatter and difference in UTS results between the two weld runs indicates that the process parameters and weld set-up did not produce fully repeatable results.



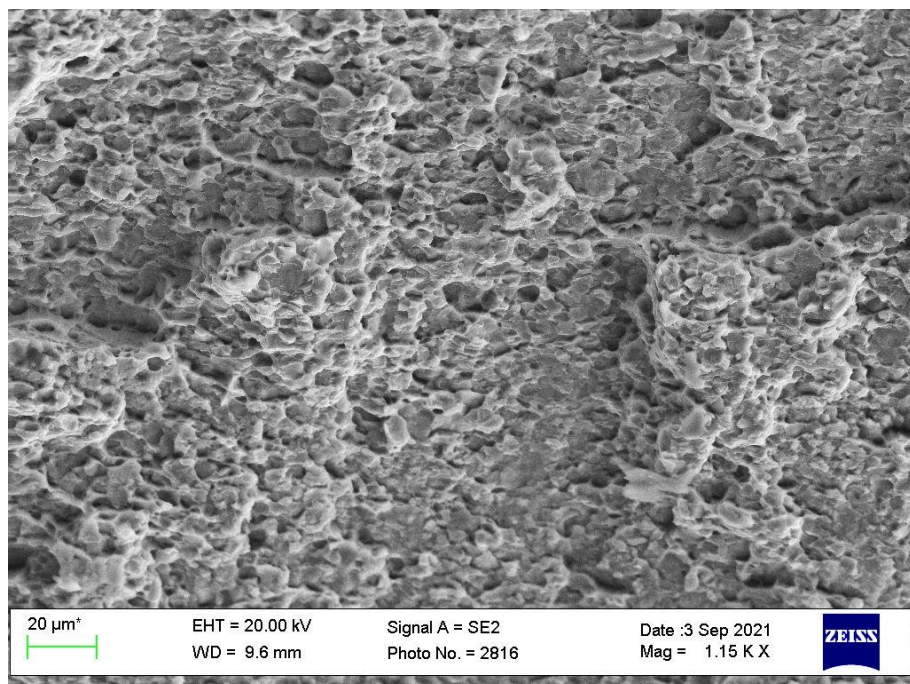
(a)



(b)



(c)



(d)

Figure 79: Showing mid-weld tensile fracture of AA8090 \perp weld; (a) micrograph showing fracture from top surface, (b) cross-section of weld showing crack path, (c) micrograph showing transition in fracture surfaces and (d) SEM image showing details of fracture surface.

6.2.2.3 Fatigue Testing

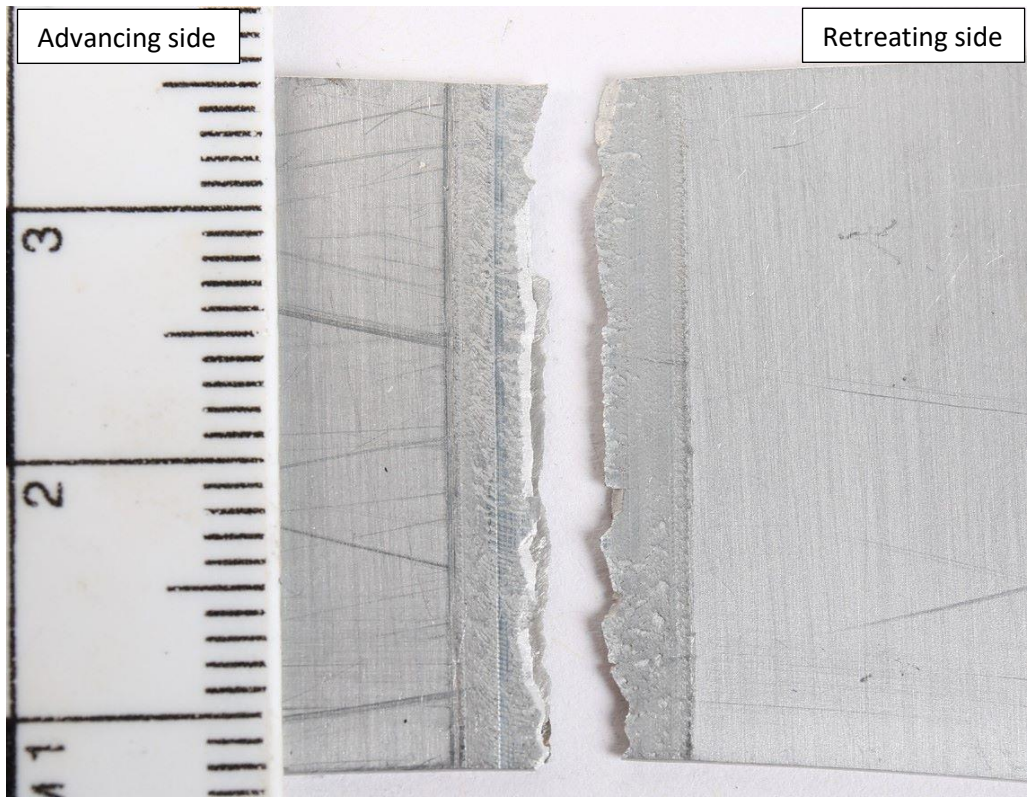
The AA8090 II weld (fatigue testing was only carried out in one weld orientation due to limited supply of material) achieved 84% mean fatigue strength efficiency when compared with the parent material, see Table 31, section 5.2.3.1. Little information is provided in the literature regarding fatigue results of AA8090 FSW, although Pedemonte et al. (2013) and Lertora and Gambaro (2010) did study it. Pedemonte et al. (2013) found that specimens tested with a maximum stress of 155 MPa achieved up to approximately 50,000 cycles, although different test parameters were used. Lertora and Gambaro (2010) results are presented as the stress range plotted against number of cycles; at 50,000 cycles the stress range achieved was 110 MPa, although the authors advised using a weld ratio of 4 (for comparison the weld ratio in this research for this configuration was 5).

Due to the staircase method being used in this research, the scatter in the fatigue strength calculated from the results is assessed from the standard deviation and coefficient of variation which, in this case, was calculated as 27.58 MPa and 0.102. These are considered to be relatively high values when compared with the standard deviation of the same parameter for the parent material of 17.66 MPa and coefficient of variation of 0.055. Although the staircase method is considered a valid one for statistical measurement with limited test specimens, this result indicates that additional testing with a larger sample size would be beneficial to add confidence in the fatigue strength of this welded material, especially for use on an aircraft.

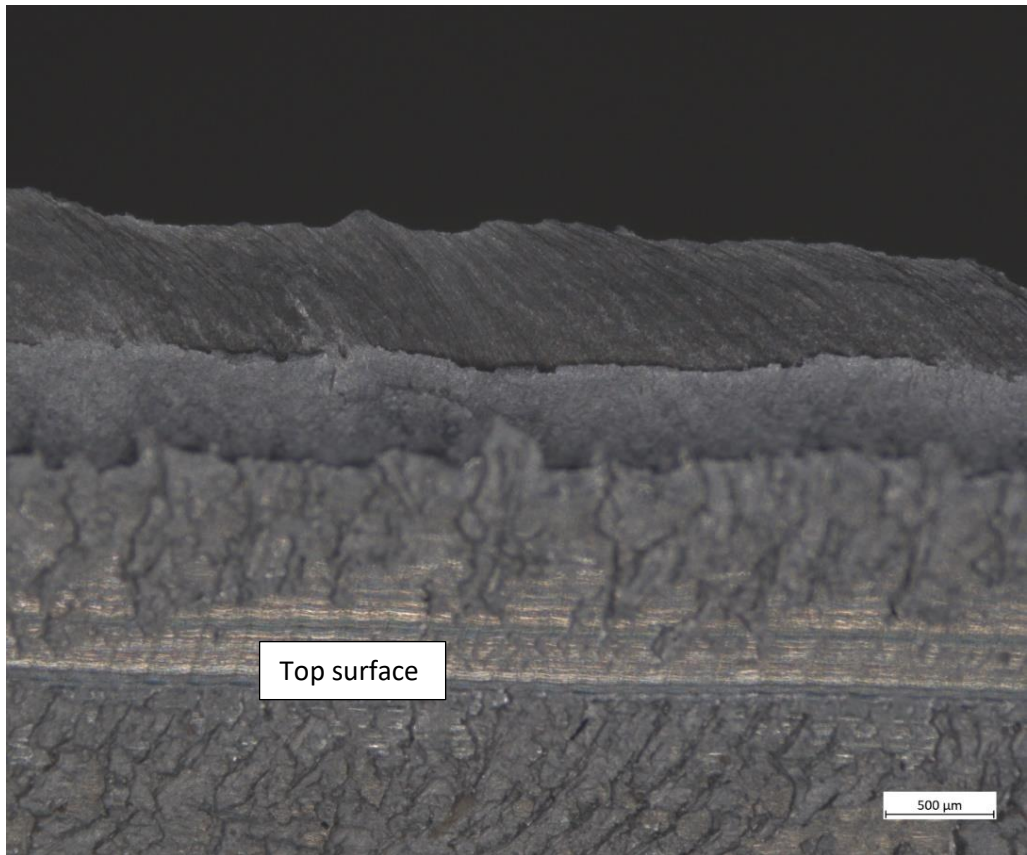
Of the 34 fatigue tests carried out for welded AA8090, 14 failed before 50,000 cycles. Of these, when viewed from the top surface, 8 failed mid-weld, 4 were within the weld but close to the advancing side visible edge of the weld and 2 were along the advancing side edge of weld. Examples of each failure with cross-sectional micrographs and SEM images of the fracture surfaces are shown in Figure 80, Figure 81 and Figure 82.

With reference to Figure 80, the mid-weld fatigue fractures failed along the approximate centre line of the weld, within the galled area but were not coincident with any surface groove. Stereo microscopy revealed that the fracture surface was in two halves, similar to that of the \perp mid-weld tensile fracture which failed partially along the kissing bond. The part of the fracture surface closest to the weld top surface was bright but not shiny, relatively smooth and sloped at approximate 45° . The other half, closest to the weld

bottom was dark, dull and presented with directional markings. When the cross-section was examined it was confirmed that the mid-weld fatigue fracture had followed the kissing bond close to the bottom surface of the weld before then failing at approximately 45° to the direction of cyclic pull when the kissing bond transitioned to a lazy S. Ruzek and Kadlec (2014) found that when specimens with a kissing bond measuring over a critical size for the material and thickness of material being welded were fatigue tested, that the presence of the kissing bond significantly decreased the number of cycles to failure, and thus has a significant impact on the weld quality. This indicates that the size/thickness of the kissing bond in these welds varied across each weld run and between each weld, and so the process is not repeatable or maintainable. Additionally, it was noted that the number of cycles to failure varied significantly for those which failed mid-weld, from 7043 to 49772 cycles (although only 3 of the 8 achieved over 25,000 cycles), again indicating that the weld quality was not maintained or repeated. Position control to ensure full penetration, more rigorous preparation when cleaning and removing the oxide layer prior to welding, and a different tool design may help alleviate this issue. The SEM analysis revealed transgranular failure through the fine recrystallised grains, with striations indicative of the cyclic progressive failure mechanism observed, as generally anticipated of fracture surfaces produced during a fatigue failure.



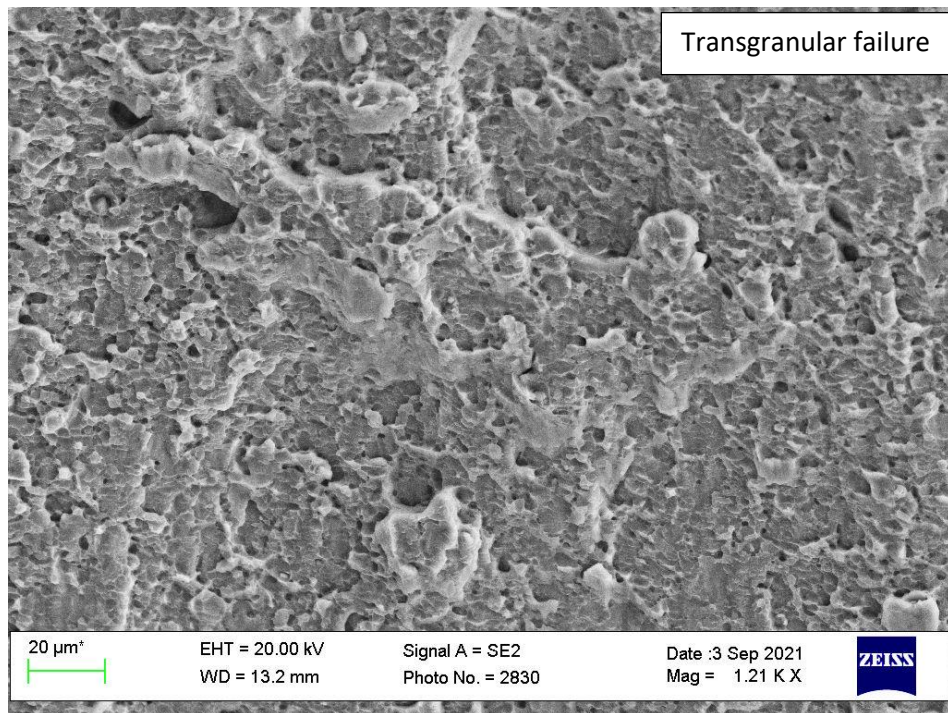
(a)



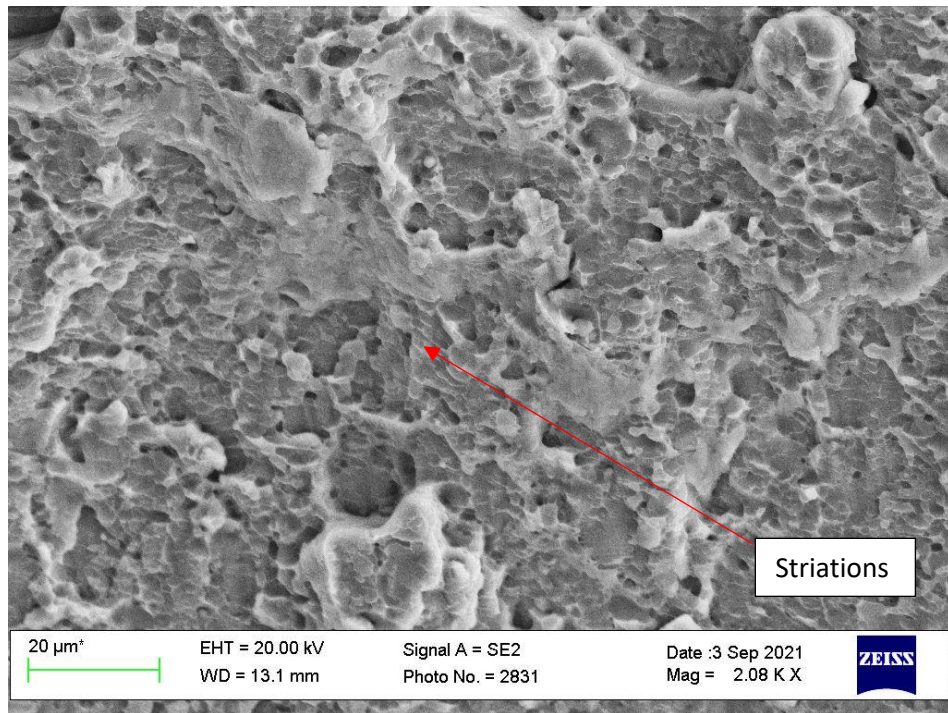
(b)



(c)



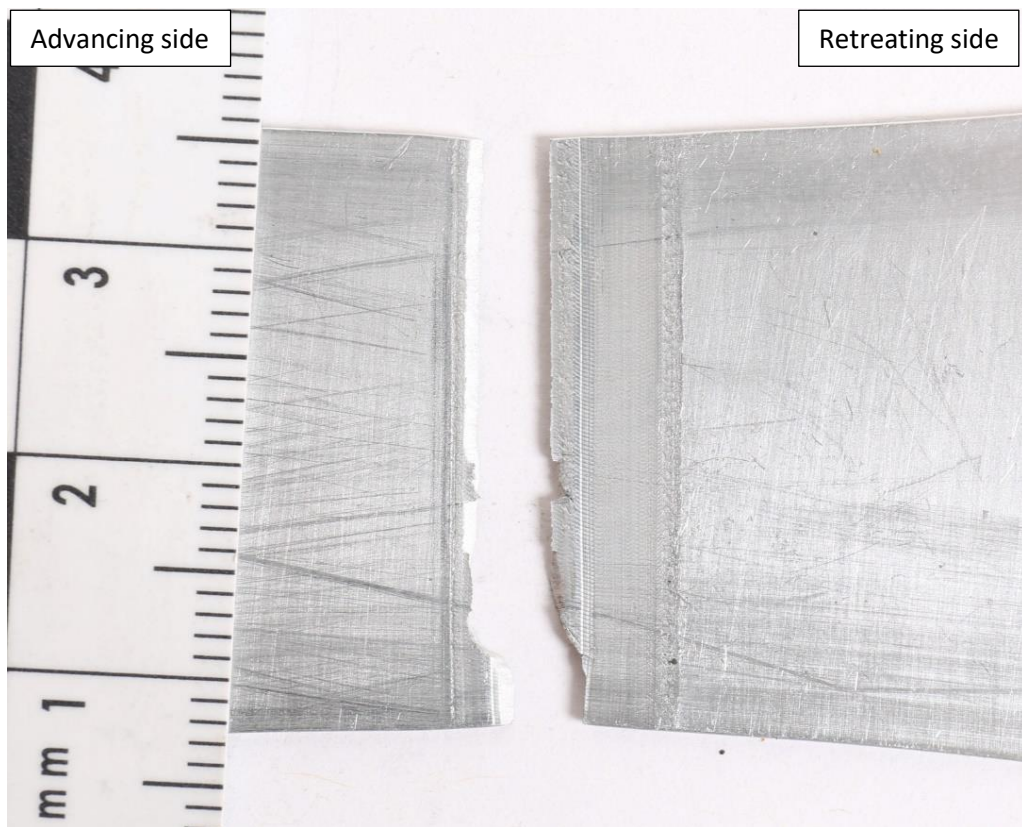
(d)



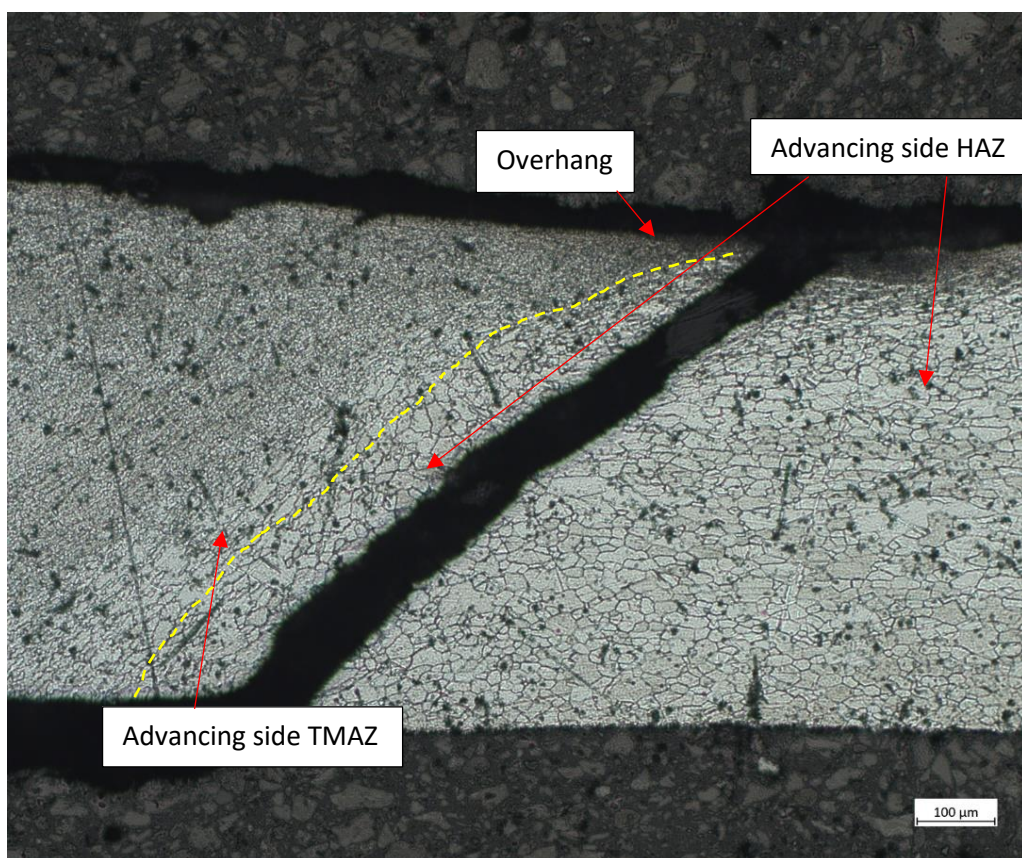
(e)

Figure 80: Showing mid-weld fatigue fracture of AA8090 weld; (a) micrograph showing fracture from top surface, (b) micrograph of fracture surface, (c) cross-section of weld showing crack path, (d) and (e) SEM images showing details of fracture surface.

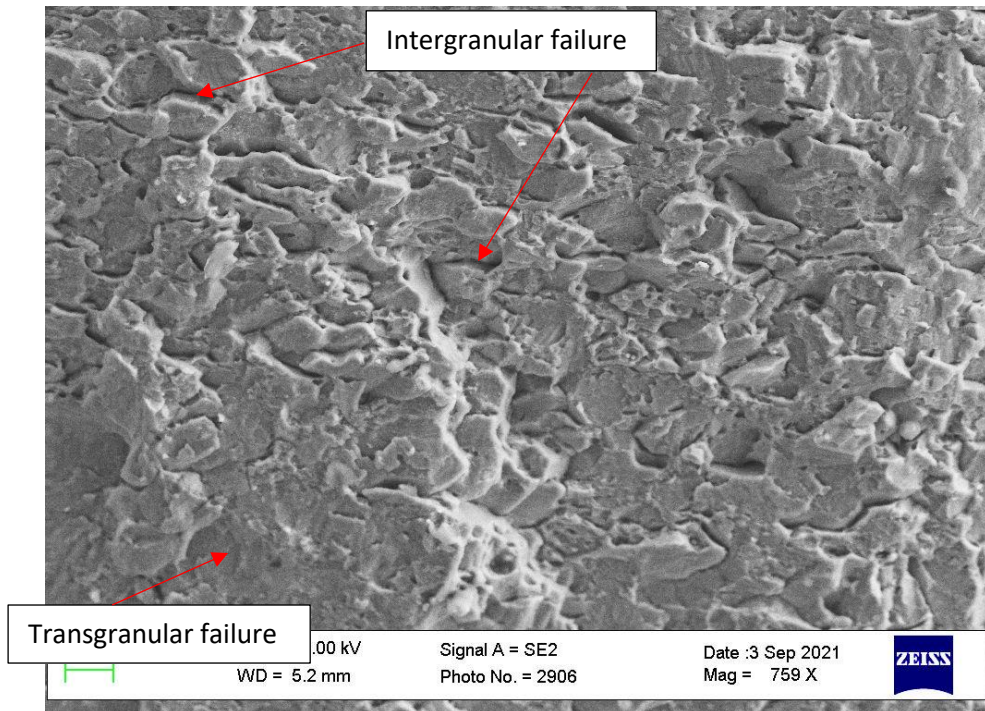
With reference to Figure 81, those fatigue fractures which occurred within the weld but close to the advancing edge failed for the most part within the recessed, rippled and galled area when viewed from the top surface. The fracture surface was bright, quite shiny and was sloped at 45° across the majority of the crack length. The cross-section revealed that the crack initiated in the overhang close to where the overhang merges with the main body of the weld nugget, propagated through the top part of the TMAZ and then through the HAZ (close to the TMAZ boundary) for the remainder of the through-thickness. SEM analysis revealed a fracture surface which was predominantly transgranular but had areas with mixed intergranular failure. Striations were observed throughout the fracture surface indicative of the cyclic progression of the failure. The areas of intergranular failure are at odds with the parent material fatigue failures which were entirely transgranular with more obvious striations. The change in fracture mode is likely due to precipitate coarsening at grain boundaries within the HAZ.



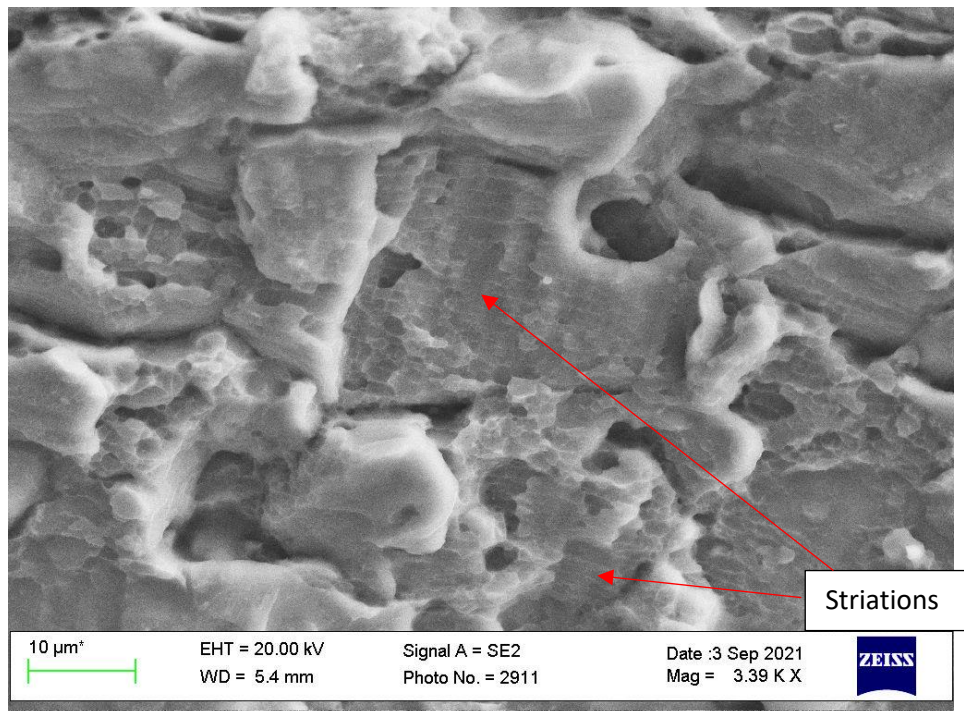
(a)



(b)



(c)



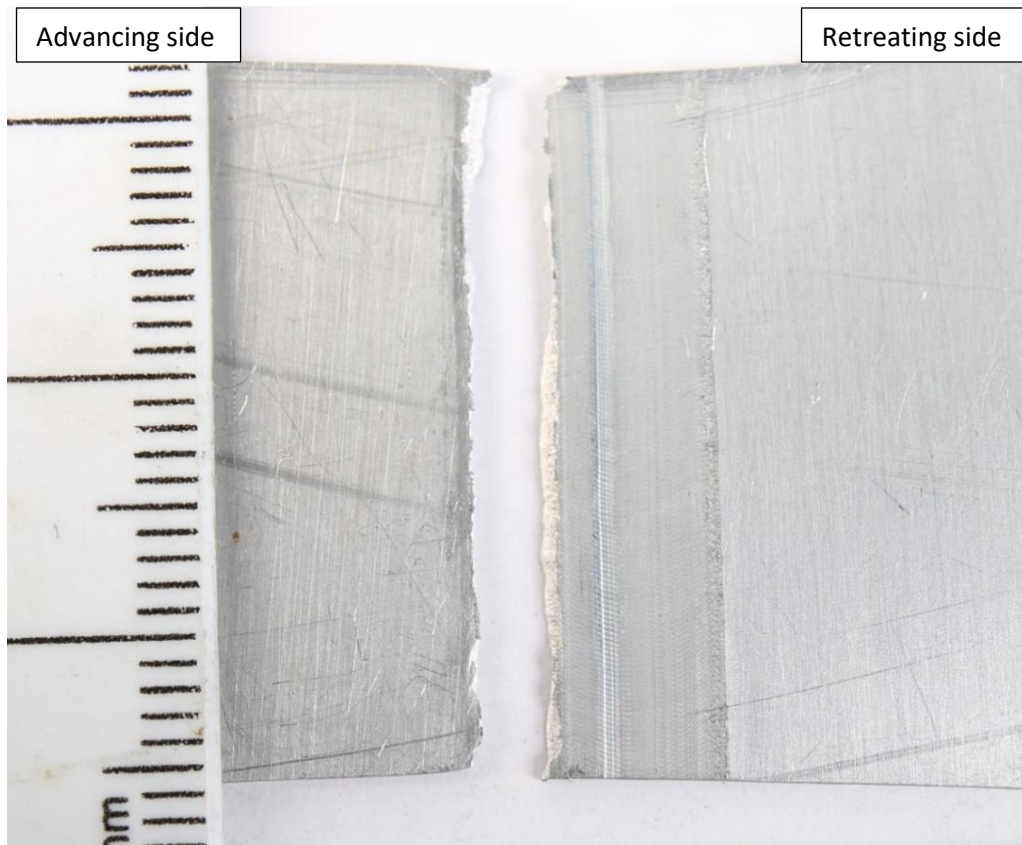
(d)

Figure 81: Showing AA8090 II fatigue fracture occurring within the weld close to the advancing edge; (a) micrograph showing fracture from top surface, (c) cross-section of weld showing crack path, (c) and (d) SEM images showing details of fracture surface.

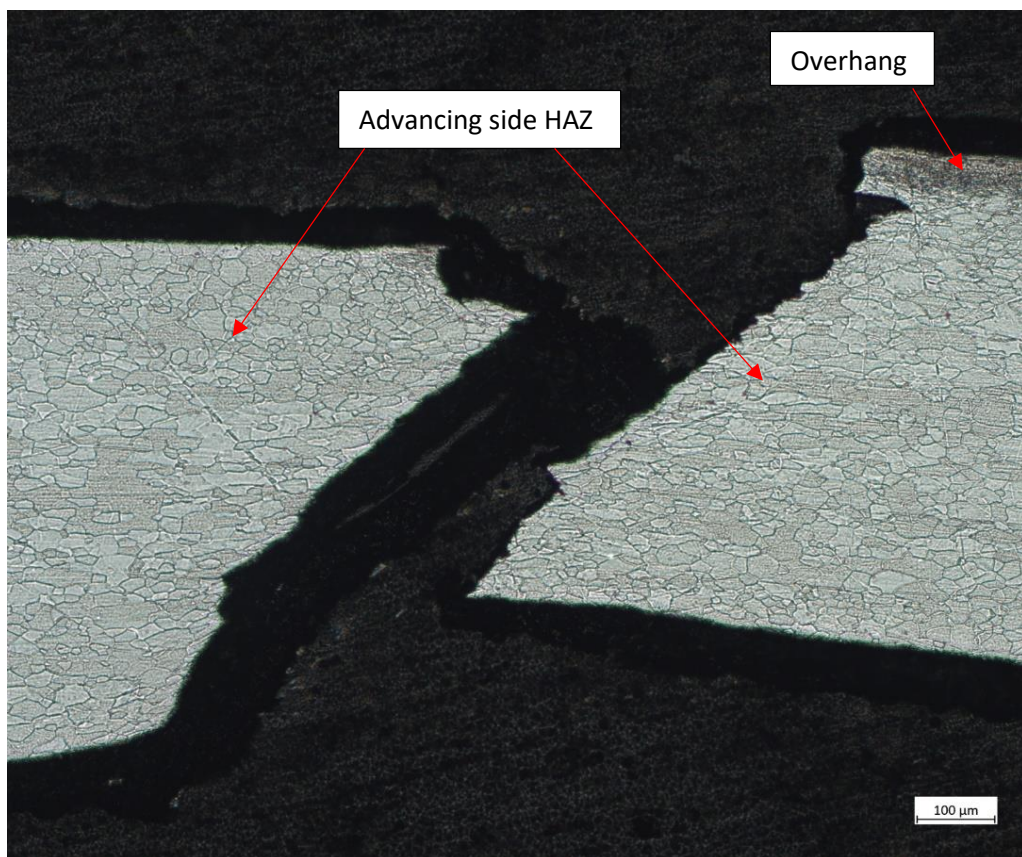
With reference to Figure 82, the two specimens which failed along the advancing side edge featured fracture surfaces orientated at 45° to the loading direction, which were bright, shiny and fairly granular in appearance. The cross-section revealed that the crack initiated at the edge of the overhang, then propagated along its underside briefly before propagating at 45° to the loading direction, indicating that the potential difference in mechanical properties between the overhang and the adjoining HAZ acted as a stress raiser in this instance. SEM analysis revealed a mix of intergranular and transgranular failure, with a higher incidence of intergranular failure than observed on those which failed within the weld. This is attributed to additional coarsening of precipitates at the grain boundaries. Clear striations were observed throughout the fracture surface.

The welds which failed at the advancing side and those within the weld close to the advancing side varied in the number of cycles to failure, but to a lesser extent than those which failed mid-weld at the kissing bond. Their range was 37,386-45632.

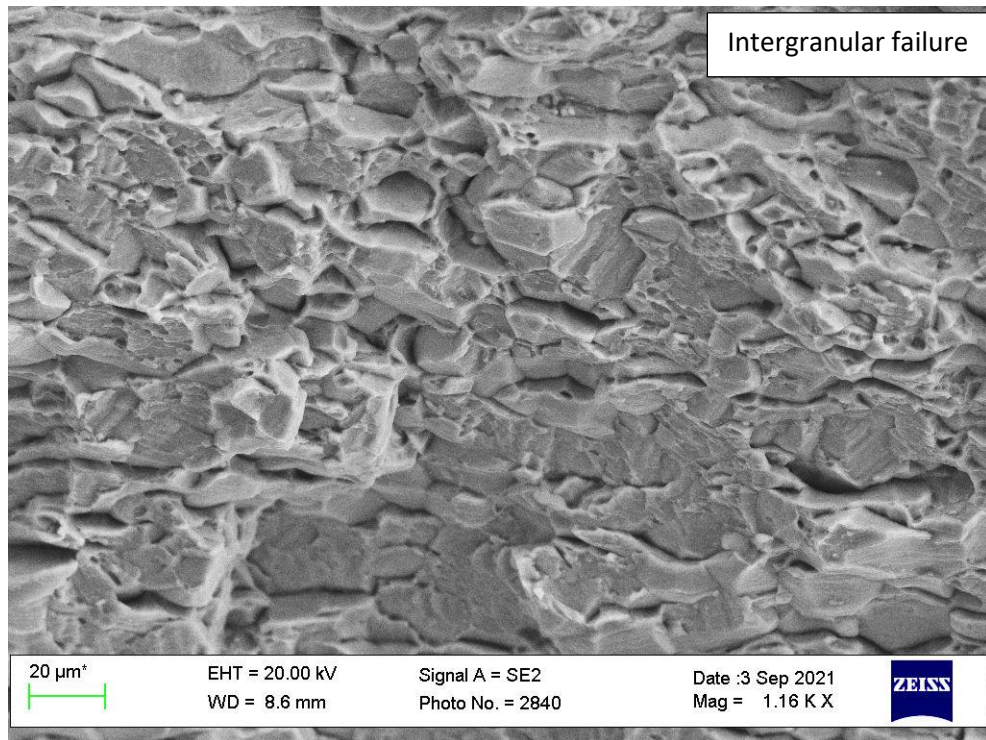
These results indicate a tendency for AA8090 welds to fail in fatigue at the hardness minima (advancing side HAZ) unless a flaw exists to change the weakest position, in this case the kissing bond. As previously noted, the kissing bond must be sufficiently defined for the fatigue crack to propagate from it.



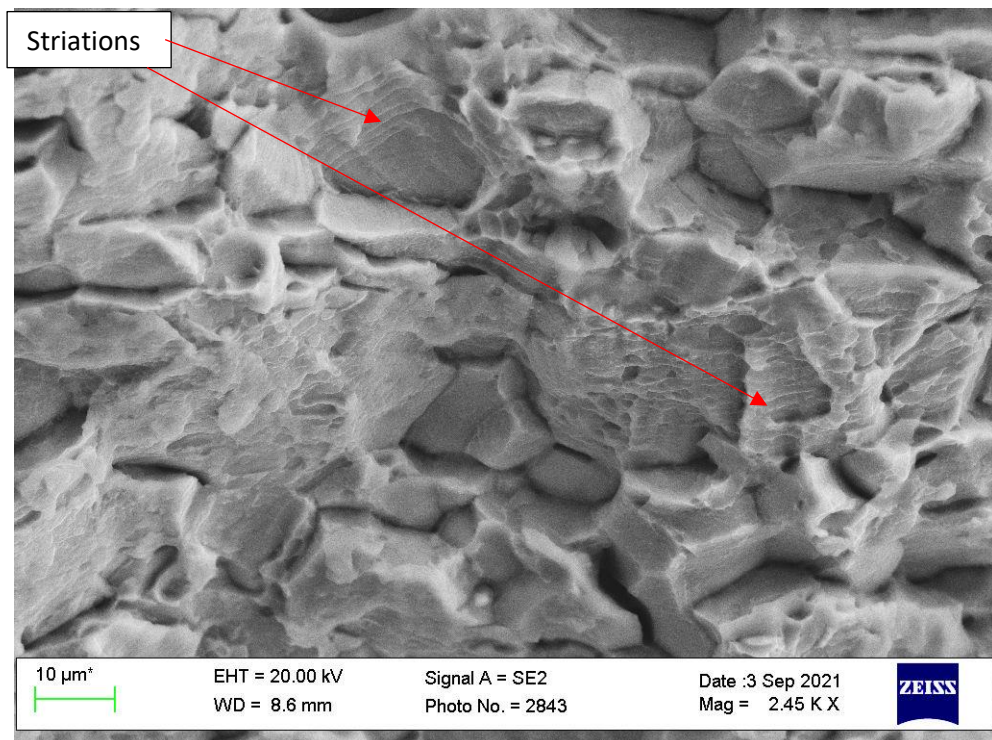
(a)



(b)



(c)



(d)

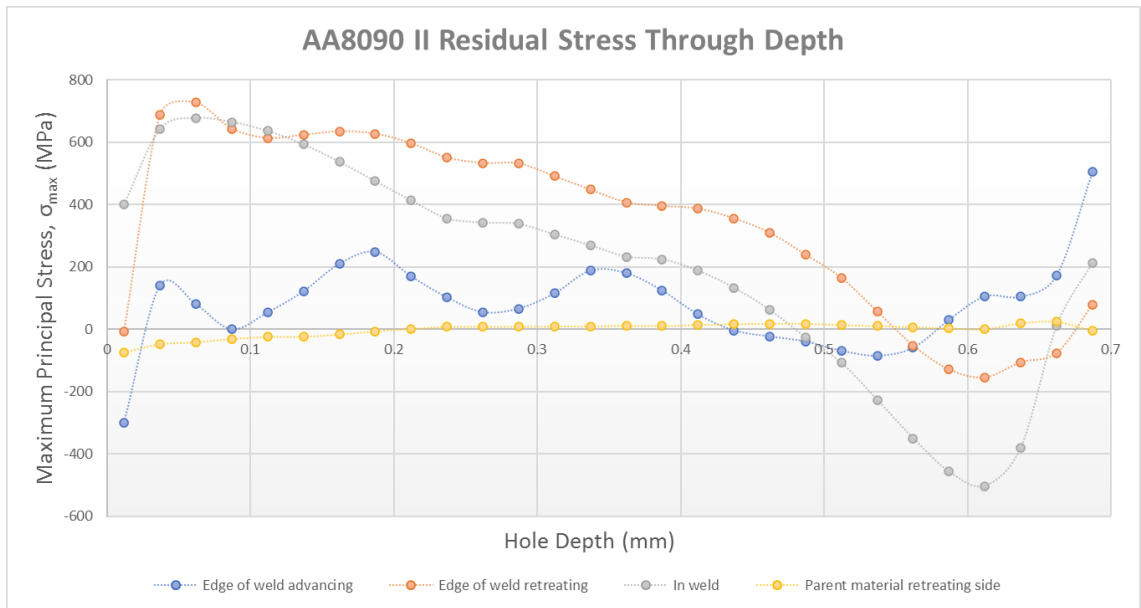
Figure 82: Showing AA8090 II fatigue fracture along the advancing edge; (a) micrograph showing fracture from top surface, (c) cross-section of weld showing crack path, (c) and (d) SEM images showing details of fracture surface.

6.2.2.4 Residual stress

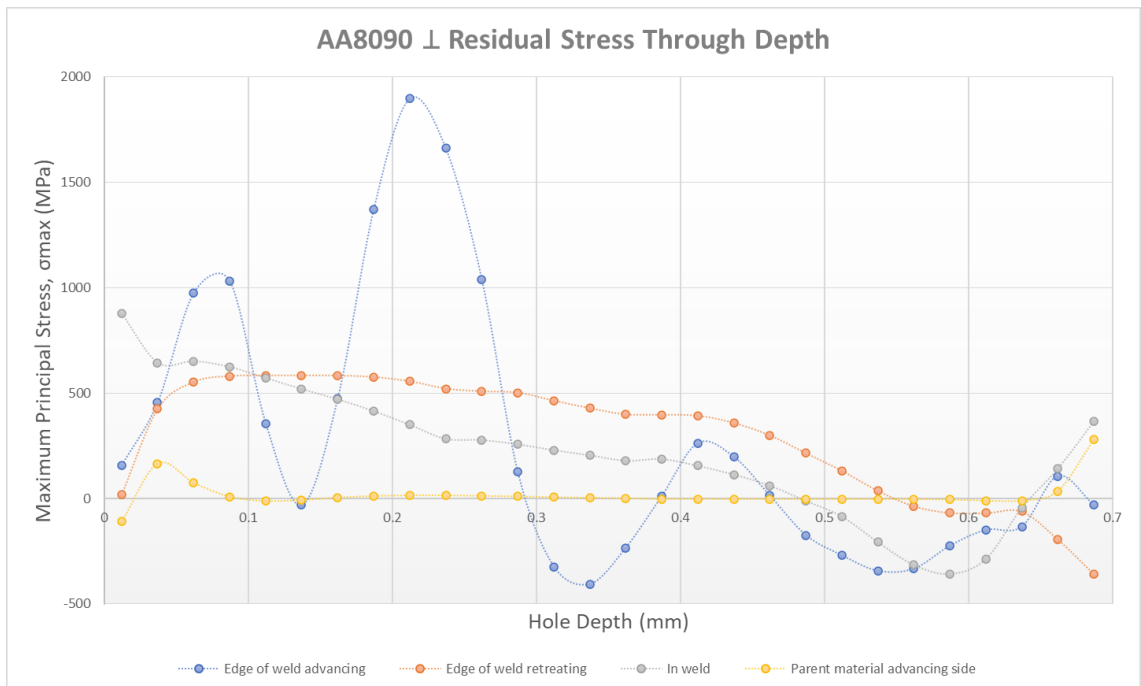
6.2.2.4.1 Residual Stress with Hole Depth

The residual stress (RS) results plotted against the drilled hole depth are shown for both configurations in Figure 83. These results show the calculated stress throughout the full drilled thickness, however as described in section 3.4.4.3 only those values occurring at depths between 0.06 mm and 0.4 mm will be considered in this analysis. The calculation of uncertainty in hole drilling residual stress has many variables and, as described previously (section 3.4.4.3), the numerical results cannot be treated as quantitative for analysis or reporting purposes if they exceed 80% of the material's yield strength. In this case, the RS numerical values far exceed that of the material's yield strength and indeed that of its UTS. Additionally, Kumar, Mishra and Baumann (2014) note that the FSW process alters the yield strength of the nugget, HAZ and TMAZ due to the thermal and mechanical processes occurring therein. Exceedance of the yield strength is not unheard of within the weld due to the large amount of plastic deformation which the material has undergone. As the material did distort both longitudinally and angularly, it is likely that the RS did exceed that of the yield strength. However, if these values were to be regarded as valid and the RS exceeded that of the material's UTS, then the material should have suffered relaxation cracking upon cooling. As such the actual calculated numerical values of RS for AA8090 welded configurations will be disregarded and the results treated as qualitative in an effort to analyse trends within the weld.

Data sets from AA8090 || parent material advancing side and AA8090 ⊥ parent material retreating side are missing as all attempts at testing these locations failed. Additionally, both Edge of Weld (EoW) advancing side data sets (particularly that from AA8090 ⊥) appear to be spurious results based on the degree of fluctuation throughout the hole depth and in comparison with the EoW retreating side; if additional time and resources had been available both the missing and spurious data sets would be repeated.



(a)



(b)

Figure 83: Showing residual stress results plotted against drilled hole depth; (a) AA8090 II, and (b) AA8090 ⊥.

As described previously, RS generation in FSW is partially generated due to the large forces involved, significant thermal gradients, and resultant rigid clamping required which prohibits material contraction during cooling and thus introduces RS (Casavola, 2018). Additionally, the undeformed and un-heated material surrounding the weld will

also impart constraints, regardless of the clamping (Mishra et al., 2014). The constraints on the welding zone which prohibit contraction result in the welded zone (nugget, TMAZ and HAZ) being in tension as it cannot contract. Considering only those results not deemed to be spurious, and only at depths 0.06-0.4 mm, it was observed that the parent material maintained almost constant near-zero RS throughout depth, as expected. For both configurations, the EoW retreating side and in-weld results showed that the RS was in tension and high close to the surface and gradually decreased with depth. This is expected to be due to the additional influence of surface friction in that area.

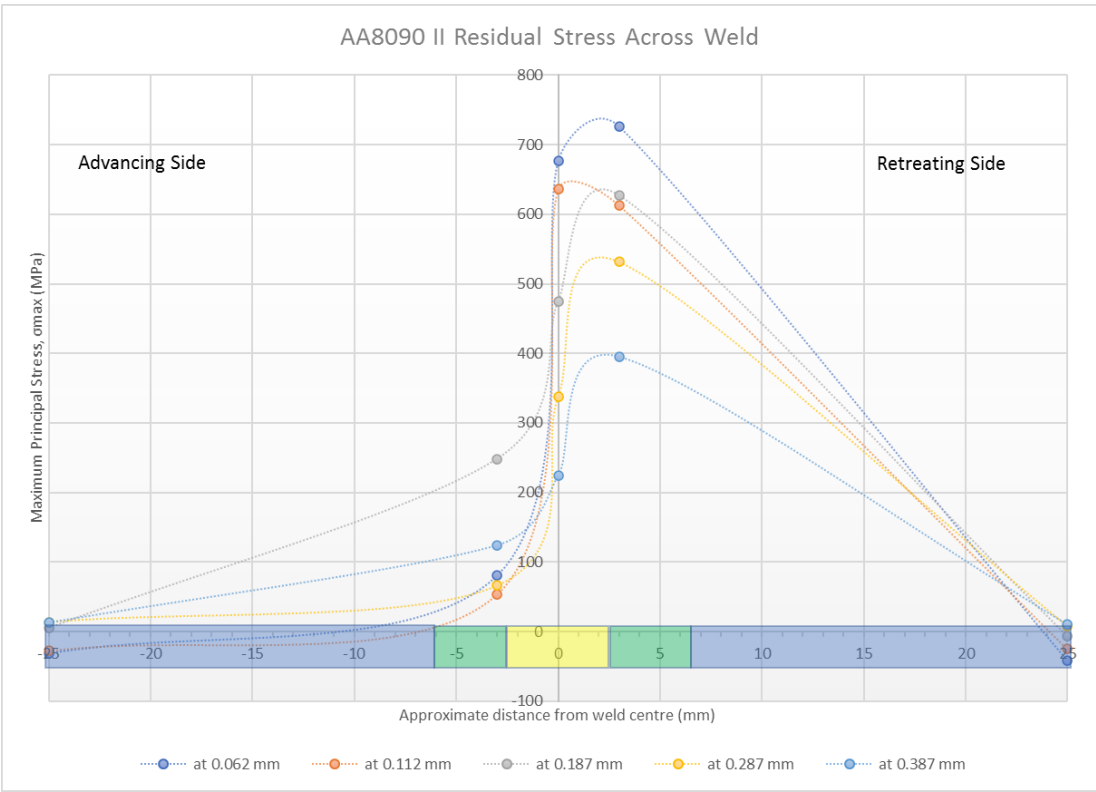
In both cases the residual stress is higher at the retreating edge of the weld than in weld. Delijaicov, de Oliverira Silva, Resende and Batalha (2018) attribute the reduction in RS within the nugget when compared to the TMAZ to significant mechanical work but reduced thermal input in the TMAZ and HAZ, and to the pressure from the tool shoulder. It is considered that the heat input leading to precipitate coarsening in the HAZ and resulting in reduced hardness in this area has increased the levels of RS there when compared to the nugget which has undergone recovery and recrystallisation thereby recovering some hardness and thus slightly alleviating the RS in that area.

Although the results are not being analysed quantitatively, there is a slight increase in RS on the II when compared with \perp . This is not excessive, especially considering the large margin for error inherent in hole drilling RS measurement. However, if the trend for RS in II welds to be larger is accurate, this is considered to be due to this grain orientation suffering greater constriction longitudinally from the surrounding cool material when thermal forces are applied, thus increasing the longitudinal tensile RS within the weld.

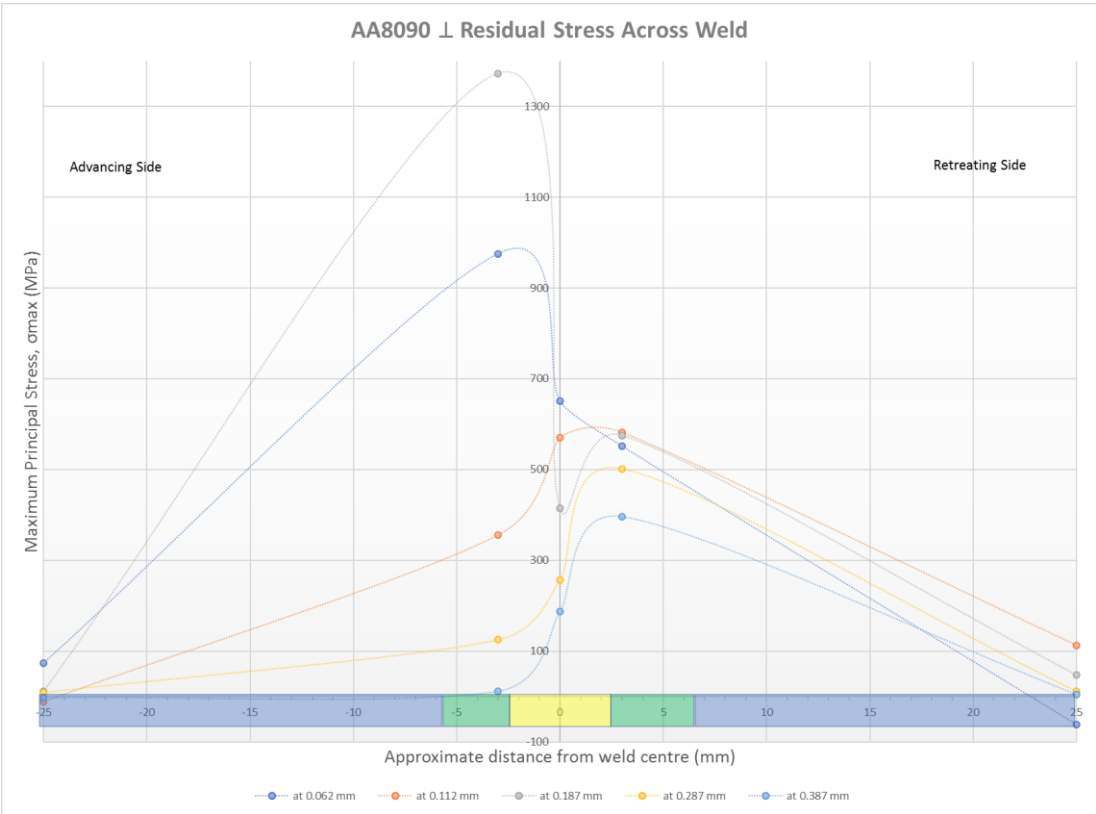
It is well documented within the literature (Hattel, Sonne, & Tutum, 2015; Mishra et al., 2014) that the existence of substantial RS in a weld can have a detrimental effect on the fatigue strength of the joint, however the quantification of this effect is difficult (Mishra et al., 2014). In this research, the fatigue specimens all failed either in-weld or EoW advancing side (noting the presence of kissing bonds for in-weld failures). It is clear that the weld (nugget, HAZ and TMAZ) is the weakest point of the material, or is the area of greatest stress concentration, as the specimens did not fail in the parent material. However it was not possible to quantify the contributing effects to fatigue strength of the presence of RS over that of the microstructural changes throughout the weld.

6.2.2.4.2 *Residual Stress Across Weld*

The residual stress across the weld, i.e., measurements taken at advancing and retreating parent materials, HAZ and within the weld nugget, is shown in Figure 84 at various hole depths. As the AA8090 II parent material advancing side and AA8090 \perp parent material retreating side measurements were unsuccessful, “stand-in” results were used from other configurations (the relevant orientation of dissimilar weld parent material) in order to complete these plots. Note, it was not possible to conduct separate measurements at the HAZ and TMAZ due to the thin nature of the TMAZ. The EoW tests were conducted adjacent to the visible part of the weld when viewed from the surface; based on the microstructural work this is mainly within the HAZ but may incorporate some overhang. The plots in Figure 84 show the approximate positions of the parent materials (blue bars), HAZ and TMAZ (green bars) and nugget (yellow bar).



(a)



(b)

Figure 84: Showing residual stress across weld at varying hole depths: (a) AA8090 II and (b) AA8090 L.

As previously described, most FSW RS cross-weld plots take the form of a “M” shape or an inverted “V” shape (section 2.3.9.3.4). From Figure 84 it is clear that this has not occurred in this case, however this is considered to be due to the spurious EoW advancing results; it was not possible to create a cross-weld plot without including the EoW advancing result. The II weld shows the start of an M shape, i.e. the EoW retreating measurement is larger than that of the nugget before reducing to the near zero at the parent material, with the exception of 0.112 mm where both measurements (EoW retreating side and nugget) are similar. This indicates that in the near-surface region, the difference in RS is not as obvious between the different weld zones. It is expected that if the EoW advancing result had been valid, a typical M shape would be observed. In the case of the \perp weld, the highly fluctuating EoW advancing result has radically changed the form of the cross-weld plot. It is again considered that had this result been valid, that the plot would take the typical M shape.

The literature overwhelmingly describes the cross-weld plots as being M or inverted V shaped, with tensile RS in-weld and at the shoulder edge of weld, before turning compressive outside of this area to balance the stresses in the structure, before returning to the unaffected parent material values (Mishra et al., 2014). No measurements in this research were compressive, however this is considered to be due to only 5 measurements being taken across the weld. It is expected that if additional measurements were taken, perhaps at 6 mm, 10 mm, 15 mm and 20 mm from the weld centreline, then the tensile to compressive shape would be observed.

6.2.3 Summary/ Conclusions for this Configuration

The following is a brief summary of the findings from the work on AA8090 weld configurations.

- Both configurations were distorted to a limited extent both longitudinally and angularly.
- The weld surface appearance was different for the two configurations and changed for different weld runs of the \perp weld.
- The weld microstructures were similar for both configurations with larger retreating side TMAZ and HAZ, however the retreating TMAZ for the \perp weld was considerably larger than the II weld.

- The II weld experienced greater heat input than the \perp weld. This was shown by:
 - The volume fraction of coarsened precipitates at the grain boundaries of the II weld was significantly greater than the \perp weld.
 - Kissing bonds observed in the \perp weld were more defined than those in the II weld.
 - Larger sized grains were observed in the II weld HAZ than in the \perp weld.
 - The \perp weld had overall greater hardness properties than the II weld.
 - Material on the retreating side of \perp was pushed upwards similarly to AA8090 II, however due to insufficient contact of the shoulder, this was not flattened and was instead deposited in a rough, uneven manner. This is contrary to the assertion that the II weld experienced greater heat input as it suggests over-plasticisation.
- The weld set-up and process parameters used do not allow for maintainable quality along the \perp weld, or repeatable results on different welds. This was indicated by:
 - Different surface appearances.
 - Large standard deviation in tensile test results.
 - Different extent of kissing bond quality.
- Kissing bonds can have a detrimental effect on the tensile and fatigue properties if the size and definition exceeds a critical point.
- Further work is required, however the RS results appear to align with the literature for both configurations. The II RS is slightly higher than that of the \perp weld.

6.3 BS L165-BS L165

6.3.1 As-Welded Examination

6.3.1.1 *Welded Sheets*

Both configurations of BS L165 welds showed distortion longitudinally for all welds, which manifested as either convex or sinusoidal curving, Figure 85(a) and (b) respectively. Transversely, the welds differed in the extent of angular distortion, with some welds (from both configurations) exhibiting very little and some with quite severe angular distortion. One of the more severe cases is shown in Figure 85(c). The

longitudinal distortion was not considered by the author to be detrimental to the weld quality, however severe angular distortion was reason for concern and those welds showing extensive distortion were not used in ensuing tensile or fatigue testing. Some indications of vertical lifting at the end of a weld run were observed, however this was not as extensive as observed with the AA8090 welds (as shown on Figure 65(c) of section 6.2.1.1). This may indicate more successful clamping for BS L165 as these welds were performed subsequent to AA8090.



(a)



(b)



(c)

Figure 85: Showing longitudinal distortion on two BS L165 II welds: (a) convex and (b) sinusoidal curving, and (c) angular distortion on a \perp weld.

Limited trials were held to find appropriate process parameters. It was more difficult to find parameters which would produce a satisfactory weld for BS L165 than for AA8090, as welds which were too “hot” resulted in severe warping and distortion along the mid-point of the weld, Figure 86. The main reason for this was considered to be the increased thermal conductivity and coefficient of thermal expansion of BS L165 over AA8090 (154.3 W/mK, $24.4 \times 10^{-6}/K$ and 95.3 W/mK, $21.4 \times 10^{-6}/K$ respectively (MatWeb Metal Material Data Sheets, (MDS), 2021), owing to the increased copper content of BS L165 over AA8090 and the alclad layer. As the tool traversed, the heat input to the preceding material built up ahead of the tool to such an extent that warping ensued. As the weld material was constrained to its maximum at this point because of the mechanical clamps and the surrounding material, when it expanded it had no progression route. As the tool progressed beyond the mid-point, the constraint from the surrounding material lessened, and the material was able to expand more comfortably. It was for this reason that a “cooler” weld was required for BS L165 and therefore a slower rotational speed of 2700 RPM (compared with 3000 RPM for AA8090) was chosen.

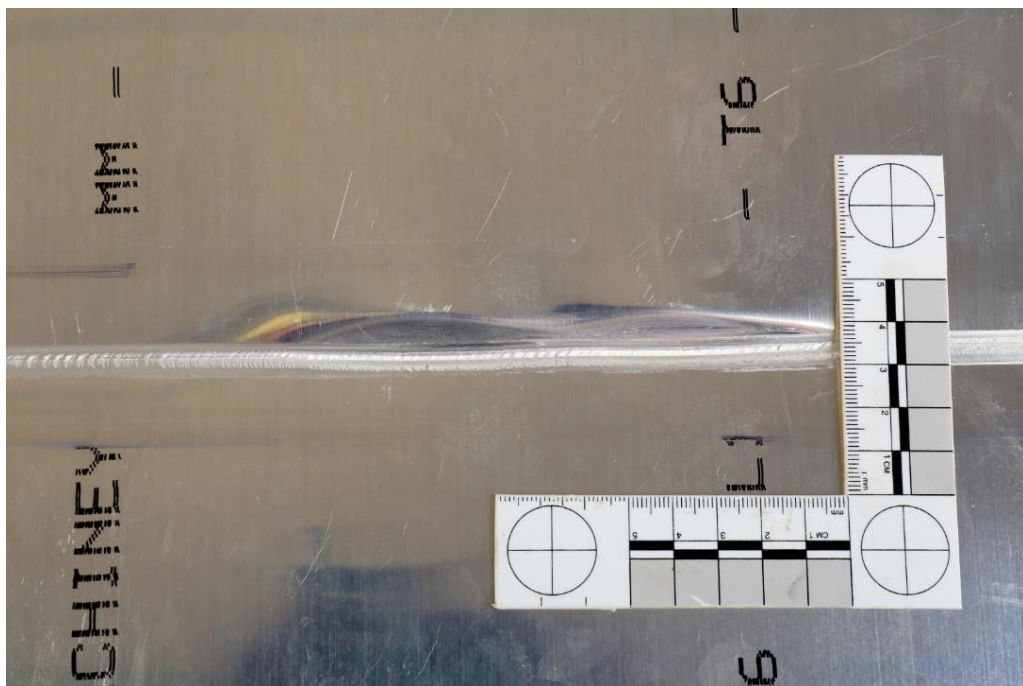


Figure 86: Showing warping and distortion to mid-point of BS L165 weld during parameter trials.

6.3.1.2 *Weld Surface*

An area of the II weld top surface representative of most of the steady state welding conditions of BS L165 is shown in Figure 87 with a scaled profile of the tool superimposed. This image indicates that the main weld width was not consistent with that of the diameter of the tool shoulder, as previously observed on AA8090 \perp welds. Instead, the main weld width was narrower than the pin maximum diameter. This was indicative that material had again been extruded from the sides, similarly to AA8090 welds, although in this case the extruded material had been flattened. Additional material was deposited on either side of the weld surface; the extent of this material deposition varied along the length of the weld as indicated by the images shown in Figure 88. It is considered that, in this case, while still not consistently achieving or maintaining full contact of the shoulder diameter to the material surface, more of the diameter than solely the trailing tilted shoulder heel was sporadically in contact as the tool traversed.

The weld had ripples across the surface, spaced at approximately 210 μm , which was broadly consistent with the weld pitch (0.222 mm/rev), however these ripples were overlaid with lines consistent with the stationary shoulder having “ironed” the weld as it progressed.

The stationary shoulder produces an ironing effect where it smooths the surface as it traverses, which eradicates the ripples on the surface caused by the trailing edge of the shoulder (this is as described in literature, these ripples are considered to be caused by the pin in this research) and produces a smooth surface appearance (Ji et al., 2017; Patel et al., 2019; Sinhmar & Dwivedi, 2020b). Only one study can be found which shows a stationary shoulder weld which has been ironed but faint ripples remain (You et al., 2020); this is only shown in an image and is not referred to in the text, however it appears that the ripples become fainter with increasing rotational speed. No explanation is provided by You et al. (2020) as to how the shoulder can both create a ripple at its trailing edge and smooth the surface. In this case it is considered that the ripples were caused by the shear layers detaching from the pin (and not from the shoulder) and being deposited, and the stationary shoulder tilted heel partially smoothed over these ripples.

Galled material which had stuck and detached from the trailing edge of the shoulder, or which had been ejected by the pin was also deposited on the weld surface. Grooves/furrows were observed on some II welds (not pictured, but can be seen in Figure 66(a), section 6.2.1.2 on AA8090 II welds), however these were intermittent and inconsistent, indicative of inconsistent and fluctuating heat input along the weld, as described previously (section 6.2.1.2).

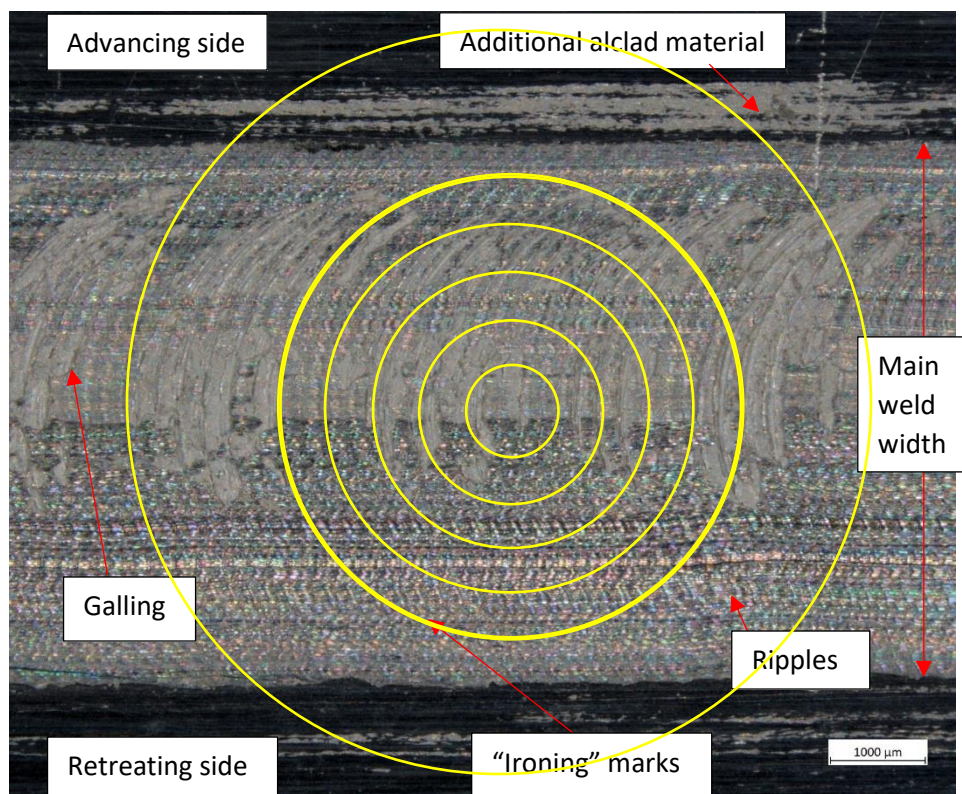


Figure 87: Showing L165 II weld surface with superimposed tool profile

The additional material deposited on either side of the weld, which varies in extent along the length of the weld, is considered to be part of the alclad layer. Zhang et al. (2011) found that during conventional FSW part of the alclad layer accumulated underneath the shoulder to a thickness far exceeding that of the original layer. It is conceivable that during welding a thick layer of alclad built up underneath the shoulder (sporadically in contact with the material) and was then extruded to the sides when it reached a critical mass. This, along with the shoulder being inconsistent in its contact, would explain the differing levels of deposit along the weld. After the alclad reached a critical mass, it was extruded and then required more time and distance along the weld to build up again. SEM-EDX was used to analyse the deposits; they were consistent with AA1050 (see section 2.2.5.1) and therefore confirmed as alclad deposits. Generally, a reduction in

flash (in the case of BS L165 likely to comprise of a mix of parent material and alclad layer) is observed during SSFSW when compared with conventional FSW as the stationary shoulder restrains the plasticised material (Li, Z. et al., 2016). It may be that as the shoulder was not in full contact with the parent material (as shown by the reduced width of the weld), that the forging pressure was insufficient to restrain this material.

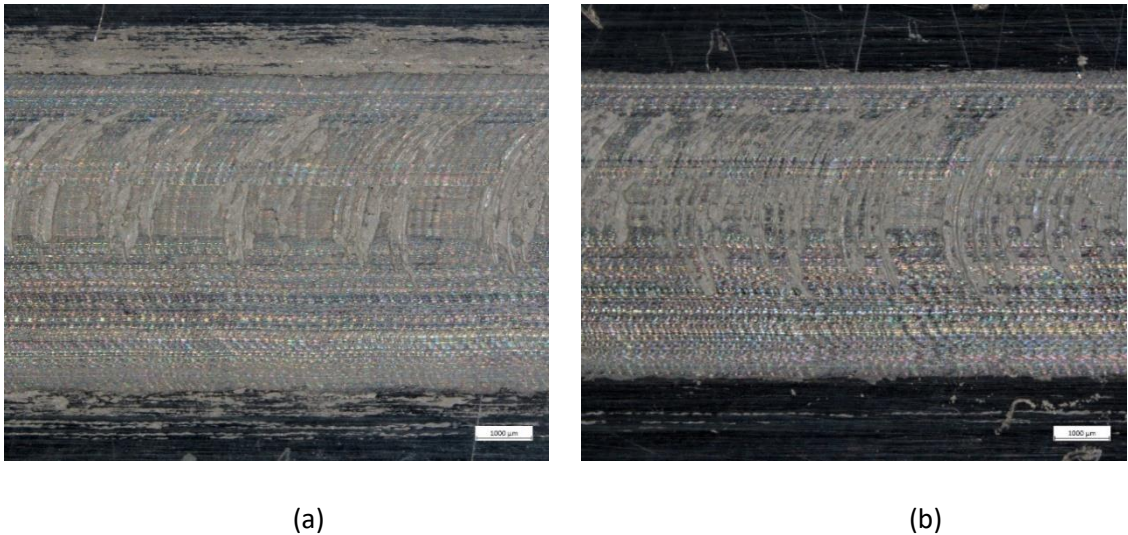
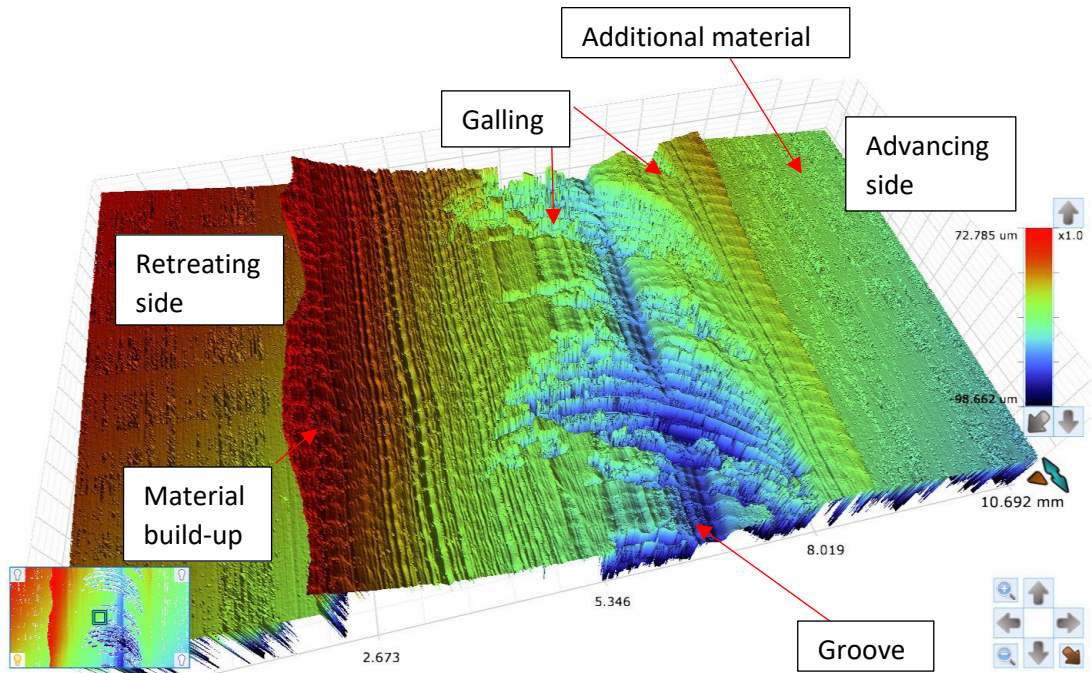
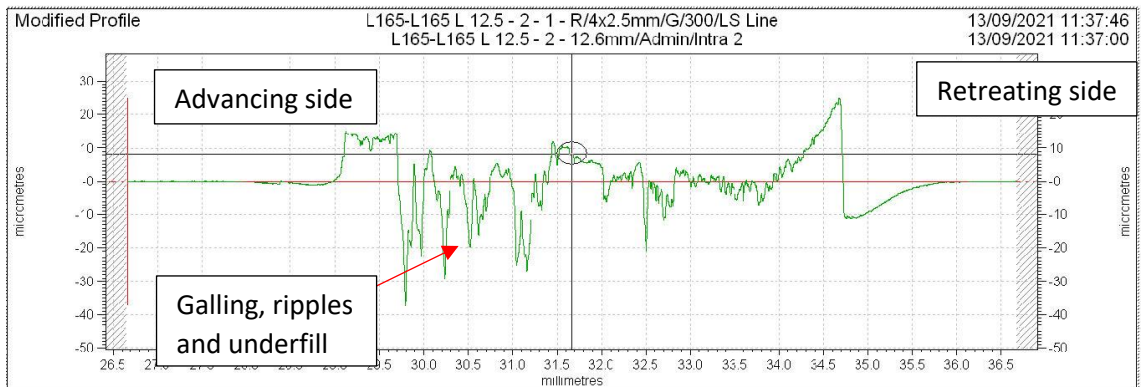


Figure 88: Images for comparison of differing quantities of additional material at side of weld along length of BS L165 II weld. Note, these images are taken from the same weld.

The topography of the weld is shown in Figure 89. The optical profilometry image indicates a groove through the galled material, with the contact profilometry plot indicating potential underfill. The “groove” can be faintly seen in Figure 87 and Figure 88 and is not considered to be similar to those observed on AA8090; instead that and the “underfill” are considered to be a disturbance caused by the galling.



(a)



(b)

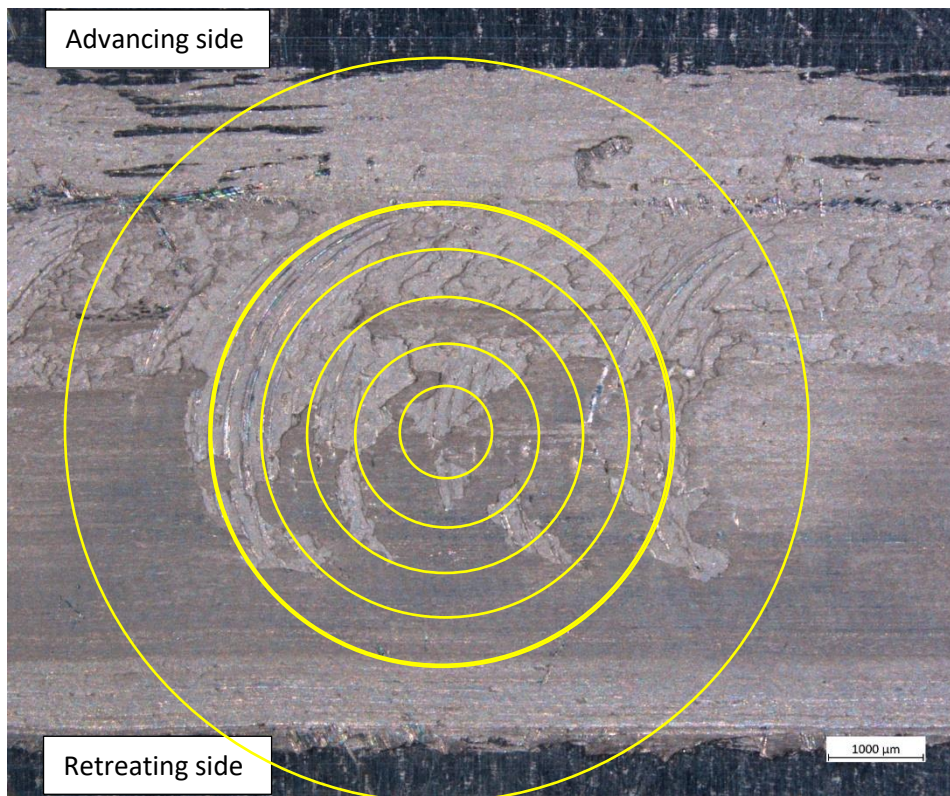
Figure 89: Showing BS L165 II weld surface topography, (a) optical profilometer 3D model image, and (b) contact profilometry surface plot.

The BS L165 \perp weld surface appearance changed dramatically both between welds and along the weld length, therefore two images are shown for comparison in Figure 90, with tool profiles superimposed. Similarities between the two were: the variation of deposited material at the sides; sporadic galling; and the width of the weld being less than the diameter of the shoulder, similar to the II welds. The main difference was that while Figure 90(b) reasonably resembled the II weld previously seen in terms of ripples being visible but ironed over to an extent (apart from close to the retreating side), no

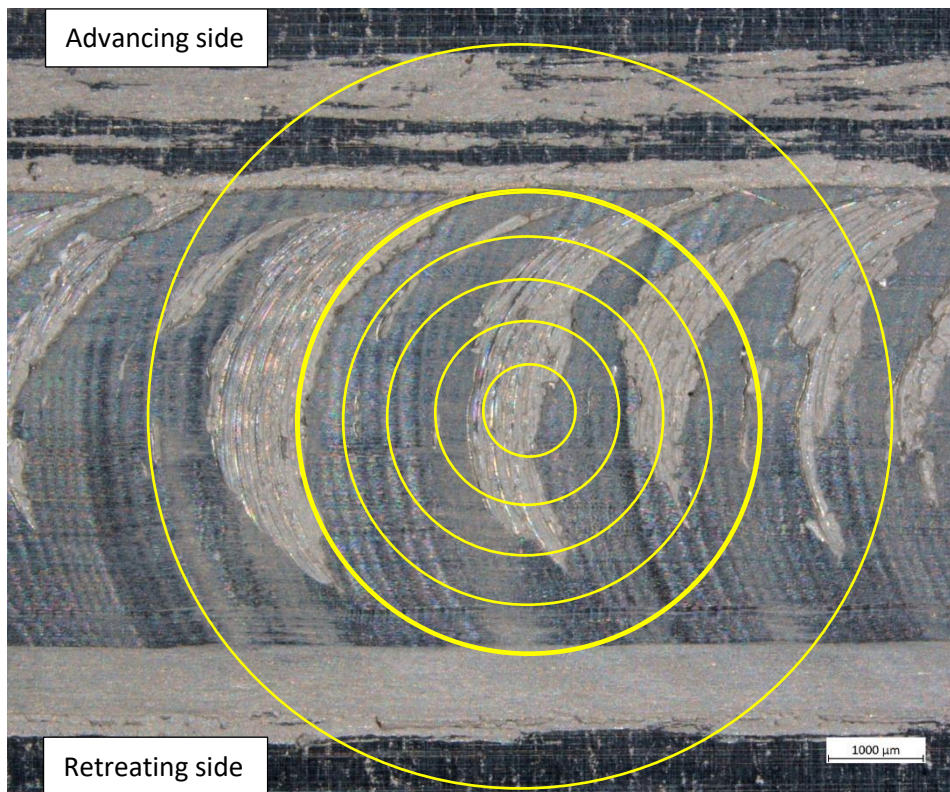
ripples other than those caused by deposited galled material were visible on Figure 90(a).

The ironing effect observed on Figure 90(a) is far more in keeping with that shown in literature (Ji et al., 2017; Patel et al., 2019; Sinhmar & Dwivedi, 2020b), and has the appearance of a “traditional” SSFSW. The shoulder smoothed the surface as it traversed, and the galling was very soft material (potentially overheated) being stuck to and then redistributed by the shoulder.

For this configuration, an explanation for the differences in surface appearance cannot be found in the literature. It is expected that it again relates to the weld force; at some instances in this weld the force was sufficient for the shoulder to make good contact, albeit not over its entire surface as shown by the weld width, allowing for the ironing effect to occur. These observations indicate that the weld process parameters/ clamping do not produce consistent results across the weld.



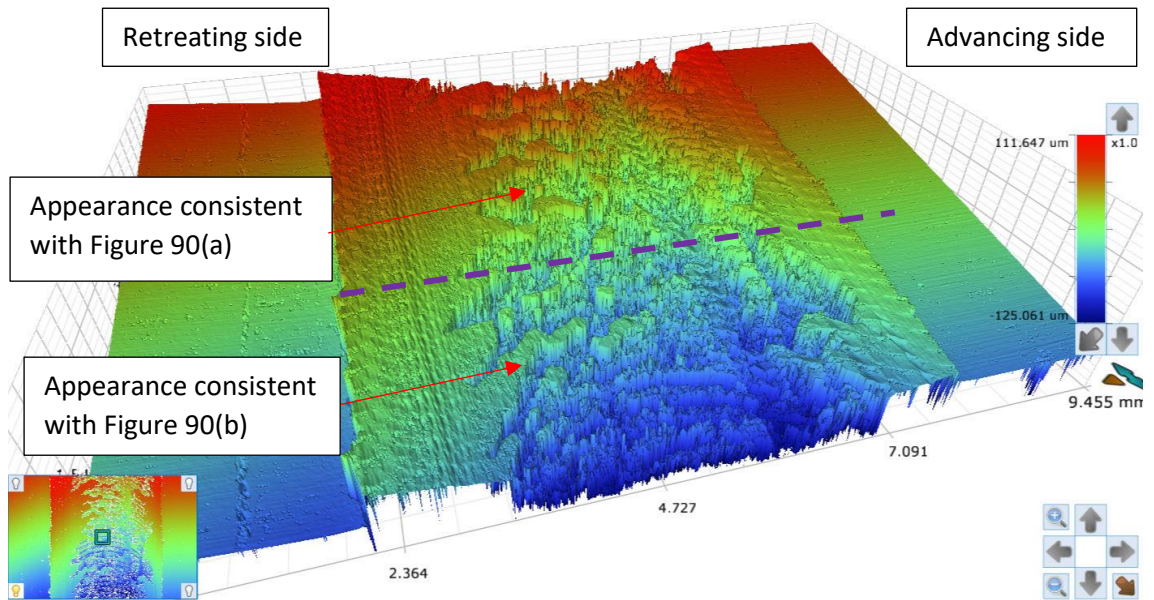
(a)



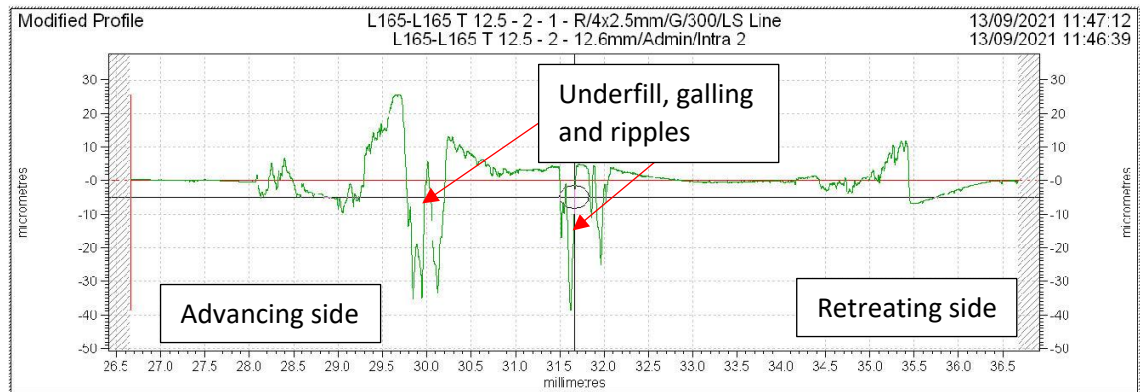
(b)

Figure 90: Showing BS L165 (⊥) weld surface. Both are from the same weld, with (b) taken from slightly further along (approx. 100 mm) from (a).

The optical and contact profilometry images are shown in Figure 91. The optical profilometry scan has been taken at a point between the two images shown in Figure 90 and further highlights the gradual shift from one appearance to another. The contact profilometry plot again indicates some underfill which may be misleading and could be a characteristic of the galled area. As the welding process used force control rather than position control, differences in the alclad layer thickness may account for the differences along the \perp weld, coupled with the influence of the grain orientation to account for the differences between the appearance of the two configurations. Zhang et al. (2011) found that the plunge depth strongly effected the surface appearance of alclad welds, and that a small plunge depth offered a smoother surface appearance (plunge depth was not altered during this current research).



(a)



(b)

Figure 91: Showing BS L165 \perp weld surface topography, (a) optical profilometer 3D model image, and (b) contact profilometry surface plot.

6.3.1.3 Weld Macro- and Micro-structures

The weld cross-section is shown in Figure 92 with weld zones differentiated by coloured, dashed lines and labelled. The advancing side is on the right-hand side of both images and the \perp image is to a slightly larger scale.

Negligible overall weld thinning was observed, however the \perp weld does show some underfill across the weld surface consistent with areas of galling previously observed via stereo microscopy and profilometry (section 6.3.1.2). As galling is caused by over-plasticised, very soft material sticking to the shoulder and subsequently being redistributed on the surface, this accounts for the underfill, as the overall mass of

material remains constant (not considering the effects of oxidisation). The \perp weld has a considerably rougher surface appearance owing to ripples, underfill and galling than that of the II weld.

A region affected by surface contact and containing an overhang is clear along the top surface and to either side of the main weld nugget. In this case, remnants of the alclad layer can be seen mixing along the top surface, combining the effects of this region and the alclad. The alclad layer can also be seen being drawn into the nugget/ TMAZ interface. Kissing bonds/ lazy S formations were evidence on all examined weld cross-sections to varying extents and severity. The alclad layer could also be seen being drawn into the kissing bond/ lazy S. This will be discussed in further detail in section 6.3.1.3.1.

Similar to the AA8090 welds, the nugget and TMAZ broadly follow the shape of the pin, although again being wider than the tapered pin diameter. In this case the nugget width measured 3.8 mm and 3.9 mm for the II and \perp weld respectively, measured at mid thickness.

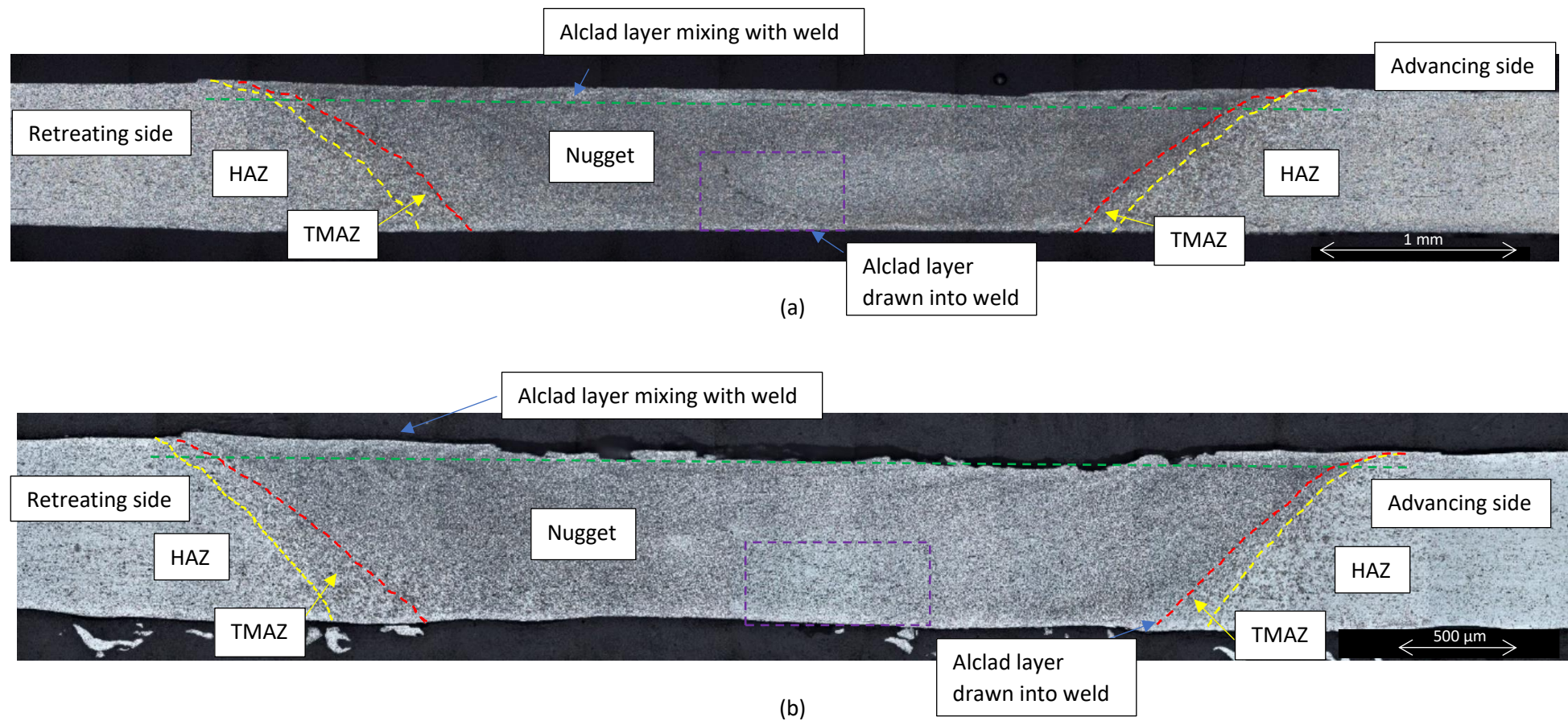


Figure 92: Showing macrograph of BS L165 weld cross-section; (a) || and (b) ⊥. The green dashed line indicates the extent of the SAZ, while the purple dashed box indicates the presence of the residual joint line/ kissing bond. The HAZ extends beyond the limits of these images.

6.3.1.3.1 Nugget

When comparing the nugget dimensions with that of the pin (and again disregarding the surface width measurement), it was observed that the \parallel weld measured approximately 3.8 mm and 3.0 mm at the mid-point and bottom surface respectively, and the \perp weld measured 3.9 mm and 3.0 mm at the same positions. When compared with the pin dimensions of 3.0 mm and 1.0 mm it is clear that the nugget of this material is of similar dimensions to AA8090 and follows a similar pattern, in that the nugget width exceeds the corresponding diameter of pin, especially at the root. As previously described, He et al. (2019) found an increase in nugget size with increasing rotational speed. A slower rotational speed was used for this material than for AA8090 however direct comparison of process parameters between different materials is not possible due to differing thermal conductivities.

No specific value could be found in the literature for the recrystallisation temperature of BS L165 (or AA2014), however Reddy (2007) states that the recrystallisation temperature of metals is approximately 30-50% of the melting temperature. When considering the Al-Cu phase diagram (shown in Figure 93) the relevant melting temperature (solidus line) is 548.2 °C. Therefore, according to Reddy (2007) the recrystallisation temperature should lie in the range of 164.46-274.1 °C. This is an approximation as it does not consider other alloying elements within BS L165. This is well below the temperatures which may be expected in the nugget, as previously discussed (section 6.2.1.3.1) and within the temperature range expected in the TMAZ. Dynamic recovery and recrystallisation was observed within the nugget, as expected and as shown in Figure 94 (see later in this section).

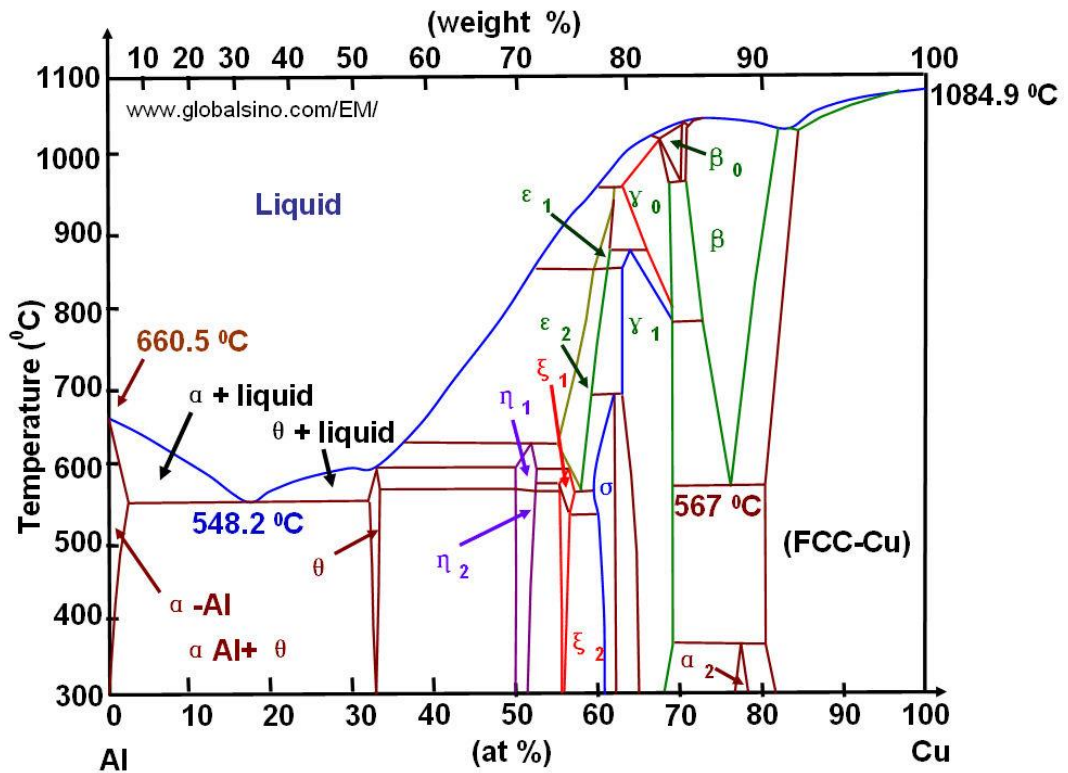


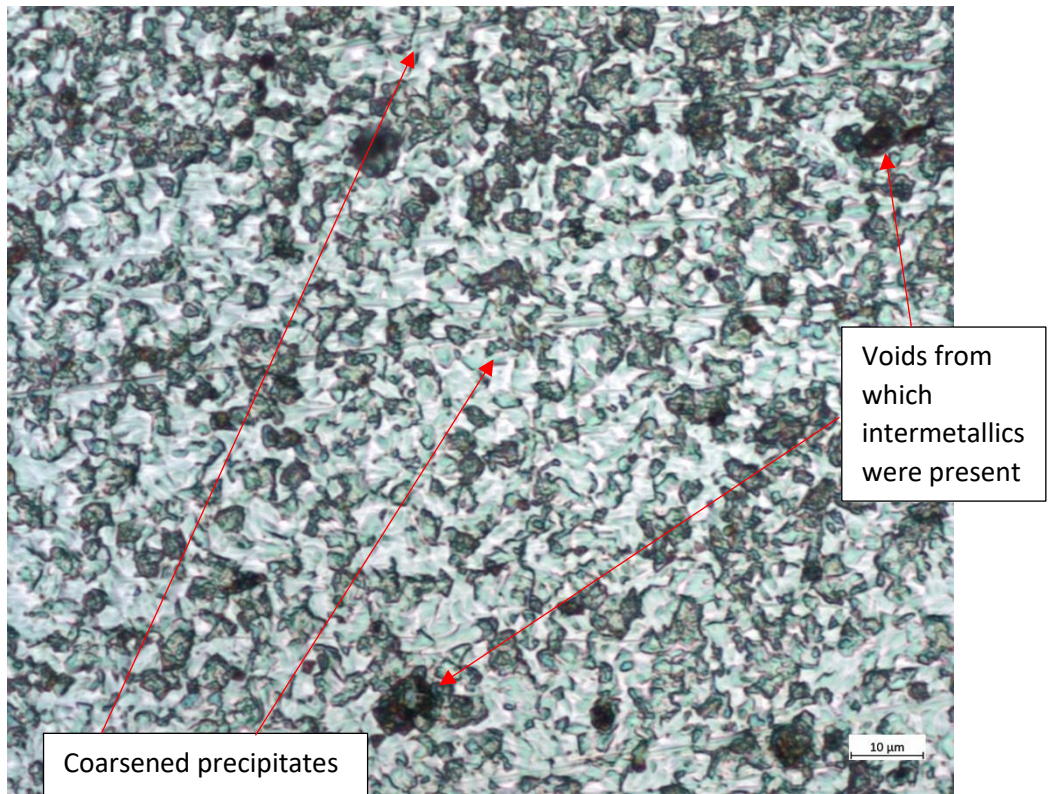
Figure 93: Showing Al-Cu phase diagram, courtesy of Liao (2006).

Grain sizes, measured at mid-thickness, are shown in Table 37. A significant reduction in grain size in the nugget was observed in comparison with the parent material; approximately 45-61% for direction 1 and 35-63% direction 2. Both \parallel and \perp orientations produced similar sized grains, indicating that the \parallel weld had a more dramatic response to the heat input and deformation forces as there was a larger change in grain size (\parallel welds are compared with the S-T parent material). The \perp weld nugget grains were closer to being equiaxed than the original parent material (\perp welds are compared with the longitudinal parent material). The difference in grain size between the two directions (for both material orientations) was less on the advancing side, as the retreating side direction 1 measurements were slightly larger than the advancing for both orientations. As previously described, although higher heat input is expected on the advancing side (which should produce larger grains), the additional shear forces and plastic strains on the advancing side result in smaller grains being produced on that side.

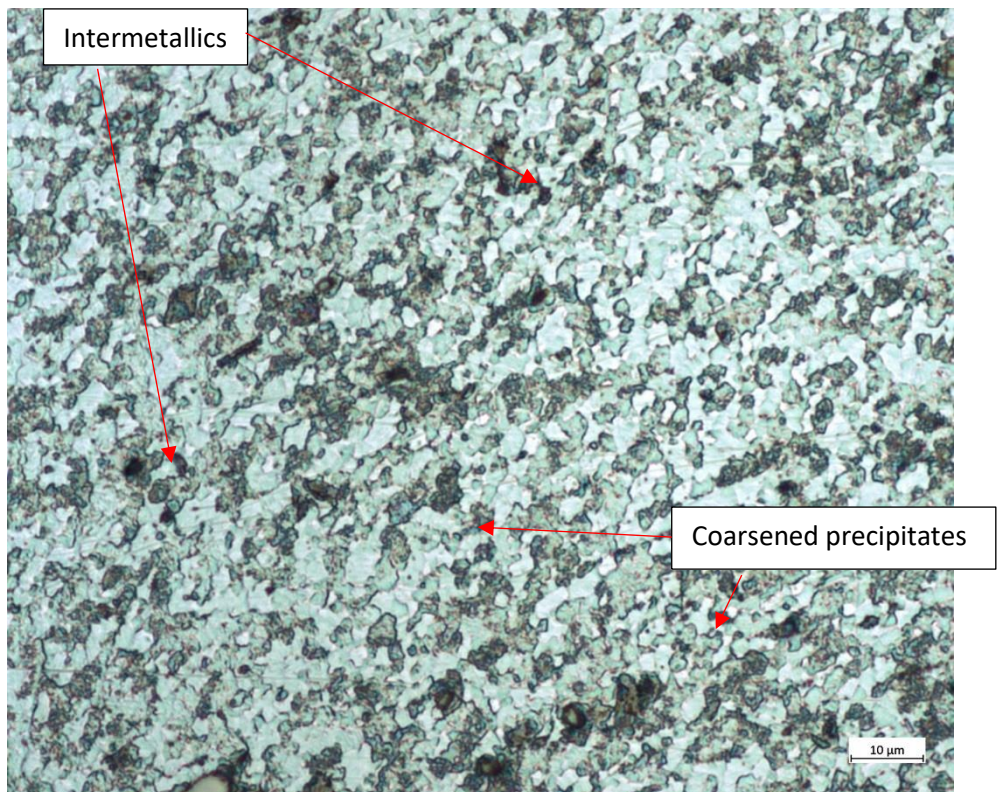
Table 37: Showing BS L165 parent material and weld nugget grain size dimensions, showing Relative Accuracy (%RA) in brackets.

Configuration	Average grain diameter (μm)			
	Advancing side		Retreating side	
	Direction 1	Direction 2	Direction 1	Direction 2
Parent material longitudinal	12.2 (4%)	7.5 (6%)	N/A	
Parent material short-transverse	14.4 (15%)	13.0 (13%)	N/A	
BS L165 II	5.6 (16%)	4.8 (11%)	6.6 (10%)	4.9 (14%)
BS L165 I	5.5 (10%)	4.8 (12%)	6.3 (13%)	4.9 (5%)

Focusing on the advancing side, micrographs of the nugget from both configurations are shown in Figure 94.



(a)



(b)

Figure 94: Showing micrographs of the advancing side of the nugget: a) BS L165 II; b) BS L165 L.

The micrographs (Figure 94) show the results of the dynamic recovery and recrystallisation previously alluded to; fine recrystallised grains. The grains have more distinct boundaries than that observed with the AA8090 nuggets, indicating that either the recovery and recrystallisation of the BS L165 was more mature than that of the AA8090 or that the grain boundaries of BS L165 were more heavily decorated with precipitates.

Babu et al. (2013) state that the temperatures reached in the nugget during Friction Stir Spot Welding (FSSW, a spot welding variant of FSW) are well above the solvus temperature of λ' ($\text{Al}_5\text{Cu}_2\text{Mg}_8\text{Si}_5$) and θ' (Al_2Cu) strengthening precipitates, and that the thermal cycle can result in the formation of incoherent equilibrium λ and θ phases in the nugget. They also consider the second-phase particles already present in the material prior to welding, showing that these, along with the equilibrium phases formed during the welding can undergo partial dissolution during FSW. Rapid cooling can result in additional formation and/ or coarsening of the equilibrium phases. They conclude that the microstructural response within the nugget is a combination of dissolution, coarsening and reprecipitation of strengthening precipitates following natural aging. In another body of work, Babu et al. (2012) identified that coarse particles were Al_2Cu , with finer equilibrium θ and λ phase particles. They found no needle-like semi-coherent strengthening precipitates such as λ' or θ' in the nugget. It is likely that the coarse particles observed in this research are incoherent θ , with the strengthening θ' having dissolved, and that incoherent λ would be apparent through use of TEM.

In this research, both configurations show a reduction in large intermetallic particles when compared with the parent material as these were likely to have been partially fractured and distributed within the nugget. However this reduction was not as apparent as that commented on by Rajendran et al. (2019) in their research, possibly indicating that the deformation and stirring in the nugget of this research did not reach that of Rajendran et al.'s (2019). Rajendran et al. (2019) identified the intermetallics of FSW AA2014-T6, via TEM-EDX analysis, as Fe-Mn-Al. Based on the similarity in microstructures of Rajendran et al.'s (2019) work (Figure 95), it is considered highly likely that the intermetallics in this research also comprise of Fe-Mn-Al.

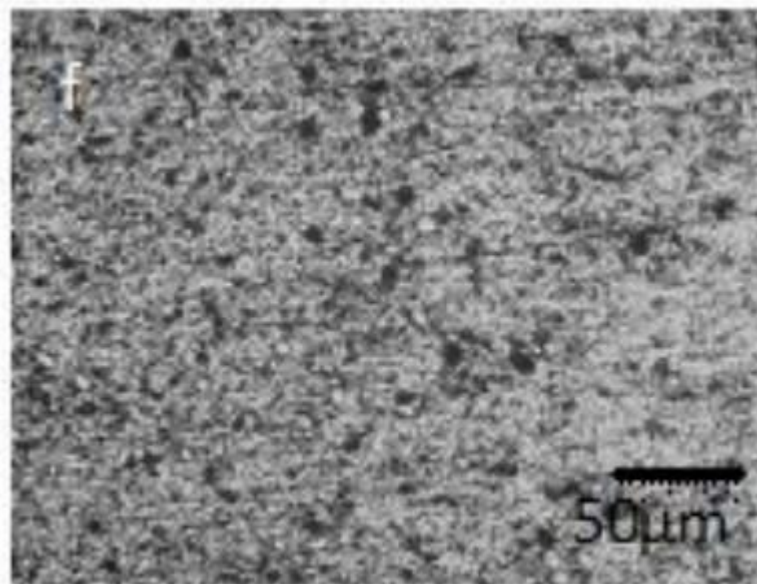


Figure 95: Showing FSW AA2014-T6 nugget, courtesy of Rajendran et al. (2019).

Kissing bonds were observed in all welds, however the extent and severity of these varied and none were as severe as those present in the AA8090 welds. All of the “kissing bonds” observed on BS L165 meet the criteria provided previously to describe these defects as “lazy S” rather than kissing bonds. The effect of these lazy S defects on the tensile mechanical properties is discussed section 6.3.2.2 and 6.3.2.3. One main difference between the lazy S/ kissing bonds observed on the AA8090 welds and these BS L165 welds is that the alclad layer present on the bottom surface of the BS L165 parent material has been drawn into the weld at this point, Figure 96. This may potentially cause a double weakness; that arising from the presence of a dense chain of Al_2O_3 particles and that arising from the presence of a layer of commercially pure aluminium (weaker and softer than the heavily alloyed BS L165 bulk material). Various researchers have reported a deterioration in weld quality when an alclad layer is drawn into the weld. Zhang et al. (2011) reported that the amount of alclad being drawn into the nugget (not necessarily at a kissing bond) was dependent on the traversing speed and plunge depth due to the effect on material flow; they considered an inward extension of the bottom alclad layer to be detrimental to the weld quality. The effect of alclad material ingress to the weld in this research is discussed in section 6.3.2.2 and 6.3.2.3.

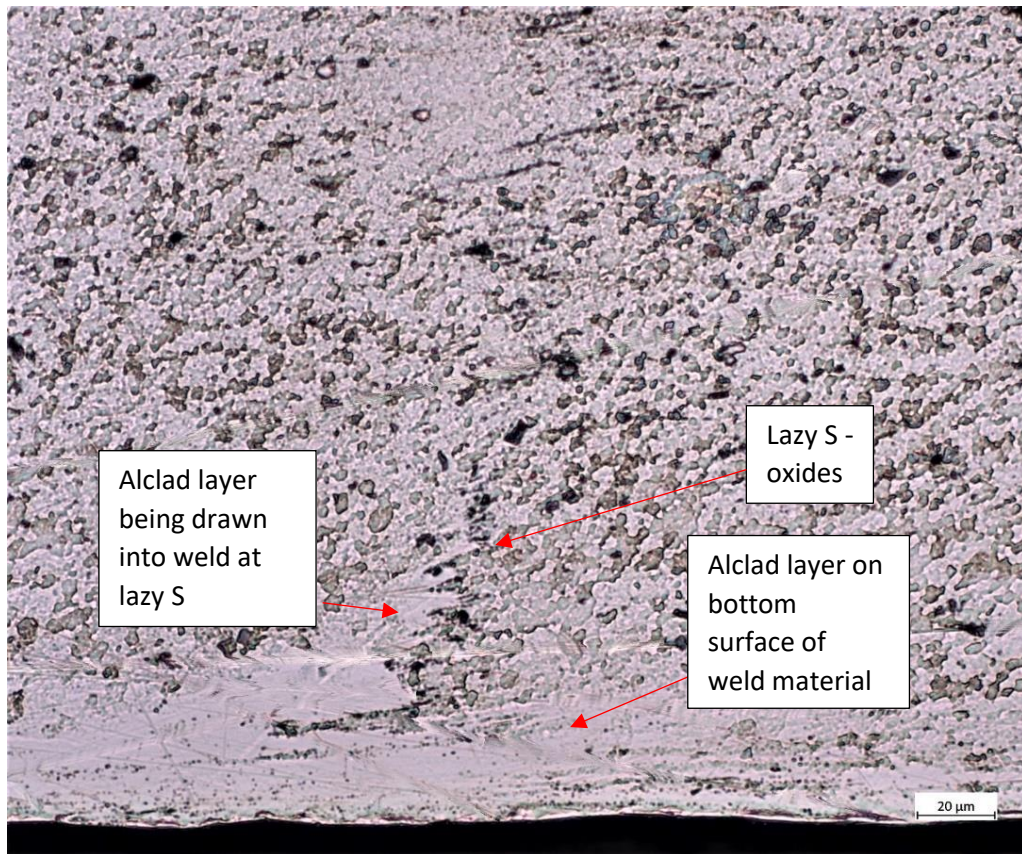


Figure 96: Showing alclad layer being drawn into the lazy S on a II weld.

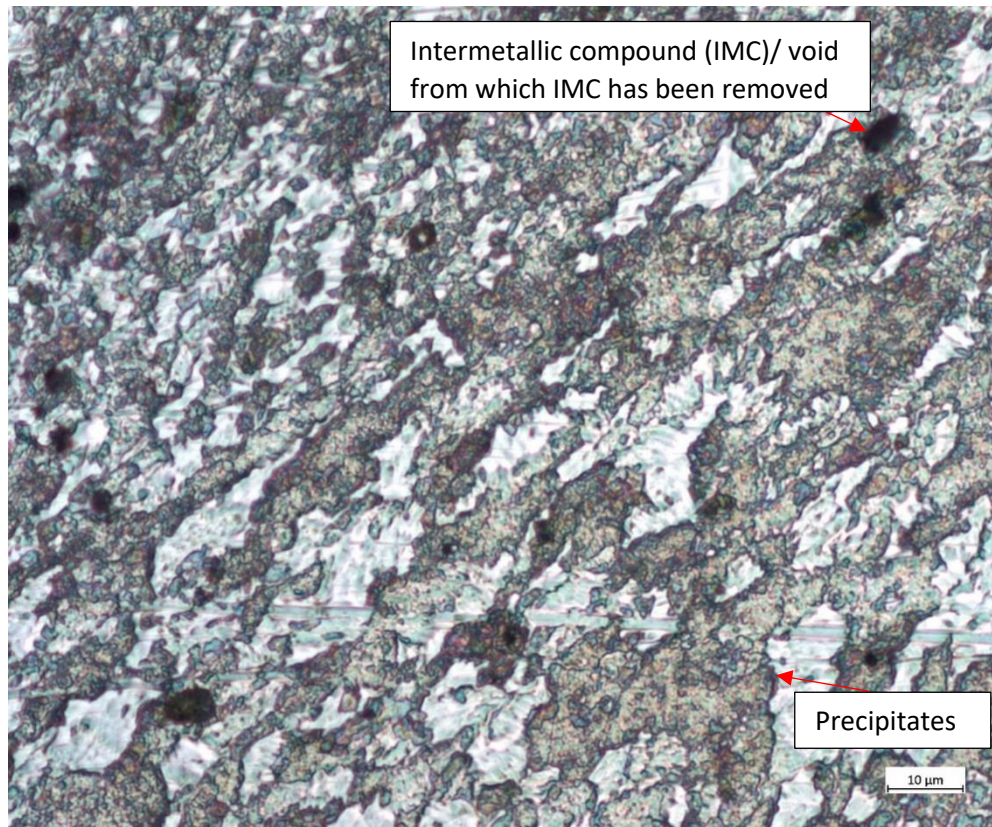
6.3.1.3.2 TMAZ

Similar to the AA8090 welds, the BS L165 TMAZ are identified by distorted and elongated, angled grains adjacent to the weld nugget, as shown in Figure 97. The nugget/ TMAZ boundary is distinct on the advancing side while being more diffuse on the retreating side, and the TMAZ is again narrower on the advancing side than retreating side. The II weld TMAZ measures approximately 170 µm wide on the advancing side and 360 µm on the retreating, while the \perp weld measures approximately 140 µm on the advancing side and 200 µm on the retreating. This is a change from the AA8090 welds where the \perp weld had a significantly wider TMAZ than the II weld. For BS L165, a narrower TMAZ indicates reduced heat input to the weld when the weld \perp is compared with the II. An explanation for this discrepancy may be that the width of the TMAZ is influenced by the material orientation. Barbini, Carstensen and dos Santos (2018) do not specifically mention the TMAZ width in their work on investigating the effect of material rolling orientation with respect to weld direction, however some of their welds did show a marked change in microstructural appearance when the rolling orientation was changed. This indicates that the rolling direction with respect to weld

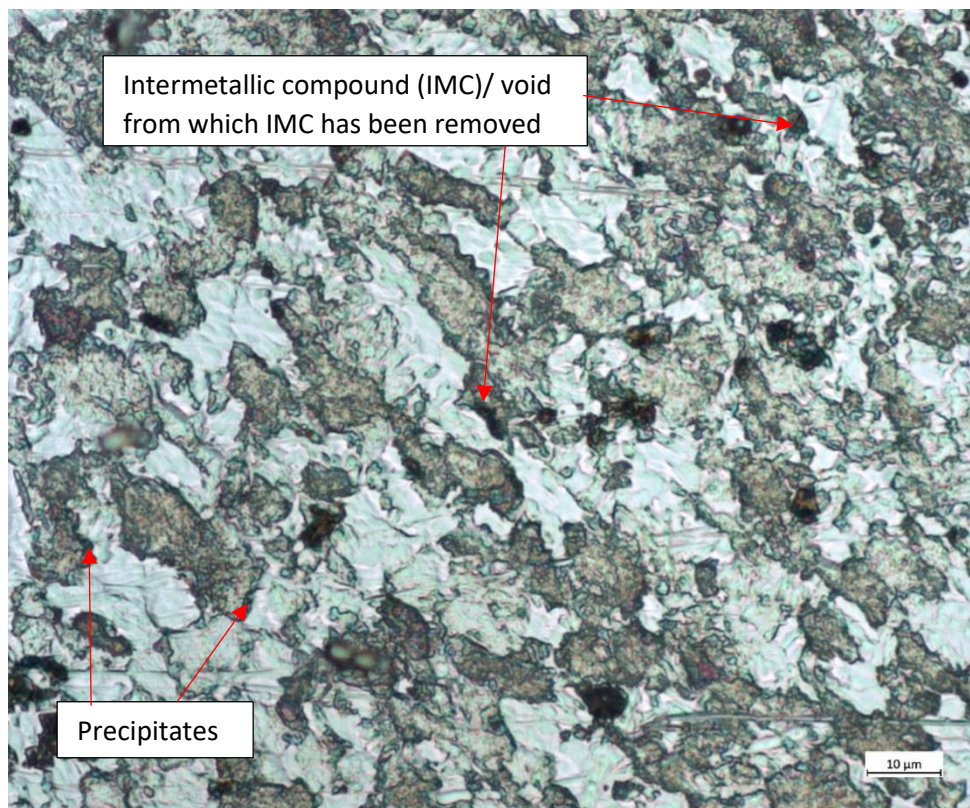
direction can have a strong influence over the weld appearance and zone width. Zolghadr, Akbari and Asadi (2019) do state that the TMAZ formation “rigorously” depended on the properties of the original parent material. They state that the width of the TMAZ is determined by the amount and combination of strain and heat within the weld.

While the width of the TMAZ appears more uniform throughout the material thickness, than that observed on the AA8090 \perp , there is still some increase in width towards the bottom surface. This is considered to be due to reasons already described in section 6.2.1.3.2.

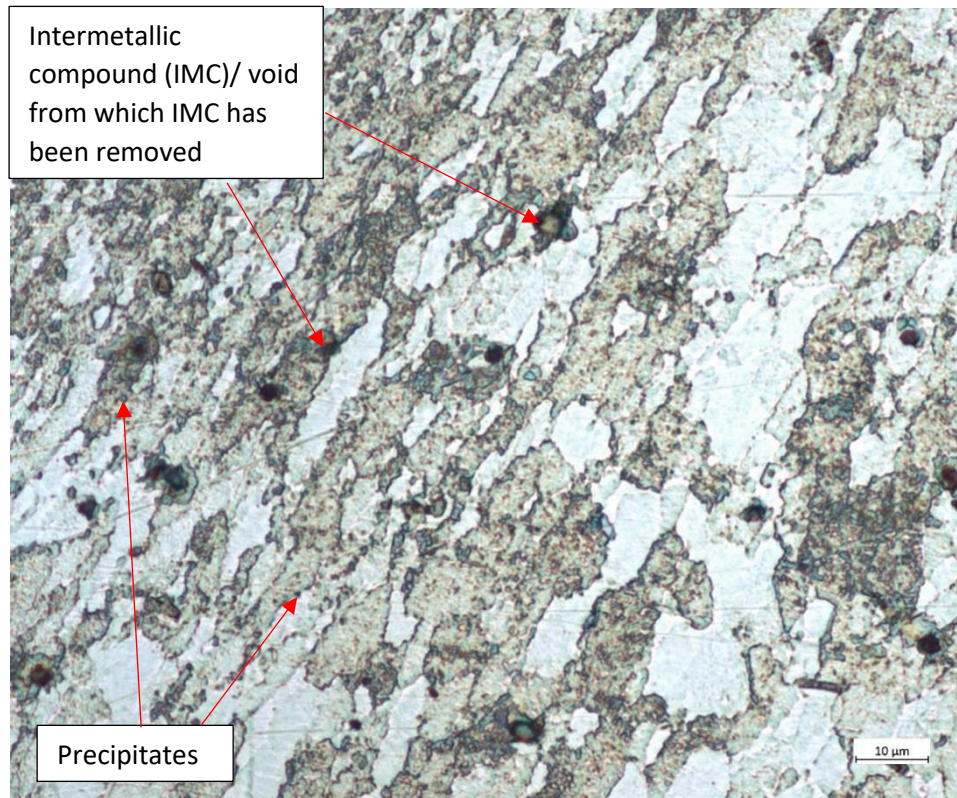
Figure 97(a) and (b) show the II weld TMAZ advancing and retreating sides respectively, with the \perp weld shown in Figure 97(c) and (d). The II weld shows larger but slightly fewer intermetallic particles on the advancing side, with more numerous but overall smaller particles on the retreating side. These particles are not evenly distributed in either case. It is considered that these intermetallics compounds (IMCs) were of similar composition as that described by Rajendran et al. (2019) and described in section 6.3.1.3.1. Coarsened precipitates, considered to be incoherent θ , can be observed having heterogeneously nucleated at grain boundaries. It is expected that TEM analysis would reveal gathering of coarsened λ particles on the grain boundaries also. The \perp weld shows significantly smaller and less numerous IMCs on the advancing side with coarser and more plentiful IMCs on the retreating side.



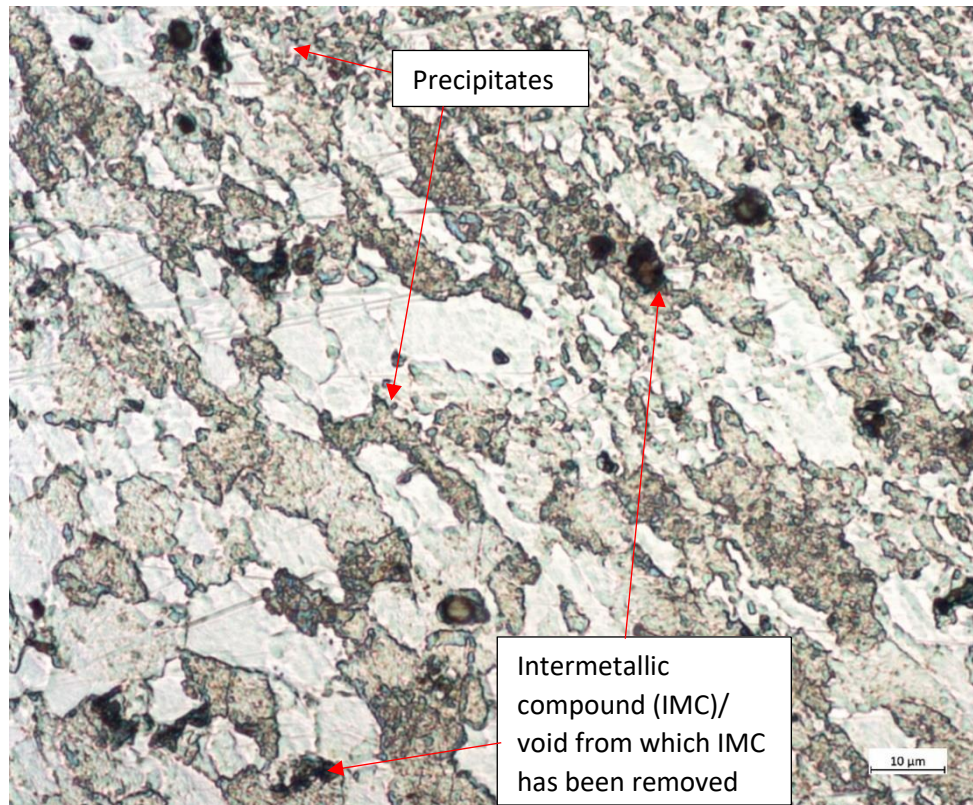
(a)



(b)



(c)



(d)

Figure 97: Showing micrographs of the TMAZ: a) BS L165 II advancing side and b) retreating side; c) BS L165 ⊥ advancing side and d) retreating side.

The alclad layer was observed to be drawn into the weld at the nugget/ TMAZ interface, as shown in Figure 98. This was also observed by Zhang et al. (2011) to differing extents depending on the plunge depth and traversing speed used, and the effect reduced with high traversing speeds and small plunge depths. This is due to the material flow conditions; inappropriate welding parameters produce welds with excess material flow which allows the alclad layer to extend into the weld at the interface. This suggests that these welds may have been too hot and reducing the heat input would have decreased the extent of the material flow. Zhang et al. (2011) comment that the extension of the alclad layer into the weld strongly affected the weld quality, however they did not provide any mechanical testing results to qualify the statement. The effect of alclad layer ingress on the quality of these welds is discussed in sections 6.3.2.2 and 6.3.2.3.

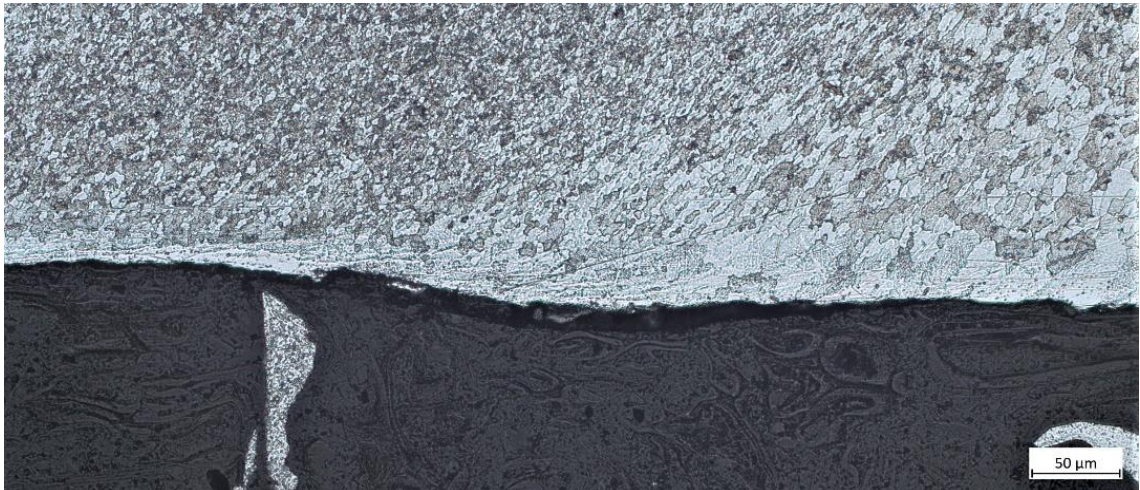


Figure 98: Showing alclad layer being drawn into the weld at the nugget/ advancing side TMAZ interface of a \perp weld.

6.3.1.3.3 HAZ

The hardness results were again used to determine the width of the HAZ as the microstructural changes from thermal input were not visually significant enough to identify the boundary through solely optical means. There was a substantial difference in HAZ widths of BS L165 and AA8090, and substantial differences between the two configurations of BS L165. BS L165 II weld HAZ width measured approximately 4.0 mm on the advancing side and 3.5 mm on the retreating side, while the \perp weld measured 1.5 mm and 2.0 mm for the advancing and retreating sides respectively. These

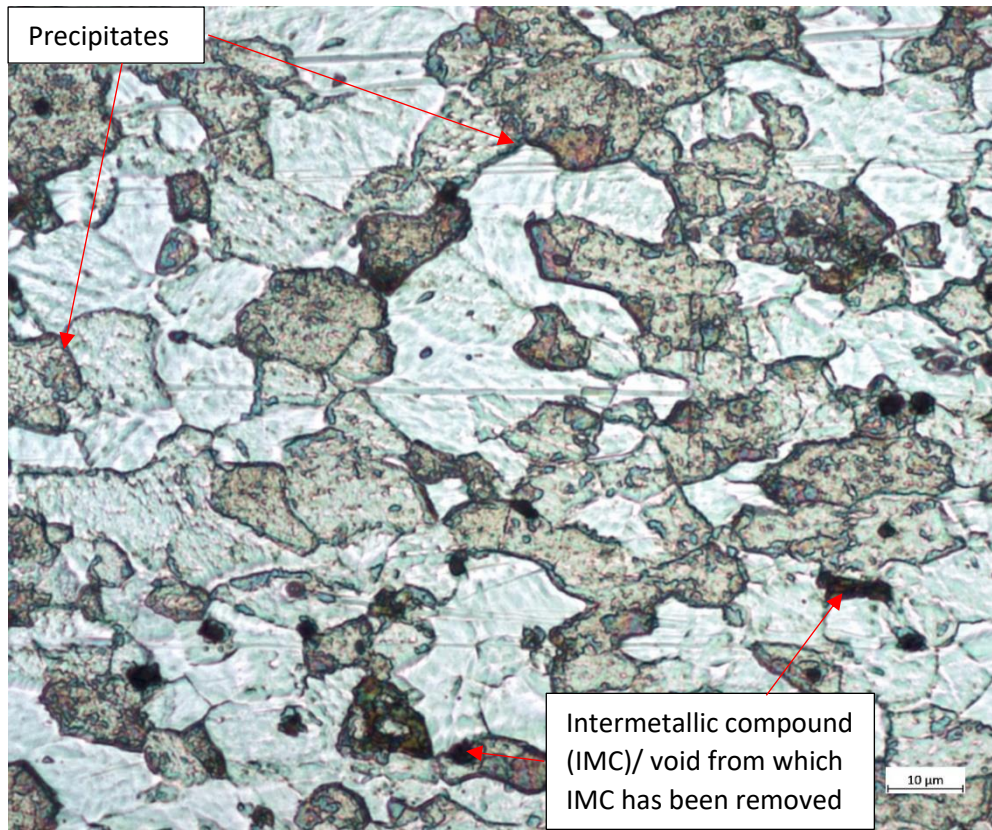
measurements imply that the \perp weld was cooler than the II weld as a narrower HAZ generally results from a cooler weld, that being one of the main perceived attractions of the SSFSW process (Wu, H. et al., 2015).

It is expected that the large HAZ widths observed on the II were a result of the increased thermal conductivity of this material when compared with AA8090. The fact that the advancing side width was measured as larger than the retreating is not truly considered to be at odds with the evidence discussed in section 6.2.1.3.3 where the AA8090 advancing side was smaller than the retreating side. The hardness measurements as the testing transitioned from HAZ to parent material showed a very gradual change in value (see section 6.3.2.1). As these measurements were only made every 0.5 mm and there is a margin of error within the hardness measurement it is conceivable that the advancing and retreating sides are of equal value, or that the retreating side actually exceeds that of the advancing, as some hardness measurements may have been mis-accounted as HAZ on the advancing side due to the gradual change. This mis-accounting arises from interpretation of the data rather than errors in testing.

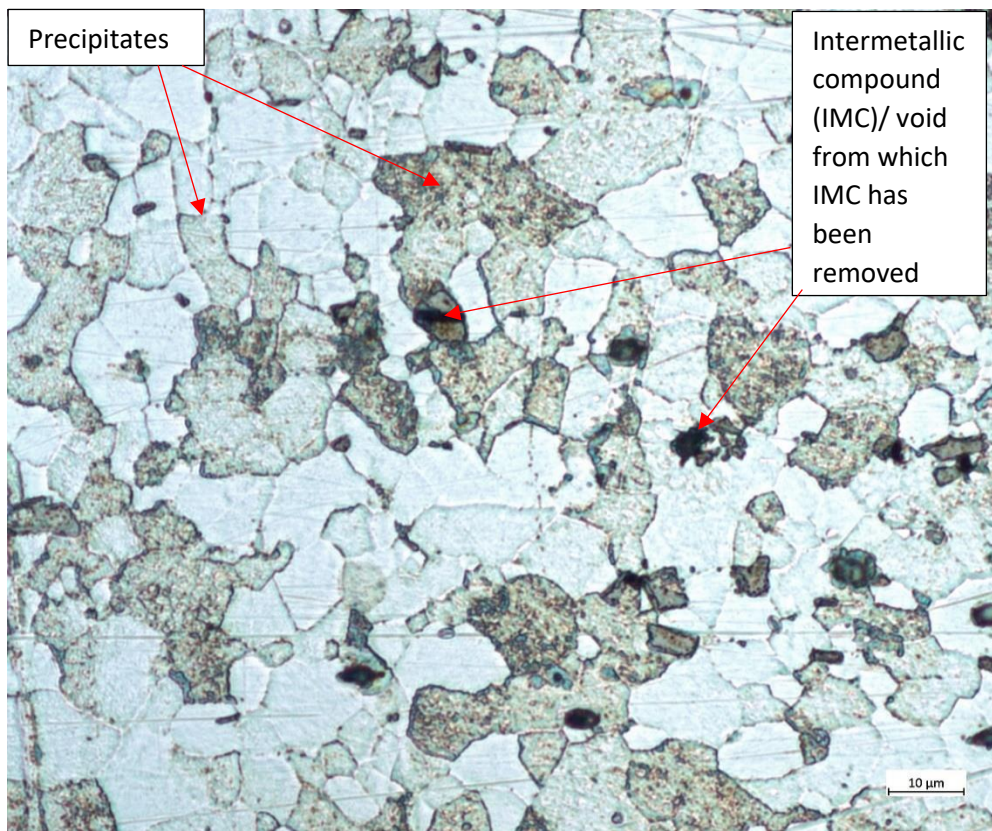
It is not clear why, if the large HAZ on the II weld was due to high thermal conductivity, how then could the narrow HAZ on the \perp weld have been caused from high thermal input; as the high thermal input on a material with high thermal conductivity should have resulted in a notably wider HAZ. It is considered that the reason for the narrow HAZ is as described previously; a high cooling rate is responsible. It is not, however, clear as to why this high cooling rate occurred on the \perp weld and not on the II weld as both welds were carried out using the same welding parameters, the same clamping and on the same day.

The advancing side HAZ microstructures are shown in Figure 99. The images show slightly fewer large intermetallic particles (considered to be similar in composition to that reported in section 6.3.1.3.1) in the microstructure when compared with the parent material. There does appear to be a coarsening of particles around the grain boundaries, expected to comprise of incoherent θ and λ . This coarsening appears to be more severe on the II weld than on the \perp weld, indicative of higher heat input to the II weld.

Evidence in support of the II weld being hotter was the narrower TMAZ and HAZ of the \perp weld, and that coarsening of precipitates at the grain boundaries of the TMAZ and HAZ of the \perp weld does not appear as severe as that for the II weld. Evidence in support of the \perp weld being hotter was the surface appearance, which was significantly galled in some areas, indicative of over plasticisation, with underfill, smaller and more evenly distributed particles within the nugget of the \perp weld. The TMAZ and HAZ widths and microstructure appear to be more compelling evidence than the surface appearance, both of which overall support the II weld being hotter.



(a)



(b)

Figure 99: Showing microstructure of advancing HAZ of BS L165, a) II and b) L.

The HAZ grain sizes for both configurations are shown in Table 38, with the parent material measurements for comparison (again, longitudinal for comparison with \perp weld, and S-T for comparison with II weld). The measured change in grain size when compared with the parent material was most significant for the II as there was a considerable change in direction 2 from the S-T parent material. These measurements were only carried out at one part of the HAZ, close to the TMAZ. Again, it is unclear as to why a change in grain size occurred in the HAZ as no deformation occurs in this area.

Table 38: Showing BS L165 parent material and weld HAZ grain size dimensions, showing Relative Accuracy (%RA) in brackets.

Configuration	Average grain diameter (μm)							
	Advancing side				Retreating side			
	Direction 1	% difference from parent material	Direction 2	% difference from parent material	Direction 1	% difference from parent material	Direction 2	% difference from parent material
Parent material longitudinal	12.2 (4%)	N/A	7.5 (6%)	N/A	N/A			
Parent material short - transverse	14.4 (15%)	N/A	13.0 (13%)	N/A	N/A			
BS L165 II	11.3 (14%)	-21.5	7.6 (10%)	-41.5	12.5 (8%)	-13.2	7.5 (12%)	-41.3
BS L165 \perp	11.0 (8%)	-9.8	7.9 (9%)	+5.3	11.3 (11%)	-7.4	7.8 (8%)	+4.0

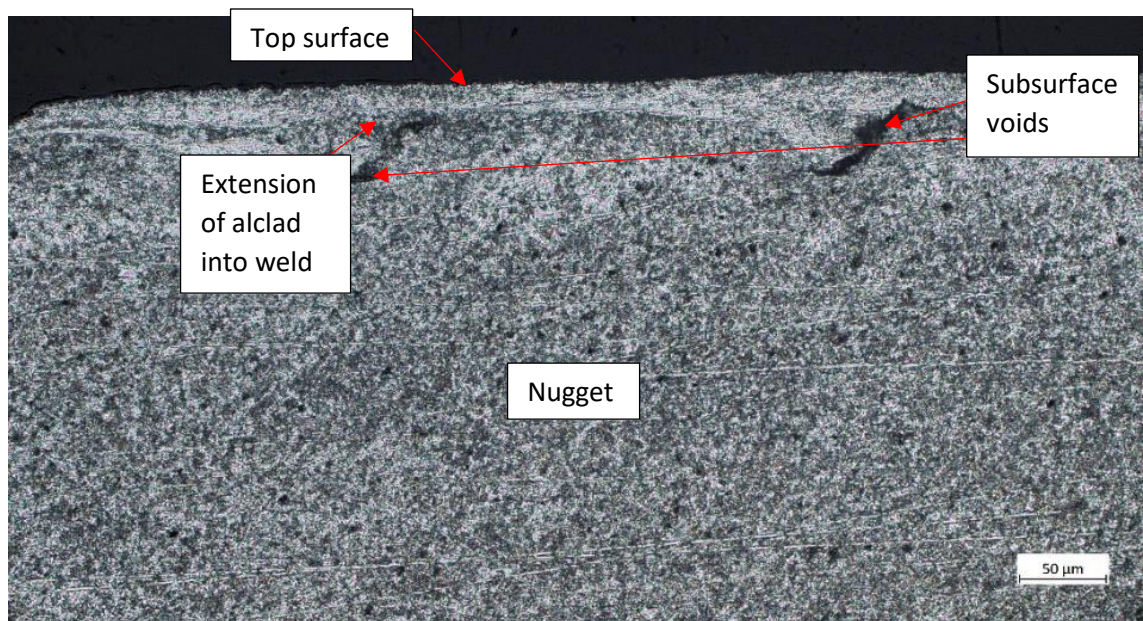
6.3.1.3.4 Alclad Mixing

Zhang et al. (2011) found that the material flow for alclad vs. unclad materials was distinctly different with the alclad layer exerting a significant effect on the material flow.

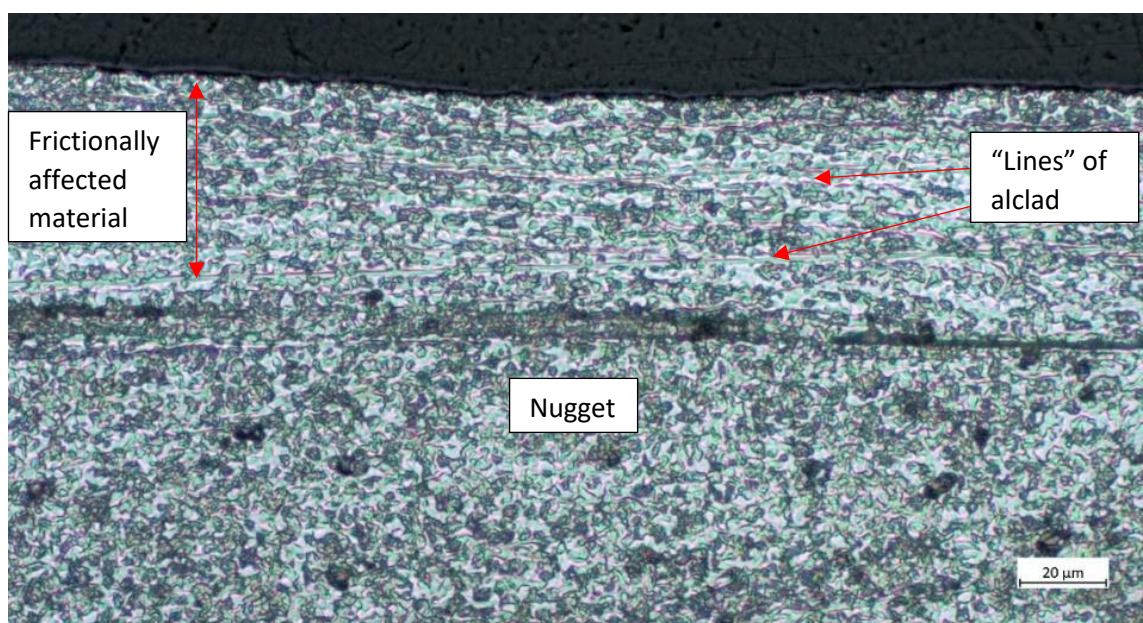
Figure 100 shows the alclad layer at various points at the top surface of the nugget of the II weld. At the advancing side the alclad layer has partially extended into the weld from the top surface. Due to insufficient mixing and therefore inadequate deposition of material as it is moved around the tool, voids have formed adjacent to these alclad extensions, Figure 100. It is reasonable to assume that these voids would not be beneficial to the weld quality, however the extent of their influence was measured through mechanical testing which will be discussed in sections 6.3.2.2 and 6.3.2.3.

The alclad layer is only subtly visible at the weld mid-point (width, rather than depth); a shallow layer of frictionally affected (from pin contact with the surface) material is visible with fine lines of alclad subsurface (Figure 100(b)). This indicates that the alclad

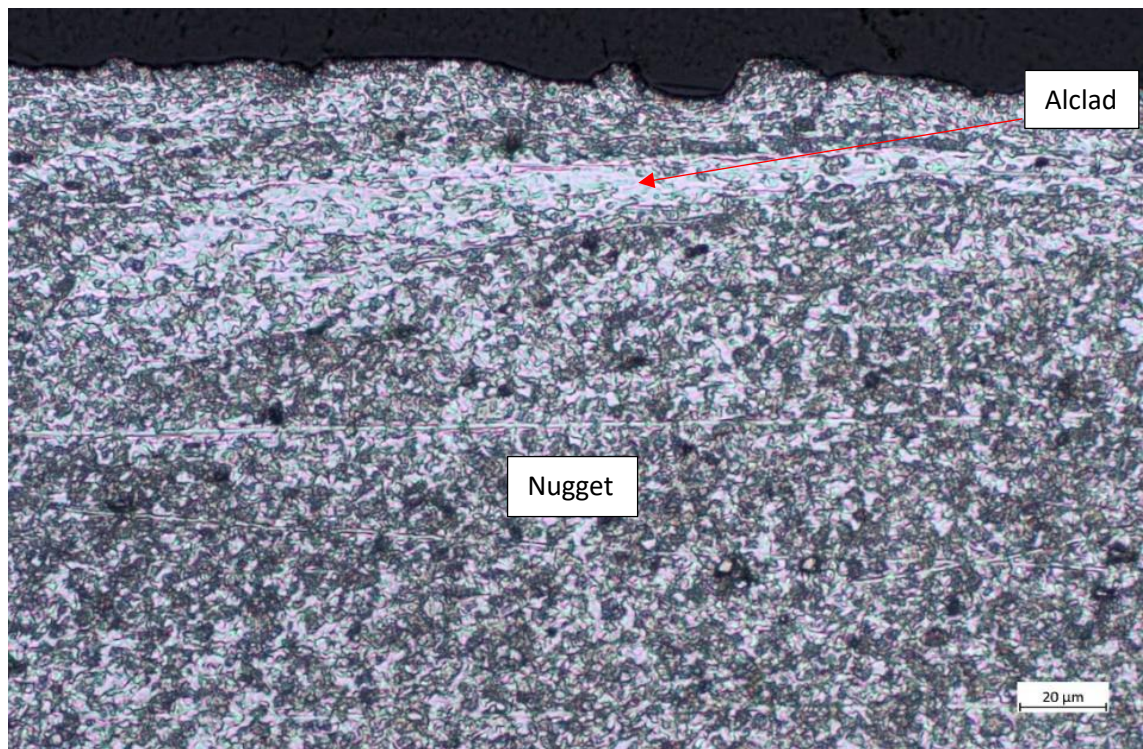
layer has either been sufficiently well mixed with the parent material to form only fine layers, or that it has been deposited elsewhere, i.e. extension into the weld at the advancing side or deposited at the side of the weld top surface, with only a small amount remaining in this area. At the retreating side the alclad layer has mixed into the weld, with non-alclad material on the top surface. This may affect the corrosion resistance of the welded material which, although considered within this research, was discontinued due to time constraints.



(a)



(b)



(c)

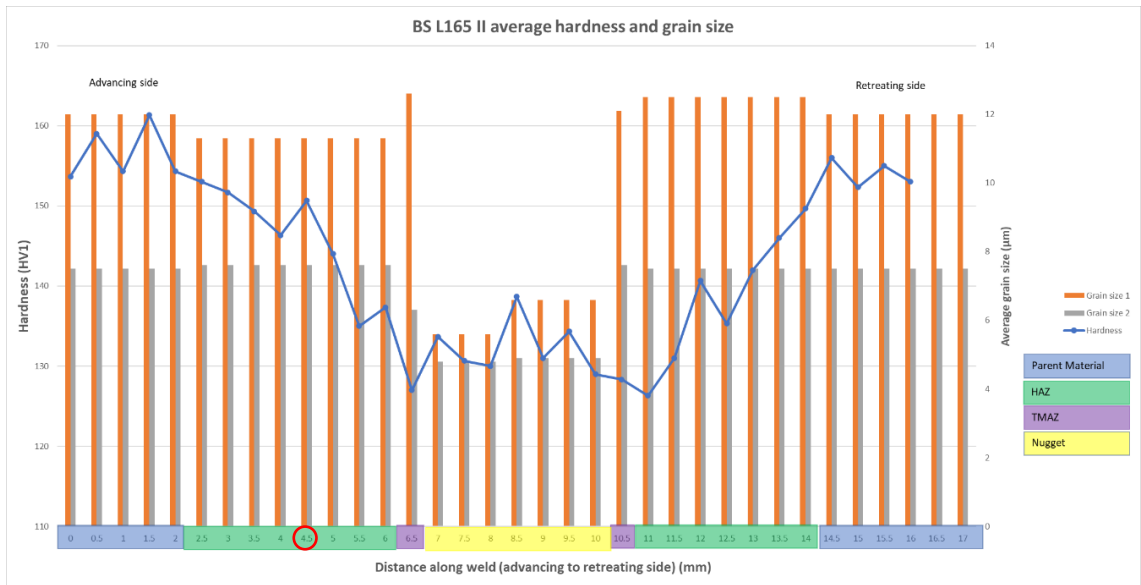
Figure 100: Showing the alclad layer response on the top surface within the nugget at (a) biased to the advancing side, (b) mid-weld, and (c) biased to the retreating side. All images are from II weld.

6.3.2 Testing

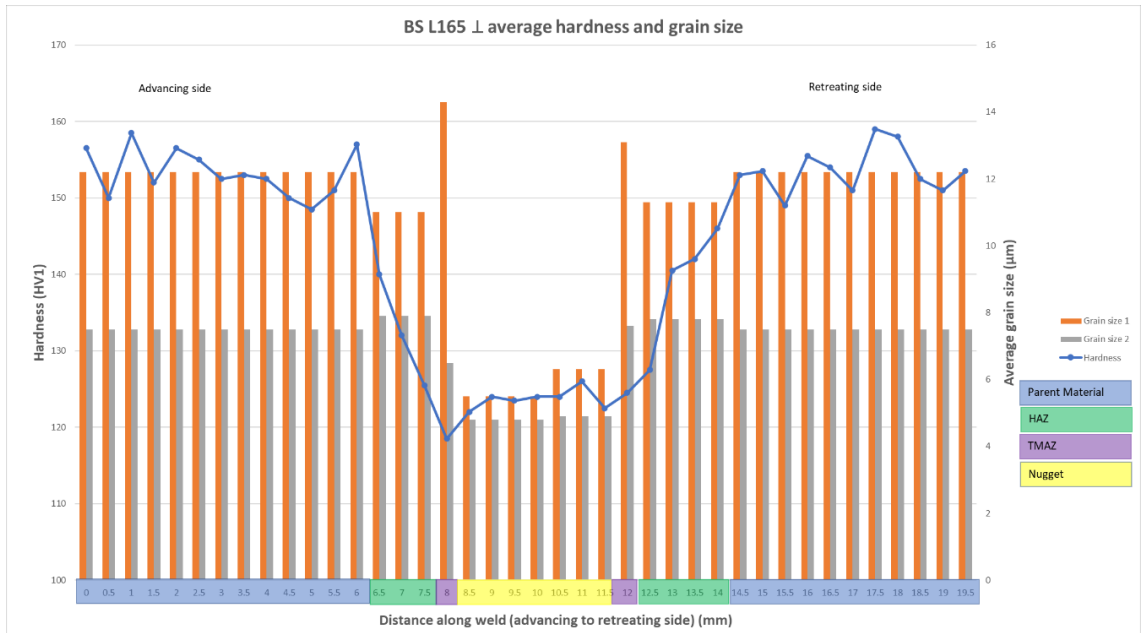
6.3.2.1 Hardness

The results of hardness testing along the weld centreline are shown in Figure 101, with grain size plotted on a secondary axis. Again, this grain size was only measured at one point within each weld area, not at each corresponding hardness measurement. The area of the weld, i.e. nugget, HAZ etc. is indicated by the coloured bars along the x-axis, however as previously discussed (section 6.3.1.3.3), the advancing HAZ for the II weld may not be as wide as indicated on the chart, due to its close correlation with the parent material hardness values. It is considered that the HAZ may actually transit to the parent material at the 4.5 mm mark on the x-axis (indicated by the red circle) and therefore only measure 1.5 mm consistent with the \perp weld. An advancing HAZ width of 1.5 mm will be used for the following analysis.

Analysis of the plots shows a steep reduction in hardness from the parent material values with very limited hardness recovery in the nugget. The II weld hardness minimum was located in the retreating HAZ, although this value was close to the hardness of the advancing side TMAZ. In the \perp weld the hardness minimum was located in the advancing side TMAZ. Both welds showed a steep reduction in hardness on the advancing side, while the retreating side gradient was slightly shallower with the HAZ spread over a larger area. Limited hardness recovery in the nugget has been reported in the literature for AA2014-T6 (John et al., 2019; Satyanarayana & Kumar, 2019) although some researchers claim that the nugget can achieve parent material hardness levels (Rajendran, Chinnasamy et al., 2019), strongly dependent on process parameters. Muhammad et al. (2021) attributes the reduction in hardness in the nugget to high temperature and severe plastic deformation causing dissolution of the hardening precipitates into the aluminium matrix, with the partial limited hardness recovery due to recrystallisation and grain refinement.



(a)



(b)

Figure 101: Showing hardness and grain size plots of a) BS L165 II, and b) BS L165 ⊥.

The II weld data shows a slight increase in hardness across the joint when compared with the ⊥ weld, however this difference is only 5-10 HV which is not considered to be significant enough to draw conclusions regarding the different weld qualities.

In the literature, the hardness minima typically occurs in the advancing side TMAZ (Rajendran, C. et al., 2021) or occasionally the advancing side HAZ (Lin et al., 2006), however some researchers do report minima occurring at the retreating side

(Rajendran, C. et al., 2016). As described, in this research the II weld hardness minimum occurs in the retreating side HAZ, however the minimum value is extremely close to that of the advancing side TMAZ. It is considered that similar levels of precipitate coarsening occurred in these areas to produce similar testing results, with this effect outweighing the hardening effect of the smaller recrystallised grain size on the advancing side TMAZ. The \perp weld has a clear hardness minimum at the advancing side TMAZ, typical for this alloy and temper. The retreating side HAZ is wider for both welds, and this can be attributed to reasons previously discussed (section 6.2.2.1).

Unlike the AA8090 alloy, the parent material hardness in the BS L165 welds did approximately recover to the previously measured hardness value, comfortably within the uncertainty margin, on each side of the weld. This is expected, as the parent material is, by definition, not affected by the weld process and therefore no changes should be apparent.

6.3.2.2 Tensile Testing

The results of the BS L165 tensile testing are shown in Table 39, and as previously, parent material longitudinal results are used for comparison with BS L165 \perp welds, and parent material transverse for comparison with BS L165 II welds. This testing showed that the BS L165 II achieved 100% of the measured parent material UTS, while the \perp weld achieved 97%. Most researchers report weld efficiencies of in the approximate range of 80-90% (Das et al., 2020; Rajendran, C. et al., 2019), however some researchers (Devaraju, 2017; Ramanjaneyulu et al., 2013) report weld efficiencies of over 100%, however for the latter it is not clear whether the efficiency is measured against the parent material specification or a measured UTS. In either case it is clear that the tensile test results for the welds in this research are at the high end of the scale and indicate successful welds.

Similar to AA8090, the BS L165 welds also experienced a significant reduction in % elongation. This can be attributed to heterogeneous nucleation of precipitates to the grain boundaries and flaws as previously described.

Both weld configurations show significant standard deviation for UTS, in both cases higher than those for the AA8090 welds. Examination of the results revealed considerable scatter in UTS of specimens taken at different parts of the weld, and on

different weld runs, with no discernible pattern in areas of strength or weakness. This indicates that despite the impressive overall weld efficiency, the weld quality was not consistent or repeatable. Based on previous analysis, this is likely to be due to inconsistent heat input and the presence of kissing bonds of varying severity.

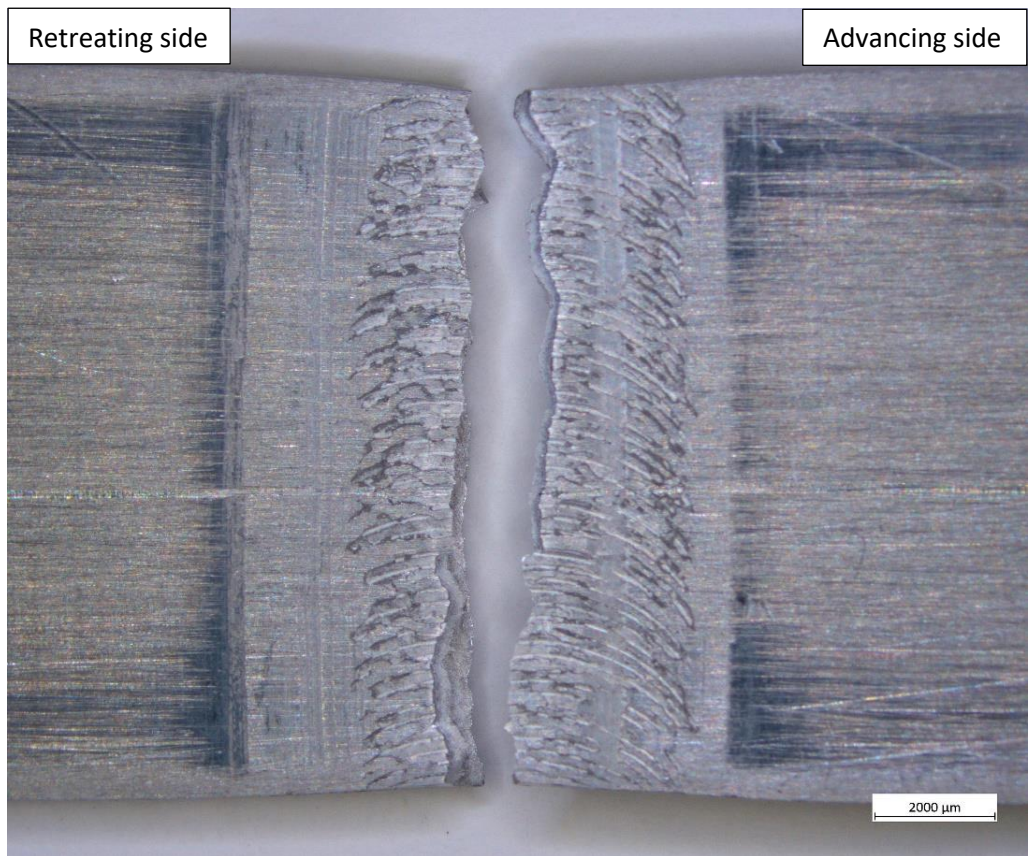
Table 39: Showing BS L165 tensile test results.

	UTS (MPa)		0.2% Proof strength (MPa)		Elongation (%)		UTS Standard Deviation	Efficiency of test when compared with parent material specification (%)	Weld efficiency, using measured parent material test results as comparison (%)
	Spec	Measured	Spec	Measured	Spec	Measured			
BS L165 parent L	415	442	345	397	7	8.7	2.82	106.5	-
BS L165 parent T	415	436	345	393	7	8.4	2.20	105.1	-
BS L165 II	415	437	345	340	7	3.3	38.90	105.3	100.2
BS L165 I	415	430	345	343	7	2.4	22.06	103.6	97.3

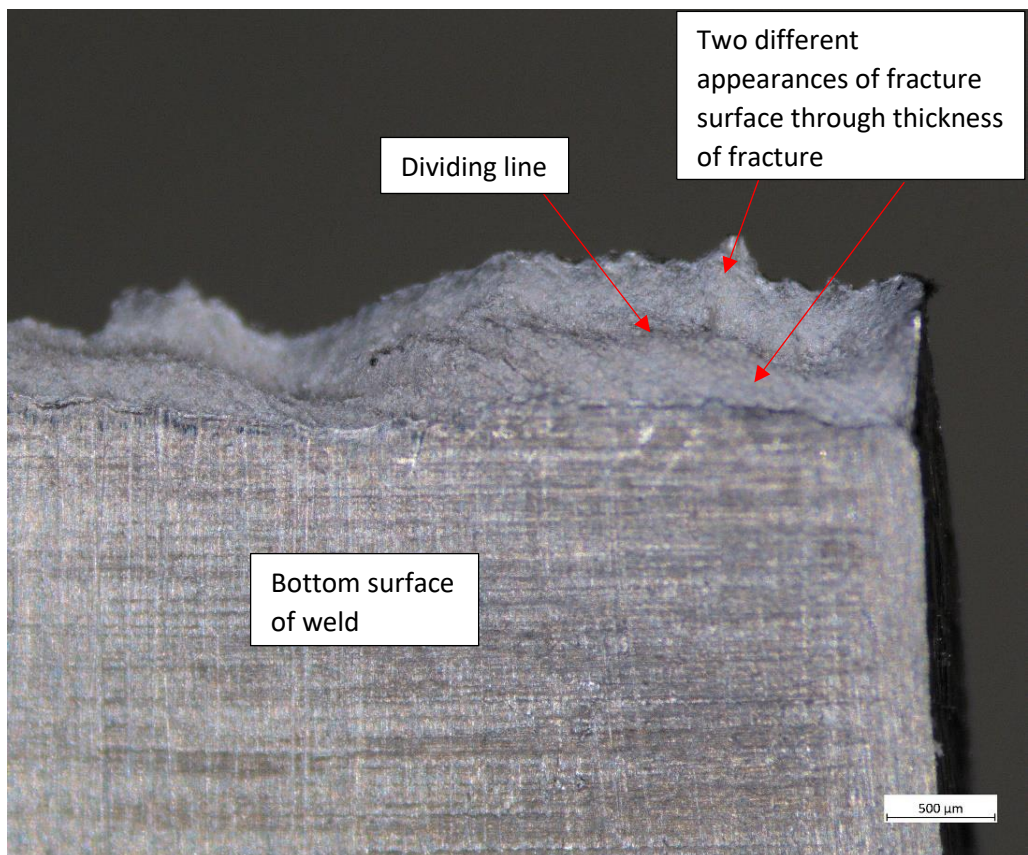
Of the 20 BS L165 II tensile tests performed, one specimen failed at the retreating side edge of weld, with all others failing mid-weld. Of those which failed mid-weld, there was a mix of ragged and rough, and smooth, fracture paths when viewed from the weld top surface. Examples of each failure type, showing position of fracture from the top surface, as a cross section and showing detailed SEM images of the fracture surface are shown in Figure 102 (mid-weld failure with rough crack path), Figure 103 (mid-weld failure with smooth crack path) and Figure 104 (retreating edge of weld).

With reference to Figure 102 and Figure 103, those mid-weld failures (all specimens except one) failed along the approximate mid-point of the weld. The fracture path propagated through the galling and underfill previously described, however these features did not appear to influence the fracture path, i.e. the fracture did not meander to follow the shape of the curve, even in the case of rough and ragged failures. The fracture surfaces of the ragged failures revealed a distinct change in appearance across the thickness of the fracture, with two separate areas and a dividing line between the two, Figure 102(b). Despite the differences in appearance of the two areas, overall the fracture surfaces were dull and matt in appearance and formed a “V” shape over most of the fracture surface. The smooth failures fracture surfaces were sloped at 45° with a small lip adjacent to the bottom surface of the weld and were bright and matt in

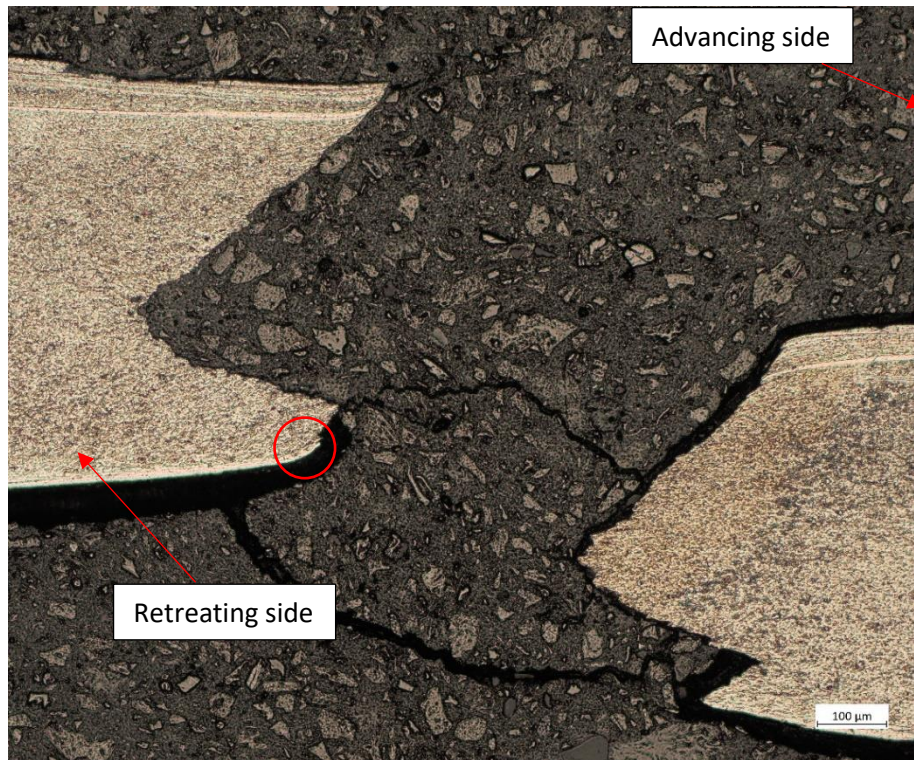
appearance. The etched cross-sections show that both the ragged and smooth failures fractured within the nugget. Although kissing bond remnants cannot be observed extending from the fracture on the cross-sections, they have the appearance of following such a flaw, Figure 102(c) and Figure 103(b), by following the “S” curve typical of a kissing bond. A small amount of alclad appears to have been drawn into the weld at the join line, as shown by the red circles on Figure 102(c) and Figure 103(b) at the end of the fracture on the bottom surface of the weld. The fracture propagated through bands of alclad close to the weld surface, with no apparent effect on the crack path. This is indicative that the alclad layer extending into the weld can have a deleterious effect on the weld quality, but perhaps only if a weakening feature (e.g. a kissing bond) is present. SEM analysis revealed that both types of failure (rough and smooth) had fracture surfaces featuring transgranular failure. Considerably smaller grains than the parent material were noted (as expected as the fracture occurred within the recrystallised nugget) and less microvoid coalescence than the parent material failures, also expected from the smaller grain size and reduction in % elongation, the latter owing to the presence of coarse precipitates rather than fine, strengthening precipitates.



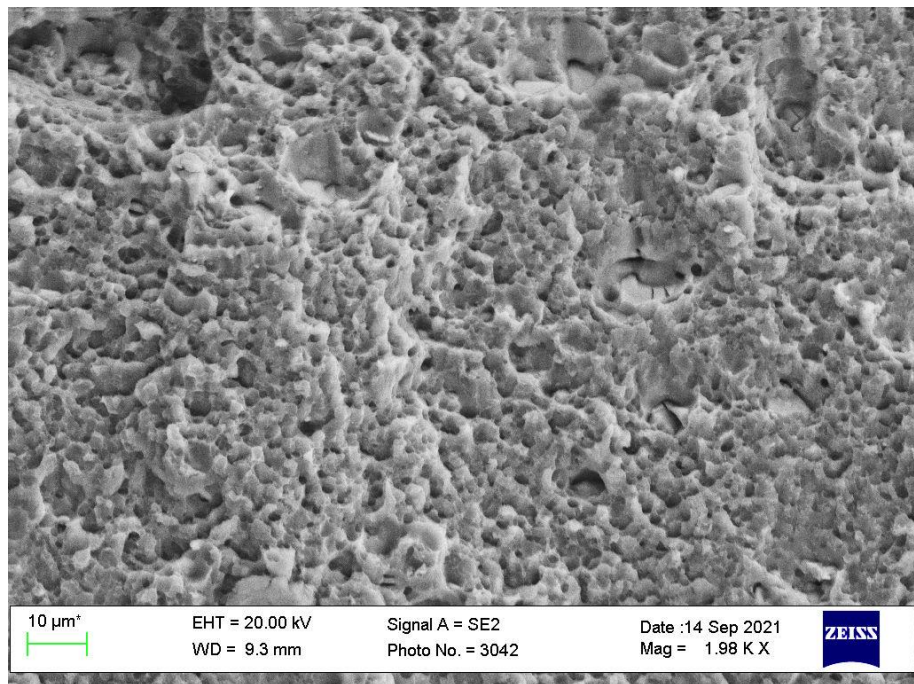
(a)



(b)

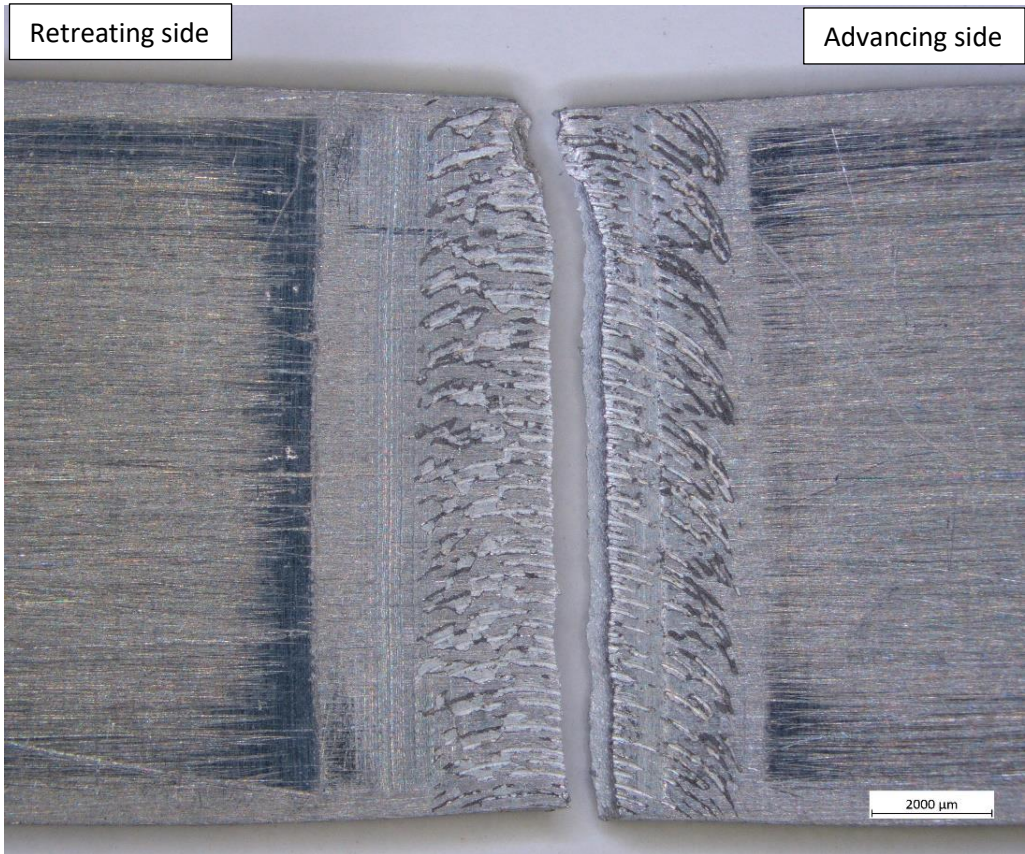


(c)

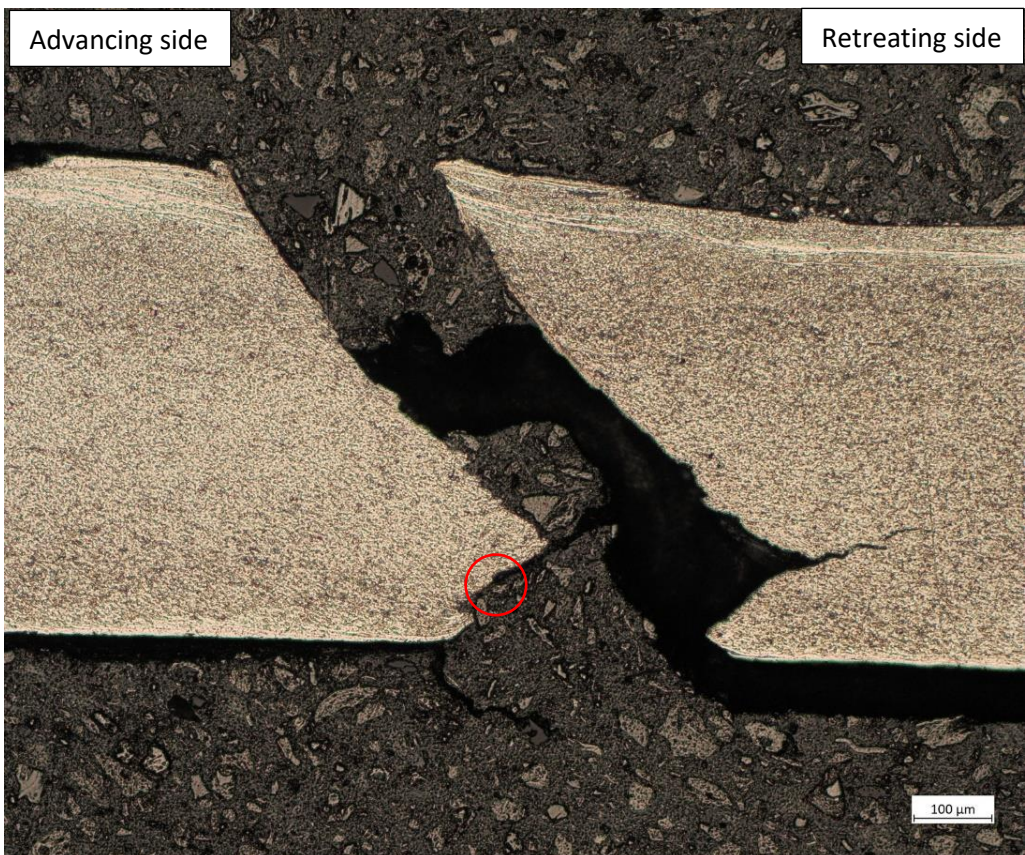


(d)

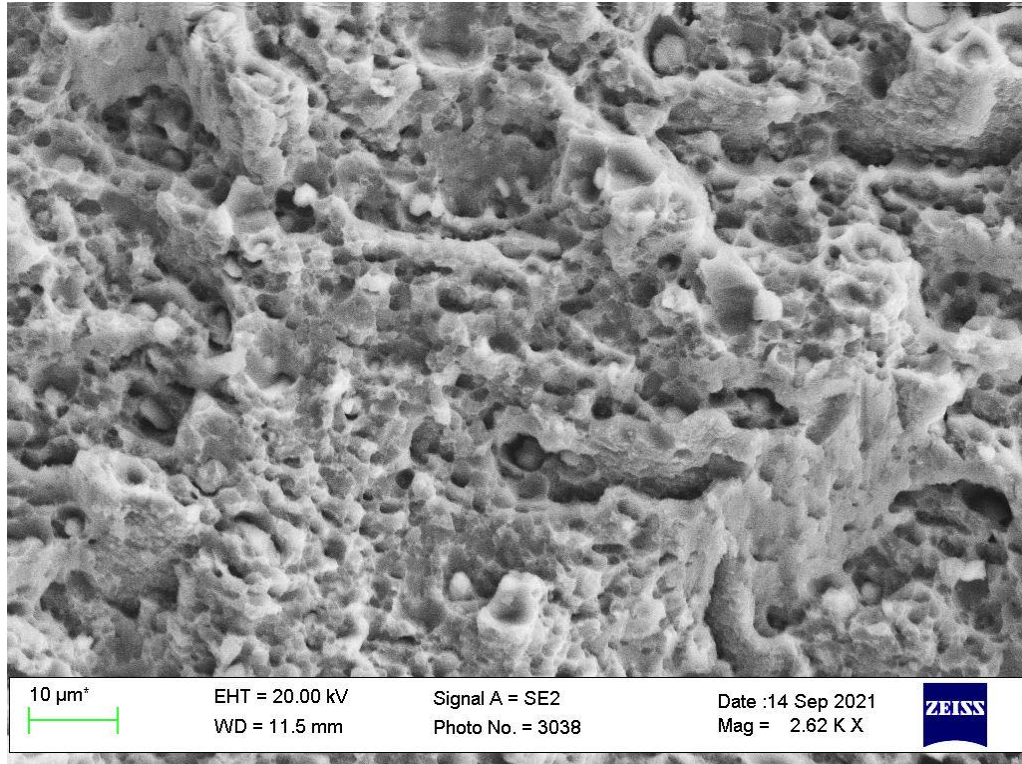
Figure 102: Showing mid-weld tensile fracture of BS L165 II weld with a rough and ragged crack path; (a) micrograph showing fracture from top surface, (b) macrograph of fracture surface (c) cross-section of weld showing crack path, and (d) SEM image showing details of fracture surface.



(a)



(b)

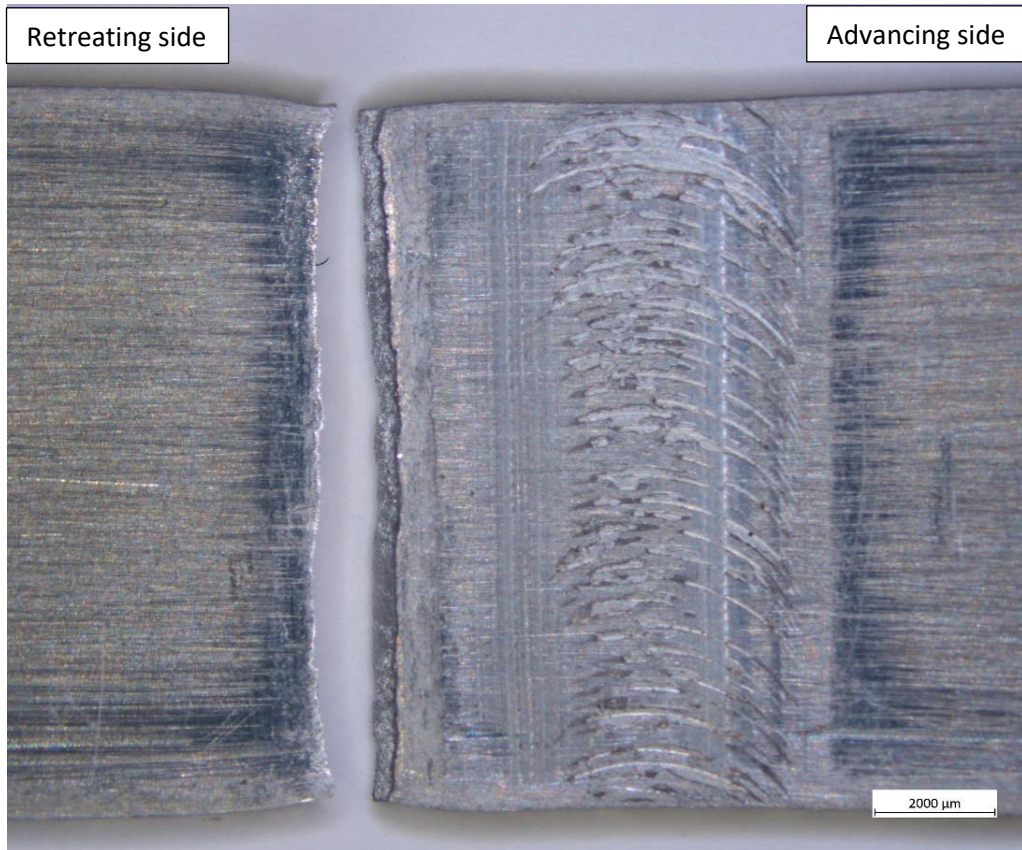


(c)

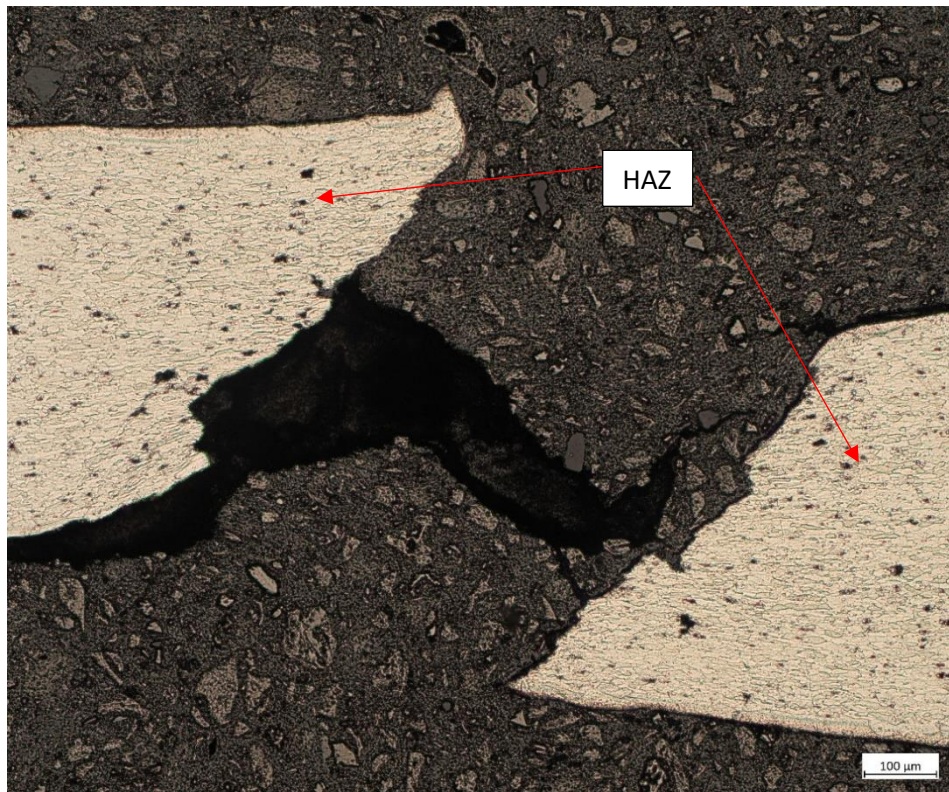
Figure 103: Showing mid-weld tensile fracture of BS L165 II weld with a smooth crack path; (a) micrograph showing fracture from top surface, (b) cross-section of weld showing crack path, and (c) SEM image showing details of fracture surface.

With reference to Figure 104, the one tensile specimen which failed at the retreating edge of weld did so adjacent to the visible edge of the weld when viewed from the top surface. When viewed from this same perspective a small amount of “necking”, i.e. a reduction in cross-sectional area immediately adjacent to the fracture, and a small reduction in cross-sectional area with respect to the material thickness was also observed via the etched cross-section. This necking is indicative of ductility, and upon examination of the test results, this particular test achieved 5% elongation, more than any other test specimen. The etched cross-section also revealed that the fracture occurred comfortably within the HAZ which is consistent with one of the hardness minima for the II welds, and does not appear to have been influenced by the overhang. SEM analysis revealed that the fracture surface was transgranular with significantly more microvoid coalescence than observed on the mid-weld failures. It was noted that,

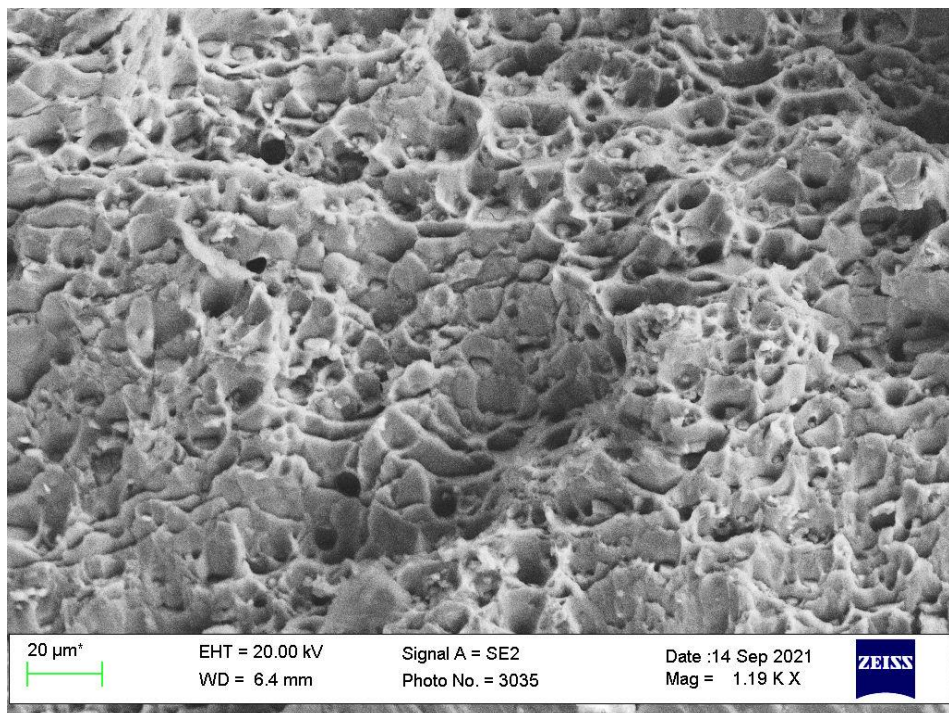
in addition to achieving the highest % elongation, this tensile specimen also achieved the highest UTS value of 447 MPa, although other mid-weld failures were very close. It is considered that this failure occurred at this position as it is likely that there was no kissing bond/ lazy S present at that area of the weld. This suggests that this may be the preferred failure position for this configuration when no weakening flaws are present.



(a)



(b)



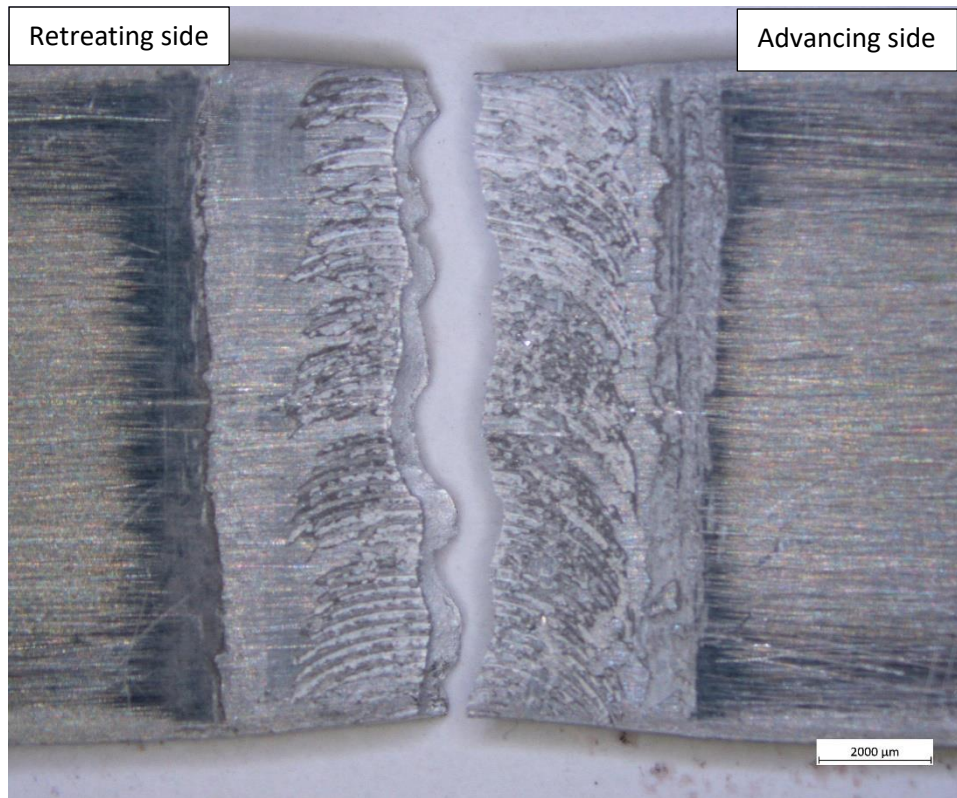
(c)

Figure 104: Showing retreating edge of weld tensile fracture of BS L165 II weld; (a) micrograph showing fracture from top surface, (b) cross-section of weld showing crack path, and (c) SEM image showing details of fracture surface.

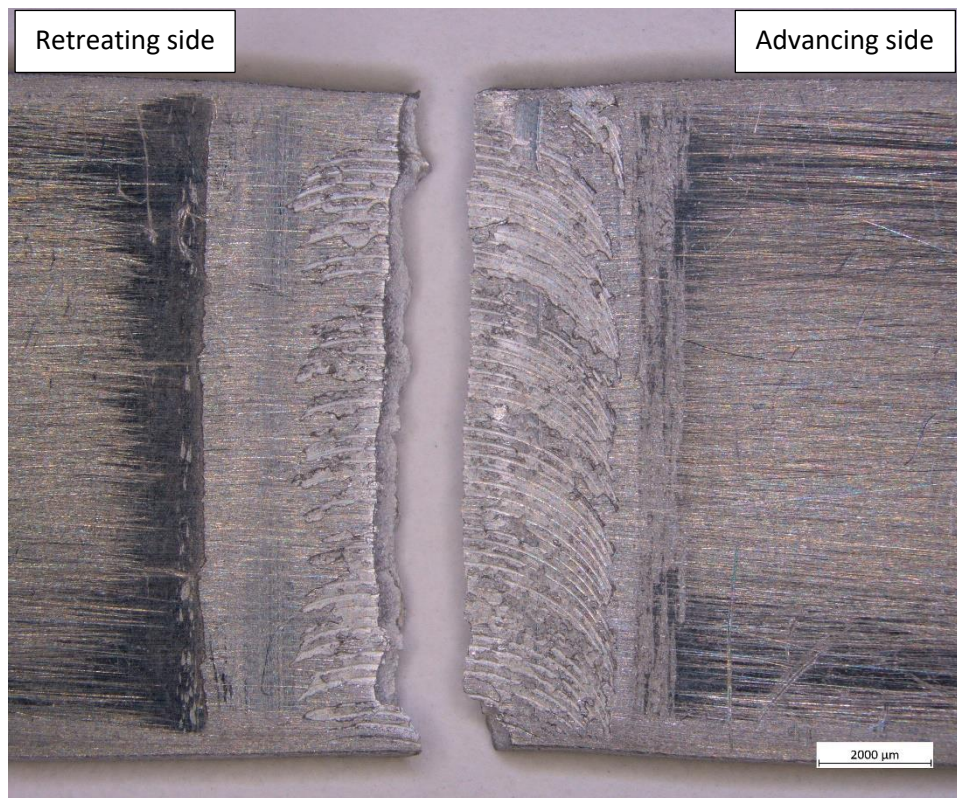
Of the 20 BS L165 \perp tensile tests performed, all failed mid-weld with varying degrees of roughness to the crack path. Images of the differing fracture paths are shown in Figure 105. Most of the test specimen fracture surfaces were dull and matt and sloped at 45° to the loading direction, although there were some with the V shape observed previously and some had a small lip adjacent to the bottom surface of the weld. Again, the crack propagated through the underfill and galling present on the top surface of the specimens, but this appeared to have no influence on the crack path. The etched cross-sections revealed that while overall all failed at 45° to the loading direction, in some cases there was evidence of a kissing bond, revealed by the shape of the failure (Figure 106(a)), while others were diagonally straight with little change in shape to indicate the influence of a kissing bond (Figure 106(b)). The welds all failed within the nugget, and while there were indications of the alclad layer being drawn into those welds with kissing bonds, there was no indication of the alclad mixing close to the weld surface influencing the failure.

For those weld specimens with kissing bonds, the SEM analysis revealed similar fracture surface morphology as observed on the mid-weld II weld failures, as shown in Figure 107(a), i.e., transgranular failure with limited microvoid coalescence. For those specimens with no indication of a kissing bond, the SEM analysis again revealed transgranular failure with limited microvoid coalescence, however those failures had a considerable increase in the volume fraction of large precipitates and intermetallic particles, Figure 107(b). It is considered that the parts of the weld from which these specimens were cut had experienced more heat input than those with kissing bonds. This led to sufficient plasticisation and mixing to avoid kissing bond formation, but also overaged the nugget, allowing re-precipitation and subsequent particle coarsening. The relatively large number of particles set within a matrix of fine grains led to areas of micro stress concentration around the particles and a route for crack propagation.

No discernible pattern could be established regarding type of failure vs. UTS achieved, i.e. there was significant scatter within the results regarding UTS and % elongation and within the type of failure, and no correlation between the two was observed.

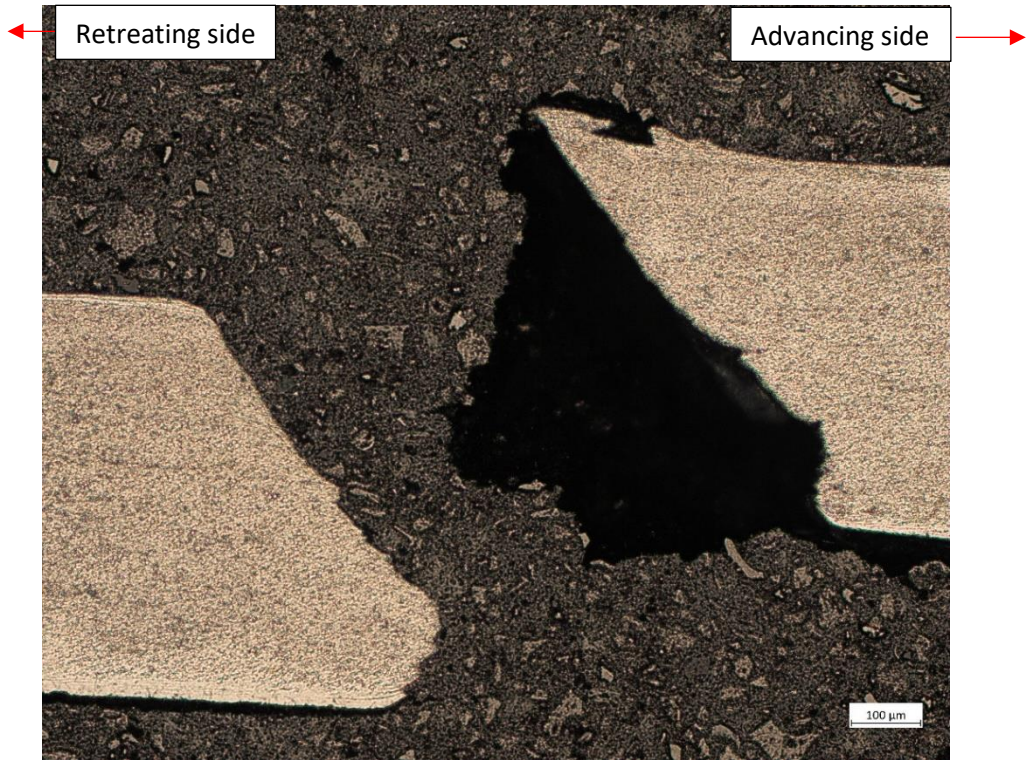


(a)

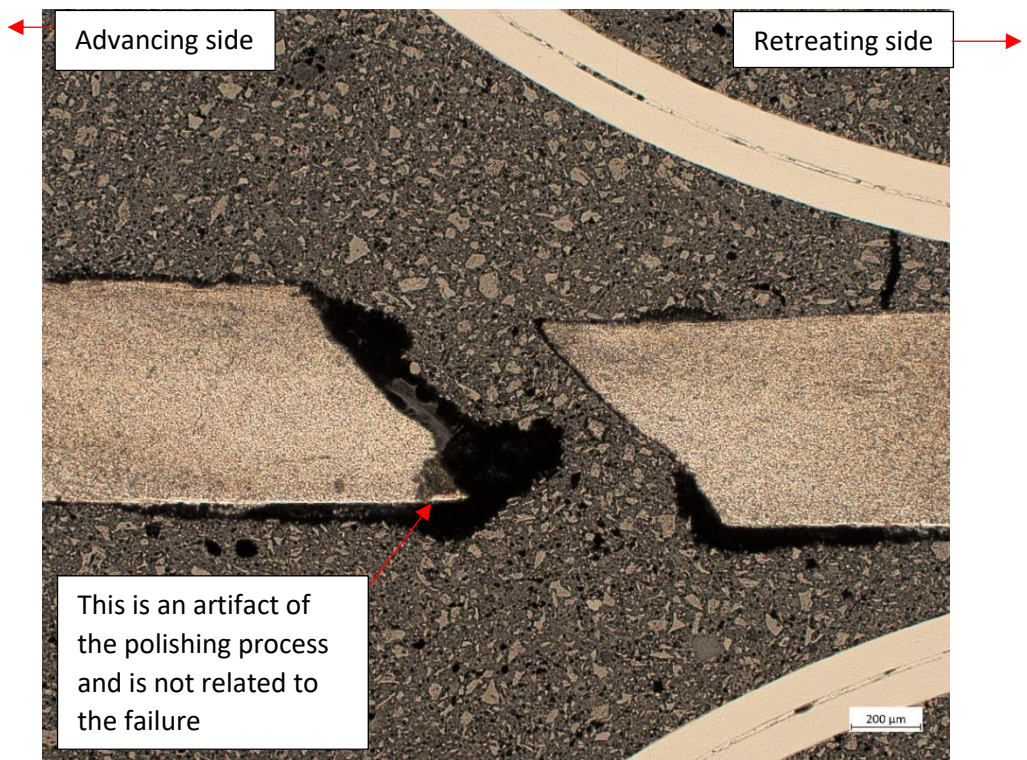


(b)

Figure 105: Showing differing fracture paths of BS L165 \perp tensile tests; (a) ragged and (b) smooth.

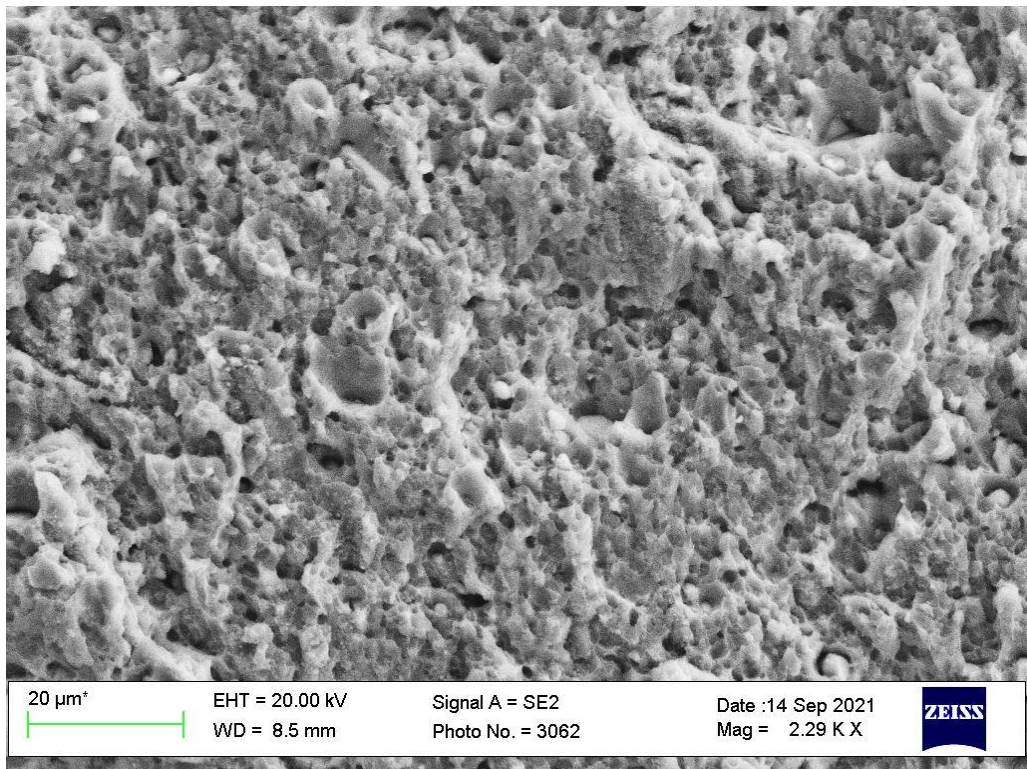


(a)

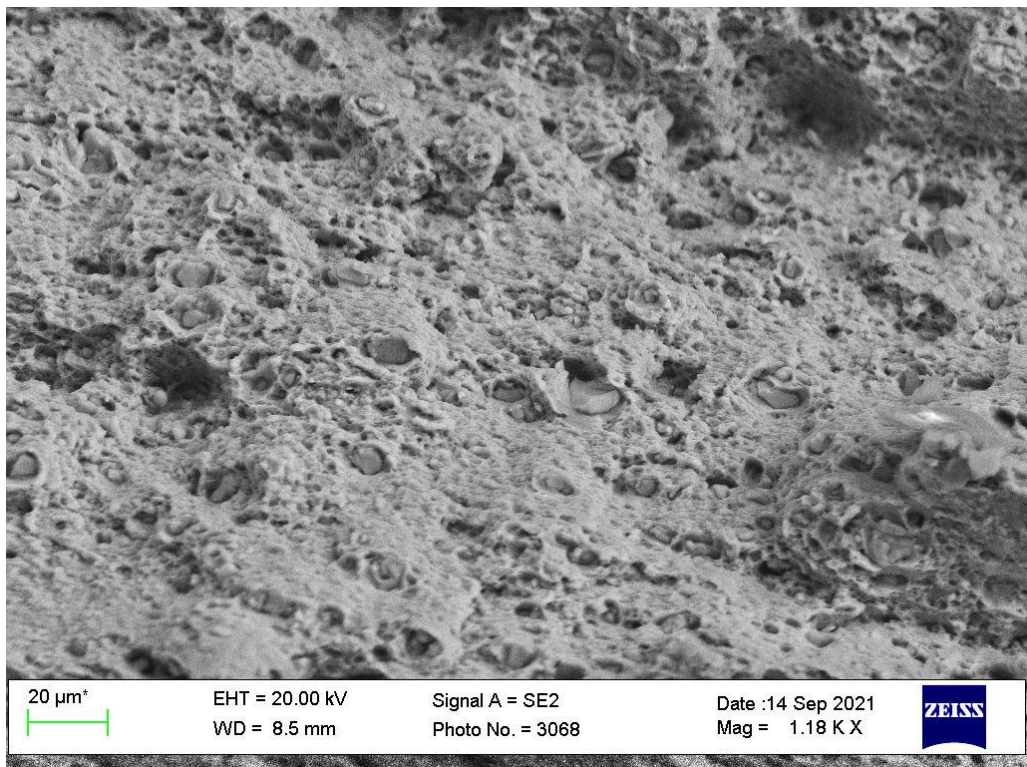


(b)

Figure 106: Showing etched cross-sections of BS L165 \perp tensile specimens; (a) with a kissing bond shape, and (b) almost diagonally straight failure.



(a)



(b)

Figure 107: Showing SEM images of BS L165 \perp tensile specimens; (a) a fracture surface from a specimen with a kissing bond, and (b) a fracture surface from a specimen with no indication of a kissing bond.

6.3.2.3 Fatigue Testing

The BS L165 fatigue results are presented in Table 31 in section 5.2.3.1. The BS L165 II weld achieved approximately 84.6% mean fatigue strength weld efficiency when compared with the parent material, very similar to the results achieved for AA8090 welds. Little research could be found assessing the fatigue strength of FSWs made in this specific alloy, although Aydin et al. (2012) found that the welded fatigue strength was always lower than that achieved by the parent material, regardless of the weld parameters used. They attributed this difference to the reduced ductility inherent in the welded specimens and the presence of different microstructural zones, e.g. TMAZ, HAZ etc. which introduced areas of stress concentration and promoted fatigue crack growth. They also found that almost all welded fatigue specimens failed within the weld, with fractures at high stresses occurring around the nugget and TMAZ on the advancing side, with fractures at low stresses occurring in the HAZ with no preference between advancing and retreating sides.

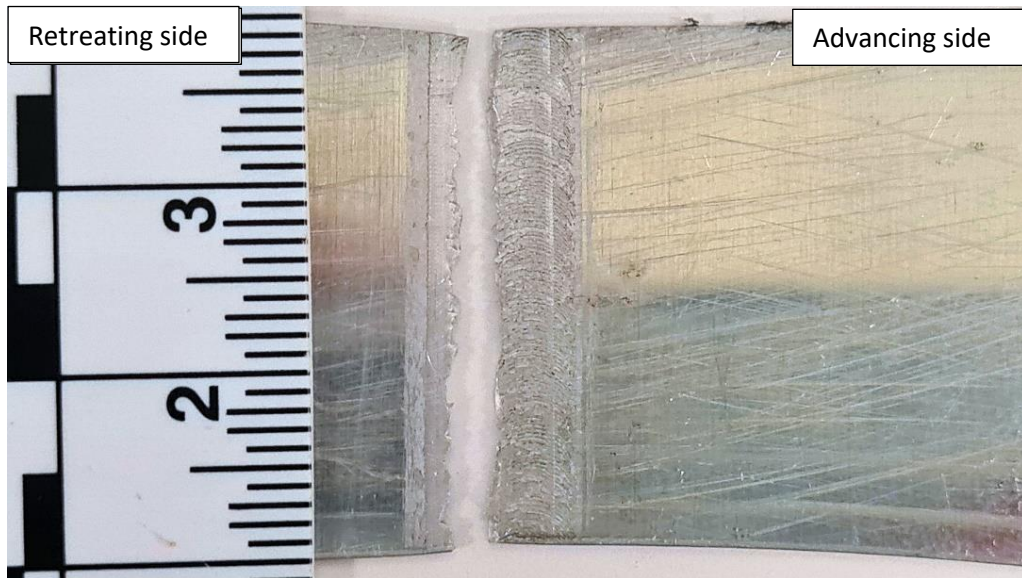
A significantly higher standard deviation and coefficient of variation, i.e. results scatter, was noted for the welded results when compared with the parent material results: 28.76 MPa (standard deviation) and 0.111 (coefficient of variation) for the welded specimens and 11.71 MPa and 0.038 for the parent material. This was similar to the scatter observed for the equivalent results in the AA8090 welds and is considered to be another indicator of the inconsistent weld quality achieved with these weld parameters.

Of the 34 fatigue tests conducted for this configuration, 16 failed prior to the 50,000-cycle cut-off. Of these 16, 13 failed within the weld; most of which were biased towards the advancing side, with three biased towards the retreating side and no failures occurred at the actual mid-weld point. Of the other 3 (of 16) failures, 2 failed at the advancing side EoW, and one failed at the retreating EoW. It was noted that one of the specimens which had the main crack within the weld, featured an additional crack which had propagated along the retreating EoW. Examples of the specimens which failed within the weld (one biased towards the advancing side and one towards the retreating side) and at the advancing and retreating EoW will be discussed. Where examination of fracture surfaces revealed failures occurring as a mix of 90° and 45° to the loading direction, attempts were made to conduct the SEM and cross-sectional analysis at the

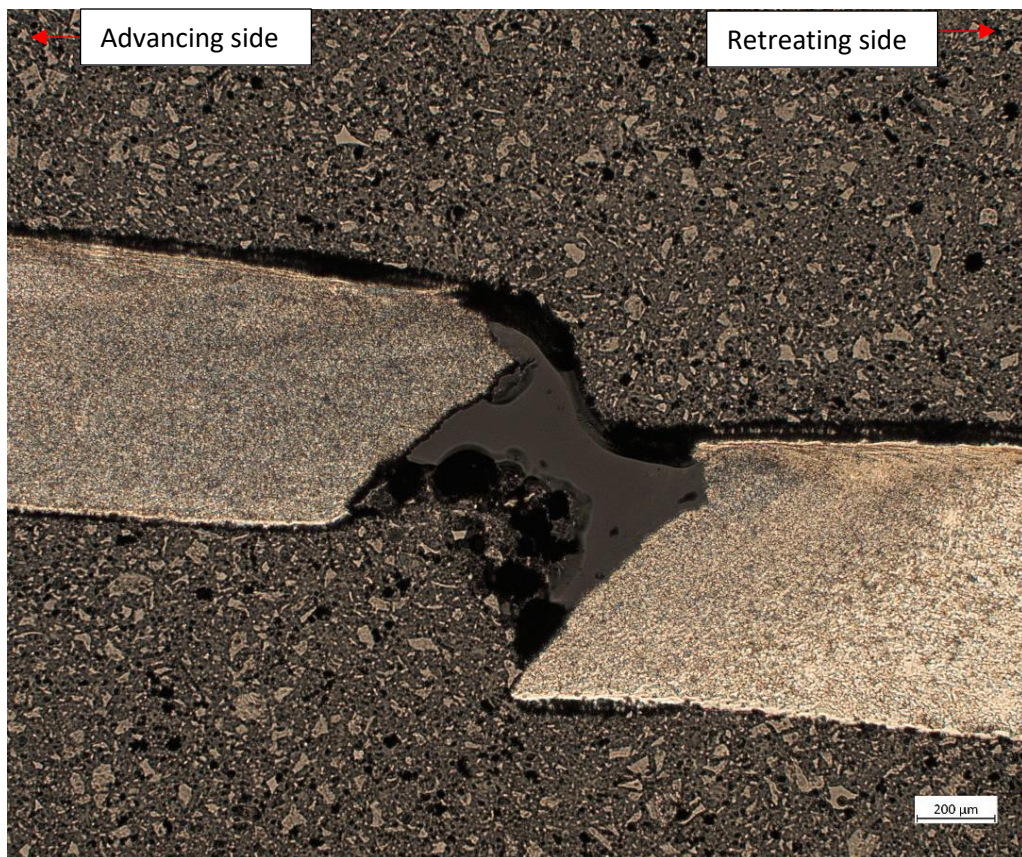
90° area as this is more typical of fatigue failures, with the 45° areas likely to be overload occurring once critical crack length had been achieved.

With reference to Figure 108, a fracture occurring within the weld but biased towards the retreating side is shown. From the top surface, this fracture occurred at the edge of the rippled area, where it changes to a relatively flat surface area. This transition area is likely to be an area of high stress concentration. The fracture surface was rough with some fracture paths orientated at 45° to the loading direction and some at 90°. The cross-section shown in Figure 108(b) shows a small 90° area adjacent to the top surface of the weld, directly below the area of alclad mixing, which then transforms to 45°. The fracture is not coincident with a kissing bond and occurs within the nugget but closer to the retreating TMAZ than to the mid-point. The SEM analysis did not reveal any striations within the 90° area; this was considered to be due to an issue with operator skill as striations were observed on other BS L165 fatigue specimens which failed within the weld. The SEM images shown in Figure 108(c) and (d) are both taken within the 45° area and show transgranular overload with limited microvoid coalescence and the presence of large particles.

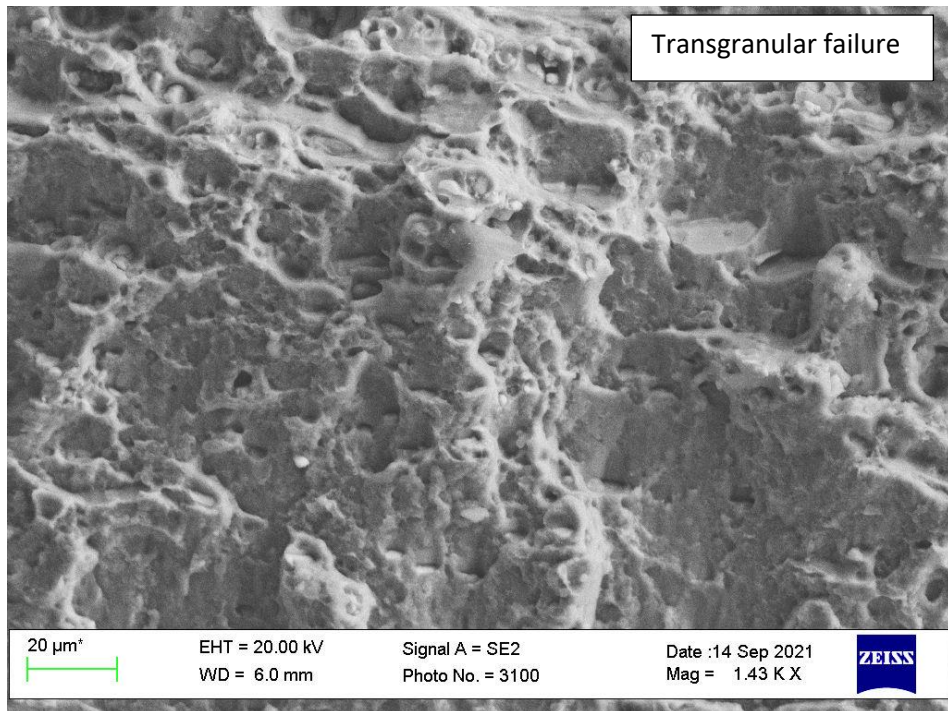
It was noted that a large variation in cycles to failure existed in those specimens which failed within the weld. Some achieved only ~19,000 cycles while others were close to the 50,000 cut-off. This indicates that there is no discernible pattern regarding cycles to failure at this position of fracture, and this can likely be attributed to variation in the thermal input, i.e. from the use of force control rather than position control during SSFSW.



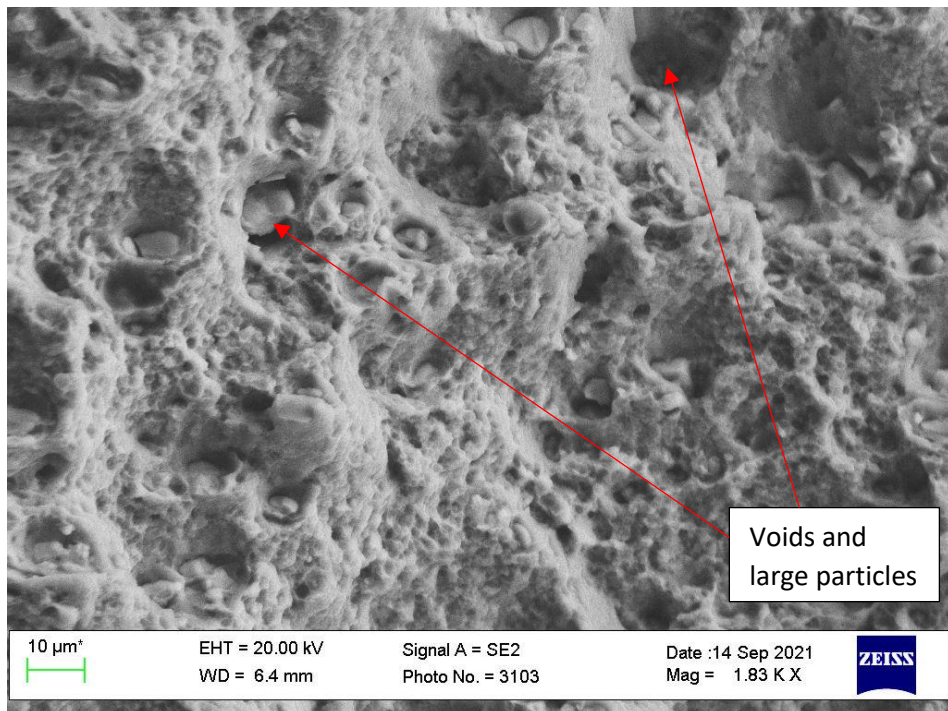
(a)



(b)



(c)

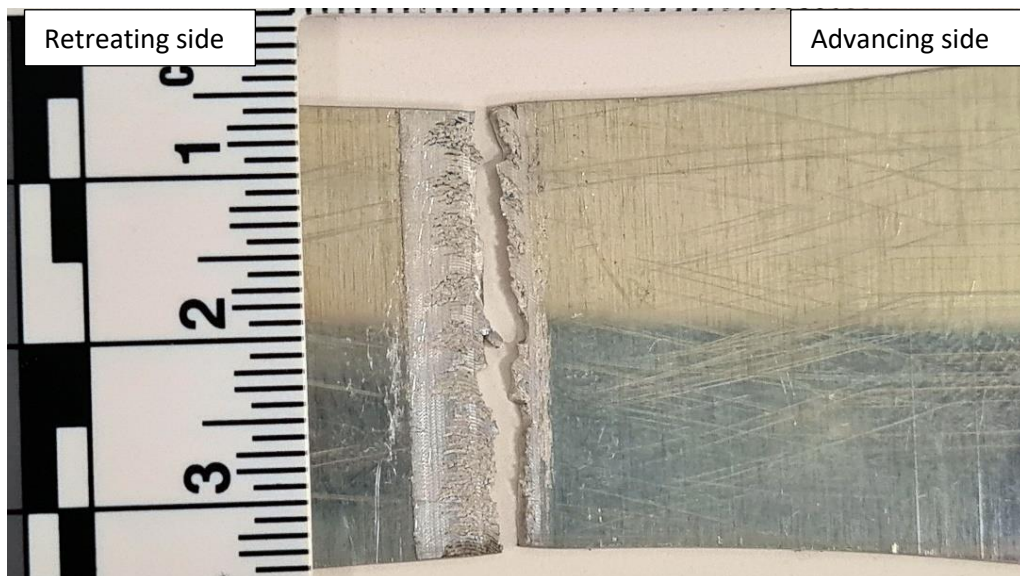


(d)

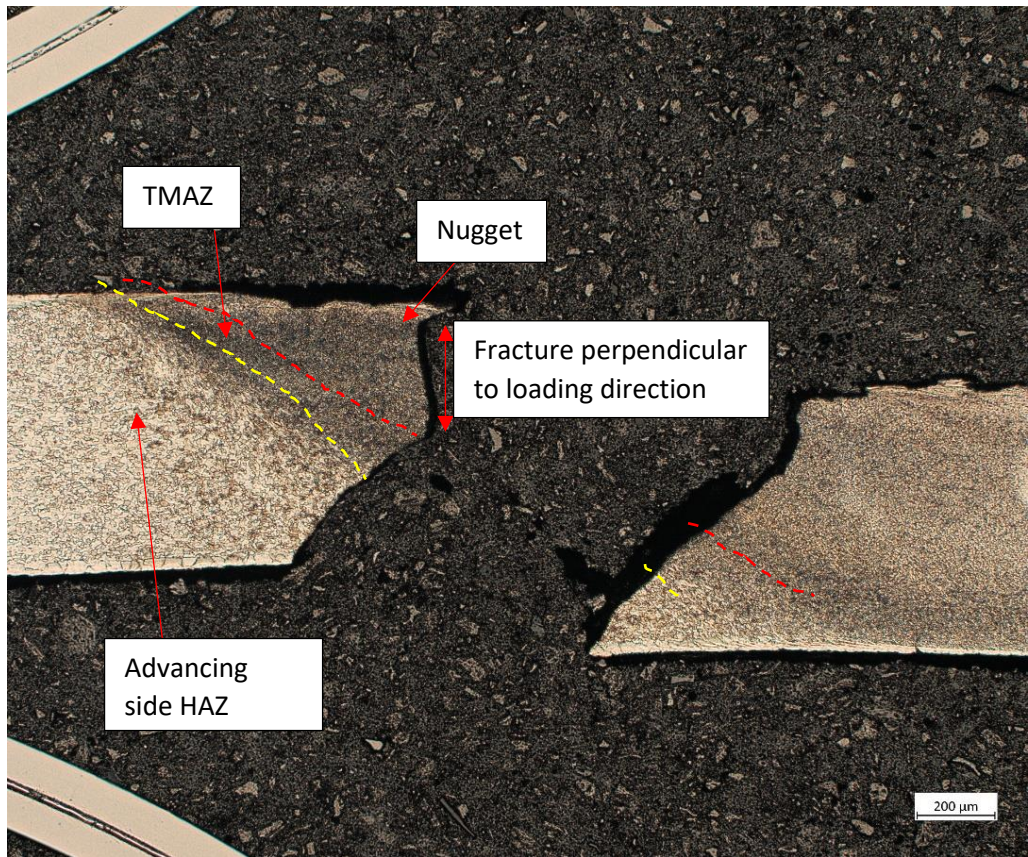
Figure 108: Showing an in-weld fatigue fracture biased towards the retreating side of a BS L165 weld; (a) micrograph showing fracture from top surface, (b) cross-section of weld showing crack path, (c) and (d) SEM images showing details of fracture surface.

Figure 109 shows an in-weld failure biased towards the advancing side. The fracture occurred close to the top of the rippled area and is again likely to be an area of stress concentration. The fracture surface was a mix of 45° and 90° orientations similar to the previous example, however this fracture was considered to have a more convoluted crack path across the weld, when compared with Figure 108(a). The cross-section of the fracture surface shows a shallow 45° area through the alclad-mixing zone on the top surface of the weld. The crack propagation then changed to perpendicular to the loading direction through a significant portion of the weld nugget and then changed back to 45°, travelling through the advancing TMAZ and HAZ. The SEM image shown in Figure 109(c) shows a thumbnail shaped area underneath the alclad-mixing region adjacent to the top surface, surrounded by areas of microvoid coalescence. It is considered that the thumbnail region is where the fatigue crack initiated, before propagating through the alclad-mix region and the surrounding area, before failing in overload once the critical crack length was reached. This was confirmed with striations being present in the thumbnail region (Figure 109(d) and ductile microvoid coalescence in the surrounding area (within the HAZ - Figure 109(e)).

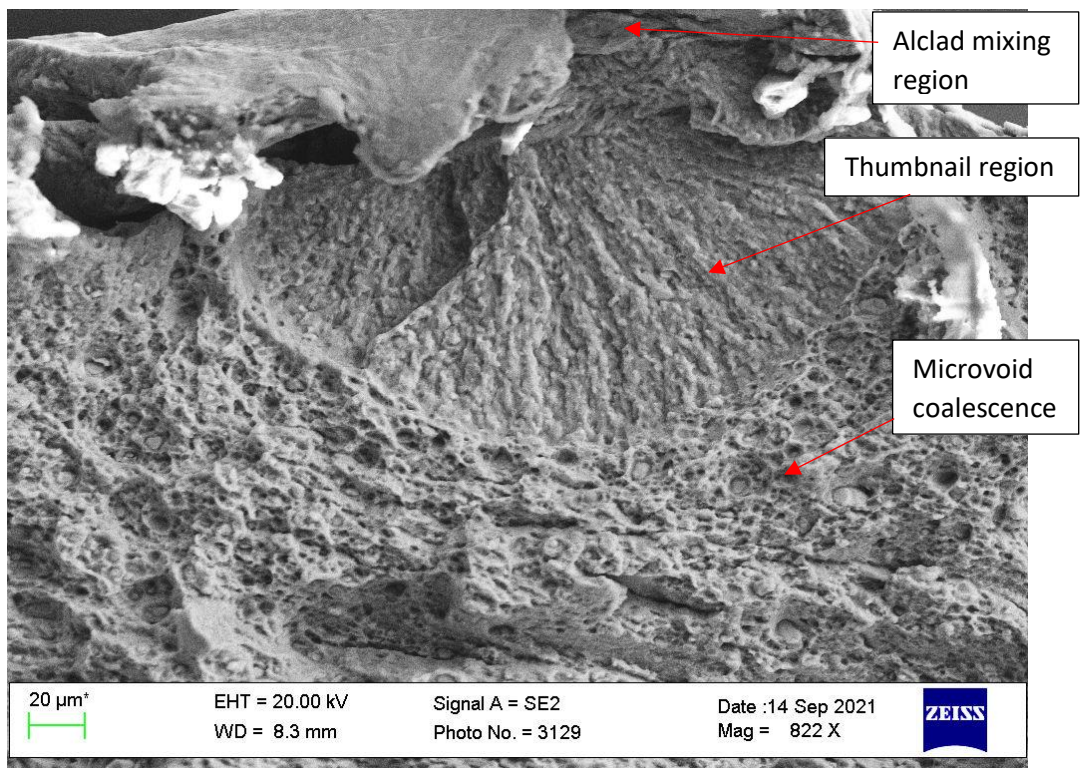
Again, no discernible pattern regarding cycles to failure was observed with this position of failure.



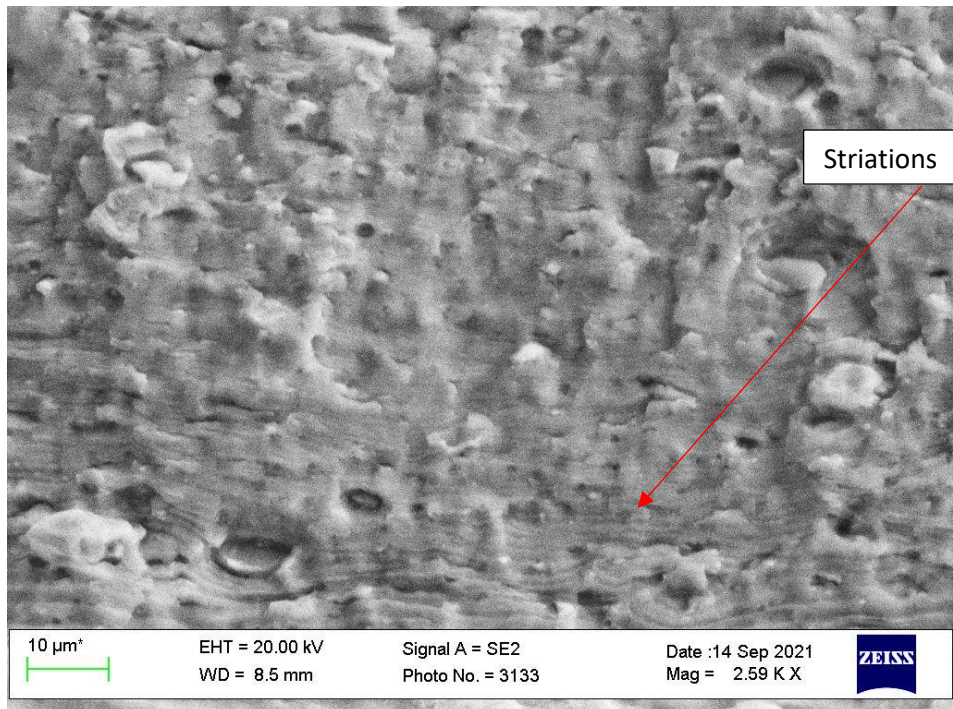
(a)



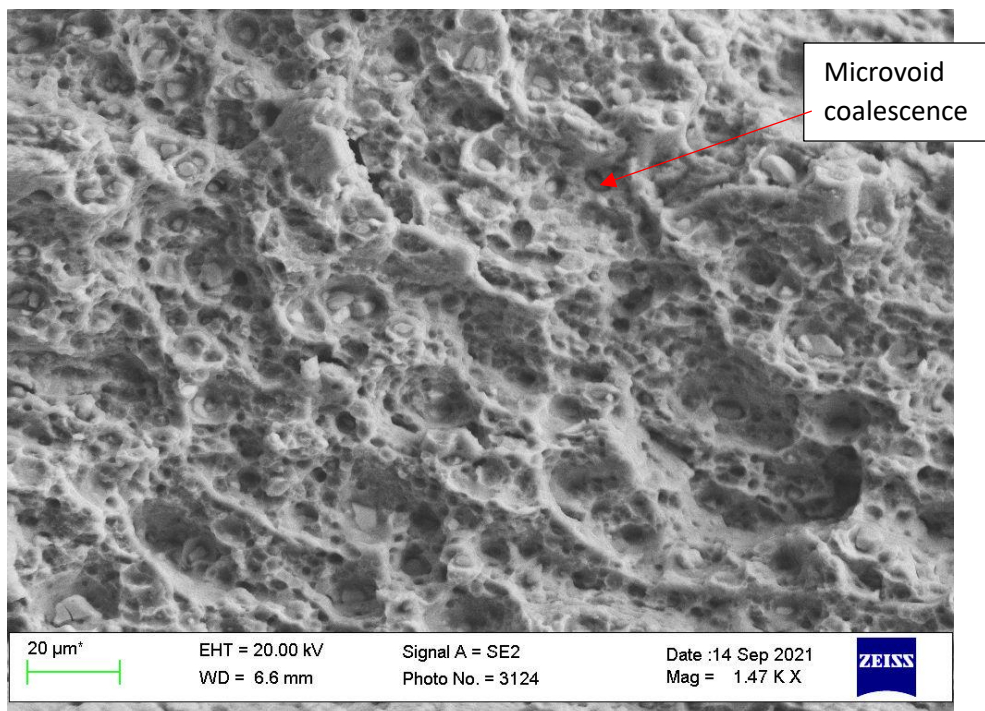
(b)



(c)



(d)

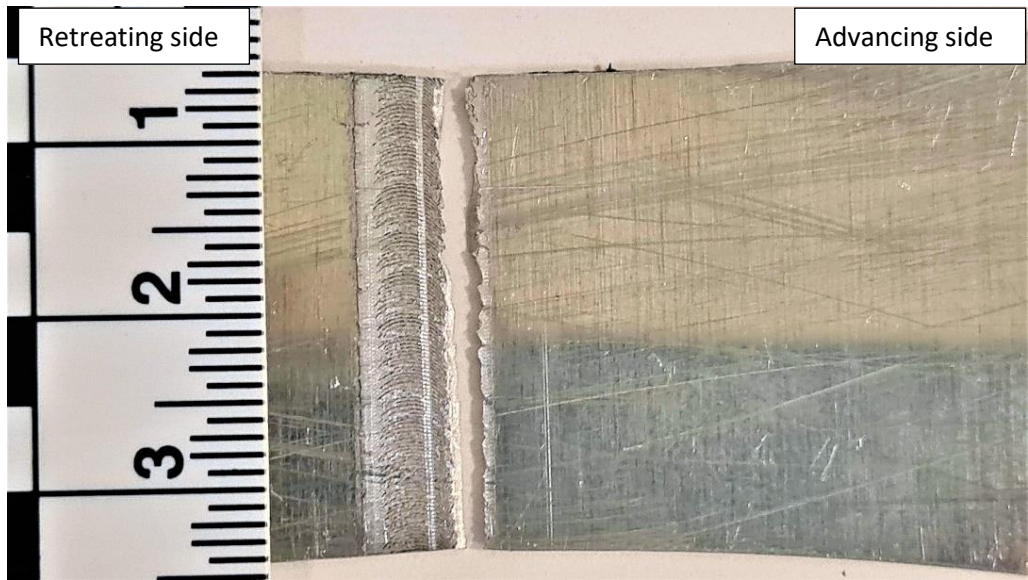


(e)

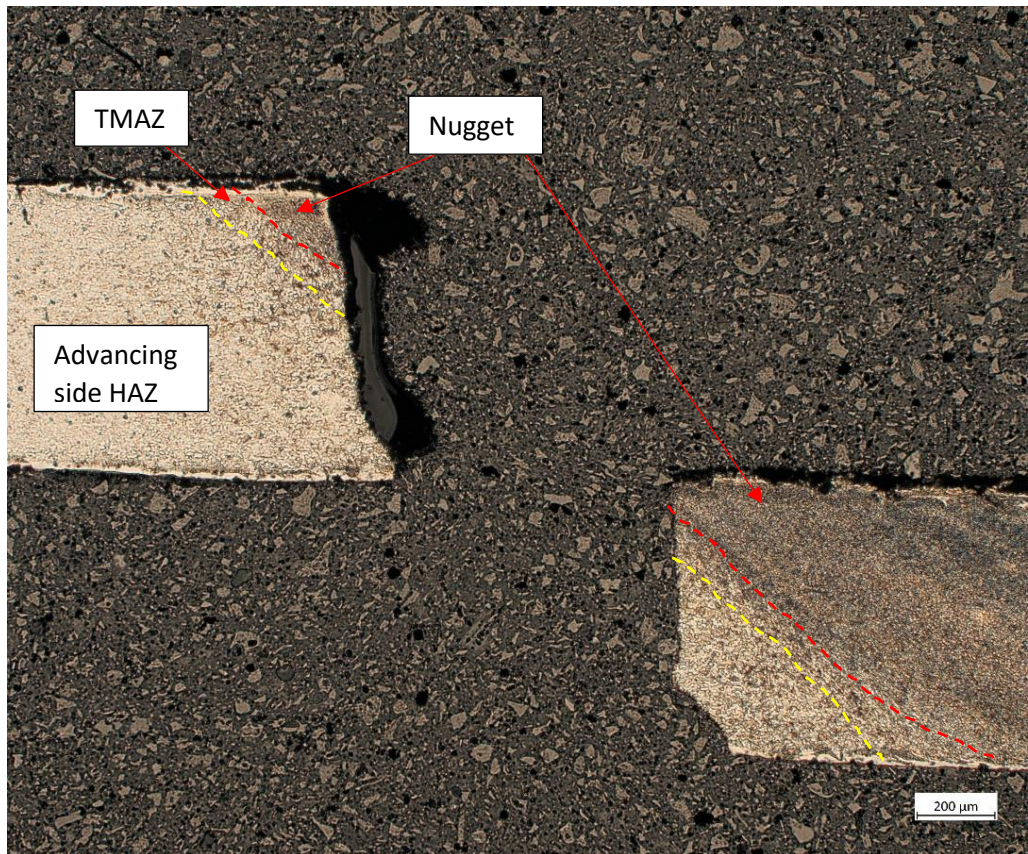
Figure 109: Showing an in-weld fatigue fracture biased to the advancing side of a BS L165 weld; (a) micrograph showing fracture from top surface, (b) cross-section of weld showing crack path, (c), (d) and (e) SEM images showing details of fracture surface.

With reference to Figure 110, an example of a failure occurring on the EoW at the advancing side is shown. Parts of the crack path appear to coincide with the tips of the rippled region, a clear area of stress concentration. The fracture surface was again a mix of 45° and 90° orientations, with each occurring at different areas along the weld length. The cross-section shows that the crack initiated at the top surface, propagated perpendicularly to the loading direction through most of the thickness with the final part failing at 45° to the loading direction. The crack propagates for only a short length through the nugget and TMAZ, before entering the HAZ for the majority of its propagation. It was considered that the majority of the crack was caused by the fatigue mechanism through the material thickness indicated by the 90° failure which was confirmed by SEM analysis. This is as anticipated of a fatigue crack propagating perpendicular to crack opening stresses. It is likely that the crack initiated from the ripple tips at the top surface, which is shown on the SEM image Figure 110(c); this shows “ratchet” marks, features located adjacent to the ripple tips which indicate multiple crack initiation points. The crack then propagated at 90°; because of the crack initiation location at the ripple tips on the advancing side EoW, only a short distance through the nugget and TMAZ was traversed. This allowed the crack to propagate within the HAZ and, owing to the increased ductility within the HAZ due to larger grain size than within the nugget, the crack could achieve a longer critical length before the material failed in final overload. Striations were observed both in the nugget fatigue area and the HAZ fatigue area (Figure 110(d)), with ductile overload shown in the area of final failure.

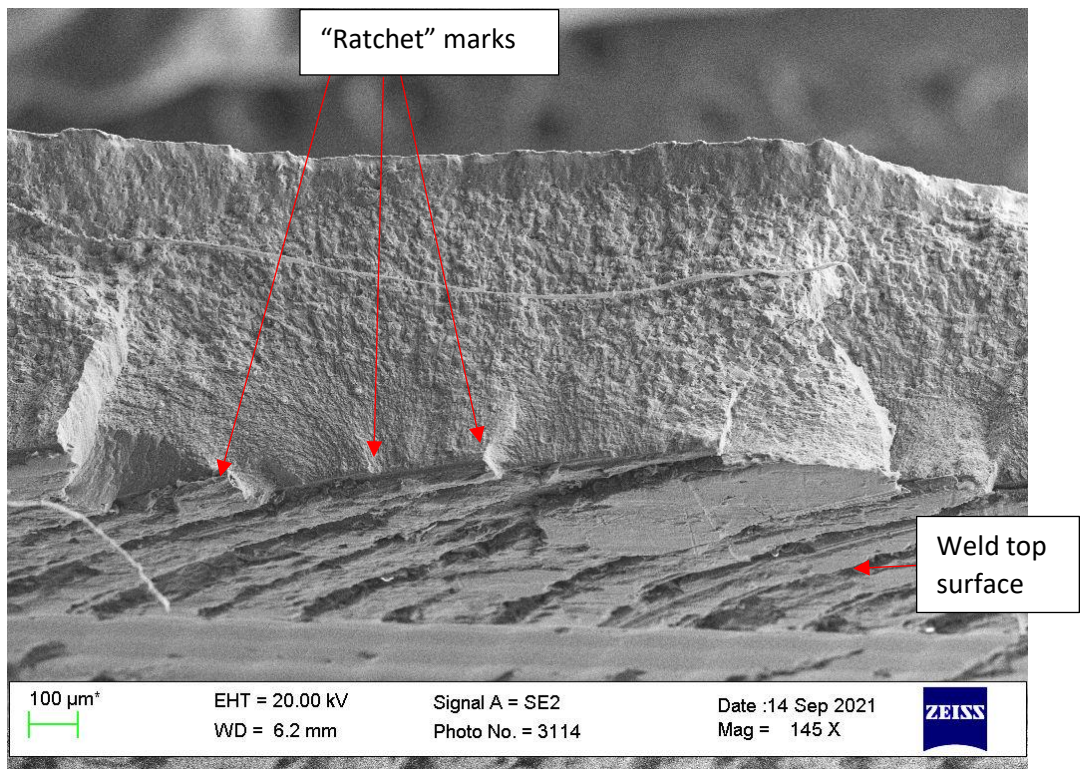
The two specimens which failed at this position achieved relatively high cycles to failure: ~42,500 and ~45,500. This is attributed to the mainly transgranular crack propagation, allowing more consistent damage tolerance than if the crack initiated within the weld.



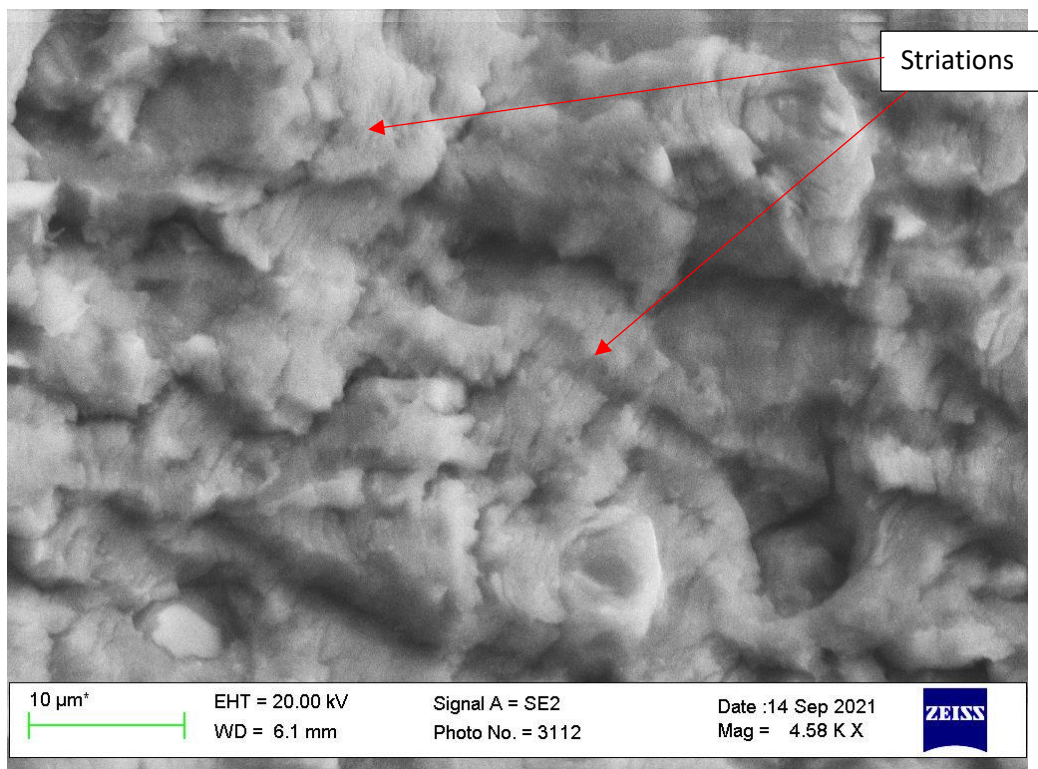
(a)



(b)



(c)

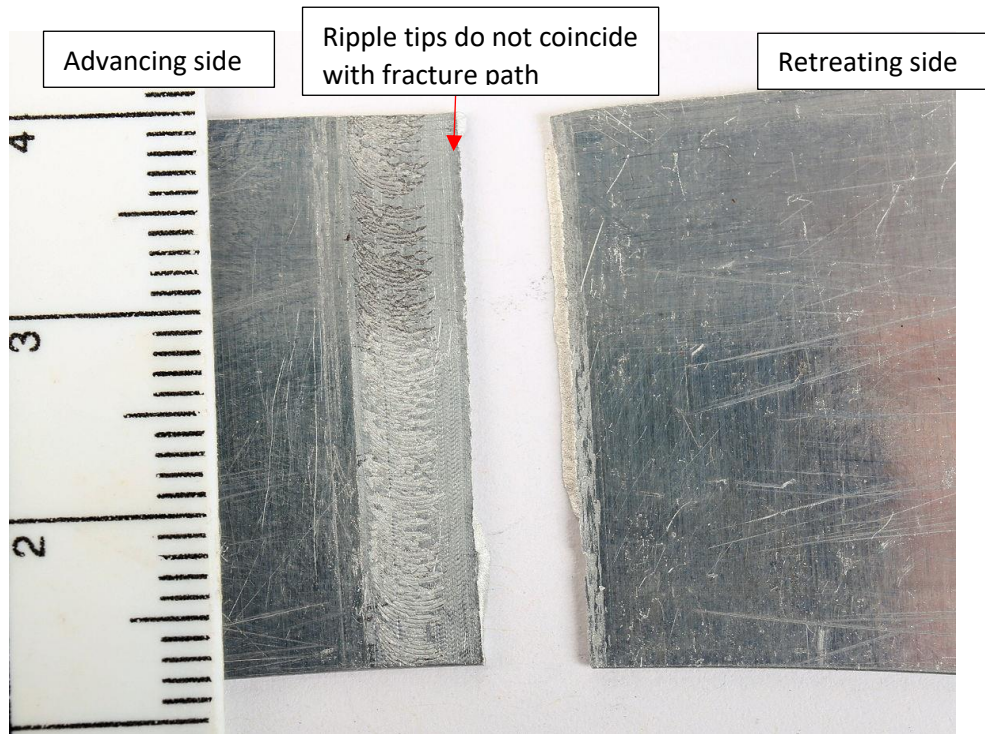


(d)

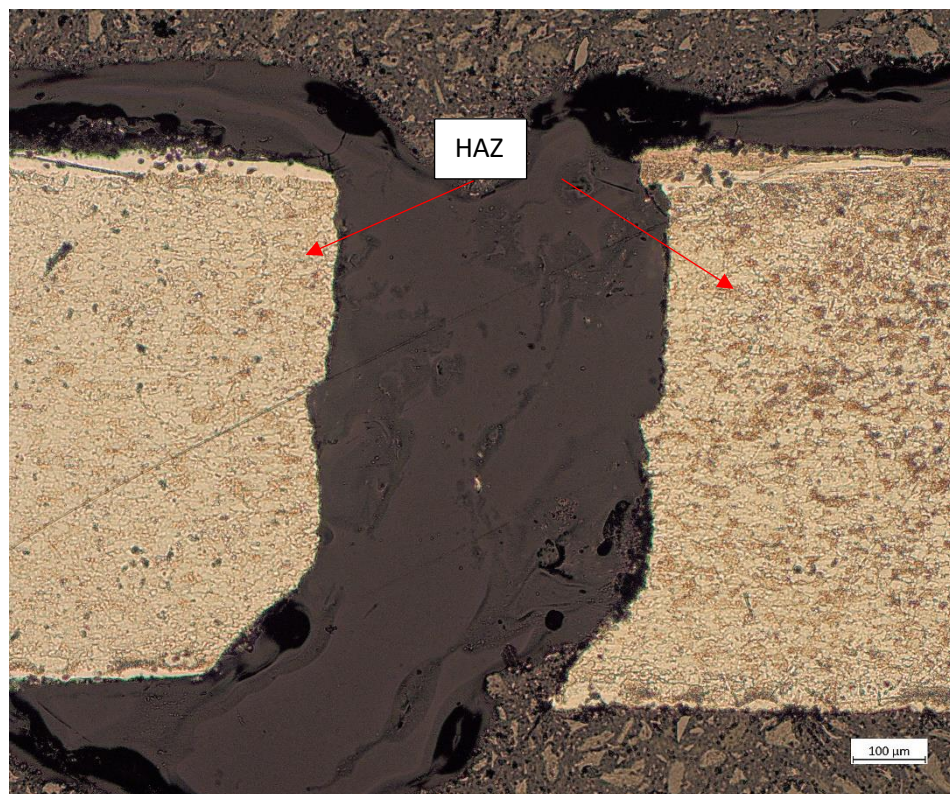
Figure 110: Showing advancing EoW fatigue fracture of BS L165 weld; (a) micrograph showing fracture from top surface, (b) cross-section of weld showing crack path, (c) and (d) SEM images showing details of fracture surface.

The specimen which failed at the retreating EoW was similar to the advancing EoW failures in fracture surface topography and appearance, and the SEM analysis revealed similar results, therefore these are not repeated here. There were however a few differences, shown in Figure 111. The image of the specimen showing the fracture from the top surface indicates that the crack did not initiate from the ripple tips as was the case for the advancing EoW failures. This is not unexpected as the ripples did not extend to the retreating EoW (section 6.3.1.2). Instead, this crack has propagated along the edge of the weld visible from the top surface, with only deposited alclad material beyond it. This area is visually flat but optical and surface profilometry did indicate a sharp rise in material at the retreating side edge (Figure 89), which would be sufficient to act as a stress raiser. The cross-section shows that the crack initiated at the edge of the surface alclad-mixing region, again an area of high stress concentration. The crack then propagated through the HAZ without entering the nugget.

This specimen achieved only ~26,000 cycles before failure. The low fatigue resistance, combined with it being a singular failure means that it is likely that a flaw existed in that specimen prior to testing, e.g., a surface scratch or defect within the weld, causing an area of high stress concentration. It is likely that had this flaw occurred within the nugget area, that the specimen would have failed at a far lower cycle value, and that it was able to survive to ~26,000 cycles due to the ductile nature of the HAZ.



(a)



(b)

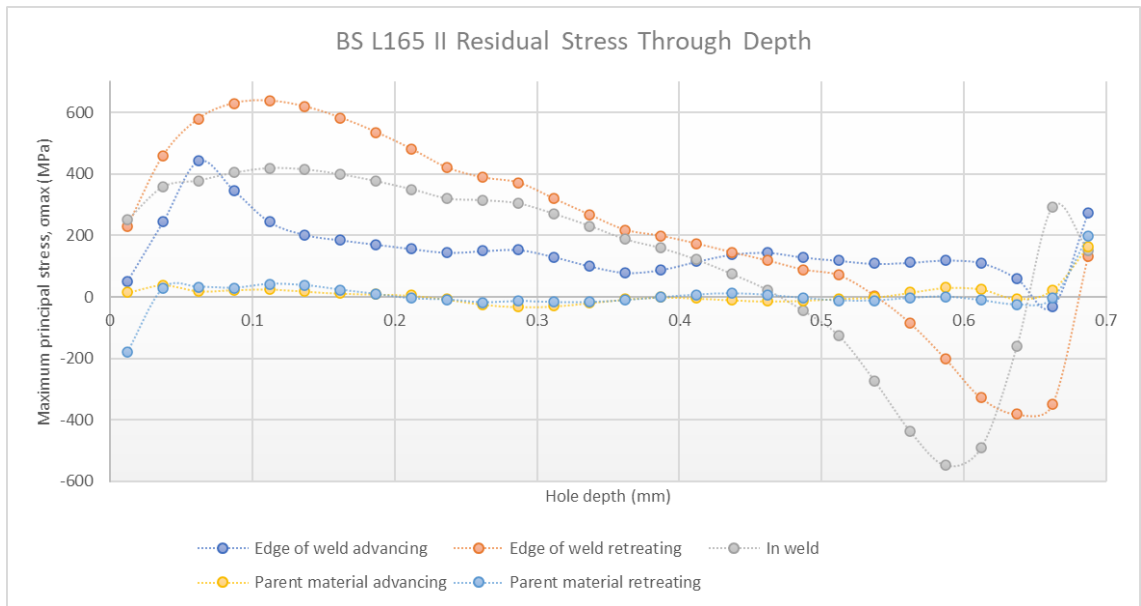
Figure 111: Showing retreating EoW fatigue fracture of BS L165 weld; (a) micrograph showing fracture from top surface, (b) cross-section of weld showing crack path.

6.3.2.4 Residual Stress (RS)

6.3.2.4.1 Residual Stress with Hole Depth

The RS results plotted against the drilled hole depth are shown for both orientations (|| and \perp) in Figure 112. Again, only the results at hole depths 0.06-0.4 mm are considered in the analysis. The results exceed 80% of the yield strength, and in many cases are well in excess of the materials UTS. For the reasons described in section 6.2.2.4.1, the calculated values have again been disregarded and the results considered only in a qualitative manner for analysis.

See sections 2.3.9.3.4 and 6.2.2.4 for reasons for RS generation within FSWs. All datasets for BS L165 II were accounted for. As expected, all parent material measurements remained at approximately zero throughout the depth. All EoW retreating and advancing sides, and the nugget RS measurements were high in tension close to the weld surface and reduced gradually with depth. This original high value is considered to be due to the surface friction influence in that area which has been significantly affected by thermal input and oxidation. It was noted that as the alclad layer has an average thickness of only 4% of the bulk material (0.028 mm average thickness), in this case this thickness does not interfere with the depths of interest, i.e. starting at 0.06 mm, therefore the high value at shallow depths is only influenced by the frictionally affected area on the surface. No specific influence of the alclad layer at greater depths, i.e. where it mixes within the nugget were observed.



(a)



(b)

Figure 112: Showing residual stress results plotted against drilled hole depth; (a) BS L165 II, and (b) BS L165 ⊥.

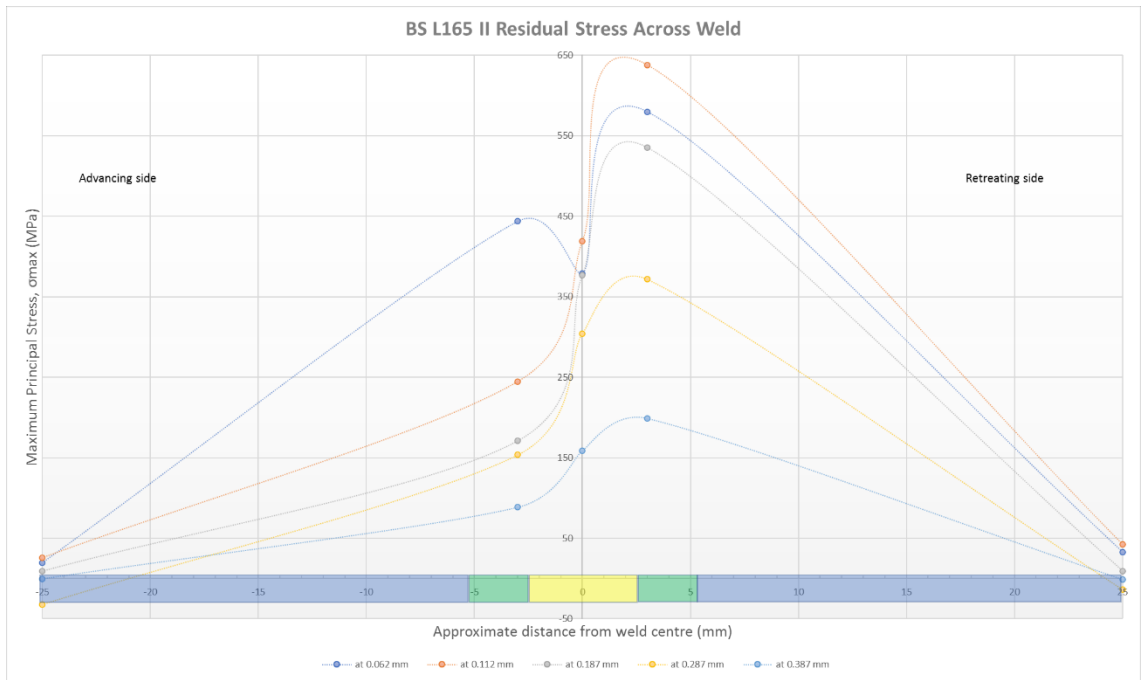
The EoW advancing side results were lower than the EoW retreating and nugget results. For all other configurations (e.g. AA8090 welds and dissimilar welds) with results considered to be valid (i.e. not excessively fluctuating), the EoW advancing side result measured equal to or higher than the nugget. In this case, although the EoW advancing does follow a similar shape as the EoW retreating and nugget (with the exception of 0.06 mm), the lower result may indicate that this dataset may be invalid. The parent material

on the retreating side was missing for BS L165 \perp , however the other results are considered to be qualitatively valid.

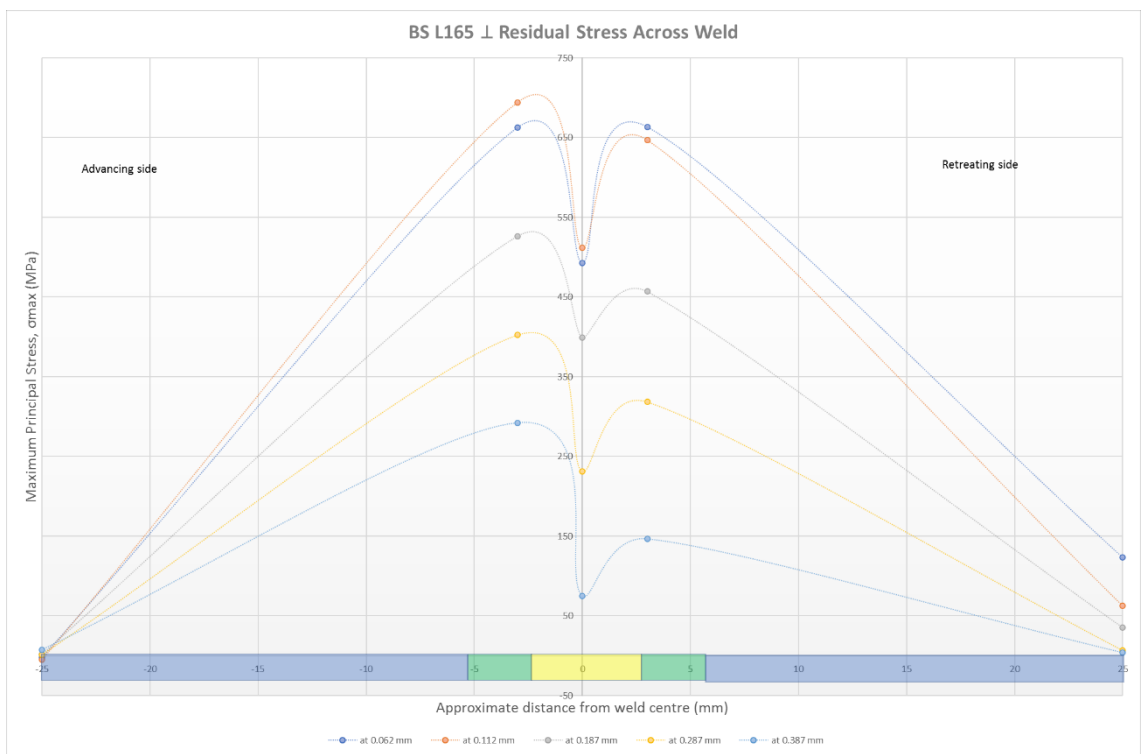
For both II and \perp welds the retreating EoW RS was higher than within the nugget; this is attributed to the same reasons as AA8090-AA8090 welds (section 6.2.2.4.1). As previously described, the advancing EoW is lower than the nugget RS in the BS L165 II welds. An explanation for this may be due to the heat input being of sufficient temperature to carry out a stress-relieving heat treatment in the advancing EoW, while overaging the nugget. The heat input is generally considered to be higher on the advancing side than the retreating side. However, no indication of this having occurred was observed in the microstructure, therefore it is unclear as to whether the heat treatment occurred, or if the result is unreliable. Further work is required to conduct additional RS testing at this position to test this theory.

6.3.2.4.2 Residual Stress Across Weld

The residual stress across the weld, i.e., measurements taken at advancing and retreating parent materials, HAZ and within the weld nugget, is shown in Figure 113 at various hole depths. There was no result for BS L165 retreating side parent material due to faulty tests and time constraints (this is missing from Figure 112(b)), therefore a “stand-in” result was used from the AA8090-BS L165 \perp weld retreating parent material to complete the plot. As with the AA8090-AA8090 RS plots, the EoW tests incorporate both HAZ and TMAZ, and the plots show the approximate weld zone of the test.



(a)



(b)

Figure 113: Showing residual stress across weld at varying hole depths: (a) BS L165 II and (b) BS L165 ⊥.

Having a reduced advancing EoW result for the II weld has influenced the shape of the cross-weld plot. Only the value at 0.062 mm resembles the classic “M” shape expected

from the literature (see section 2.3.9.3.4), with the retreating arms of the M in that case heavily outweighing that of the advancing side. All other depths are of an “S” shape, with reducing gradients with increasing depth. No FSW RS research can be found which takes this S-shape, suggesting that the advancing EoW in this case was an erroneous result. The \perp weld RS plots all take the classic M-shape, with the advancing EoW predominantly exceeding that of the retreating. The advancing side RS exceeding that of the retreating can be attributed to the increased thermal input to this side as discussed previously.

No compressive measurements were recorded in this testing, similar to the AA8090-AA8090 welds. Again, this can likely be attributed to insufficient data points, and if additional tests were conducted between the EoW points and the parent material measurements it is expected that compressive readings, which would balance the tensile measurements, would be obtained within the HAZ.

6.3.3 Summary/ Conclusions for this Configuration

The following is a brief summary of the findings from the work on BS L165 weld configurations.

- It was more challenging to find appropriate weld parameters for BS L165 compared with AA8090 due to the higher thermal conductivity of BS L165 leading to severe distortion.
- Both configurations were longitudinally and angularly distorted in the finished welds.
- The weld macrostructures were similar for both configurations with a larger retreating side TMAZ and HAZ, although additional analysis had to be carried out to find the true width of the II HAZ.
- The weld surface appearance varied between the configurations, between different weld runs and along each individual weld, particularly in the case of the \perp weld, suggesting inconsistent heat input as the tool traversed.
- The alclad layer was deposited inconsistently adjacent to the weld on each side of the top surface. The alclad layer was also mixed close to the top surface, and was drawn into the weld to varying degrees at the bottom surface TMAZ, and at kissing bonds where applicable.

- Contradictory evidence suggested the each of the configurations may be hotter than the other. This is likely due to the varying heat input along the weld as discussed, but overall it was considered that the heat generation within the II weld was greater.

6.4 AA8090-BS L165

6.4.1 As-Welded Examination

6.4.1.1 Welded Sheets

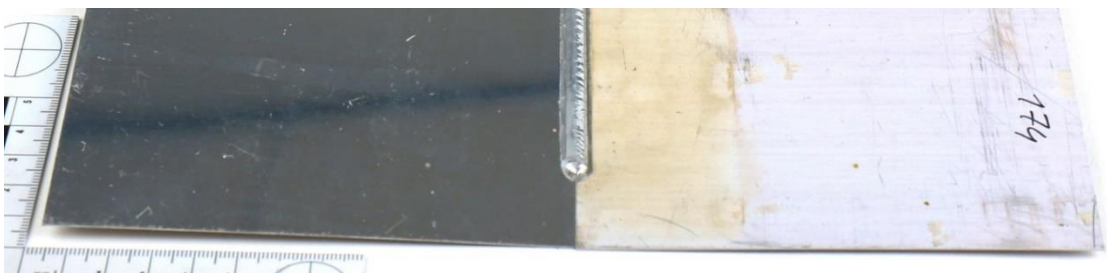
Longitudinal distortion observed on the similar welds was present on the AA8090-BS L165 welds, i.e. convex and sinusoidal, Figure 114. Additionally, transverse angular distortion which again varied in severity between the individual welds was present, with an example shown in Figure 114(c). The angular distortion was a concern as they were an indicator of additional stresses within the welded material which may affect the mechanical testing results. Vertical lifting was negligible for this configuration in successful welds but was observed during weld parameter trials.



(a)



(b)



(c)

Figure 114: Showing longitudinal distortion on AA8090-BS L165 welds: (a) sinusoidal and (b) convex curving on \parallel and \perp welds respectively, and (c) angular distortion on a \perp weld.

It was again only possible to carry out limited trials in pursuit of the appropriate weld process parameters, and the difference in thermal conductivity and coefficient of thermal expansion between the two materials further complicated this process. Warping similar to that observed on the BS L165-BS L165 welds (Figure 86, section 6.3.1.1) was produced when there was excessive heat within the weld, and insufficient mixing, identified by failed root bend tests was found when there was insufficient heat within the weld. It was necessary to strike a balance between the BS L165 requiring a

“cooler” weld to avoid warping, and the “hotter” weld required to successfully plastically stir the AA8090.

Successful welds, i.e. those with no visible warping and which passed root and crown bend tests, were produced using an increased weld (down) force; this was increased by 300 N from the similar welds to 3300 N, which would act to increase frictional heat generation. The rotational speed used matched that of the BS L165 similar welds at 2700 RPM, thereby reducing the heat input to the weld in comparison with the AA8090 similar welds, however the traversing speed was decreased to 8 mm/s (this was 10 mm/s for the similar welds), thereby increasing the heat input to the weld. It is considered that the decreased rotational speed reduced shear (in comparison with AA8090 similar welds), and thus the adiabatic heat generation, which was beneficial for the BS L165, while the increased heat input from the reduced traverse speed and higher down force allowed adequate mixing of the materials.

6.4.1.2 Weld Surface

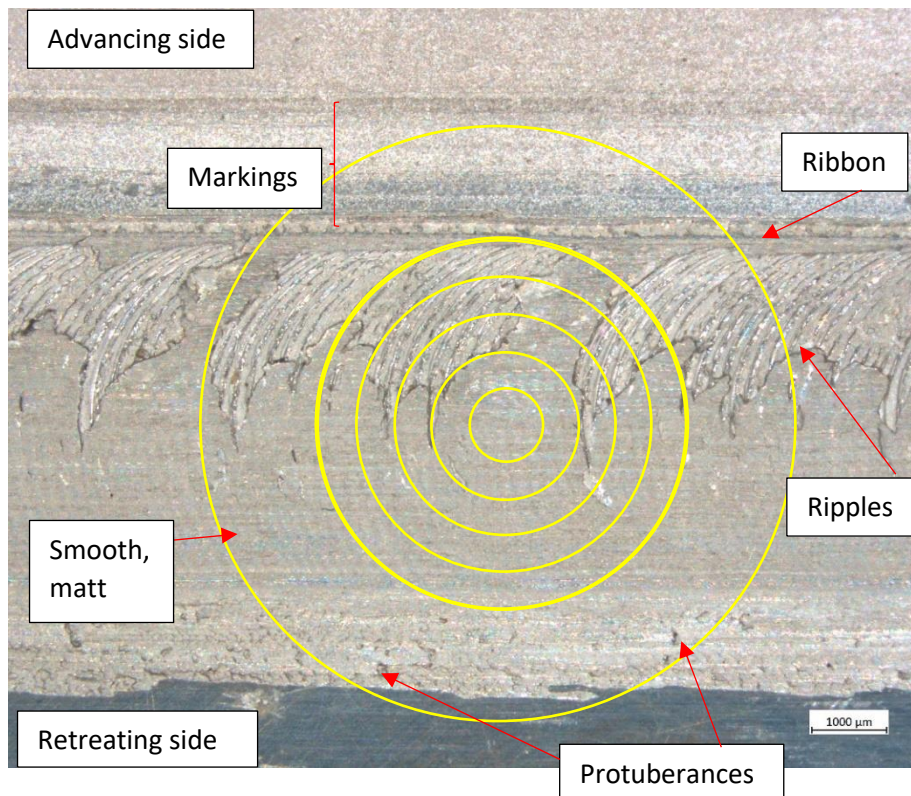
The weld surface of both AA8090-BS L165 configurations changed between weld runs and along the weld as the tool progressed. The II weld is shown in Figure 115 with the tool profile superimposed on to Figure 115(a). The tool profile was positioned on the weld to best fit the ripples which can be partially seen in the image. This area of the weld (Figure 115(a)) featured partial ripples overlaid with smooth (ironed) material with a matt appearance. Rougher, deposited material with protuberances was observed along the retreating edge and a ribbon of material was present along the advancing edge. Adjacent to the advancing edge was a band of directional markings which varied in hue and width as the weld progressed, this is apparent when Figure 115(a) is compared with Figure 115(b), another area of the weld. This part of the weld Figure 115(b) also featured rough deposited material with protuberances along the retreating edge, and a ribbon of material at the advancing edge. It differed from the area shown in Figure 115(a), in that the band of directional markings adjacent to the advancing edge was wider but fainter at its extremity, and that the ripples were themselves had a rougher, more ill-formed appearance. The smooth, ironed material on the surface of the weld (with the exception of the ripples), particularly towards the retreating side of the weld, varied from a matt appearance to shiny and reflective.

The ripple spacings were broadly consistent with the weld pitch (0.178 mm/rev) at approximately 169 μm . The ripples shown on Figure 115(a) had a “cleaner” appearance than those shown in Figure 115(b). As the ripples are formed from plasticised shear layer material detaching from the pin, it is suspected that the material at the area shown in Figure 115(b) was more plasticised than that in Figure 115(a), and was thus deposited in a less controlled manner, indicating that there was a higher heat input to the weld at that area. The ripples in both cases allow for underfill as they lie beneath the overlaid ironed material. This is shown in the profilometry images in Figure 116. Voids and grooves are usually formed on the advancing side as material is moved from the advancing side (creating a void) and then moved from the retreating side to be deposited. It is considered that the ripples underneath the overlaid material are visible from the surface due to insufficient material being moved to that position to completely cover the surface; the additional material has been lost to the sides as the ribbon at the advancing side and the rough deposited material with protuberances at the retreating side.

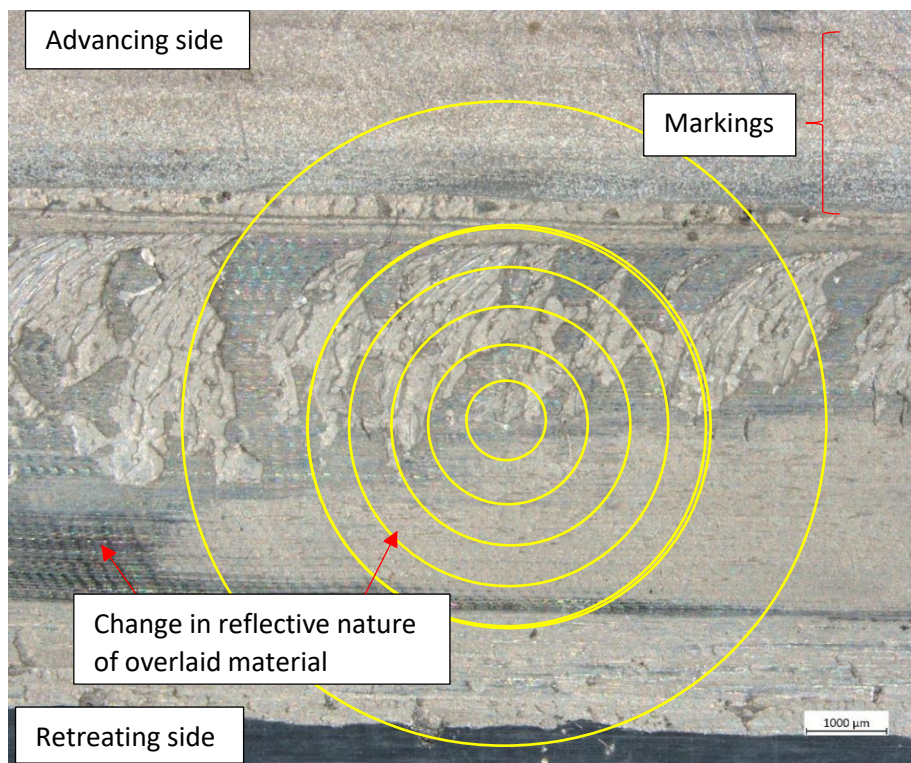
The directional markings adjacent to the advancing side were not observed on either AA8090 similar welds, were only observed to a very narrow extent on the \perp weld, and no reference to this feature was found within the literature. There are two suspected reasons for these markings. The first is that they were caused as the shoulder made contact with the material surface and are frictional contact marks. The second is that it may have occurred as a function of oxidation due to the heat input to the weld, which has affected only the AA8090 in this manner. This is likely to be due to the advancing side being hotter than the retreating side as previously described, and the BS L165 having an element of protection from its alclad layer. This dissimilar weld had a lower rotational speed than the similar AA8090, however for the dissimilar weld both the down force was increased and the traverse speed was decreased, thus higher overall heat generation arose in this weld when compared with the similar weld. This explains why this feature was not observed on the similar weld: insufficient heat input to the AA8090 weld. The markings appear only on the \parallel weld. This is considered to be due to the material texture of longitudinally orientated grains. It is suspected that these grains and their boundaries are orientated at the surface such that the heat input has discoloured them over a specific distance. In the \perp weld, due to the transversely

orientated grains and grain boundaries, the texture would not be as uniform and thus the heat input did not affect them in the same manner. The width and hue of the markings change along the length of the weld. As shown by other surface features, the heat input to the weld changed along the length, likely due to the force control used rather than position control changing depth of tool insertion into the material. As the markings extend beyond that of the shoulder diameter, the second reason is considered to be most likely.

The change of surface appearance of the ironed areas from matt to reflective is expected to be a result of the variance of heat input and thus oxidation of the material, and a mix of alclad, BS L165 and AA8090 being mixed within the weld and deposited on the surface. The rough material with protuberances at the retreating side is considered to be alclad material.

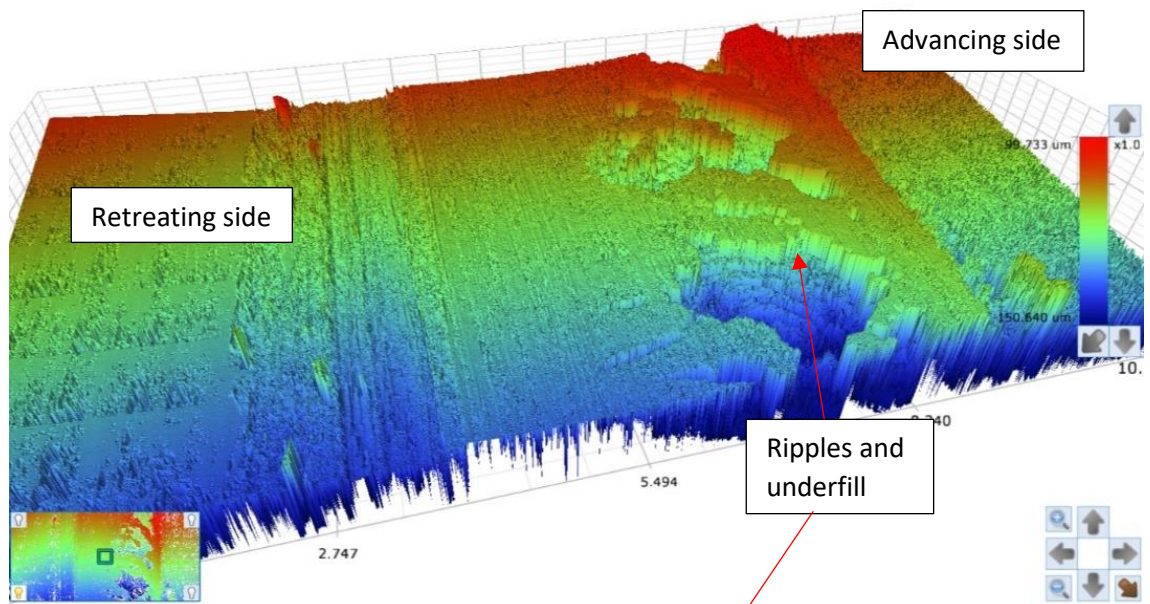


(a)

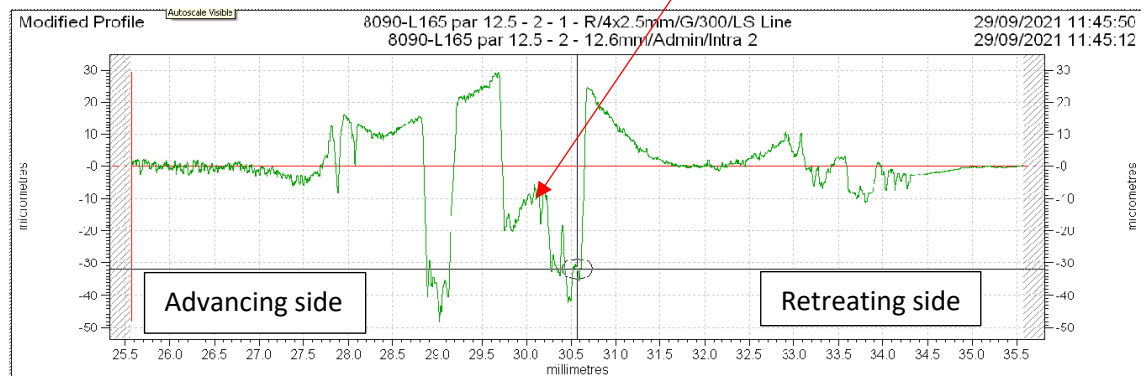


(b)

Figure 115: Showing AA8090-BS L165 II weld surface with superimposed tool profile: (a) shows area representative of the average weld, (b) shows how the surface appearance can change.



(a)

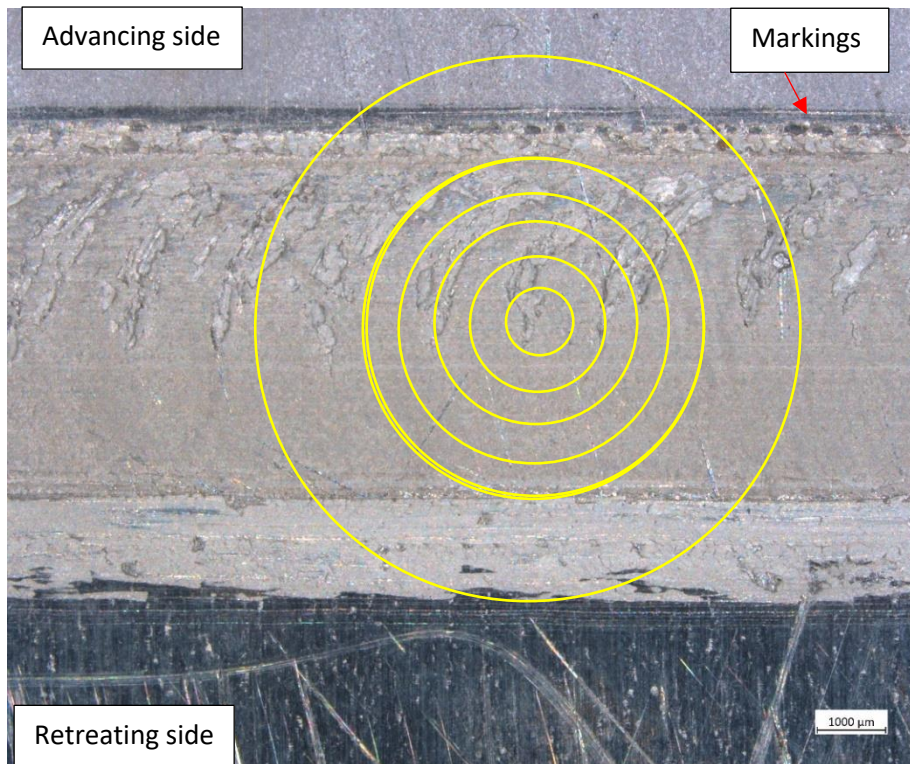


(b)

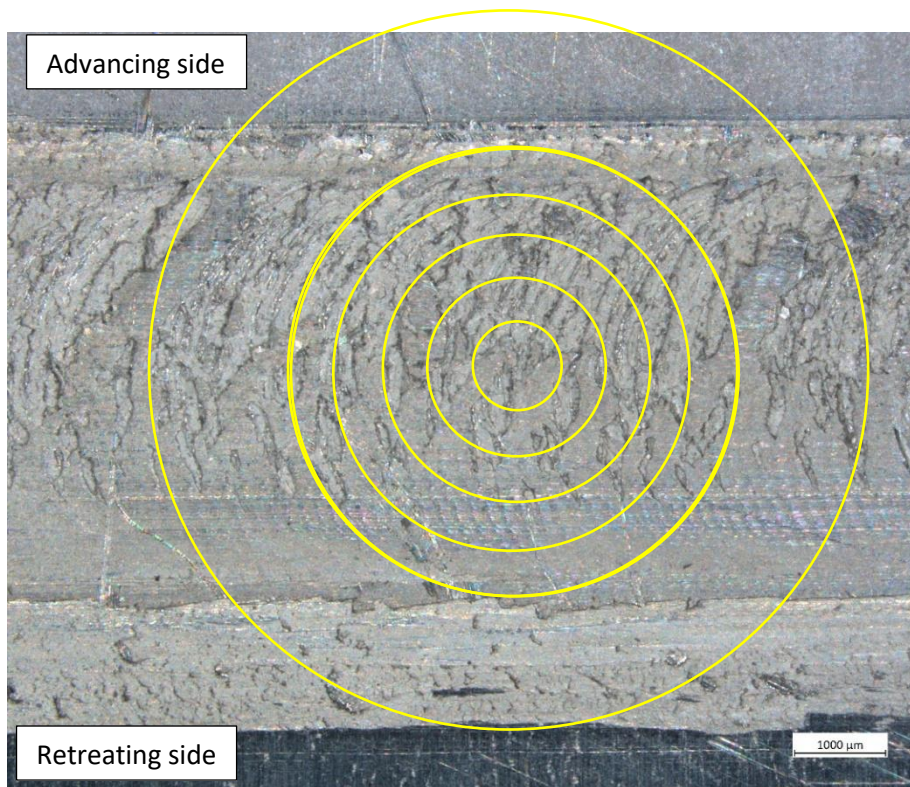
Figure 116: Showing AA8090-BS L165 II weld surface topography, (a) optical profilometer 3D model image, and (b) contact profilometry surface plot.

The \perp weld is shown in Figure 117 with the tool profile superimposed. There are many similarities between the surface appearance of this configuration and the II weld: partial ripples overlaid with smooth deposited material which vary in roughness along the weld length; a ribbon along the advancing edge; an area of rough material with protuberances along the retreating edge; a change in the appearance of the ironed material from matt to reflective. These features can all be attributed to the reasons previously discussed for the II weld. The main differences between the two configurations are that while the surface roughness changes along the length of the weld (similar to the II weld), the roughest parts of this weld exceed that of the II weld, as identified by the profilometry

images shown in Figure 118. Additionally, only a very narrow area of discolouration is present adjacent to the advancing side, the reasons for which have previously been described.



(a)



(b)

Figure 117: Showing AA8090-BS L165 \perp weld surface with superimposed tool profile: (a) shows area representative of the average weld, (b) shows how the surface appearance can change.

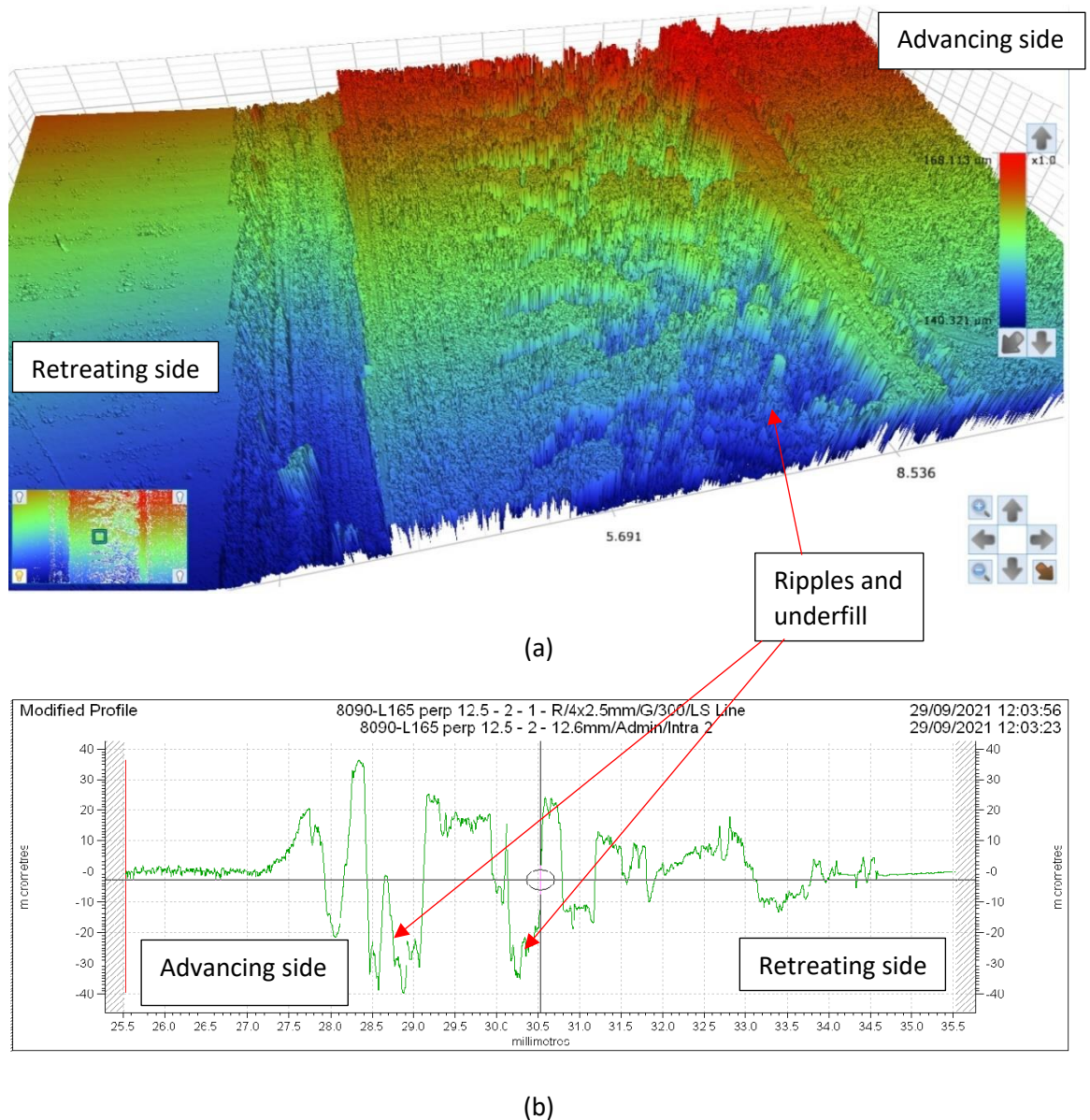


Figure 118: Showing AA8090-BS L165 \perp weld surface topography, (a) optical profilometer 3D model image, and (b) contact profilometry surface plot.

6.4.1.3 Weld Macro- and Micro-structures

Cross-sections of AA8090-BS L165 welds are shown in Figure 119, with the advancing side on the right in both cases and the \perp weld image is to a slightly larger scale. The material mixing is more easily visible on these dissimilar welds when compared to the similar welds due to the contrast between the materials when etched. There is clear mixing of the materials on the advancing side of the nugget on the II weld, and on the region near to the surface of the retreating side, however this is likely to include

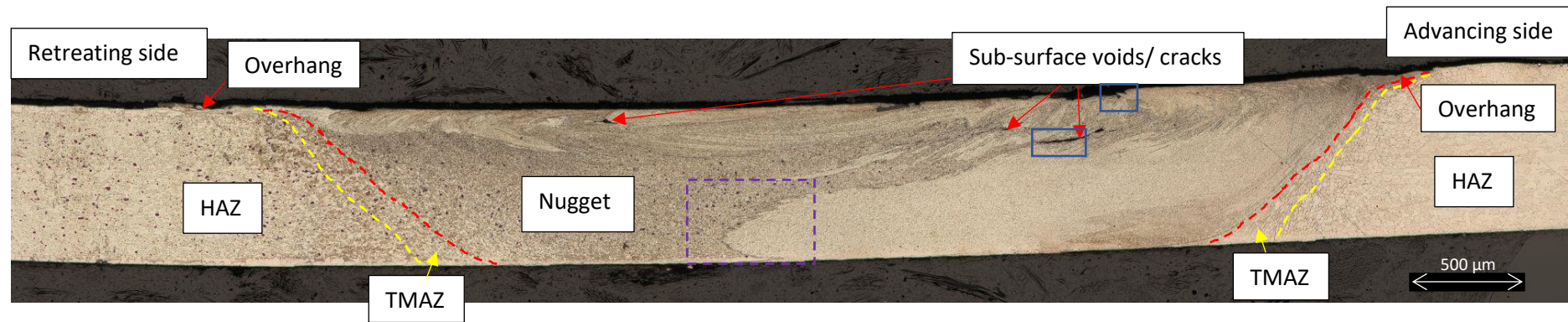
significant amounts of alclad material also, as previously observed on the BS L165 similar welds. The II weld shows more mixing than the \perp weld indicating greater material flow in the II weld, therefore suggesting a hotter weld than the \perp .

Negligible weld thinning was observed on the cross-sections shown in Figure 119, in fact the \perp weld has a slightly increased cross-sectional thickness across the weld nugget. This weld does however show significant underfill at the weld surface on the advancing side, which accounts for the additional material. Less underfill was observed on the II weld, however this was consistent with this cross-section having been taken from one of the smoother surface areas shown in Figure 115.

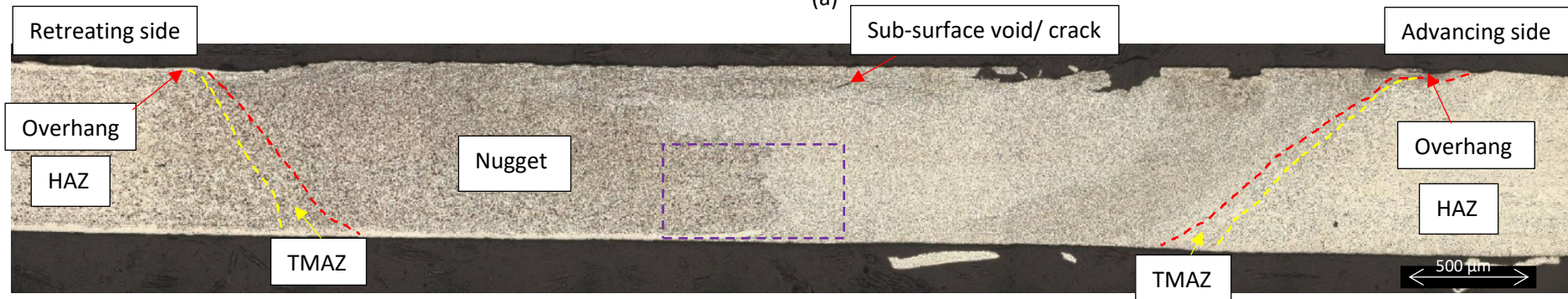
Both surface breaking and sub-surface voids and cracks were observed close to the top surface of the \perp weld, particularly along mix lines, with one small sub-surface crack present on the \perp weld. Examples of these voids/ cracks are shown in greater detail in Figure 120. These voids/ cracks are different from the more common voids described within the literature which occur at or close to the bottom of the nugget on the advancing side, and are caused by insufficient material flow usually caused by inadequate heat input to the weld (Threadgill et al., 2009; Zettler et al., 2010). When FSW aluminium and copper dissimilar welds, Xue, Ni, Wang, Xiao and Ma (2011) found that both surface-breaking and sub-surface cracks and voids were produced when the rotational speed was low and when a small pin offset was used as the result of intermetallic compounds being formed. They found that sound welds were produced at higher rotational speeds and when a large (2.5 mm) pin offset was made to the advancing side when the harder Cu was positioned at that side. In this current research AA8090 parent material does have a lower hardness (approximately 11%) than BS L165 so it is possible that further optimisation of the process parameters and repositioning of the materials (see section 6.5) would resolve this defect, although faster rotational speeds resulted in warping of BS L165 in this case.

On the images shown in Figure 119, the kissing bond/ lazy S feature is more prominent on the II weld than on the \perp weld although the alclad layer has been drawn into the \perp weld at this point. In some welds clear indications of oxide entrapment were observed, however in others only the adjoining line between the materials was visible. This kissing bond/ lazy S feature varied in prominence throughout both weld configurations

indicating unstable weld conditions along the length of the weld and between separate weld runs.

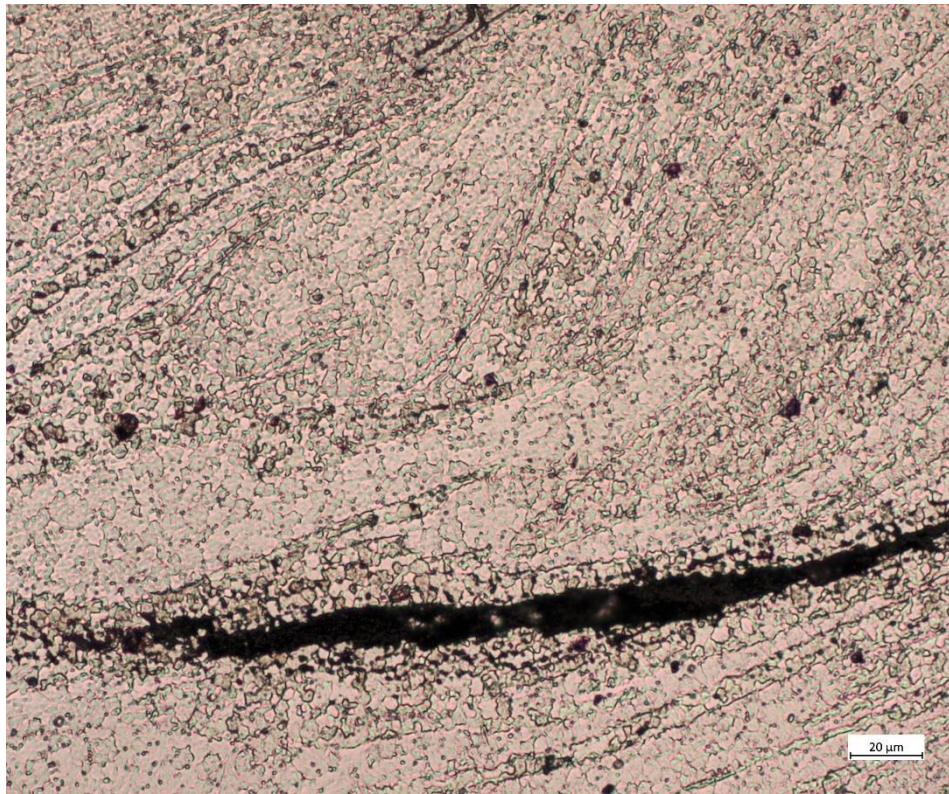


(a)

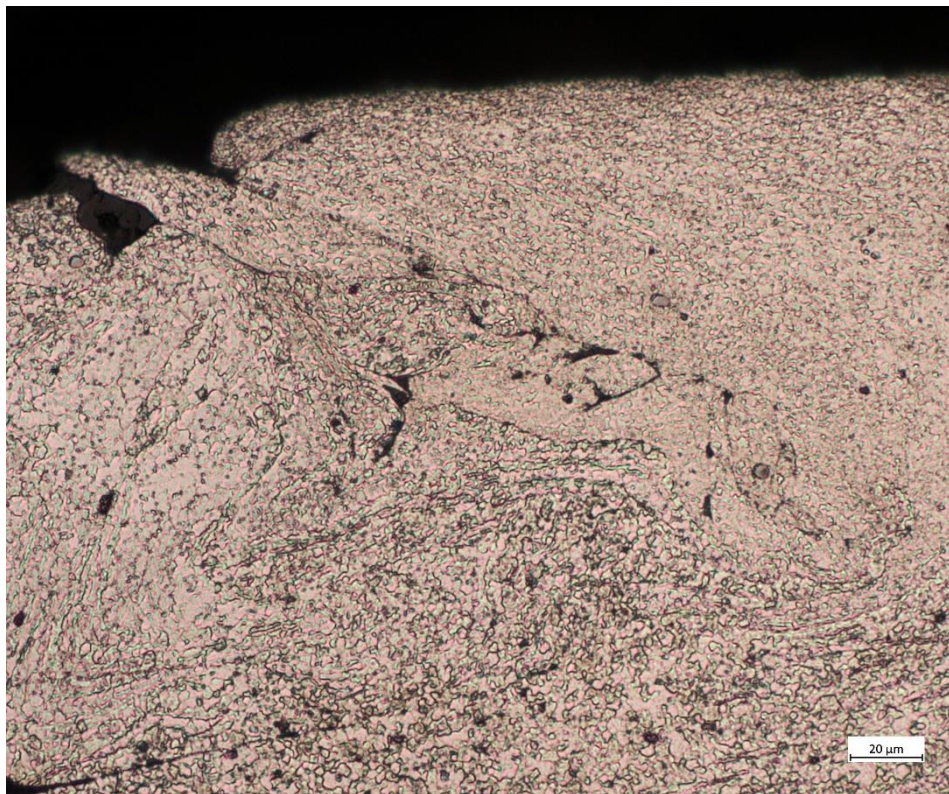


(b)

Figure 119: Showing macrograph of AA8090-BS L165 weld cross-section; (a) \parallel and (b) \perp . The areas indicated by the blue boxes in (a) are shown in greater detail in Figure 120.



(a)



(b)

Figure 120: Showing cracks/ voids within the II weld nugget: (a) sub-surface; and (b) both sub-surface and surface breaking.

6.4.1.3.1 Nugget

Comparison of the nugget dimensions with that of the pin revealed that the II weld width measured approximately 4.2 mm and 3.2 mm at the mid-thickness and bottom surface respectively, and that the \perp weld width measured approximately 4.2 mm and 3.4 mm at the same positions. These nugget zones were slightly wider than the two sets of similar welds; as previously described, the findings of He, Li, Song, Lui and Hu (2019) were that increased rotational speed produced larger nugget zones. As the rotational speed was equivalent to that used for the BS L165 similar welds, and slower than that for the AA8090 similar welds, these measurements do not support that research. However a combination of materials with different thermal conductivities will inevitably affect the nugget growth and so direct comparison is not possible. It is thought that the increased nugget zone width in this configuration was influenced by the slower traversing speed, i.e. greater heat input to the weld.

Micrographs of the II and \perp weld nugget zones are shown in Figure 121 and Figure 122 respectively, where it is clear that dynamic recovery and recrystallisation occurred when compared with the parent materials (Figure 31, section 4.1.2 and Figure 36, section 4.2.2). Grain sizes used in the analysis were measured at mid-thickness; these are shown in Table 40. For this configuration the grain sizes were compared with both the parent material and with the relevant similar weld configuration. With regards to Table 40, the column labelled "Advancing side" refers to areas of the nugget comprised solely of AA8090, while "Retreating side" to areas solely comprised of BS L165. The grains produced in the nugget of the \perp weld were slightly larger than those in the II weld, possibly indicating a cooler weld in the II configuration. As previously described, higher temperatures are generally reached on the advancing side, however when combined with the severe deformation, smaller grains are usually produced on that side. Interestingly, despite both similar sets of weld configurations producing grains consistent with that trend, i.e. the advancing side grains being smaller than the retreating side, for AA8090-BS L165 this is true for the II configuration, however the \perp weld has smaller grains on the retreating side. The BS L165 parent material grains were of course initially far smaller (by approximately 40%) than the AA8090 parent material grains. It does not appear improbable to expect that when these materials are SSFSW together, that the AA8090 grains would remain larger than the BS L165 regardless of

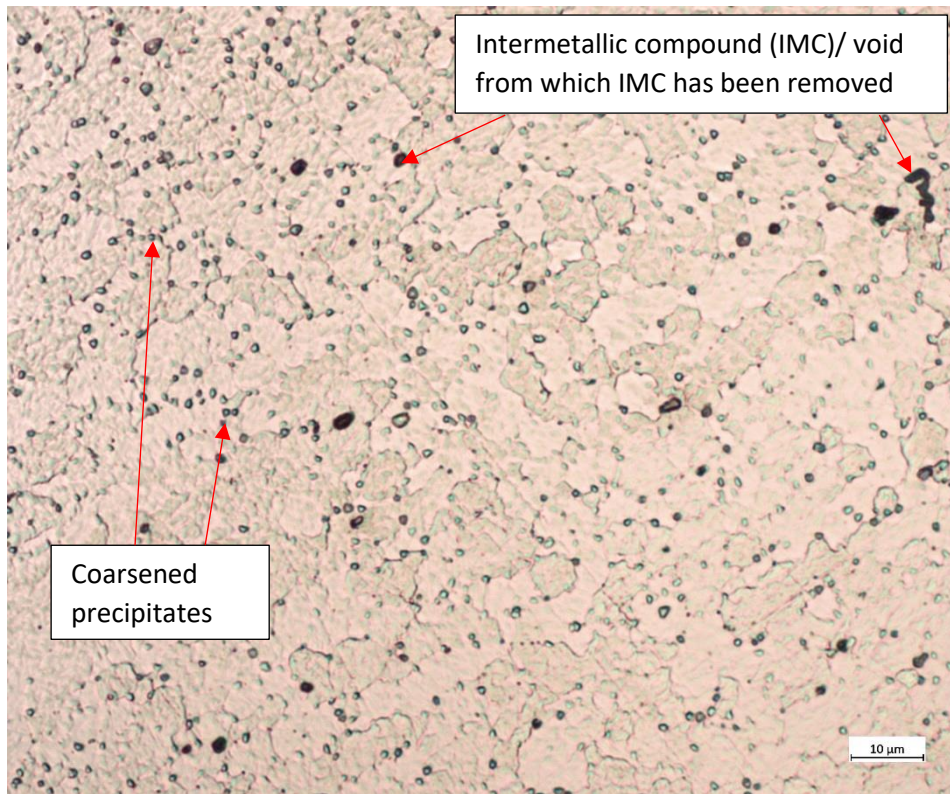
material positioning. However this does not explain the disparity between the two orientations. In any case, recrystallisation would destroy the original grain structure. The simplest explanation is that higher amounts of mechanical deformation were generated at the advancing side of the II weld (causing an increased number of new grains' nucleation sites) than at the advancing side of the \perp weld, and apart from the weld parameters and clamping producing unstable weld conditions, no further reasoning can be given.

It was noted that the AA8090-BS L165 weld produced smaller AA8090 grains on the advancing side than on the similar AA8090 weld advancing side and larger BS L165 grains on the retreating side than on the BS L165 similar weld retreating side. Singh, Sahlot, Paliwal and Arora (2019) found that although most models use an average of the dissimilar parent material properties, the stir zone (nugget) is actually a hybrid mixture of the two, and the thermo-physical properties, e.g. specific heat capacity, thermal diffusivity, thermal conductivity, and density are unique to each weld dependent on material composition and initial thermal history, material orientation, weld parameters and tool dimensions. For this reason, direct comparison with the similar welds is not truly illustrative of the material transformations which occur.

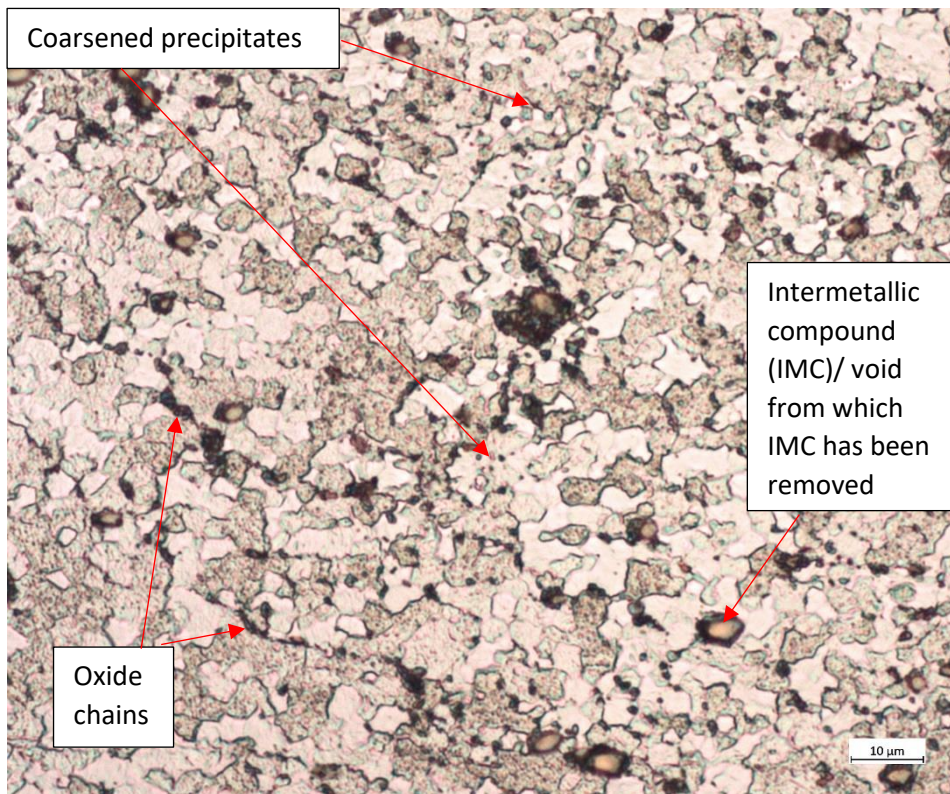
Table 40: Showing AA8090-BS L165 weld nugget grain size dimensions with similar weld grain sizes for comparison, showing Relative Accuracy (%RA) in brackets.

Configuration	Average Grain Diameter (μm) Measured Across Two Directions											
	Advancing Side						Retreating Side					
	Direction 1	% Change from Parent Material	% Change from Relevant Similar Weld Configuration	Direction 2	% Change from Parent Material	% Change from Relevant Similar Weld Configuration	Direction 1	% Change from Parent Material	% Change from Relevant Similar Weld Configuration	Direction 2	% Change from Parent Material	% Change from Relevant Similar Weld Configuration
AA8090 Parent Material (L)	21.2 (9%)	-	-	16.2 (6%)	-	-	-	-	-	-	-	-
AA8090 Parent Material (S-T)	28.0 (4%)	-	-	25.4 (16%)	-	-	-	-	-	-	-	-
BS L165 Parent Material (L)	12.2 (4%)	-	-	7.5 (6%)	-	-	-	-	-	-	-	-
BS L165 Parent Material (S-T)	14.4 (15%)	-	-	13.0 (13%)	-	-	-	-	-	-	-	-

Configuration	Average Grain Diameter (μm) Measured Across Two Directions											
	Advancing Side						Retreating Side					
	Direction 1	% Change from Parent Material	% Change from Relevant Similar Weld Configuration	Direction 2	% Change from Parent Material	% Change from Relevant Similar Weld Configuration	Direction 1	% Change from Parent Material	% Change from Relevant Similar Weld Configuration	Direction 2	% Change from Parent Material	% Change from Relevant Similar Weld Configuration
AA8090 II	7.9 (8%)	-71.8	-	7.8 (10%)	-69.3	-	10.6 (19%)	-62.1	-	8.8 (13%)	-65.4	-
AA8090 I	8.8 (9%)	-58.5	-	7.4 (8%)	-54.3	-	9.4 (14%)	-55.7	-	8.3 (10%)	-48.8	-
BS L165 II	5.6 (16%)	-61.1	-	4.8 (11%)	-63.1	-	6.6 (10%)	-54.2	-	4.9 (14%)	-62.3	-
BS L165 I	5.5 (10%)	-54.9	-	4.8 (12%)	-36.0	-	6.3 (13%)	-48.4	-	4.9 (5%)	-34.7	-
AA8090-BS L165 II	6.8 (7%)	-75.7	-13.9	6.6 (5%)	-74.0	-15.4	7.4 (15%)	-48.6	+21.1	5.4 (9%)	-58.5	+10.2
AA8090-BS L165 I	8.5 (12%)	-59.9	-3.4	6.8 (11%)	-58.0	-8.1	7.8 (10%)	-36.1	+23.8	6.1 (12%)	-18.7	+24.5

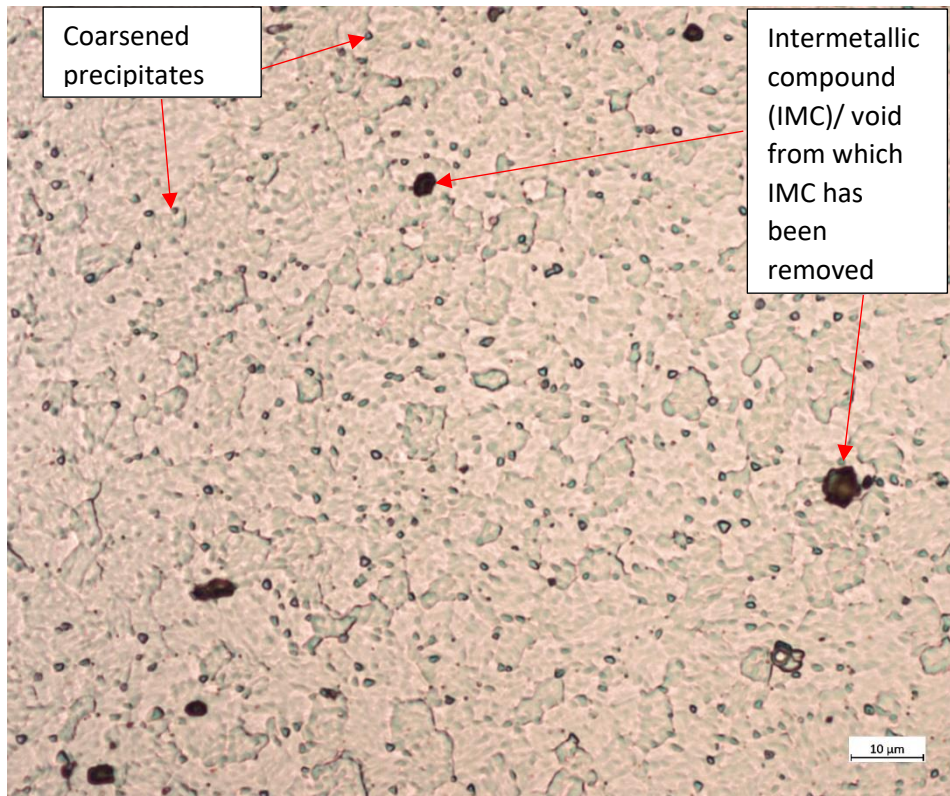


(a)

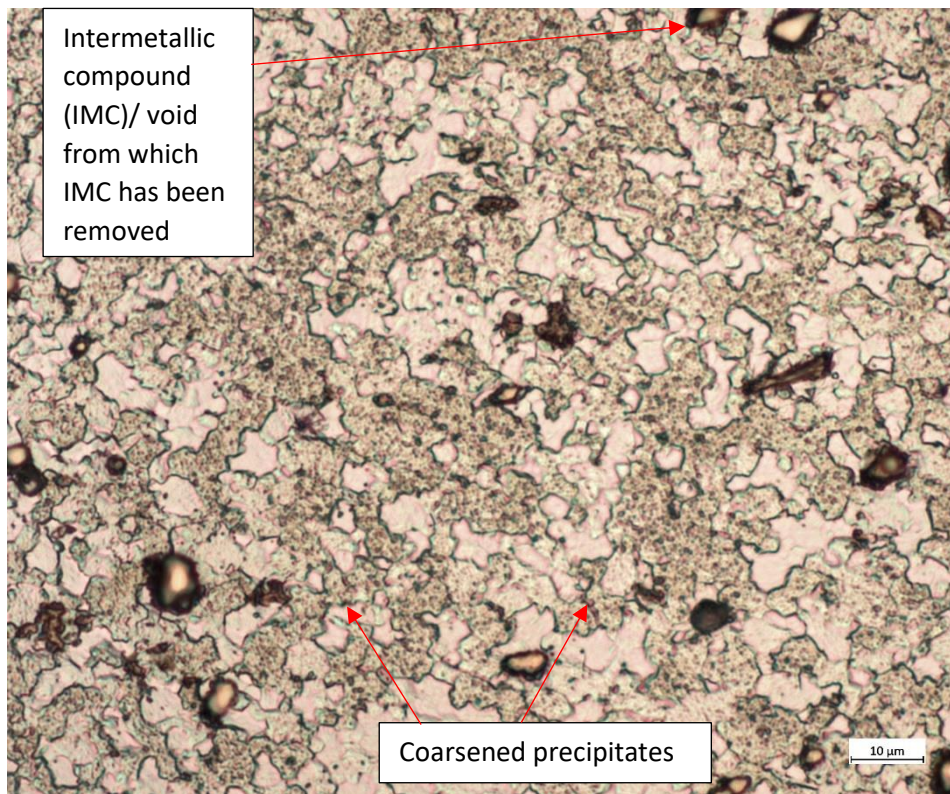


(b)

Figure 121: Showing micrographs of the II weld nugget: (a) advancing side AA8090 material and (b) retreating side BS L165 material.



(a)



(b)

Figure 122: Showing micrographs of the \perp weld nugget: (a) advancing side AA8090 material and (b) retreating side BS L165 material.

Analysis of the AA8090 part of the nugget (advancing side, II shown on Figure 121(a) and \perp shown on Figure 122(a)) revealed a significant increase in the volume of fine black, approximately spherical particles gathered at grain boundaries, considered to be heterogeneously nucleated incoherent δ (section 6.2.1.3.1). Coarse intermetallic compounds (IMCs) generally located at the grain boundaries were also observed. The volume fraction of precipitates and IMCs was approximately equal between the two configurations. The composition of the IMCs was considered to be similar to that observed by Vigraman et al. (2021) and reported in section 6.2.1.3.1, although it is acknowledged that some transfer of IMCs from the retreating side (AA2014) of the nugget may have occurred.

The BS L165 part of the nugget (retreating side, II shown in Figure 121(b) and \perp shown in Figure 122(b)) show the presence of large intermetallic compounds, considered to be similar in composition to that identified by Rajendran et al. (2019) and reported in section 6.3.1.3.1. Again, it was however noted that some transfer of IMCs from the advancing (AA8090) side may have occurred. Heterogeneous nucleation of coarsened precipitates, considered to be incoherent θ were observed at the grain boundaries. More θ particles were observed overall on the II weld than on the \perp weld, which suggests that further coarsening occurred in the II weld than in the \perp weld. Additionally, oxide chains were observed within the nugget; these are discussed in section 6.5.1.3.1.

The alclad layer being drawn into the weld referred to previously, and shown in Figure 119(b), is shown in greater detail in Figure 123. The materials have mixed in such a manner that the alclad layer has been positioned with AA8090 material underneath it, and the AA8090 forming the bottom surface at the joint line. The alclad layer has been drawn into the joint line remnant, and the presence of oxides which were also drawn into the weld has formed a kissing bond at this point. The alclad layer splits, with some of it drawn into the joint line as described, and some drawn further into the AA8090 material. This forms a sharp interface of material properties between the fine, recrystallised grains of the nugget material and the alclad layer. This will likely introduce stress concentrations owing to the sharp interface, and may result in a deterioration of mechanical properties.

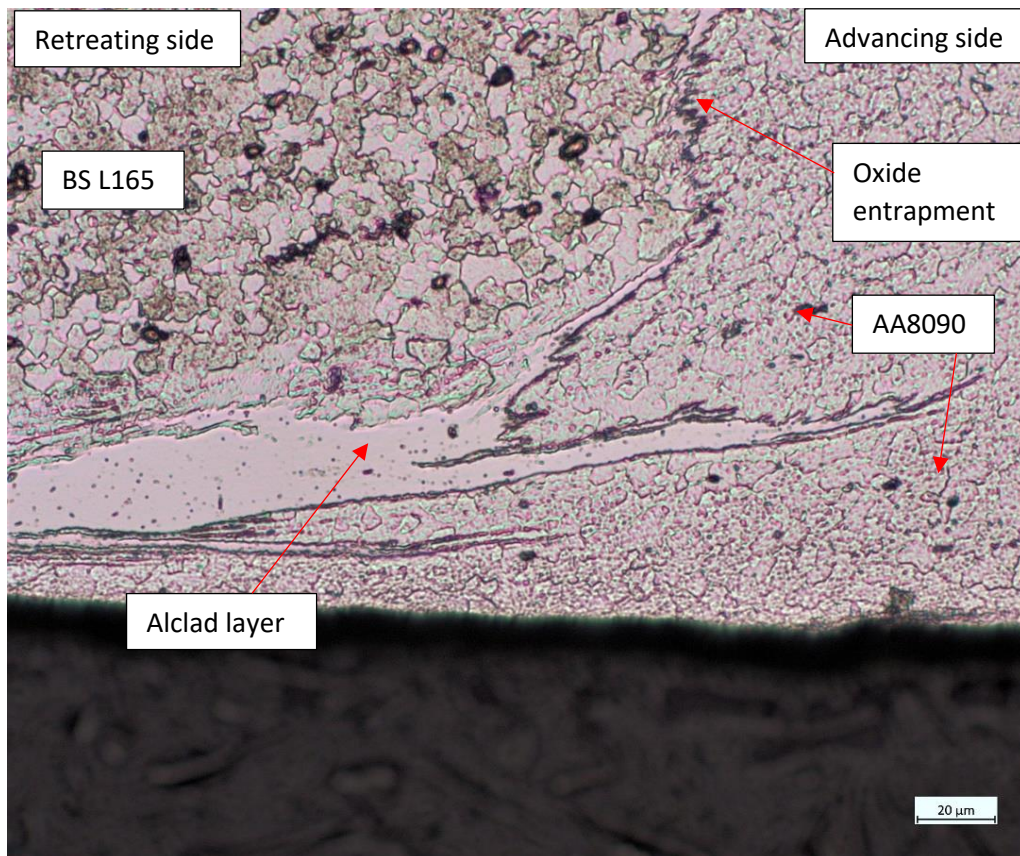


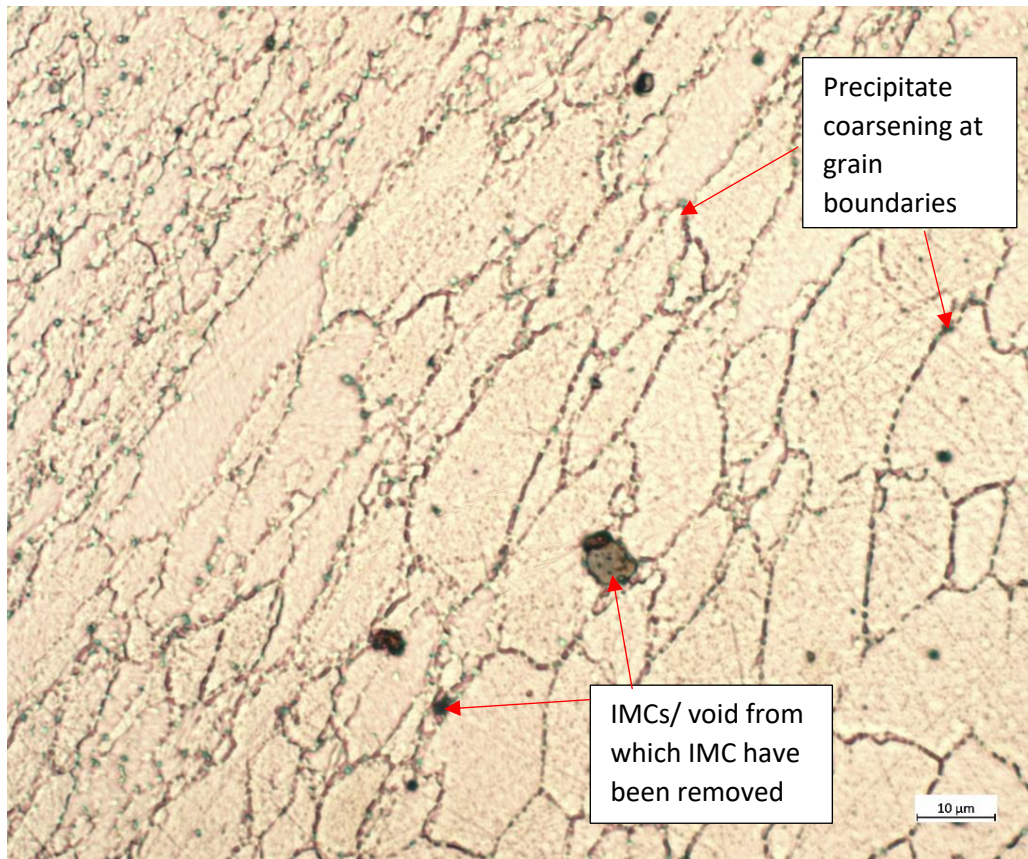
Figure 123: Showing alclad layer being drawn into the weld and kissing bond on a AA8090-BS L165 \perp weld.

6.4.1.3.2 TMAZ

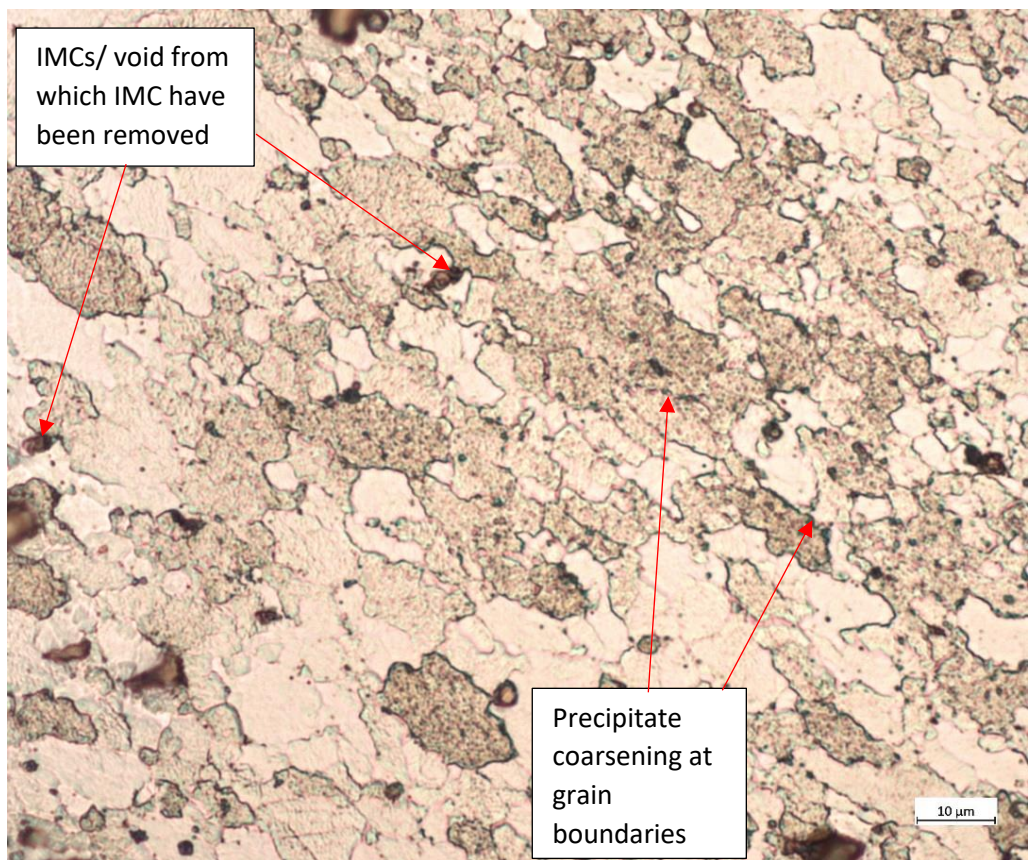
As expected, the TMAZ was identified by distorted and elongated grains. The nugget/TMAZ boundary was sharp on the advancing side of both configurations and diffuse on the retreating side with the advancing side TMAZ being slightly narrower than the retreating side. The II weld TMAZ measured approximately 95 μm wide on the advancing side and 190 μm on the retreating, while the \perp weld measures approximately 85 μm on the advancing side and 140 μm on the retreating. These values are significantly smaller than those observed on the similar welds; this can be attributed to the different weld parameters used and to the effect of mixing materials within the nugget having a corresponding effect on the material thermo-physical properties. The TMAZ width increased close to the bottom surface of the weld, as observed on previous welds.

The TMAZ microstructure is shown in Figure 124 for both configurations. The advancing (AA8090) side shows precipitates, assumed to be incoherent δ gathered at the grain boundaries, with several coarse IMCs. There are larger but fewer coarse IMCs in the II

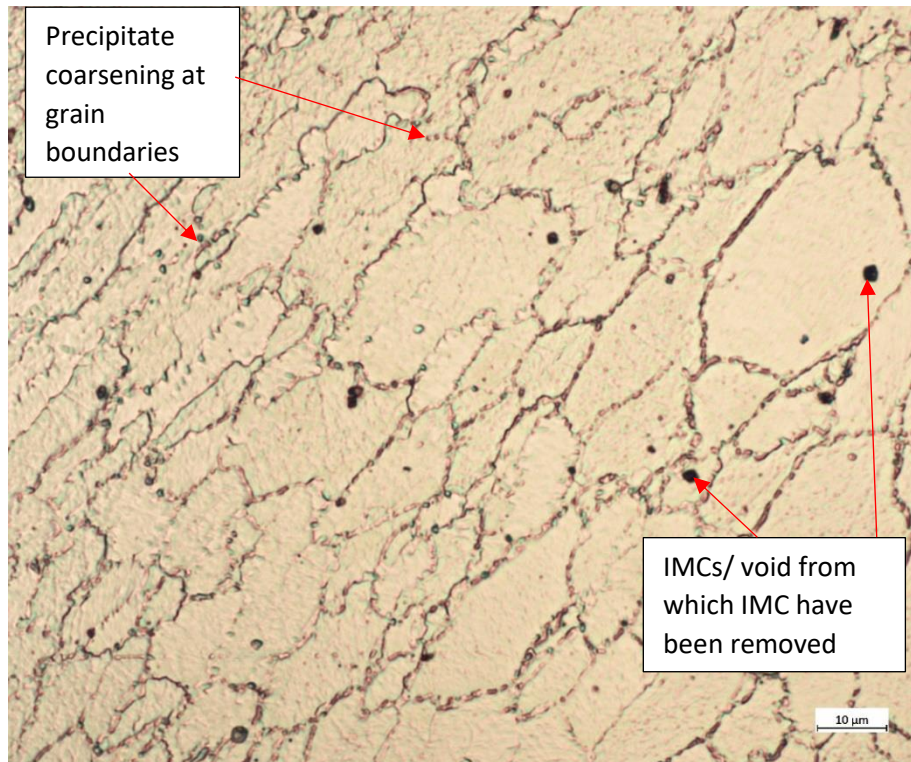
than the \perp weld, which is at odds with the observations from the nugget. The retreating side (BS L165) TMAZ shows coarsened precipitates, presumed to be incoherent θ , and considerably larger IMCs on the \perp weld than on the II. The IMCs on the TMAZ of both sides are considered to be compositionally consistent with that described by Vigraman et al. (2021) (advancing side) and Rajendran et al. (2019) (retreating side).



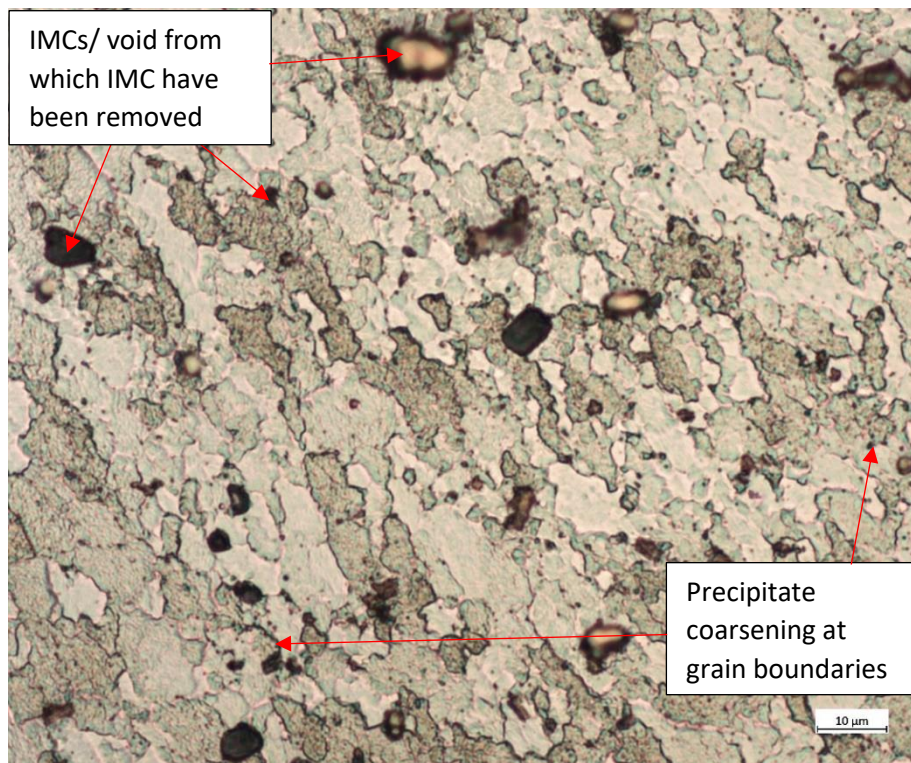
(a)



(b)



(c)



(d)

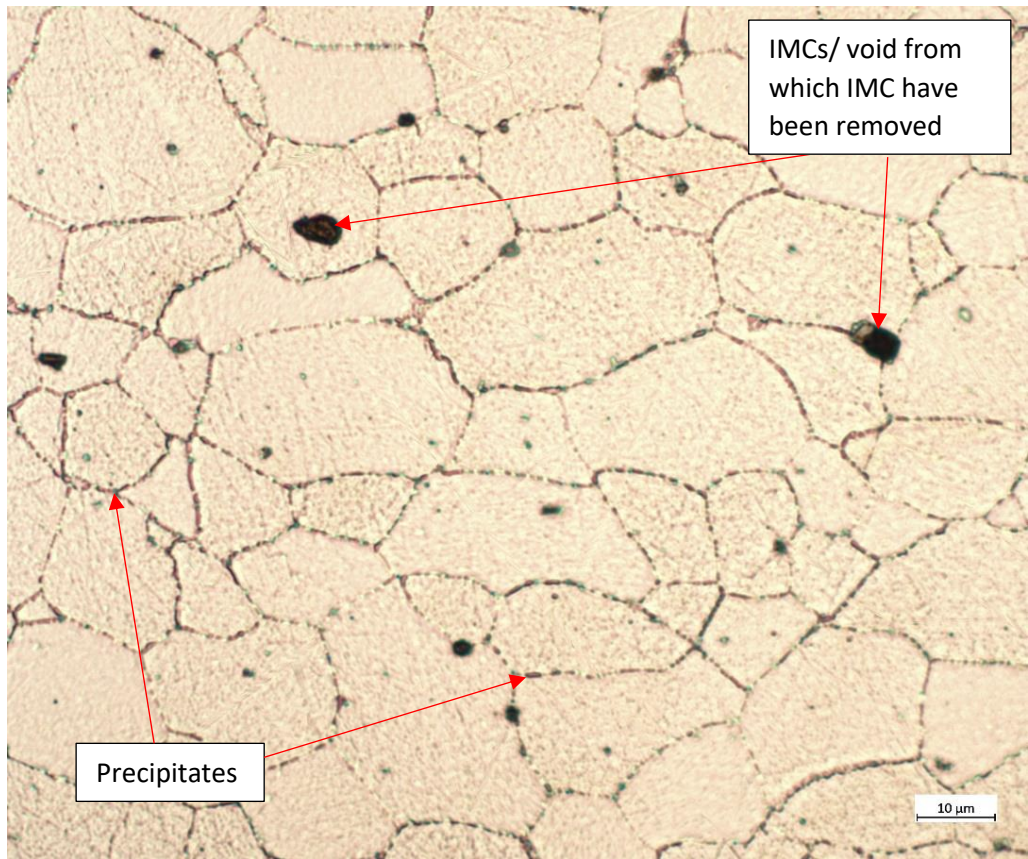
Figure 124: Showing micrographs of the TMAZ: a) AA8090-BS L165 II advancing side and b) retreating side; c) AA8090-BS L165 \perp advancing side and d) retreating side.

6.4.1.3.3 HAZ

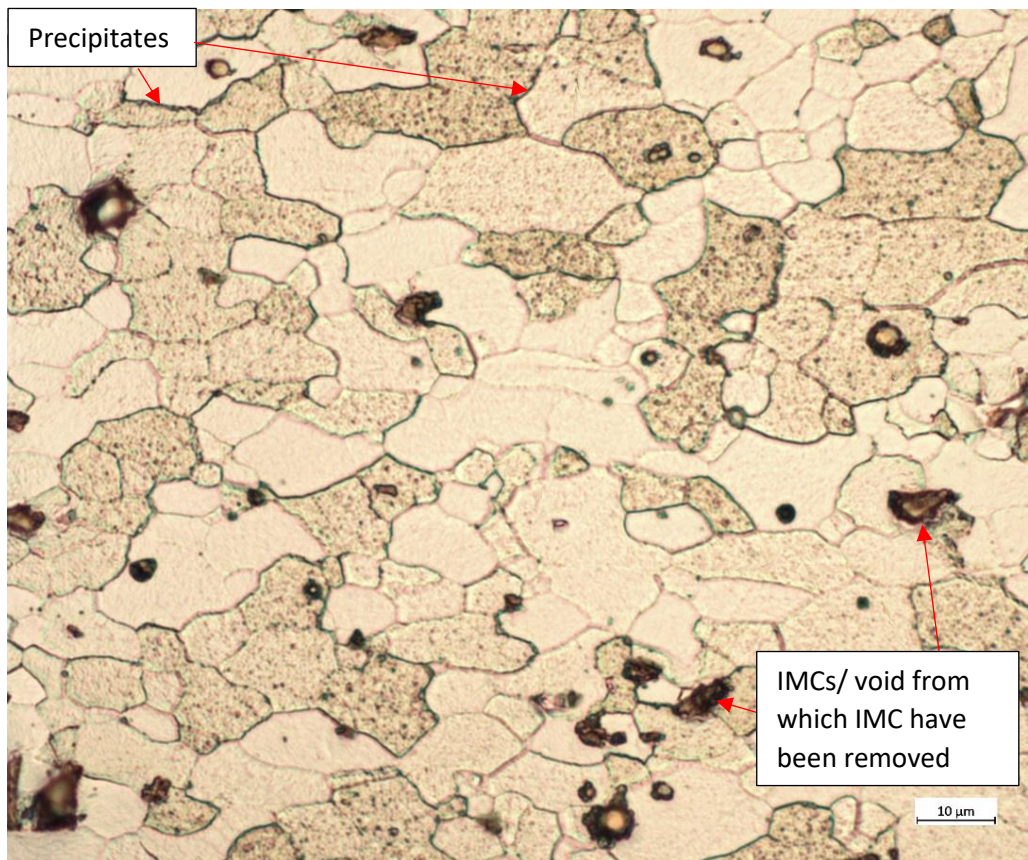
Again, the transition from HAZ to parent material was not visually obvious and therefore the width of the HAZ was analysed using the hardness data. This indicated that the advancing side HAZ was approximately (based on hardness tests every 0.5 mm) 2.0 mm wide and the retreating side 3.0 mm for both configurations. As previously described, it is expected for the retreating side HAZ to be wider than the advancing side.

Micrographs of the HAZ are shown in Figure 125. The microstructures are similar to that of the relevant similar weld configuration, i.e. the advancing side HAZ of AA8090-BS L165 resembles that of the AA8090-AA8090 weld HAZ, and the retreating side resembles that of the BS L165-BS L165 weld HAZ. As such, all images show precipitate coarsening around the grain boundaries. The images shown were taken close to the TMAZ border and the degree of precipitate coarsening decreases as the parent material is approached.

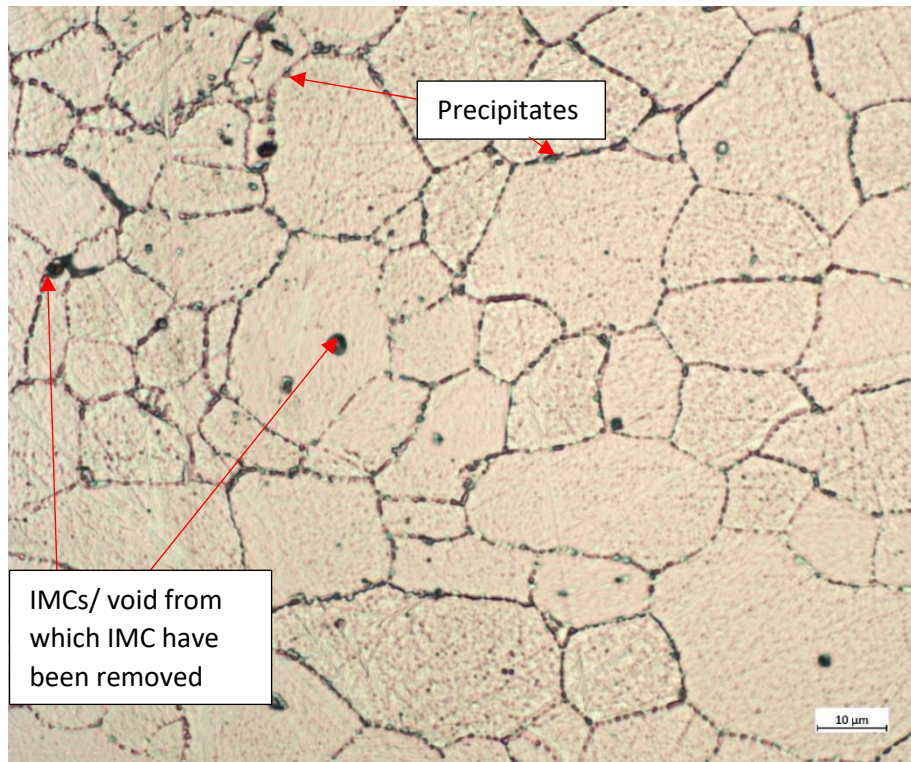
The grain sizes of the HAZ areas are shown in Table 41 where the measured grain sizes for these configurations are compared with both the parent material and with the relevant similar welds. Analysis of the II weld shows that on the advancing (AA8090) side of the AA8090-BS L165, a reduction in grain size in both measured directions was experienced when compared with the parent material. When compared with the AA8090 similar welds, the AA8090-BS L165 advancing side on the II weld featured smaller grain sizes, while there was a slight increase in grain size on the \perp weld. The retreating side of the AA8090-BS L165 II featured a grain size decrease in both directions when compared with the BS L165 parent material, and when compared with the similar BS L165 II weld retreating side there was a reduction of direction 1 and a small increase in direction 2. The retreating side of the AA8090-BS L165 \perp weld featured an increase in grain size when compared with both the BS L165 parent material and the retreating side of the BS L165 \perp similar weld.



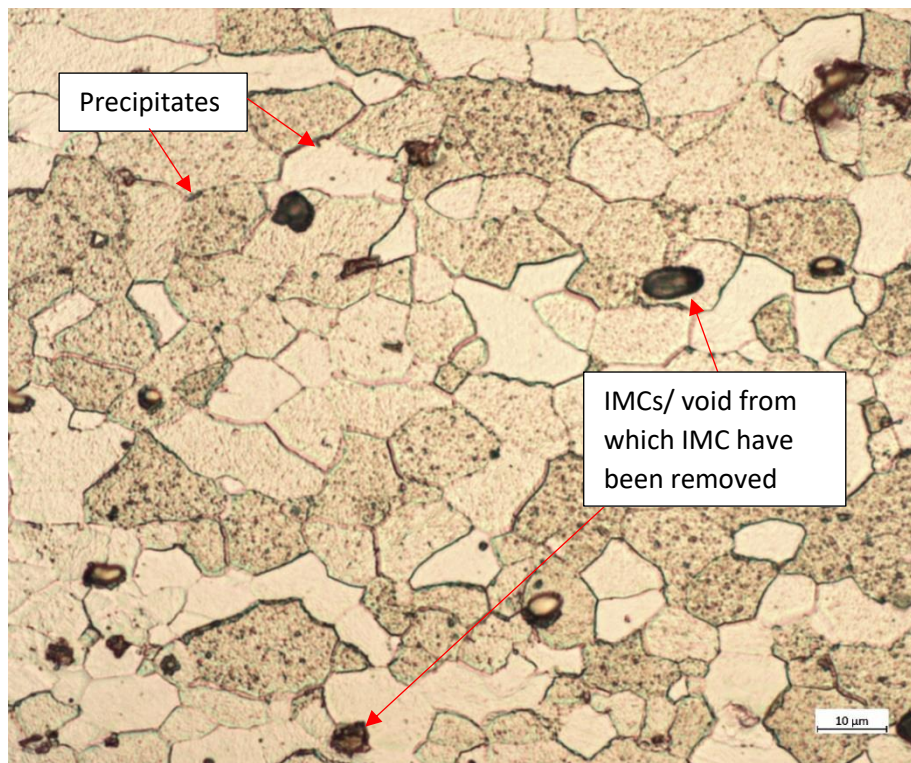
(a)



(b)



(c)



(d)

Figure 125: Showing micrographs of the HAZ: a) AA8090-BS L165 || advancing side and b) retreating side; c) AA8090-BS L165 ⊥ advancing side and d) retreating side

Table 41: Showing AA8090-BS L165 weld HAZ grain size dimensions with parent material and similar weld grain sizes for comparison, showing Relative Accuracy (%RA) in brackets.

Configuration	Average Grain Diameter (μm) Measured Across Two Directions											
	Advancing Side						Retreating Side					
	Direction 1	% Change from Parent Material	% Change from Relevant Similar Weld Configuration	Direction 2	% Change from Parent Material	% Change from Relevant Similar Weld Configuration	Direction 1	% Change from Parent Material	% Change from Relevant Similar Weld Configuration	Direction 2	% Change from Parent Material	% Change from Relevant Similar Weld Configuration
AA8090 Parent Material (L)	21.2 (9%)	-	-	16.2 (6%)	-	-	-	-	-	-	-	-
AA8090 Parent Material (S-T)	28.0 (4%)	-	-	25.4 (16%)	-	-	-	-	-	-	-	-
BS L165 Parent Material (L)	12.2 (4%)	-	-	7.5 (6%)	-	-	-	-	-	-	-	-
BS L165 Parent Material (S-T)	14.4 (15%)	-	-	13.0 (13%)	-	-	-	-	-	-	-	-
AA8090 II	25.3 (19%)	-9.6	-	18.9 (13%)	-25.6	-	17.2 (14%)	-38.6	-	15.3 (11%)	-39.8	-

Configuration	Average Grain Diameter (μm) Measured Across Two Directions											
	Advancing Side						Retreating Side					
	Direction 1	% Change from Parent Material	% Change from Relevant Similar Weld Configuration	Direction 2	% Change from Parent Material	% Change from Relevant Similar Weld Configuration	Direction 1	% Change from Parent Material	% Change from Relevant Similar Weld Configuration	Direction 2	% Change from Parent Material	% Change from Relevant Similar Weld Configuration
AA8090 \perp	15.3 (6%)	-27.8	-	12.2 (6%)	-24.7	-	17.0 (11%)	-19.8	-	13.4 (8%)	-17.3	-
BS L165 II	11.3 (14%)	-21.5	-	7.6 (10%)	-41.5	-	12.5 (8%)	-13.2	-	7.5 (12%)	-42.3	-
BS L165 \perp	11.0 (8%)	-9.8	-	7.9 (9%)	+5.3	-	11.3 (11%)	-7.4	-	7.8 (8%)	+4.0	-
AA8090-BS L165 II	15.3 (11%)	-45.4	-39.5	12.4 (7%)	-51.2	-34.4	10.0 (12%)	-30.6	-20.0	8.2 (6%)	-39.6	+9.3
AA8090-BS L165 \perp	17.5 (11%)	-17.5	+14.4	13.2 (9%)	-18.5	+8.2	13.0 (5%)	+6.6	+15.0	8.2 (11%)	+9.3	+5.1

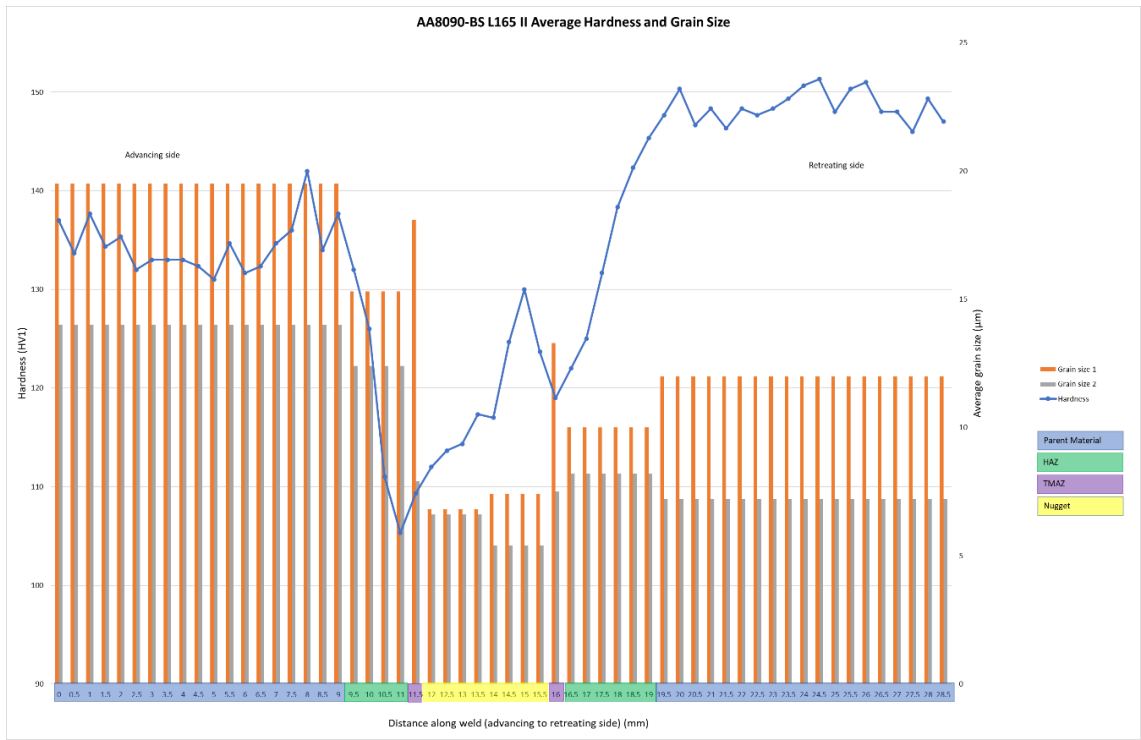
6.4.2 Testing

6.4.2.1 Hardness

The results of hardness testing conducted approximately mid-thickness across each weld are shown in Figure 126 with indications of weld zones indicated as in previous plots. Analysis of the II weld shows a sharp decrease in hardness from the AA8090 parent material into the HAZ, with the advancing side hardness minima occurring in the HAZ. A slight increase in hardness occurs in the advancing side TMAZ, with a gradual rise in hardness within the AA8090-dominated part of the nugget. The hardness value then both rises and decreases sharply within the BS L165-dominated part of the nugget. A spurious result at the 15.0 mm test point was considered, however these plots were generated from tests from multiple welds, all of which demonstrated this sharp rise and reduction within the retreating side of the nugget. It is considered that differing degrees of recovery and recrystallisation have occurred within the nugget with changes to the volume fraction of strengthening precipitates and coarsened incoherent precipitates. The retreating side hardness minima occurs in the TMAZ, with a subsequent sharp increase in the hardness values through the HAZ until the unaffected parent material is reached. Neither side reached the measured parent material original hardness value (although they both met their respective minimum specified hardness), suggesting that although the hardness did plateau, the extent of the heat input to the weld was more far reaching than anticipated, perhaps due to the thin gauge of the material.

Analysis of the \perp weld hardness again showed a sharp decrease from the AA8090 parent material through the HAZ, however in this case there was a small amount of hardness recovery in the HAZ. This was again observed on hardness testing of several \perp welds. The advancing side hardness minima occurred within the TMAZ. Similar to the II weld, the AA8090-dominated part of the nugget showed a gradual increase in hardness as the centreline was approached. Upon reaching the BS L165-dominated part of the nugget, the hardness values levelled (albeit with some oscillation) across that part of the nugget. The hardness within the TMAZ was equivalent to that of the nugget, with a subsequent reduction and the retreating side hardness minima occurring approximately 1 mm into the HAZ. The hardness then increased throughout the remainder of the HAZ until the

parent material was reached. In this case the AA8090 side met the parent material original hardness, while the BS L165 side fell short until well into the parent material, suggesting that the retreating side HAZ may actually extend by several additional millimetres.



(a)



(b)

Figure 126: Showing hardness and grain size plots of a) AA8090-BS L165 II, and b) AA8090-BS L165 I.

The hardness data analysis regarding dissimilar welds within the literature is highly influenced by the welding parameters, the materials used and their respective position (i.e. which of the dissimilar materials is positioned on the advancing and retreating sides). As no research could be found in which AA8090 and BS L165 were joined by FSW, no direct comparison can be made. Mishra et al. (2014) describe research in which the degree of variation in hardness within the nugget was dependent on which side the AA6061 and AA5052 alloys were positioned; in this study the hardness minima were located within the HAZ and it was at this point that tensile fracture occurred. Robe et al. (2015) reported hardness maps of AA2024 and Al-Li AA2198 dissimilar welds which showed variation within each “half” of the nugget, with higher values reported close to the weld centreline. They also state that for FSW precipitation hardening aluminium alloys the grain size is not a reliable indication of hardness. Saravanan et al. (2015) used AA2014-T6 within a dissimilar weld and found that the hardness minima occurred within the HAZ. They assert that the hardness within the nugget depends greatly on the amount of material mixing which occurs within the weld. In their research on AA2198-AA2024, Khalilabad et al. (2018) found that the hardness minima occurred in the TMAZ/ HAZ area but did not specify exactly which area.

In this current research, apart from close to the top surface of the II weld, little actual mixing has occurred, i.e. there are no onion rings, which is itself dependent on the weld parameters and the degree of plasticity achieved within the weld. Perhaps if hotter weld parameters (acknowledging the challenges that this poses with regards to BS L165 warping) were used, greater mixing between the materials would have occurred within the nugget and the hardness would have been less varied.

6.4.2.2 Tensile Testing

The results of AA8090-BS L165 tensile testing are shown in Table 42. For comparison, and in addition to the parent material (transverse parent material test results for comparison with II welds), the similar material weld test results are also shown. Dissimilar weld efficiency is typically measured against the weaker of the two parent materials (Bandhu et al., 2017; Barbini et al., 2018; Park et al., 2020; Venkateswara Rao & Senthil Kumar, 2020), however AA8090 and BS L165 have comparable minimum UTS

specifications and extremely similar measured UTS values. The difference in measured UTS for the two parent materials falls within the uncertainty of the measurement (refer to sections 3.4.2, 4.1.3.2 and 4.2.3.2) and so the materials can be considered to have equivalent measured UTS (when compared with the relevant orientation). However, the similar weld testing showed that the AA8090-AA8090 welds were weaker than the BS L165-BS L165 welds (with the parameters used) and so the AA8090 (advancing) side of the weld was deemed to be weaker in the welded condition, despite the similarities in the parent material properties. Thus, these tensile tests have been compared with the AA8090 parent material to determine weld efficiency.

Table 42: Showing AA8090-BS L165 tensile test results with parent material and similar welds shown for comparison.

	UTS (MPa)		0.2% Proof strength (MPa)		Elongation (%)		UTS Standard Deviation	% UTS Parent Material Spec	% UTS Measured Parent Material	% UTS Measured AA8090 similar material weld	% UTS Measured BS L165 similar material weld
	Spec	Measured	Spec	Measured	Spec	Measured					
AA8090 parent L	400	443	280	343	6	9.5	3.17	110.8	-	-	-
AA8090 parent T	410	438	280	307	9	11.1	2.52	106.8	-	-	-
BS L165 parent L	415	442	345	397	7	8.7	2.82	106.5	-	-	-
BS L165 parent T	415	436	345	393	7	8.4	2.20	105.1	-	-	-
AA8090	410	357	280	256	9	3.3	8.39	87.1	81.5	-	-
AA8090 ⊥	400	359	280	266	6	2.0	23.57	89.8	81.0	-	-
BS L165	415	437	345	340	7	3.3	38.9	105.3	100.2	-	-
BS L165 ⊥	415	430	345	343	7	2.4	22.06	103.6	97.3	-	-
AA8090-BS L165	410	345	280	284	9	1.4	21.08	84.1	78.8	96.6	78.9
AA8090-BS L165 ⊥	400	320	280	Note 1	6	Note 1	31.35	80.0	72.2	89.1	74.4

Table 42 notes:

Note 1: The 0.2% proof strength was inconclusive for this configuration owing to elongation being below the tolerance measurable by the equipment.

The weld efficiency of both dissimilar welds decreased in comparison with the similar welds, with the II weld achieving 78.8% efficiency and the \perp weld achieving 72.2%. When considering 6 relevant⁷ studies in the literature ((Bandhu et al., 2017) regarding AA2014-AA6061 welds, (Barbini et al., 2018) regarding AA2024-AA7050 welds, (Venkateswara Rao & Senthil Kumar, 2020) regarding AA6061-AA2014 welds, (Masoumi Khalilabad et al., 2021) regarding AA2198-AA2024 welds, (Masoumi et al., 2016) regarding AA2024-AA2198 welds and (Sivaraman et al., 2021) regarding AA2014-AA2075 welds) it was found that the weld efficiency of germane dissimilar materials varied between 42.9% and 94% for the most successful welds produced, with an average (of the 6 results from literature considered) of 71.5%. The results achieved in this research are therefore consistent with that produced in the wider research community. Rao and Kumar (2020) attribute the lower tensile strength of dissimilar joints to a different⁸ microstructure being formed within the nugget, creating a non-uniform stress distribution within the weld. They state that dissimilar joint strength is generally attributed to mechanical interlocking of the materials rather than metallurgical bonding, thus the lower tensile strength. Differing degrees of mixing occurred between weld runs in this current research, however none were mixed to the degree that onion rings were formed. This suggests that the overall degree of mixing was poor.

A reduction in % elongation was also observed, beyond that even of the similar welds. It is considered that the heterogeneous nucleation of coarsened incoherent precipitates to the grain boundaries, and weaknesses associated with kissing bonds were the cause, in addition to the frictionally affected surface.

Although not the greatest observed so far, the AA8090-BS L165 weld UTS standard deviations were considerable. Significant scatter was revealed, with results varying from 228 MPa to 339 MPa in just one \perp weld. However, similar to the BS L165-BS L165 welds no discernible pattern with respect to areas of strength and weakness were found, i.e. the two \perp specimens achieving the highest and lowest values both failed mid-weld. This was an indication that the weld quality was not consistent across each weld or

⁷ Relevance was judged based on the materials used.

⁸ Presumed by this author to mean a different and unique microstructure to either of the original parent material's microstructure, however no clarification is provided as to the definition of "different" in the study.

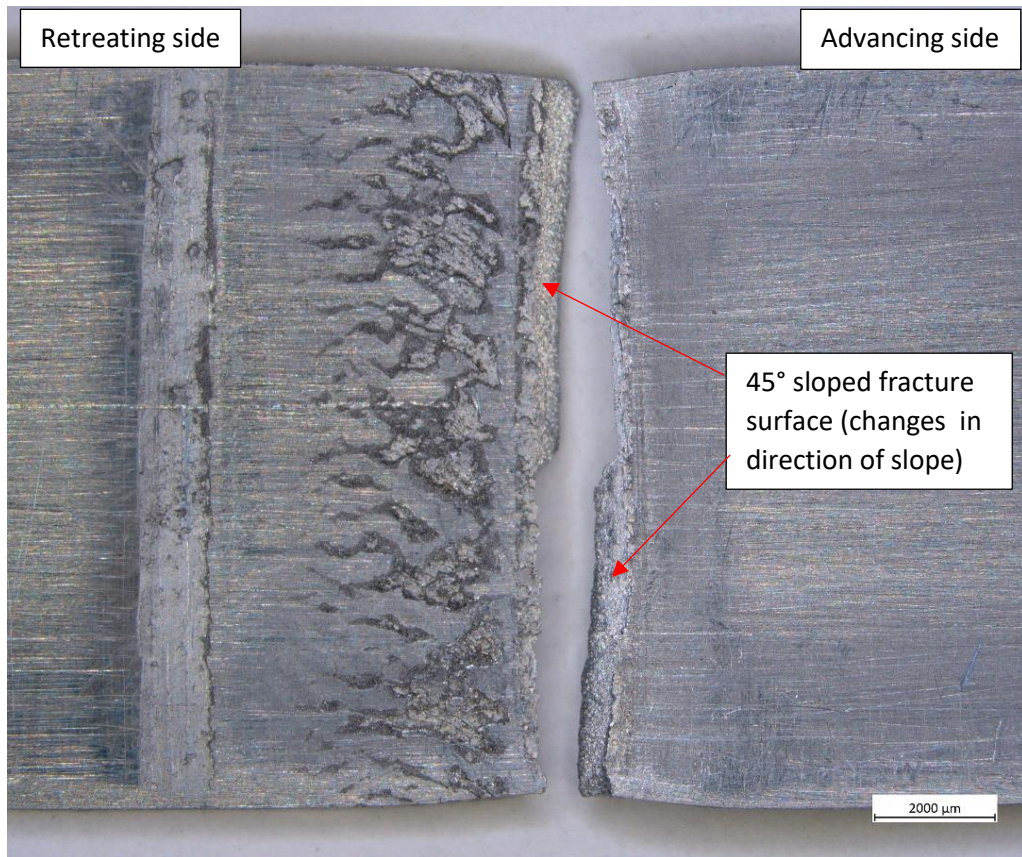
repeatable between weld runs, most likely as a result of inconsistent heat input to the weld.

Of the 20 AA8090-BS L165 II weld tensile tests performed, 12 failed at the advancing edge of weld and 8 failed mid-weld. Rao and Kumar (2020) state that a general “rule of thumb” for weld qualification in dissimilar welding is that the joint should fail in the HAZ of the weaker material rather than within the nugget. They assert that joints which failed within the nugget generally experienced inadequate mixing of plasticised material or suffered excessive heat input. Other research is in agreement with this statement (Bandhu et al., 2017; Barbini et al., 2018; Masoumi et al., 2016; Sivaraman et al., 2021), and this research is broadly in agreement as the majority of the welds failed at the advancing (AA8090) side of the weld. Examples of each failure type, showing position of fracture from the top surface, as a cross section and showing detailed SEM images of the fracture surface are shown in Figure 127 (advancing edge of weld failure) and Figure 128 (mid-weld failure).

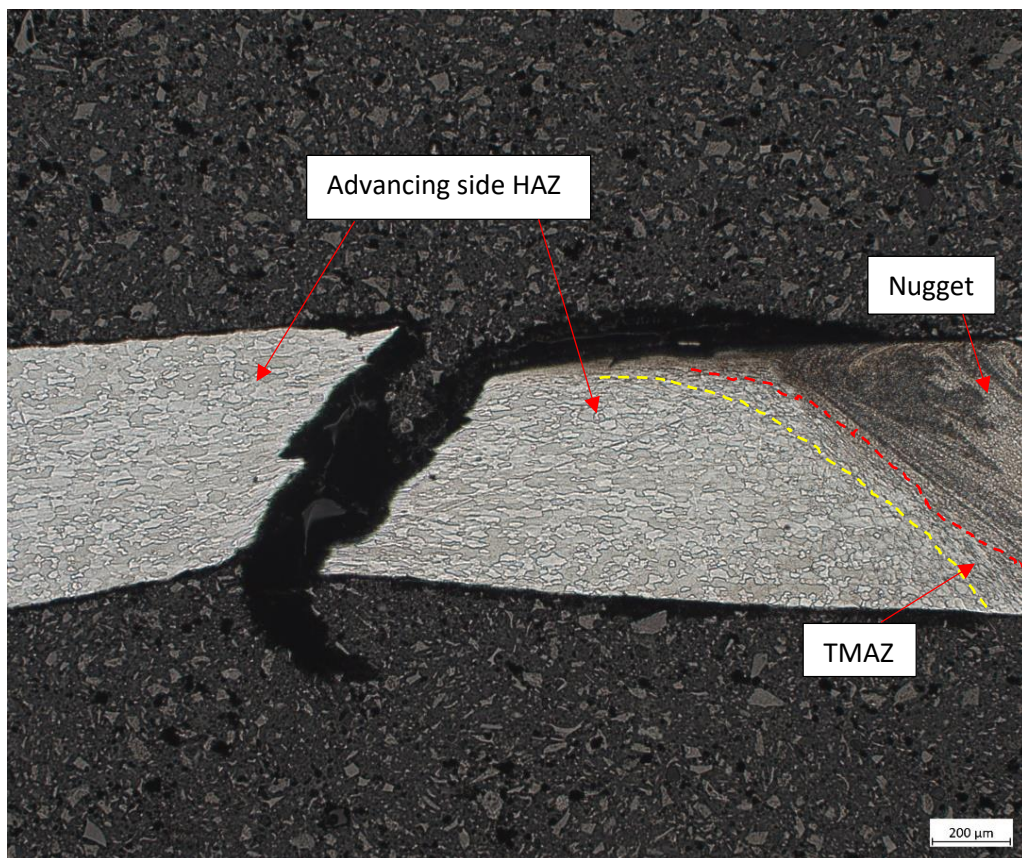
With reference to Figure 127, the 12 tensile specimens which failed along the advancing edge of the weld did so along the edge of the visible part of the weld as viewed from the top surface. The fracture surfaces were dull but relatively smooth and orientated at 45° to the loading direction, although the direction of the 45° slope varied and on some occasions (as shown in Figure 127(a)) alternated along the crack length. The etched cross-section (Figure 127(b)) revealed that the failure initiated at the edge of the overhang and then propagated within the advancing side HAZ. The advancing side HAZ was identified as the softest area of the weld in Figure 126(a) and it is suspected that the crack initiated and propagated at this location due to the combination of the stress intensifier (edge of overhang) and it being the weakest area of the weld.

SEM analysis revealed a mix of intergranular (Figure 127(c)) and transgranular failure (Figure 127(d)) featuring slip planes on the grain boundaries on the intergranular regions (Figure 127(c)) similar to that observed on the AA8090-AA8090 II welds. Also consistent with the AA8090 II similar welds were small pockets of microvoid coalescence located on the grain boundaries. Upon examination of the test results it was found that all 12 advancing edge of weld failures achieved relatively high UTS (although the % elongation was still dramatically reduced from the parent material value) with far less scatter than observed on the \perp welds previously noted. It was also noted that on one II weld, all

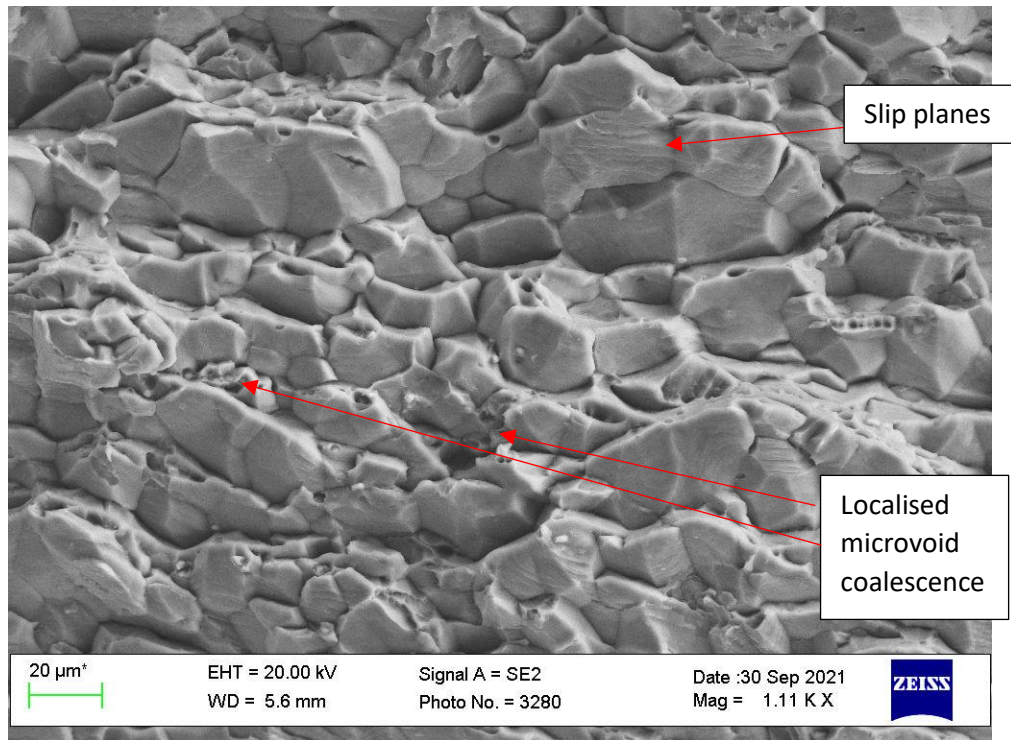
except one of the specimens failed at the advancing edge of weld. This is indicative of a more successful weld, with the failure occurring at the weakest and softest (see Figure 126(a)) point.



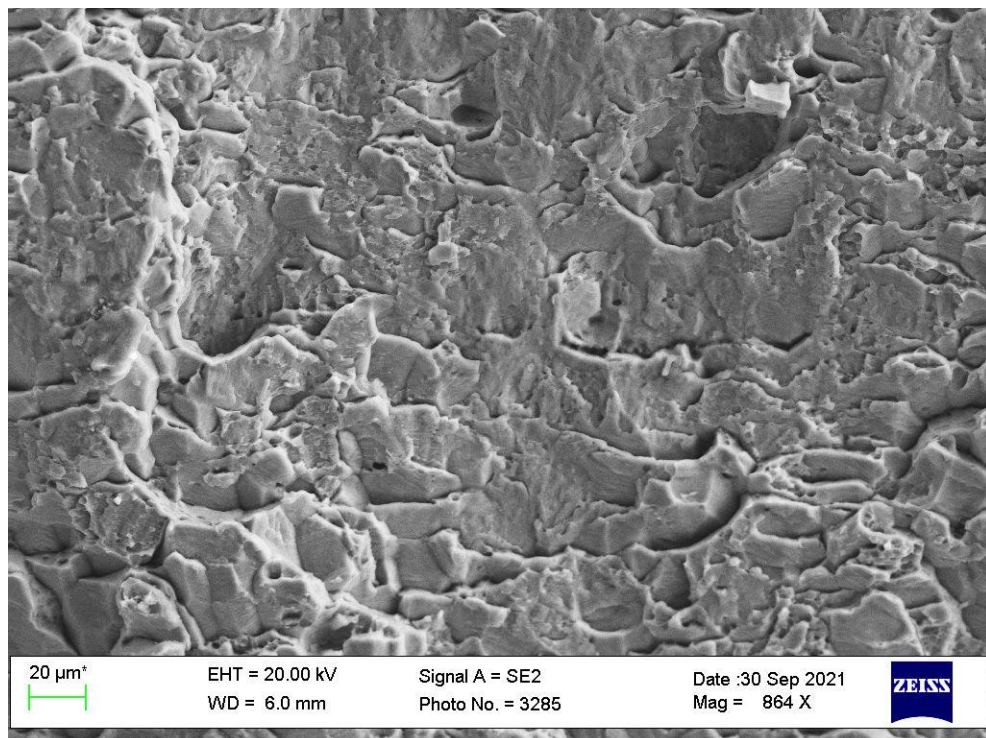
(a)



(b)



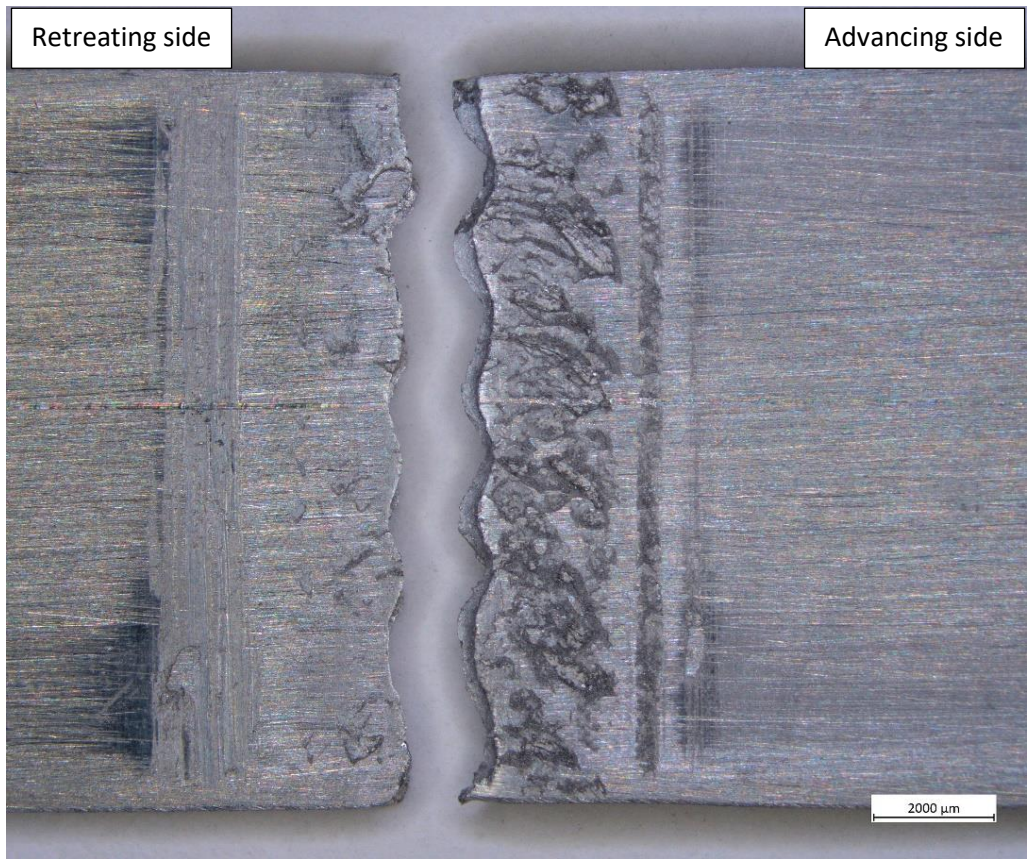
(c)



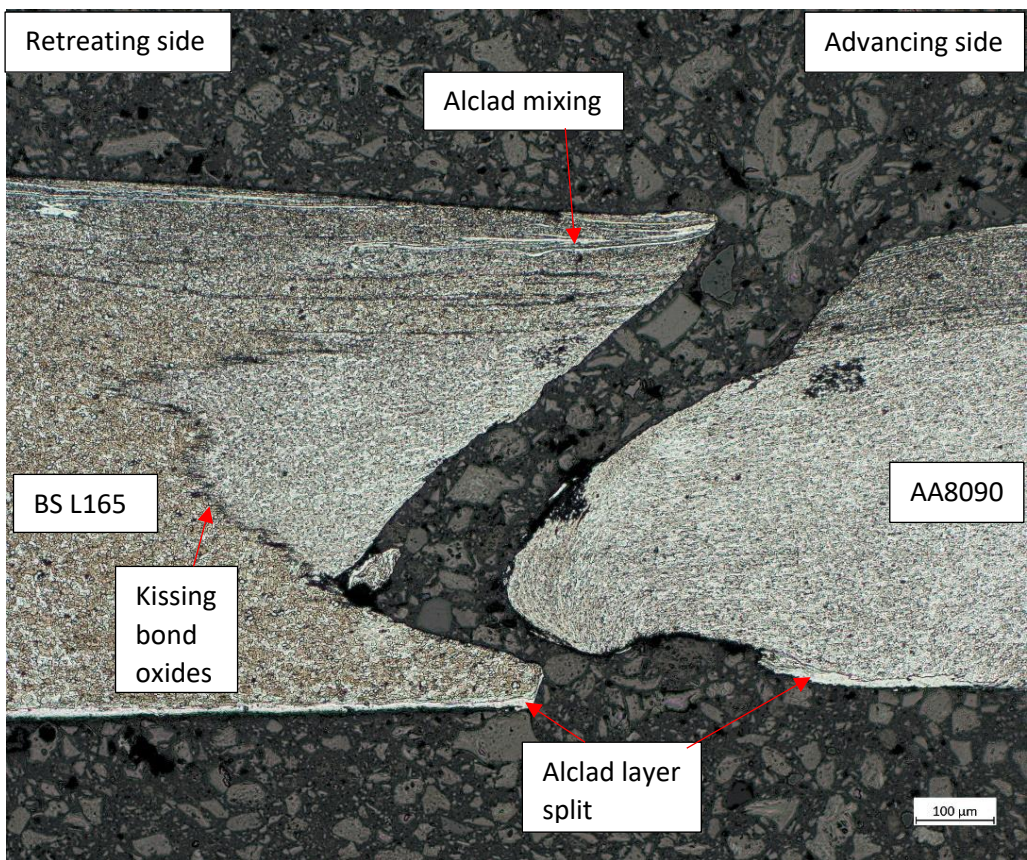
(d)

Figure 127: Showing tensile fracture of AA8090-BS L165 II weld occurring at the advancing side EoW; (a) macrograph showing fracture from top surface, (b) cross-section of weld showing crack path, (c) and (d) SEM image showing detail of fracture surface.

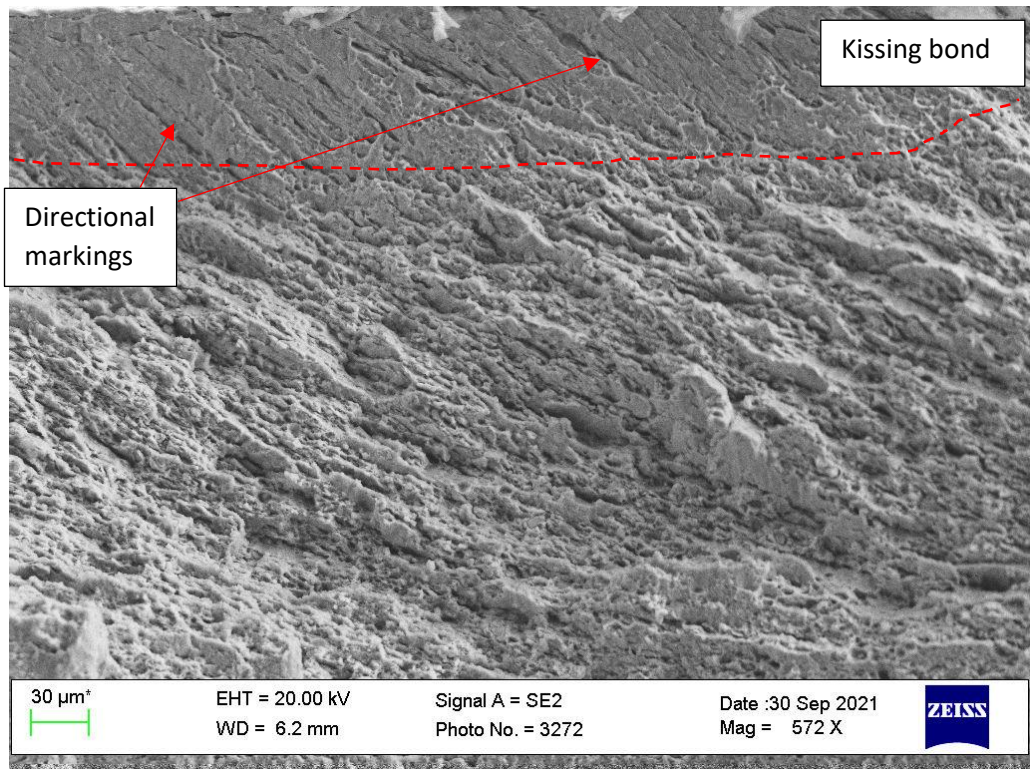
With reference to Figure 128, the 8 tensile test specimens which failed mid-weld did so within or along the edge of the rough and underfilled rippled area, and generally followed a ragged wavy line as shown on Figure 128(a). The fracture surfaces were dull and matt in appearance. The etched cross-section shows that the failure partially occurred at the joint line remnant, where the two materials met mid-weld. The alclad layer can be seen to split, similar to that on a \perp weld examined in Figure 123 (section 6.4.1.3.1). It is considered that a partial kissing bond was the weakest point of this weld and so the crack propagated along this line until such a point that the materials were more fully bonded. At this point the AA8090 nugget material was weaker than the mixed material and the crack then propagated through this part of the nugget 45° to the loading direction. Some plastic deformation can be seen on the predominantly AA8090 half of the failure, likely arising during final failure. SEM analysis confirmed the presence of the kissing bond as the corresponding area showed only directional markings from mixing with no features consistent with material failure; this is indicative of an area which was not properly joined. The main part of the crack propagation was through AA8090-dominated material. This part of the fracture surface was a mix of microvoid coalescence and transgranular failure, similar to that observed on the AA8090 II tensile test specimen which failed mid-weld.



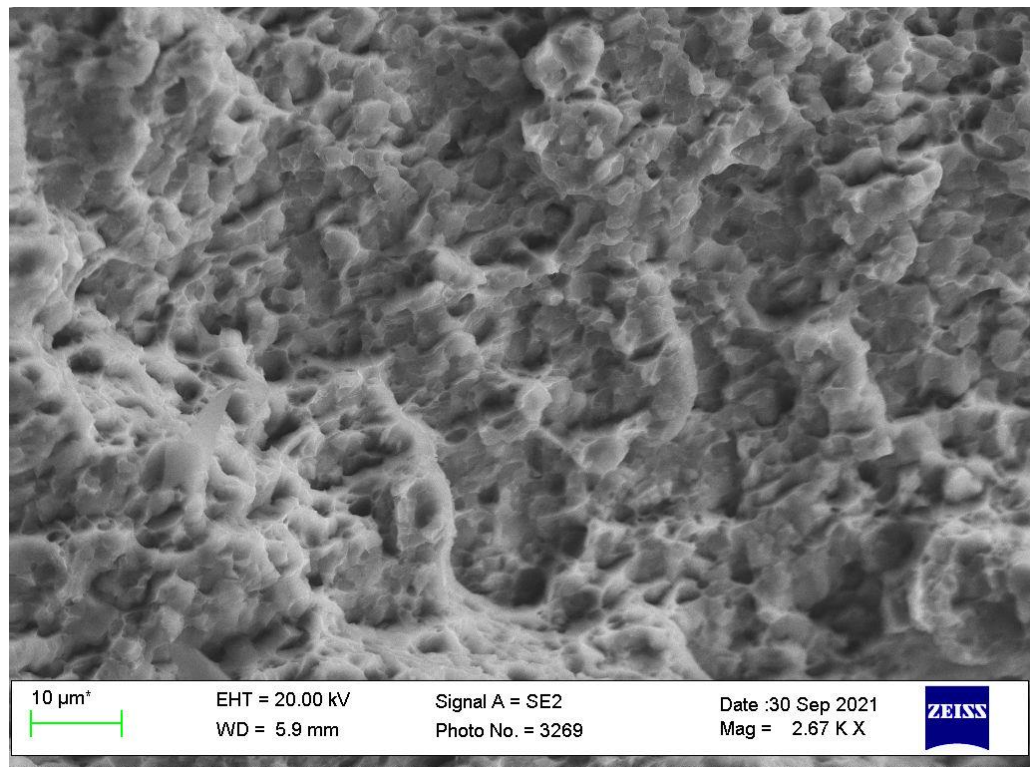
(a)



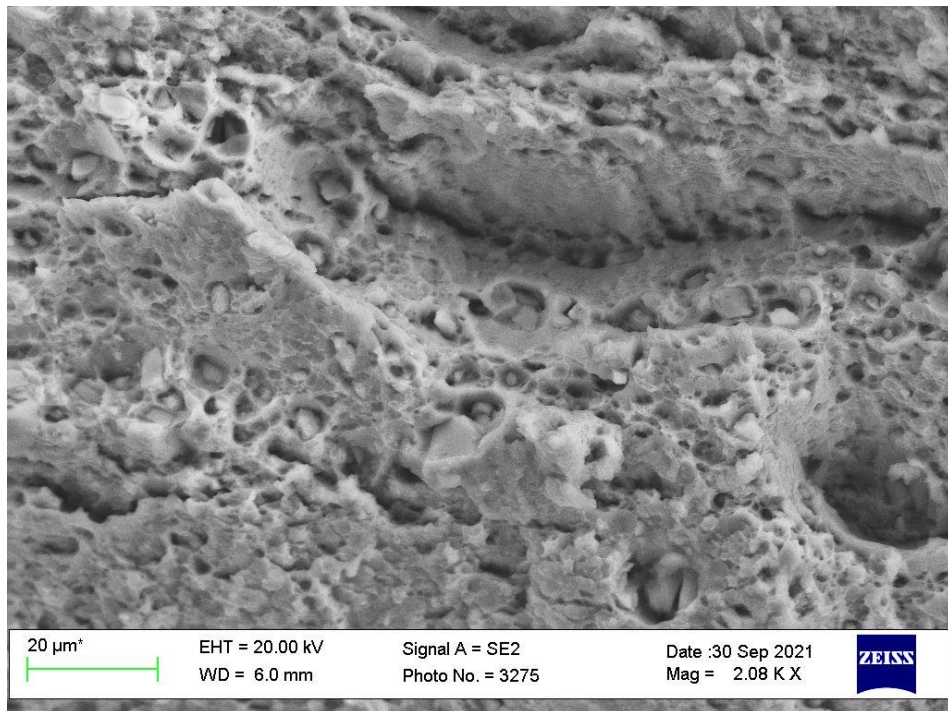
(b)



(c)



(d)



(e)

Figure 128: Showing tensile fracture of AA8090-BS L165 II weld occurring mid-weld; (a) macrograph showing fracture from top surface, (b) cross-section of weld showing crack path, (c), (d) and (e) SEM image showing detail of fracture surface.

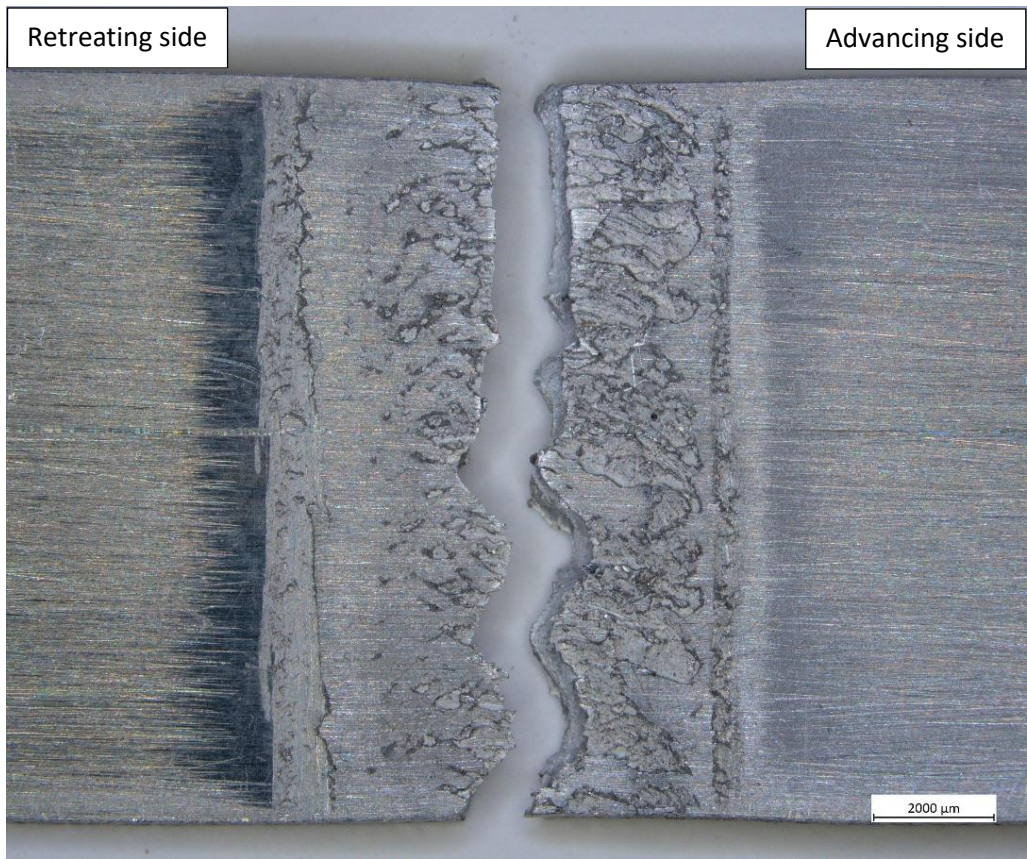
Of the 20 AA8090-BS L165 \perp tensile test specimens, 17 failed mid-weld and 3 failed at the advancing side edge of weld. Based on the previous discussion, this suggests overall poor or inconsistent weld quality as the majority have not failed through the softest area of the weld (advancing TMAZ for \perp welds, see Figure 126 in section 6.4.2.1). Examples of each failure location, showing the position of fracture from the top surface, as a cross section and showing detailed SEM images of the fracture surface are shown in Figure 129 (mid-weld failure) and Figure 130 (advancing edge of weld failure).

With reference to Figure 129, those failures occurring mid-weld did so in a similar manner to the II welds, through the rough, underfilled and rippled areas as viewed from the top surface. Again, similarly to the II welds, they failed with a ragged wavy line as shown on Figure 129(a). The fracture surface observed was at 45° to the direction of loading, however a small lip was observed adjacent to the bottom surface. The etched cross-section revealed that this corresponded to a small kissing bond, although the alclad material had not been drawn into this weld as seen on previous examples. It is

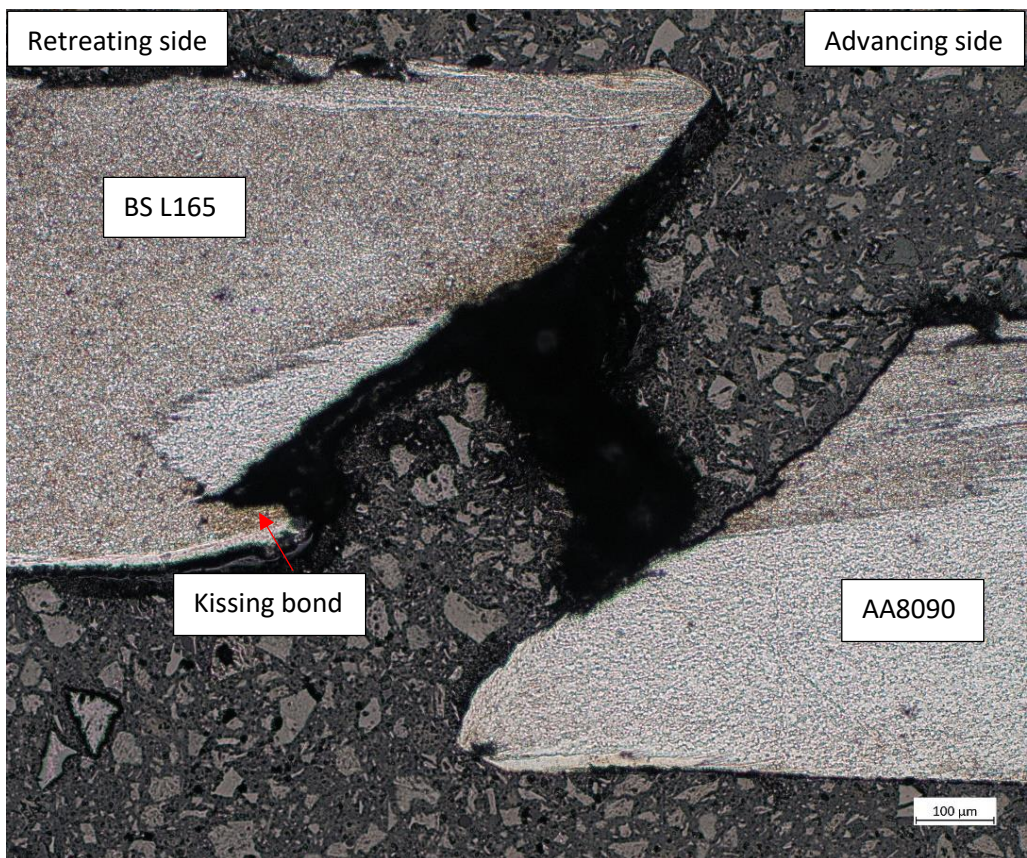
considered that the small kissing bond opened under modest loading, and as the tensile test progressed and additional loading was applied, this opening acted as a stress raiser and caused the specimen to fail at an already weakened position. The weld then failed when the load reached the corresponding UTS of the nugget. The crack propagated through an AA8090-dominated part of the nugget and then through a BS L165-dominated part of the nugget. As observed from the similar weld tensile tests, AA8090 is weaker than BS L165 in the welded condition (with the weld parameters used), therefore it is likely that the crack propagated from the opened kissing bond, through the AA8090 material and then finally through BS L165 material when the overall reduced cross-section weakened the weld.

SEM analysis confirmed the presence of the kissing bond (Figure 129(c)), along with clearly differentiated areas of the different materials. The AA8090 part of the fracture surface (as indicated in Figure 129(c) and shown in detail in Figure 129(d)) had directional markings, retaining the indicators of movement from the pin as it was stirred. This may indicate a lack of plasticity in the material and that the AA8090 part of the weld nugget did not fully consolidate. This introduced weaker areas along these stir planes and thus the material failed along the grain boundaries, although some localised ductility was observed. When the fracture progressed to the BS L165-dominated part of the nugget, it failed in a ductile manner influenced by the large intermetallic particles observed (Figure 129(e)).

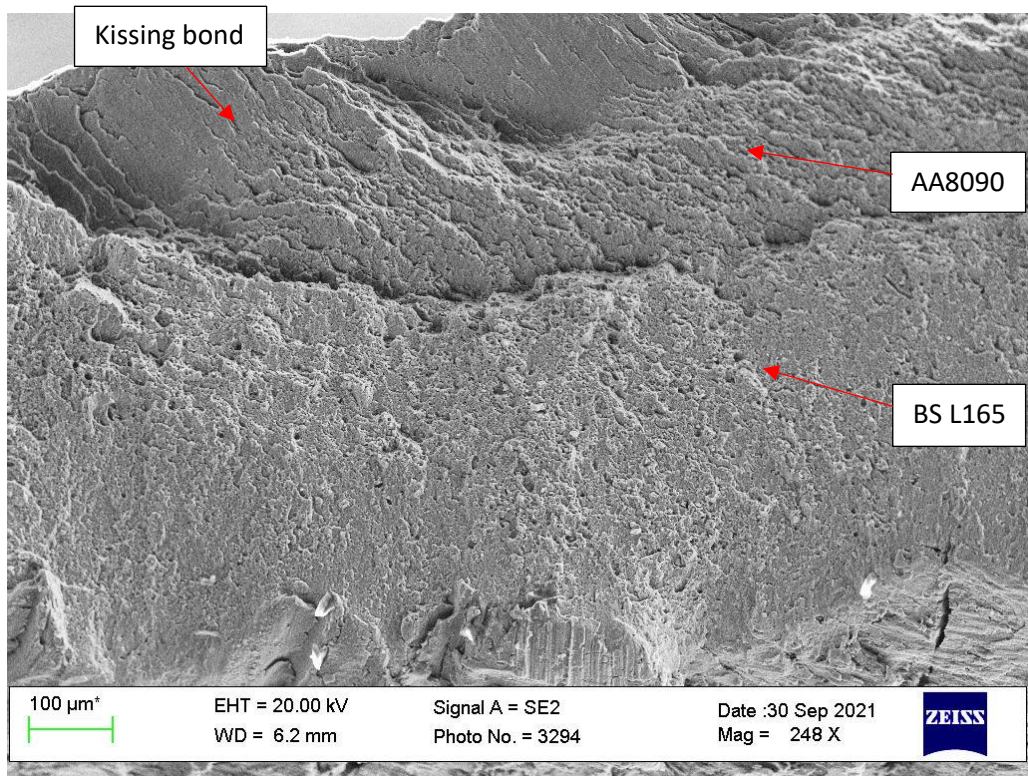
As previously described, the 17 mid-weld failures achieved a wide range of UTS results. This is considered to be due to a variation in both the length of the kissing bond present at that part of the weld, and to the extent of the mechanical interlock (or more precisely lack of) at that area. This coupled with the adequacy or deficiency of the plasticisation, mixing and therefore consolidation of the AA8090 determined the quality of the weld and the value of UTS that it could achieve. These criteria are all determined by the level of heat input to the weld and is therefore another indicator of the lack of consistency across and between welds.



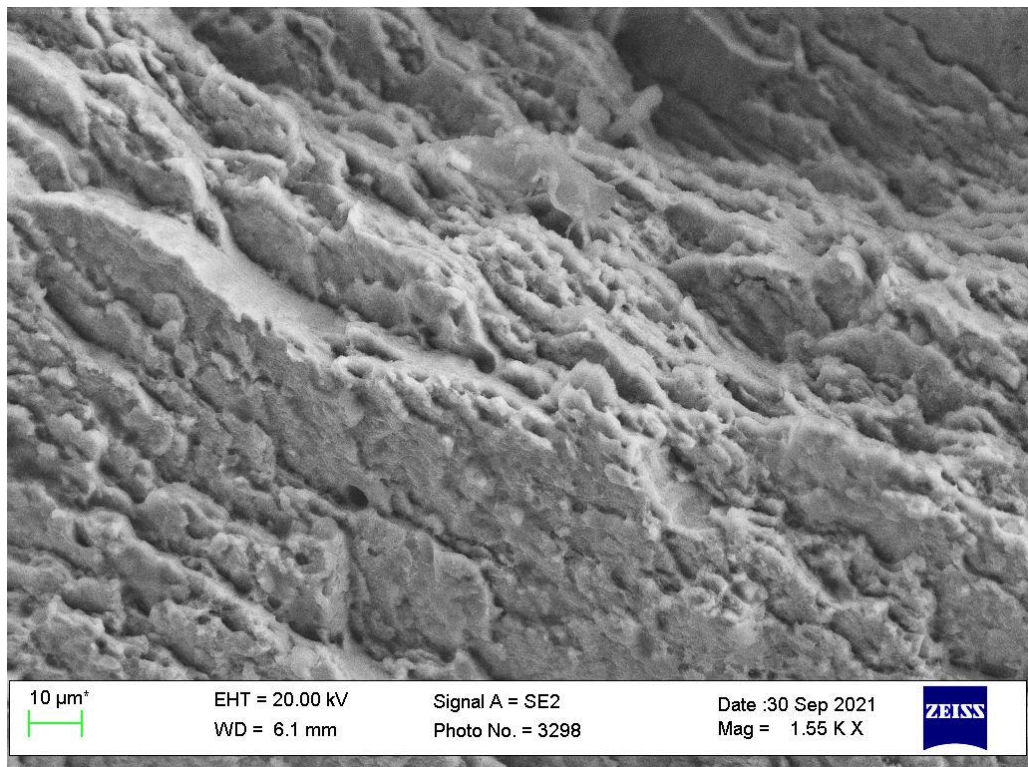
(a)



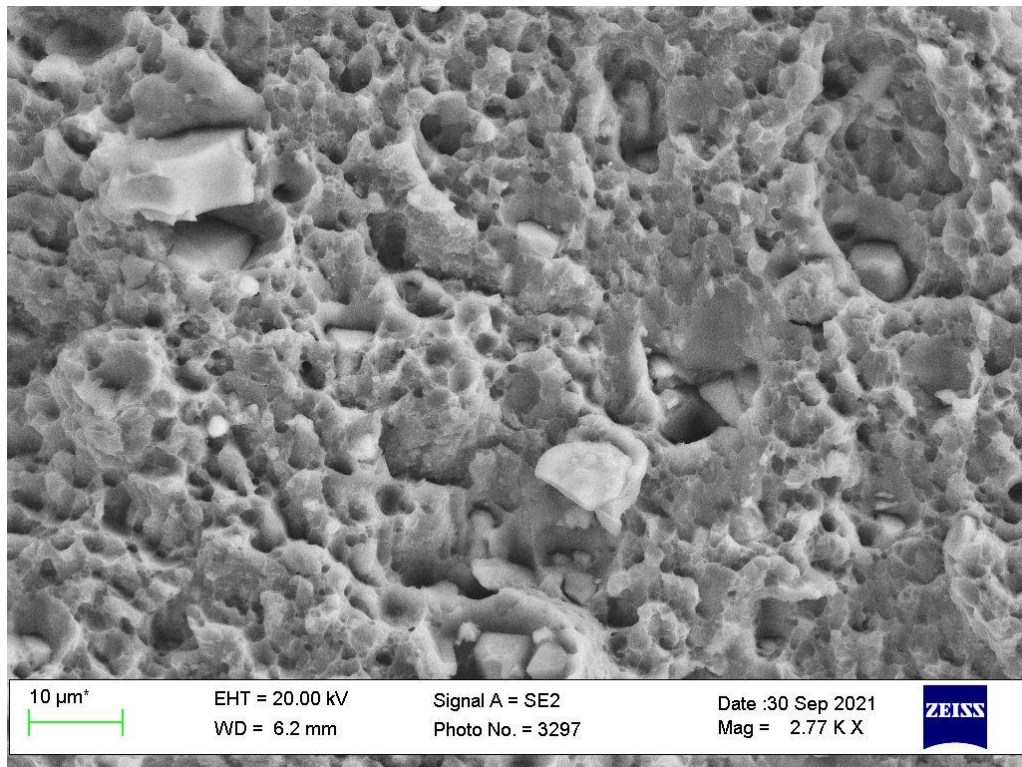
(b)



(c)



(d)



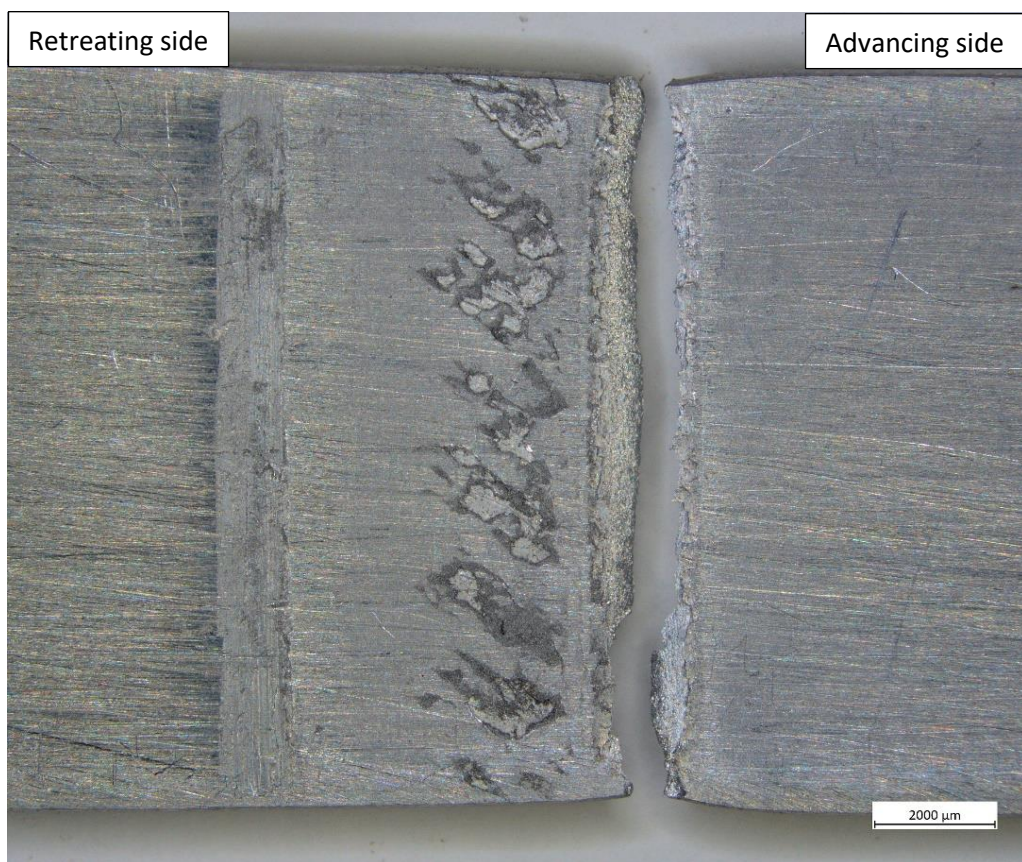
(e)

Figure 129: Showing tensile fracture of AA8090-BS L165 \perp weld occurring mid-weld; (a) macrograph showing fracture from top surface, (b) cross-section of weld showing crack path, (c) low magnification SEM image showing fracture surface full-thickness, (d) SEM image showing predominantly AA8090 fracture surface (e) SEM image showing predominantly BS L165 fracture surface.

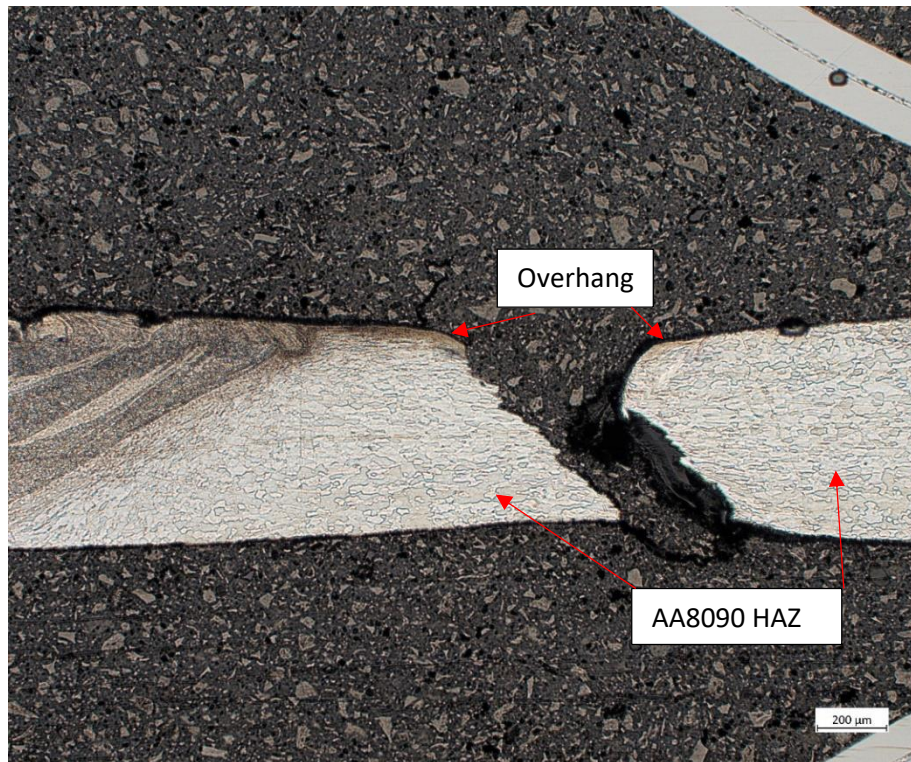
With reference to Figure 130, the three AA8090-BS L165 \perp specimens which failed at the advancing side edge of weld did so in a manner similar to those II welds, i.e. along the visible edge of the weld as viewed from the top surface, in a relatively straight line with smooth dull and matt fracture surfaces orientated 45° to the direction of loading. The etched cross-section shows that the material's failure initiated within the overhang and then propagated through the HAZ with some plastic deformation at the top surface, likely occurring during final failure. SEM analysis revealed a mix of inter and transgranular failure with slip planes visible on the grain faces, similar to that observed on the AA8090 \perp weld advancing and retreating edge of weld tensile tests.

Analysis of the test results revealed that although these three test specimens did not achieve the highest UTS results, all were close to the top of the range. This is indicative

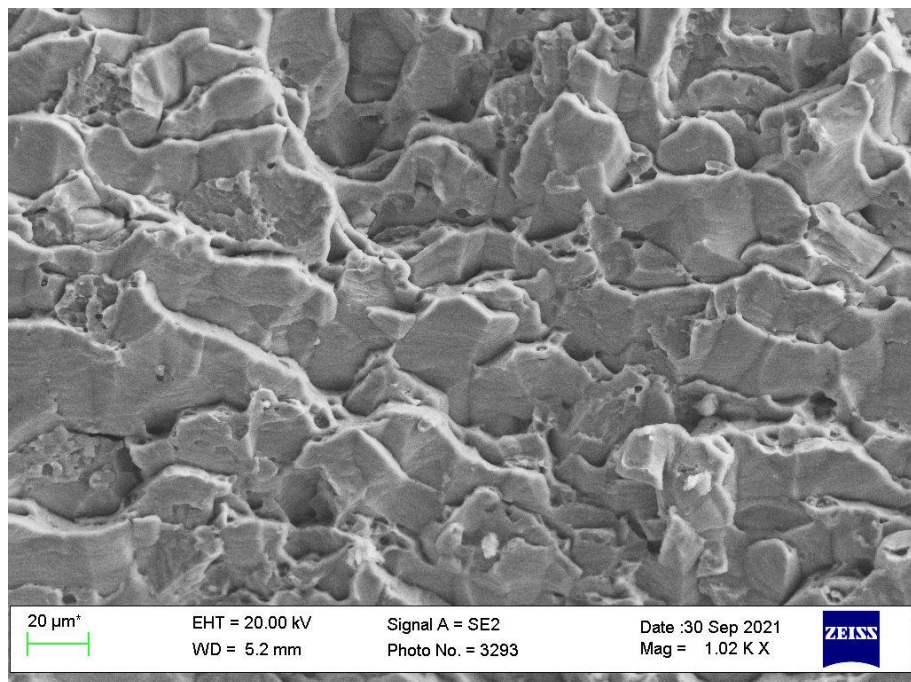
that at these points of the weld, the nugget did not contain a kissing bond, and that the materials were sufficiently mixed such that the weakest point was not within the nugget, but within the HAZ. Interestingly, the softest part of this weld fell in the advancing side TMAZ (Figure 126(b) in section 6.4.2.1), not at the HAZ. Although the TMAZ grains size was large in one direction (Table 28 in section 5.1.3.2), they were smaller in direction 2, while the HAZ grains were relatively large in both directions with grain boundary precipitate coarsening reducing their strength, which is considered to be the reason for failure in the HAZ.



(a)



(b)



(c)

Figure 130: Showing tensile fracture of AA8090-BS L165 \perp weld occurring at the advancing EoW; (a) macrograph showing fracture from top surface, (b) cross-section of weld showing crack path, (c) SEM image showing fracture surface detail.

6.4.2.3 Fatigue Testing

Although the AA8090-BS L165 tensile test samples were compared with AA8090 parent material for determining weld efficiency due to AA8090 being weaker (in UTS) than BS L165 in the welded condition, the results of fatigue testing show that the mean fatigue strength of both BS L165 parent material and the BS L165-BS L165 similar welds was lower than AA8090 parent material and AA8090-AA8090 similar welds. For that reason, the AA8090-BS L165 fatigue tests have been compared with BS L165 for determining weld efficiency. AA8090-BS L165 welds achieved 70.8% weld efficiency when compared with the parent material and achieved 83.7% of the mean weld strength achieved during BS L165 similar weld tests. It is expected that the considerable loss of ductility of these dissimilar welds (see section 6.4.2.2), beyond that even of the similar welds was a significant factor in the loss of fatigue strength. The literature states that generally dissimilar aluminium FSW have lower fatigue strength than the base materials (Wang et al., 2018). Cavaliere, De Santis, Panella and Squillace (2009) found that the positioning of the materials, i.e. what parent material is positioned on the advancing side, has a significant effect on the fatigue strength, with best results for AA2024-AA6082 being produced with the stronger material (AA2024) on the retreating side. Cavaliere and Panella (2008) also found that even if the stronger material is positioned on the advancing side, fatigue results can be improved if an advancing side tool offset (see section 2.3.9.1.4) is utilised. However, Sillapasa, Mutoh, Miyashita and Seo (2017) positioned the harder 7N01 aluminium alloy on the advancing side of a 7N01-6N01 weld and reported a fatigue strength of 83.7% of the weaker material. They also found that the lowest fatigue strength occurs within the HAZ, followed by the nugget (TMAZ was not considered). As fatigue strength is measured via different methods (for example: determining the number of cycles (N) that the material can withstand before failure at a particular stress amplitude (s); determining the maximum s for which failure would not occur at a given N; or studying the growth rate of fatigue cracks within the material (Wang et al., 2018)), and the results are rarely reported as a mean fatigue strength, comparison with the literature is challenging.

The AA8090-BS L165 fatigue tests had the lowest standard deviation and coefficient of variation for measured fatigue strength values of all test configurations, being significantly lower than even the parent materials tests at only 7.38 MPa and 0.034

respectively (Table 31 in section 5.2.3.1) (for comparison the next closest is BS L165 parent material at 11.71 MPa and 0.038). This indicates a reasonably high degree of confidence in the accuracy of the results.

Of the 32 fatigue tests conducted for this configuration, 17 failed prior to the 50,000-cycle cut-off. Of these, all failed within the weld with 9 in-weld but close to the advancing edge, 5 mid-weld and 3 within the weld but close to the retreating edge. Examples of each failure location, showing the position of fracture from the top surface, as a cross section and showing detailed SEM images of the fracture surface are shown in Figure 131 (close to the advancing edge), Figure 132 (mid-weld) and Figure 133 (close to the retreating edge). With regards to the mid-weld failures and to the failures biased towards the retreating edge, the images showing the fracture when viewed from the top surface (Figure 132(a) and Figure 133(a) respectively) look to be in similar positions. The difference in location can however be clearly seen in the etched cross-sections (Figure 132(b) and Figure 133(b) and (c) respectively).

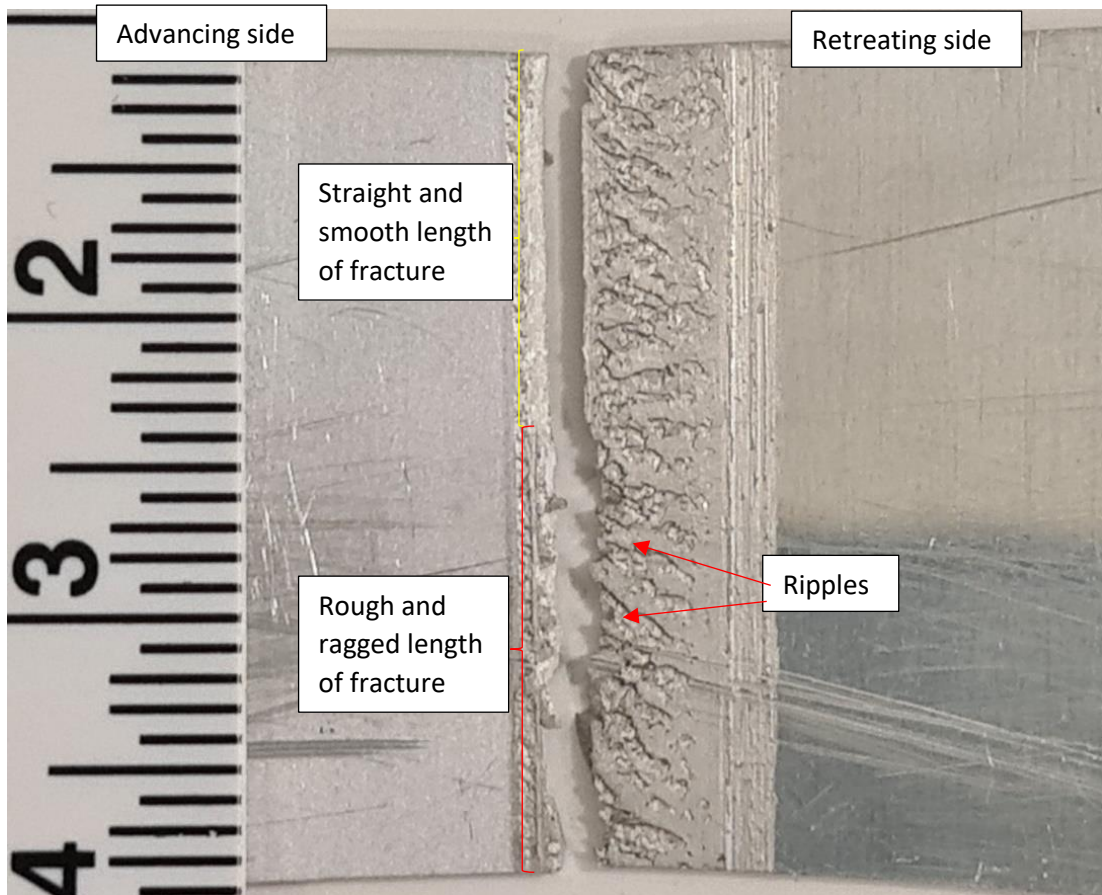
More than half of the failures occurred close to the advancing edge. This is interesting as BS L165 parent material achieved a lower mean fatigue strength than AA8090 parent material, and in the similar welds, BS L165 welds were weaker in mean fatigue strength than the AA8090 welds. When not influenced by flaws such as kissing bonds, the majority of similar welds (both AA8090 and BS L165) failed at or close to the advancing side (Table 32 in section 5.2.3.2). The hardness minima for this AA8090-BS L165 II weld occurred in the advancing side HAZ (Figure 126(a)), as was the case for the AA8090 II weld (only II were considered for fatigue testing) (Figure 75(a) in section 6.2.2.1). The BS L165 II weld hardness minima actually occurred in the retreating side HAZ (Figure 101 in section 6.3.2.1) however this value was extremely close to that of the advancing side minimum hardness value. It is considered that fatigue initiation location is closely related to the location of hardness minima, which is in turn produced by coarsening of the precipitates which heterogeneously nucleate at grain boundaries, weakening the material in that area.

With reference to Figure 131, a fracture occurring within the weld but heavily biased towards the advancing side is shown. The fracture occurred along the edge of the rough and underfilled area, but not at the actual boundary of the visible weld when viewed from the surface. Approximately one half of the fracture length was ragged and strongly

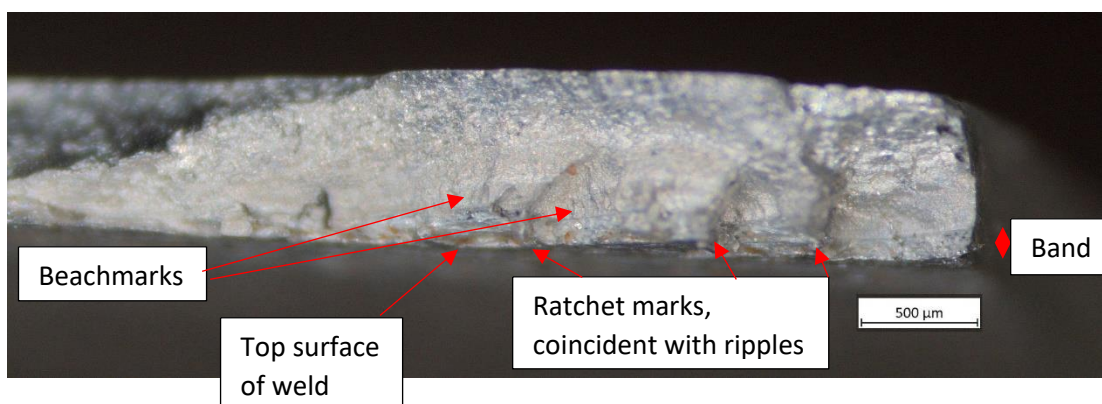
influenced by the rough surface ripples while the other approximate half was straight and smooth; these areas are indicated on Figure 131(a). Stereo microscopy revealed that the fracture surface associated with the ragged length of the fracture was itself quite rough with “ratchet” marks indicative of multiple fatigue initiation sites (Figure 131(b)); these corresponded to rough surface ripples suggesting that the fatigue response in this case was influenced by the ripples acting as stress raisers. The fracture surface corresponding to the straight length of the fracture was orientated at approximately 45° to the direction of loading and had a small distinct band (approximately 100-150 µm depth) adjacent to the top surface of the weld which had a different appearance to the rest of the fracture surface (Figure 131(c)); ratchet marks were also visible through the band. This band was also visible on the fracture surface corresponding to the rough crack length with the ratchet marks proliferating along it. It is considered that this band corresponded to the area of mixing along the surface of the weld.

The etched cross-section showed that the crack had initiated within the band observed via stereo microscopy and then propagated through part of the nugget, ending within the TMAZ. While this has not failed at the area of minimum hardness as described earlier in this section, the hardness within the TMAZ is low in comparison with other areas, and the ripples on the surface of this specimen gave rise to a stress raiser, thereby relocating the point of initiation. The mating fracture surface on the right-hand side of Figure 131(d) is a different shape to that on the left-hand side because the failure occurred within the underfilled area of the weld surface. Additionally, as the specimen was cut part-way through the length, there may be some irregularity to the alignment of the adjoining fracture surfaces, i.e. they may not have been cut exactly and so misaligned although all attempts at precision were made. It is considered that the rough ripples, combined with the area of surface mixing acted as stress raisers initiating fatigue at multiple points adjacent to the top surface of the weld. These cracks propagated to a greater extent in the length corresponding to the rough crack length, but arrested within the straight edged length, before final overload failure when the critical crack length was reached. SEM analysis revealed striations consistent with fatigue failure within the band, with transgranular overload failure occurring elsewhere.

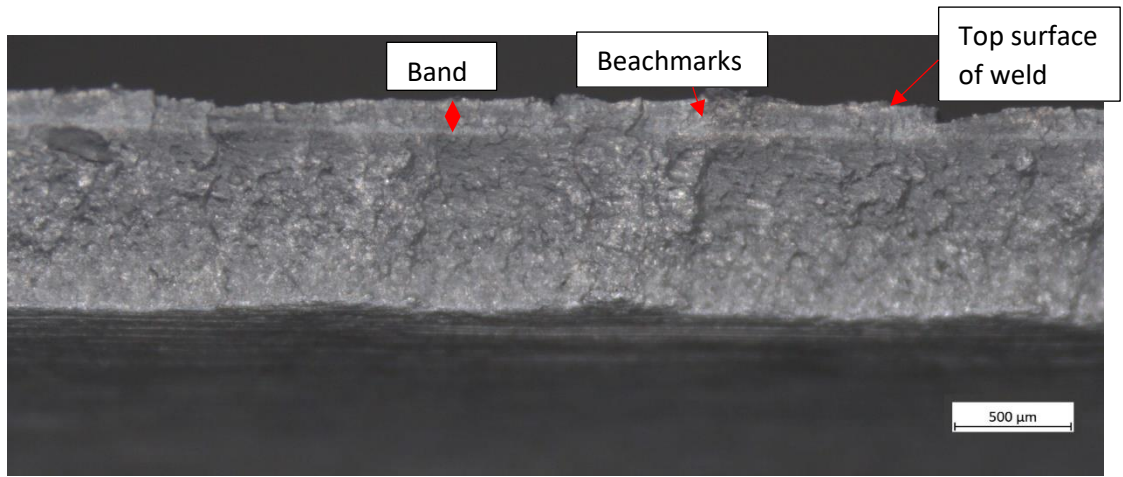
The specimens which failed close to the advancing edge all achieved mid-range to high (approaching the 50,000 cycle) cut-off cycles before failure. It is expected that if the region of chaotic mixing was reduced through improved process parameters, the fatigue strength would improve.



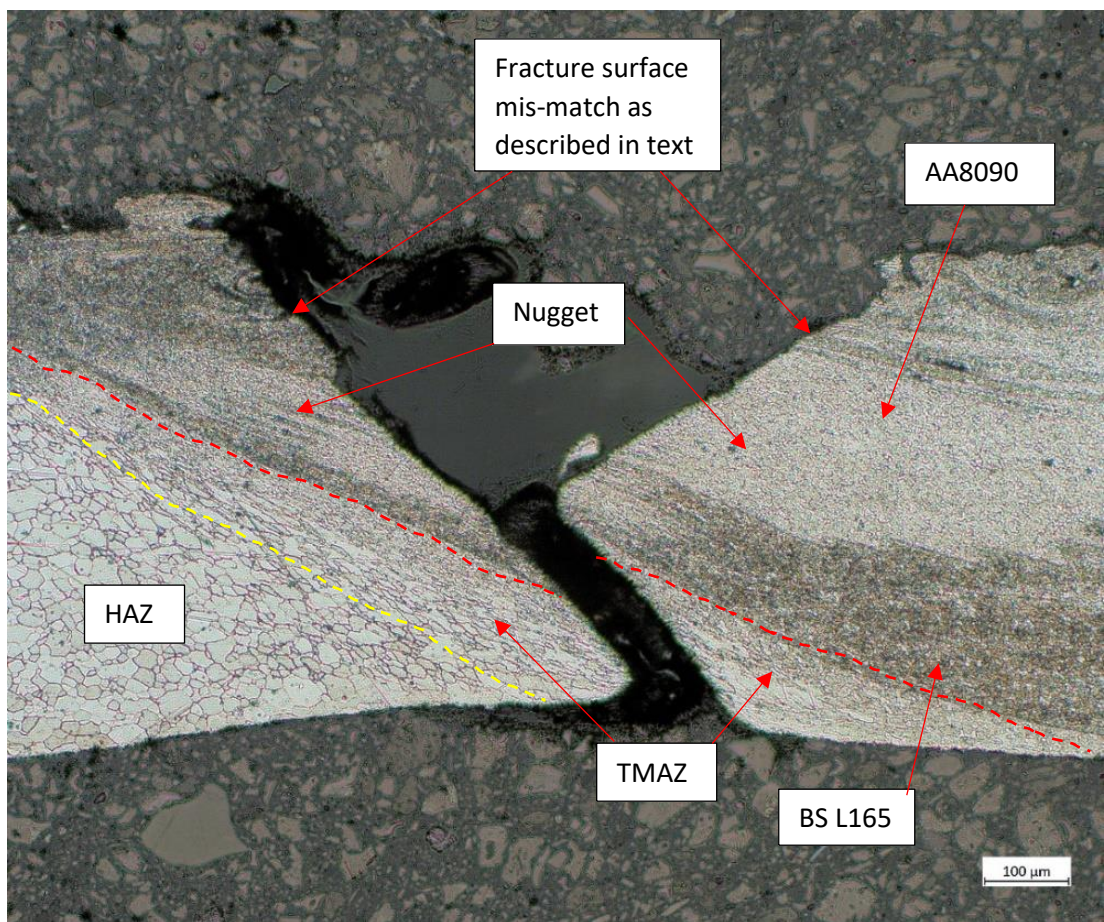
(a)



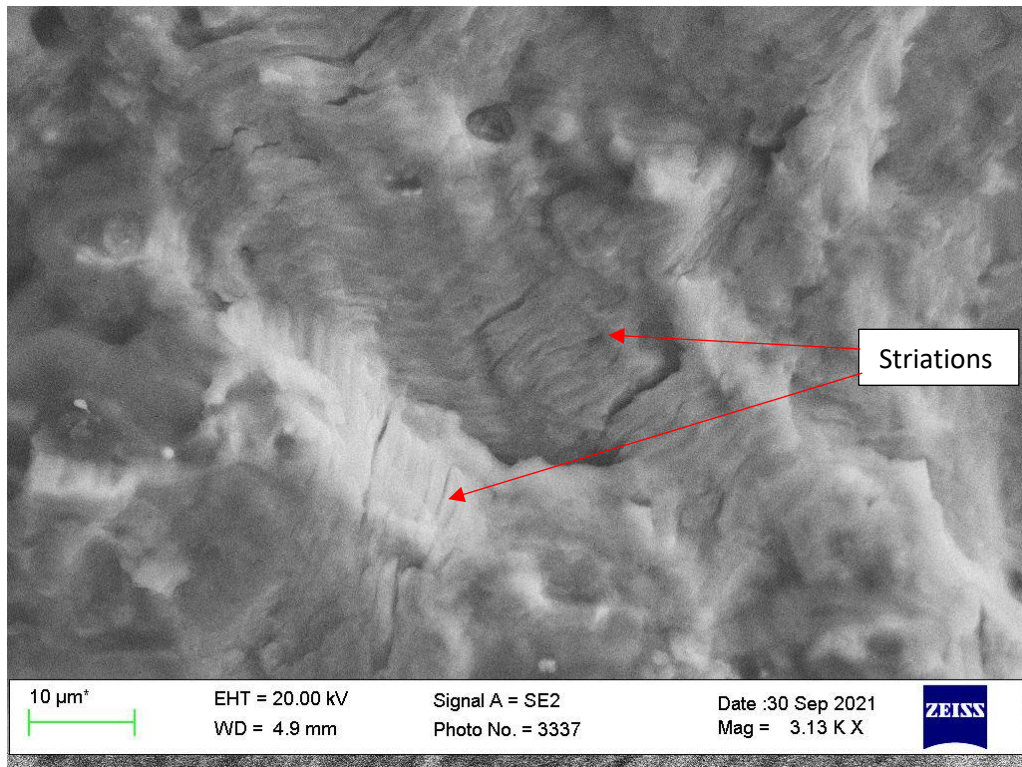
(b)



(c)



(d)



(e)

Figure 131: Showing fatigue fracture of AA8090-BS L165 II weld occurring close to the advancing edge of the weld; (a) macrograph showing fracture from top surface, (b) image showing fracture surface corresponding to ragged length of fracture, (c) image showing fracture surface corresponding to straight length of fracture, (d) cross-section of weld showing crack path, (e) SEM image showing detail of fracture surface.

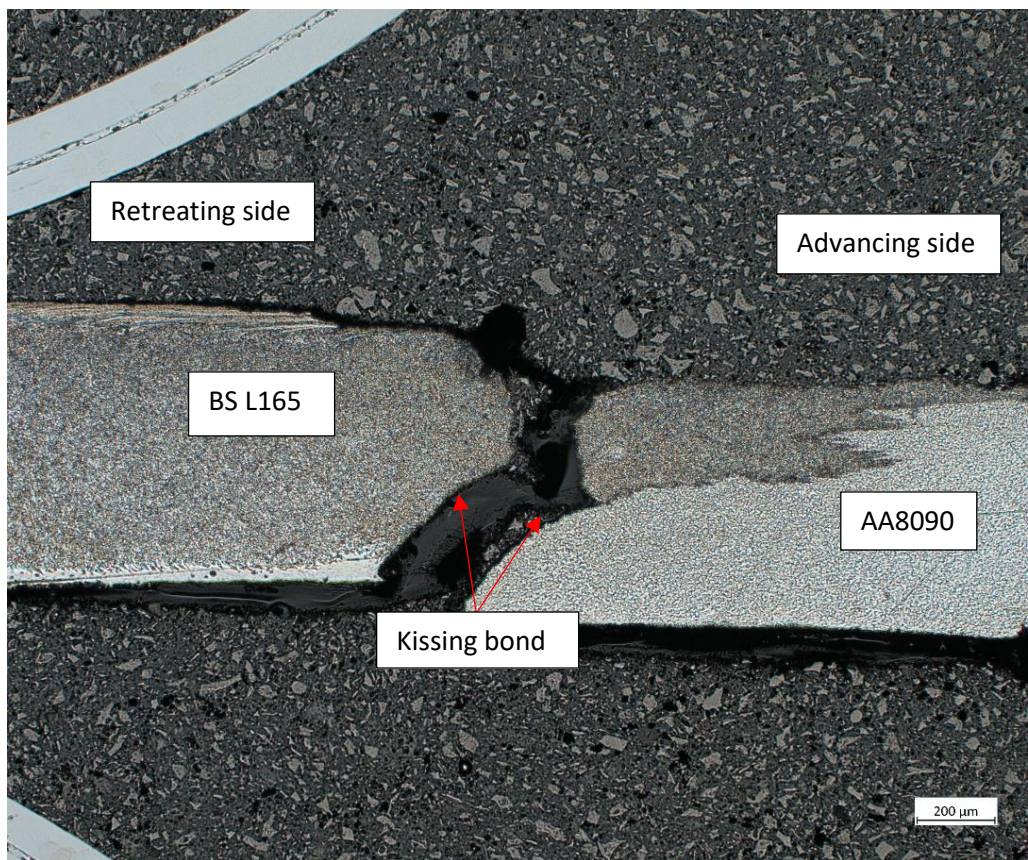
With reference to Figure 132, the fatigue test specimens which failed mid-weld did so within the rough rippled region, with a slight bias to the retreating side, Figure 132(a). The crack lengths were fairly straight and smooth, and stereo microscopy revealed that the fracture surfaces had two regions; one which was dull with directional markings and another which was bright but matt in appearance, Figure 132(c). This was similar to mid-weld fracture surfaces examined previously on similar welds in which a kissing bond was present. Indeed, the etched cross-section revealed that the materials had separated at the join line remnant before propagating through the BS L165 material. The material mixing in this part of the weld was considered to be particularly ineffective. Figure 119 (section 6.4.1.3) shows that the join line of II weld macrostructure examined previously curved slightly towards the retreating side adjacent to the bottom surface of the weld,

before curving towards the advancing side, with AA8090 material mixed through the BS L165 material above this main curve. The \perp weld macrostructure showed that the join line was almost vertical from the bottom surface to approximately mid-thickness, before curving into the retreating side and then doubling back to curve towards the advancing side. Although in the \perp weld there was no mixing adjacent to the bottom surface of the weld, both of these macrographs showed mixing in the top half, or at the very least, material transfer from one side to the other. This weld (Figure 132(b)) shows only BS L165 transfer to the advancing side, with no mixing of the two materials either below or above the main curve. This particular fatigue specimen only achieved 376 cycles prior to failure, indicating that the bond between the materials was superficial. None of the specimens which failed mid-weld achieved over 19000 cycles prior to failure, with 4 of the 5 under 6000 cycles. The lack of join (kissing bond) covering approximately half of the weld thickness resulted in the remaining BS L165 material being unable to support the cyclic load.

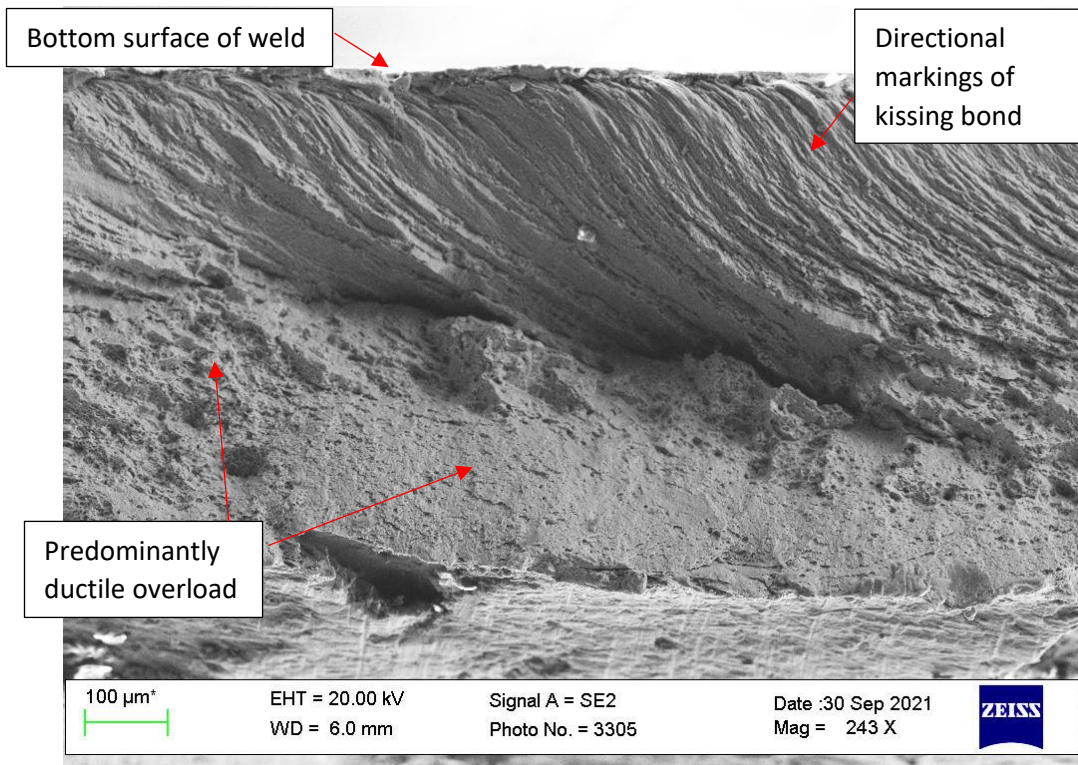
SEM analysis confirmed the presence of the directional lines. Faint striations were observed close to the kissing bond/ failed material boundary (observed on the failed material), with the majority of the fracture surface comprised of ductile microvoid coalescence, consistent with overload. Elongated ductile dimples (Figure 132(e)) confirmed that the final failure occurred adjacent to the top edge of the weld.



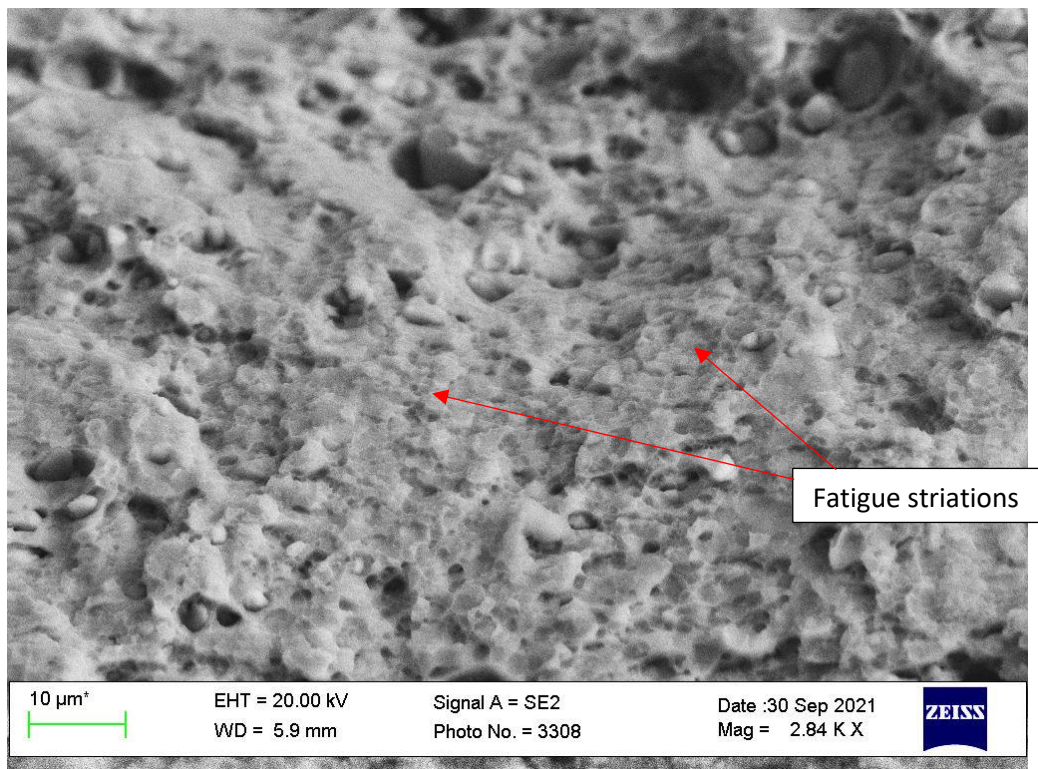
(a)



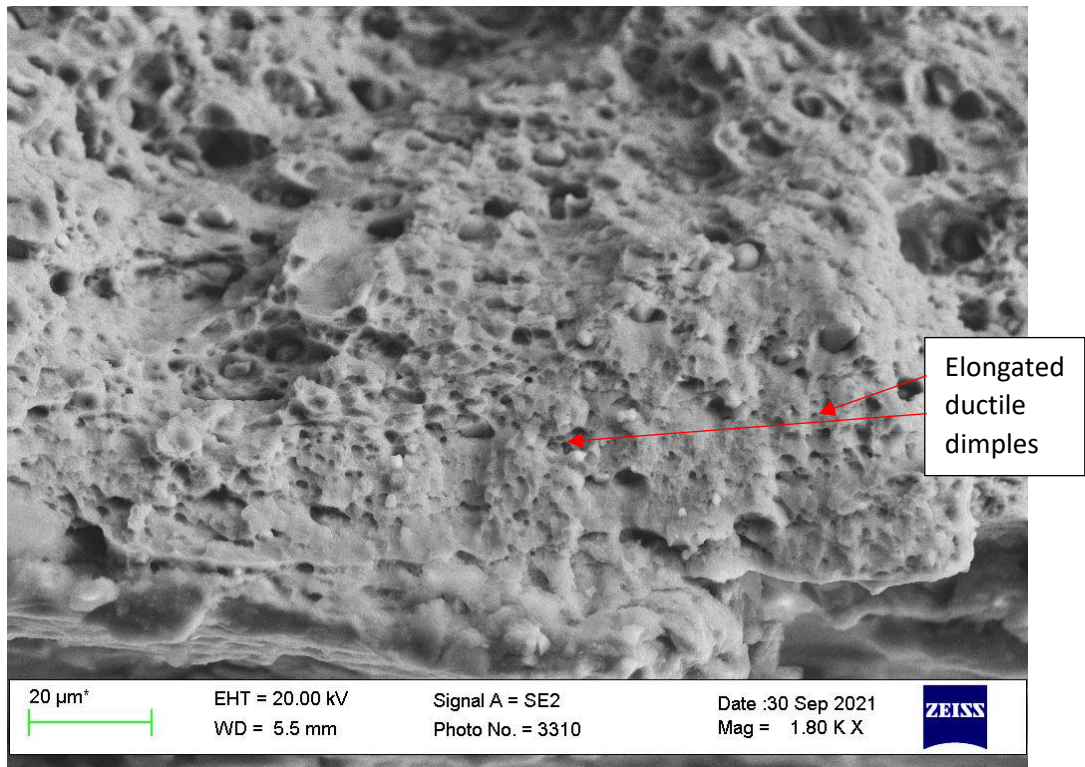
(b)



(c)



(d)



(e)

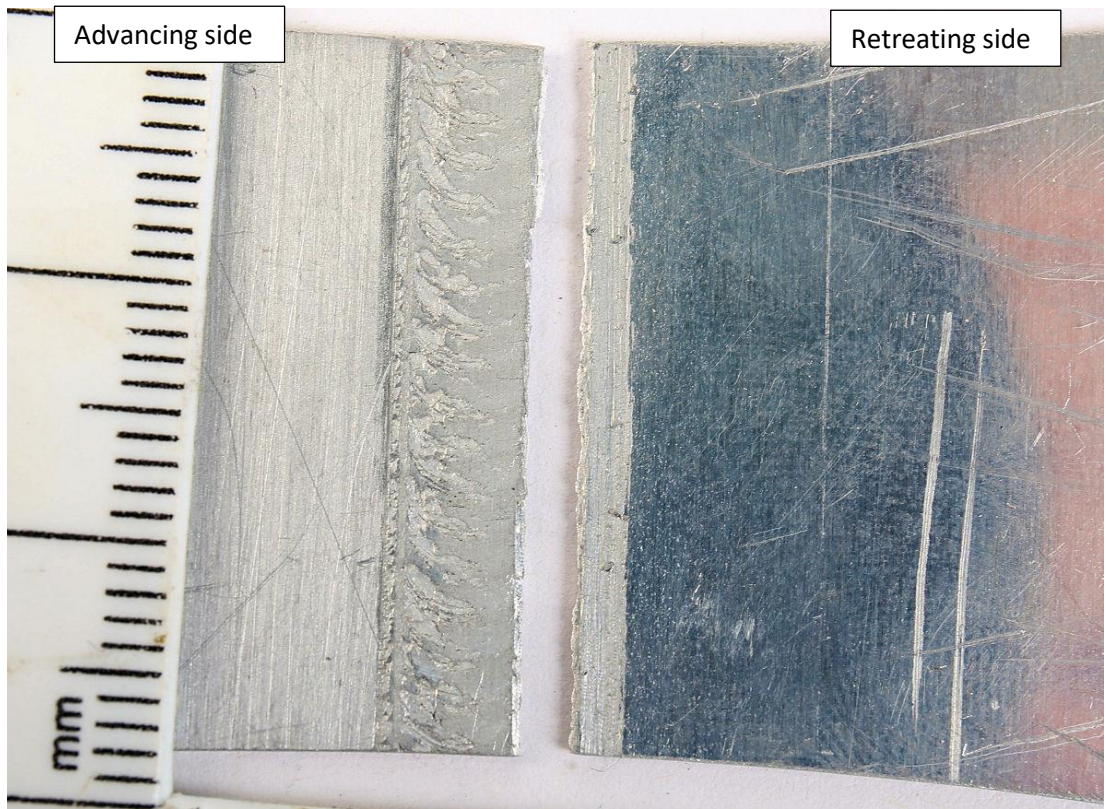
Figure 132: Showing fatigue fracture of AA8090-BS L165 II weld occurring mid-weld; (a) macrograph showing fracture from top surface, (b) cross-section of weld showing crack path, (c) low magnification SEM image fracture surface full thickness, (d) and (e) SEM image showing detail of fracture surface.

With reference to Figure 133, the fatigue specimens which failed in-weld, close to the retreating edge as viewed from the top surface of the weld, did so separate from the rough rippled region, along a smooth area of material. Stereo microscopy revealed a ledge of material, too thick to be only the alclad layer present adjacent to the fracture surface (Figure 133(b)). This ledge was of an almost constant thickness across the length of the crack. The fracture surface material adjacent to the ledge had separated from it in places, and thumbnail markings and ratchet marks consistent with fatigue failure were present propagating from it. Due to there being no sharp boundary between the nugget/TMAZ/HAZ interfaces it was difficult to pin-point the exact location of the fracture from one image; Figure 133(c)-(e) show the etched cross-section gradually narrowing in on the failure point with each image location shown on the previous image via a green dashed box. This, together with the stereo microscopy analysis, showed that the fatigue

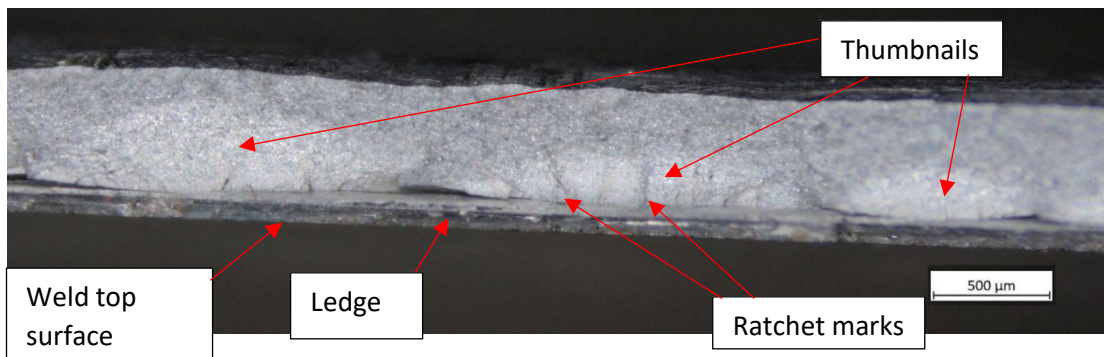
crack initiated sub-surface, in the material adjacent to the ledge. The fatigue crack then propagated through the retreating HAZ, with final overload in the HAZ and ledge. SEM analysis revealed fatigue striations (Figure 133(f)) within the thumbnail markings (Figure 133(b)) and ductile microvoid coalescence present elsewhere on the fracture surface (not shown).

It is considered that the ledge was formed as a combination of alclad layer and the material response to the tool frictional influence. This acted as a stress raiser promoting fatigue failure to initiate from that point. These three failures all achieved mid values with regards to cyclic performance, ranging from 22000-30000 cycles prior to failure. This indicates that this would not be the material's preferred failure location had the surface not exerted such a strong influence.

From the author's experience, the fracture location for relevant dissimilar aluminium FSWs is rarely reported in the literature. Sillapasa et al. (2017) did however cut small round bar test specimens to test the fatigue strength of different weld locations and found that the HAZ was the weakest area with regards to fatigue. This suggests that the failure location in these welds should be the HAZ, but which side? The advancing side (AA8090) in this configuration has the weakest welded tensile strength (from previous testing) however the retreating side (BS L165) has the lowest welded fatigue resistance, but Cavaliere et al. (2009) found that positioning the strongest material on the retreating side (as is the case here) improved fatigue resistance. For this research, only 3 specimens failed in the HAZ however contributory factors such as kissing bonds and "reinforced" surfaces strongly influenced the position of failure. The testing shows that the favoured location with the current weld parameters is close to the advancing side, initiating from the surface and propagating through the nugget and TMAZ. It is considered that with optimal parameters to produce higher quality welds that the failure location would move to the HAZ. Without further testing it is unknown if this would be on the advancing or retreating HAZ, however due to the hardness minima occurring at the advancing side HAZ (Figure 126(a), section 6.4.2.1) it is suspected that this would be the preferred position.



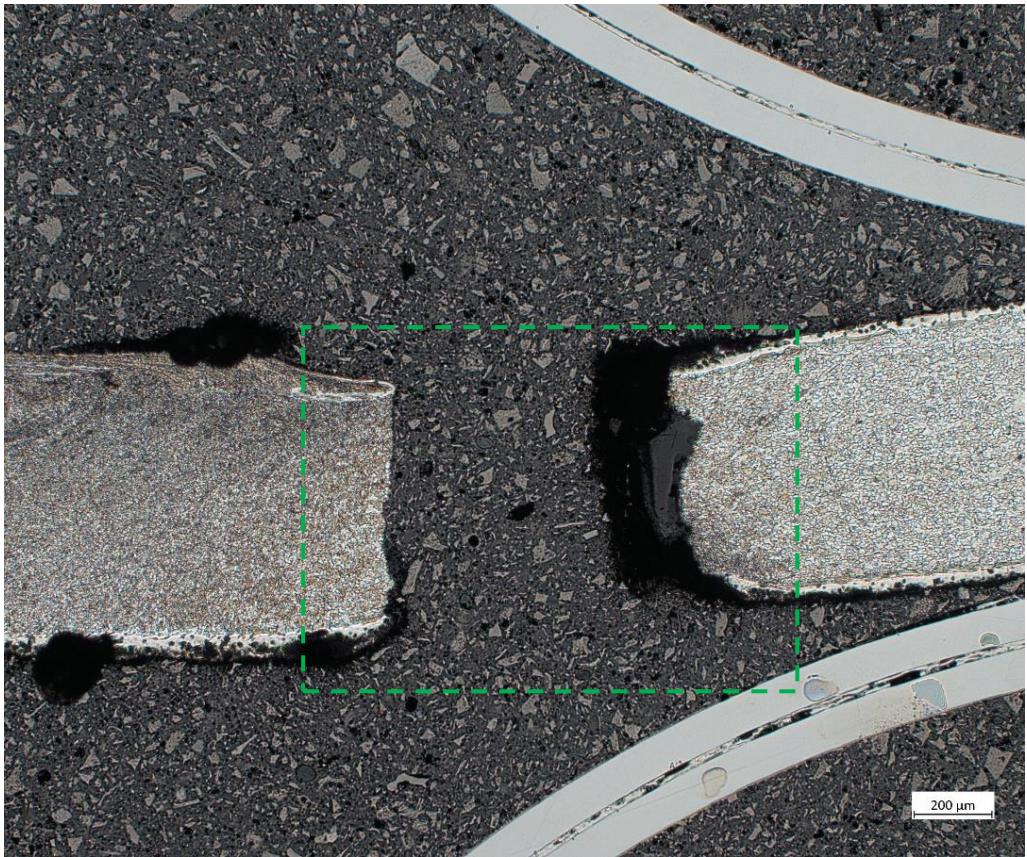
(a)



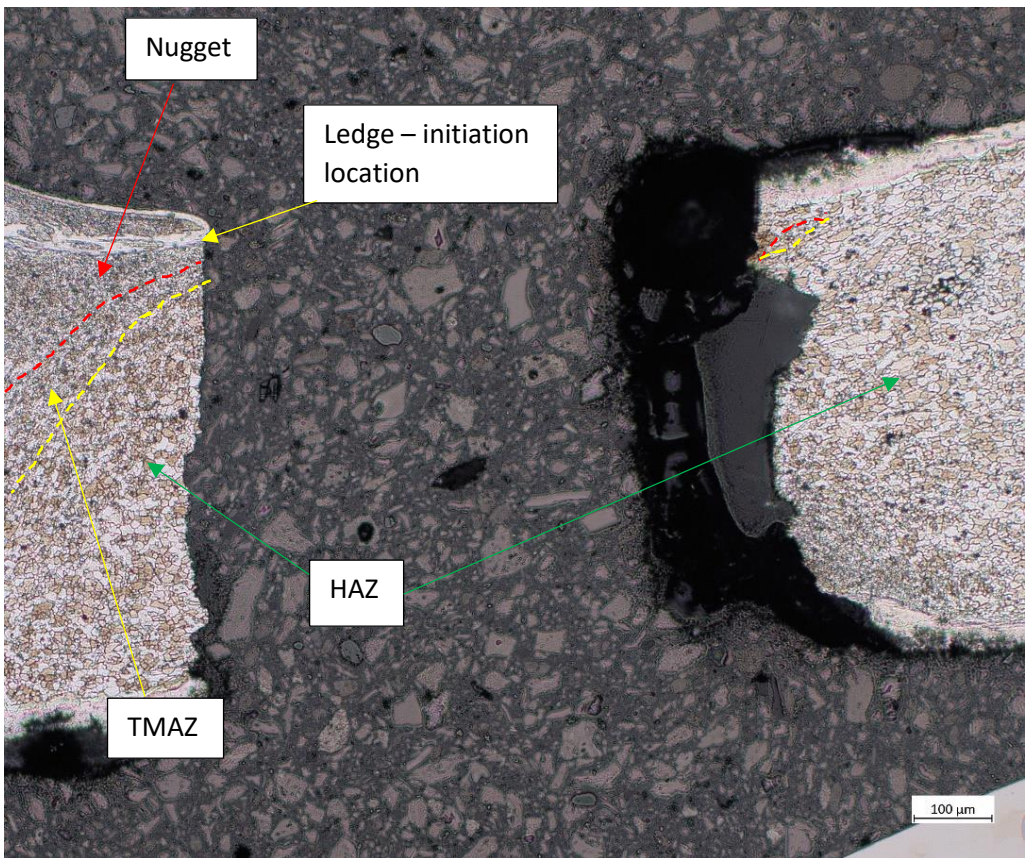
(b)



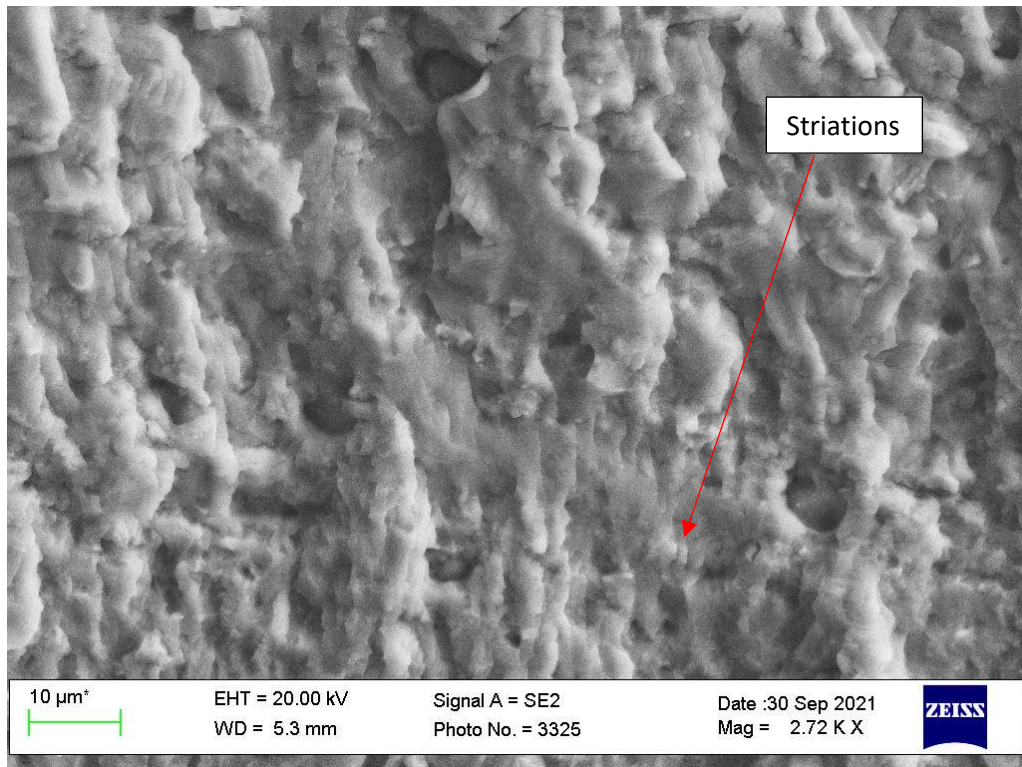
(c)



(d)



(e)



(f)

Figure 133: Showing fatigue fracture of AA8090-BS L165 II weld occurring close to the retreating edge of the weld; (a) macrograph showing fracture from top surface, (b) stereo microscope image showing fracture surface, (c), (d) and (e) cross-sections of weld showing crack path, (f) SEM image showing detail of fracture surface.

6.4.2.4 Residual Stress

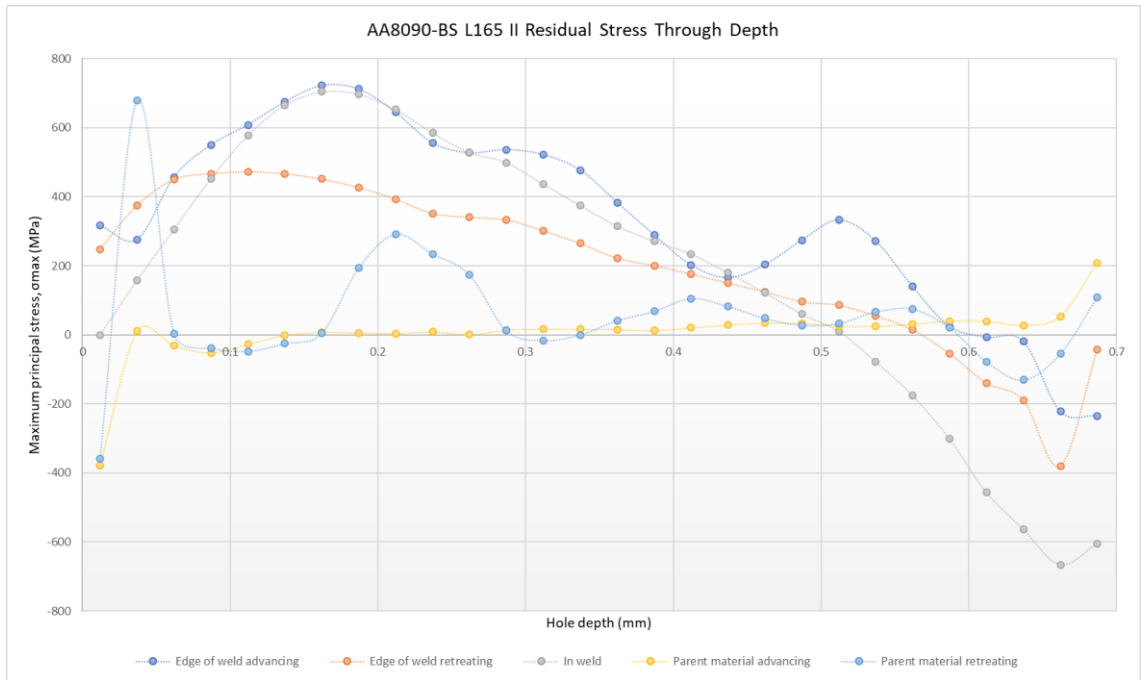
6.4.2.4.1 Residual Stress with Hole Depth

The RS results plotted against the drilled hole depth are shown for both configurations in Figure 134. Again, only values occurring at depths 0.06-0.4 mm are considered in the analysis. The values produced are well in excess of the materials yield strength (and UTS) and so again cannot be used for quantitative analysis.

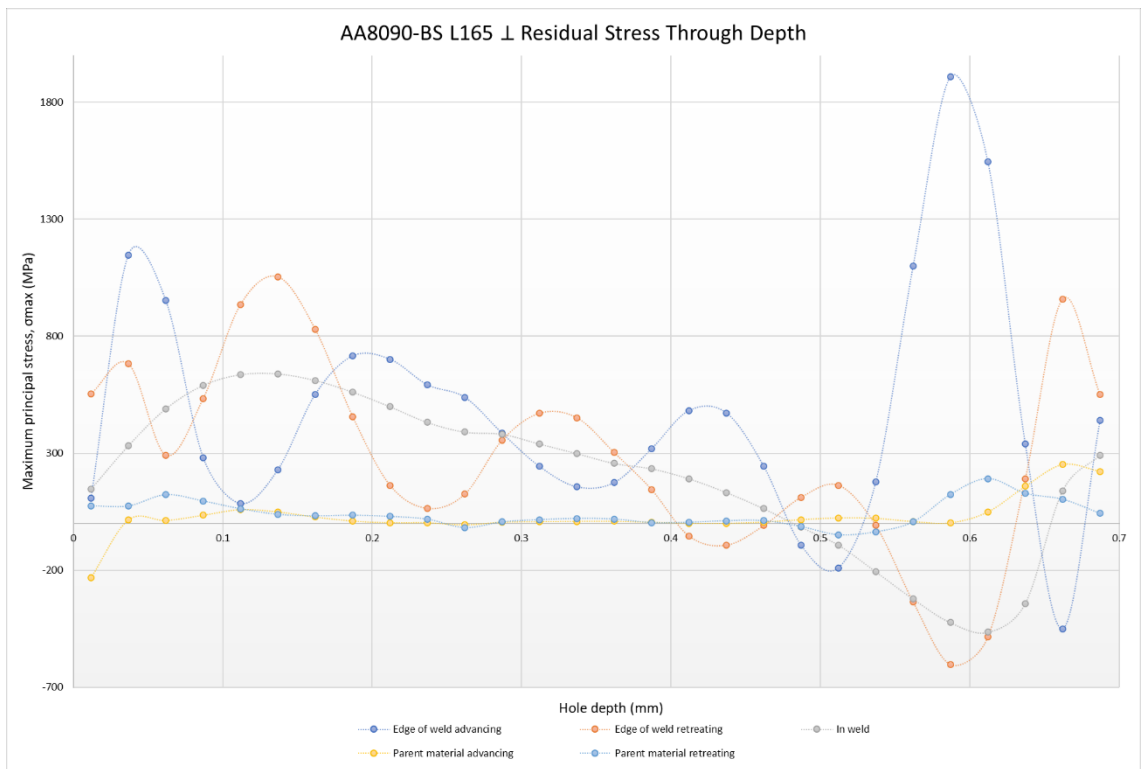
As expected, all parent material measurements remained at approximately zero throughout depth (with the exception of AA8090-BS L165 II retreating side parent material - see following paragraph for further explanation). With regards to the AA8090-BS L165 II plot (Figure 134(a)) and disregarding the actual measurement values, the

nugget and EoW advancing (AA8090) had comparable RS profiles through depth (0.06-0.4 mm). Unlike with previous tests which started at high values (after 0.06 mm), these continued to grow in tensile RS before reaching a peak at approximately 0.16 mm and then gradually reducing with depth. The EoW retreating (BS L165) RS was similar in profile to that testing performed previously (high initially and gradually decreasing with depth), and the overall measurement was below that of the nugget and EoW advancing side. Little analysis is possible with regards to the AA8090-BS L165 \perp RS due to the spurious results at the edge of the weld, although the nugget profile is similar to previous testing with the RS peak occurring at a deeper position.

All data sets were accounted for in both AA8090-BS L165 configurations, however several are considered to be spurious based on the degree of fluctuation including AA8090-BS L165 II parent material retreating side (Figure 134(a)). Based on previous testing, i.e. BS L165-BS L165 II parent material retreating side RS tests, this value should measure around zero throughout the depth. A flaw or some unobserved mechanical damage may have caused the initial spike in this test and the subsequent rise and fall from approximately 0.16-0.28 mm, however the more likely scenario is a deficient test. Additionally, both edge of weld specimens (advancing and retreating) from AA8090-BS L165 \perp (Figure 134(b)) show considerable fluctuation. The edge of weld tests were performed immediately adjacent to the visible weld when viewed from the surface; by positioning the tests there, they should avoid the TMAZ and nugget and, although there may be some influence from the overhang/ frictionally affected surface material (up to approximately 100-150 μm), the hole should only be drilled through the HAZ of the weld. Although there cannot be direct read-across from the similar welds to this configuration due to the difference in welding parameters and the unique thermo-mechanical properties produced by the materials mixing, it is considered that the profile for these tests should be similar to that seen previously. The advancing edge of weld tests on both AA8090-AA8090 configurations were considered to be spurious based on the degree of fluctuation. Had the AA8090-BS L165 II weld advancing EoW test not followed a more sensible profile, the author would consider whether the fluctuating profile was in fact accurate, however from positioning of the test and the microstructure of the HAZ throughout depth there appears to be no logical explanation for the fluctuating profile to be accurate.



(a)



(b)

Figure 134: Showing residual stress results plotted against drilled hole depth; (a) AA8090-BS L165 II, and (b) AA8090-BS L165 \perp .

6.4.2.4.2 Residual Stress Across Weld

The residual stress measurements taken across the weld are shown in Figure 135. As previously, the approximate positions of the parent material, HAZ (not TMAZ) and nugget are shown along the x-axis. The AA8090-BS L165 \perp results must be analysed with caution due to the fluctuating and spurious nature of the edge of weld tests.

The AA8090-BS L165 \parallel results (Figure 135(a)) show a peak at the advancing side EoW and then gradual reduction in RS through the nugget and then retreating side EoW, for all depths with the exception of 0.062 mm where the advancing and retreating EoWs are almost identical (as shown in Figure 134(a)) and the profile takes the form of the typical “M” shape. Disregarding the 0.062 mm result however and concentrating on the other 4 depths, the profile is at odds with those recorded in literature. Studies using relevant dissimilar aluminium alloys (e.g. AA2024-AA7075, AA2024-AA6061, AA7075-AA6062) were examined and all produced results with a double peak, i.e. an asymmetric “M” shape (Guo et al., 2020; Hadji et al., 2018; Jamshidi Aval, 2015; Zapata et al., 2016) with the peaks at the edges of the weld and a dip in RS within the nugget, see section 2.3.9.3.4. It should however be noted that these studies all used either XRD, neutron diffraction or ultrasonic methods; the XRD studies (Jamshidi Aval, 2015; Zapata et al., 2016) are only valid for near surface measurements. There are conflicting reports in the literature as to where the maximum residual stress is measured within the weld. Guo et al. (2020) and Jamshidi Aval (2015) both reported that the maximum RS occurred at the edge of the weld at the side corresponding to the stronger material, with Guo attributing this to the higher heat input at the advancing side combined with the higher mechanical properties of AA7075 over AA2024. However, Zapata et al. (2016) reported the maximum RS at the side corresponding to the weaker material, which was attributed to the properties, chemical composition and heat treatments of the materials used as the weaker material had higher RS when similar welding was conducted. Hadji et al. (2018) reported that the RS was at a maximum on the retreating side regardless of material positioning of AA2024 and AA7075, however when the weaker AA2024 was positioned on the advancing side, the RS increased overall. These results were attributed to the local mechanical properties and inhomogeneous temperature distributions before and after welding.

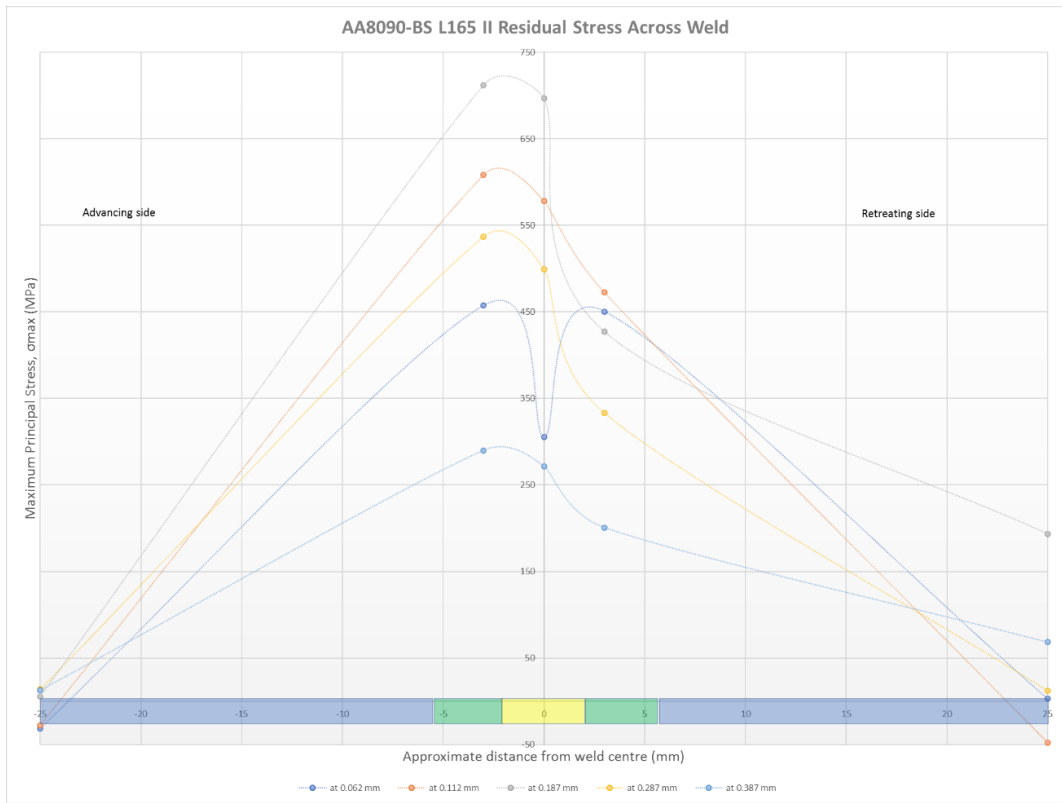
This all suggests that the RS measurement and profile is highly dependent on a number of factors, including but not limited to:

- the material composition
- original mechanical properties
- heat input during welding and the material response to that heat, both individually and the response of the mixed material
- unique combined thermo-mechanical properties produced
- degree of mixing
- positioning of materials.

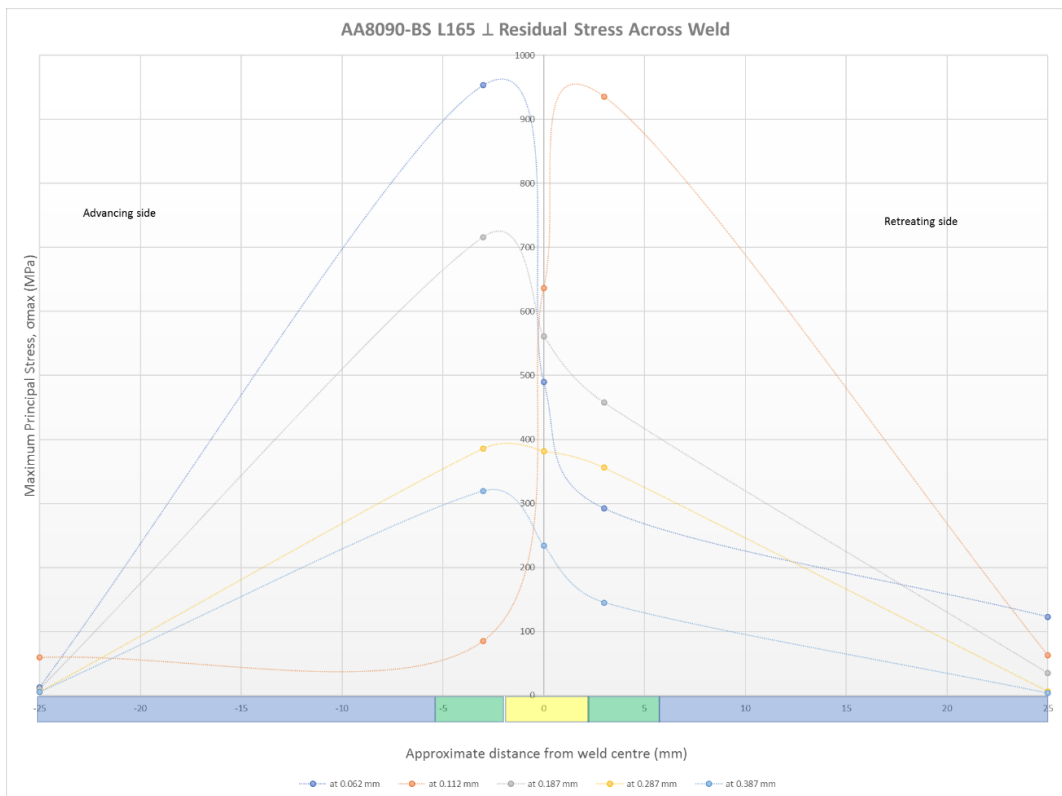
As all testing produced results which cannot be used for qualitative analysis, it is not possible to determine which of the materials had the overall stronger RS response to welding in the similar welds (AA8090-AA8090 and BS L165-BS L165).

The \perp RS results show a similar profile (with the exception of 0.112 mm) to the II weld, however as stated previously, these results must be treated with caution due to the high degree of fluctuation produced in the EoW tests.

Again, there are no balancing compressive RS results shown on either plot in Figure 135, however as previously discussed, had additional measurements been take at positions within the HAZ and parent material, it is expected that compressive results would have been generated.



(a)



(b)

Figure 135: Showing residual stress across weld at varying hole depths: (a) AA8090-BS L165 II and (b) AA8090-BS L165 ⊥.

6.4.3 Summary/ Conclusions for this Configuration

The following is a brief summary of the findings from the work on AA8090-BS L165 weld configurations.

- There was little direct read-across from the similar weld configurations, i.e. the behaviour of AA8090-AA8090 or BS L165-BS L165 did not necessarily determine the behaviour when combined as AA8090-BS L165. This was apparent in the weld parameters required to allow welding without warping BS L165, the fatigue results and in the RS results. The influence of each material's thermo-physical properties combined to produce unique ones, especially within the nugget.
- Differing degrees of mixing of the materials were noted along each weld, between weld runs and between the configurations. Generally it was suspected that the welds would have experienced greater mixing with potentially improved mechanical testing results had the heat input been greater, however this had to be balanced with the distortion reaction of BS L165.
- The welds were inconsistent along each weld, between runs and between configurations. In addition to the differences in material mixing described above, the extent of kissing bond present also varied (although this is strongly related to material mixing) and dramatic changes in the weld surface appearance were observed.
- The frictionally affected surface region (included mixed alclad) had a strong influence on the fatigue properties of the welds.
- The tensile properties were generally consistent with the literature.
- Additional work is required regarding fatigue testing to determine the preferential failure position in the absence of kissing bonds or influential surface area. This would require a systematic programme to determine optimal process parameters.
- Additional RS work is required before any definitive conclusions can be drawn.

6.5 BS L165-AA8090

6.5.1 As-Welded Examination

6.5.1.1 *Welded Sheets*

The SSFSW was conducted at TWI in Rotherham by the author and a TWI specialist, however, as insufficient material was transported to the facility during the initial welding period this configuration (BS L165-AA8090 II and \perp) was welded separately, with material being posted and the welding carried out solely by the TWI specialist. As such, testing and analysis was carried out on this configuration at different times than the other configurations and, as an unfortunate consequence, initial photography of the as-received SSFSW sheets was not carried out. Detailed notes on the author's observations were however taken which describe the sheet's appearance. The sheets were similar in appearance to other configurations with respect to varying degrees of longitudinal and angular distortion, and vertical lifting at the end of the weld run.

Only welds considered to be sound (with the parameters used having passed bend testing) were returned from TWI, therefore the author did not have sight of any failed welds produced during trials. As a result no comment can be made on any warping or distortion which may have occurred during trials to the BS L165 (as per the similar BS L165 welds, see (Figure 86 in section 6.3.1.1) and whether this was more or less extensive than that observed on AA8090-BS L165 configurations.

6.5.1.2 *Weld Surface*

6.5.1.2.1 *BS L165-AA8090 II welds*

An area of the II weld top surface representative of the surface appearance during steady state welding conditions is shown in Figure 136 with a scaled profile of the tool superimposed.

Significant amounts of deposited material were present adjacent to the advancing edge varying in volume deposited, roughness and width along the length of each weld. They were, in parts, relatively smooth and even, but with protuberances/ galling of material interspersed along the length. These protuberances were occasionally relatively large as

shown in Figure 137. This material was similar to that observed adjacent to the retreating edge of the AA8090-BS L165 II weld (Figure 115 in section 6.4.1.2) and was considered to be redistributed alclad material. Deposited material was also present at the retreating edge, however this was far reduced in volume from the advancing edge and was generally of a smooth and even appearance.

The advancing “half” of the weld width exhibited ripples with irregular overlaid ironed material while the retreating “half” was of the ironed appearance observed previously. The ripple spacings were broadly consistent with the weld pitch (0.178 rev/mm), measuring approximately 173 μm . Similarly to the AA8090-BS L165 II configuration, the ripples varied in their roughness and definition, with this attributed to differences in the heat input along the weld changing the plasticity of the material. The ripples were positioned below the overlaid ironed material, resulting in underfill of the weld at those areas which can be observed in the profilometry images shown in Figure 138. It is considered that the ripples are visible with underfill present for the same reasons as described for AA8090-BS L165 II (section 6.4.1.2), however in this case additional material (in the form of the alclad layer) was deposited on the advancing side due to the parent material’s positioning.

Directional markings observed adjacent to the advancing edge of the AA8090-BS L165 II weld (section 6.4.1.2) were not observed on this configuration, nor were they present at the retreating (AA8090) edge. These markings were originally attributed to discolouration owing to oxidation from excess heat on the advancing side of the weld, with the BS L165 being spared due to its positioning on the retreating side plus its protection via the alclad layer. As such, although in this case the BS L165 is on the (hotter) advancing side, it still retains some protection from discolouration through the alclad layer and thus these markings were not formed. Another difference between this configuration and AA8090-BS L165 was that this weld had no change in reflectivity. This change from matt to reflective on the AA8090-BS L165 II weld was, again, partially attributed to oxidation, thus would not be experienced here. It was also partially attributed to the mix of alclad, BS L165 and AA8090 within the materials being stirred; these are all present within this weld, however their original positions differ from the AA8090-BS L165. As such, the materials’ final positions will differ within the weld with alternative materials being located at the top surface.

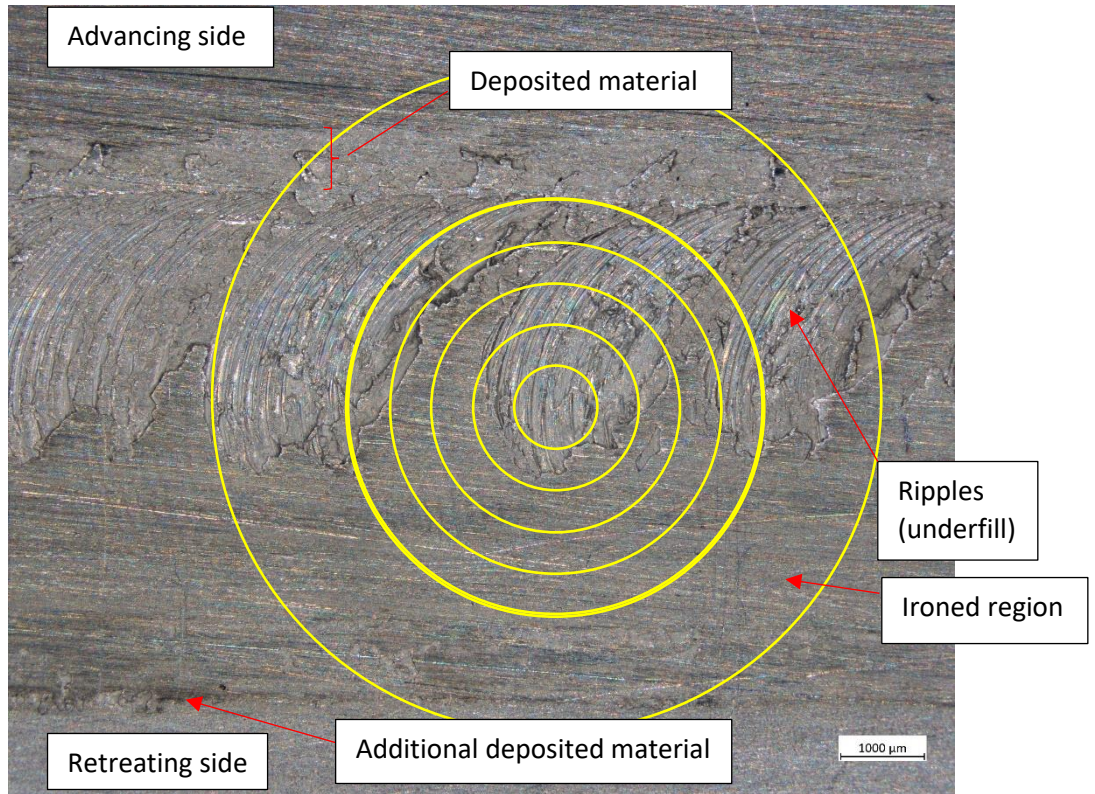


Figure 136: Showing BS L165-AA8090 II weld with superimposed tool profile.



Figure 137: Showing relatively large deposit of material on the advancing side edge of BS L165-AA8090 II weld.

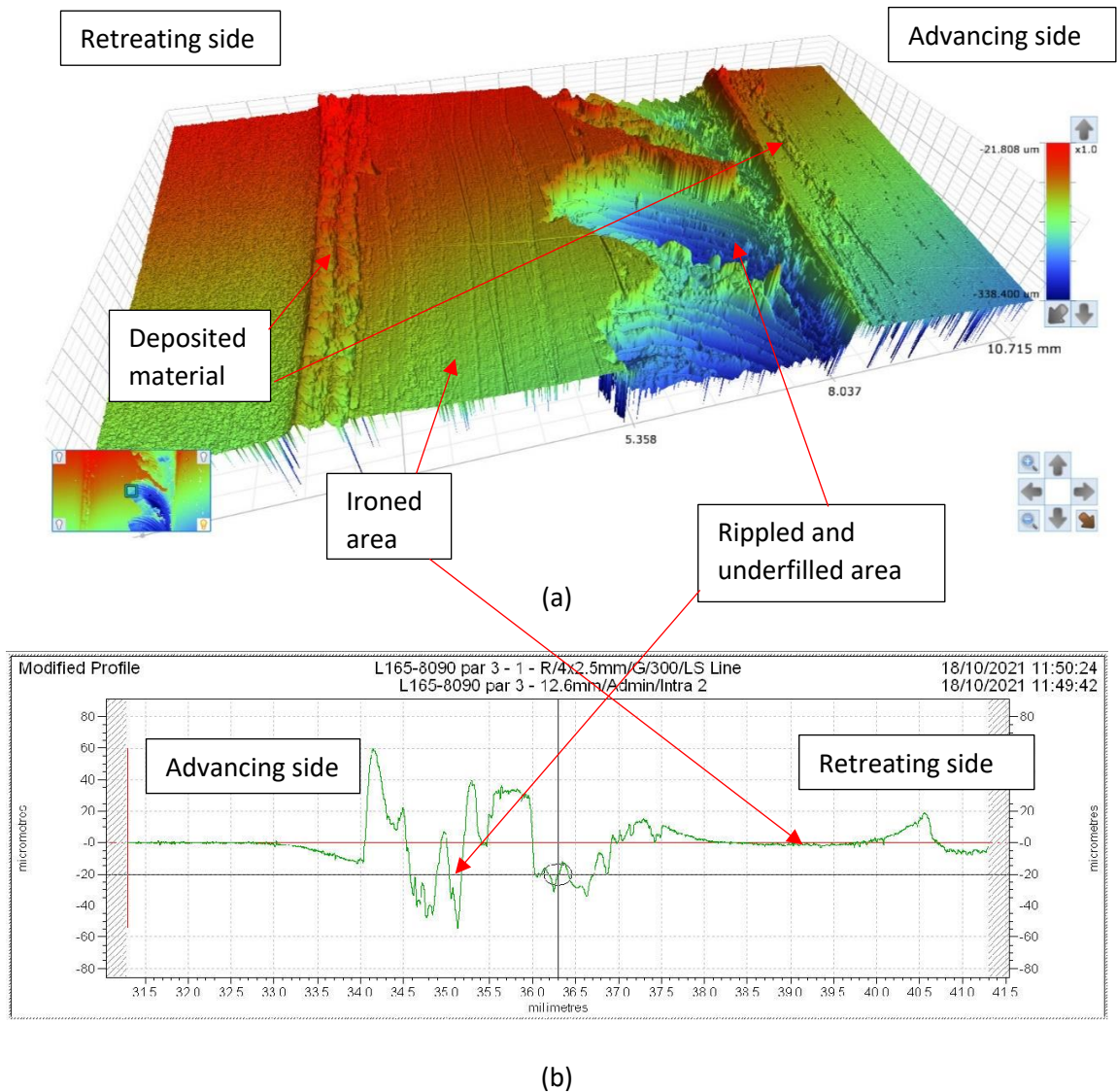


Figure 138: Showing BS L165-AA8090 II weld surface topography: (a) optical profilometry image, and (b) contact profilometry surface plot.

6.5.1.2.2 BS L165-AA8090 \perp welds

An image representative of the BS L165-AA8090 \perp weld top surface appearance is shown in Figure 139. There were several features which were similar to the II weld: visible ripples overlaid with ironed material and deposited material adjacent to the advancing side and to a lesser extent on the retreating side. There were however some differences. The \perp weld had an overall “neater” appearance, with the ironed material covering a more extensive area and less deposited material on the advancing side. The material adjacent to the advancing side was deposited finely and barely visible over some lengths of the weld; it is considered that the fine deposit was clad material, which due to its greater ductility than the other materials, was extruded to a finer

thickness but greater width. Additionally, a material “ribbon”, similar to that observed on the AA8090-BS L165 \perp weld, was observed. The ribbon was considered to be mixed weld material which had been extruded out from the edge of the pin, but due to its, albeit slightly, reduced ductility and density gathered into a thicker mass adjacent to the pin without spreading. It is likely that this weld had lower heat input than the II weld and thus reduced plasticity, hence the neater appearance, thinner alclad deposits and limited galling to the advancing side.

Also observed on the \perp weld were several lines on the ironed material. These were slightly “wavy” along the length of the weld and can be seen pictured in Figure 139 and on the optical profilometry image in Figure 140(a), and are indicated on the surface profilometry plot in Figure 140(b). Based on the narrow width of these markings and reasonably shallow depth it is considered that they were caused by material adhered to the tool shoulder trailing edge which gouged the marks as it traversed, while ironing the rest of the weld face.

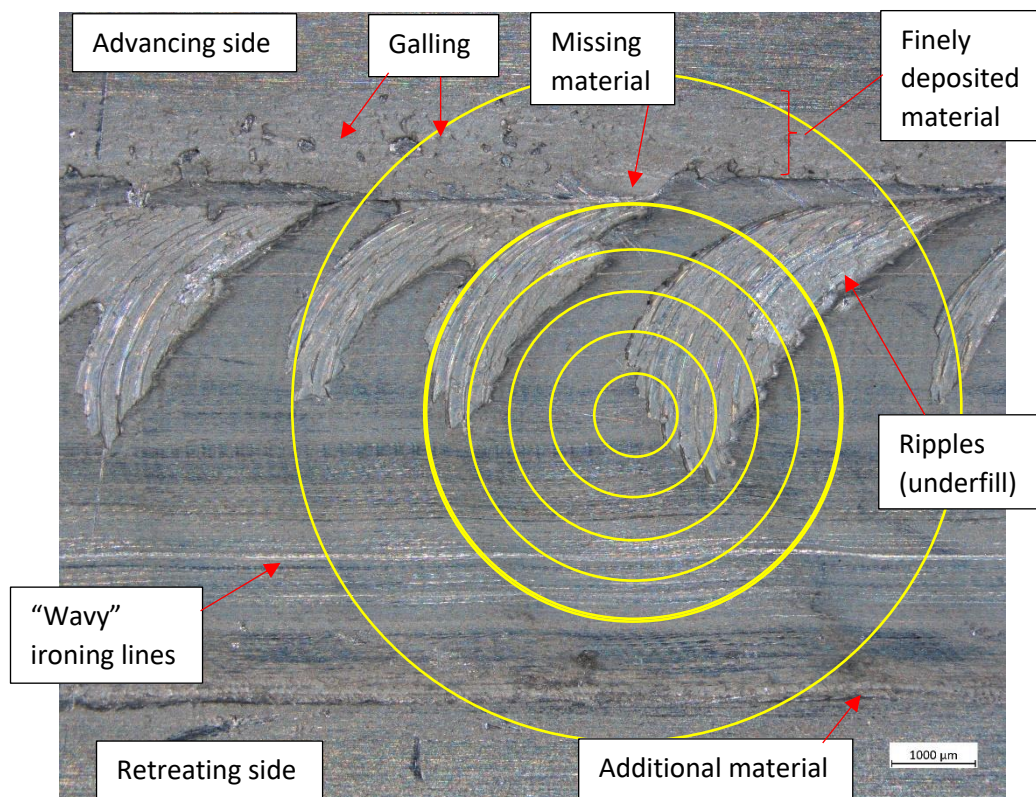


Figure 139: Showing BS L165-AA8090 \perp weld with superimposed tool profile.

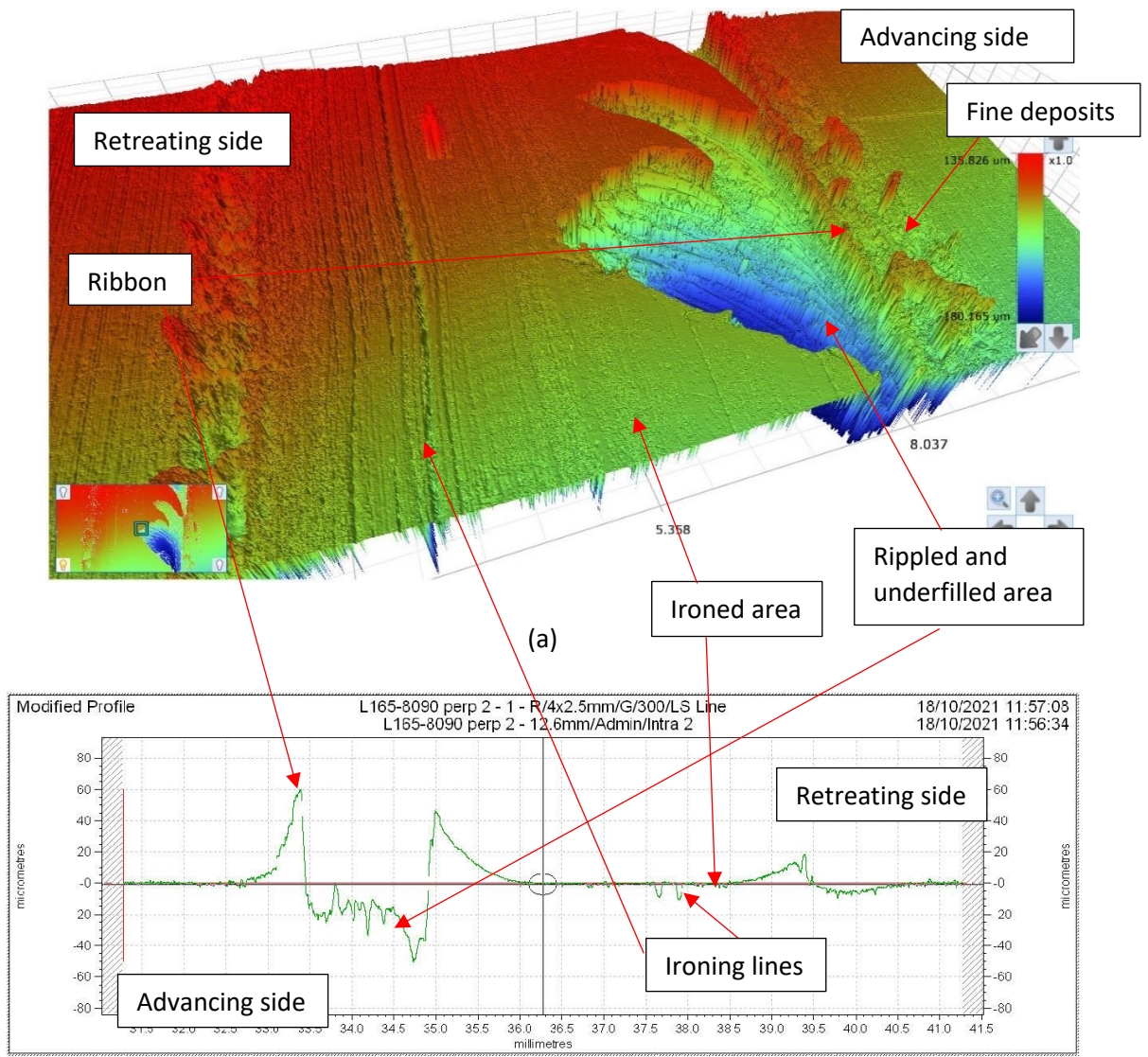


Figure 140: Showing BS L165-AA8090 \perp weld surface topography: (a) optical profilometry image, and (b) contact profilometry surface plot.

6.5.1.3 Weld Macro- and Micro-structures

Etched cross sections of both BS L165-AA8090 weld configurations are shown in Figure 141; in both cases the advancing side is on the right. The materials have not mixed as successfully for the II weld as was observed for the AA8090-BS L165 II weld (Figure 119 in section 6.4.1.3), with distinct “block” of each material. The AA8090 does extend over to the advancing side along the top surface of the weld and mixing of the alclad layer present on the BS L165 has occurred in that area, although this is not clear from Figure 141, and the BS L165 extends into the AA8090 on the retreating side at approximately 1/3rd thickness, but that is the extent of the mixing indicative of low plasticity in the material during welding, suggestive of relatively low heat generation. There is a similar level of mixing on the ⊥ weld, although this was reasonably similar to that of the AA8090-BS L165 ⊥ weld. It is considered that less heat was generated in the BS L165-AA8090 II welds than in the AA8090-BS L165 II weld. This resulted in reduced mixing which indicates diminished plasticity of the materials.

Minimal weld thinning was observed on either weld, actually both welds increased in thickness across the retreating half (corresponding to the overlaid ironed area described in 6.5.1.2). Underfill was observed on the advancing side of both welds, coinciding with the visible ripples as previously described; this is not weld thinning which is caused due to the forging pressure of the shoulder compressing the weld, rather due to insufficient material transfer from the retreating side to the advancing side during stir.

Oxide chains were visible along the joint line, indicating the presence of kissing bonds (rather than the more benign lazy S). These oxide chains extend from the bottom surface of the weld, through to approximately 2/3rd of the weld thickness and are particularly abundant at the approximate mid-thickness of the weld (highlighted by blue boxes in Figure 141(a)). Additional oxide chains extend into the nugget remote from the joint line; these are discussed further in section 6.5.1.3.1. Fewer subsurface voids were observed on these configurations when compared with AA8090-BS L165, although some were present. Instead, oxide chains extended close to the top surface, following the dissimilar material interfaces. A large inclusion is present mid thickness on the joint line of the ⊥ weld (highlighted by a green box on Figure 141(b); this is also discussed in section 6.5.1.3.1. The alclad layer was not drawn into the weld at the bottom surface.

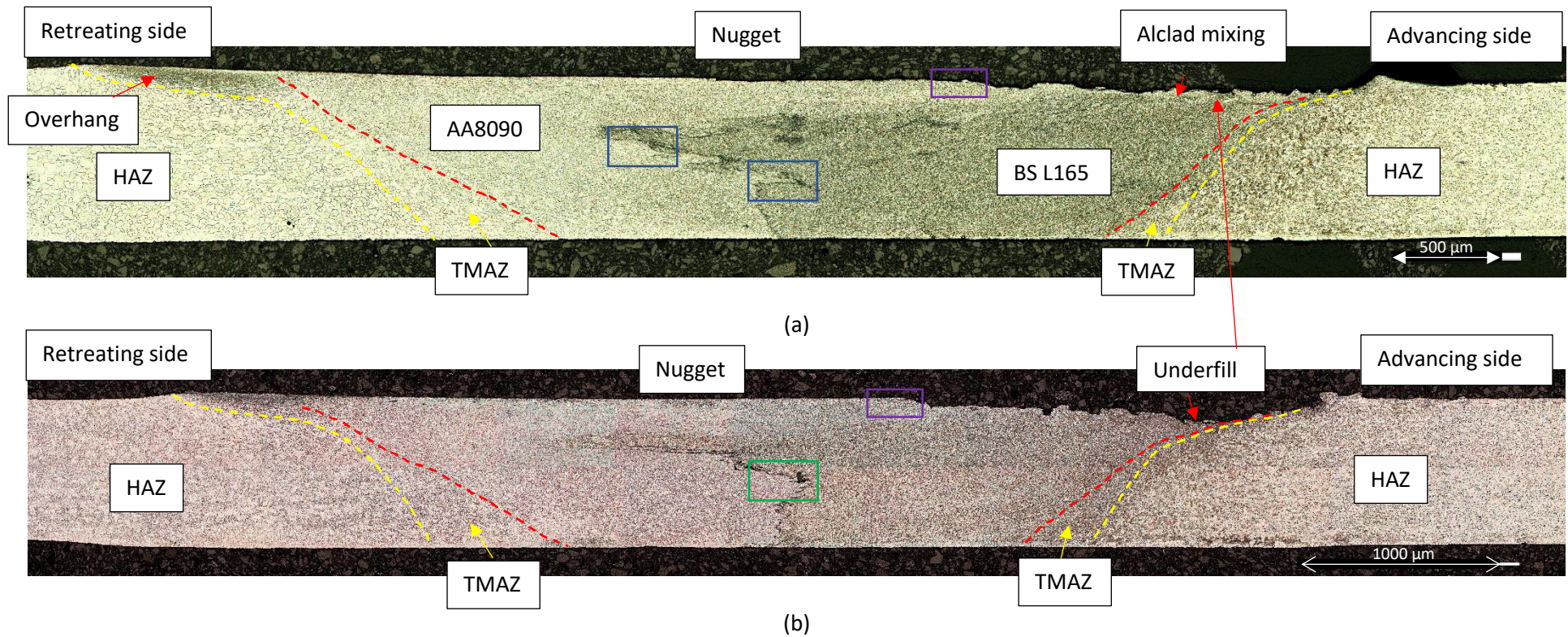


Figure 141: Showing macrograph of BS L165-AA8090 weld cross-section; (a) || and (b) ⊥. The areas indicated by the blue boxes in (a) highlight oxide chains and are discussed in section 6.5.1.3.1, as is the area indicated by the green box in (b) which highlights a large inclusion. The areas indicated by the purple boxes in (a) and (b) highlight the surface transition from the smooth ironed area to the rough and rippled area, and are discussed in section 6.5.1.3.4.

6.5.1.3.1 Nugget

Comparison of the nugget dimensions with that of the pin revealed that the II nugget width measured approximately 3.8 mm and 2.6 mm at the mid-thickness and bottom surface respectively, and that the \perp nugget width measured approximately 3.4 mm and 2.3 mm at the same positions. While slightly smaller than the AA8090-BS L165 welds at all positions, the dimensions for this configuration were comparable with the similar welds, Table 43. The smaller nugget suggests that, despite using the same welding parameters as AA8090-BS L165, the heat generation within these welds was reduced, especially at the bottom surface. Barbini, Carstensen and dos Santos (2018) found that the heat generation was affected by the positioning of their dissimilar materials, although their parent materials had significantly different tensile strengths. It is suspected that the differing thermal properties of the two materials played a significant role in this case. When BS L165 was on the (hotter) advancing side it was better able to conduct heat away from the nugget zone due to its higher thermal conductivity (this was also true of the BS L165 similar welds); with AA8090 on the hotter side less heat was conducted away from the nugget, resulting in an increased nugget size. The dissimilar welds used different weld parameters than the similar welds, thus the AA8090 similar weld nuggets are not considerably larger than this dissimilar configuration.

Table 43: Showing nugget width dimensions for all configurations.

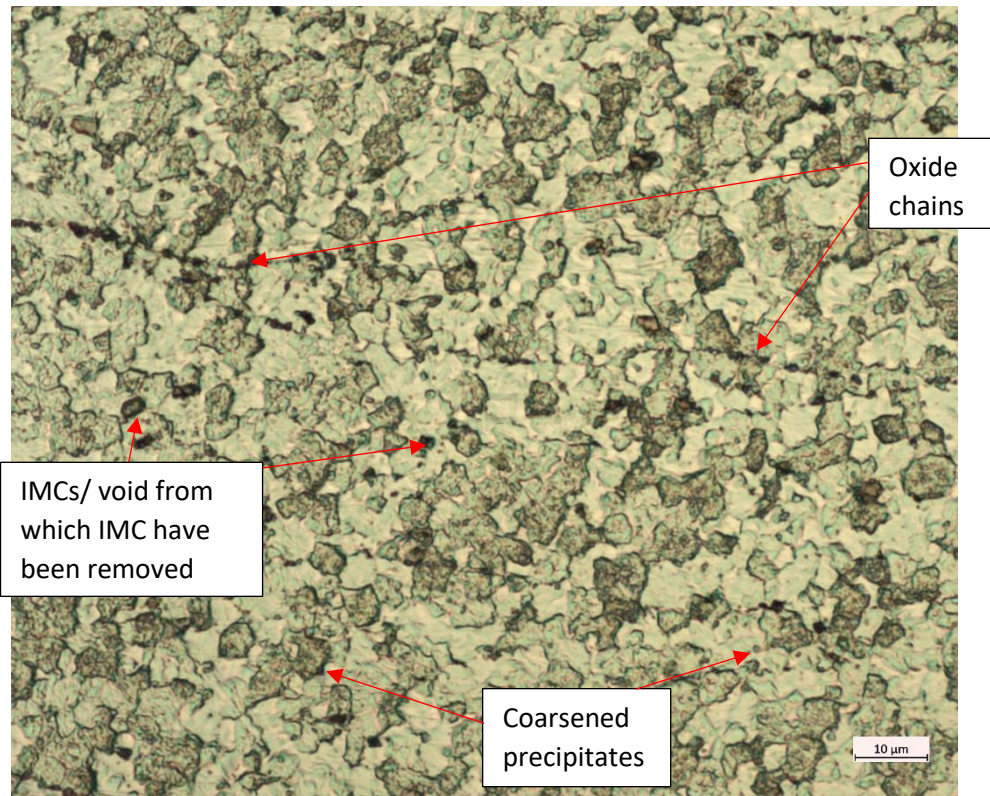
Configuration	Top surface measurement (mm)	Mid-thickness measurement (mm)	Bottom surface measurement (mm)
AA8090 II	4.4	3.7	2.6
AA8090 \perp	4.8	3.8	2.9
BS L165 II	4.6	3.8	3.0
BS L165 \perp	4.6	3.9	3.0
AA8090-BS L165 II	4.9	4.2	3.2
AA8090-BS L165 \perp	5.0	4.2	3.4
BS L165-AA8090 II	4.8	3.8	2.6
BS L165-AA8090 \perp	4.7	3.4	2.3

Micrographs of the II and \perp weld nugget zones are shown Figure 142 and Figure 143 respectively. These show that dynamic recovery and recrystallisation has occurred

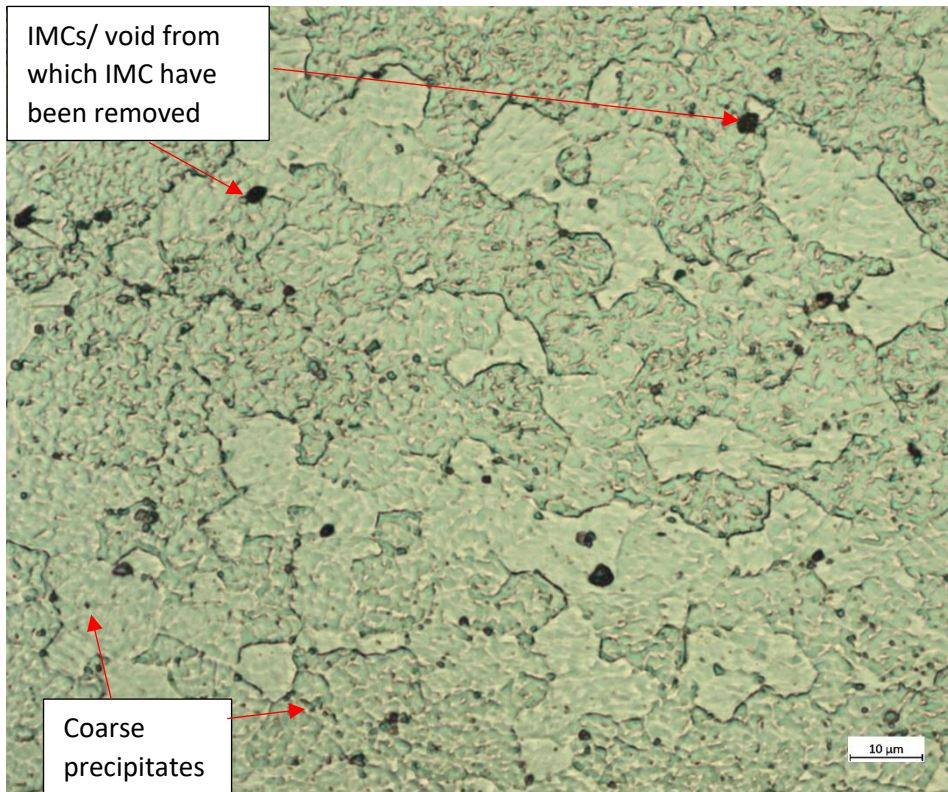
within the nugget in comparison with the parent materials (Figure 31 in section 4.1.2 and Figure 36 in section 4.2.2).

Analysis of the BS L165 (advancing side) area of the nugget (Figure 142(a) and Figure 143(a)) revealed the presence of large intermetallic compounds and coarsened incoherent θ precipitates which had heterogeneously nucleated at the grain boundaries. The intermetallic compounds were larger within the \perp weld, indicating that they had been fractured during the stirring process in the II weld. These IMCs were considered to be compositionally consistent with those discussed previously (section 6.3.1.3.1) and reported by Rajendran et al. (2019).

As with other configurations, analysis of the AA8090 area of the nugget (Figure 142(b) and Figure 143(b)) revealed an increase in black spherical particles congregated at grain boundaries, considered to be heterogeneously nucleated incoherent δ precipitates (see section 6.2.1.3.1). Coarse IMCs generally located at the grain boundaries were also observed. These IMCs were considered to be compositionally consistent with those discussed previously (section 6.2.1.3.1) and reported by Vigraman et al. (2021).

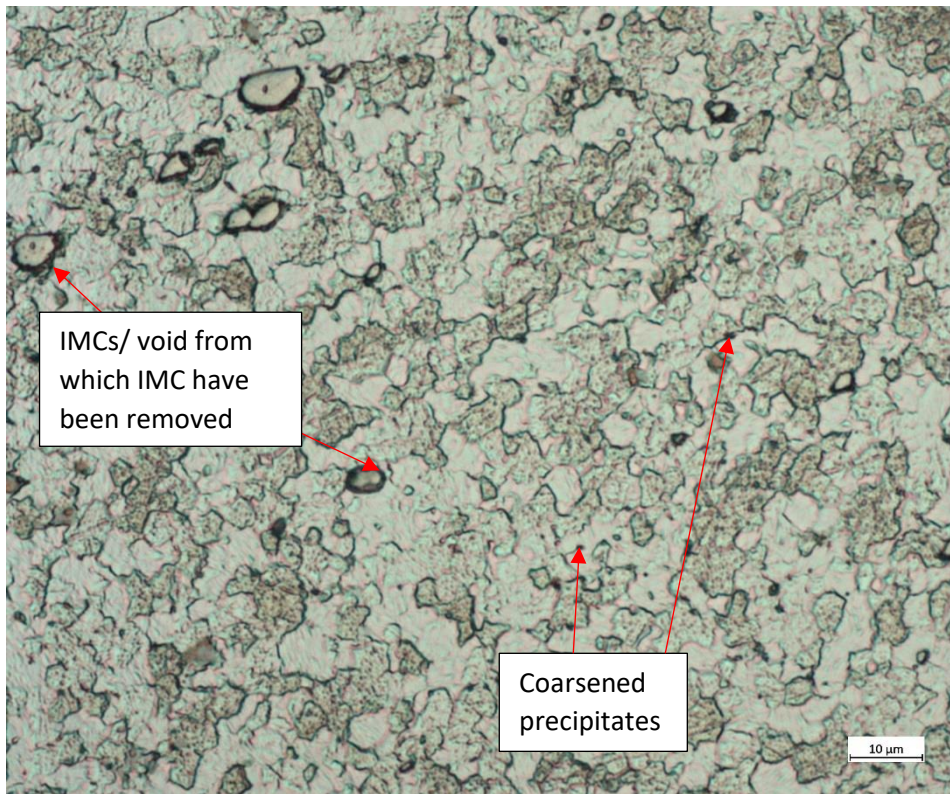


(a)

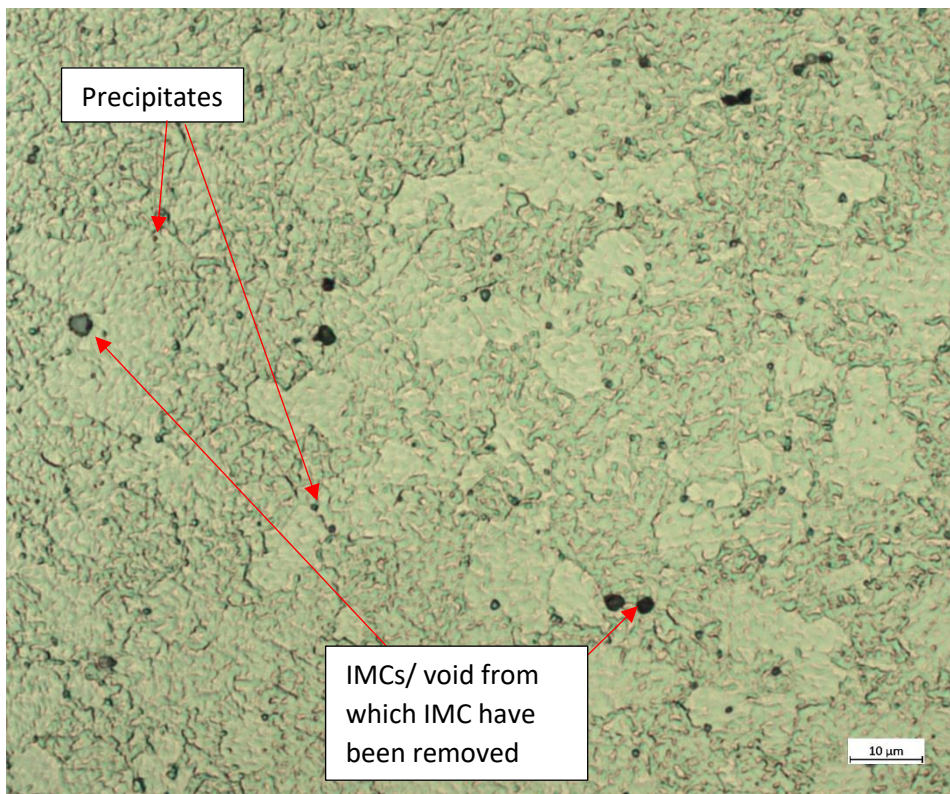


(b)

Figure 142: Showing micrographs of the II weld nugget: (a) advancing side BS L165 material and (b) retreating side AA8090 material.



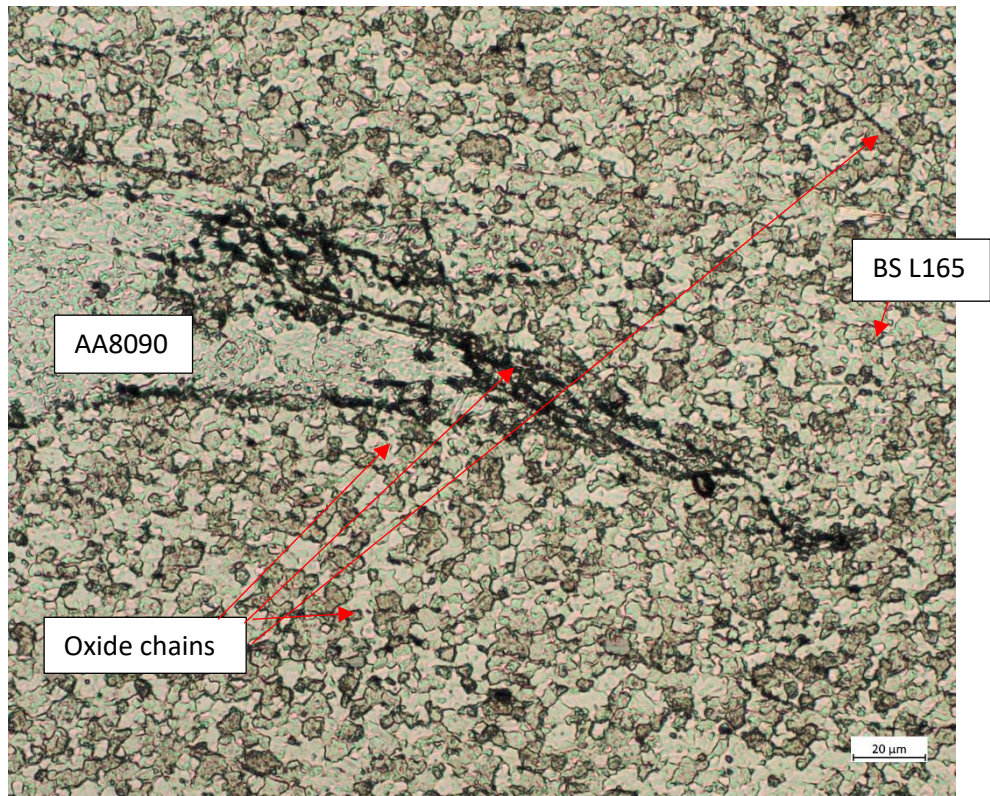
(a)



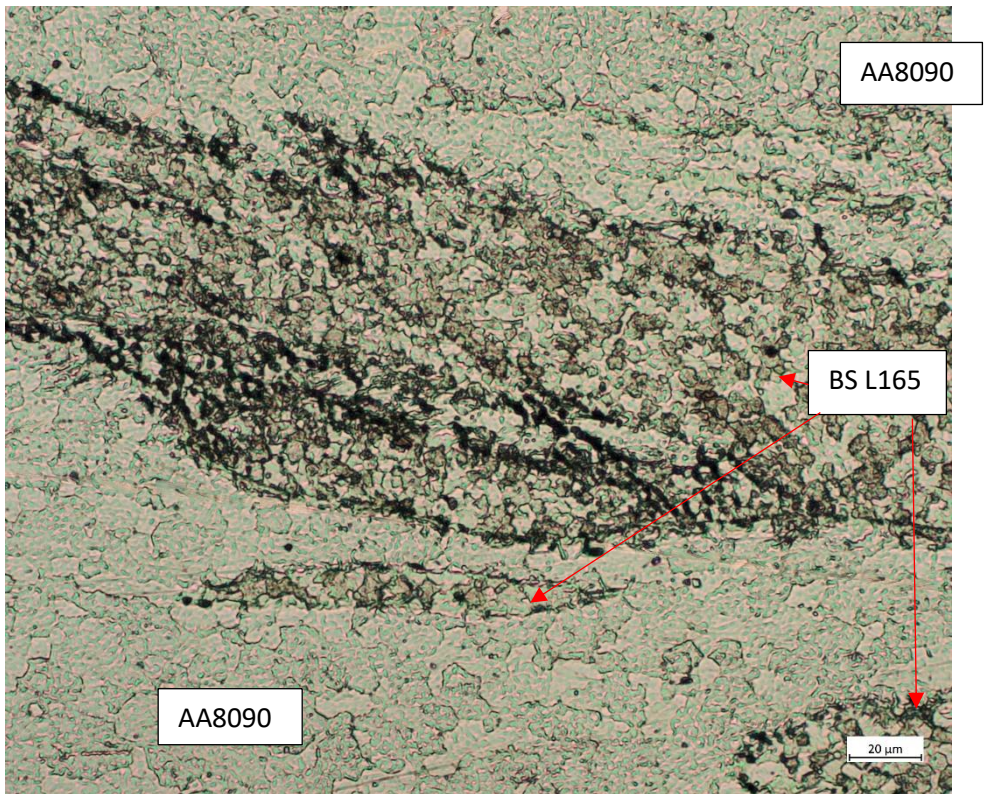
(b)

Figure 143: Showing micrographs of the \perp weld nugget: (a) advancing side BS L165 material and (b) retreating side AA8090 material.

Oxide chains were present along the joint line of both configurations, indicative of kissing bonds. These extended from the bottom surface of the weld, along the joint line to approximately 2/3rd of the weld thickness and also extended into the BS L165 part of the weld. The oxide chains on the joint line are highlighted in Figure 141(a) with blue boxes and are shown in greater detail in Figure 144. Some oxide chains are shown within the weld nugget (BS L165 area) in Figure 142(a), however these are also shown in greater detail in Figure 145. Although oxide clusters and chains were present in other configurations (see Figure 121), these considered to be far in excess to that seen previously. Additionally, a large inclusion is present mid joint line on the \perp weld, shown in Figure 146. SEM-EDX confirmed this inclusion to be aluminium oxide. It is considered that this inclusion was picked up from the material surface, in the same manner to the typical smaller oxides, however the reason for such a large (approximately 20 x 40 μm) oxide remaining intact during the welding process is unknown. It should be noted that aluminium oxide is not involved in the metallographic preparation process. There are consequences for such a large inclusion; although no other inclusion of this size was observed on any micrographs taken from elsewhere on that particular weld, or on any other weld, is not proof that no other sizeable inclusions exist within the weld. These could easily act as stress raisers, deteriorating the mechanical properties of the weld even beyond that due to the presence of the small oxides within the kissing bond. Likewise, the oxide chains could undoubtedly act as fracture paths under tensile loading and their presence on and radiating from the joint line, and within the BS L165 part of the nugget could also deteriorate the mechanical properties of the weld. The cause of the oxide presence is likely to be insufficient preparation of the parent material surfaces prior to welding. As previously stated, these welds were conducted at a different time than the other configurations, and not under the author's supervision, therefore it is feasible that insufficient preparation occurred.



(a)



(b)

Figure 144: Showing areas highlighted by blue boxes in Figure 141(a).

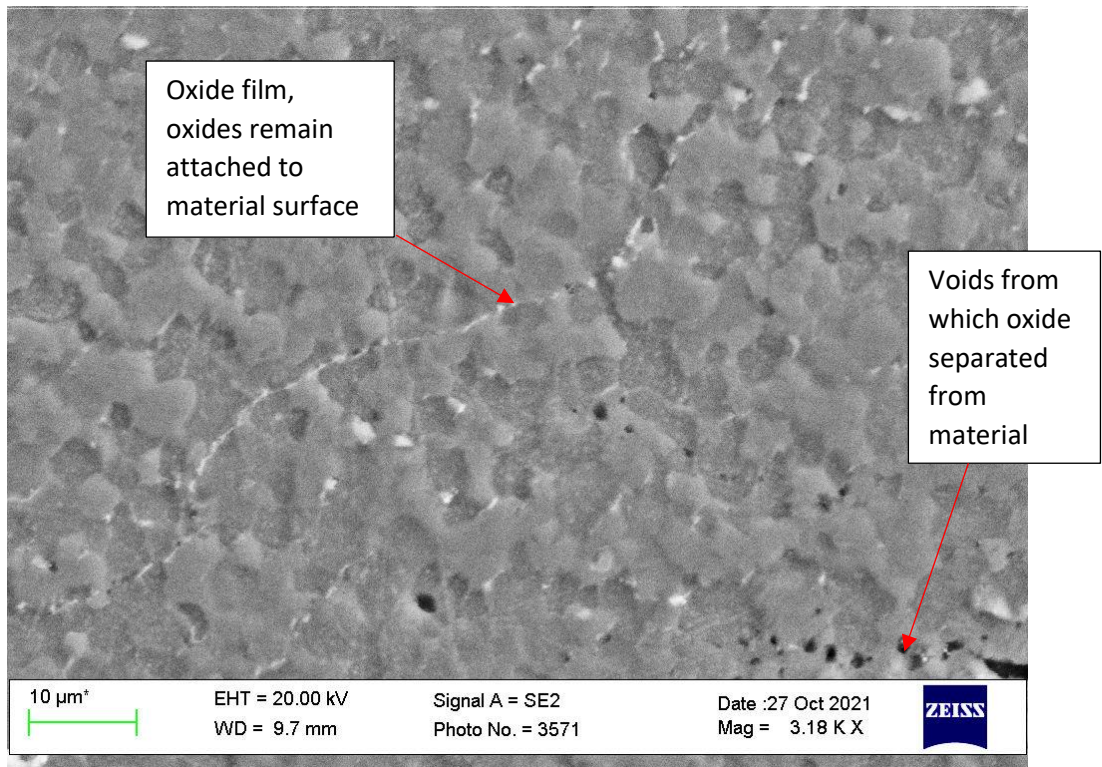


Figure 145: Showing oxide chains within BS L165 area of \perp weld nugget.

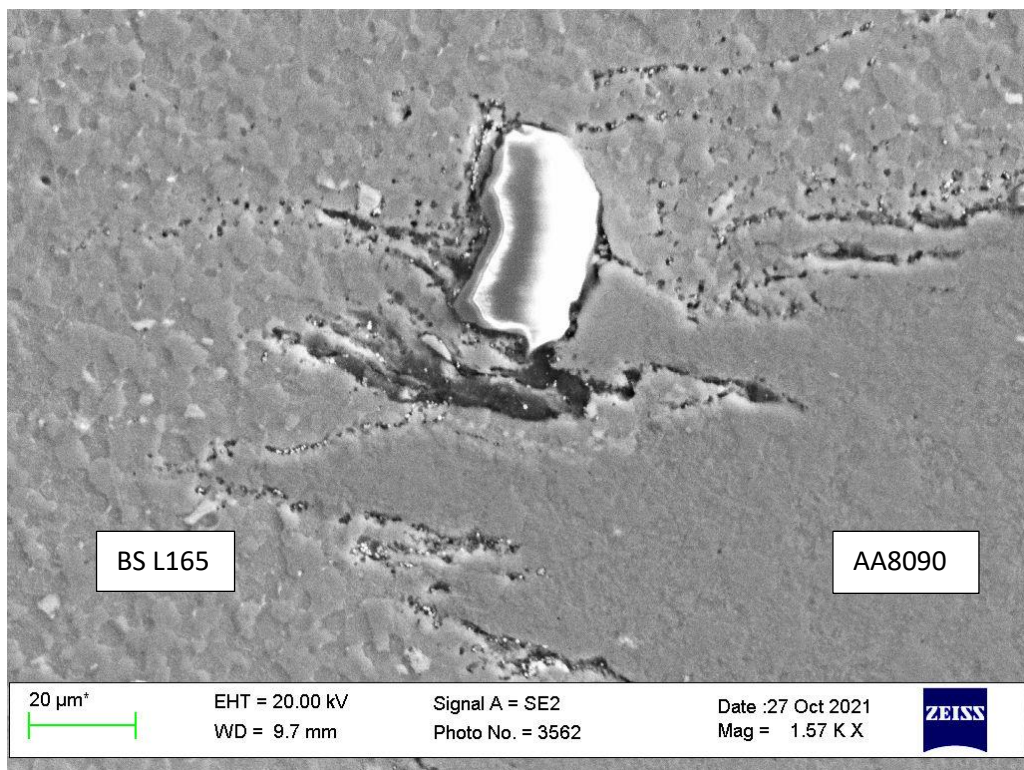


Figure 146: Showing large oxide inclusion in centre of weld, highlighted by green box in Figure 141(b), and oxide chains emanating from the joint line.

The average grains sizes were compared with the parent materials and all other welded configurations, Table 44. In Table 44 the column labelled “Advancing side” refers to areas of the nugget comprised solely of BS L165, while “Retreating side” refers to areas solely comprised of AA8090. When comparing the two BS L165-AA8090 configurations, the grain size of the II weld was slightly larger than the \perp weld at the advancing side and slightly smaller than the \perp weld on the retreating side. This suggests that slightly more deformation (plasticisation) occurred on the \perp weld at the advancing side and more of the heat generated during the plasticisation transferred to the retreating side. This is likely as a result of the grain orientation in the parent materials where the high energy grain boundaries affected heat transfer.

While the AA8090-BS L165 \perp weld had the unusual situation (owing to the BS L165 (retreating) side parent material being originally of far smaller grain size than AA8090 (advancing) parent material) of the retreating side grains being larger than the advancing side, in this configuration (BS L165-AA8090) both orientations of weld have the more typical condition of the advancing side grains being smaller, as expected due to the larger amount of deformation occurring at that position. Having said that, the analysis of the AA8090-BS L165 welds showed that mixing of dissimilar materials influenced the final grain sizes whereby the AA8090 reduced in size and the BS L165 grew in size in comparison with the similar material weld. This was attributed to the dissimilar weld nugget being a hybrid of the two materials. In this case (BS L165-AA8090), for both weld orientations the advancing side grains were larger than the advancing sides of the similar BS L165 weld configurations as expected, while the II retreating side grains were similar in size to the similar AA8090 II retreating side, but the \perp weld grains were slightly larger than the similar AA8090 \perp retreating side. One would expect the AA8090 retreating side grains to reduce in size in a similar hybrid manner to the AA8090-BS L165 weld however this has not occurred. It is suggestive of more heat being transferred to the retreating side of these BS L165-AA8090 welds and is likely to be a function of the thermal conductivity of the combination owing to the BS L165 being on the advancing side, the argument for the smaller nugget size described earlier in this section notwithstanding.

Table 44: Showing BS L165-AA8090 weld nugget grain size dimensions with grain sizes of all other configurations shown for comparison, showing Relative Accuracy (%RA) in brackets.

Configuration	Average Grain Diameter (μm) Measured Across Two Directions											
	Advancing Side						Retreating Side					
	Direction 1	% Change from Parent Material	% Change from Relevant Similar Weld Configuration	Direction 2	% Change from Parent Material	% Change from Relevant Similar Weld Configuration	Direction 1	% Change from Parent Material	% Change from Relevant Similar Weld Configuration	Direction 2	% Change from Parent Material	% Change from Relevant Similar Weld Configuration
AA8090 Parent Material (L)	21.2 (9%)	-	-	16.2 (6%)	-	-	-	-	-	-	-	-
AA8090 Parent Material (S-T)	28.0 (4%)	-	-	25.4 (16%)	-	-	-	-	-	-	-	-
BS L165 Parent Material (L)	12.2 (4%)	-	-	7.5 (6%)	-	-	-	-	-	-	-	-
BS L165 Parent Material (S-T)	14.4 (15%)	-	-	13.0 (13%)	-	-	-	-	-	-	-	-

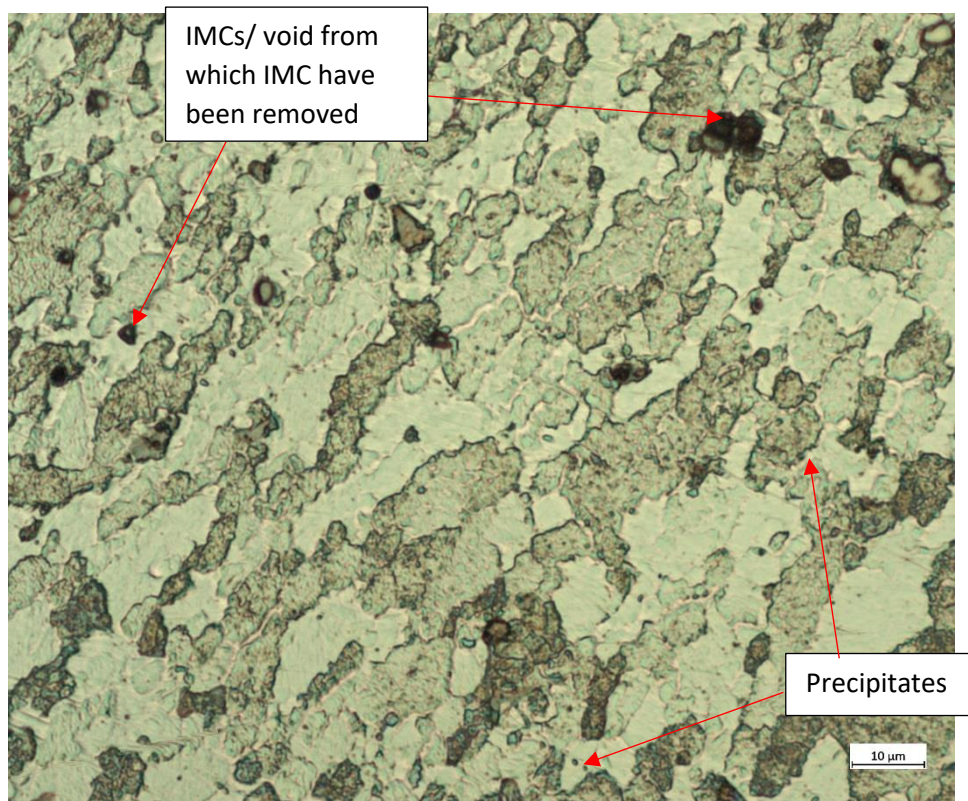
Configuration	Average Grain Diameter (μm) Measured Across Two Directions											
	Advancing Side						Retreating Side					
	Direction 1	% Change from Parent Material	% Change from Relevant Similar Weld Configuration	Direction 2	% Change from Parent Material	% Change from Relevant Similar Weld Configuration	Direction 1	% Change from Parent Material	% Change from Relevant Similar Weld Configuration	Direction 2	% Change from Parent Material	% Change from Relevant Similar Weld Configuration
AA8090 II	7.9 (8%)	-71.8	-	7.8 (10%)	-69.3	-	10.6 (19%)	-62.1	-	8.8 (13%)	-65.4	-
AA8090 I	8.8 (9%)	-58.5	-	7.4 (8%)	-54.3	-	9.4 (14%)	-55.7	-	8.3 (10%)	-48.8	-
BS L165 II	5.6 (16%)	-61.1	-	4.8 (11%)	-63.1	-	6.6 (10%)	-54.2	-	4.9 (14%)	-62.3	-
BS L165 I	5.5 (10%)	-54.9	-	4.8 (12%)	-36.0	-	6.3 (13%)	-48.4	-	4.9 (5%)	-34.7	-
AA8090-BS L165 II	6.8 (7%)	-75.7	-13.9	6.6 (5%)	-74.0	-15.4	7.4 (15%)	-48.6	+21.1	5.4 (9%)	-58.5	+10.2
AA8090-BS L165 I	8.5 (12%)	-59.9	-3.4	6.8 (11%)	-58.0	-8.1	7.8 (10%)	-36.1	+23.8	6.1 (12%)	-18.7	+24.5
BS L165-AA8090 II	7.2 (10%)	-50.0	+28.6	5.8 (6%)	-55.4	+20.8	10.4 (10%)	-62.9	-1.9	8.8 (9%)	-65.4	0
BS L165-AA8090 I	6.9 (12%)	-43.4	+25.5	5.0 (11%)	-33.3	+4.2	10.9 (10%)	-48.6	+16.0	7.7 (11%)	-52.5	-7.3

6.5.1.3.2 TMAZ

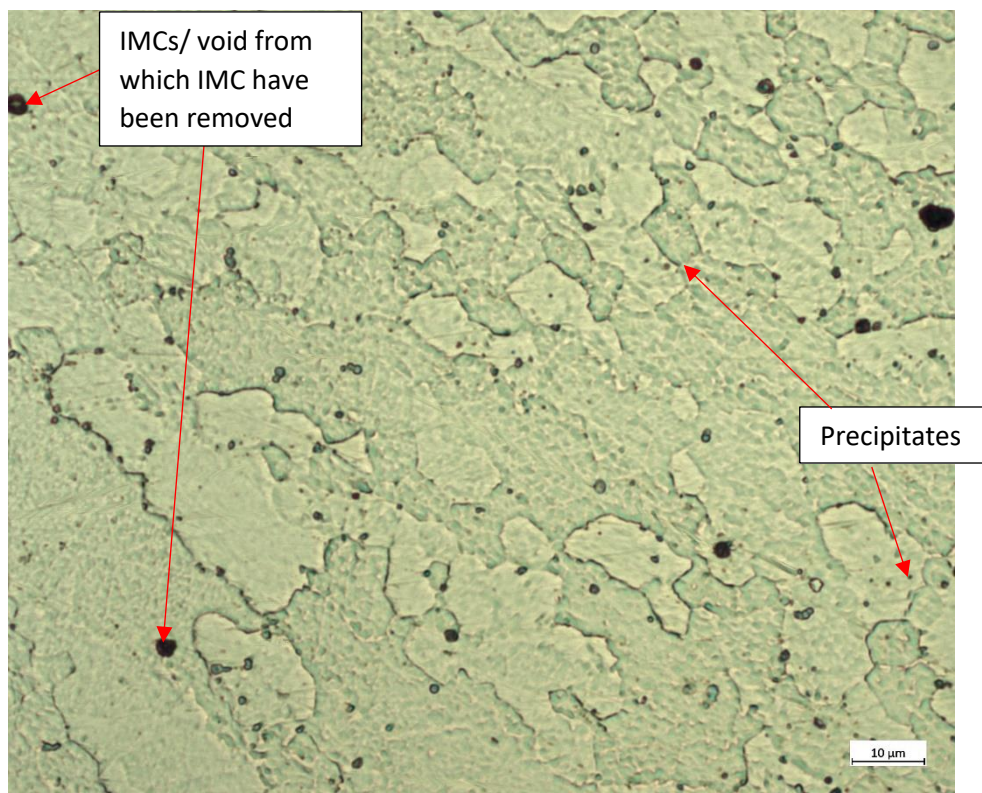
The TMAZ was characterised by distorted and elongated grains with a sharp nugget/TMAZ transition on the advancing side and a diffuse boundary on the retreating side. These boundaries are shown in Figure 141 and the microstructures of the II and \perp weld TMAZ are shown in Figure 147 and Figure 148 respectively. The II weld TMAZ measured approximately 115 μm in width on the advancing side and 300 μm on the retreating side, while the \perp weld TMAZ measured approximately 140 μm in width on the advancing side and 295 μm on the retreating side. These measurements are significantly larger than the AA8090-BS L165 welds and are more in keeping with those found on the similar welds. It is suspected that this is again related to the higher thermal conductivity of BS L165 directing heat outside the weld, combined with the different welding parameters used (compared with the similar welds) as discussed in section 6.5.1.3.1. In the case of the nugget, because the BS L165 was mixed with AA8090 to an extent, or at least in intimate contact with it, this resulted in an overall smaller nugget. In the case of the TMAZ, the BS L165 conducted the heat away from the nugget zone, travelling through the adjacent material on the advancing side; the welding parameters resulted in sufficient heat to be conducted through this area to produce a larger TMAZ than encountered in the AA8090-BS L165 welds. On the retreating side, while less heat was conducted from the advancing side during welding, the retreating side does still generate its own heat, which in the case of the predominantly AA8090 had a lower conduction rate and thus resulted in a larger TMAZ on the retreating side than the AA8090-BS L165 welds. As with all other configurations, the advancing side TMAZ was narrower than the retreating side, and the TMAZ increased in width towards the bottom surface of the weld.

On the advancing (BS L165) side there are a number of large intermetallic compounds and coarsened incoherent θ precipitates which have heterogeneously nucleated at grain boundaries. The intermetallic compounds visually appeared to be of a larger size in the II weld TMAZ than within the II weld nugget. Aside from the change in grain size and shape, the retreating (AA8090) sides were also similar in appearance to that observed in the nugget, with coarse intermetallic compounds (IMCs) and incoherent δ precipitates heterogeneously nucleated at the grain boundaries. The IMCs on the TMAZ of both sides

are considered to be compositionally consistent with that described by Rajendran et al. (2019) (advancing side) and Vigraman et al. (2021) (retreating side).

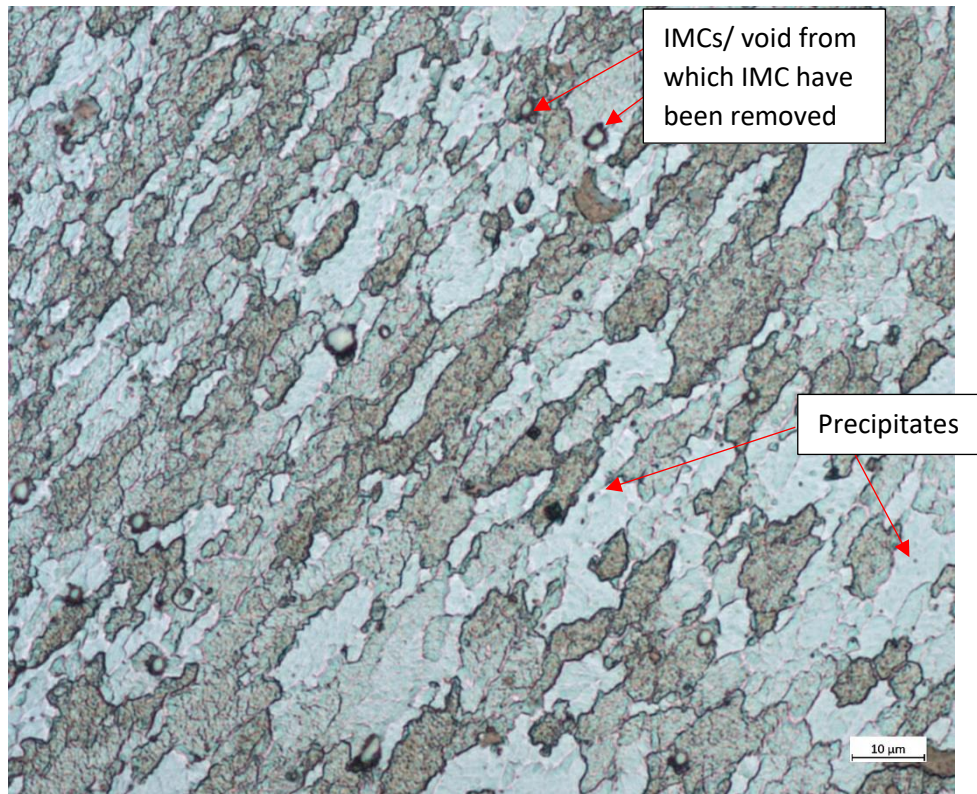


(a)

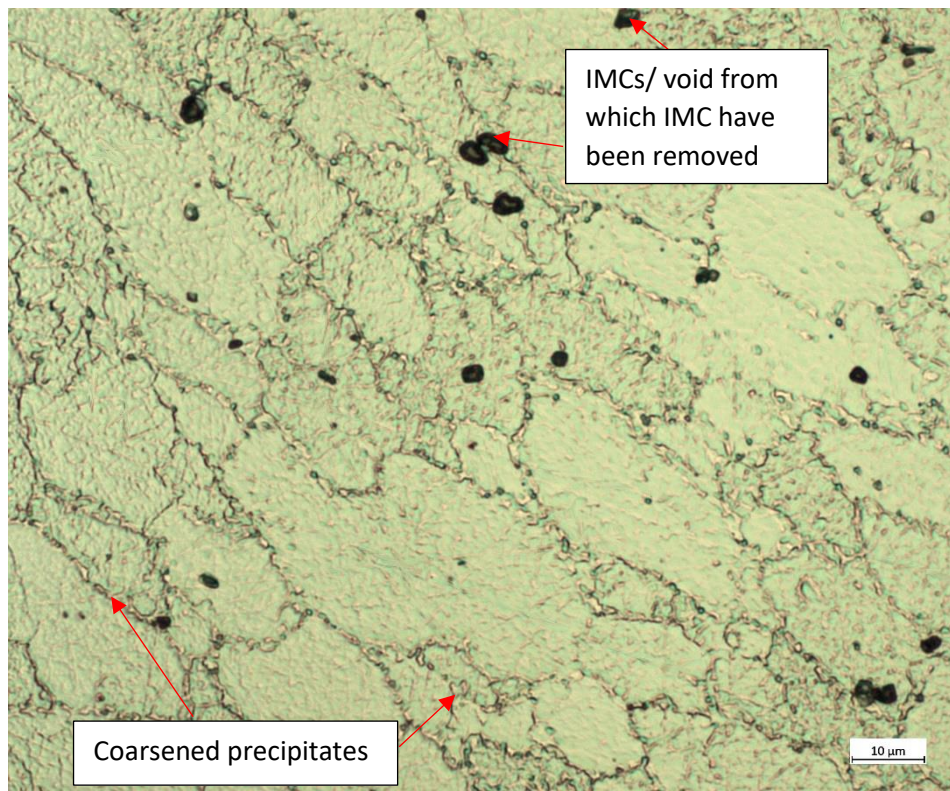


(b)

Figure 147: Showing micrographs of the BS L165-AA8090 II TMAZ: (a) advancing side, and (b) retreating side.



(a)



(b)

Figure 148: Showing micrographs of the BS L165-AA8090 \perp TMAZ: (a) advancing side, and (b) retreating side.

6.5.1.3.3 HAZ

As with other configurations the HAZ width was ascertained using hardness testing data. This indicated that the II weld HAZ (based on measurements every 0.5 mm) measured approximately 2.5 mm on the advancing side and 4.0 mm on the retreating side, while the \perp weld measured approximately 3.0 mm on the advancing side and 3.5 mm on the retreating side. As expected, the retreating side HAZ was wider than on the advancing side. These measurements were overall larger than observed on any other configuration, Table 45. This was considered to be due to the reasons previously given for the larger TMAZ in section 6.5.1.3.2, i.e. the higher conduction rate of BS L165 and the welding parameters used.

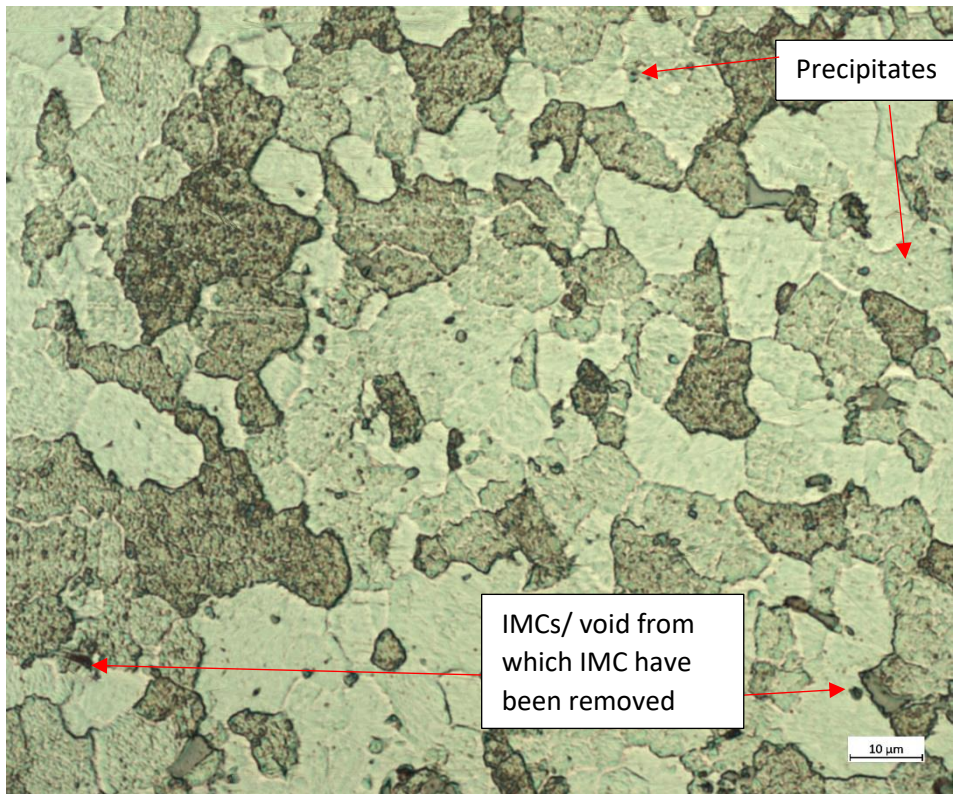
Micrographs of the HAZ are shown for the II and \perp welds in Figure 149 and Figure 150 respectively. The microstructures were similar to those of the relevant similar weld configurations, i.e. the advancing side HAZ of BS L165-AA8090 resembles that of the BS L165-BS L165 weld HAZs and the retreating side resembles that of the AA8090-AA8090 weld HAZs, with coarsening around the grain boundaries and some large intermetallic particles (considered to be similar to those described previously in sections 6.2.1.3.1 and 6.3.1.3.1) dispersed heterogeneously. As with previous configurations these images were taken close to the TMAZ boundary, and the degree of coarsening reduced as the HAZ nearer the parent material.

Table 45: Table showing HAZ widths of all weld configurations.

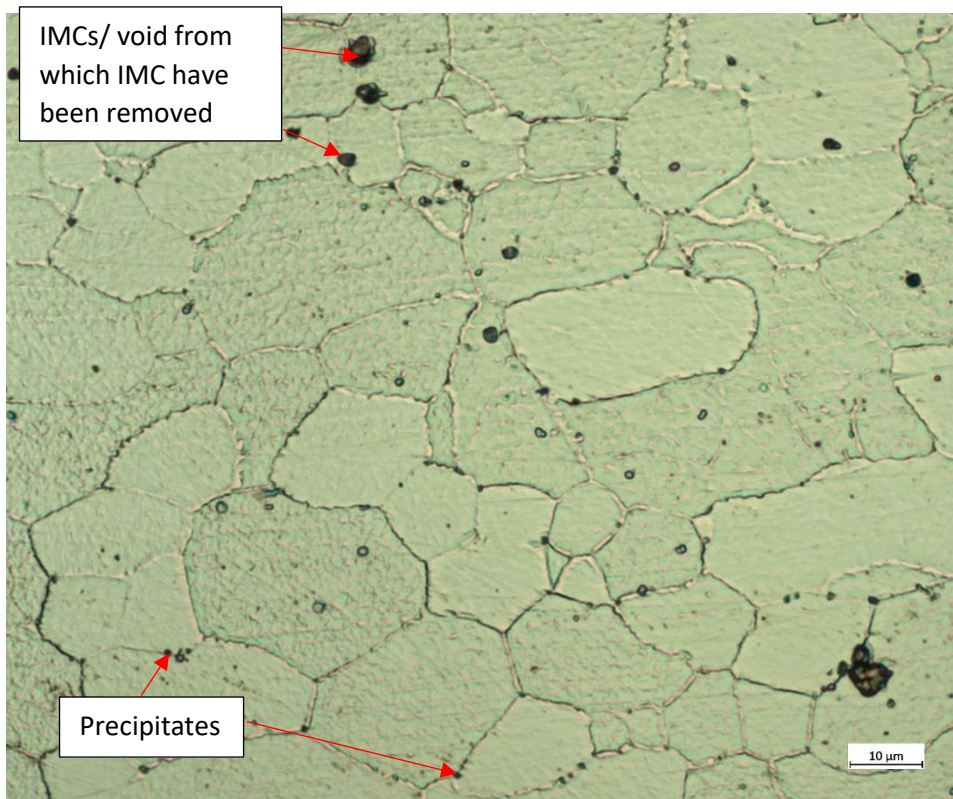
Configuration	Advancing side HAZ width (mm)	Retreating side HAZ width (mm)
AA8090 II	2.0	2.5
AA8090 I	2.0	2.5
BS L165 II	1.5 ¹	3.5
BS L165 I	1.5	2.0
AA8090-BS L165 II	2.0	3.0
AA8090-BS L165 I	2.0	3.0
BS L165-AA8090 II	2.5	4.0
BS L165-AA8090 I	3.0	3.5

Table 45 notes:

- 1 Originally measured as 4.0 mm but following further analysis determined to be 1.5 mm. See sections 6.3.1.3.3 and 6.3.2.1

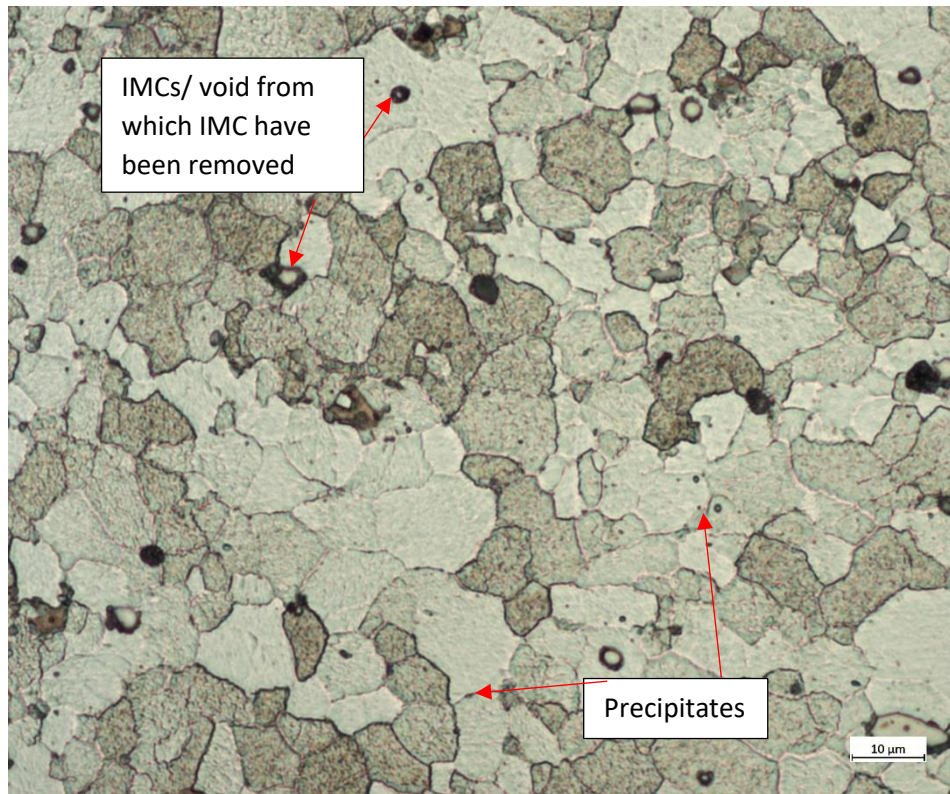


(a)

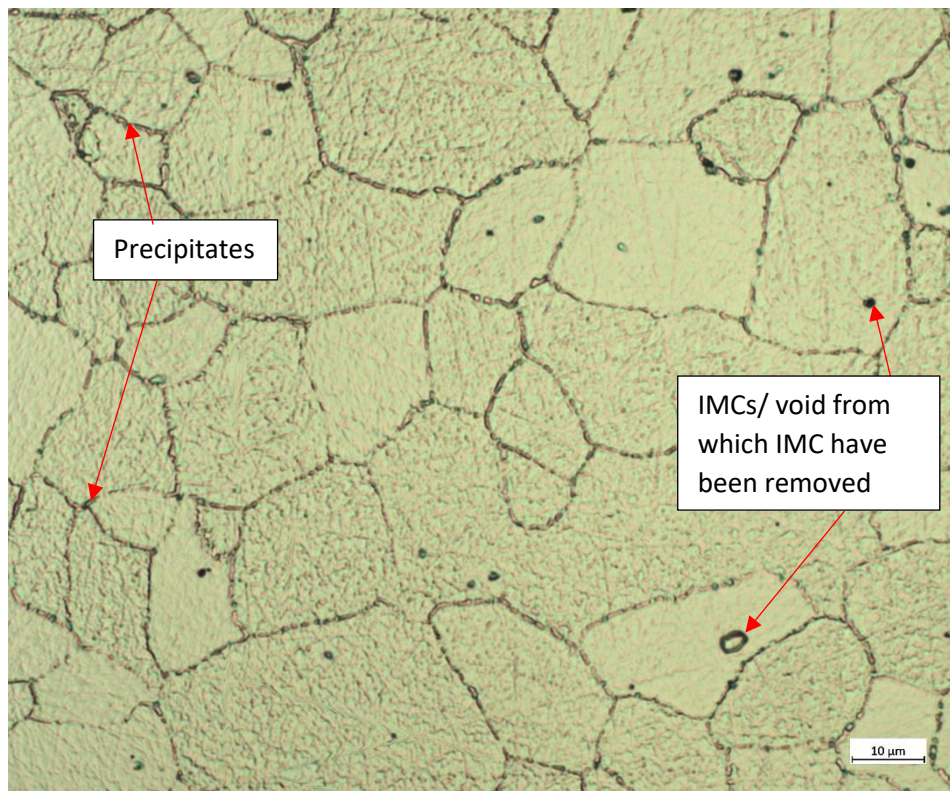


(b)

Figure 149: Showing micrographs of the BS L165-AA8090 II HAZ: (a) advancing side, and (b) retreating side.



(a)



(b)

Figure 150: Showing micrographs of the BS L165-AA8090 \perp HAZ: (a) advancing side, and (b) retreating side.

The average measured grain sizes of the HAZ areas are shown in Table 46 where the measured size for this configuration is compared with all other configurations. Analysis of the II weld shows a change in grain size on the advancing side in both directions when compared with both the BS L165 parent material and the BS L165-BS L165 II weld, and an overall reduction in grain size on the retreating side when compared with the corresponding values (AA8090 S-T parent material and AA8090-AA8090 II weld). This was also observed for the \perp weld. This suggests that the heat input to the HAZ has affected the grain structure despite no deformation occurring in this area, although the RA must of course be brought into consideration. The combined RA of the grain sizes being compared may account for the difference in grain size in some respects, however some grain size directions have calculated changes of approximately 44.5% which is outside the scope of the RA. Again, it is unclear as to why the grain size has changed with no deformation occurring in that area.

When compared with the AA8090-BS L165 welds, the differences in grain sizes were attributed to the different positioning of the materials influencing heat transfer through the weld. There are differences between the grain sizes (comparing advancing side of AA8090-BS L165 to retreating side of BS L165-AA8090), however it is expected that the grains would not have an identical response to reversed positioning within the weld and subsequent changes in thermal distribution.

Table 46: Showing BS L165-AA8090 weld HAZ grain size dimensions with parent material and grain sizes of all other configurations shown for comparison, showing Relative Accuracy (%RA) in brackets.

Configuration	Average Grain Diameter (μm) Measured Across Two Directions											
	Advancing Side						Retreating Side					
	Direction 1	% Change from Parent Material	% Change from Relevant Similar Weld Configuration	Direction 2	% Change from Parent Material	% Change from Relevant Similar Weld Configuration	Direction 1	% Change from Parent Material	% Change from Relevant Similar Weld Configuration	Direction 2	% Change from Parent Material	% Change from Relevant Similar Weld Configuration
AA8090 Parent Material (L)	21.2 (9%)	-	-	16.2 (6%)	-	-	-	-	-	-	-	-
AA8090 Parent Material (S-T)	28.0 (4%)	-	-	25.4 (16%)	-	-	-	-	-	-	-	-
BS L165 Parent Material (L)	12.2 (4%)	-	-	7.5 (6%)	-	-	-	-	-	-	-	-
BS L165 Parent Material (S-T)	14.4 (15%)	-	-	13.0 (13%)	-	-	-	-	-	-	-	-
AA8090 II	25.3 (19%)	-9.6	-	18.9 (13%)	-25.6	-	17.2 (14%)	-38.6	-	15.3 (11%)	-39.8	-

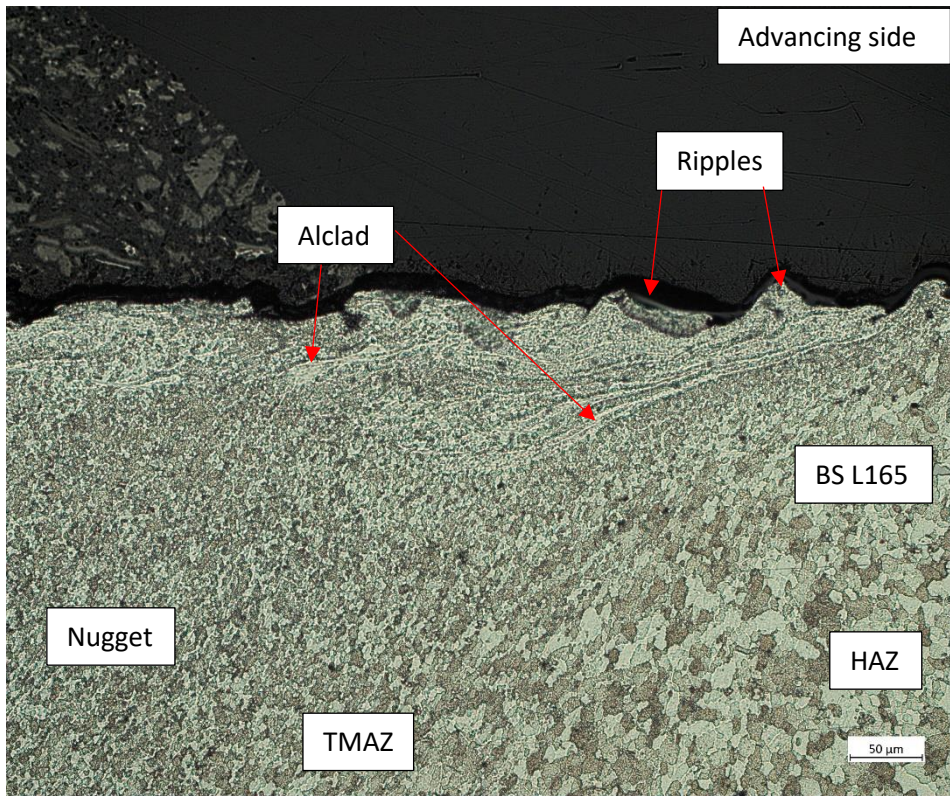
Configuration	Average Grain Diameter (µm) Measured Across Two Directions											
	Advancing Side						Retreating Side					
	Direction 1	% Change from Parent Material	% Change from Relevant Similar Weld Configuration	Direction 2	% Change from Parent Material	% Change from Relevant Similar Weld Configuration	Direction 1	% Change from Parent Material	% Change from Relevant Similar Weld Configuration	Direction 2	% Change from Parent Material	% Change from Relevant Similar Weld Configuration
AA8090 1	15.3 (6%)	-27.8	-	12.2 (6%)	-24.7	-	17.0 (11%)	-19.8	-	13.4 (8%)	-17.3	-
BS L165 II	11.3 (14%)	-21.5	-	7.6 (10%)	-41.5	-	12.5 (8%)	-13.2	-	7.5 (12%)	-42.3	-
BS L165 1	11.0 (8%)	-9.8	-	7.9 (9%)	+5.3	-	11.3 (11%)	-7.4	-	7.8 (8%)	+4.0	-
AA8090-BS L165 II	15.3 (11%)	-45.4	-39.5	12.4 (7%)	-51.2	-34.4	10.0 (12%)	-30.6	-20.0	8.2 (6%)	-39.6	+9.3
AA8090-BS L165 1	17.5 (11%)	-17.5	+14.4	13.2 (9%)	-18.5	+8.2	13.0 (5%)	+6.6	+15.0	8.2 (11%)	+9.3	+5.1
BS L165-AA8090 II	12.7 (10%)	-11.8	+12.4	7.4 (11%)	-43.1	-2.6	17.2 (14%)	-38.6	0	14.1 (9%)	-44.5	-7.8
BS L165-AA8090 1	12.7 (14%)	+4.1	+15.5	7.9 (20%)	+5.3	+9.7	16.3 (7%)	-23.1	-4.1	13.5 (7%)	-16.7	+0.7

6.5.1.3.4 *Weld Surface Region*

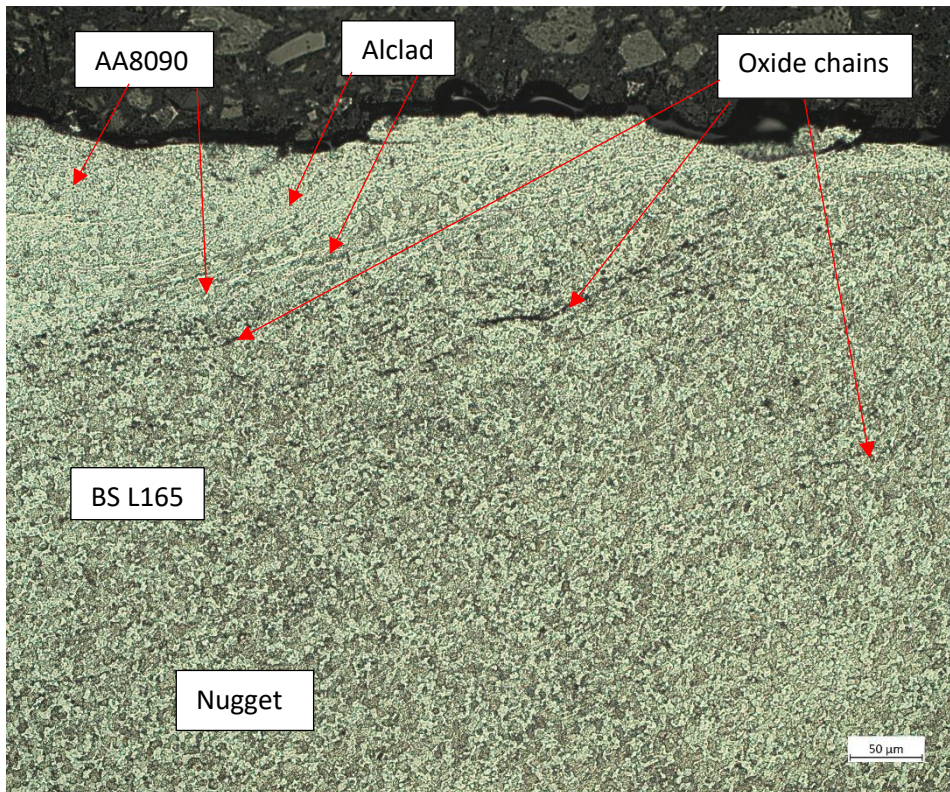
The surface regions of these dissimilar welds are quite chaotic, made more so by the presence of the alclad layer.

On the advancing side of the nugget within the rippled region the alclad material can be seen to partially remain on the surface (on some ripples) but also to mix within the BS L165 to a shallow depth, Figure 151(a). Remaining on the advancing side of the nugget but away from the rippled area, the AA8090 material has extended across at the top surface into the BS L165 region and the alclad material on the surface of the BS L165 has mixed with it, Figure 151(b). There is also intimate mixing between AA8090 and BS L165 at a shallow subsurface depth and oxide chains, described in section 6.5.1.3.1, are present within the BS L165 material, emanating from (but not necessarily present on) the joint line. These features: alclad mixing to a shallow depth within the weld; materials mixing close to the surface and oxide chains may all create weaknesses within the weld. The softer alclad mixing subsurface could create sharp strength gradients and act as stress raisers, risking potential failure through fatigue or overload when subjected to tensile loading. The same could be said for the two materials mixing, as there is a significant difference in the material's strengths in the as-welded state (Table 29 in section 5.2.2.1). The oxide chains introduce a weakness to the weld and offer a convenient fracture path.

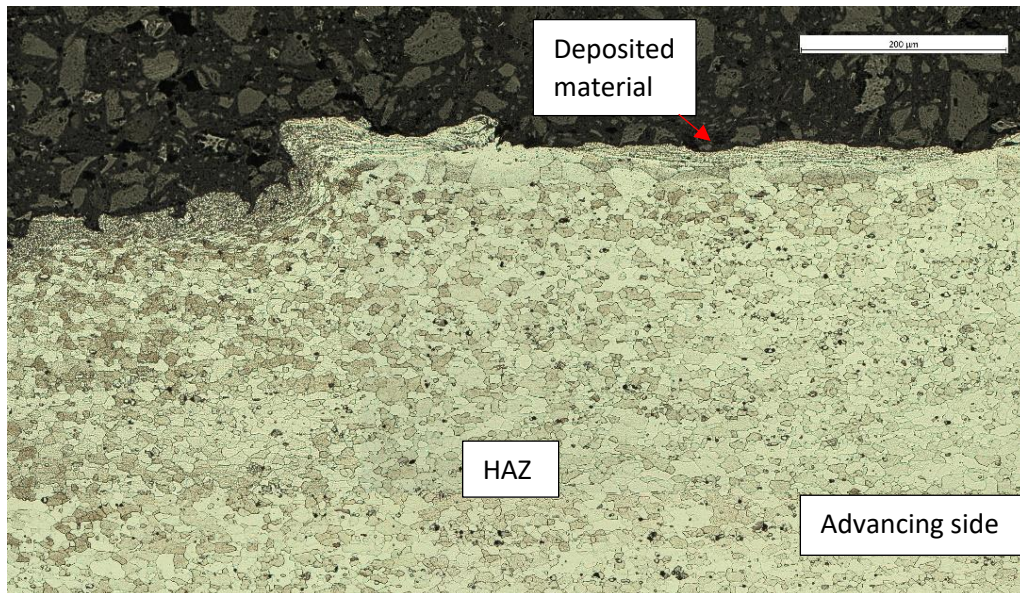
Adjacent to the weld (nugget and TMAZ), i.e. on the surface of the AA8090 and alclad BS L165 parent materials, is a layer of deposited alclad material, as previously discussed in 6.5.1.2 and shown in Figure 136. This layer varied in thickness over both weld configurations and is shown in Figure 151(c) as a fine layer on a \perp weld. The author can see little detriment to the weld quality due to the presence of this material deposit, except that it may be considered "untidy" and post weld processing may be required if used on an aircraft. However, if the extruded alclad left an area of BS L165 unclad, this may also present corrosion challenges.



(a)



(b)



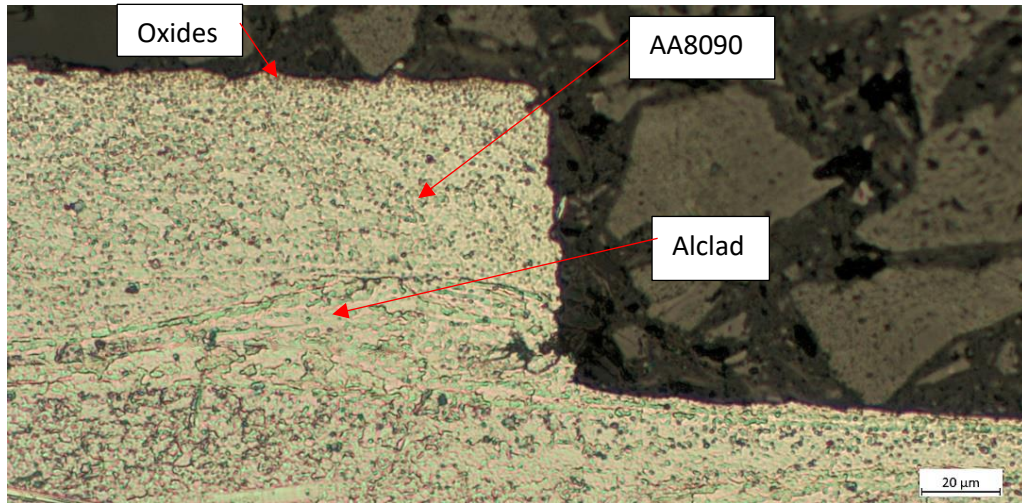
(c)

Figure 151: Showing weld surface region on advancing side of the weld: (a) alclad mixing into weld at rippled area of the nugget (II weld); (b) alclad mixing with AA8090 along top surface of weld, and mixing with BS L165 sub-surface, showing oxide chains (II weld); (c) deposited alclad material adjacent to weld as previously shown in Figure 136 (⊥ weld).

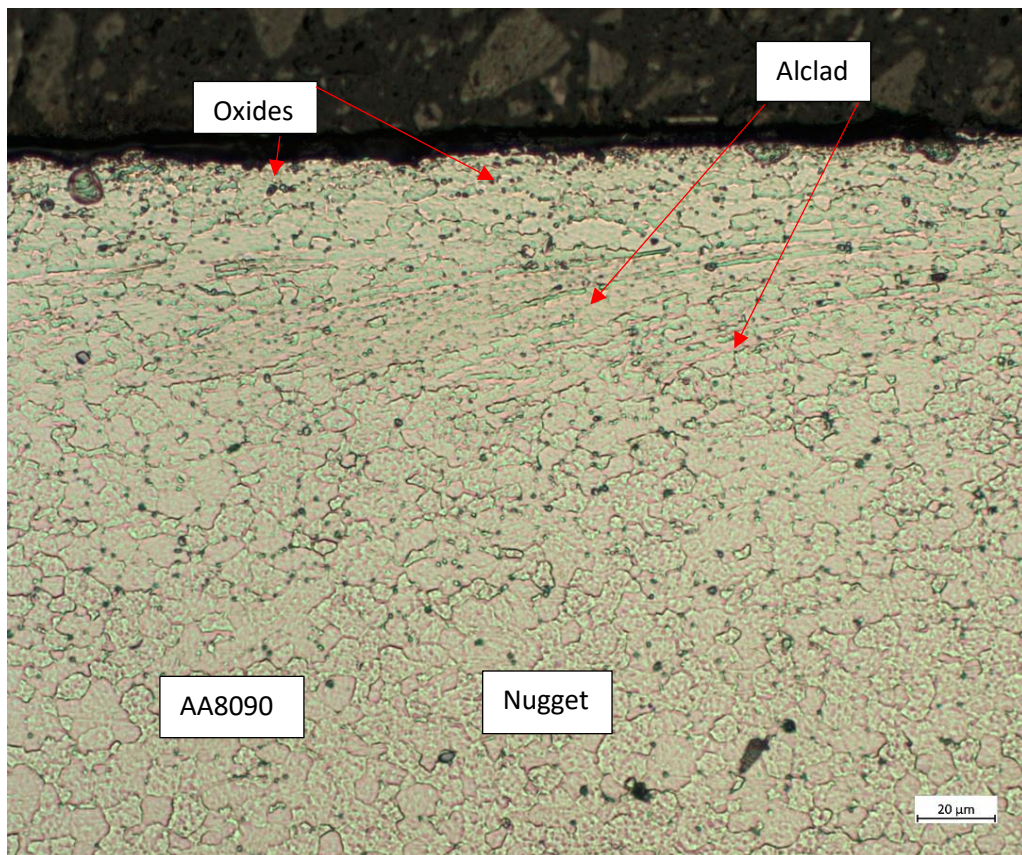
Still on the advancing side on the weld, i.e. before the mid-point within the nugget, the weld surface transitions from the rough, uneven, rippled area to a smooth, flat, ironed area. Figure 141 (highlighted by the purple boxes) shows this as a smooth, gradual, sloped transition for both configurations, however this was not the case on all welds. Figure 152(a) shows an example of a ⊥ weld which has a sharp, almost 90° transition between the two areas. This is a potential fatigue initiation site, and such a sharp corner radius can act as a stress raiser. The fact that the transition differs on different weld runs indicates inconsistent weld quality despite using the same parameters throughout this configuration.

Within the flat, ironed area on the retreating side of the nugget, the alclad material donated from the BS L165 parent material can be seen mixing with AA8090 subsurface, Figure 152(b). This could have the same potential consequences as previously discussed on the advancing side of the weld surface region. Also observed within a shallow layer at the top of the surface region were small oxides with a relatively dense distribution. Parts of the flat ironed area achieved good mixing without voids, however in other areas

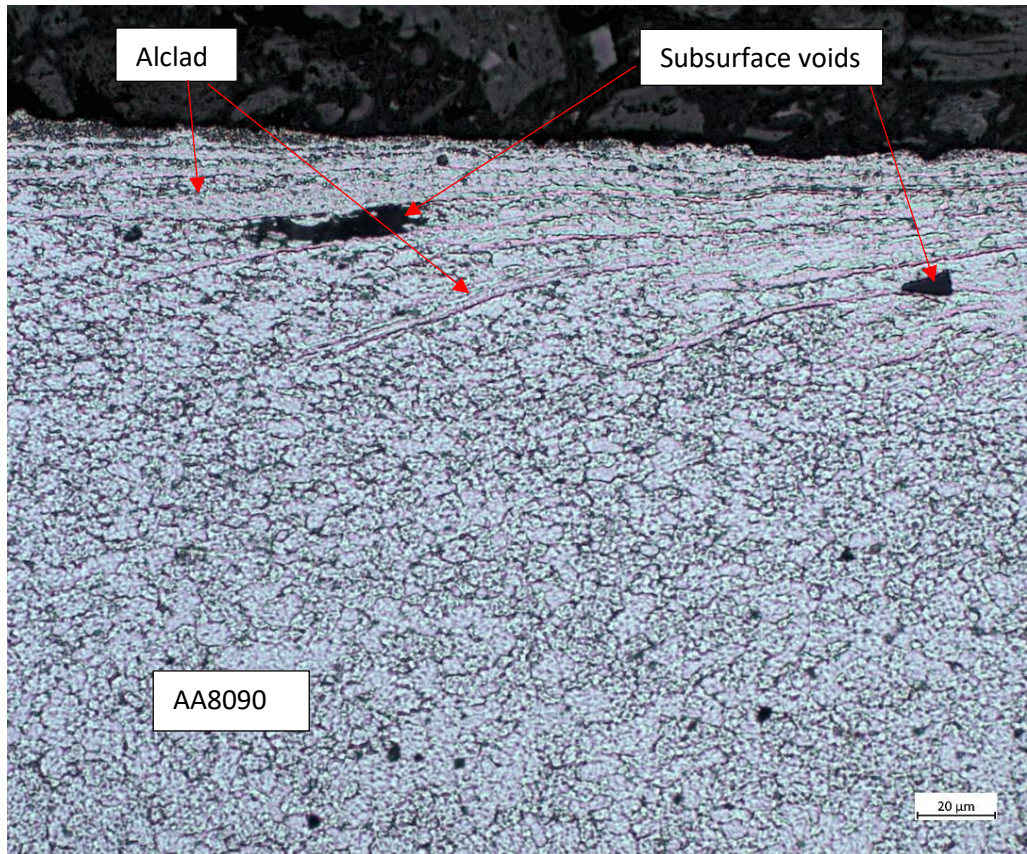
subsurface voids were present close to the weld surface, Figure 152(c). These were particularly prevalent where heavy mixing of the alclad material with AA8090 occurred. These are clearly detrimental to the weld quality and act to weaken the material by introducing stress raisers, essentially reducing the material cross-section, and acting as a blocker to consolidated mixing of the materials.



(a)



(b)



(c)

Figure 152: Showing the weld surface region within advancing and retreating side of nugget: (a) showing sharp step between rough, uneven, rippled area and ironed area of the weld top surface (\perp weld); (b) showing alclad mixing with AA8090 (II weld); (c) showing alclad mixing with AA8090 and subsurface voids (\perp weld).

6.5.2 Testing

6.5.2.1 Hardness

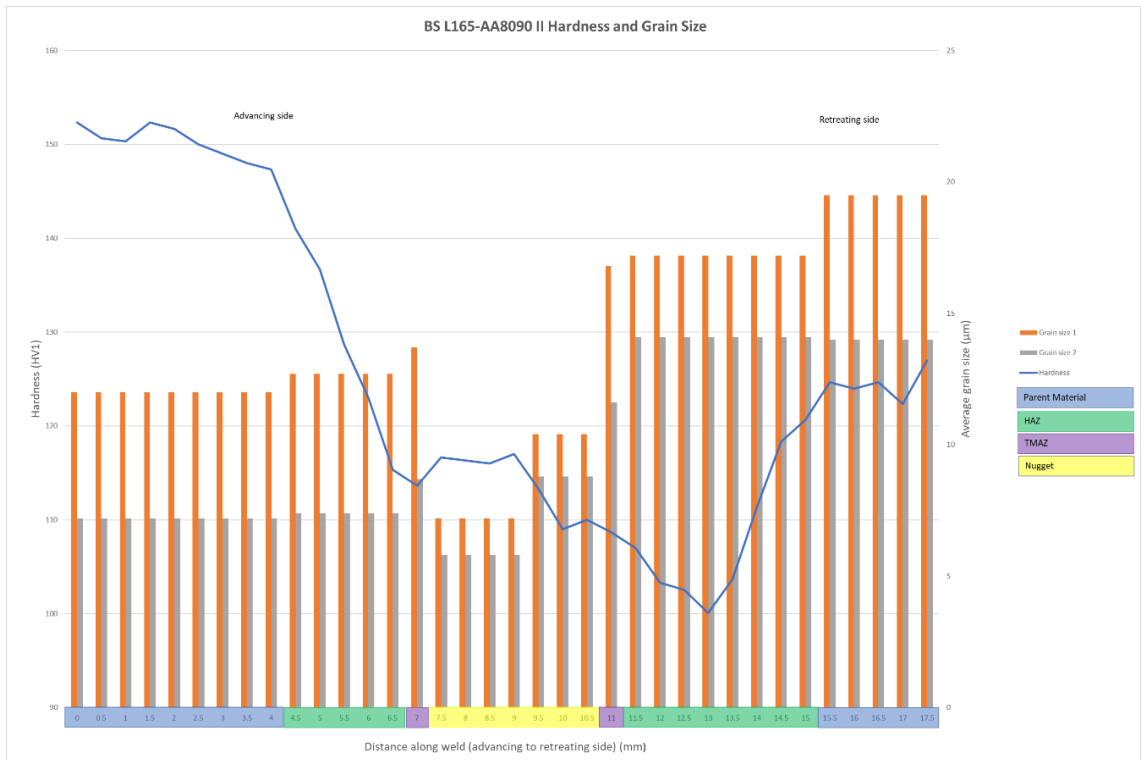
The results of hardness testing conducted approximately mid-thickness across each weld are shown in Figure 153 with weld zones indicated as in previous plots. Analysis of the II weld (Figure 153(a)) shows a decline in hardness from the BS L165 parent material advancing side through the HAZ with the advancing side minima occurring within the TMAZ. The hardness only marginally recovered in the BS L165 dominated part of the nugget where it remained relatively consistent. The hardness then dropped in the AA8090 dominated part of the nugget and continued to drop through the TMAZ and HAZ, reaching the retreating side (and whole weld) hardness minima well into the HAZ. Upon reaching the minima, the hardness then increased until that of the parent material was reached. The minima being located well into the retreating side HAZ is an indication of how the HAZ microstructure varies across its width. One may expect the minima to occur at the position within the HAZ which experienced the most heat, i.e. close to the TMAZ. However it is likely that the actual position was created through maximum coarsening of incoherent precipitates without the corresponding grain refinement observed in the TMAZ (grain size refinement in the TMAZ in one direction only). Neither materials recovered to their full parent material measured hardness values, although the BS L165 advancing side was very close (approximately 95%). The retreating side AA8090 was below the measured parent material hardness (Table 20 in section 4.1.3.1) achieving approximately 90%, making it likely that the HAZ actually extended further and the levelling of measurements observed at points 15.5-16.5 on Figure 153(a) was a change in the microstructure of the HAZ rather than the unaffected parent material being reached.

Analysis of the \perp weld (Figure 153(b)) shows a similar hardness profile to the II weld on the advancing side, with a fairly sharp decline through the HAZ and the advancing side minima being located in the TMAZ. Although still only a fraction of the original parent material hardness, more hardness recovery occurred in the BS L165 dominated region of the nugget than that which occurred in the II weld. The hardness then dropped within the AA8090 dominated part of the nugget where it oscillated briefly before dropping through the TMAZ with the minima again being reached well into the HAZ. Following the

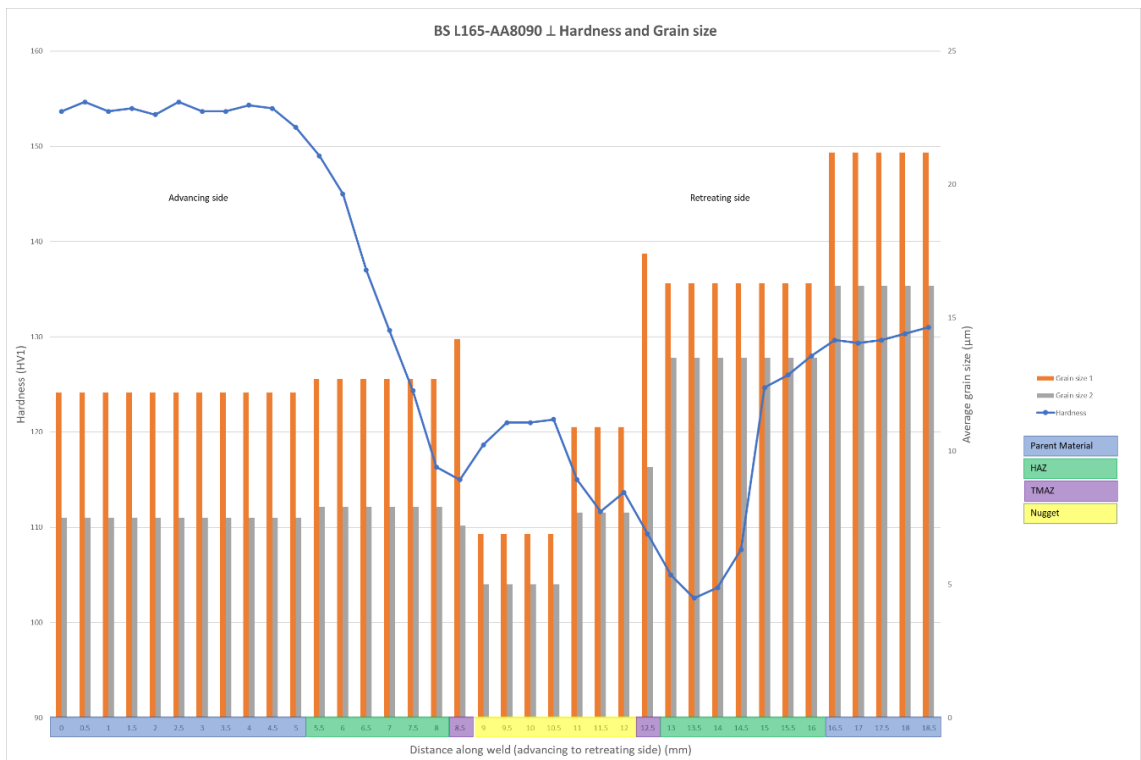
minima the hardness recovery was gradual at first and then rose sharply. Prior to the HAZ, the advancing side achieved approximately 99% of the measured parent material hardness, and the retreating side achieved approximately 94%. Considering the uncertainty of the measurement, it is believed that both materials achieved their original parent material hardness values.

Comparison with the AA8090-BS L165 welds (Figure 126 in section 6.4.2.1) showed that the BS L165 suffers far more variation of hardness value in the nugget when positioned on the retreating side, although at the hardness peaks more hardness recovery in the nugget was observed when this material was on the retreating side.

In the case of BS L165-AA8090 both hardness minima occurred in the AA8090 (retreating) HAZ, and while in the AA8090-BS L165 II weld the minima also occurred in the AA8090 (now advancing) HAZ, on the \perp weld the minima occurred in the AA8090 TMAZ. On the AA8090-BS L165 II weld, the softest part of the BS L165-dominated part of the weld occurred at the TMAZ which is in keeping with the softest parts of the BS L165-dominated areas on both BS L165-AA8090 welds; only the AA8090-BS L165 \perp weld has the BS L165-dominated softest area in the HAZ.



(a)



(b)

Figure 153: Showing hardness and grain size plots of a) BS L165-AA8090 II, and b) BS L165-AA8090 L.

6.5.2.2 Tensile Testing

The results of BS L165-AA8090 tensile testing are shown in Table 47 and have been compared with all other configurations. To ascertain UTS weld efficiencies the welds have been compared with the AA8090 parent material values due to this material being weaker in the welded condition as described in section 6.4.2.2. This configuration achieved the lowest weld efficiencies of any of the welds tested in this study, achieving only 74.4% (II weld) and 64.1% (\perp weld). Based on the literature previously examined in section 6.4.2.2 (Bandhu et al., 2017; Barbini et al., 2018; Masoumi Khalilabad et al., 2021; Masoumi et al., 2016; Sivaraman et al., 2021; Venkateswara Rao & Senthil Kumar, 2020), the II weld was slightly above the average result of 71.5% for germane dissimilar materials, and the \perp weld slightly below. Both are well within the range of results achieved in other research.

In comparison with the AA8090-BS L165 welds, this configuration achieved 94.5% and 88.8% UTS for the II and \perp welds respectively. On first inspection this suggests that the dissimilar welds were stronger with AA8090 on the advancing side. However, when the fracture position was examined it became apparent that for AA8090-BS L165 II welds, 12 of the 20 test specimens failed at the advancing (AA8090) edge of weld, the softest part of the weld. The literature (as discussed in section 6.4.2.2) states that the softest part of the weld should be the weakest point and thus the expected point of fracture. All others of that configuration failed within the nugget and were influenced by a kissing bond. Of the BS L165-AA8090 II welds only 2 of the 20 test specimens failed at the supposed weakest position of retreating (AA8090) HAZ; all others failed within the nugget and were influenced by kissing bonds (this will be discussed in more detail shortly). As such, the fact that the BS L165-AA8090 II weld achieved 94.5% of the AA8090-BS L165 II weld tensile strength when 90% of its test specimens failed due to a flaw rather than at its material-influenced weakest point, is indicative that in the absence of flaws the dissimilar materials may actually be stronger with BS L165 on the advancing side when welded parallel to the rolling direction. Such a statement cannot be made regarding the \perp welds as both configurations had only 3 test specimens which failed at the supposed weakest point, and the remaining 17 (in each case) failing mid-nugget due to kissing bonds. When one considers the UTS of each tensile test specimen

which failed at the material-influenced (position of lowest hardness) weakest point, these were:

- AA8090-BS L165 \perp : 326 MPa, 337 MPa and 335 MPa – average 332.7 MPa
- BS L165-AA8090 \perp : 317 MPa, 334 MPa and 330 MPa – average 327 MPa

Acknowledging the small sample size, this suggests that when welded perpendicularly to the rolling direction the weld is slightly stronger with AA8090 on the advancing side. The difference is however marginal, especially when the uncertainty of ± 4.6 MPa (see section 3.4.2) is considered, and thus inconclusive.

Section 2.3.9.3.2 describes the debate within the literature as to the most appropriate positioning of materials for optimum mechanical properties. For example, Verma and Misra (2021) state that the stronger material should be positioned on the advancing side due to the increased heat generation at this location, which allows greater plasticisation of the stronger material and subsequently superior mixing. However, Barbini et al. (2018) found that positioning the stronger material on the advancing side resulted in lower torque and thus lower heat input due to the material's higher strength and lower ductility. They found that increasing the heat input by lowering the traversing speed cause intolerable coarsening of precipitates in the other material, but reducing the heat input by increasing the traversing speed did not allow for adequate mixing between the two materials. The parent materials tested in this research have similar UTS prior to welding, however when welded AA8090 is the weaker of the two. This would suggest that this research supports the opinion of Verma and Misra (2021) and the BS L165 as the stronger material should be positioned on the advancing side for the \perp dissimilar welds only.

There is little research within the literature on the effect of the rolling direction on the weld quality, however Barbini et al. (2018) did study it. They found that for AA2024 the yield strength was strongly affected by the weld orientation but that UTS was only affected at low traversing speeds with the specimens welded perpendicularly to the rolling direction achieving significantly lower results.

In this current research the yield strength of the dissimilar weld configurations was only measurable for AA8090-BS L165, with the other dissimilar configurations producing inconclusive results owing to the extremely low ductility of the welds, mainly due to the

presence of kissing bond flaws (see later within this section). Due to this, it is not possible to say if the yield strength was affected by the change in the materials' positioning or the change in weld orientation. The BS L165-AA8090 \perp welds did achieve lower UTS results than the II welds however, again due to the widespread kissing bond flaw influencing the results, conclusions cannot be reached regarding the \perp weld with respect to tensile strength. This means that no recommendation can be provided from the current research as to the positioning of the materials when welded in the \perp orientation, nor can a recommendation be made as to the optimum orientation to weld these materials with respect to rolling direction. Additional work on finding optimum welding parameters to achieve welds with sound mixing and which are absent of kissing bonds is required at which point these questions can be answered.

Table 47 shows that the ductility achieved with these welds was the lowest of all configurations and was actually below the tolerance for the equipment to accurately measure, the uncertainty of $\pm 0.3\%$ notwithstanding. Nevertheless, the fact that they are so low is valuable information in itself; the ductility of these specimens was severely affected by the welding process. It is considered that this considerable reduction in ductility was due mainly to the severe kissing bonds present, but was also influenced by the changes in microstructure as described in section 6.2.2.2.

As with most of the weld configurations, Table 47 shows that these tensile tests had high standard deviations in UTS. Examination of the results revealed significant scatter with the II configuration having a variation of 85 MPa in just one weld and 91 MPa overall, while the \perp weld had variation of 108 MPa in just one weld and 125 MPa overall. Again, no strong pattern was observed; as previously discussed, most failed mid-weld due to a kissing bond, and while all of those which did fail at the retreating edge of weld achieved some of the highest results, some of those which failed mid-weld achieved comparable results (although others were much lower). This was an indication of inconsistent weld quality both along weld lengths and between welds, likely due to inconsistent heat input affecting the presence and severity of kissing bonds.

Table 47: Showing BS L165-AA8090 tensile test results with parent material with all other configurations shown for comparison.

	UTS (MPa)		0.2% Proof strength (MPa)		Elongation (%)		UTS Standard Deviation	% UTS Parent Material Spec	% UTS Measured Parent Material	% UTS Measured AA8090 similar material weld	% UTS Measured BS L165 similar material weld	% UTS of Measured Relevant AA8090-BS L165 configuration
	Spec	Measured	Spec	Measured	Spec	Measured						
AA8090 parent L	400	443	280	343	6	9.5	3.17	110.8	-	-	-	-
AA8090 parent T	410	438	280	307	9	11.1	2.52	106.8	-	-	-	-
BS L165 parent L	415	442	345	397	7	8.7	2.82	106.5	-	-	-	-
BS L165 parent T	415	436	345	393	7	8.4	2.20	105.1	-	-	-	-
AA8090	410	357	280	256	9	3.3	8.39	87.1	81.5	-	-	-
AA8090 ⊥	400	359	280	266	6	2.0	23.57	89.8	81.0	-	-	-
BS L165	415	437	345	340	7	3.3	38.9	105.3	100.2	-	-	-
BS L165 ⊥	415	430	345	343	7	2.4	22.06	103.6	97.3	-	-	-
AA8090-BS L165	410	345	280	284	9	1.4	21.08	84.1	78.8	96.6	78.9	-
AA8090-BS L165 ⊥	400	320	280	Note 1	6	Note 1	31.35	80.0	72.2	89.1	74.4	-
BS L165-AA8090	410	326	280	Note 1	9	Note 1	14.64	79.5	74.4	91.3	74.6	94.5
BS L165-AA8090 ⊥	400	284	280	Note 1	6	Note 1	26.96	71.0	64.1	79.1	66.0	88.8

Table 47 notes:

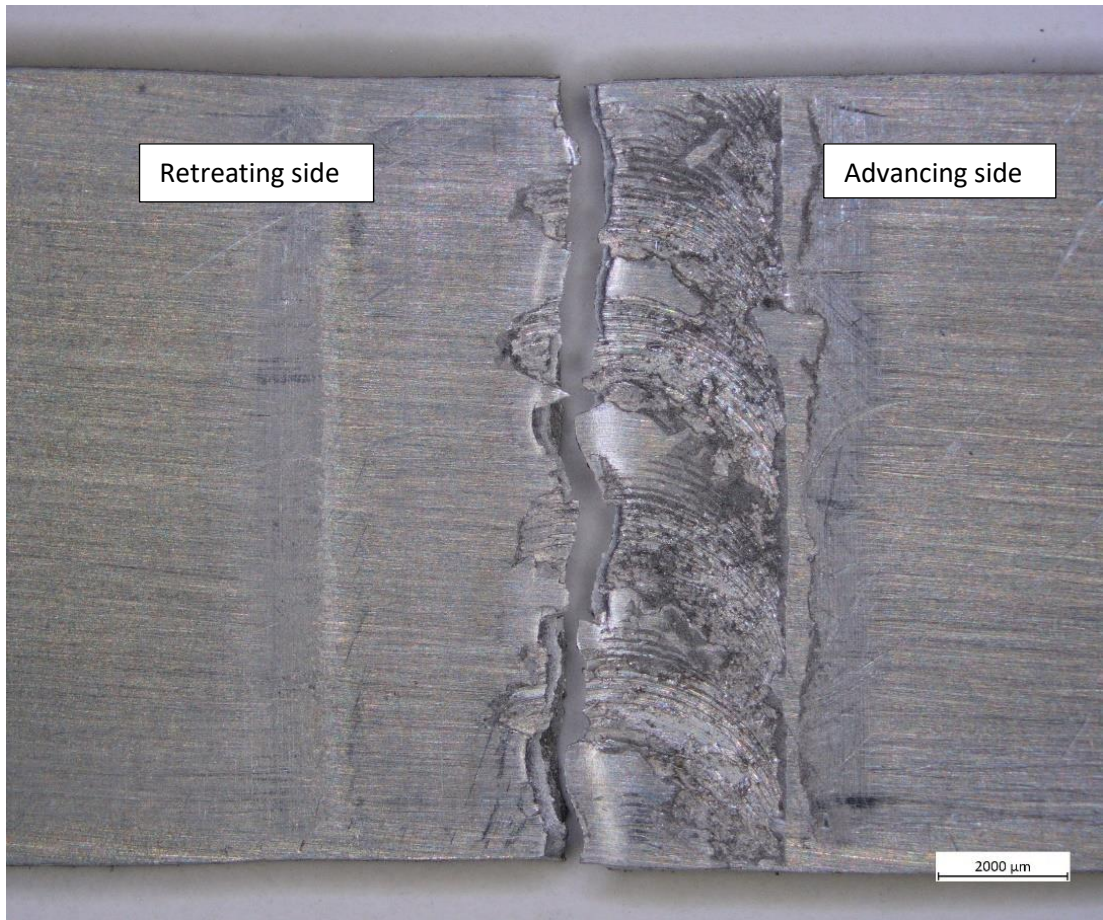
1 The 0.2% proof strength was inconclusive for this configuration owing to elongation being below the tolerance measurable by the equipment.

Of the 20 BS L165-AA8090 II tensile tests performed, 18 failed mid-weld and two failed at the retreating edge of weld when observed from the top surface. Of those 18 which failed mid-weld there was considerable variation in the fracture path appearance, with some having smooth and straight paths across the fracture length and others following a ragged and wavy fracture path. For this reason, one ragged mid-weld failure has been discussed along with one straight mid-weld failure, in addition to the retreating edge of weld failure. Examples of each failure type, showing position of fracture from the top surface, as a cross section and showing detailed SEM images of the fracture surface are shown in Figure 154 (ragged mid-weld), Figure 155 (straight mid-weld) and Figure 156 (retreating edge of weld).

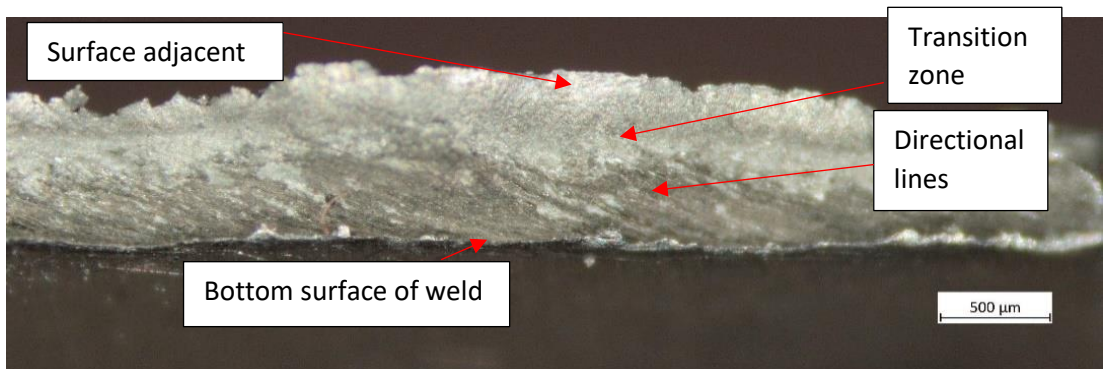
With reference to Figure 154, the crack propagated partially through the rippled area although the fracture path was not influenced by these features. The fracture surfaces were heavily dominated by the dull directional markings which were previously associated with kissing bonds over approximately half of the fracture surface thickness. The etched cross-section (Figure 154(c)) shows that the fracture followed the kissing bond from the bottom surface of the weld, then traversed through a small AA8090 dominated area before final failure through the BS L165 dominated surface area. Note that the BS L165 material has mixed across the top of the weld at this position, which conflicts with that shown in Figure 141 where tendrils of AA8090 extend along the top of the weld thickness, indicating that the material mixing varies along the length of the weld.

SEM analysis revealed three different zones to the fracture surface as shown in Figure 154(d); a kissing bond adjacent to the bottom surface of the weld (Figure 154(e)), then a transition zone which contained a mix of the directional lines typical of the kissing bond together with microvoid coalescence indicative of ductile failure, Figure 154(f), with the final area adjacent to the top surface of the weld corresponding to the BS L165 dominated SAZ, which showed transgranular cleavage failure, Figure 154(g). Within the kissing bond (close to the transition zone) large oxides were observed consistent with that shown in Figure 141 and Figure 146, shown here in Figure 154(e). Those large oxides shown previously were observed on a \perp weld; this is a II weld (despite what appears to be a \perp rolling direction on Figure 154(a); these markings were related to the seemingly inadequate preparation process and were not the rolling direction). This indicates that

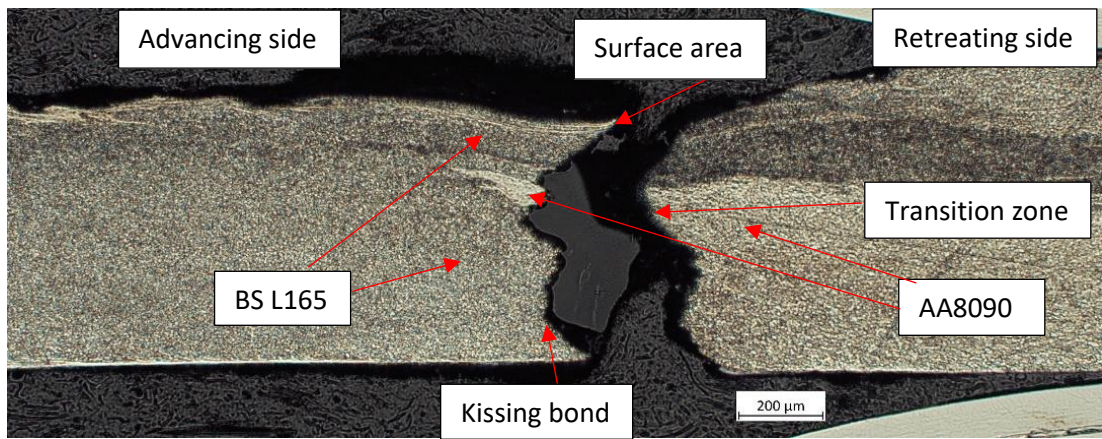
several of the sheets were ill prepared prior to welding and highlights the importance of carrying out this process properly.



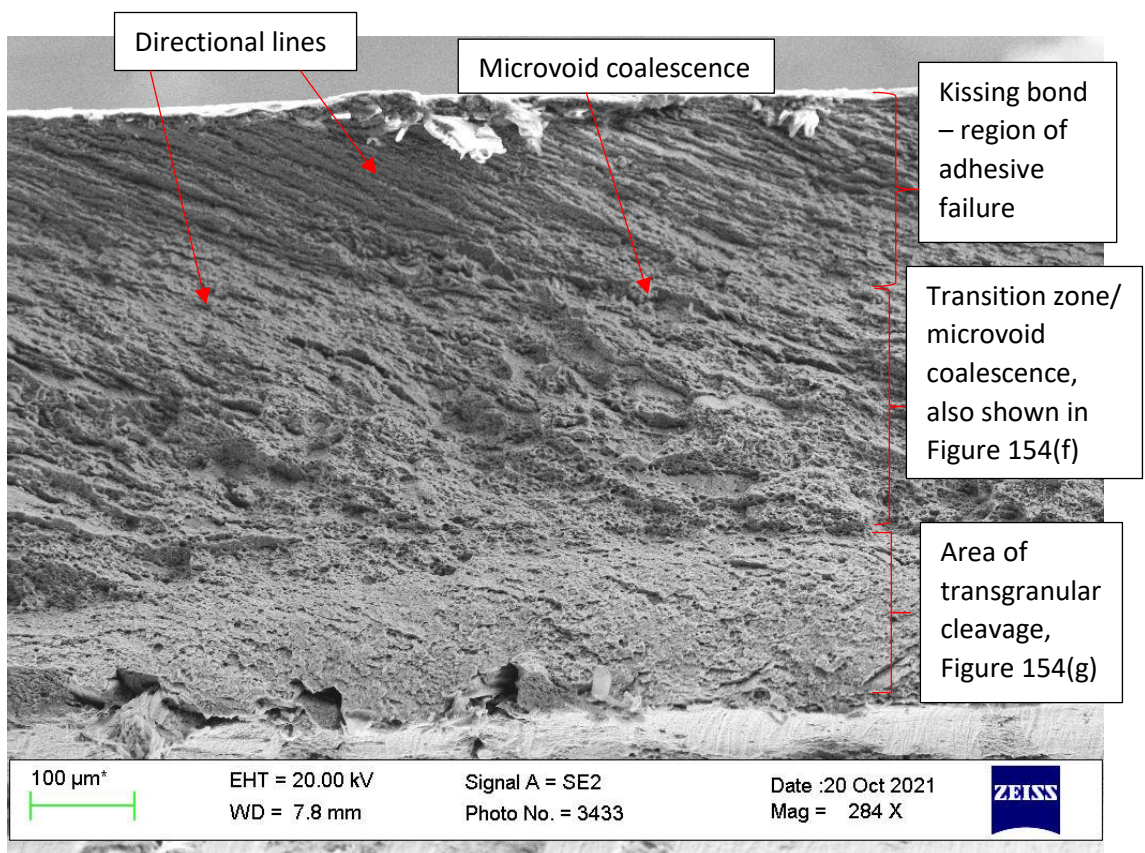
(a)



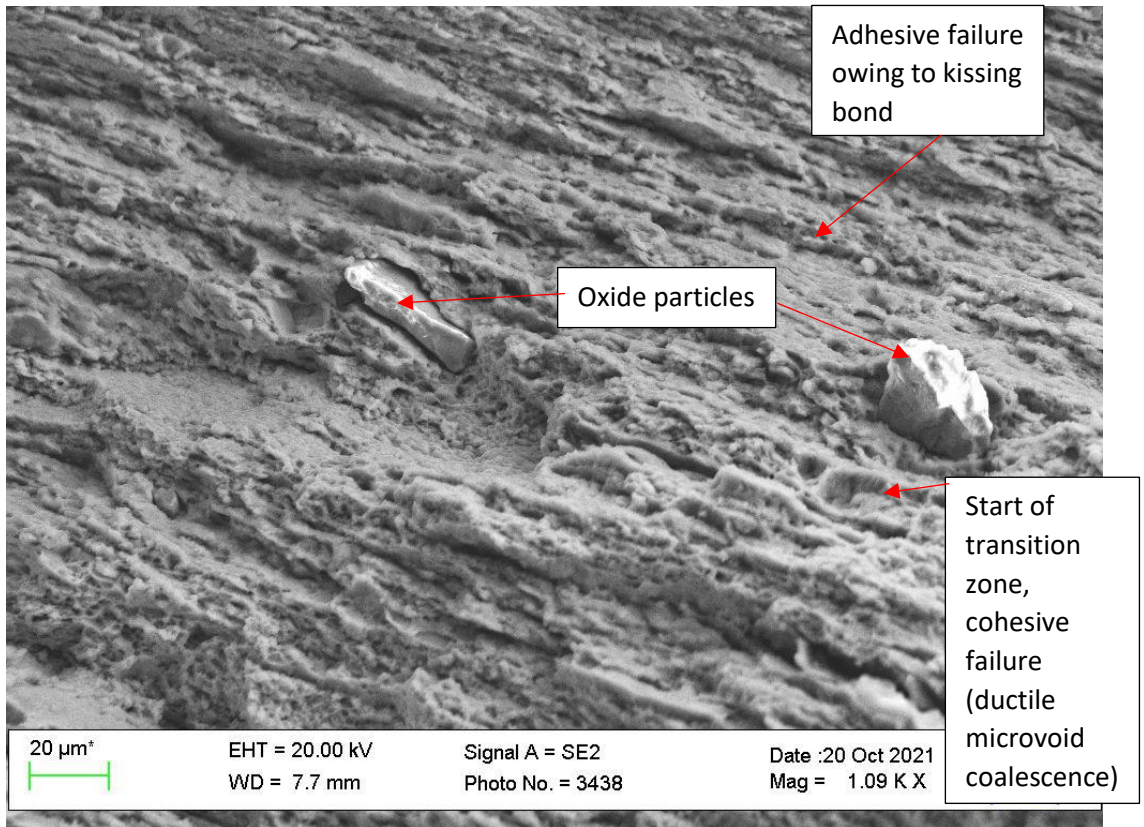
(b)



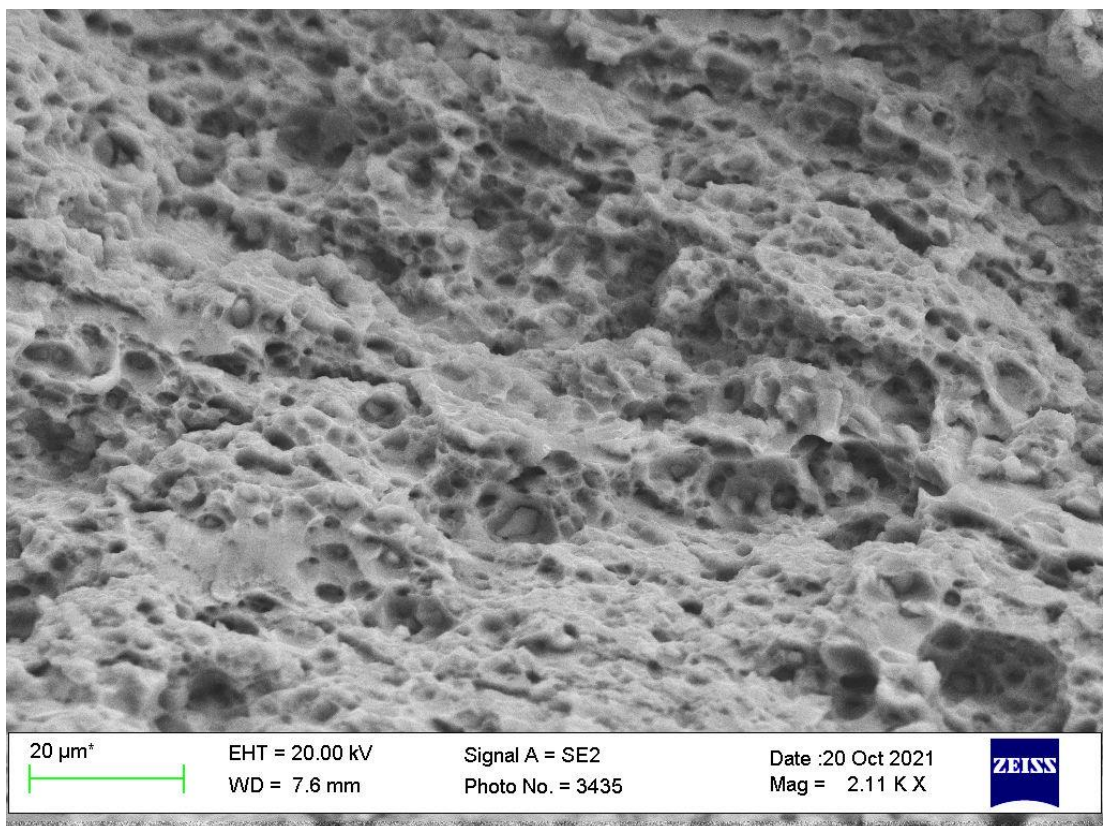
(c)



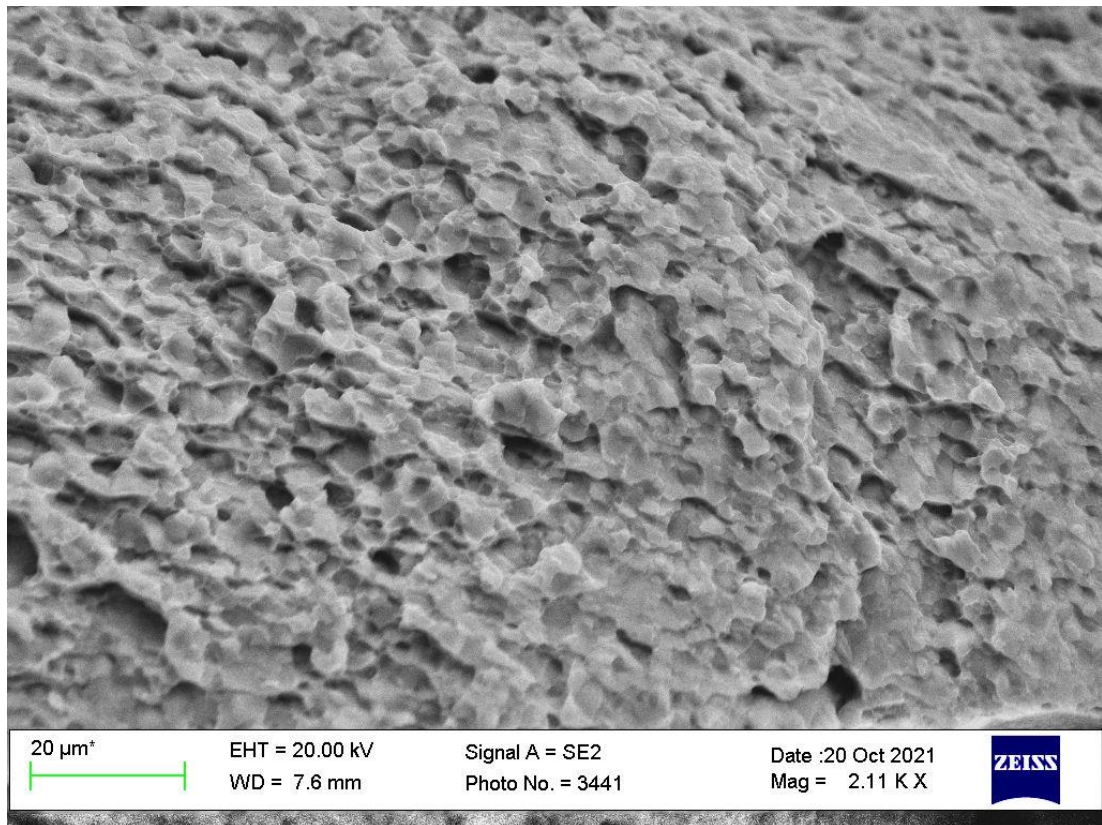
(d)



(e)



(f)

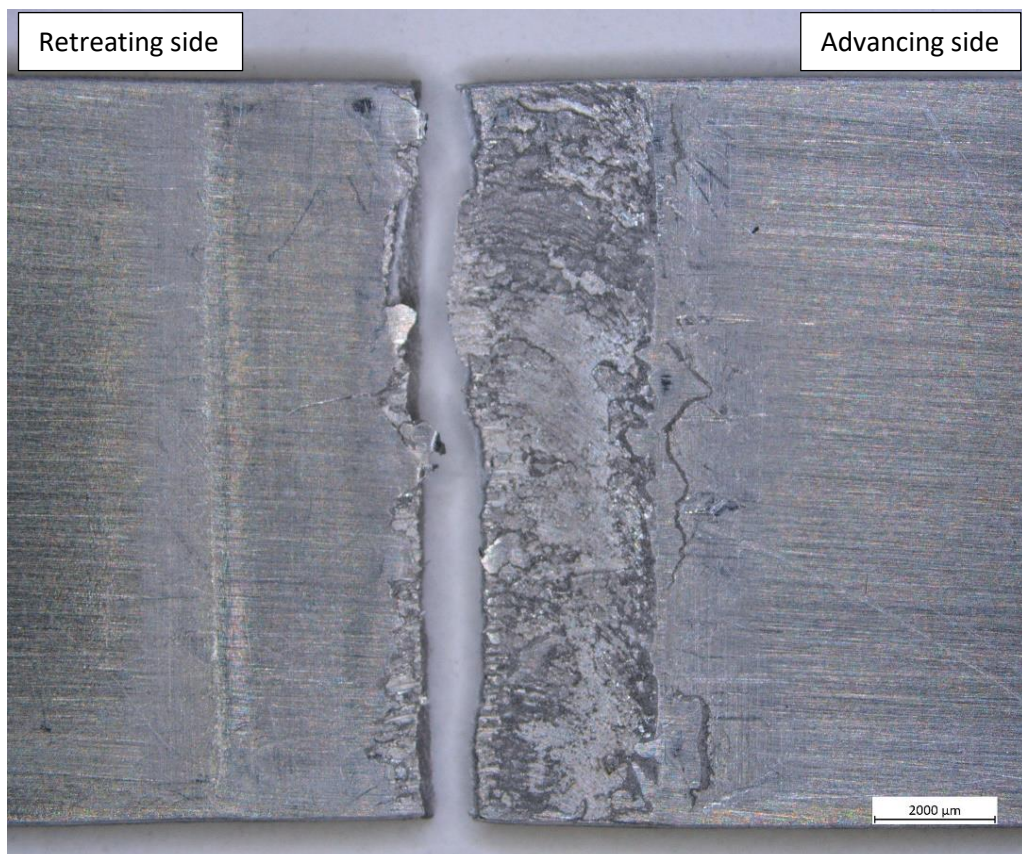


(g)

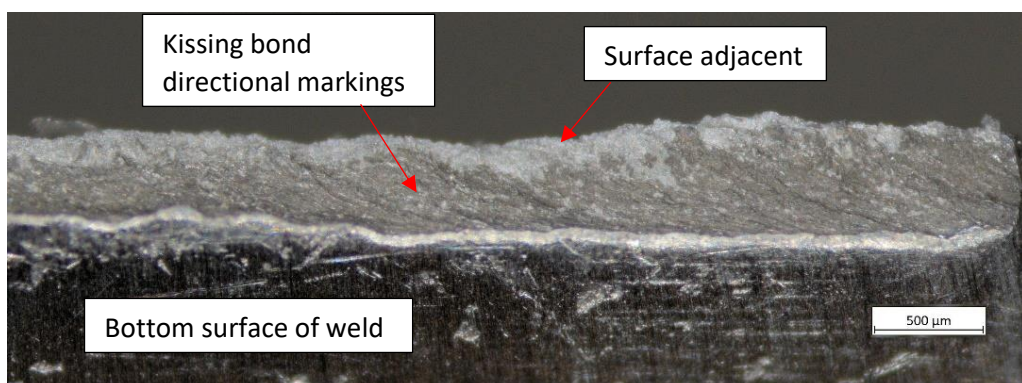
Figure 154: Showing tensile fracture of BS L165-AA8090 II weld which failed mid-weld with a ragged appearance: (a) macrograph showing fracture from top surface; (b) macrograph showing part of fracture surface; (c) cross-section of weld showing crack path; (d), (e), (f) and (g) SEM images showing detail of fracture surface.

With reference to Figure 155, those mid-weld fractures which followed a straight fracture path did so close to the edge of the rippled area. Although it was previously stated that the rippled surface did not influence the fracture path, when the two surfaces were compared, Figure 154(a) shows a more intermittent rippled appearance, while Figure 155(a) has a more consistently rippled, rough appearance. This suggests that the intermittency of the ripples influenced the fracture path, i.e. where the ripples covered a significant length of the weld consistently the fracture path followed a straight rather than ragged path. The fracture surface was again heavily dominated by the kissing bond which was also shown via the etched cross-section. This cross-section showed the crack propagated from the kissing bond adjacent to the bottom surface of the weld, through a BS L165 dominated area before finally propagating through the AA8090

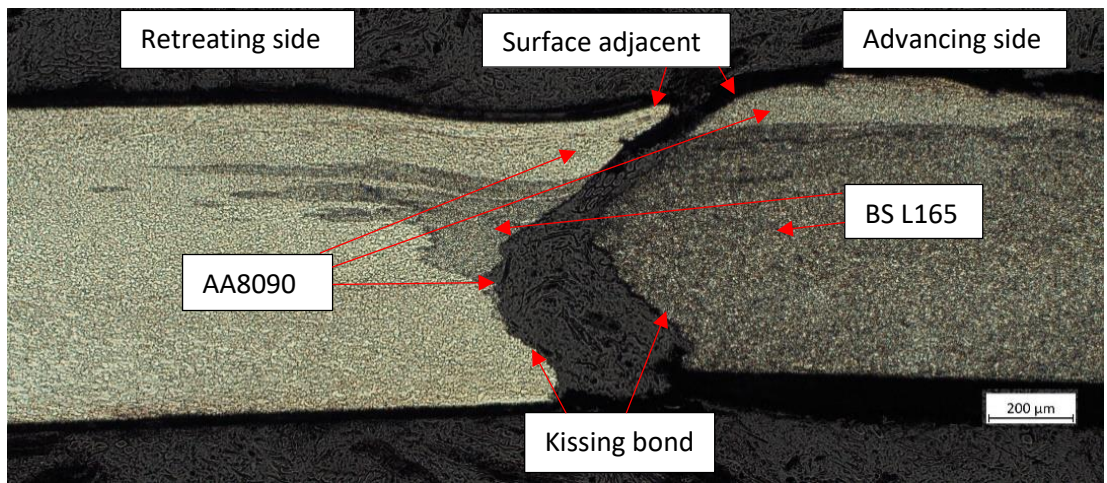
dominated area close to the top surface. Note, that the materials are again mixed such that the AA8090 was adjacent to the top surface of the weld as per Figure 141. SEM analysis revealed a similar fracture surface to that described for the ragged mid-weld fracture, although in this case there was little transition zone and rather the fracture surface changed from kissing bond to microvoid coalescence almost immediately (Figure 155(d)). The final area close to the top surface was comprised predominantly of transgranular failure with some elongated voids, indicative of a shear failure, Figure 155(e).



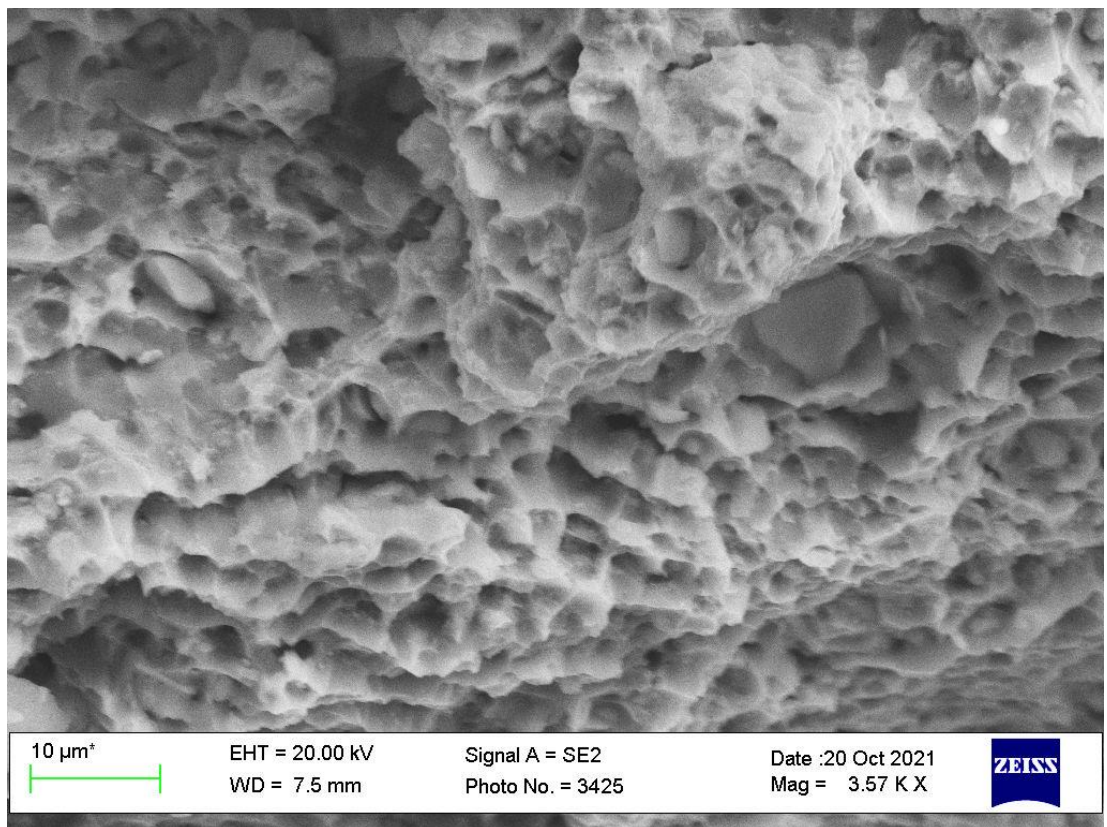
(a)



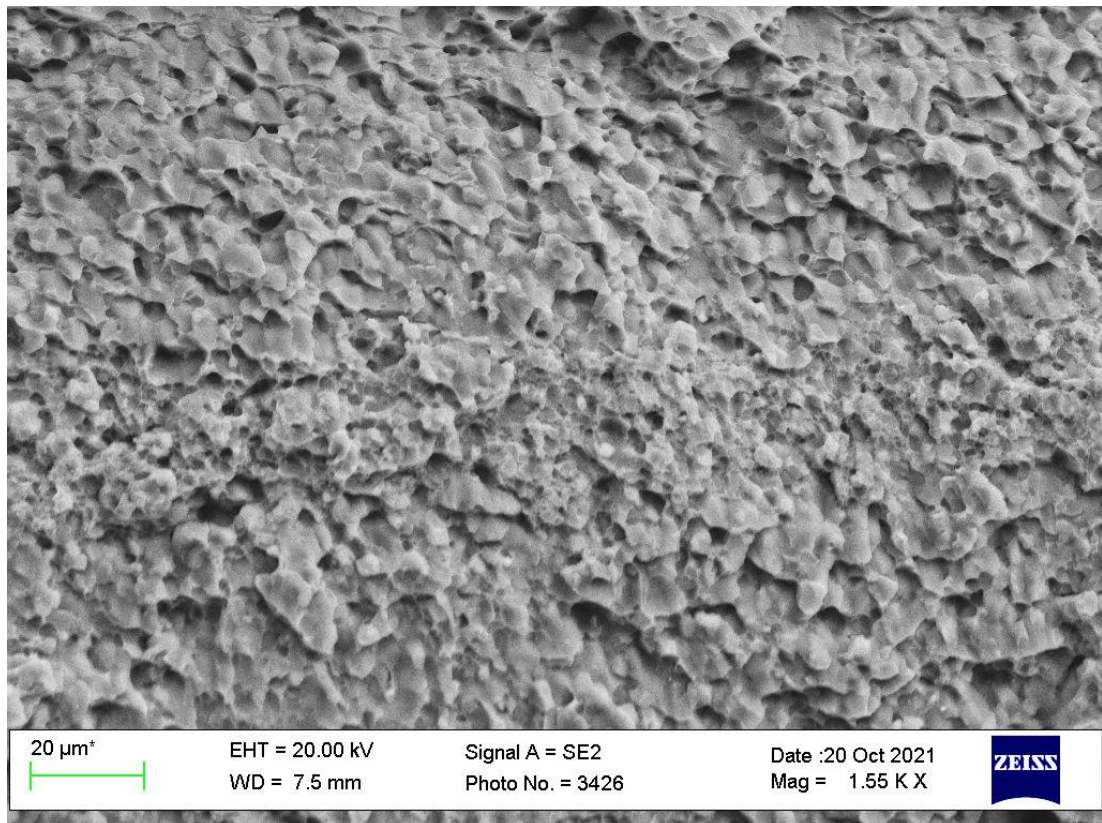
(b)



(c)



(d)

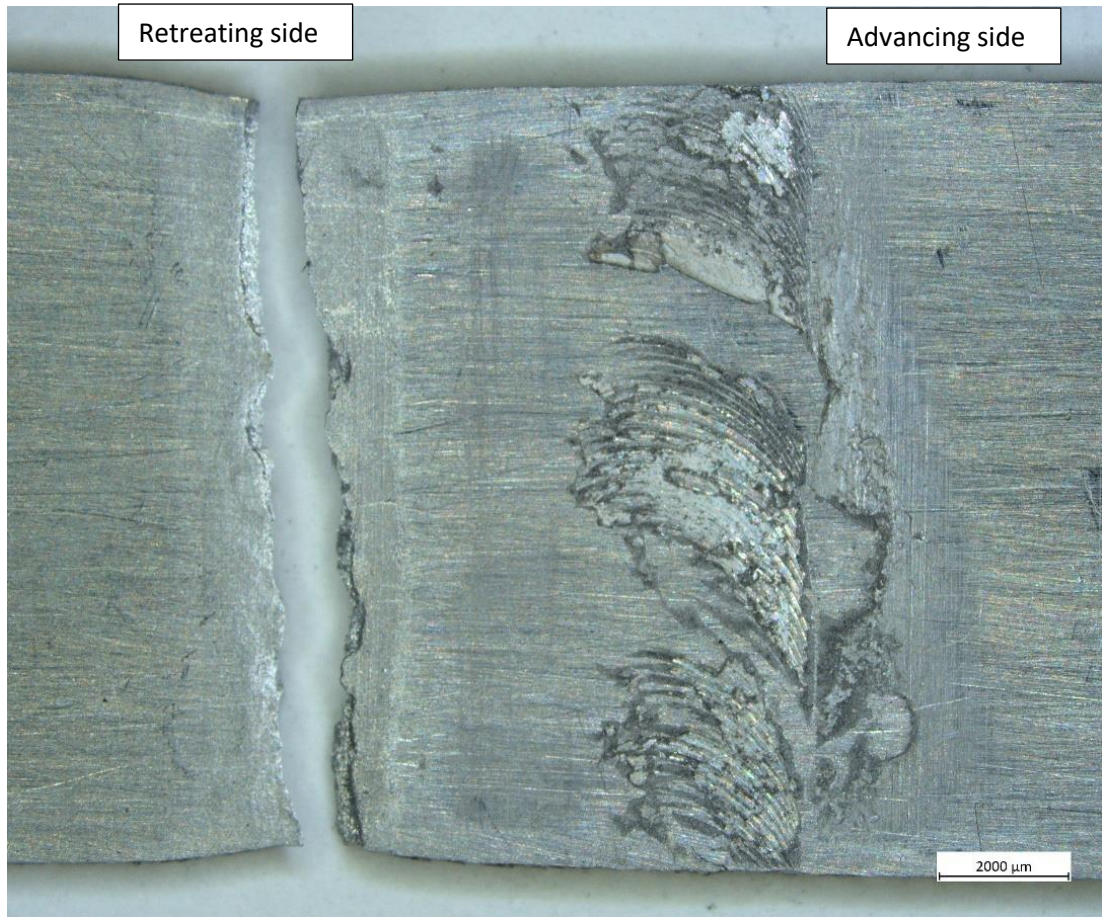


(e)

Figure 155: Showing tensile fracture of BS L165-AA8090 II weld which failed mid-weld with a straight appearance: (a) macrograph showing fracture from top surface; (b) stereo micrograph showing part of fracture surface; (c) cross-section of weld showing crack path; (d) and (e) SEM images showing detail of fracture surface.

With reference to Figure 156, the two tensile specimens which failed adjacent to the retreating edge of weld did so fairly remotely from the weld TMAZ and nugget, and failure occurred well into the HAZ as shown by the two etched microsections. There is good correlation between the point of failure and the position of the hardness minima (Figure 153(a)) which was found to be well within the retreating HAZ, approximately 2 mm from the TMAZ. This is indicative of a good quality weld with no substantial flaws which have acted to prematurely weaken the weld. However, as only two specimens failed in this manner, it is clear that the quality was erratic using these weld parameters, clamping and material preparation, and further work is required to improve this. SEM analysis showed intergranular failure with localised microvoid coalescence occurring at the grain boundaries where coarsened precipitates are known to have heterogeneously

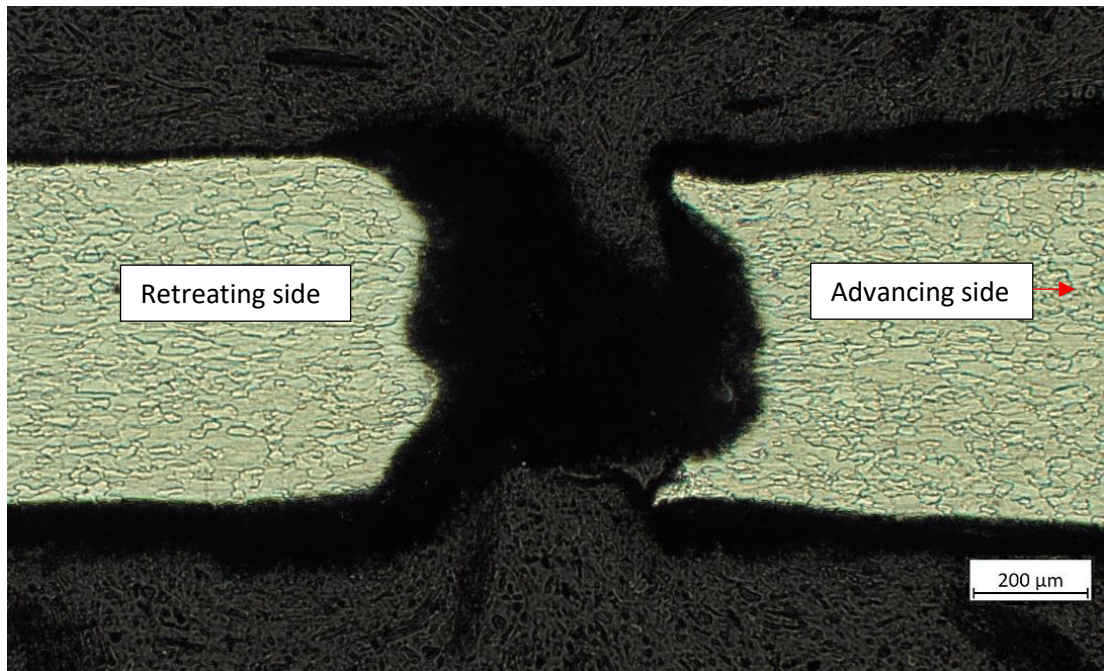
nucleated within the HAZ, likely leaving ductile precipitate free zones at the grain boundaries. Additionally, evidence of slip steps was visible on grain faces indicative of the operation of dislocation movement being confined only to favourably orientated slip systems.



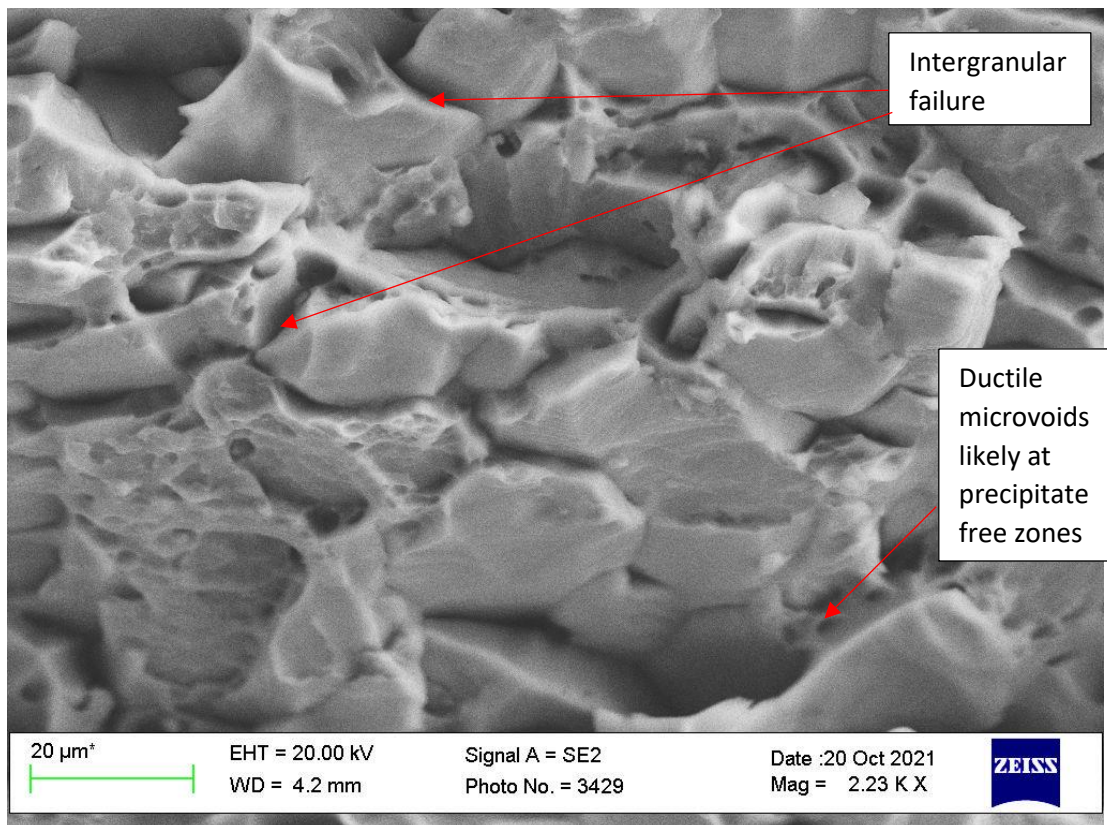
(a)



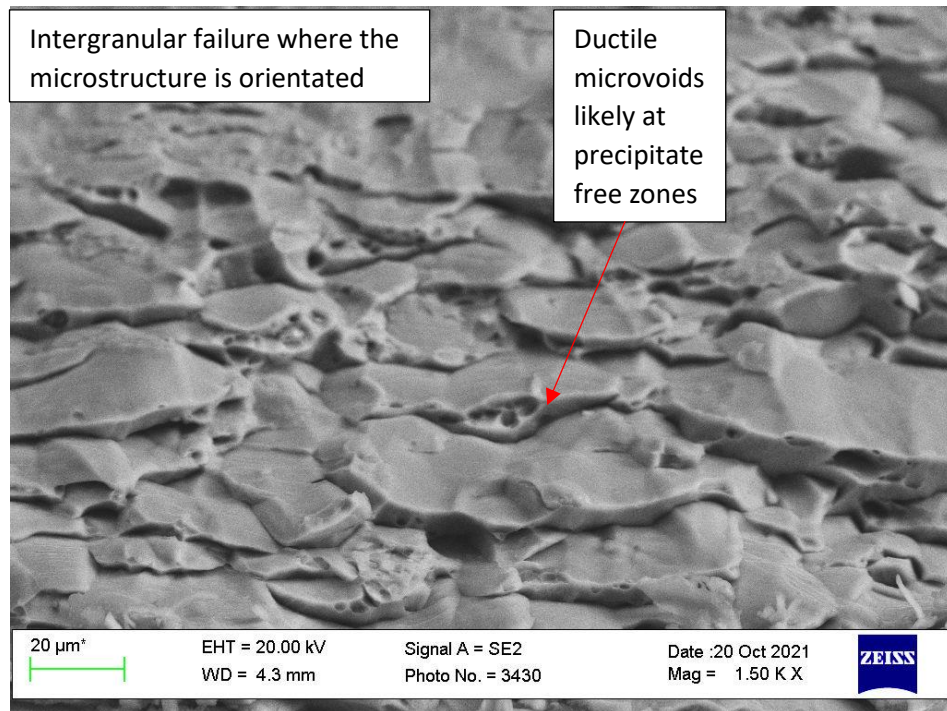
(b)



(c)



(d)



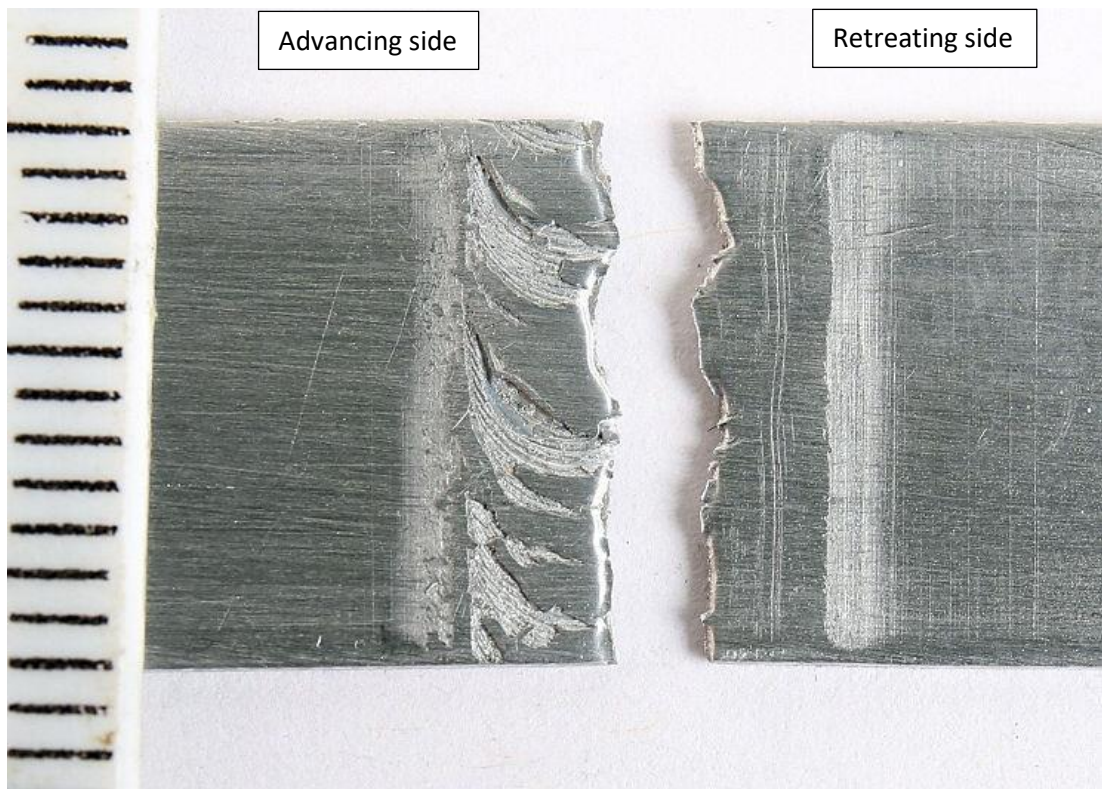
(e)

Figure 156: Showing tensile fracture of BS L165-AA8090 II weld which failed at the retreating edge of weld: (a) macrograph showing fracture from top surface; (b) and (c) cross-sections of weld showing crack path; (d) and (e) SEM images showing detail of fracture surface.

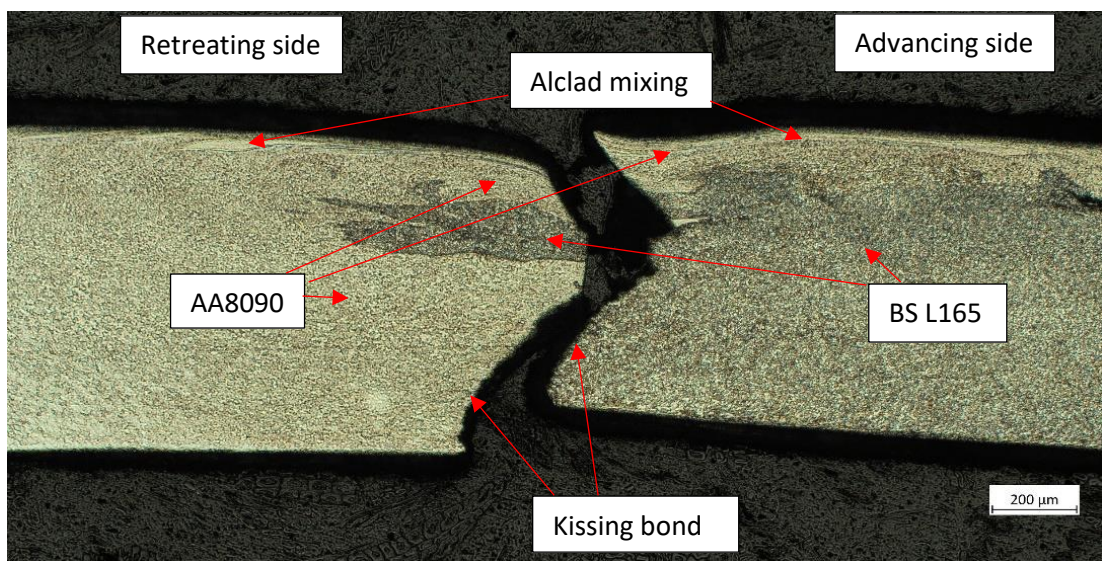
Of the 20 BS L165-AA8090 \perp tensile tests performed, 17 failed mid-weld and only three failed at the retreating edge of the weld. Contrary to that observed on the II welds, little variation in the raggedness/ straightness of the fracture path was observed, with all fractures having a mix of both across their crack length. Although there was some change in the surface appearance along the \perp welds this was not as significant as on the II welds, with the welds generally having a “neater” appearance with intermittent ripples. The degree of raggedness or straightness along each individual specimen was influenced by the length of the rippled areas, showing that for the \perp welds the fracture path is influenced by these features.

With reference to Figure 157, the fracture path described above can be seen for those BS L165-AA8090 \perp specimens which failed mid-weld. Similar to that observed previously, the fracture surface was heavily dominated by a kissing bond. The etched cross-section shows that the crack propagated from the kissing bond, then through a BS L165 dominated part of the microstructure, before final failure within the AA8090

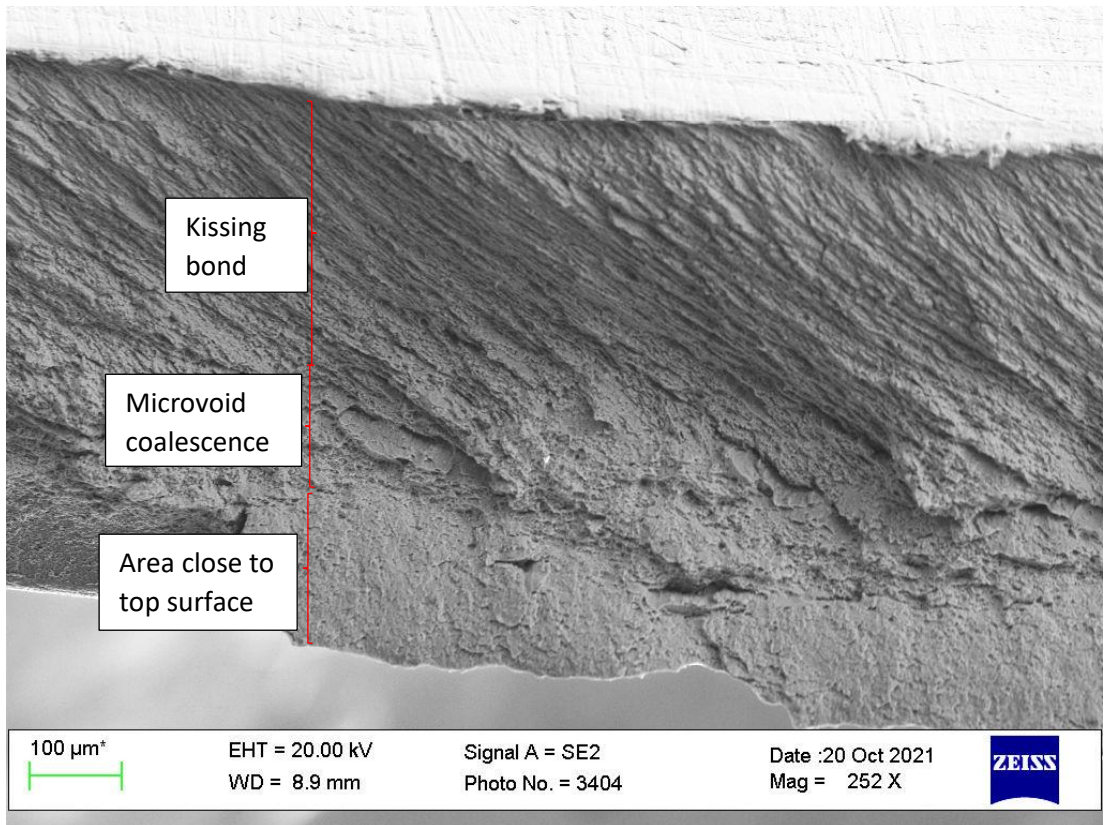
dominated area close to the top surface. As observed on the II welds, SEM analysis revealed 3 zones (Figure 157(c)), however like the straight mid-weld II fracture, there was little transition zone, with the BS L165 dominated area featuring significant microvoid coalescence, Figure 157(d). The fracture area close to the top surface was predominantly transgranular with elongated voids indicative of shear failure, Figure 157(e).



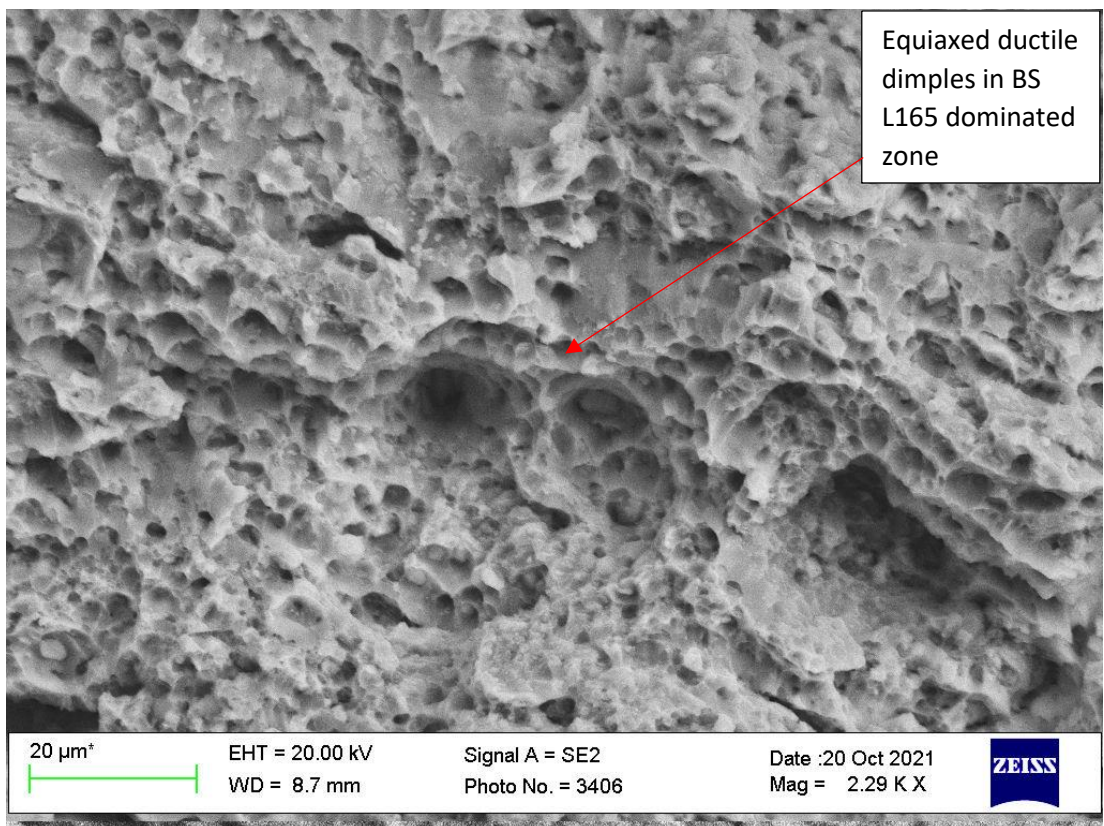
(a)



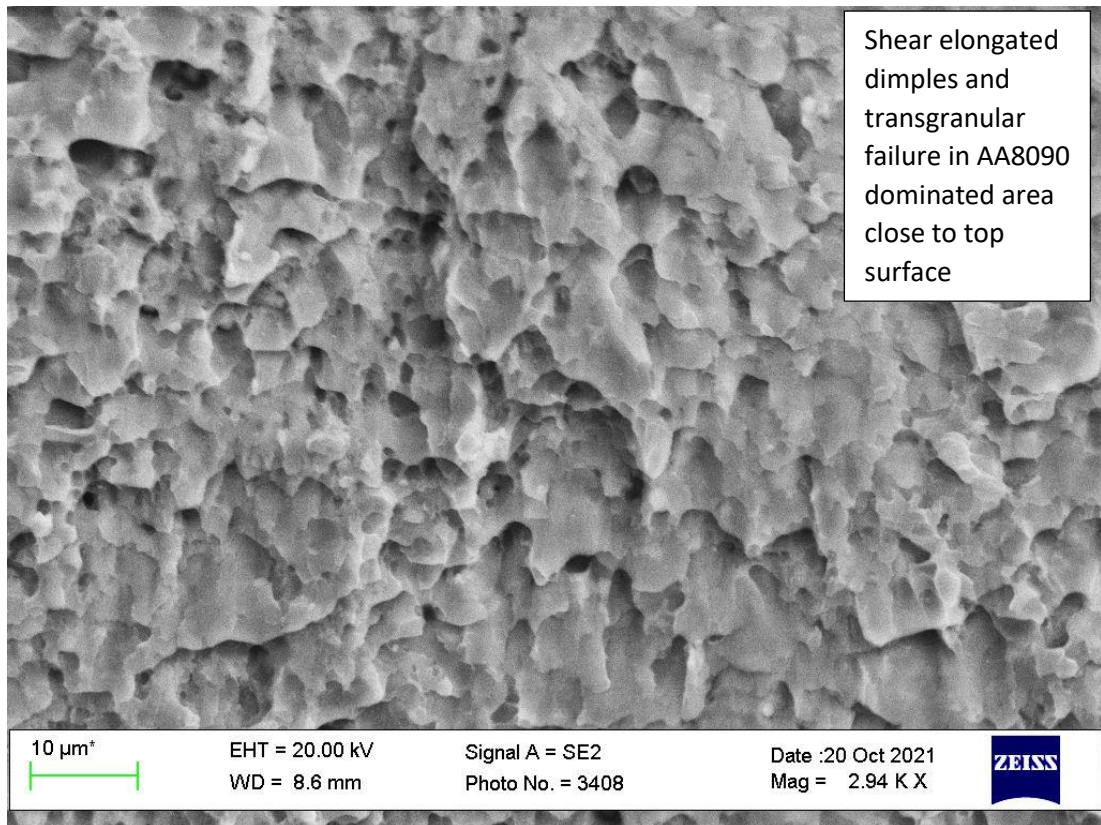
(b)



(c)



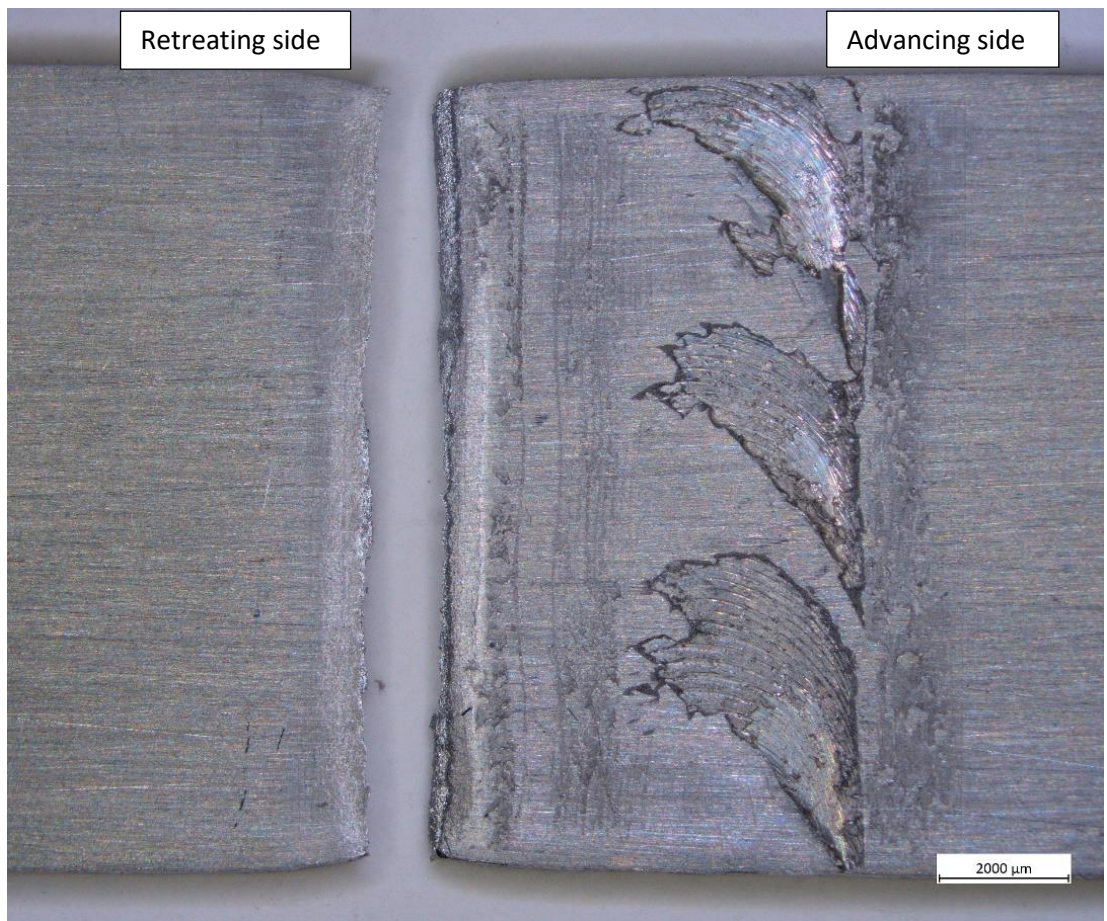
(d)



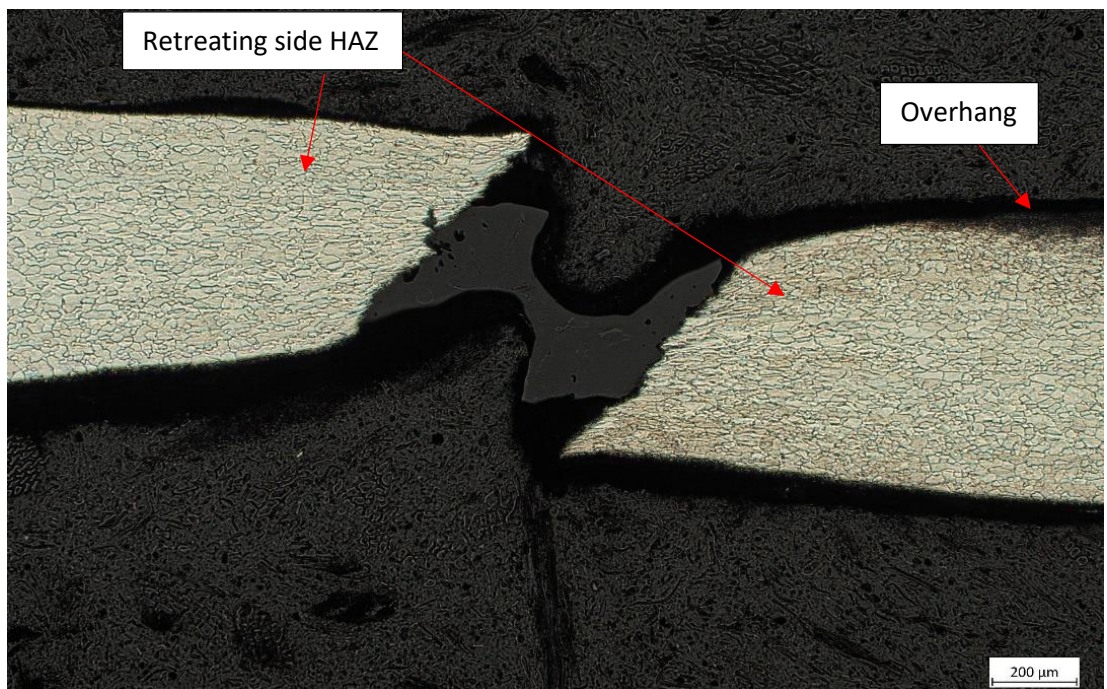
(e)

Figure 157: Showing tensile fracture of BS L165-AA8090 \perp weld which failed mid-weld: (a) macrograph showing fracture from top surface; (b) cross-section of weld showing crack path; (c), (d) and (e) SEM images showing detail of fracture surface.

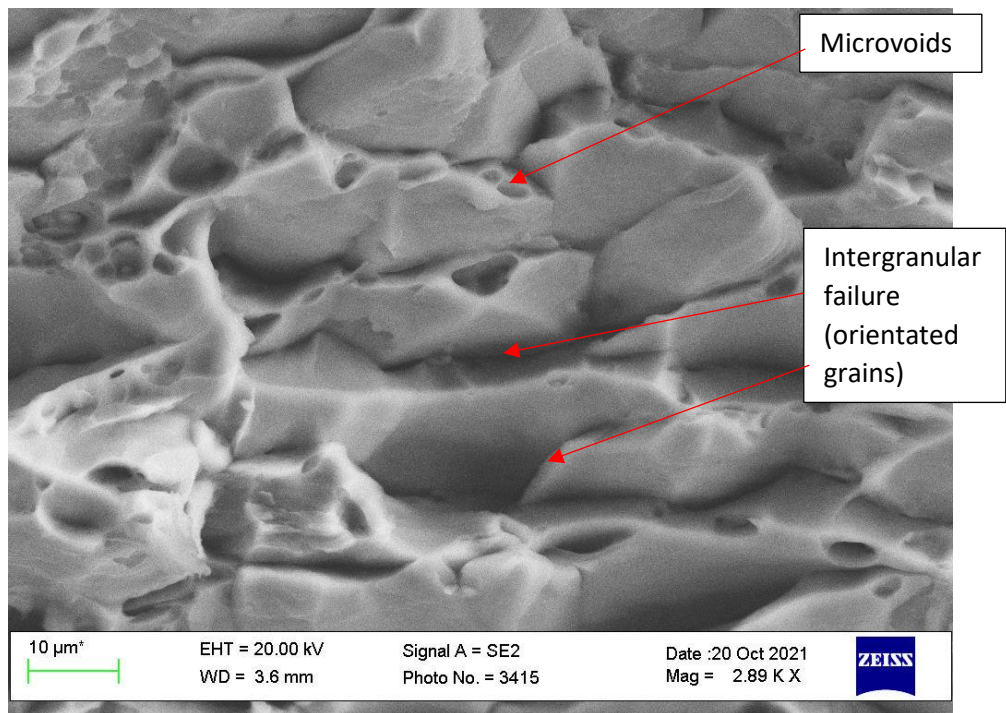
With reference to Figure 158, those BS L165-AA8090 \perp tensile test specimens which failed at the retreating edge did so close to the visible edge as viewed from the top surface. When the etched cross-section was examined, it was observed that the failure occurred within the HAZ, approximately 1.2 mm from the retreating TMAZ (measured on another macrograph, not shown on Figure 158(b)). This showed reasonable correlation to the position of hardness minima which was shown to be approximately 1 mm from the TMAZ, however as the hardness tests were only carried out every 0.5 mm, inaccuracies in measurement are expected. SEM analysis showed a mix of intergranular and transgranular failure with localised microvoid coalescence between the grains with slip planes visible on the grain faces.



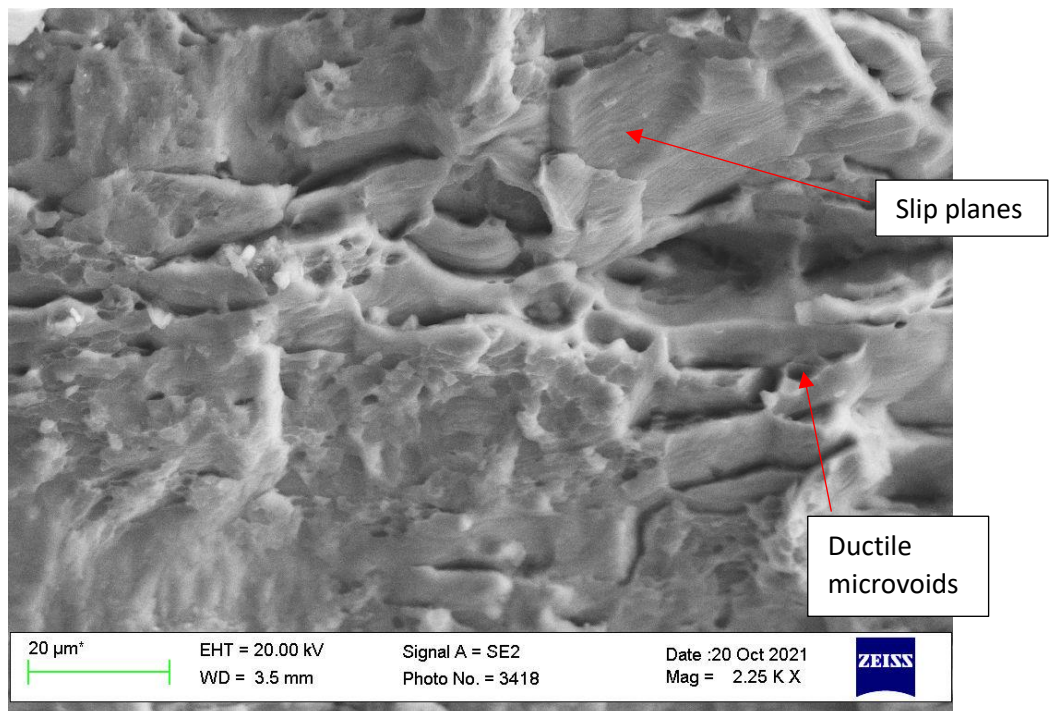
(a)



(b)



(c)



(d)

Figure 158: Showing tensile fracture of BS L165-AA8090 \perp weld which failed at the retreating side edge of weld: (a) macrograph showing fracture from top surface; (b) cross-section of weld showing crack path; (c) and (d) SEM images showing detail of fracture surface.

6.5.2.3 Fatigue Testing

Similar to the AA8090-BS L165, the BS L165-AA8090 weld fatigue tests were compared with BS L165 parent material for determining weld efficiency due to it and its similar weld achieving a poorer fatigue performance than the AA8090 parent material and that similar weld. The BS L165-AA8090 welds achieved a mean fatigue strength of 185.7 MPa (Table 31 in section 5.2.3.1) which accounted for a fatigue weld efficiency of approximately 60% of the parent material and 72% of the BS L165 similar weld. When compared with AA8090-BS L165, the BS L165-AA8090 welds had a reduction in mean fatigue strength of approximately 14%. Cavaliere, De Santis, Panella and Squillace (2009) found that superior fatigue results were achieved when the stronger material was positioned on the retreating side. Both parent materials have similar strengths (although BS L165 has higher hardness properties than AA8090), however AA8090 was weaker in the welded condition (in the similar welds). Thus it would appear that this research supports Cavaliere et al.'s, (2009) theory, i.e. the AA8090-BS L165 configuration achieved higher mean fatigue strength with the harder material positioned on the retreating side. However, the kissing bonds present in the BS L165-AA8090 welds were more severe than observed in other configurations, although this severity did vary along the length of the weld and between different weld runs. As a result, at least part of the reason for the reduction in fatigue strength must be attributed to the overall poor weld quality of BS L165-AA8090 and true comparisons cannot be made until weld parameter optimisation has been carried out to achieve the best possible weld quality.

The BS L165-AA8090 weld fatigue tests produced the largest standard deviation and coefficient of variation of all configurations, far in excess of the next closest (standard deviation 77.08 MPa compared with next largest value of 28.76 MPa for BS L165 similar welds, Table 31 in section 5.2.3.1. In the similar welds (both AA8090 and BS L165), the relatively high standard deviations were attributed to a lack of consistency in weld quality. This result illustrates an even greater lack of consistency in the weld quality. Again, it demonstrates the need for methodical weld parameter optimisation. Additionally, a larger sample size may have helped to achieve results with less scatter and should be considered for future work.

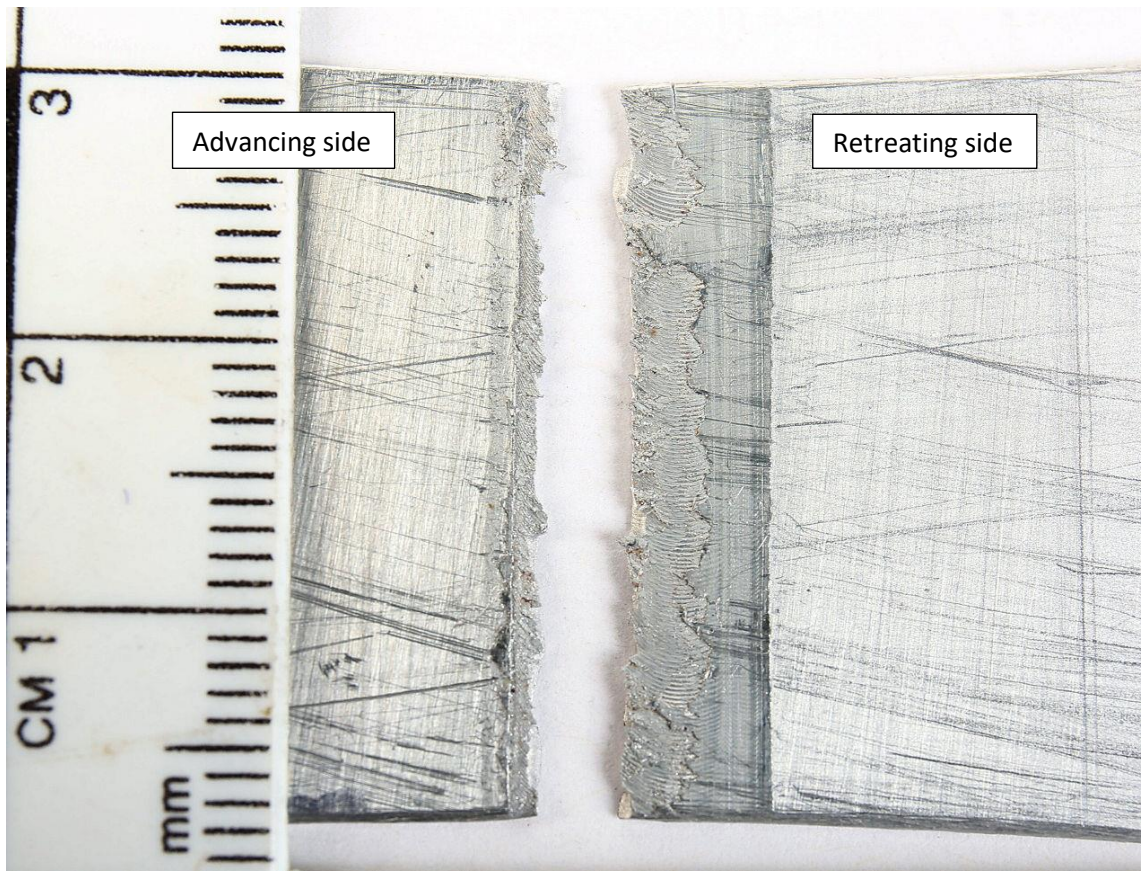
Of the 33 tests conducted for this configuration, 18 failed prior to the 50,000-cycle cut-off. Of these 18, all failed within the weld but at different positions. Seven failed in-weld

but were biased towards the advancing edge, one failed at the approximate mid-weld point, and 10 failed with multiple cracks occurring both at the approximate mid-weld point and simultaneously in-weld but biased towards the advancing edge. Examples of each failure location, showing the position of fracture from the top surface, as a cross section and showing detailed SEM images of the fracture surface are shown in Figure 159 (in-weld biased towards the advancing edge), Figure 160 (mid-weld), and Figure 161 (multiple cracks at both locations).

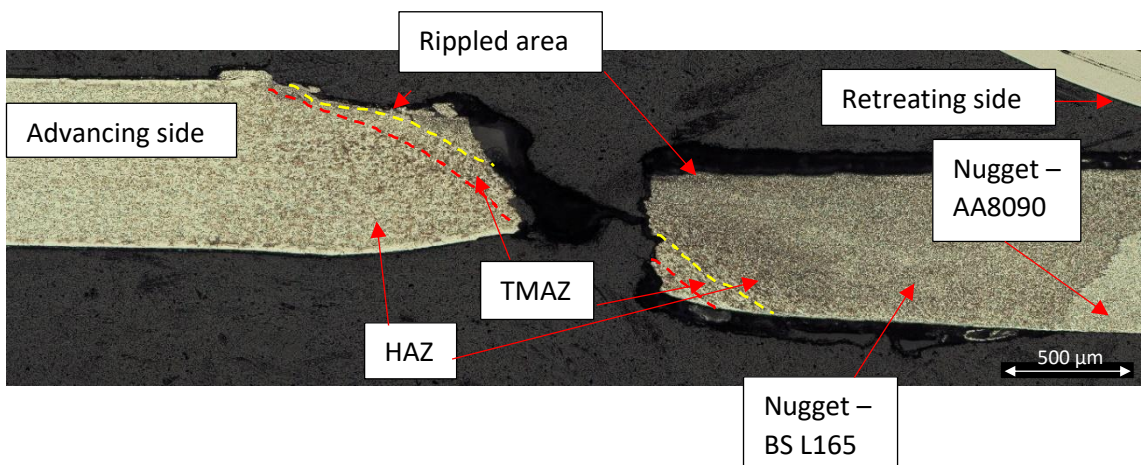
With reference to Figure 159, the fractures occurring within the weld but biased towards the advancing side propagated through the rippled area. The specimen shown was cut from a length of the weld which was heavily rippled, rather than one of the more intermittently rippled parts, however it was noted that all specimens which failed at this position were cut from heavily rippled sections of the weld (although not all heavily rippled sections failed at that location). The crack path was relatively straight although ragged protuberances along the top of the fracture surface suggested that the path may have been influenced by the ripples. The approximate positions of the nugget and TMAZ boundaries have been marked on the etched cross-section, Figure 159(b) (the yellow dashed line denotes the nugget/ TMAZ boundary and the red dashed line denotes the TMAZ/ HAZ boundary). This indicates that while the crack most likely initiated at the top surface, due to the ripples acting as stress raisers, it propagated through the area close to the top surface (within the nugget), then the nugget, the TMAZ and the HAZ.

SEM analysis revealed ratchet and “beach marks” underneath the mixed material (BS L165 and alclad) deposited on the weld surface (mixed material shown in Figure 151(a)), Figure 159(c), typical of fatigue mechanisms. Striations were observed in this mixed material, however as these ratchet marks were subsurface it is considered that the main crack initiated from that position rather than directly from the surface. The ripples would still be able to act as a stress raiser due to the thin nature of the mixed layer, which combined with the hardened predominantly BS L165 material allowed crack initiation in the area close to the top surface and propagation through the material nugget with final overload failure in the TMAZ and HAZ. Within the beach-marked areas, SEM analysis revealed striations typical of fatigue failure. Large intermetallic compounds (IMCs) created voids during failure. Most of the specimens which failed at this position

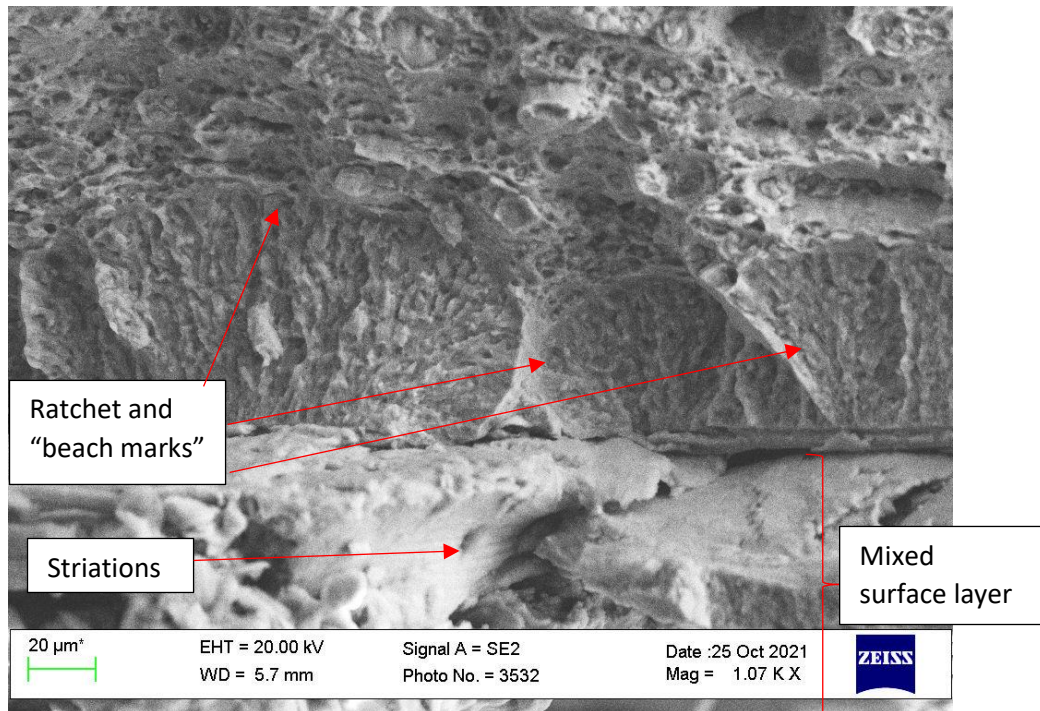
achieved relatively high cycles-to-failure (mid-30,000s to high 40,000s), although this did vary with one achieving only 24,272.



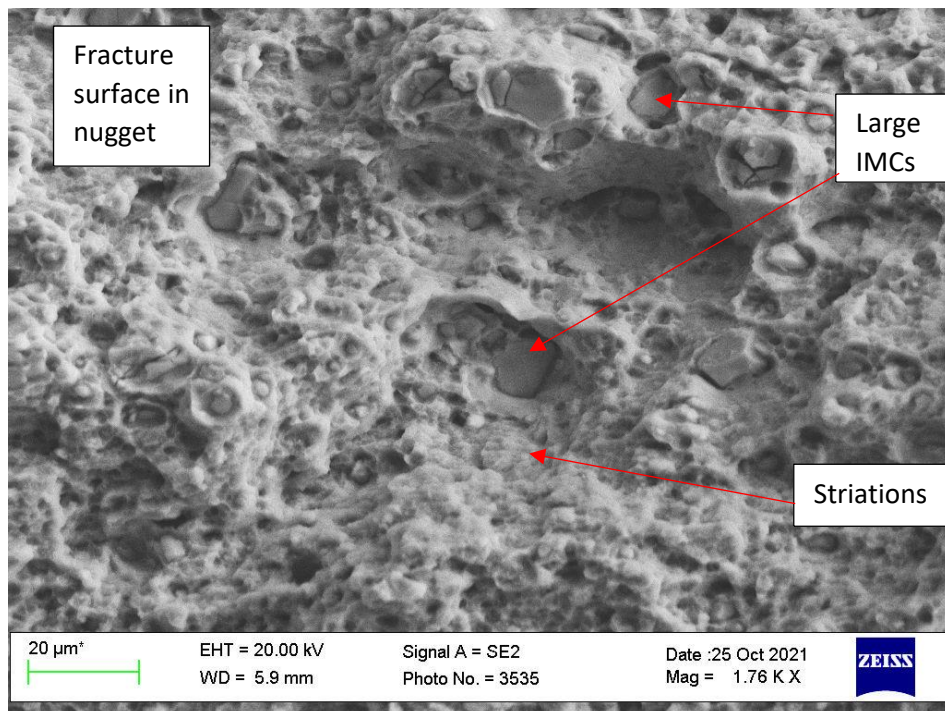
(a)



(b)



(c)



(d)

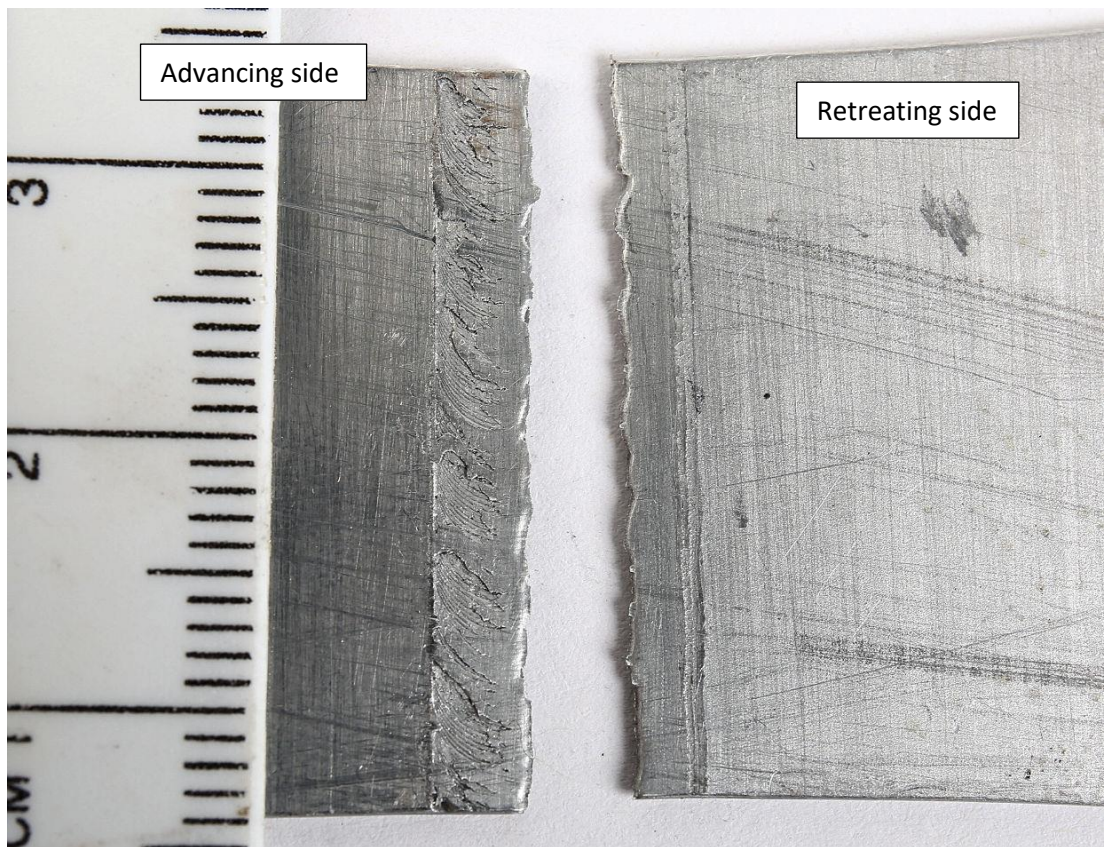
Figure 159: Showing fatigue fracture of BS L165-AA8090 II weld which failed in-weld but biased towards the advancing side: (a) macrograph showing fracture from top surface; (b) cross-section of weld showing crack path; (c) and (d) SEM images showing detail of fracture surface.

With reference to Figure 160, the one fatigue specimen which failed at the approximate mid-weld point was cut from a length of weld with intermittent ripples. The fracture path did not coincide with the ripples at any point and so they did not influence the failure position, Figure 160(a). Stereo microscopy revealed a fracture surface typical of those featuring a kissing bond as described for previous configurations.

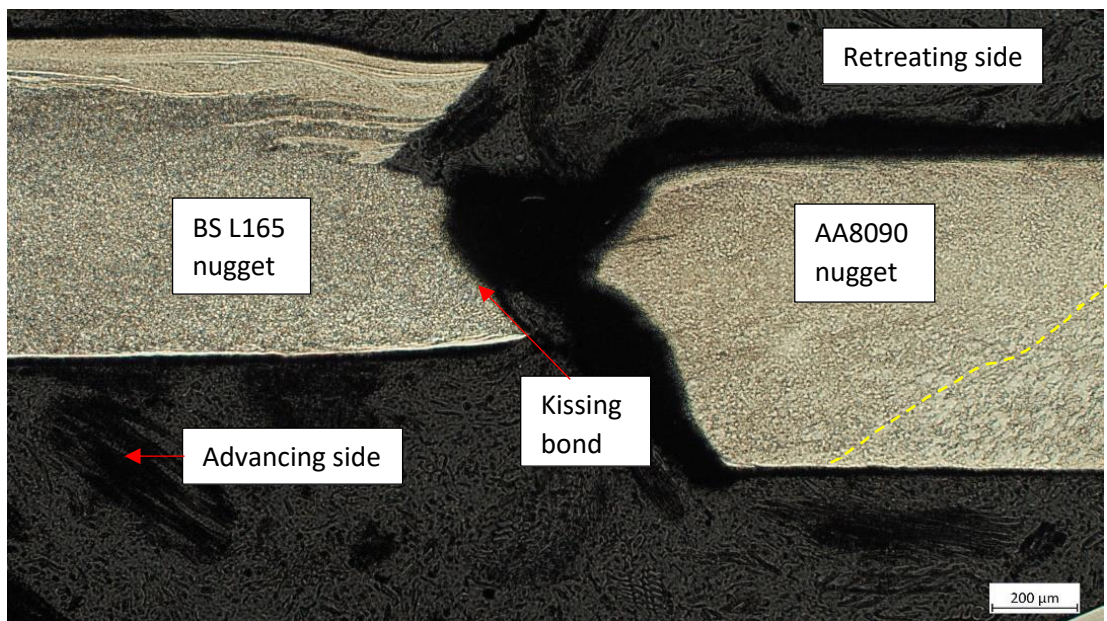
The etched cross-section shows that the fracture follows a kissing bond for almost half of the weld thickness from the bottom surface, before failing through a mixed region at approximately 45° to the loading direction. It should be noted that the fracture surfaces shown in the etched cross-section (Figure 160(b)) do not properly mate; the advancing side clearly follows the kissing bond with the full BS L165 part of the nugget shown to the left-hand side of the image, while the retreating side shows that the nugget/ TMAZ boundaries is inexplicably close to the fracture. Comparison with Figure 141 suggested that the nugget should extend approximately 1-1.5 mm from the joint line to the TMAZ boundary. It is not known exactly what has happened with the creation of this macro-section however, despite the similar shape to the fracture surfaces it is clear (based on the mixing patterns close to the top surface) that the two halves do not mate. It is considered that the fracture surface on the right-hand side may have been inadvertently mounted at an angle and upon polishing the mismatch was created. Based on the stereo microscopy and SEM analysis it is considered that the left-hand side shows the accurate fracture path.

The SEM analysis showed 3 regions (Figure 160(c)); the directional markings which have become associated with a kissing bond, a transition zone of microvoid coalescence (MVC) (Figure 160(d)), transverse fracture and limited striations (Figure 160(e)), and a final zone close to the weld top surface which featured transverse failure with elongated pores, typical of a shear overload failure.

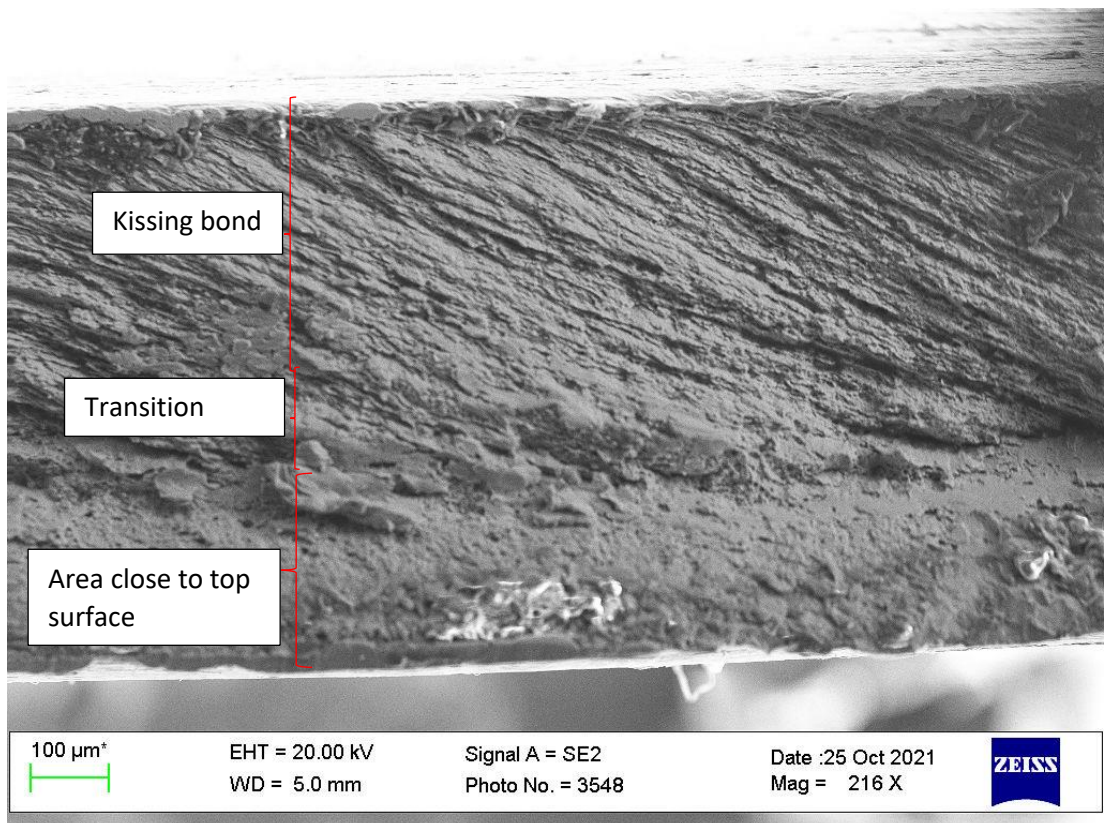
As stated, only one specimen failed solely at the mid-point. This specimen achieved only 6139 cycles to failure and was considered to be prematurely weakened by the poor weld quality producing a large and weak kissing bond.



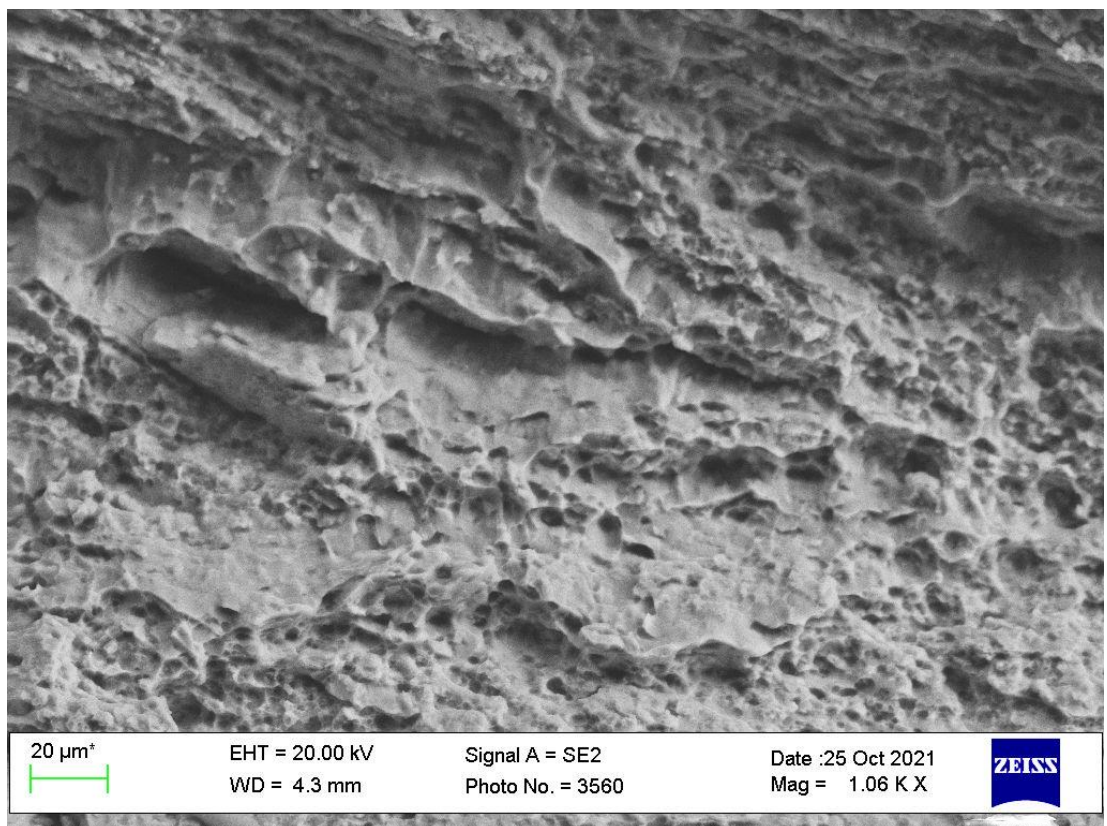
(a)



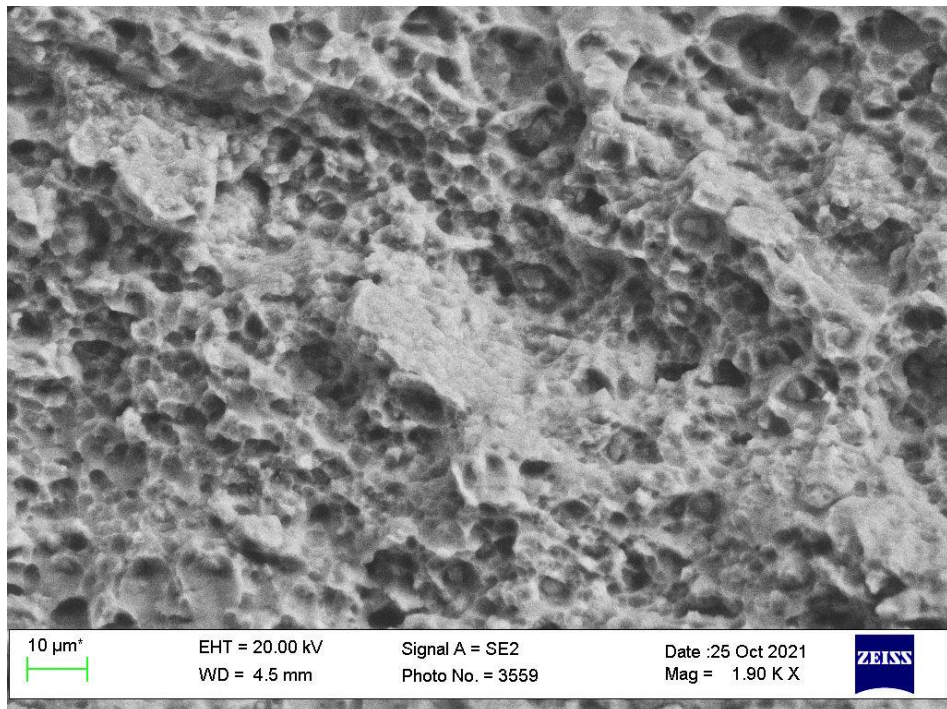
(b)



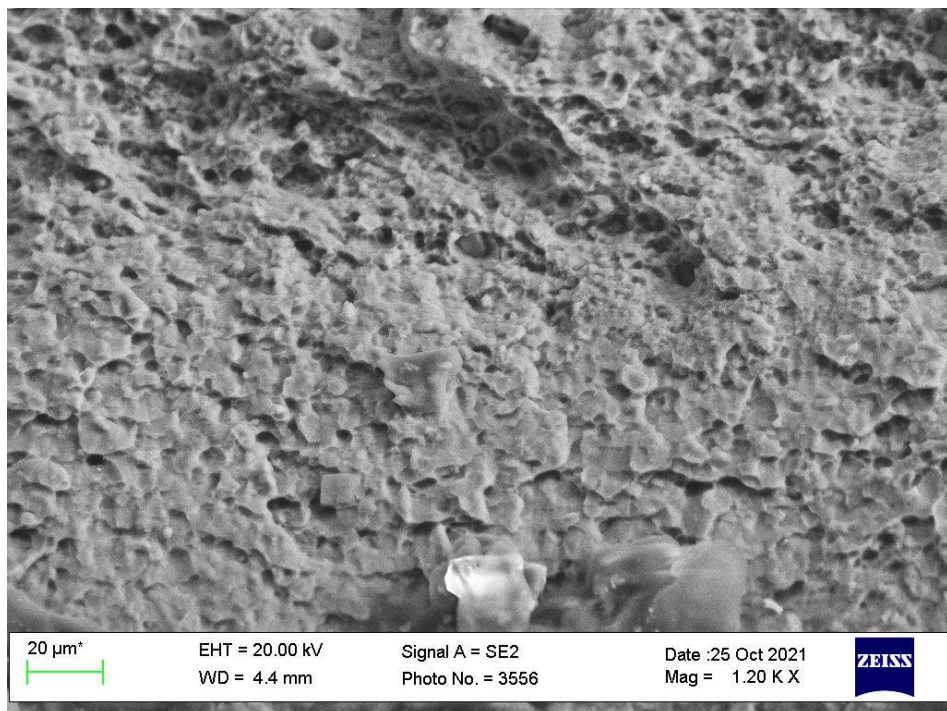
(c)



(d)



(e)



(f)

Figure 160: Showing fatigue fracture of BS L165-AA8090 II weld which failed mid-weld: (a) macrograph showing fracture from top surface; (b) cross-section of weld showing crack path; (c), (d), (e) and (f) SEM images showing detail of fracture surface.

With reference to Figure 161, those specimens which failed at multiple locations did so at the approximate mid-point of the weld (similar to the specimen discussed in reference to Figure 160, although in this case (Figure 161) it did propagate through the edges of the ripples) and within the weld biased towards the advancing side (similar to the specimen discussed in reference to Figure 159). The specimen examined here had an additional partial fracture within the advancing side HAZ as shown in Figure 161(a), however this was not typical of all of these failures. Figure 161(b), another of these failures, shows that these two fractures (the mid-weld and one biased to the advancing side) propagated simultaneously.

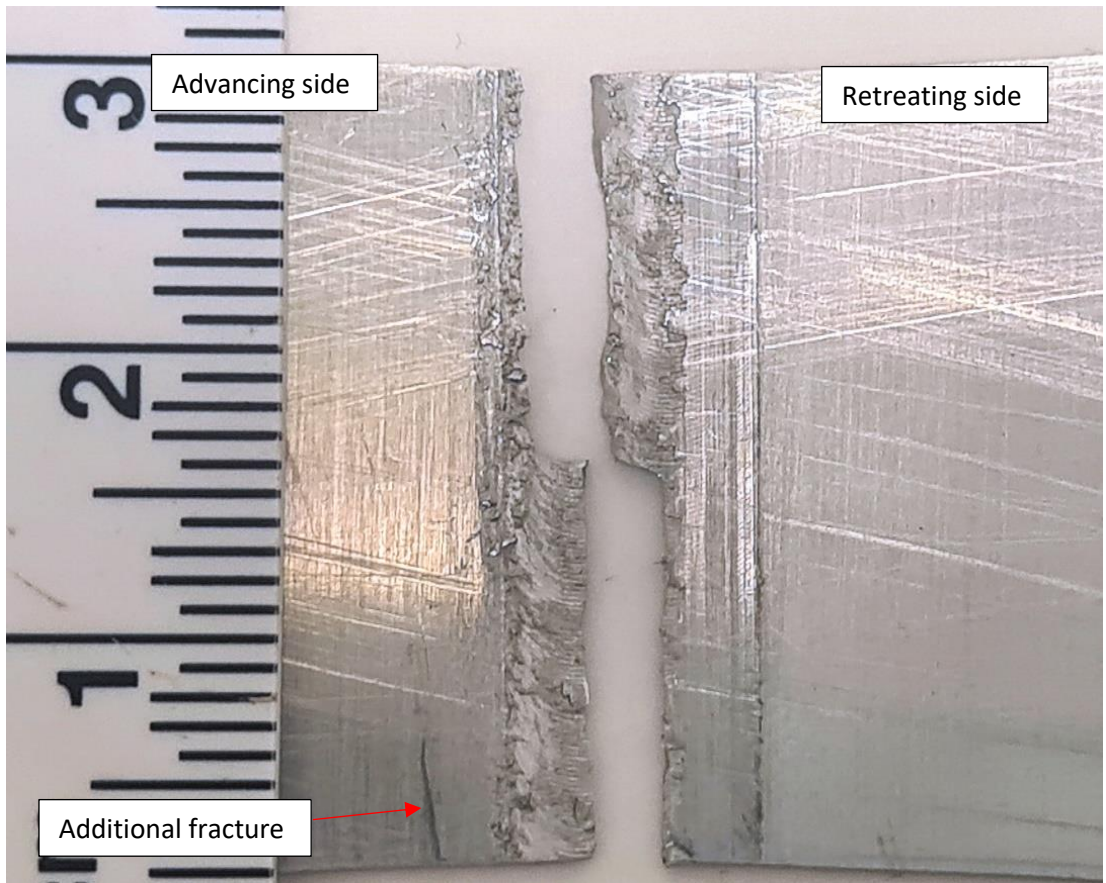
Etched cross-sections were produced of both fractures. The mid-weld cross-section (Figure 161(c) and (d)) shows that the fracture occurred at the joint line before propagating through to the weld surface. While at the advancing side, the cross-section (Figure 161(e) and (f)) shows the fracture initiated from the rippled area on the top surface then propagated through the nugget before propagating through the TMAZ and HAZ at 90° to the direction of loading (Figure 161(f)).

SEM analysis of the mid-weld fracture showed the three zones previously observed: kissing bond; transition zone and area close to the top surface, shown in Figure 161(g), (h) and (i).

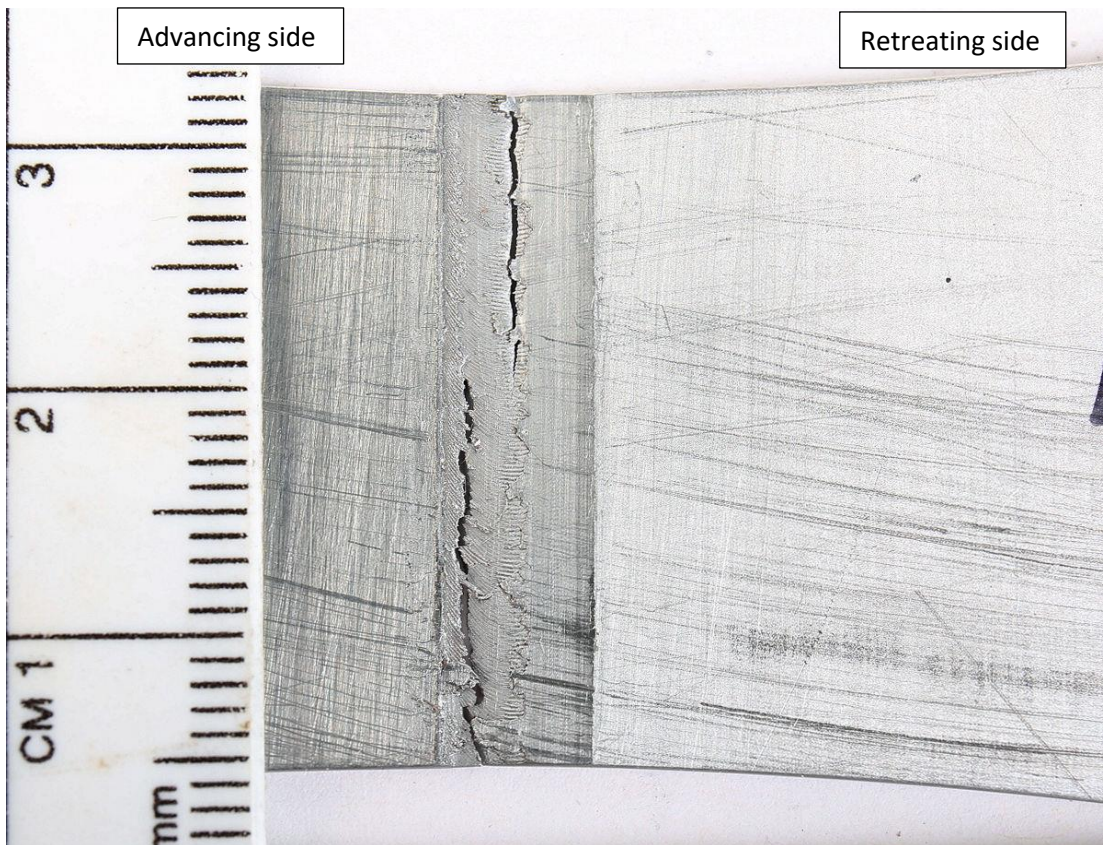
SEM analysis of the fracture biased towards the advancing side revealed ratchet marks and beach-marks underneath the rippled mixed material containing striations, although the extent of these beach-marks varied in depth along the length of the advancing side fracture (Figure 161(j), (k) and (l)). Close to the bottom surface of the weld, on those parts of the fracture on which the fatigued region extended for the majority of the weld thickness (Figure 161(j)), the fracture surface was transgranular with elongated pores, Figure 161(m). On those parts of the fracture on which the fatigued region extended only partially into the weld thickness (Figure 161(k)), the remaining fracture surface exhibited microvoid coalescence typical of ductile overload mixed with transgranular failure (Figure 161(n)).

It is considered that in the absence of any flaws such as kissing bonds, or detrimental surface features such as ripples, that the preferred position of fracture would be within the advancing side HAZ, based on BS L165 having lower fatigue resistance than AA8090

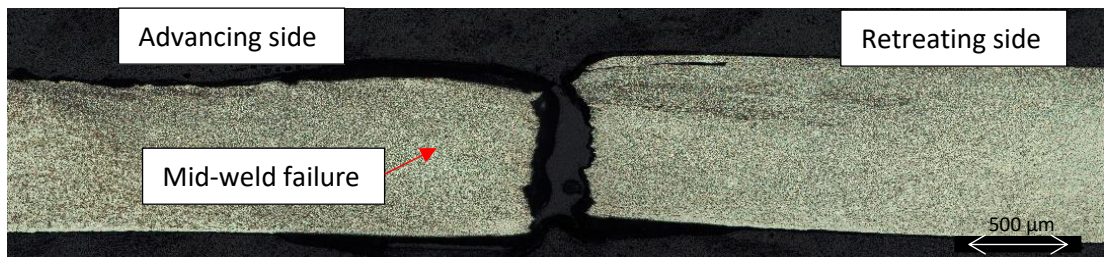
(both in terms of parent material and in the welded condition on the similar welds) and the presence of a partial crack on Figure 161. However, position of lowest hardness was located in the retreating side HAZ, at which point the literature suggests fatigue failure should occur (Cavaliere et al., 2009; Sillapasa et al., 2017). Therefore, no definite conclusions can be drawn without further parameter optimisation and testing being carried out. It is likely that those specimens which failed in multiple locations did so due to the presence of both a kissing bond and a heavily rippled surface creating two areas of weakness and stress concentration.



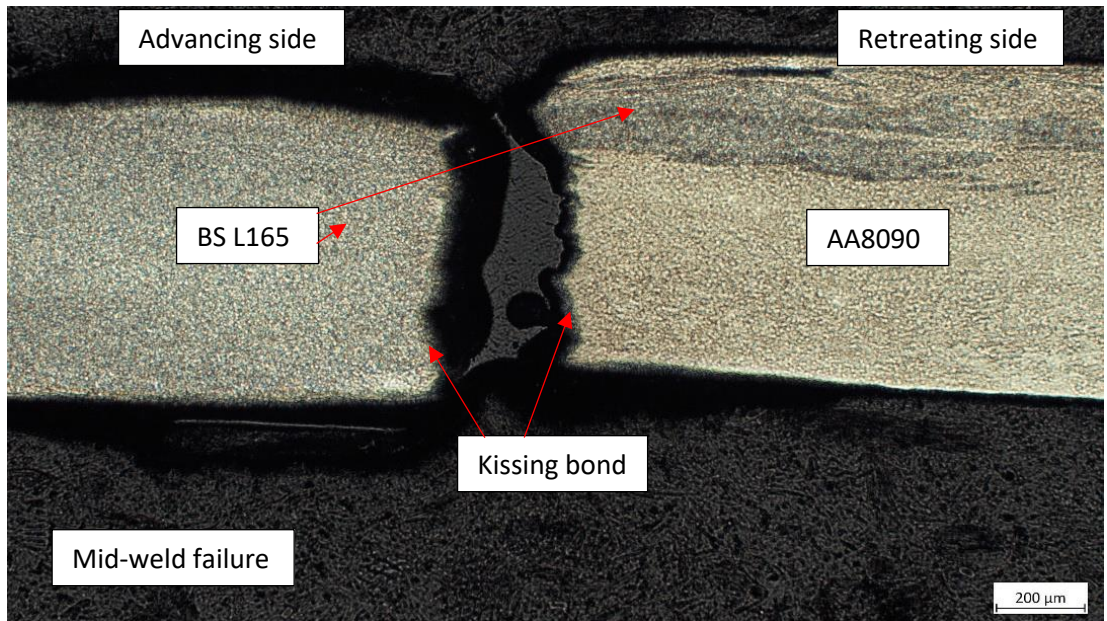
(a)



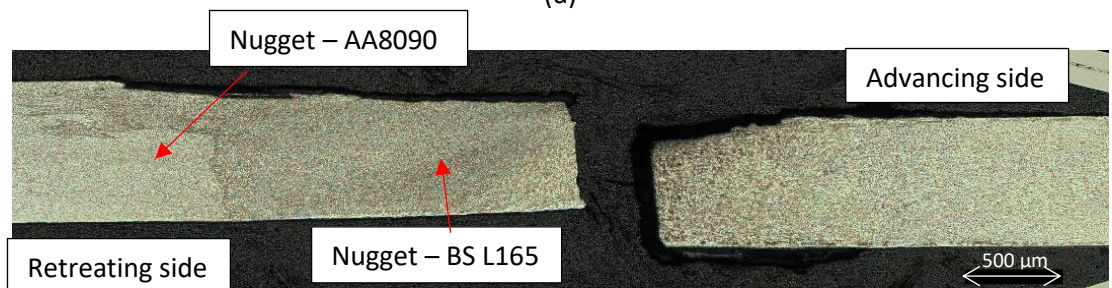
(b)



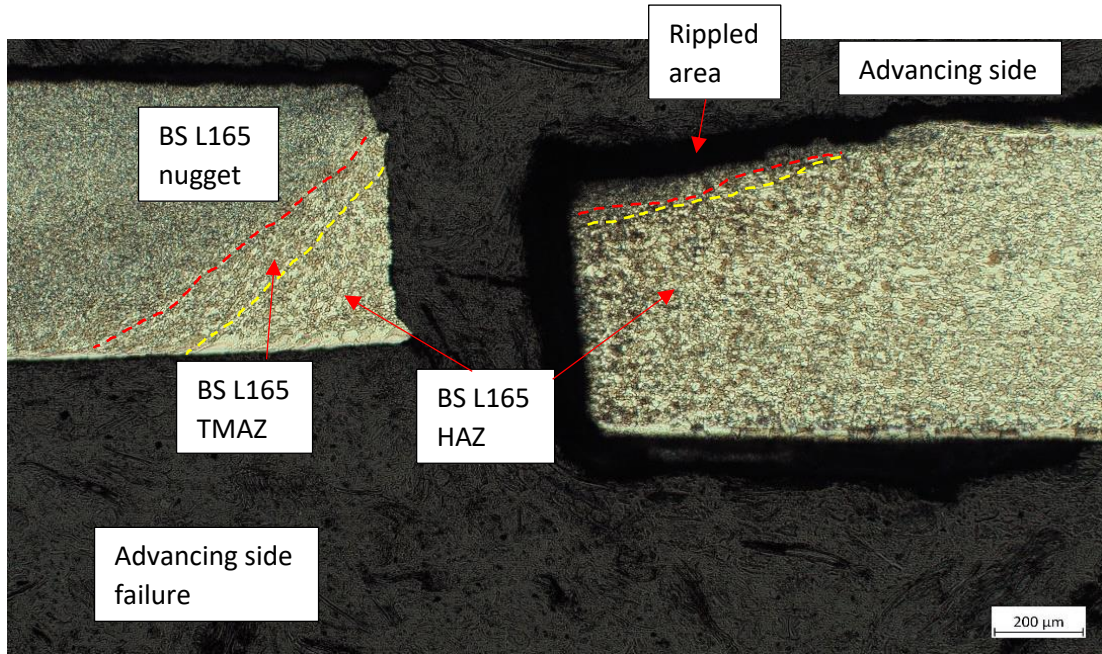
(c)



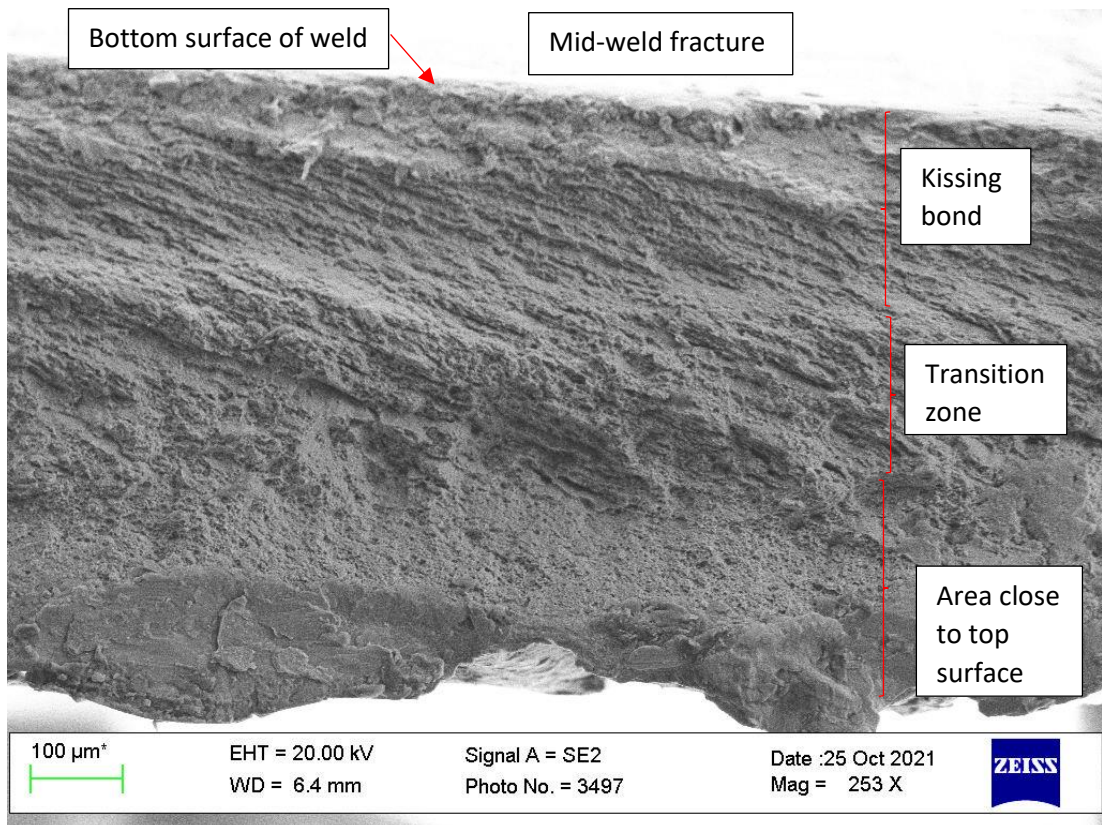
(d)



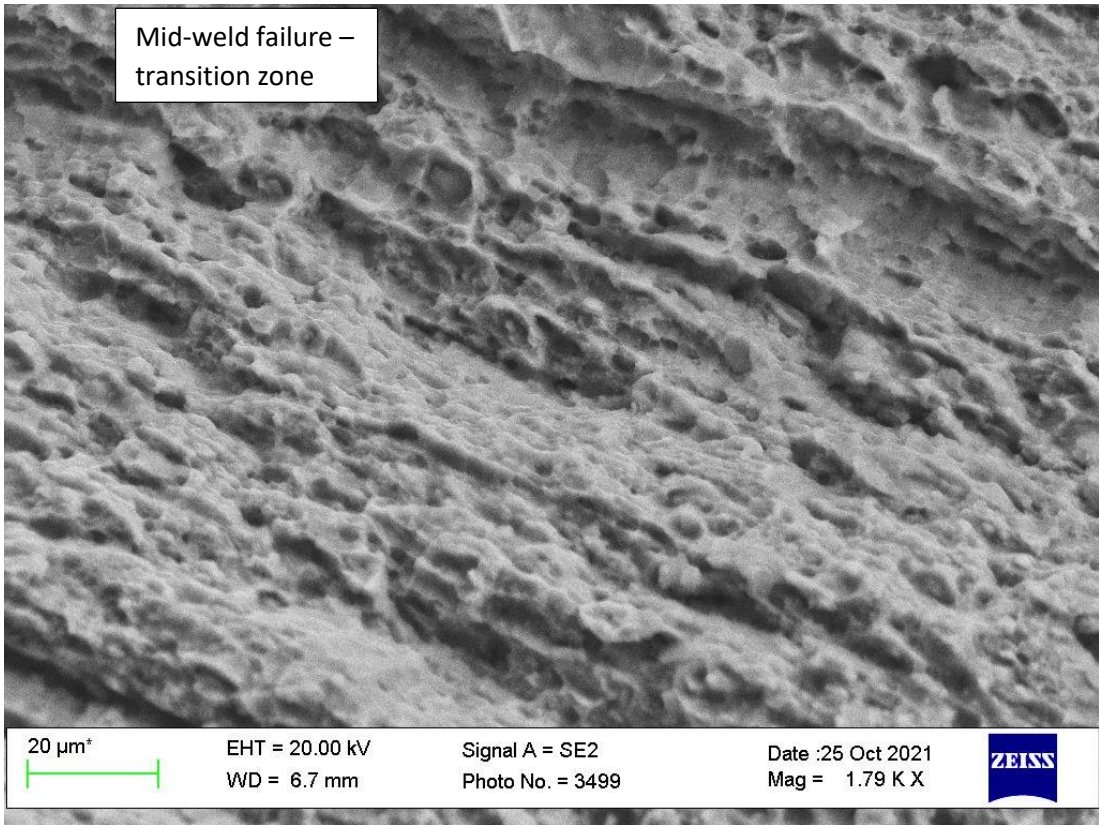
(e)



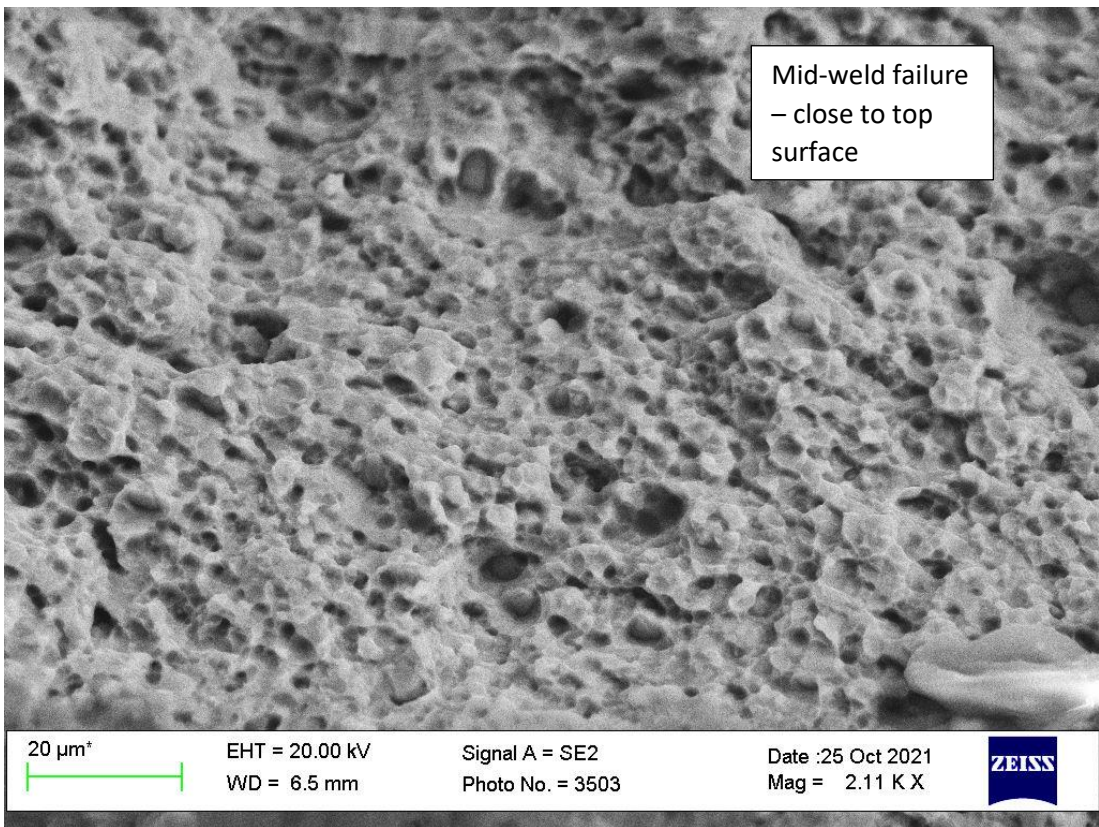
(f)



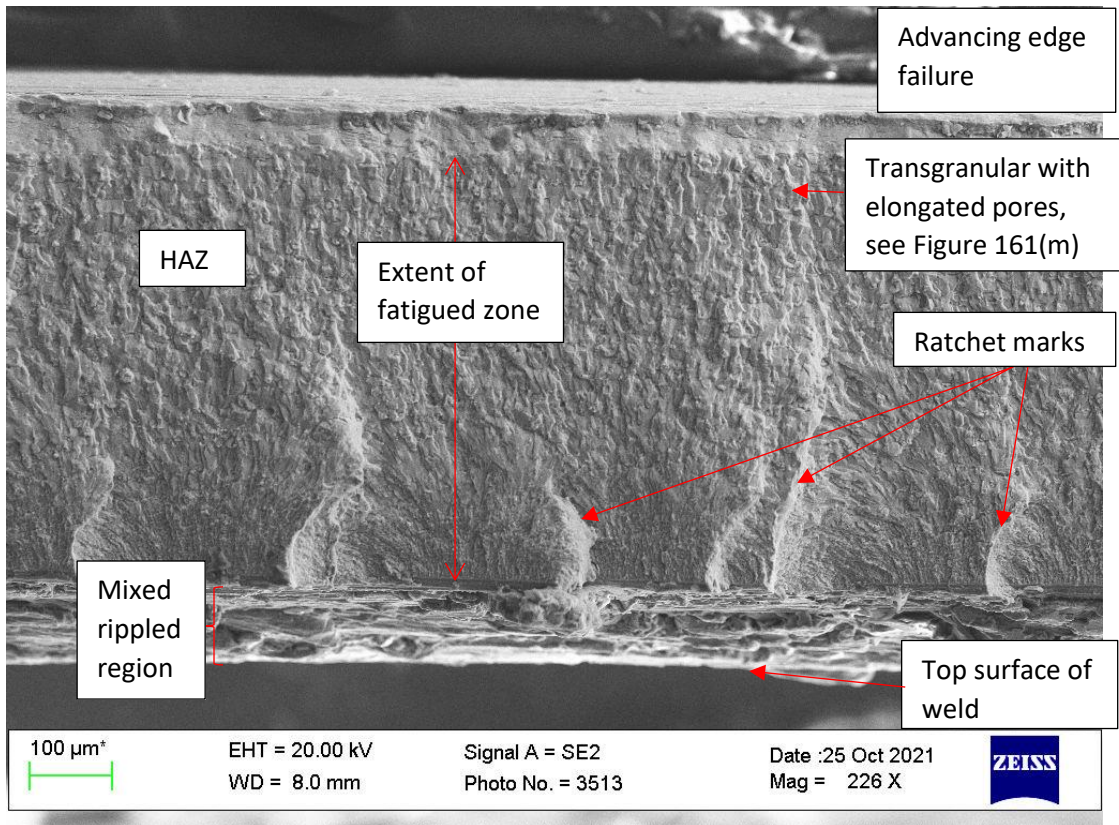
(g)



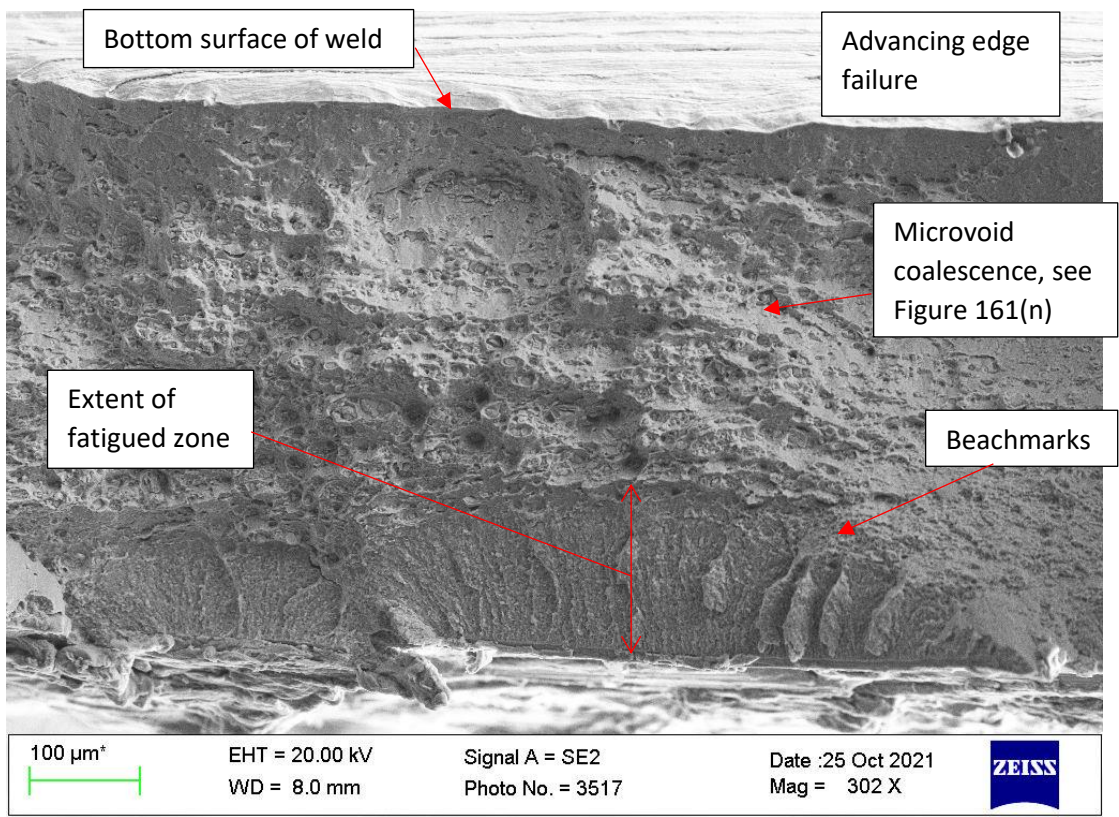
(h)



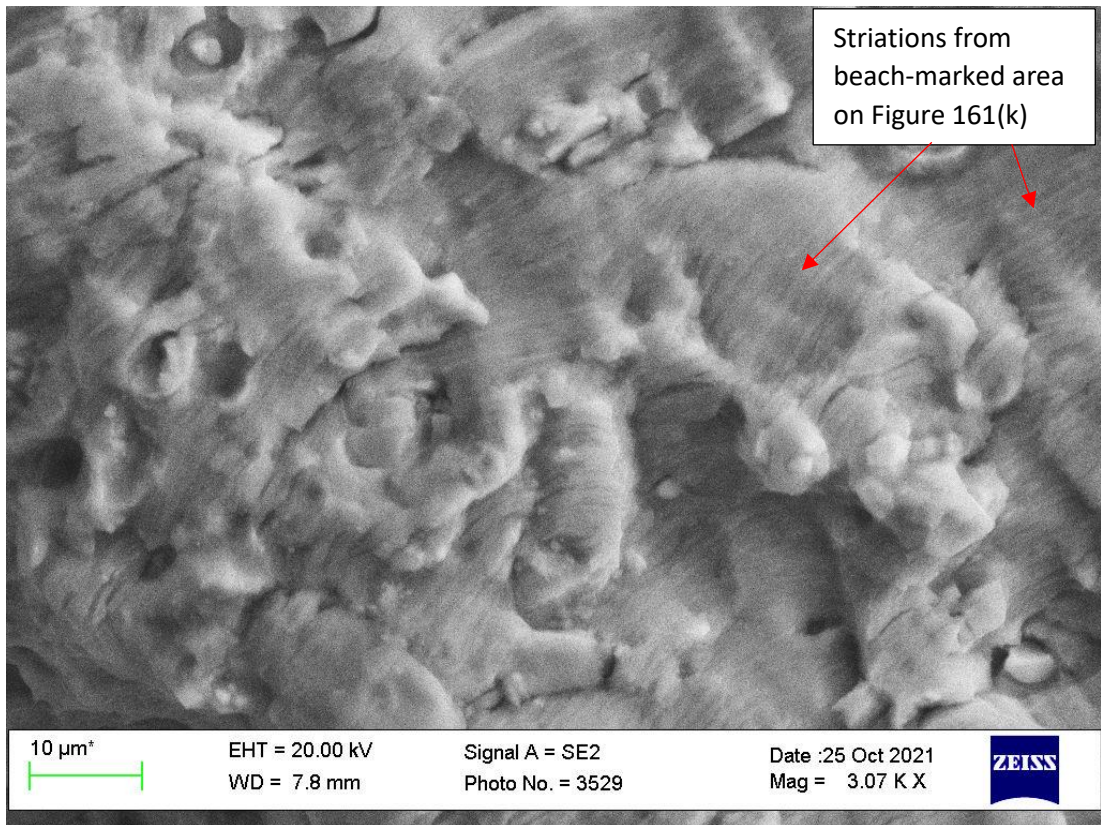
(i)



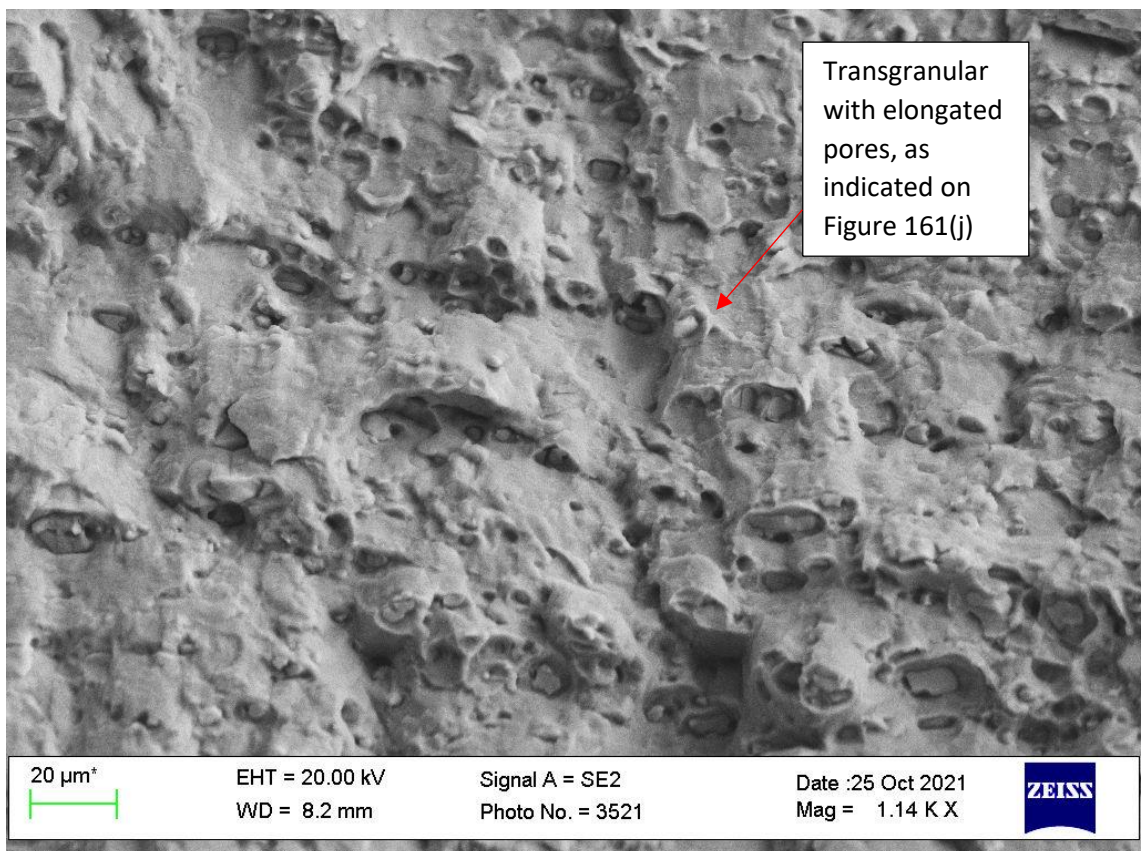
(j)



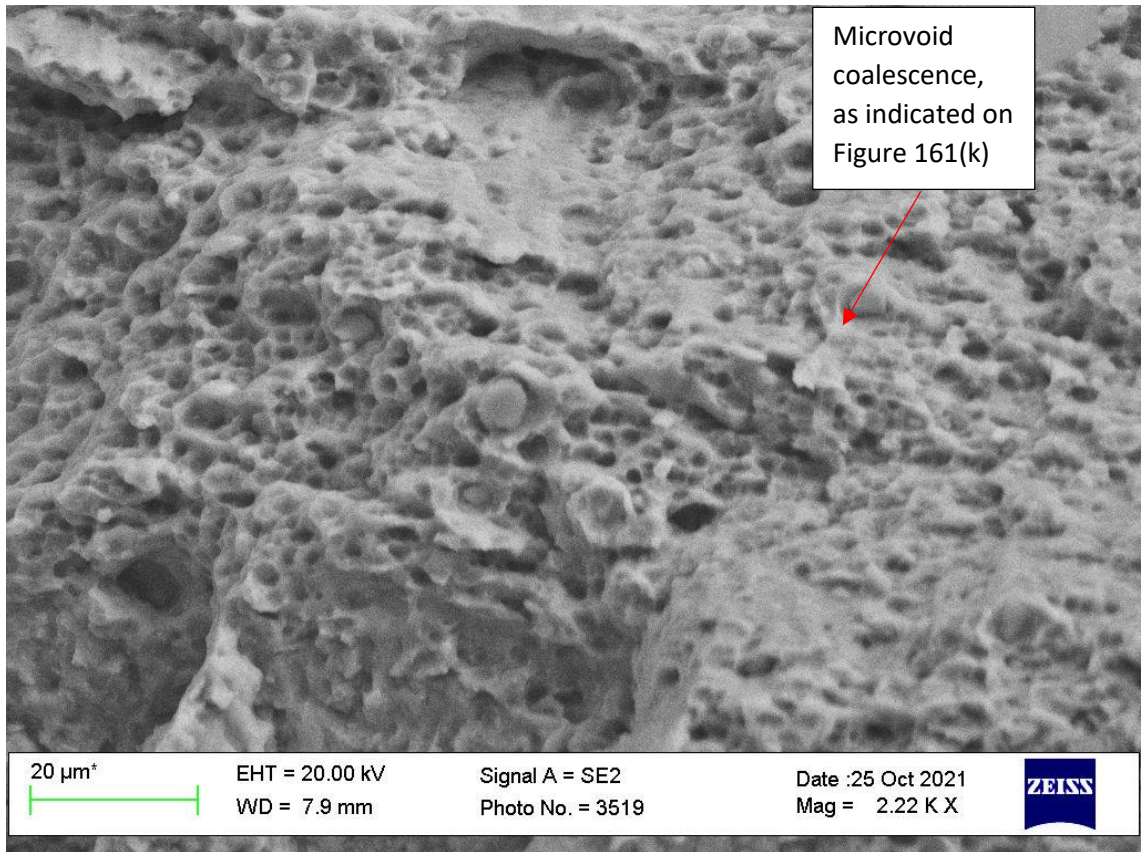
(k)



(l)



(m)



(n)

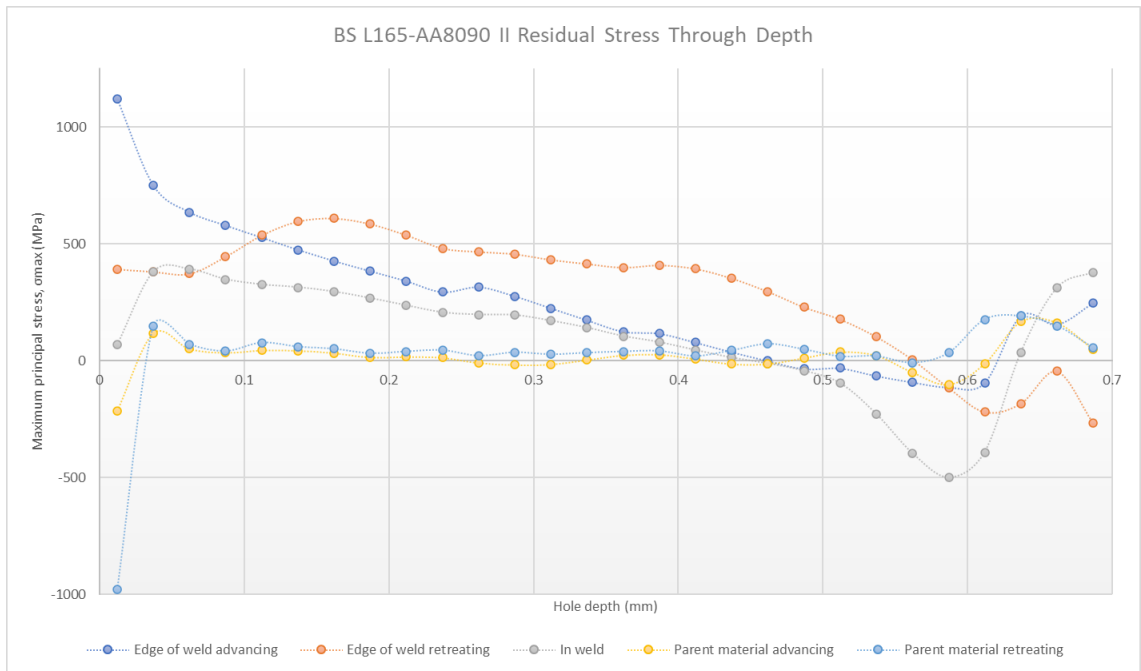
Figure 161: Showing fatigue fracture of BS L165-AA8090 II weld which failed partially mid-weld and partially in-weld but biased towards the advancing edge: (a) macrograph showing fracture from top surface; (b) macrograph showing another multi-site failure; (c) and (d) cross-section of weld showing crack path at mid-weld position; (e) and (f) cross-section of weld showing crack path at in-weld towards advancing edge position; (g), (h) and (i) SEM images showing detail of fracture surface at mid-weld position; (j), (k), (l), (m) and (n) SEM images showing detail of fracture surface at advancing edge position.

6.5.2.4 Residual Stress

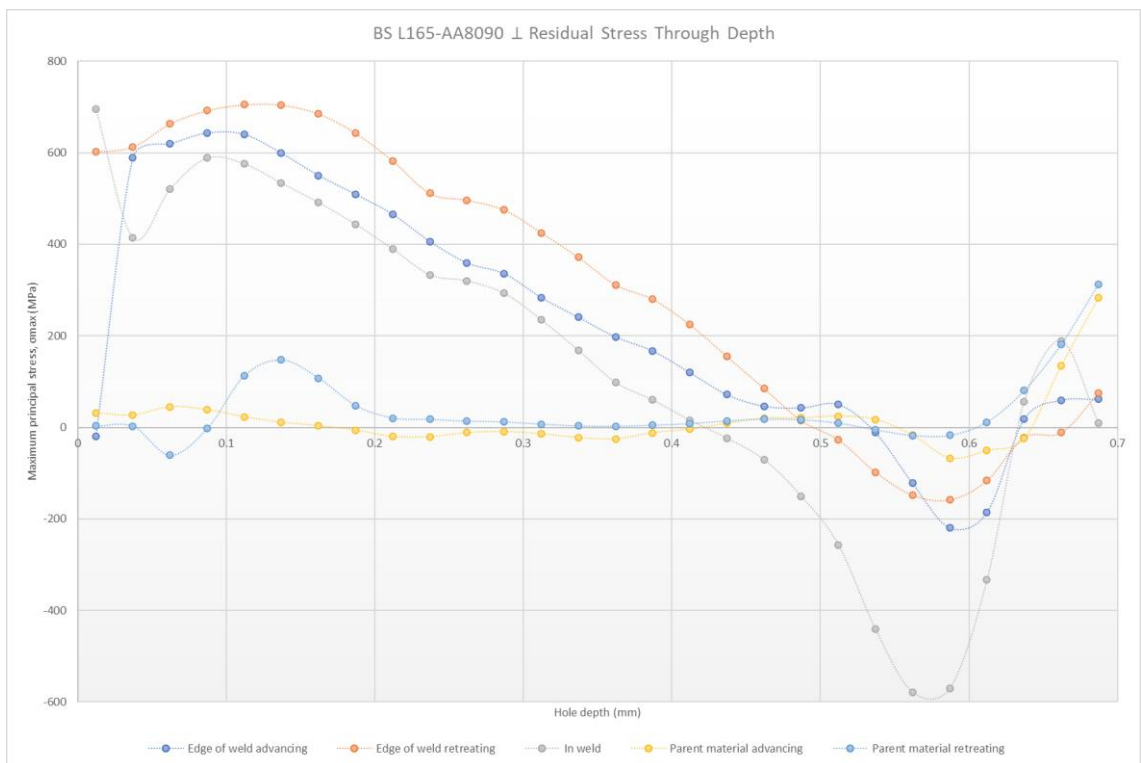
6.5.2.4.1 Residual Stress with Hole Depth

The RS results plotted against the drilled hole depth are shown for both configurations in Figure 162. Again, only values occurring at depths 0.06-0.4 mm are considered in the analysis. As with all previous configurations, the results are significantly in excess of the material yield strength (and UTS) and therefore cannot be used quantitatively.

All datasets are accounted for in both BS L165-AA8090 configurations, and only the \perp weld retreating side parent material is considered to be potentially spurious. It is considered that a flaw or mechanical damage within the material caused the significant fluctuation from approximately 0.1-0.18 mm depth. The profiles of the other data sets are all in keeping with that seen previously. It can be seen that the II weld has a high RS close to the weld surface and then remains fairly constant with depth, decreasing only gradually (although the retreating EoW does rise slightly close to the surface before reducing). The \perp weld data sets all begin high close to the surface and then the RS reduces sharply with depth. The difference in profile shapes for the two configurations are considered be due to the differing grain orientations affecting the heat profile within the weld which has consequences for heat dissipation rate and the material's reaction to this, hence a difference in RS throughout the weld depth. As expected, with the exception of the fluctuation in the \perp weld retreating side, the parent materials remained at approximately zero throughout depth.



(a)



(b)

Figure 162: Showing residual stress results plotted against drilled hole depth; (a) BS L165-AA8090 II, and (b) BS L165-AA8090 I.

6.5.2.4.2 *Residual Stress Across Weld*

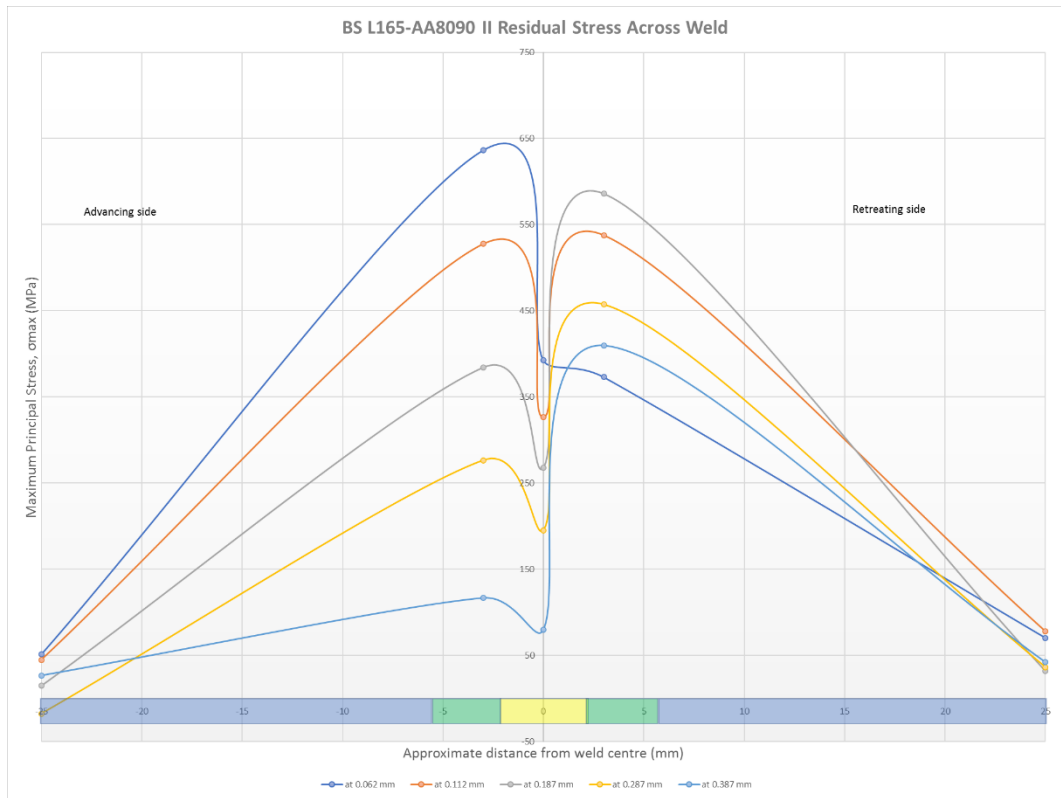
The residual strength measurements plotted across the weld at various depths are shown in Figure 163 with the approximate positions of nugget, HAZ/ TMAZ and parent materials shown along the x-axis. Almost all depth measurements follow the typical “M” shaped profile expected from the literature (see section 2.3.9.3.4), at odds with the highly spurious results observed in the AA8090-BS L165 tests. It is expected that had the results for AA8090-BS L165 been more reliable, that they would have followed this shape also. Figure 163 shows that the measurements taken at all depths have the maximum RS peak arising in the retreating side of the weld, with the exception of the 0.062 mm measurement on the II weld. As discussed previously (section 6.5.2.4.1), the retreating edge of weld RS measurement rises (Figure 162(a)) before reaching its peak at approximately 0.16 mm, with the 0.062 mm measurements being almost identical for the retreating edge of weld and in-weld. This has produced a profile more in keeping with that observed for the AA8090-BS L165 for that depth measurement only. It is suspected that material mixing close to the surface of the weld accounts for this disparity.

If that result is disregarded, the RS measurements show higher values on the retreating (AA8090) side of the weld. As previously discussed (section 6.4.2.4.2), there is disagreement within the literature at which point the highest RS should occur. These findings disagree with Guo et al. (2020) and Jamshidi Aval (2015) who attributed higher RS values on the advancing side to superior mechanical properties of the advancing side material. If the BS L165 is considered to be the stronger material (this is true in the welded condition) then the results concur with Zapata et al. (2016) and Hadji et al. (2018) who measured the RS to be highest on the retreating side which corresponded with the weaker material, similar to these results. Zapata et al. (2016) attributed this to the differences in the materials (composition, properties and thermal history of the materials).

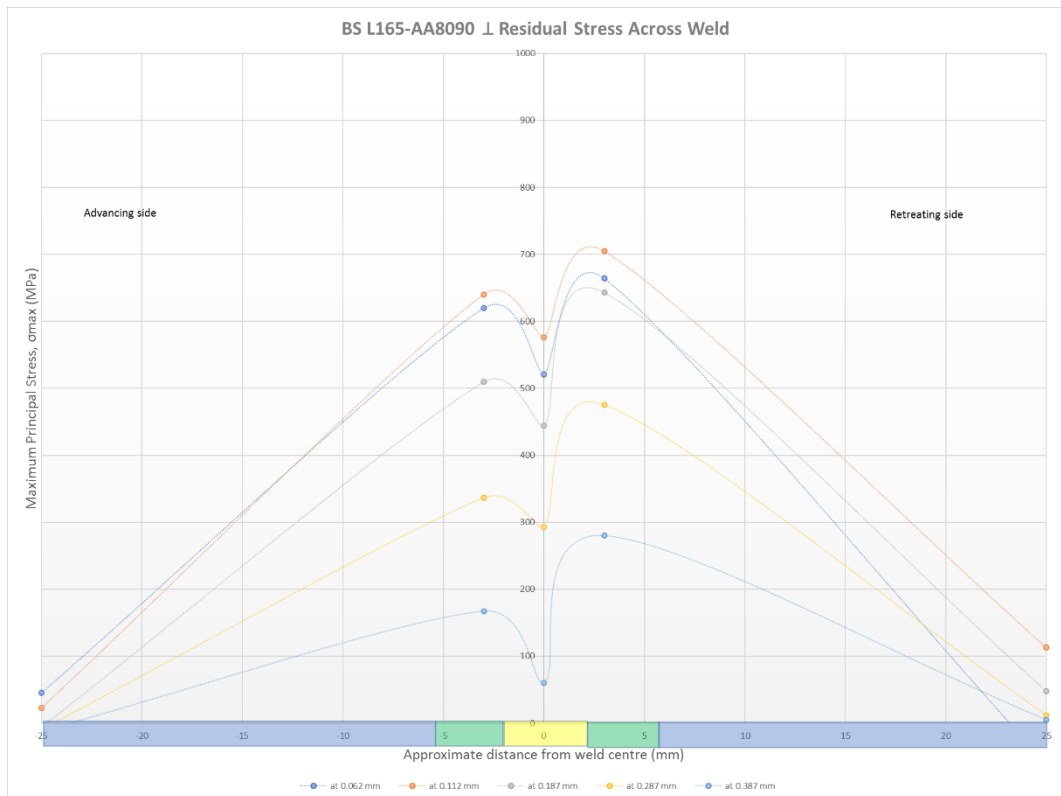
Again disregarding the potentially spurious 0.062 mm measurement, the II weld shows that, although following the expected order in terms of RS of 0.112 mm, 0.187 mm, 0.287 mm and then 0.387 mm on the advancing side and in-weld, i.e. the RS should reduce with depth, this is not true on the retreating side. On the retreating side the RS is highest at 0.187 mm, then reduces at 0.112 mm, 0.287 mm and 0.387 mm (again

disregarding the 0.062 mm measurement). It is unexpected for the mid thickness measurement to be lower than those closer to the top as the residual stress should reduce with depth. This suggests an anomaly within the weld at that depth which may reasonably be attributed to the drill passing through the TMAZ and into the HAZ and the differences in RS arising as a result in the change in microstructure, although if that were the case one would expect to see evidence of this on other configurations. The \perp weld RS is slightly higher at 0.112 mm than at 0.062, and then follows the expected decline in RS with depth. As the results cannot be analysed quantitatively the small difference between the 0.112 mm and 0.062 mm measurements is not considered to be significant and cannot be validated owing to time constraints.

When discussing the AA8090-BS L165 RS results it was not possible to determine which of the materials had an overall stronger RS response to SSFSW due to the spurious results. In this case (BS L165-AA8090), although the results cannot be analysed quantitatively, the overall consistent profiles (noting the exception of the II weld at 0.062 mm) suggests that the weaker (in the welded condition) AA8090 had a stronger RS response to SSFSW for both configurations due to higher RS values being recorded at the retreating side.



(a)



(b)

Figure 163: Showing residual stress across weld at varying hole depths: (a) BS L165-AA8090 II and (b) BS L165-AA8090 ⊥.

6.5.3 Summary/ Conclusions for this Configuration

The following is a brief summary of the findings from the work on BS L165-AA8090 weld configurations.

- Again little read-across from the similar weld configurations was possible. This was due to the influence of each material's thermo-physical properties combining to produce unique properties.
- The weld surface appearance changed along each weld and between welds which was apparent through the differences in ripple definition, roughness and coverage.
- Less mixing was apparent in the nugget of the II than in the AA8090-BS L165 II weld.
- There was a significant presence of oxide chains on the joint line and into the nugget which weakened the weld overall. Additionally large oxide inclusions were observed on the kissing bond which also acted to weaken the bond.
- Other stress concentrations were observed in the form of alclad mixing close to the top surface of the weld, and sharp transitions from the rippled area on the surface to the ironed area.
- The hardness minimum was located a significant distance into the retreating side HAZ, rather than close to the TMAZ boundary.
- This configuration experienced the lowest tensile weld efficiency of all configurations. However, as more of these specimens failed at a kissing bond it is expected that by using optimised weld parameters, the weld quality would improve, and this would change.
 - Based on the current data, the recommendation can be made to position BS L165 (the stronger material in the welded condition) on the advancing side for material with the rolling direction orientated parallel to the weld.
 - Further work is required before a recommendation can be made on the \perp welds.
 - No recommendation can currently be made on the overall optimal material orientation, i.e. on an aircraft no specification could yet be made as to which rolling direction to position the materials.

- This configuration also had the lowest fatigue weld efficiency of all configurations. However due to the number of failures which occurred at kissing bonds, this low efficiency cannot currently be attributed to the positions of the materials, i.e. which is on the advancing or retreating side. Instead, the low fatigue efficiency must be, at least partially, attributed to the poor weld quality as indicated by kissing bonds, poor mixing, oxide chains etc. It is clear that significant further work is required to find optimal weld parameters to produce the highest quality welds.
- The data suggests that the retreating side, occupied by the weaker material (AA8090) in the welded condition has the strongest response with regard to residual stress. However, it is acknowledged that considerably more data is required for full analysis, i.e. additional testing at more positions.

6.6 Comparison of Weld Configurations

A summary of salient features of each weld configuration is shown on Table 48.

Table 48: Showing summary of most salient features of welds, as discussed previously in Chapter 6.

Configuration	Feature or Property		⊥
8090-8090	Weld distortion	Longitudinal and transverse	Longitudinal and transverse
	Surface appearance	Ripples only visible over small amount of surface (with underfill), additional material covers the rest.	Ripples visible over greater width of weld (with underfill)
		Smaller rough area on retreating side, no underfill on that side. Limited galling	Rough surface on retreating side with additional material and underfill
	Grooves on surface	Grooves not on all surfaces	

Configuration	Feature or Property		⊥
	Microstructure	Nugget: grains equiaxed on advancing side. Larger with less equality in directions on retreating side. More numerous heterogeneously nucleated precipitates at grain boundaries than ⊥. Similar number of IMCs in both. Kissing bonds in both	Nugget: grains slightly larger than on advancing side with less equality in directions, smaller than on retreating side (still larger than on advancing) TMAZ: Considerably larger retreating TMAZ. Reduced volume fraction of coarsened precipitates than . More IMCs HAZ: significantly smaller advancing side grains than
	Hardness	Minimum is advancing side HAZ	Slightly better hardness recovery in nugget than . Minimum is retreating side HAZ
	Tensile strength	81.5% weld efficiency Most failed in advancing side HAZ, consistent with hardness minimum	Reduction of 1.3% in elongation from 81% weld efficiency Only 3 failed at retreating side HAZ (where hardness minimum is located). Most failed mid-weld due to kissing bonds.
	Fatigue	84% weld efficiency Most failed mid-weld due to kissing bonds, the rest were at or close to the hardness minimum	N/A
	Residual Stress	Spurious result at advancing EoW Largest RS at retreating EoW Plot does not show traditional "M" or "V" shape	Spurious result at advancing side of weld Largest RS at retreating EoW Plot does not show traditional "M" or "V" shape
L165-L165	Weld distortion	Longitudinal and transverse and warping when using some welding parameters	Longitudinal and transverse and warping when using some welding parameters

Configuration	Feature or Property	∥	⊥
	Surface appearance	<p>Inconsistent material deposits adjacent to tool pin width</p> <p>Ironing marks on retreating side</p> <p>Intermittent grooves present on some welds</p> <p>Ripples concentrated on advancing side with underfill in this area</p>	<p>Stronger ironing effect than on ∥ weld</p> <p>Ripples cover more surface area of weld (intermittently) than on ∥ weld, with underfill</p> <p>Significant change in appearance along weld length</p>
	Microstructure	<p>Alclad layer drawn into weld at joint line</p> <p>Nugget: smaller grain size than for AA8090</p> <p>Nugget and TMAZ: Fewer but larger IMCs than ⊥ weld</p>	<p>Alclad layer drawn into weld at advancing side TMAZ</p> <p>Nugget: smaller grain size than for AA8090</p>
	Hardness	<p>Greater hardness recovery in nugget than for ⊥ weld</p> <p>Hardness minimum in retreating HAZ (but very close in value to advancing TMAZ)</p>	<p>Hardness minimum in advancing TMAZ</p>
	Tensile strength	<p>100% weld efficiency</p> <p>All but one failed mid-weld due to kissing bonds</p>	<p>97% weld efficiency</p> <p>All failed mid-weld partially due to kissing bonds</p>
	Fatigue	<p>84.6% weld efficiency</p> <p>Most failed mid-weld, not owing to kissing bonds</p>	<p>N/A</p>
	Residual Stress	<p>Largest RS in retreating EoW</p> <p>M shape not achieved</p>	<p>Overall largest RS in advancing EoW</p> <p>M shape achieved</p>
	8090-L165	Weld distortion	<p>Longitudinal and transverse and warping when using some welding parameters</p>

Configuration	Feature or Property	II	⊥
	Surface appearance	<p>Obvious ironing effect over varying portion of surface area, with underlying ripples and underfill.</p> <p>Change in surface appearance from reflective to dull.</p> <p>Band of oxidation markings adjacent to weld on advancing side</p>	<p>Intermittent ironing effect over retreating side of weld</p> <p>Ripples and underfill on advancing side</p>
	Microstructure	<p>Greater degree of materials mixing than on ⊥ weld</p> <p>Fewer coarse IMCs in advancing side TMAZ than ⊥ weld</p> <p>Nugget larger (for II and ⊥) than on any other configuration</p>	<p>Slightly increased cross-sectional thickness than parent material on retreating side, significant underfill on advancing side</p> <p>Surface breaking and sub-surface voids present close to the top surface</p> <p>Smaller grains on retreating side of nugget</p> <p>Overall larger grains in HAZ than II weld</p>
	Hardness	<p>Hardness minimum in advancing side HAZ</p>	<p>More consistent hardness recovery in retreating side (BS L165) nugget than II weld.</p> <p>Hardness minimum in advancing side TMAZ</p>
	Tensile strength	<p>78.8% weld efficiency</p> <p>12 failed at advancing side HAZ consistent with hardness minimum and 8 failed mid-weld owing to kissing bonds</p>	<p>72.2% weld efficiency</p> <p>17 failed mid-weld due to kissing bonds, and 3 failed at the advancing HAZ (not consistent with hardness minimum)</p>
	Fatigue	<p>70.8% weld efficiency (compared with parent material)</p> <p>All failed in weld, but the position changed.</p>	N/A
	Residual Stress	Spurious parent material retreating side (BS L165) result	Spurious results at both advancing and retreating EoW

Configuration	Feature or Property		⊥
		Overall similar highest RS results for advancing EoW and in-weld	Highest RS position not clear due to spurious results
		M shape not achieved	M shape not achieved
L165-8090	Weld distortion	Longitudinal and transverse, warping unknown	Longitudinal and transverse, warping unknown
	Surface appearance	Varying amounts of deposited material on advancing side	Less deposited material adjacent to advancing side
		Ironing effect over retreating side, underlying ripples and underfill on advancing side	Ironing effect over retreating side, underlying ripples and underfill on advancing side
	Microstructure	Oxide chains present in nugget and large inclusions observed in kissing bond	Oxide chains present in nugget and large inclusions observed in kissing bond
		Smaller nugget width than AA8090-L165 welds TMAZ larger width than AA8090-L165 welds	Smaller nugget width than AA8090-L165 welds TMAZ larger width than AA8090-L165 welds Sharp transition from smooth ironed area to rough rippled area on top surface of weld
	Hardness		Slightly more hardness recovery in nugget than in weld.
Hardness minimum in retreating side HAZ		Hardness minimum in retreating side HAZ.	
Tensile strength	74.4% weld efficiency	64.1% weld efficiency	
	Analysis shows that positioning BS L165 on the advancing side produces a stronger weld than in the previous configuration Most failed mid-weld due to kissing bonds, remainder failed at retreating HAZ consistent with hardness minimum.	Analysis was inconclusive as to comparable strengths when BS L165 is positioned on the advancing or retreating sides. Most failed mid-weld due to kissing bonds, remainder failed at retreating HAZ consistent with hardness minimum.	
Fatigue	60% weld efficiency (compared with parent material)	N/A	

Configuration	Feature or Property		⊥
		All failed in weld, but the position changed. Multiple cracks were observed on several specimens.	
	Residual Stress		Potentially spurious result at the retreating (AA8090) parent material.
		Overall largest RS at retreating EoW	Overall largest RS at retreating EoW
		Overall M shape achieved	M shape achieved

6.7 Property Relationships

Attempts were made to find relationships between different mechanical properties of the SSFSW materials with varying success. The experiments included:

1. Fitting a polynomial trendline to the residual stress results when plotted across the weld. Despite best efforts using MS Excel no trendline would fit satisfactorily, with the “best fit” differing significantly in shape rendering it unfeasible for residual stress prediction across the weld.
2. Plotting the residual stress with depth for the nugget, advancing EoW and retreating EoW and fitting best fit linear and polynomial trendlines. The residual stress was plotted between 0.1 mm depth and 0.4 mm, the former being where most results established more steady state conditions following the initial sharp changes near surface. Reasonable correlation was achieved between the 6th order polynomial trendlines and the results, however the linear trendlines showed significant scatter. Some of the data sets, however, adopted differing patterns/ plot shape and so the results of this analysis were not considered to be meaningful enough to justify further exploration.
3. Similarly to the residual stress, attempts were made to fit a polynomial trendline to the hardness data taken across the weld mid-thickness. It was not possible to fit a trendline in MS Excel with sufficient accuracy and correlation to the results.
4. The hardness data was then plotted against position across the weld (only HAZ, TMAZ and nugget, discounting the parent materials) and a far superior

correlation between the trendlines and results was achieved (compared with those plots including the parent materials), although the level of correlation was not consistent across all configurations with considerable scatter present on several.

5. The advancing and retreating HAZ hardness results were then considered in isolation. The polynomial trendlines which were applied were not consistent across the different configurations, with some best fits having 3rd order polynomials and some having 6th order. The linear trendlines were more promising, with most configurations adopting similar gradients, although considerable scatter existed and some configurations did not follow the trend.

None of the preceding experiments were considered worthy of further analysis. Instead work focused on ascertaining the relationship between hardness and tensile strength, and the relationships between the residual strength, hardness and grain size.

6.7.1 Relationship Between Hardness and Tensile Strength

Inspired by the work of Sillapasa et al. (2017) attempts were made to develop a relationship between the hardness results and UTS. While Sillapasa et al. (2017) were able to cut small round bar specimens to test the UTS at specific parts of the weld, e.g. testing only the advancing side HAZ or only the nugget, this was not possible in the current research due to the thin material used. Using the theory that under tensile loading the FSW material should fail at the region of lowest tensile strength, which should coincide with the region of lowest hardness (Sillapasa et al., 2017), the author considered only those tensile specimens (for each configuration) which did fail at the location of minimum hardness. This discounted all specimens which failed at other locations due to welding flaws, such as within the nugget due to a kissing bond or stress concentrations arising from the top surface.

Listing the relevant specimens, an average UTS at the hardness minima (typically either the advancing or retreating side HAZ) was found for each configuration. This value differed from the overall UTS reported for each configuration previously as those values included failures at all locations. The average tensile strength for each configuration was then divided by the average minimum hardness of the same configuration to reveal the relationship shown in Equation 24, reported to two decimal places. It is acknowledged

that specific relationships for each of the two alloys may differ slightly, and for the dissimilar welds, however all data was combined in this case.

$$\sigma_{UTS} = 3.23H \quad (\text{Equation 24})$$

Where:

σ_{UTS} = the UTS of the SSFSW material at the position of hardness minimum in the absence of any flaws (MPa)

H = the hardness of the material at its softest/ weakest point (HV₁)

The same method used by Sillapasa et al. (2017) was then used to find the percentage of scatter of the results, shown below in Equation 25:

$$S = \frac{1}{n} \sum_{i=1}^n \left(\frac{\sigma_{UTS}^{est} - \sigma_{UTS}^{exp}}{\sigma_{UTS}^{exp}} \times 100 \right) i \quad (\text{Equation 25})$$

Where:

σ_{UTS}^{est} = the UTS estimated by Equation 24 (MPa)

σ_{UTS}^{exp} = the UTS obtained experimentally (MPa)

This produced a calculated scatter of 7.04%. The experimental results are shown alongside the predicted values (“Estimated” trendline) and scatter (“Estimated + 7.04%” and “Estimated – 7.04%”) in Figure 164. It can be seen that most experimental results fit comfortably within or close to the estimated range, with only 2 results significantly outside. These outliers are the BS L165 longitudinal and transverse parent (unwelded) materials meaning that close correlation was obtained for all welded material configurations. It should however be noted that no value was obtainable for the BS L165-BS L165 \perp welds as all tensile test specimens failed within the nugget due to the presence of kissing bonds. It is considered likely that the BS L165-BS L165 \perp welds would agree with Equation 24 if the kissing bonds were not present. Additionally, if further work was conducted to optimise the process parameters and produce welds of improved and consistent quality, Equation 24 may change slightly. Despite these limitations, a reasonably accurate means of predicting the UTS of AA8090 and BS L165 SSFSW materials, based on measured hardness values, has been found.

Sillapasa et al. (2017) produced the equation $\sigma_{UTS} = 3.05 \text{ HV}$ with a scatter of 7.3 % for aluminium alloys 6N01 and 7N01. They also report on other research, which produced relationships of $\sigma_{UTS} = 3.0\text{-}3.5 \text{ HV}$ (Sillapasa et al. (2017) referred to the research of Sato and Endo (1986⁹), for aluminium alloys. The exact relationship in Sato and Endo's (1985) work depended upon the type of aluminium alloy, e.g. work hardening or precipitation hardening. For precipitation hardening alloys with a T6 temper, they appear to suggest a relationship of approximately $\sigma_{UTS}=0.3\text{HV}$. This shows reasonable correlation between the current research with the work conducted on parent materials (Sato & Endo, 1985), and on FSW specimens (Sillapasa et al. (2017)).

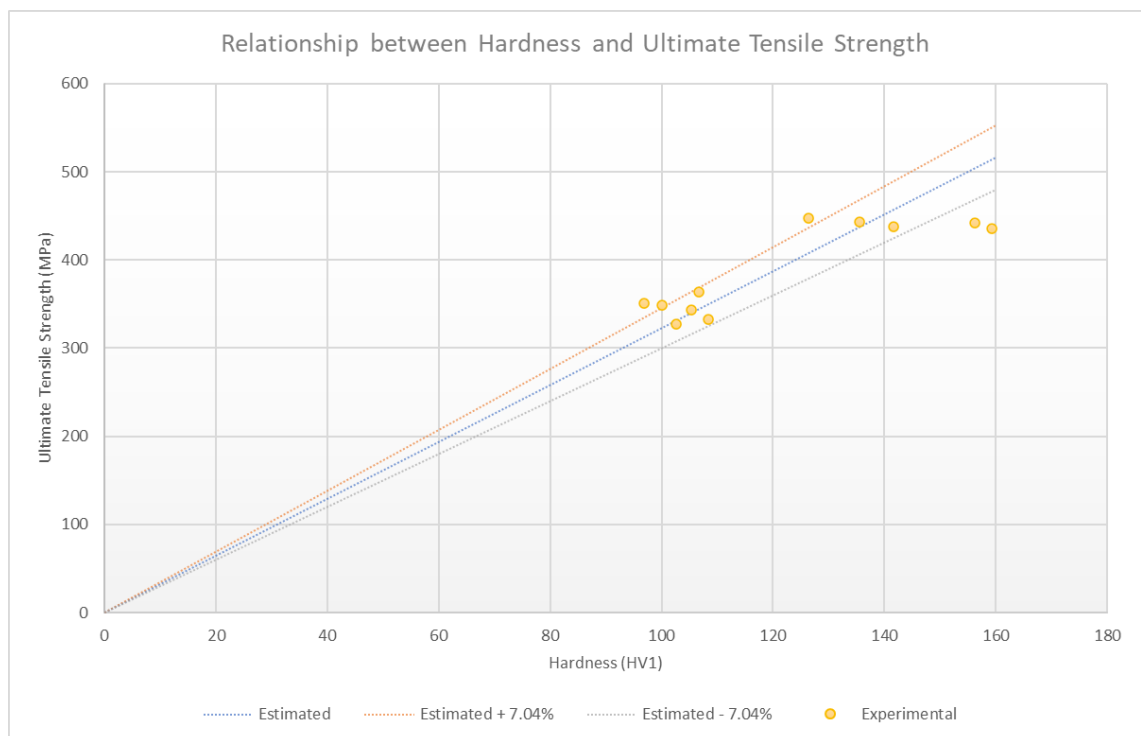


Figure 164: Showing relationship between hardness and UTS for AA8090 and BS L165 and their SSFSW configurations.

Sillapasa et al. (2017) were also able to produce a relationship between fatigue strength, tensile strength and hardness. While this was acknowledged as valuable, it was not possible in the current research. This was due to the mean fatigue strength having been calculated using the staircase method, and incorporating data from tests which had failed at numerous locations. Sillapasa et al. (2017) were able to manufacture small bars at each weld location (HAZ, nugget etc) and find the fatigue strength of each weld zone

⁹ Note: the author could not acquire an English-language version of this work, and has only reviewed the abstract in this comparison.

at 10^7 cycles. The current research did not produce fatigue strengths for individual weld zones, and while consideration was given to analysis of each specimen based on the number of cycles to failure at the fatigue amplitude increment, that the specimen was tested at (see section 3.4.3.2), this was judged to be sufficiently inaccurate to dissuade the author from further analysis.

6.7.2 Regression Analysis

Regression analysis is a method often used in business settings to analyse the relationship between two or more variables, e.g. how sales are affected by the use of promotions. The variable that one wishes to determine the value of (i.e. predicted sales) is termed the dependent variable, and those variables that one wishes to analyse the effect are termed independent variables (i.e. use of promotions, other competitors product launches etc) (Gallo, 2015). Regression analyses which use linear relationships (rather than polynomial) and utilise multiple independent variables are known as multiple linear regression (Ganiyu, 2019). In a regression analysis, the data sets are plotted on a scatter chart and a “best-fit” line applied, with a confidence band and variance determined (Wong, 2020).

In the case of this research it was considered to be beneficial to determine if a meaningful relationship existed between the residual stress, hardness and grain size, therefore regression analysis was carried out using MS Excel. It was suspected that the heat input and cooling rate experienced within the weld may have an influence on the generation residual stress. As the grain size and hardness are both heavily influenced by the heat input to the weld, this was the reason that a relationship between residual stress, hardness and grain size was considered. The aim was to accurately predict the residual stress value (dependent variable), with respect to the hardness and grain size at that measured point (independent variables). As two grain size measurements were obtained at each position due to the typically non-equiaxed grains, three independent variables were used in this analysis: hardness (measured in HV_1), grain size one and grain size 2 (measured in μm). Several limitations to this analysis were noted from the outset as listed below:

- Small data-set. Only one measurement of residual stress was typically taken at each point on the weld, with these measurements only occurring in one position

on each of the advancing and retreating parent materials and HAZ/ TMAZ and the nugget. There were therefore only 5 measurements for each configuration.

- The grain size was only measured at one position within the HAZ (both advancing and retreating sides) and within the nugget. It was previously acknowledged that the HAZ microstructure subtly changed as it progressed from the TMAZ boundary towards the unaffected parent material, therefore this is a potentially significant source of error.
- As the residual stress measurement was taken at the edge of the weld (potentially through the HAZ/ TMAZ/ combination of both), the hardness measurements across these zones in each configuration were averaged for this analysis.
- Similarly, the HAZ and TMAZ grain sizes were averaged (advancing and retreating sides treated separately) for use in this analysis.
- Several of the residual stress measurements were previously considered to be spurious. This will likely have a significant impact on the results of this analysis.
- Not all RS data sets are accounted for.

The regression analysis was carried out using residual stress data acquired at 0.112 mm depth, where surface influence should be minimised. The summary output of the MS Excel analysis for the AA8090 II configuration is shown in Figure 165, with the most important items highlighted in yellow and post-analysis interpretation conducted with the assistance of Frost (2020). The results of the analysis, indicating a best-fit equation are then shown in Table 49 with the models plotted in Figure 166; see the following paragraphs for details of the analysis and structure of best-fit equation.

The R-square value accounts for the variance. In linear regression the analysis finds the smallest sum of squared residuals (the difference between the measured and predicted values) possible for the dataset (Frost, 2018). The R-square value is always between 0 and 100% (shown in Figure 165 as a value between 0-1). Typically the higher the R-square value, the more successfully the regression model fits the source data, however this is dependent on the residual plot (not shown here) being unbiased. Although not a statistician, upon examination of the relevant residual plot the author did not consider them to be biased. The result of this analysis shows the R-square value to be ~0.999, or that this model accounts for approximately 99.9% of the dependent variable's variance.

The ANOVO (Analysis of Variance) test is a means of determining if results are significant, i.e. that a relationship exists between the variables. Frost (2020) describes this as returning the p-value (the probability that one would obtain the effect observed in the sample, or larger, if the null hypothesis is true for the populations) for the F-test ((p-value/ Significant F), these are statistical values shown in Figure 165) of overall significance. This determines whether the regression model with its independent variables explains the dependent variable's variability better than a model with no/ fewer independent variables. Frost (2021) describes the null hypothesis as that in experiments there is an effect or difference between groups that the researcher is testing, the null hypothesis states that the true effect size equals zero, i.e. there is no difference between the groups; if the F-test result is statistically significant, it suggests the model is sound and the null hypothesis can be rejected. The Significance F and p values are generally considered statistically significant if they are below 0.05 (5%) (Andrade, 2019); in this case the value is 0.01 (both for Significance F, and the p-values for the intercept and independent variables) and the model can therefore be considered sound.

SUMMARY OUTPUT								
<i>Regression Statistics</i>								
Multiple R	0.999965198							
R Square	0.999930397							
Adjusted R Square	0.999721588							
Standard Error	5.727717109							
Observations	5							
<i>ANOVA</i>								
	<i>df</i>	<i>SS</i>	<i>MS</i>	<i>F</i>	<i>Significance F</i>			
Regression	3	471308.1064	157102.7021	4788.732023	0.010622312			
Residual	1	32.80674328	32.80674328					
Total	4	471340.9132						
	<i>Coefficients</i>	<i>Standard Error</i>	<i>t Stat</i>	<i>P-value</i>	<i>Lower 95%</i>	<i>Upper 95%</i>	<i>Lower 95.0%</i>	<i>Upper 95.0%</i>
Intercept	-10662.81167	289.2498945	-36.86366659	0.017265339	-14338.08005	-6987.543293	-14338.0801	-6987.543293
Average hardness in that area	-91.37505379	1.789943608	-51.04912433	0.012469134	-114.1184437	-68.63166384	-114.118444	-68.63166384
ave grain size 1 in that area	-3202.38727	70.26026405	-45.57892449	0.013965175	-4095.12857	-2309.64597	-4095.12857	-2309.64597
ave grain size 2 in that area	6097.75429	135.5498928	44.98531252	0.014149395	4375.4296	7820.07898	4375.4296	7820.07898
<i>RESIDUAL OUTPUT</i>								
	<i>Predicted Residual stress @ 0.112 mm depth</i>	<i>Residuals</i>						
<i>Observation</i>								
1	-23.43811386	-4.055886135						
2	53.80679383	-0.026793829						
3	635.6853537	-0.026353684						
4	612.6265834	0.065416557						
5	-28.92061709	4.043617092						

Figure 165: Showing MS Excel summary output of AA8090 II regression analysis. As a MS Excel summary output each term is not defined here, rather those terms deemed most important are highlighted.

The equation of the best fit line (and means therefore of predicting the residual stress is comprised of the intercept and coefficients for each independent variable, shown for AA8090 II in Figure 165 under “Coefficients”. In the case of the AA8090 II configuration, the relationship is shown in Equation 26:

$$RS = -10662.812 - 91.375H - 3202.387GS_1 + 6097.754GS_2 \quad \text{Equation 26}$$

Where:

RS = Residual Stress (MPa)

H = Hardness (HV₁)

GS₁ = Grain size 1 (μm)

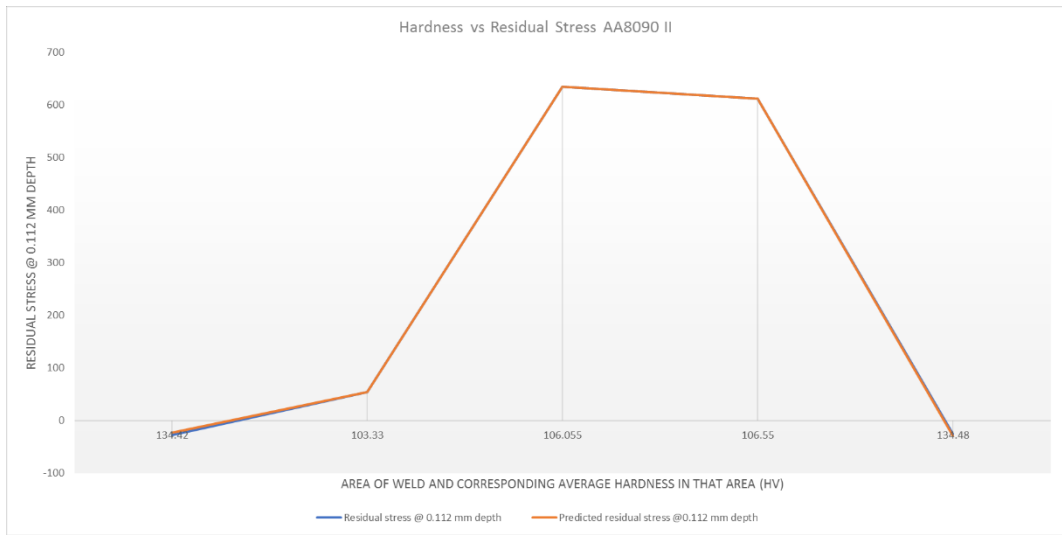
GS₂ = Grain size 2 (μm)

The residual output in Figure 165 shows the predicted values using Equation 26. It can be seen that there is close correlation between the predicted and measured results for this configuration based on the residuals noted.

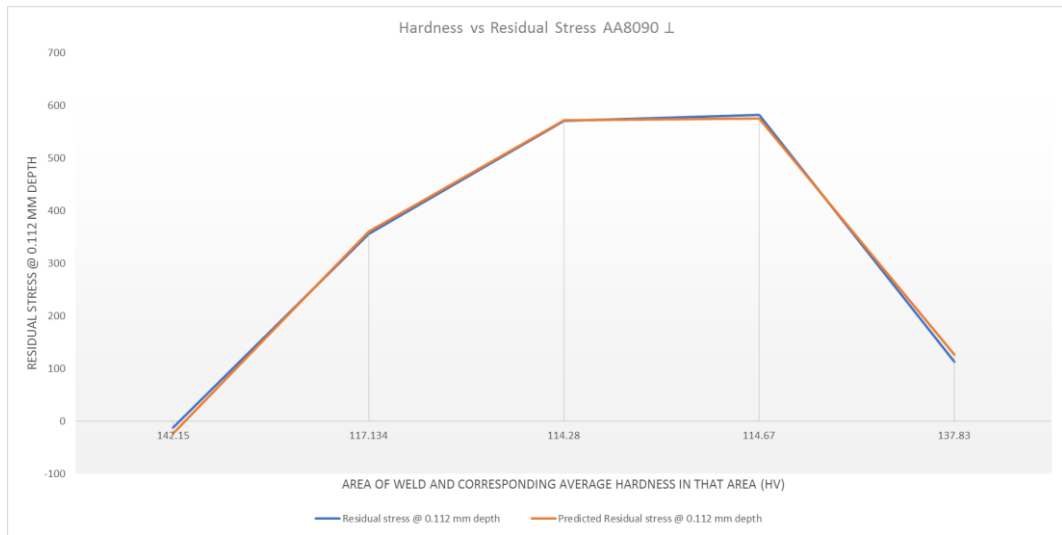
The results for all configurations are shown in Table 49, with the measured vs. predicted results of RS against hardness values shown in Figure 166.

Table 49: Showing results of residual stress regression analysis based on hardness and grain size.

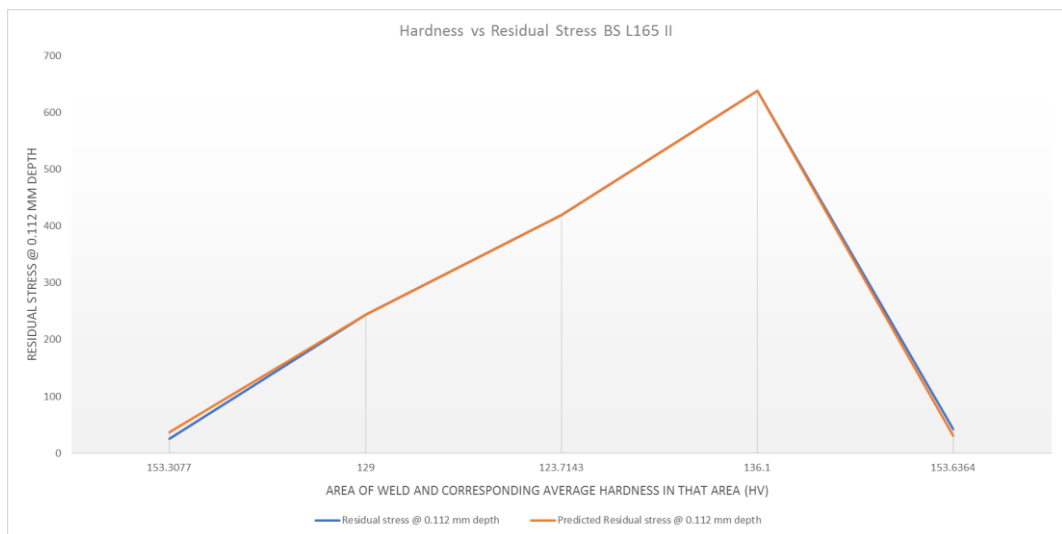
Configuration	R-square	Significance F	P-value				Relationship
			Intercept	Average hardness	Grain size 1	Grain size 2	
AA8090 II	0.9999	0.0106	0.0173	0.0125	0.0140	0.0141	RS = -10662.812 - 91.375H - 3202.378GS ₁ + 6097.754GS ₂
AA8090 I	0.9986	0.0477	0.0389	0.0527	0.0897	0.0946	RS = 4088.953 - 34.747H - 45.164GS ₁ + 110.129GS ₂
BS L165 II	0.9990	0.0399	0.5390	0.0252	0.0311	0.0288	RS = -120.633 - 19.253H - 416.951GS ₁ + 1126.802GS ₂
BS L165 I	0.9931	0.1055	0.0617	0.0571	0.8282	0.3806	RS = 3387.157 - 29.609H - 13.137GS ₁ + 179.539GS ₂
AA8090-BS L165 II	0.9674	0.2288	0.1057	0.1273	0.4640	0.3162	RS = 3235.611 - 18.977H + 44.636GS ₁ - 112.410GS ₂
AA8090-BS L165 I	0.5727	0.7685	0.5004	0.6154	0.7190	0.8737	RS = 3114.787 - 16.316H - 68.071GS ₁ + 40.139GS ₂
BS L165-AA8090 II	0.9697	0.2205	0.1065	0.1143	0.1542	0.1433	RS = 4389.631 - 29.905H - 221.682GS ₁ - 350.892GS ₂
BS L165-AA8090 I	0.9401	0.3084	0.1540	0.1680	0.4287	0.3564	RS = 3406.850 - 24.073H + 82.981GS ₁ - 122.444GS ₂



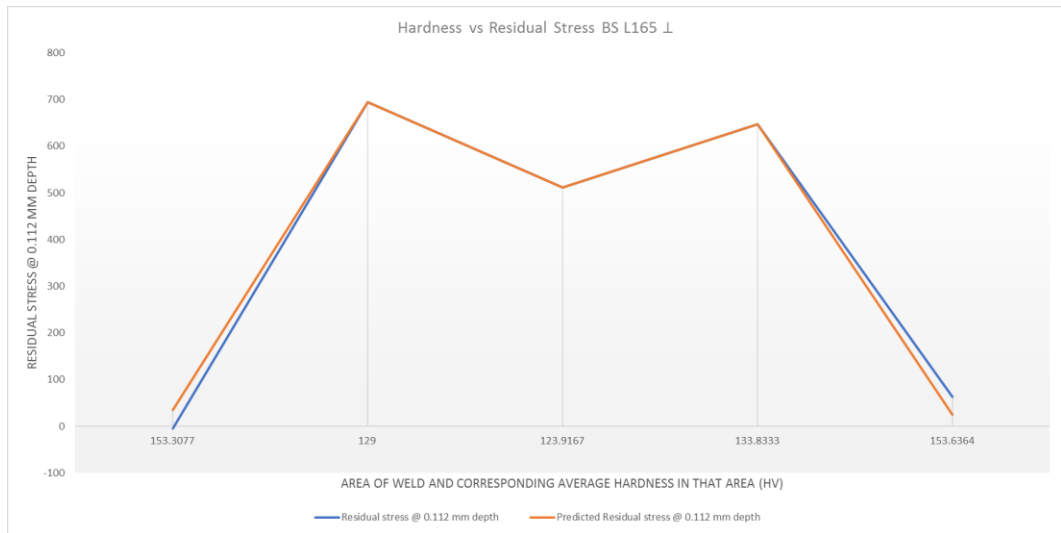
(a)



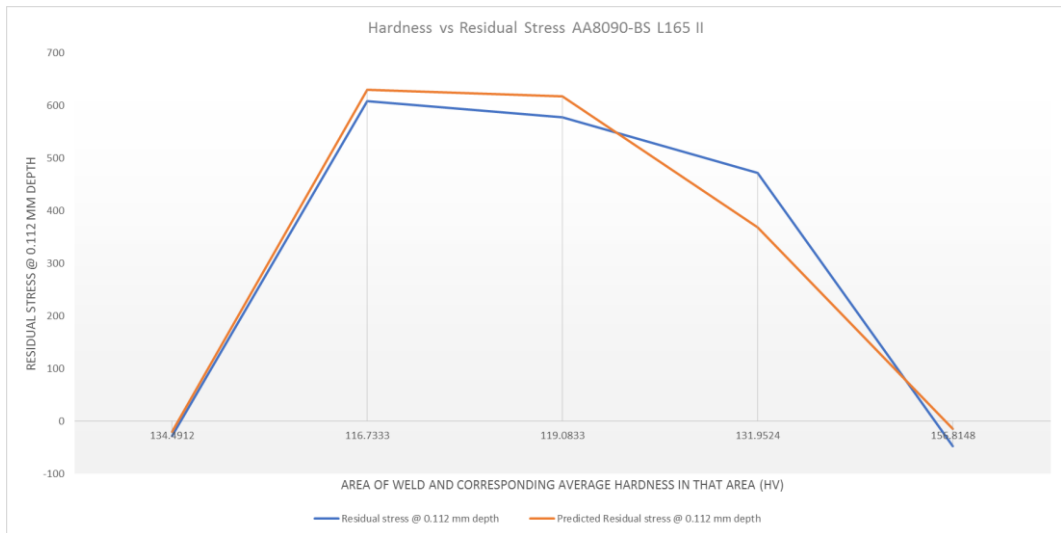
(b)



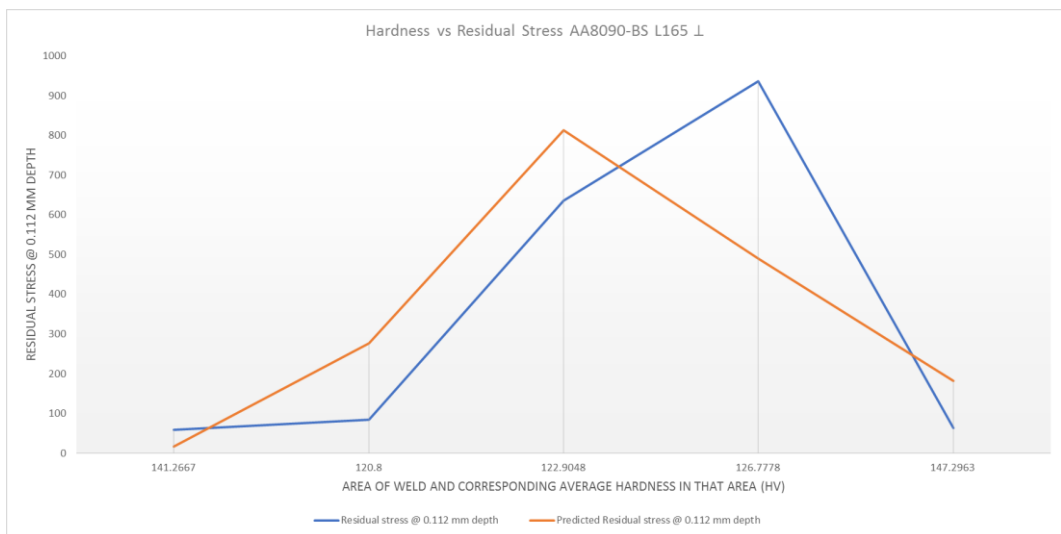
(c)



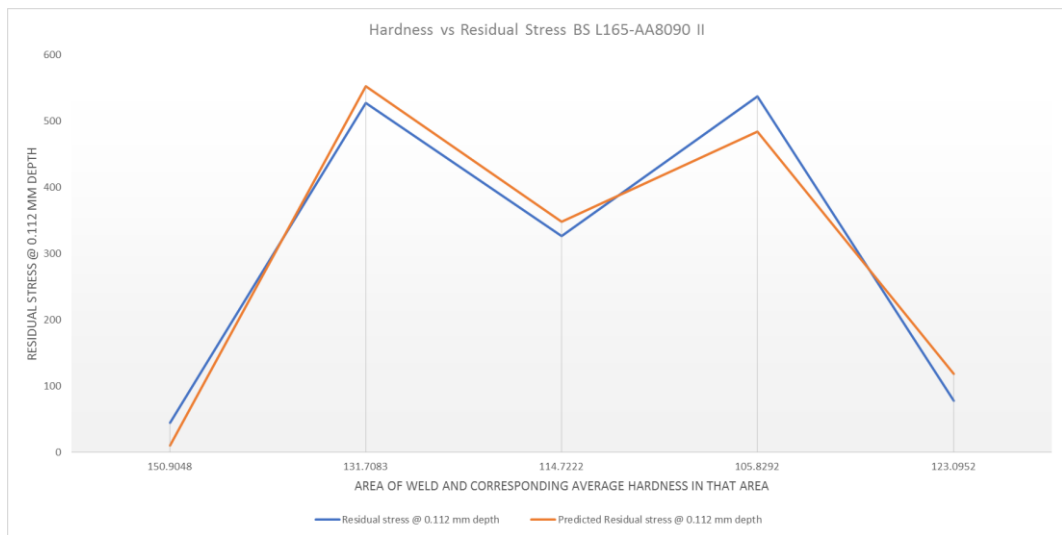
(d)



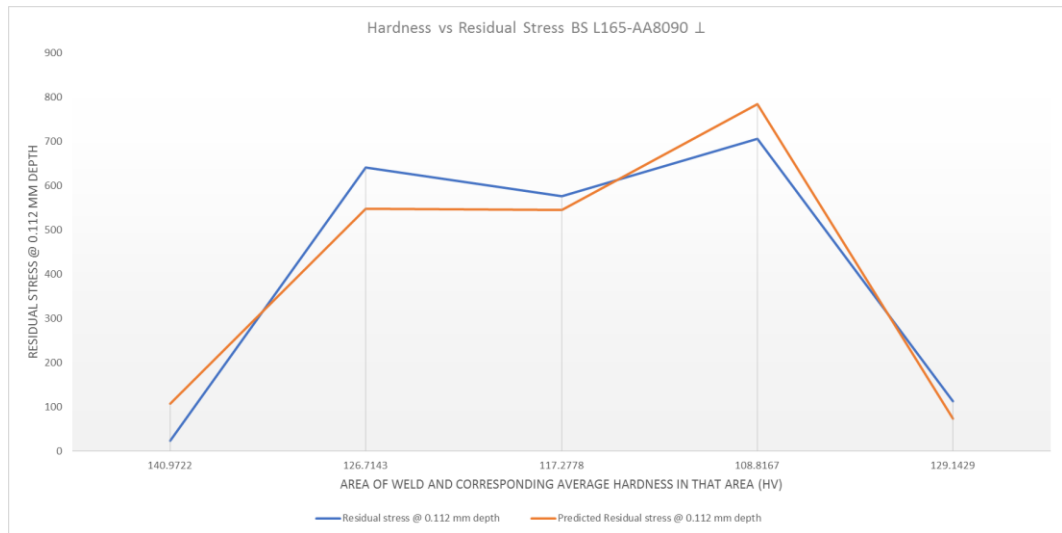
(e)



(f)



(g)



(h)

Figure 166: Showing plots of measured vs. predicted RS for each configuration: (a) AA8090 II; (b) AA8090 \perp ; (c) BS L165 II; (d) BS L165 \perp ; (e) AA8090-BS L165 II; (f) AA8090-BS L165 \perp ; (g) BS L165-AA8090 II; (h) BS L165-AA8090 \perp .

Clearly from the plots in Figure 166 the predicted data matches the measured data more successfully for some configurations compared with others. This is likely owing to spurious data-sets and to the very limited number of measured results. It is considered that if the original RS data was more reliable (remembering that most of the measured results were in excess of the yield strength and cannot therefore be reliably depended upon for quantitative analysis) and if significantly more RS testing was undertaken that

this method could be used to determine a relationship between the RS, hardness and grain size. Table 49 shows that only AA8090 II fulfils the requirement of Significant F and the p values to be <0.05 , thus the null hypothesis cannot be rejected for all other configurations. Analysis of the plots shows that all similar weld configurations have reasonable correlation between the measured and predicted data and so there may be some merit in this approach for those welds, despite not meeting the statistical criteria.

Although this current analysis was unsuccessful in some areas, it still added value to the overall research in that it shows that a relationship is currently not always obtainable from the testing conducted to date but that one may be possible in future.

7 Conclusions and Further Work

7.1 Main Conclusions from Analysis

The aim of this research was to determine whether SSFSW is a suitable joining technique for 0.7 mm AA8090-T81 and BS L165 in various configurations, based on the quality of welds and focusing on the metallurgy of the welds produced. SSFSW was performed in eight configurations to demonstrate the suitability of the two materials when joined similarly, dissimilarly, when alternating the material positioned on the advancing side and when joined in different orientations. It was found that the 0.7 mm thick materials are suitable for SSFSW in the butt-weld configuration based on the microstructures and associated mechanical properties but, as there were inconsistencies with the quality of the welds (both along individual weld runs and between different welds), further work is required to determine optimum welding parameters and clamping conditions.

The following conclusions were drawn from the analysis:

- The width of the weld was not consistent with the dimensions of the tool shoulder. Instead, it appeared that the tool shoulder had, in most cases, had little to no contact with the material surface, and that the weld width was solely dependent on the pin dimensions and process parameters.
- No configuration produced a fully ironed top surface, as would be expected from the literature (see section 2.3.2). It is expected that optimised welding parameters may produce this fully ironed surface and that the current partially rough, rippled and underfilled surface appearance is a function of the heat input and generation within the weld, and a result of incomplete contact with the shoulder.
- The welding parameters, clamping set-up and preparation produced welds of inconsistent quality. This was indicated by changes to the surface appearance, variations in the degree of mixing between materials, and inconsistent tensile and fatigue testing results due to the intermittent presence of kissing bonds. These changes occurred both between different welds of the same materials and orientations using the same parameters, and also changed along single weld runs

from one point along the length to another. It is expected that this would improve with optimised parameters and conditions.

- The hardness minimum was located in the HAZ or TMAZ in all configurations. For the similar welds the position of the AA8090 II minimum was on the advancing side, with the \perp weld hardness minimum on the retreating side, and the BS L165 II the hardness minimum was on the retreating side, and the \perp weld on the advancing side. For the dissimilar welds, the hardness minimum was consistently on the side corresponding to the softer material (AA8090).
- The highest tensile strength weld efficiency was achieved on BS L165 similar welds, followed by AA8090 similar welds, then AA8090-BS L165 and finally BS L165-AA8090. Despite this order, analysis regarding those which failed at the softest position indicated that the dissimilar welds were actually stronger (in the absence of kissing bonds) when the BS L165 was positioned on the advancing side for the II orientation. Analysis of the \perp welds in this respect was inconclusive.
- The AA8090-AA8090 and BS L165-BS L165 welds achieved similar fatigue weld efficiencies, when compared with the mean fatigue strength of the relevant parent materials, however, despite being stronger in tensile tests, BS L165 achieved a lower main fatigue strength than AA8090. The point of failure was found to be influenced by kissing bonds, coarse precipitates in the nugget, the location of hardness minima and by stress concentrations on the surface of the weld.
- The analysis of residual stress was hindered by spurious data sets and results exceeding the yield strength (and in some cases the UTS) of the materials. The spurious data sets confused the results and subsequent analysis, while the excessive measured values necessitated the results being treated as qualitative rather than quantitative. The typical "M" shape observed in literature was only achieved in a few cases.
- The positioning of each material, i.e. which was on the advancing side, on dissimilar welds, and the orientation of the materials with respect to welding and the rolling direction influenced the weld appearance and quality. This was indicated by: changing surface appearances; degree of material mixing; hardness, tensile, fatigue and RS test results. The effect of these changes is apparent when the results of the testing previously listed are compared between

the dissimilar welds, and when the orientation is compared between each configuration.

- A relationship was defined, relating the hardness and tensile strength of the welded materials. This was $\sigma_{UTS} = 3.23H$ (Equation 24) and had a calculated scatter of 7.04%. This allows for a degree of predictability when determining these properties when SSFSW 0.7 mm AA8090 and BS L165. This relationship is consistent with relationships for other alloys found in literature.
- Regression analysis was attempted to compare any relationships between grain size, hardness and residual stress. This produced mixed results, with relationships for some configurations showing strong correlation with the measured results, while others were less predictable. This was considered to be due to the spurious data sets produced by the residual stress testing.

The contribution of this work to scientific knowledge has been discussed throughout, in which various gaps in the literature were found. This work has acted to partially address these holes, and are summarised below:

- No other work in literature was found in which any type of FSW was conducted using BS L65 (although the significant volume of work on the very similar AA2014-T6 was acknowledged).
- No other research was found in which SSFSW was used to join AA8090.
- No other research was found in which BS L165 and AA8090 were joined using any form of FSW.
- While AA2014-T6 and AA8090 (other tempers) have been joined using FSW in various studies, none were found which combined these materials (similarly and dissimilarly), and the additional complications of ultra-thin sheet and an alclad coating.

7.2 Further Work

The following areas are considered to be important to the progression of this research.

- Weld parameter trials. As previously determined, the welding parameters, clamping and material preparation used in this research have led to welds of inconsistent quality. A controlled and systematic process is required to

determine the optimal parameters for each configuration. Such a process will require:

- A bespoke clamp assembly to hold the materials firmly without allowing deformation or movement (either lateral or vertical) to occur during welding.
- A thorough material cleaning process. In this research the materials were prepared as per section 3.2.3, however as indicated by the presence of oxides along the joint line and inclusions on kissing bonds, this was determined to be insufficient. Further work is required to determine the extent of material preparation required for these materials.
- A systematic trial programme. For example, begin by determining a rotational speed and traversing speed sufficient to pass a bend test. Then vary one parameter while keeping the other constant. Carry out full testing on the welds, i.e. microstructural analysis, hardness, tensile strength and fatigue strength to determine optimum parameters. This would be time consuming, expensive and would require a large supply of material. Additionally, other welding parameters would have to be considered, e.g. down force, tilt angle, as would the design of the tool itself.
- It is considered that this should be broken down into smaller work packages. The current research became rather unwieldy due to 2 materials being considered and the change in orientation requiring a full suite of testing to be carried out on 8 different configurations. Had the research been limited to one material only, the work and subsequent output would have been more manageable.
- A study is required to determine the full effect of the higher heat input on the top surface of the weld on material and weld mechanical properties, for example hardness mapping.
- Further residual stress testing is required due to the spurious results and excessive values produced. It is suspected that the author's technique requires improvement, hence the unreliable results therefore this work may be suitable for outsourcing to a specialist, or a different RS technique considered.

- In addition to the residual stress testing required to replace unreliable results, further testing is required at additional points between the EoW and parent material measurements. These would be used to determine if the RS moves to compressive in nature in this area to balance the tensile results already found, before returning to approximately zero remote from the weld.
- Corrosion testing. The author of this research did carry out a year-long corrosion trial using welded test specimens on the roof of 1710 NAS, however there was insufficient time to fully analyse the corroded specimens and thus the work was discarded. This corrosion work is important as any tendencies for corrosion as a result of SSFSW of the two materials must be understood prior to use on military aircraft.
- Transmission Electron Microscopy (TEM) is required to fully understand the precipitation phenomena occurring within the welds and how this differs from the parent material. This will allow the changes in strength, ductility and hardness to be fully understood, rather than depending on literature for analysis.
- The full suite of testing and analysis should be conducted on materials welded in alternating orientations, e.g. advancing side AA8090 positioned parallel to weld and retreating side positioned perpendicular to weld, or advancing side BS L165 positioned perpendicular to weld and retreating side AA8090 positioned parallel to weld.
- For the technique to be feasible for adoption as an expedient repair technique on the Merlin helicopter, all other alloys utilised in its structure would need to be proven for suitability.
- Portability of equipment. As previously described in section 1.2, the development of portable equipment was outside the scope of this research. However, in order for SSFSW to be truly beneficial as a repair technique for military aircraft, it would have to become portable and lightweight, and progress would have to occur regarding clamping of the materials to be welded

8 References

1710 Naval Air Squadron. (2014). Aircraft repair task information management system (ARTIMS) [computer software]. UK Ministry of Defence:

ABB Robotics. (2015a). *Irb 7600* ABB Robotics.

ABB Robotics. (2015b). *Release notes: RobotStudio 6.02*. Sweden: ABB Robotics.

Aerospace and Defence Industries Association of Europe - Standardization (ASD-STAN).

(2008a). *BS EN 4632-001:2008*

aerospace series. welded and brazed assemblies for aerospace constructions. weldability and brazeability of materials. general requirements The British Standards Institution.

Aerospace and Defence Industries Association of Europe - Standardization (ASD-STAN).

(2008b). *BS EN 4632-002:2008*

aerospace series. welded and brazed assemblies for aerospace constructions. weldability and brazeability of materials. homogeneous assemblies aluminium and aluminium alloys The British Standards Institution.

Agha Amini Fashami, H., Bani Mostafa Arab, N., Hoseinpour Gollo, M., & Nami, B. (2021).

Numerical and experimental investigation of defects formation during friction stir processing on AZ91. *SN Applied Sciences*, 3(1) doi:10.1007/s42452-020-04032-y

Agusta Westland International Ltd. (2010). *EM 101: Aluminium-lithium alloy al-P8090-sheet in*

T81 temper. $0.6\text{ mm} \leq a \leq 4.0\text{ mm}$. Agusta Westland International Ltd.

Agusta Westland International Ltd. (2014). Merlin Mk1, Mk2, Mk3 and Mk3a compound

interactive electronic technical publication (CIETP) DAP101C-1701-series [computer software]. Accessed via Sun Secur Global Desktop Software for Intel Solaris 10+:

Agusta-Westland International Ltd. (2013). *Engineering repair instructions*. (). C-IETP Software accessed via Sun Secur Global Desktop Software for Intel Solaris 10+: Agusta-Westland International Ltd.

Ahmad Shah, L. H., Midawi, A., Walbridge, S., & Gerlich, A. (2020). Influence of tool offsetting and base metal positioning on the material flow of AA5052-AA6061 dissimilar friction stir welding. *Journal of Mechanical Engineering and Sciences*, 14(1), 6393-6402.
doi:10.15282/jmes.14.1.2020.15.0500

Ahmed, M. M. Z., Wynne, B. P., Rainforth, W. M., & Threadgill, P. L. (2011). Through-thickness crystallographic texture of stationary shoulder friction stir welded aluminium. *Scripta Materialia*, 64(1), 45-48. doi:<https://doi.org/10.1016/j.scriptamat.2010.08.060>

Ahmed, M., Wynne, B. P., Rainforth, W. M., & Threadgill, P. L. An investigation of hardness, microstructure and crystallographic texture in thick sectioned friction stir welded AA6082. Paper presented at the *7th International Friction Stir Welding Symposium, Awaji Island, Japan, 22*.

Ahmed, S., & Saha, P. (2018). Development and testing of fixtures for friction stir welding of thin aluminium sheets. *Journal of Materials Processing Technology*, 252, 242-248.
doi:10.1016/j.jmatprotec.2017.09.034

Akhtar, N., Jin, H. J., & Wu, S. J. (2018). Aerospace grade aluminum lithium material and its welding characteristics. *Journal of Space Technology*, 8(1), 45-51.

Al-moussawi, M., Smith, A. J., Young, A., Cater, S., & Faraji, M. (2017). Modelling of friction stir welding of DH36 steel. *International Journal of Advanced Manufacturing Technology*, 92(1), 341-360. doi:10.1007/s00170-017-0147-y

- Altenkirch, J., Steuwer, A., Peel, M. J., & Withers, P. J. (2009). The extent of relaxation of weld residual stresses on cutting out cross-weld test-pieces. *Powder Diffraction Suppl.*, 24(S1), S31-S36.
- Altenkirch, J., Steuwer, A., Peel, M., Richards, D. G., & Withers, P. J. (2008). The effect of tensioning and sectioning on residual stresses in aluminium AA7749 friction stir welds. *Materials Science & Engineering.A, Structural Materials : Properties, Microstructure and Processing*, 488(1), 16-24. doi:10.1016/j.msea.2007.10.055
- Aluminum Alloy Database. (2021). *Table 11b. typical fatigue properties of wrought and cast aluminum alloys (metric units)* Retrieved from <https://app.knovel.com/hotlink/itble/rcid:kpAAD00001/id:kt00UBBSC2/aluminum-alloy-database/table-11b-typical-fatigue>
- Andrade, C. (2019). The P value and statistical significance: Misunderstandings, explanations, challenges, and alternatives. *Indian Journal of Psychological Medicine*, 41(3), 210-215. doi:10.4103/IJPSYM.IJPSYM_193_19
- Aoh, J. N., Huang, C. W., & Lin, P. C. (2013). Material flow and mechanical properties on friction stir lap welds of alclad AA2024 sheet. In H. Fujii (Ed.), *Proceedings of the 1st international joint symposium on joining and welding* (pp. 45-49) Woodhead Publishing. doi:<https://doi.org/10.1533/978-1-78242-164-1.45> Retrieved from <http://www.sciencedirect.com/science/article/pii/B9781782421634500067>
- Ashok, K., Maruthupandian, K., Ganesh Kumar, K., & Sundar Vishal, C. (2015). Micro-mechanical behaviour of AA2014 alloy during hot tensile testing. *Transactions of the Indian Institute of Metals*, 68, 19-24. doi:10.1007/s12666-015-0580-2

ASM International Handbook Committee (Ed.). (1990). *ASM handbook volume 2: Properties and selection: Nonferrous alloys and special purpose materials* (10th ed.). USA: ASM International.

ASTM International. (2013a). *ASTM E112-13: Standard test methods for determining grain size*. Pennsylvania, USA: ASTM International. doi:10.1520/E0112-13

ASTM International. (2013b). *E837-13 standard test method for determining residual stresses by the hole-drilling strain-gage method*. West Conshohocken, PA: ASTM International.

ASTM International. (2014). *ASTM B209M-14 standard specification for aluminium and aluminium-alloy sheet and plate (metric)*. USA: ASTM International.

ASTM International. (2015). *ASTM E466-15 standard practice for conducting force controlled constant amplitude axial fatigue tests of metallic materials*. Pennsylvania, USA: ASTM International.

ASTM International. (2020). *ASTM E837-20 standard test method for determining residual stresses by the hole-drilling strain-gage method*. West Conshohocken, PA: ASTM International.

Aydin, H., Tutar, M., Durmuş, A., Bayram, A., & Sayaca, T. (2012). Effect of welding parameters on tensile properties and fatigue behavior of friction stir welded 2014-T6 aluminum alloy. *Transactions of the Indian Institute of Metals*, 65(1), 21-30. doi:10.1007/s12666-011-0069-6

Babu, S., Ram, G. D. J., Venkitakrishnan, P. V., Reddy, G. M., & Rao, K. P. (2012). Microstructure and mechanical properties of friction stir lap welded aluminum alloy AA2014. *Journal of Materials Science & Technology*, 28(5), 414-426. doi:[https://doi.org/10.1016/S1005-0302\(12\)60077-2](https://doi.org/10.1016/S1005-0302(12)60077-2)

- Babu, S., Sankar, V. S., Janaki Ram, G. D., Venkitakrishnan, P. V., Madhusudhan Reddy, G., & Prasad Rao, K. (2013). Microstructures and mechanical properties of friction stir spot welded aluminum alloy AA2014. *Journal of Materials Engineering and Performance*, 22(1), 71-84. doi:<https://doi-org.hallam.idm.oclc.org/10.1007/s11665-012-0218-z>
- Bandhu, D., Kumar, R., Nishant, A., & Thakur, A. (2017). *Characterization of friction stir welding for AA 2014-6061 and influence of aging on their mechanical behavior*
- Baqerzadeh Chehreh, A., Grätzel, M., Bergmann, J. P., & Walther, F. (2020). Effect of corrosion and surface finishing on fatigue behavior of friction stir welded EN AW-5754 aluminum alloy using various tool configurations. *Materials*, 13(14), 3121. doi:10.3390/ma13143121
- Barbini, A., Carstensen, J., & dos Santos, J.,F. (2018). Influence of a non-rotating shoulder on heat generation, microstructure and mechanical properties of dissimilar AA2024/AA7050 FSW joints. *Journal of Materials Science & Technology; Journal of Materials Science & Technology*, 34(1), 119-127. doi:10.1016/j.jmst.2017.10.017
- Barbini, A., Carstensen, J., & Santos, J. F. d. (2018). Influence of alloys position, rolling and welding directions on properties of AA2024/AA7050 dissimilar butt weld obtained by friction stir welding. *Metals (Basel)*, 8(4), 202. doi:10.3390/met8040202
- Bassani, P., Gariboldi, E., & Vimercati, G. (2007). Calorimetric analyses on aged Al–4.4Cu–0.5Mg–0.9Si–0.8Mn alloy (AA2014 grade). *Journal of Thermal Analysis and Calorimetry*, 87(1), 247-253. doi:10.1007/s10973-006-7836-3
- Benedyk, Joseph C. (2010, August). International Temper Designation Systems for Wrought Aluminium Alloys: Part 2 - Thermally Treated (T Temper) Aluminium Alloys. *Light Metal Age*. 16-22

- Besharati-Givi, M. K., & Asadi, P. (2014). *Advances in friction stir welding and processing* (1st ed.). Cambridge: Woodhead Publishing. doi:<https://doi.org/10.1016/C2013-0-16268-X>
- Bhadeshia, H.K.D.H (no_date). *Friction Stir Welding*. www.phase-trans.msm.cam.ac.uk
- Bhattacharyya, M., Kundu, A., Raja, K. S., Darsell, J., Jana, S., & Charit, I. (2021). Processing-microstructure-property correlations for temperature-controlled friction stir welding of 304L SS plates. *Materials Science & Engineering.A, Structural Materials : Properties, Microstructure and Processing*, 804, 140635. doi:10.1016/j.msea.2020.140635
- Biradar, N. S. (2016). Effect of transverse mechanical arc oscillation on hot cracking (solidification & liquation) and weld metal properties of AA2014 T6 TIG welds. *AIMS Materials Science*, 3(4), 1544-1560. doi:10.3934/mat.2016.4.1544
- Bjerregaard, L., Geels, K., Ottesen, B., & Rückert, M. (2000). *Metallog guide* (3rd ed.). Denmark: Struers A/S.
- Blankenship, C. P., Hornbogen, E., & Starke, E. A. (1993). Predicting slip behavior in alloys containing shearable and strong particles. *Materials Science & Engineering.A, Structural Materials : Properties, Microstructure and Processing*, 169(1), 33-41. doi:10.1016/0921-5093(93)90596-7
- Bonaccorsi, L., Costanza, G., Missori, S., Sili, A., & Tata, M. E. (2012). Mechanical and metallurgical characterization of 8090 Al–Li alloy welded joints. *Metallurgist (New York)*, 56(1), 75-84. doi:10.1007/s11015-012-9539-2
- Boss, C. B., & Fredeen, K. J. (1999). *Concepts, instrumentation, and techniques in inductively coupled plasma optical emission spectrometry* (2nd ed.). USA: Perkin-Elmer.

- Bregianos, A. C., Crosky, A. G., Munroe, P. R., & Hellier, A. K. (2010). A study aimed at determining and understanding the fracture behaviour of an Al–Li–Cu–Mg–Zr alloy 8090. *International Journal of Fracture*, 161(2), 141-159. doi:10.1007/s10704-009-9439-z
- Brungraber, R. J., & Nelson, F.,G. (1973). *Effect of welding variables on aluminum alloy weldments* Welding Research Council.
- Burzić, Z., Čurović, J., Grahovac, N., & Stefanović, V. M. (1993). Strengthening of alloy 8090 and its fracture mechanics parameters. *Journal of Materials Science*, 28(22), 6136-6146. doi:10.1007/BF00365034
- Casavola, C. (2018). *Residual stress in friction stir welding and laser-assisted friction stir welding by numerical simulation and experiments* IntechOpen. doi:10.5772/intechopen.72271
- Cavaliere, P., De Santis, A., Panella, F., & Squillace, A. (2009). Effect of welding parameters on mechanical and microstructural properties of dissimilar AA6082–AA2024 joints produced by friction stir welding. *Materials & Design*, 30(3), 609-616. doi:<https://doi.org/10.1016/j.matdes.2008.05.044>
- Cavaliere, P., & Panella, F. (2008). Effect of tool position on the fatigue properties of dissimilar 2024-7075 sheets joined by friction stir welding. *Journal of Materials Processing Technology*, 206(1), 249-255. doi:10.1016/j.jmatprotec.2007.12.036
- Çengal, Y. A., & Turner, R. H. (2001). *Fundamentals of thermal-fluid sciences* (International Edition ed.). Singapore: McGraw-Hill Higher Education.
- Chand, S., Madhusudhan, D., Sravani, K. B., Uma, A., Sindhu, V., Devi, S. P., & Padmava, G. (2016). Study of microstructure, hardness and aging behaviour of 2014 aluminium alloy. *International Journal of Advances in Mechanical and Civil Engineering*, 3(3), 79-83.

- Concurrent Technologies Corporation. (2021a). CTC-led repair technologies deployed on navy ship. Retrieved from <https://www.ctc.com/public/newsandmedia/releases.aspx?ID=142>
- Concurrent Technologies Corporation. (2021b). Portable friction stir welder. Retrieved from https://www.ctc.com/public/files/factsheets/portable_fsw.pdf
- Dada, O. J. (2020). Review paper: Production and microstructural phenomena affecting friction stir welding mechanical behaviour and applications. *Acta Materialia Turcica*, 4, 1-39.
- Das, J., Robi, P. S., & Sankar, M. R. (2020). Assessment of parameters windows and tool pin profile on mechanical property and microstructural morphology of FSWed AA2014 joints. *SN Applied Sciences*, 2(1) doi:10.1007/s42452-019-1895-0
- Dawood, H. I., Mohammed, K. S., & Rajab, M. Y. (2014). Advantages of the green solid state FSW over the conventional GMAW process. *Advances in Materials Science and Engineering*, 2014, 1-10. doi:10.1155/2014/105713
- de Backer, J. (2015). In Puckrin E. (Ed.), *Conversation*
- Delijaicov, S., Silva, Patricia Aparecida de Oliveira, Resende, H. B., & Batalha, M. H. F. (2018). Effect of weld parameters on residual stress, hardness and microstructure of dissimilar AA2024-T3 and AA7475-T761 friction stir welded joints. *Materials Research (São Carlos, São Paulo, Brazil); Mat.Res*, 21(6) doi:10.1590/1980-5373-mr-2018-0108
- Devaraju, A. (2017). Influence of post-weld rapid cooling on grain size and mechanical properties of friction stir welded AA 2014. *Materials Today : Proceedings*, 4(2), 3722-3727. doi:10.1016/j.matpr.2017.02.267
- Dixon, W. J., & Mood, A. M. (1948). A method for obtaining and analyzing sensitivity data. *Journal of the American Statistical Association*, 43(241), 109-126. doi:10.1080/01621459.1948.10483254

- Dolgarrog Aluminium Limited. (2005). *Certificate of conformity approved certificate to EN10204 3.1 serial no. 73881*. Dolgarrog, Wales: Dolgarrog Aluminium Limited.
- Dong, Z., Yang, K., Ren, R., Wang, G., Wang, L., & Lv, Z. (2019). Friction stir lap welding 0.8-mm-thick 2024 aluminum alloy with the assistance of stationary shoulder. *Journal of Materials Engineering and Performance*, 28(11), 6704-6713. doi:10.1007/s11665-019-04395-3
- Dutta, I., Harper, C. P., & Dutta, G. (1994). Role of Al₂O₃ particulate reinforcements on precipitation in 2014 al-matrix composites. *Metallurgical and Materials Transactions.A, Physical Metallurgy and Materials Science*, 25(8), 1591-1602. doi:10.1007/BF02668525
- Eswara Prasad, N., Gokhale, A. A., & Wanhill, R. J. H. (2014). *Aluminium-lithium alloys: Process, properties and applications* (1st ed.). Oxford, UK: Butterworth-Heinemann.
doi:<https://doi.org/10.1016/C2012-0-00394-8> Retrieved from <https://www-sciencedirect-com.hallam.idm.oclc.org/book/9780124016989/aluminum-lithium-alloys#book-info>
- Frost, J. (2018). How to interpret R-squared in regression analysis. Retrieved from <https://statisticsbyjim.com/regression/interpret-r-squared-regression/>
- Frost, J. (2020). How to perform regression analysis using excel. Retrieved from <https://statisticsbyjim.com/regression/regression-analysis-excel/>
- Gallo, A. (2015, A refresher on regression analysis. *Harvard Business Review*, , Online.
Retrieved from <https://hbr.org/2015/11/a-refresher-on-regression-analysis>
- Ganiyu, M. (2019). How regression analysis works: Different forms of regression analysis and their applications. Retrieved from <https://towardsdatascience.com/how-regression-analysis-works-10f44c37b20a>
- Gazizov, M. R., Dubina, A. V., Zhemchuzhnikova, D. A., & Kaibyshev, R. O. (2015). Effect of equal-channel angular pressing and aging on the microstructure and mechanical

properties of an al-cu-mg-si alloy. *Physics of Metals and Metallography*, 116(7), 718-729.

doi:10.1134/S0031918X15070066

Gibson, B. T., Lammlein, D. H., Prater, T. J., Longhurst, W. R., Cox, C. D., Ballun, M. C., . . .

Strauss, A. M. (2014). Friction stir welding: Process, automation, and control. *Journal of Manufacturing Processes; Recent Developments in Welding Processes*, 16(1), 56-73.

doi:<https://doi.org/10.1016/j.jmapro.2013.04.002>

Giglio, M., Manes, A., Fossati, M., Mariani, U., & Giani, C. (2010). Comparison of fatigue crack

propagation behavior of al 2024 and al-li 8090 helicopter fuselage panels. *Journal of*

Testing and Evaluation, 38(1), 1-10. doi:10.1520/JTE101909

Grant, P. V., Lord, J. D., & Whitehead, P. S. (2006). *A national measurement good practice*

guide no. 53. the measurement of residual stresses by the incremental hole-drilling

technique - issue 2. (). Middlesex, UK: National Physical Laboratory. Retrieved from

[/eprintspublications.npl.co.uk//mgpg53.pdf](http://eprintspublications.npl.co.uk//mgpg53.pdf)

Grechnikov, F. V., & Nosova, E. A. (2017). Effect of composition and distribution of phases after

aging on stamp ability for aluminum alloy D16 (AA2014) sheets. *Russian Journal of Non-*

Ferrous Metals, 58(6), 625-631. doi:10.3103/S1067821217060037

Gregson, P. J., & Sinclair, I. (1996). Deviant crack path behaviour of aluminium-lithium alloy

AA8090 plate. *Proceedings of the Institution of Mechanical Engineers, Part G: Journal of*

Aerospace Engineering, 210(2), 117-121. doi:10.1243/PIME_PROC_1996_210_352_02

Griffee, C. C., Jensen, G. A., & Reinhart, T. L. Factors influencing the quality and properties of

aluminium lithium alloy welds. Paper presented at the *Fifth International Aluminum-*

Lithium Conference, Williamsburg, Virginia, 1425-1434.

- Guo, Y., Ma, Y., Zhang, X., Qian, X., & Li, J. (2020). Study on residual stress distribution of 2024-T3 and 7075-T6 aluminum dissimilar friction stir welded joints. *Engineering Failure Analysis, 118*, 104911. doi:10.1016/j.engfailanal.2020.104911
- Hadji, I., Badji, R., Gaceb, M., Kherrouba, N., & Rabahi, L. (2018). *Investigation of the effect of aluminum alloy position on residual stresses in dissimilar fsw weld by using the ultrasonic method* IOP Publishing. doi:10.1088/1757-899X/461/1/012022
- Hamilton, C., Kopyściański, M., Senkov, O., & Dymek, S. (2013). A coupled thermal/material flow model of friction stir welding applied to sc-modified aluminum alloys. *Metallurgical and Materials Transactions.A, Physical Metallurgy and Materials Science, 44(4)*, 1730-1740. doi:10.1007/s11661-012-1512-y
- Hattel, J. H., Sonne, M. R., & Tutum, C. C. (2015). Modelling residual stresses in friction stir welding of al alloys—a review of possibilities and future trends. *International Journal of Advanced Manufacturing Technology, 76(9)*, 1793-1805. doi:10.1007/s00170-014-6394-2
- He, W., Li, M., Song, Q., Liu, J., & Hu, W. (2019). Efficacy of external stationary shoulder for controlling residual stress and distortion in friction stir welding. *Transactions of the Indian Institute of Metals, 72(5)*, 1349–1359. doi:<https://doi-org.hallam.idm.oclc.org/10.1007/s12666-019-01630-2>
- Heller, K. (2019). *BR190025003, general rotary wing aviation onboard HMS queen elizabeth*. North Atlantic: Royal Navy.
- Hema, P., Sai Kumar Naik, K., & Ravindranath, K. (2017). Prediction of effect of process parameters on friction stir welded joints of dissimilar aluminium alloy AA2014 & AA6061 using taper pin profile. *Materials Today : Proceedings, 4(2)*, 2174-2183. doi:10.1016/j.matpr.2017.02.064

- Hendry, E. L., Bush, A., Ives, S., Board, I., Burton, M., info@metalweb.co.uk, . . . Forrest, H. (2014). *Emails from 10 metal stockists*
- Henry, S. D. (1995). *Fatigue data book : Light structural alloys* ASM International.
- Hepplewhite, M. (2013). In Hendry E. (Ed.), *RE: Business case*
- Hess, W. F., Wyant, R. A., & Winsor, F. J. (1947). *Technical note no. 1322. the spot welding of dissimilar aluminum alloys in the 0.040-inch thickness*. Washington, USA: National Advisory Committee for Aeronautics.
- Higgins, Raymond A. (1993). *Engineering Metallurgy. Part 1: Applied Physical Metallurgy* (6th Edition). Arnold.
- Holmes, T. M., Chin, E. S. C., Huang, P. J., & Pasternak, R. E. (1992). *Evaluation of 8090 and weldalite-049 aluminum-lithium alloys*. (). Massachusetts, USA: U.S. Army Materials Technology Laboratory. Retrieved from <https://apps.dtic.mil/dtic/tr/fulltext/u2/a258121.pdf>
- Huang, Y., Meng, X., Zhang, Y., Cao, J., & Feng, J. (2017). Micro friction stir welding of ultra-thin al-6061 sheets. *Journal of Materials Processing Technology*, 250, 313-319.
doi:10.1016/j.jmatprotec.2017.07.031
- Jamshidi Aval, H. (2015). Microstructure and residual stress distributions in friction stir welding of dissimilar aluminium alloys. *Materials & Design*, 87, 405-413.
doi:10.1016/j.matdes.2015.08.050
- Jeong, G., Park, J., Nam, S., Shin, S. -, Shin, J., Bae, D., & Choi, H. (2015). The effect of grain size on the mechanical properties of aluminum. *Archives of Metallurgy and Materials*, 60(2), 1287-1291. doi:10.1515/amm-2015-0115

- Ji, S., Li, Z., Zhou, Z., & Zhang, L. (2017). Microstructure and mechanical property differences between friction stir lap welded joints using rotating and stationary shoulders. *International Journal of Advanced Manufacturing Technology*, 90(9-12), 3045-3053. doi:10.1007/s00170-016-9640-y
- John, J., Shanmuganatan, S. P., Kiran, M. B., Senthil Kumar, V. S., & Krishnamurthy, R. (2019). Investigation of friction stir processing effect on AA 2014-T6. *Materials and Manufacturing Processes*, 34(2), 159-176. doi:10.1080/10426914.2018.1532577
- Jolu, T. L., Morgeneyer, T. F., & Gourgues-Lorenzon, A. (2010). Effect of joint line remnant on fatigue lifetime of friction stir welded Al–Cu–Li alloy. *Science and Technology of Welding and Joining*, 15(8), 694-698. doi:10.1179/136217110X12813393169453
- Kandil, F. A., Lord, J. D., Fry, A. T., & Grant, P. V. (2001). *A review of residual stress measurement methods – a guide to technique selection*. Middlesex, UK: National Physical Laboratory.
- Kaufman, J. Gilbert (2000). Understanding the Aluminium Temper Designation System. *Introduction to Aluminium Alloys and Tempers*. (pp 39-76). ASM International.
- Kebriyaei, A., Mirdamadi, S. S., & Saghafian, H. (2017). Effect of heat treatment on the mechanical and tribological properties of AA8090/6% SiCp composite. *Science and Engineering of Composite Materials*, 24(1), 129-138. doi:10.1515/secm-2014-0133
- Kostrivas, A., & Lippold, J. C. (1999). Weldability of li-bearing aluminium alloys. *International Materials Reviews*, 44(6), 217-237. doi:10.1179/095066099101528289
- Kramer, L. S., Heubaum, F. H., & Pickens, J. R. The weldability of high-strength al-cu-li alloys. Paper presented at the *Fifth International Aluminum-Lithium Conference, Williamsburg, Virginia*, 1415-1424.

- Ku, M., Hung, F., & Lui, T. (2019). Embrittlement due to excess heat input into friction stir processed 7075 alloy. *Materials; Materials (Basel)*, 12(2), 227. doi:10.3390/ma12020227
- Kulkarni, G. J., Banerjee, D., & Ramachandran, T. R. (1989). Physical metallurgy of aluminium-lithium alloys. *Bulletin of Materials Science*, 12(3-4), 325-340.
doi:<https://doi.org/10.1007/BF02747140>
- Kumar, N., Mishra, R. S., & Baumann, J. A. (2014). *Residual stresses in friction stir welding*. Waltham, MA: Butterworth-Heinemann.
- Latuta, E. (2021). In Puckrin E. (Ed.), *RE: Call#051N002307 FW: -[EXT] - NanoAnalysis contact form - EDS*
- Lee, H., Lee, Y. R., & Min, K. J. (2016). Effects of friction stir welding speed on AA2195 alloy. *MATEC Web of Conferences*, 45, 1003. doi:10.1051/mateconf/20164501003
- Leonardo. (2016). Leonardo: First royal navy AW101 merlin Mk4 makes its maiden flight.
Retrieved from <https://www.leonardocompany.com/en/press-release-detail/-/detail/volo-inaugurale-aw101-royal-navy-maiden-flight>
- Lertora, E., & Gambaro, C. (2010). AA8090 al-li alloy FSW parameters to minimize defects and increase fatigue life. *International Journal of Material Forming*, 3(1), 1003-1006.
doi:<https://doi-org.hallam.idm.oclc.org/10.1007/s12289-010-0939-1>
- Li, D., Yang, X., Cui, L., He, F., & Shen, H. (2014). Effect of welding parameters on microstructure and mechanical properties of AA6061-T6 butt welded joints by stationary shoulder friction stir welding. *Materials and Design*, 64, 251-260.
doi:10.1016/j.matdes.2014.07.046

- Li, D., Yang, X., Cui, L., He, F., & Zhang, X. (2015). Investigation of stationary shoulder friction stir welding of aluminum alloy 7075-T651. *Journal of Materials Processing Technology*, 222, 391-398. doi:10.1016/j.jmatprotec.2015.03.036
- Li, Y., Sun, D., & Gong, W. (2019). Effect of tool rotational speed on the microstructure and mechanical properties of bobbin tool friction stir welded 6082-T6 aluminum alloy. *Metals (Basel)*, 9(8), 894. doi:10.3390/met9080894
- Li, Z., Yue, Y., Ji, S., Chai, P., & Zhou, Z. (2016). Joint features and mechanical properties of friction stir lap welded alclad 2024 aluminum alloy assisted by external stationary shoulder. *Materials & Design*, 90, 238-247.
doi:<https://doi.org/10.1016/j.matdes.2015.10.056>
- Liao, Y. (2006). Practical electron microscopy and database. *An Online Book*,
- Lin, S. B., Zhao, Y. H., & Wu, L. (2006). Integral and layered mechanical properties of friction stir welded joints of 2014 aluminium alloy. *Materials Science and Technology*, 22(8), 995-998.
doi:10.1179/174328406X102408
- Lippold, J. C. Weldability of commercial aluminium-lithium alloys. Paper presented at the *Fifth International Aluminum-Lithium Conference, Williamsburg, Virginia*, 1365-1376.
- Liu, H. J., Li, J. Q., & Duan, W. J. (2013a). Friction stir welding characteristics of 2219-T6 aluminum alloy assisted by external non-rotational shoulder. *International Journal of Advanced Manufacturing Technology*, 64(9), 1685-1694. doi:10.1007/s00170-012-4132-1
- Long, T., Tang, W., & Reynolds, A. P. (2007). Process response parameter relationships in aluminium alloy friction stir welds. *Science and Technology of Welding and Joining*, 12(4), 311-317. doi:10.1179/174329307X197566

- Longhurst, W. R., Cox, C. D., Gibson, B. T., Cook, G. E., Strauss, A. M., Wilbur, I. C., & Osborne, B. E. (2017). Development of friction stir welding technologies for in-space manufacturing. *International Journal of Advanced Manufacturing Technology*, 90(1), 81-91. doi:10.1007/s00170-016-9362-1
- Lynch, S. P. (1991). Fracture of 8090 Al–Li plate I. short transverse fracture toughness. *Materials Science & Engineering.A, Structural Materials : Properties, Microstructure and Processing*, 136, 25-43. doi:10.1016/0921-5093(91)90439-T
- Lynch, S. P., Wilson, A. R., & Byrnes, R. T. (1993). Effects of ageing treatments on resistance to intergranular fracture of 8090 Al–Li alloy plate. *Materials Science & Engineering.A, Structural Materials : Properties, Microstructure and Processing*, 172(1-2), 79-93. doi:10.1016/0921-5093(93)90428-H
- Magnier, A., Zinn, W., Niendorf, T., & Scholtes, B. (2017). Residual stress analysis on thin metal sheets using the incremental hole drilling method - fundamentals and validation. *Experimental Techniques*, 43(1), 65-79.
- Martin, J. P. (2013). Stationary shoulder friction stir welding. In H. Fujii (Ed.), *Proceedings of the 1st international joint symposium on joining and welding* (pp. 477-482) Woodhead Publishing. doi:<https://doi.org/10.1533/978-1-78242-164-1.477> Retrieved from <http://www.sciencedirect.com/science/article/pii/B978178242163450078X>
- Masoumi Khalilabad, M., Zedan, Y., Texier, D., Jahazi, M., & Bocher, P. (2018). Effect of tool geometry and welding speed on mechanical properties of dissimilar AA2198–AA2024 FSWed joint. *Journal of Manufacturing Processes*, 34, 86-95. doi:10.1016/j.jmapro.2018.05.030
- Masoumi Khalilabad, M., Zedan, Y., Texier, D., Jahazi, M., & Bocher, P. (2021). Effect of heat treatments on microstructural and mechanical characteristics of dissimilar friction stir

welded 2198/2024 aluminum alloys. *Journal of Adhesion Science and Technology*, , 1-19.

doi:10.1080/01694243.2021.1917868

Masoumi, M., Zedan, Y., Texier, D., Jahazi, M., & Bocher, P. (2016). *Friction stir welding of AA2024 and AA2198 aluminum alloys: Effect of tool geometry and process parameters*

MatWeb Metal Material Data Sheets, (MDS). (2021). *Table 2. metals material properties (metric units)* Knovel.

Miller, W. S., White, J., & Lloyd, D. J. (1987). The physical metallurgy of aluminium-lithium-copper-magnesium-zirconium alloys - 8090 and 8091. *Journal De Physique Colloques*, 48 (C3)(3), C3 139-149. doi:<http://dx.doi.org/10.1051/jphyscol:1987317>

Ministry of Defence. (no_datea). 1710 squadron. Retrieved from

<https://www.royalnavy.mod.uk/our-organisation/the-fighting-arms/fleet-air-arm/support-and-training/1710-squadron>

Ministry of Defence. (no_dateb). Merlin. Retrieved from <https://des.mod.uk/what-we-do/navy-procurement-support/merlin-helicopter/>

Mishra, R. S., De, P. S., & Kumar, N. (2014). *Friction stir welding and processing*. Switzerland: Springer.

Moradi, M. M., Jamshidi Aval, H., Jamaati, R., Amirkhanlou, S., & Ji, S. (2018). Microstructure and texture evolution of friction stir welded dissimilar aluminum alloys: AA2024 and AA6061. *Journal of Manufacturing Processes*, 32, 1-10. doi:10.1016/j.jmapro.2018.01.016

Muhammad, W., Husain, W., Tauqir, A., Wadood, A., Zaigham, H., & Ur rehman, M. A. (2021). Assessment of microstructure and mechanical properties of friction stir welded AA2014-O and AA2014-T6 sheets. *International Journal of Advanced Manufacturing Technology*, doi:10.1007/s00170-021-07249-2

- Nadikudi, B. K. B. (2021). Effect of friction stir welding tool profiles on mechanical properties of dissimilar welded aluminum alloy plates. *International Journal of Structural Integrity, ahead-of-print(-)* doi:10.1108/IJSI-10-2020-0097
- Narender, G., Ramjee, E., & Prasad, N. E. (2019). In-plane anisotropy and tensile deformation behaviour of aluminium alloy AA 2014 forge plates. *Sadhana (Bangalore)*, 44(1), 1-14. doi:10.1007/s12046-018-0994-8
- NavalToday.com. (2018). Royal navy receives first upgraded merlin Mk4 helicopter. Retrieved from <https://www.navaltoday.com/2018/05/25/royal-navy-receives-first-upgraded-merlin-mk4-helicopter/>
- Neto, D. M., & Neto, P. (2013). Numerical modeling of friction stir welding process: A literature review. *The International Journal of Advanced Manufacturing Technology*, 65(1-4), 115-126. Retrieved from <https://doi-org.hallam.idm.oclc.org/10.1007/s00170-012-4154-8>
- Oettel, R. (2000). The determination of uncertainties in residual stress measurement (using the hole-drilling technique). *Standards Measurement & Testing Project no. SMT4-CT97-2195. Manual of Codes of Practice for the Determination of Uncertainties in Mechanical Tests on Metallic Materials*, 15(1), COP 15. Retrieved from npl.co.uk/getmedia/71c7d09a-9df3-4484-ad0e-ba57e9570a34/cop15
- Oxford Instruments. (2010). *Installation and user's guide: Inca x-stream and mics*. Buckinghamshire: Oxford Instruments.
- Padmasubashini, V., Sunilkumar, B., Krishnakumar, M., & George, J. (2020). A comparative study of the principal approaches for the estimation of measurement uncertainty for the ICP-OES determination of the light rare earth elements, yttrium and uranium in rock samples. *Journal of Radioanalytical and Nuclear Chemistry*, 325(1), 229-236.

- Panthri, S., Joshi, A., & Pathak, M. K. (2019). Effect of room temperature rolling followed by annealing on tensile and fracture behaviour of bulk ultrafine-grained Al–Li 8090 alloy. *Metallography, Microstructure, and Analysis*, 8(5), 581-590. doi:10.1007/s13632-019-00570-z
- Panwar, R., & Chandna, P. (2021). An experimental investigation of al-li alloy 8090 joint fabricated with friction stir welding (FSW) process by taguchi-based DOE, for predicting thermal behaviour, mechanical and metallurgical characteristics. *Ilkogretim Online - Elementary Education Online*, 20(4), 285-299.
- Park, S., Joo, Y., & Kang, M. (2020). Effect of backing plate materials in micro-friction stir butt welding of dissimilar aa6061-t6 and aa5052-h32 aluminum alloys. *Metals (Basel)*, 10(7), 1-9. doi:10.3390/met10070933
- Patel, V., Li, W., Liu, X., Wen, Q., & Su, Y. (2019). Through-thickness microstructure and mechanical properties in stationary shoulder friction stir processed AA7075. *Materials Science and Technology*, 35(14), 1762-1769. doi:10.1080/02670836.2019.1641459
- Pedemonte, M., Gambaro, C., Lertora, E., & Mandolino, C. (2013). Fatigue assessment of AA 8090 friction stir butt welds after surface finishing treatment. *Aerospace Science and Technology*, 27(1), 188-192. doi:<https://doi.org/10.1016/j.ast.2012.08.006>
- Peral, D., de Vicente, J., Porro, J. A., & Ocana, J. L. (2017). Uncertainty analysis for non-uniform residual stresses determined by the hole drilling strain gauge method. *Measurement: Journal of the International Measurement Confederation*, 97(02), 51-63.
- Pittman, R. (2017). *The merlin EH(AW) 101 from design to front line* Amberley Publishing.

- Pollak, R., Palazotto, A., & Nicholas, T. (2006). A simulation-based investigation of the staircase method for fatigue strength testing. *Mechanics of Materials*, 38(12), 1170-1181.
doi:<https://doi.org/10.1016/j.mechmat.2005.12.005>
- Ponte, M. (2007). *Studio teorico ed applicativo della tecnologia friction stir welding su leghe di alluminio e materiali compositi a matrice metallica*
- Prasad, K. Satya (1999). *Solid state transformations in AA8090 Al-Li alloys* [Doctoral dissertation, University of Roorkee].
- Prasad, N. E., Gokhale, A. A., & Rao, P. R. (2003). Mechanical behaviour of aluminium-lithium alloys. *Sadhana (Bangalore)*, 28(1), 209-246. doi:10.1007/BF02717134
- Raabe, D. (2014). 23 - recovery and recrystallization: Phenomena, physics, models, simulation. In D. E. Laughlin, & K. Hono (Eds.), *Physical metallurgy (fifth edition)* (pp. 2291-2397). Oxford: Elsevier. doi:<https://doi.org/10.1016/B978-0-444-53770-6.00023-X> Retrieved from <https://www.sciencedirect.com/science/article/pii/B978044453770600023X>
- Rajendran, C., Anudeep, S., & Ajith, R. (2019). Influences of welding speed on mechanical properties of friction stir welded joints of AA2014-T6 aluminium alloys. *International Journal of Innovative Technology and Exploring Engineering (IJITEE)*, 8(4S), 2278-3075.
- Rajendran, C., Parthiban, G., Pranav, K., & Nithi Balaji, S. P. (2021). Influence of solution treatment and artificial aging on Fracture load of friction stir welded lap joints of AA2014-T6. *IOP Conference Series. Materials Science and Engineering; IOP Conf.Ser.: Mater.Sci.Eng*, 1059(1), 12037. doi:10.1088/1757-899X/1059/1/012037
- Rajendran, C., Srinivasan, K., Balasubramanian, V., Balaji, H., & Selvaraj, P. (2016). Influences of post weld heat treatment on tensile strength and microstructure characteristics of friction

stir welded butt joints of AA2014-T6 aluminum alloy. *Journal of Mechanical Behaviour of Materials*, 25(3), 89-98. doi:10.1515/jmbm-2016-0011

Rajendran, C., Srinivasan, K., Balasubramanian, V., Balaji, H., & Selvaraj, P. (2019a). Evaluation of load-carrying capabilities of friction stir welded, TIG welded and riveted joints of AA2014-T6 aluminium alloy. *Aircraft Engineering and Aerospace Technology*, 91(9), 1238-1244. doi:10.1108/AEAT-11-2017-0233

Rajendran, C., Srinivasan, K., Balasubramanian, V., Balaji, H., & Selvaraj, P. (2019b). Identifying combination of friction stir welding parameters to maximize strength of lap joints of AA2014-T6 aluminium alloy. *Australian Journal of Mechanical Engineering*, 17(2), 64-75. doi:10.1080/14484846.2017.1304843

Rajendran, C., Srinivasan, K., Balasubramanian, V., Balaji, H., & Selvaraj, P. (2018). Identifying the combination of friction stir welding parameters to attain maximum strength of AA2014-T6 aluminum alloy joints. *Advances in Materials and Processing Technologies (Abingdon, England)*, 4(1), 100-119. doi:10.1080/2374068X.2017.1410687

Rajendran, C., Srinivasan, K., Balasubramanian, V., Balaji, H., & Selvaraj, P. (2019). Mechanical properties and microstructural characteristics of friction stir welded AA2014-T6 aluminium alloy joints. *Journal of Mechanical Behaviour of Materials*, 28(1), 169-185. doi:10.1515/jmbm-2019-0019

Ramanjaneyulu, K., Madhusudhan Reddy, G., Venugopal Rao, A., & Markandeya, R. (2013). Structure-property correlation of AA2014 friction stir weld: Role of tool pin profile. *Journal of Materials Engineering and Performance*, 22(8), 2224-2240. doi:[https://doi-org.hallam.idm.oclc.org/10.1007/s11665-013-0512-4](https://doi.org.hallam.idm.oclc.org/10.1007/s11665-013-0512-4)

- Raturi, M., & Bhattacharya, A. (2020). *Post corrosion tensile strength and failure of dissimilar friction stir welded aluminium alloys*. Les Ulis: EDP Sciences.
doi:10.1051/mateconf/202032604008
- Raturi, M., Garg, A., & Bhattacharya, A. (2019). Tensile strength and failure of dissimilar friction stir welded joints between 6061-T6 and 2014-T6 aluminum alloys. *Procedia Structural Integrity*, 17, 495-502. doi:10.1016/j.prostr.2019.08.065
- Reddy, L. K. (2007). *Principles of engineering metallurgy* New Age International (P) Limited.
Retrieved from <https://books.google.co.uk/books?id=-blz0lpQwiIC>
- Robe, H., Zedan, Y., Chen, J., Monajati, H., Feulvarch, E., & Bocher, P. (2015). Microstructural and mechanical characterization of a dissimilar friction stir welded butt joint made of AA2024-T3 and AA2198-T3. *Materials Characterization*, 110, 242-251.
doi:10.1016/j.matchar.2015.10.029
- Rohith Renish, R., Pranesh, M. A., & Logesh, K. (2018). Design and analysis of a portable friction stir welding machine. *Materials Today : Proceedings*, 5(9), 19340-19348.
doi:10.1016/j.matpr.2018.06.293
- Royal Navy. (no_date). Merlin Mk2. Retrieved from <https://www.royalnavy.mod.uk/the-equipment/aircraft/helicopters/merlin-mk2>
- Roylance, D. (2001). *Fatigue*. Massachusetts, USA: Massachusetts Institute of Technology.
- Ruzek, R., & Kadlec, M. (2014). Friction stir welded structures: Kissing bond defects. *International Journal of Terraspace Science and Engineering*, 6(2), 77-83.
- Saleh, A. A. (2018). Effect of heat treatment on the mechanical properties of AA2014 alloy. *Contemporary Engineering Sciences*, 11(69), 3409-3419.

- Saravanan, V., Banerjee, N., Amuthakkannan, R., & Rajakumar, S. (2015). Microstructural evolution and mechanical properties of friction stir welded dissimilar AA2014-T6 and AA7075-T6 aluminum alloy joints. *Metallography, Microstructure, and Analysis*, 4(3), 178-187. doi:10.1007/s13632-015-0199-z
- Sato, Shiro & Endo, Takashi (1986). Relation between tensile strength and hardness of aluminium alloys. *Keikin-zoku; J. Japan Inst. Light Metals*, 36(1), 29-35. Doi: 10.2464/jilm.36.29
- Sattari, S., Bisadi, H., & Sajed, M. (2012). Mechanical properties and temperature distributions of thin friction stir welded sheets of AA5083. *International Journal of Mechanics and Applications*, 2(1), 1-6. doi:10.5923/j.mechanics.20120201.01
- Satyanarayana, M., & Kumar, A. (2019). Effect of heat treatment on AA2014 alloy processed through multi-pass friction stir processing. *Journal of Physics.Conference Series; J.Phys.: Conf.Ser*, 1240(1), 12077. doi:10.1088/1742-6596/1240/1/012077
- Schajer, G. S. (1988). Measurement of non-uniform residual stresses using the hole drilling method. *J. Eng. Materials and Technology*, 110(4), Part 1 pp338-349.
- Schajer, G. S., & Altus, E. (1996). Stress calculation error analysis for incremental hole-drilling residual stress measurements. *Journal of Engineering Materials and Technology*, 118(1), 120-126.
- Schajer, G., & Whitehead, P. S. (2013). Hole drilling and ring coring. *Practical residual stress measurement methods* (pp. 29-50). Chichester, UK: John Wiley & Sons Inc.
- Schempp, P., Cross, C. E., Häcker, R., Pittner, A., & Rethmeier, M. (2013). Influence of grain size on mechanical properties of aluminium GTA weld metal. *Welding in the World*, 57(3), 293-304. doi:10.1007/s40194-013-0026-6

- Schneider, J., Brooke, S., & Nunes Jr, A.,C. (2016). Material flow modification in a FSW through introduction of flats. *Metallurgical and Materials Transactions B*, 47(1), 720-730.
doi:10.1007/s11663-015-0523-7
- Scialpi, A., De Giorgi, M., De Filippis, L., Nobile, R., & Panella, F. W. (2008). Mechanical analysis of ultra-thin friction stir welding joined sheets with dissimilar and similar materials. *Materials and Design*, 29, 928-936. Retrieved from <https://pdf.sciencedirectassets.com/271569/1-s2.0-S0261306908X00032/1-s2.0-S0261306907000891/>
- Sejani, D., Li, W., & Patel, V. (2021). Stationary shoulder friction stir welding – low heat input joining technique: A review in comparison with conventional FSW and bobbin tool FSW. *Null*, , 1-50. doi:10.1080/10408436.2021.1935724
- Serio, L. M., Palumbo, D., De Filippis, L., Alberto Ciro, Galietti, U., & Ludovico, A. D. (2016). Effect of friction stir process parameters on the mechanical and thermal behavior of 5754-H111 aluminum plates. *Materials; Materials (Basel)*, 9(3), 122.
doi:10.3390/ma9030122
- Sidhy, M. S., & Chatha, S. S. (2012). Friction stir welding – process and its variables: A review. *International Journal of Emerging Technology and Advanced Engineering*, 2(12), 275-279.
- Sillapasa, K., Mutoh, Y., Miyashita, Y., & Seo, N. (2017). Fatigue strength estimation based on local mechanical properties for aluminum alloy FSW joints. *Materials*, 10(2), 186.
doi:<http://dx.doi.org/10.3390/ma10020186>
- Singh, A. K., Sahlot, P., Paliwal, M., & Arora, A. (2019). Heat transfer modeling of dissimilar FSW of al 6061/AZ31 using experimentally measured thermo-physical properties. *International Journal of Advanced Manufacturing Technology*, 105(1), 771-783. doi:10.1007/s00170-019-04276-y

- Singh, S., & Goel, D. B. (2005). Influence of thermomechanical aging on fatigue behaviour of 2014 Al-alloy. *Bulletin of Materials Science*, 28(2), 91-96. doi:10.1007/BF02704225
- Sinhmar, S., & Dwivedi, D. K. (2020a). Art of friction stir welding to produce weld joint without rotation of shoulder with narrow heat-affected zone and high corrosion resistance. *Science and Technology of Welding and Joining*, 25(6), 490-495. doi:10.1080/13621718.2020.1746512
- Sinhmar, S., & Dwivedi, D. K. (2020b). Mechanical behavior of FSW joint welded by a novel designed stationary shoulder tool. *Journal of Materials Processing Technology*, 277, 116482. doi:10.1016/j.jmatprotec.2019.116482
- SINT Technology. (None). *RESTAN. system for measuring residual stress by the hole-drilling method. EVAL software. back calculation manual*. Calenzano (FI), Italy: SINT Technology.
- Sivaprasad, K., Muthupandi, V., Shankar, M. P., & Sokkalingam, R. (2019). Correlating tensile properties with microstructures of various regions in gas tungsten arc welded AA2014 alloy. *Materials Science Forum*, 969, 22-26. doi:10.4028/www.scientific.net/MSF.969.22
- Sivaraman, P., Nithyanandhan, T., Karthick, M., Kirivasan, S. M., Rajarajan, S., & Sundar, M. S. (2021). Analysis of tensile strength of AA 2014 and AA 7075 dissimilar metals using friction stir welding. *Materials Today : Proceedings*, 37, 187-192. doi:10.1016/j.matpr.2020.04.895
- Slater, A. (2018a). *SMI rec 003 1474 tensile testing uncertainties*. Portsmouth, UK: 1710 Naval Air Squadron.
- Slater, A. (2018b). *SMI rec 005 hardness uncertainty*. Portsmouth, UK: 1710 Naval Air Squadron.

- Slater, A. (2019). *SMI pro 109 estimating uncertainty*. Portsmouth, UK: 1710 NAvAl Air Squadron.
- Smith, A. F. Uses and properties of Al-Li on the new EH101 helicopter. Paper presented at the *67th Structures and Materials Panel*, Chapter 19, 1-19.
- Sohn, K., Lee, S., & Kim, N. J. (1993). In situ observation of microfracture processes in an 8090 Al-Li alloy plate. *Materials Science and Engineering: A*, 163(1), 11-21.
doi:[https://doi.org/10.1016/0921-5093\(93\)90573-W](https://doi.org/10.1016/0921-5093(93)90573-W)
- Srivatsan, T. S., & Place, T. A. (1989). Microstructure, tensile properties and fracture behaviour of an Al-Cu-Li-Mg-Zr alloy 8090. *Journal of Materials Science*, 24(5), 1543-1551.
doi:10.1007/BF01105669
- Styles, M. J., Marceau, R. K. W., Bastow, T. J., Brand, H. E. A., Gibson, M. A., & Hutchinson, C. R. (2015). The competition between metastable and equilibrium S (Al₂CuMg) phase during the decomposition of Al-Cu-Mg alloys. *Acta Materialia*, 98, 64-80.
doi:10.1016/j.actamat.2015.07.011
- Sun, T., Roy, M. J., Strong, D., Withers, P. J., & Prangnell, P. B. (2017). Comparison of residual stress distributions in conventional and stationary shoulder high-strength aluminum alloy friction stir welds. *Journal of Materials Processing Technology*, 242, 92-100.
doi:10.1016/j.jmatprotec.2016.11.015
- Tao, Y., Zhang, Z., Ni, D. R., Wang, D., Xiao, B. L., & Ma, Z. Y. (2014). Influence of welding parameter on mechanical properties and fracture behavior of friction stir welded Al-Mg-Sc joints. *Materials Science & Engineering.A, Structural Materials : Properties, Microstructure and Processing*, 612, 236-245. doi:10.1016/j.msea.2014.06.051

Teh, N. J., Goddin, H. & Whitaker, A. (no_date). Developments in micro applications of friction stir welding. Retrieved from . <https://www.twi-global.com/technical-knowledge/published-papers/developments-in-micro-applications-of-friction-stir-welding>

The British Standards Institution. (1978a). *British standards aerospace series BS L165:1978 specification for sheet and strip of aluminium-coated aluminium-copper-magnesium-silicon-manganese alloy (solution treated and artificially aged) (cu 4.4, mg 0.5, si 0.8, mn 0.8)*. London: British Standards Institution (BSI).

The British Standards Institution. (1978b). BS L 157:1978 specification for sheet and strip of aluminium-copper-magnesium-silicon-manganese alloy (solution treated and artificially aged) (cu 4.4, mg 0.5, si 0.8, mn 0.8).

The British Standards Institution. (2003). *BS ISO 12107:2003 metallic materials - fatigue testing - statistical planning and analysis of data*. UK: The British Standards Institution.

The British Standards Institution. (2006). *BS EN 2002-1:2005 aerospace series. metallic materials. test methods. tensile testing at ambient temperature*. UK: The British Standards Institution.

The British Standards Institution. (2016). BS L167:1978 bibliographic data. Retrieved from <https://bsol.bsigroup.com/Bibliographic/BibliographicInfoData/00000000030069640>

The British Standards Institution. (2017). *Bs en iso/ iec 17025:2017*. UK: The British Standards Institution.

The British Standards Institution. (2018). *BS EN ISO 6507-1:2018 metallic materials. vickers hardness test. test method*. UK: The British Standards Institution.

The British Standards Institution. (2020a). *BS EN ISO 25239-4. friction stir welding. aluminium. specification and qualification of welding procedures*. BSI.

The British Standards Institution. (2020b). *BS EN ISO 6892-1:2019 metallic materials. testing testing. method of testing at room temperature*. UK: The British Standards Institution.

The Welding Institute. (2013). *Friction stir welding operator* The Welding Institute.

Thomas, W. M. Friction stir welding and related friction process characteristics . Paper presented at the *INALCO '98, 7th International Conference on Joints in Aluminium*,

Thomas, W. M., Nicholas, E. D., Needham, J. C., Murch, M. G., Temple-Smith, P., & Dawes, C. J. (1991). In The Welding Institute (Ed.), *Improvements relating to friction welding*. Europe:

Threadgill, P. L., Leonard, A. J., Shercliff, H. R., & Withers, P. J. (2009). Friction stir welding of aluminium alloys. *International Materials Reviews*, 54(2), 49-93.

doi:10.1179/174328009X411136

Threadgill, P. L., & Leonard, A. J. (1999). *Macro and microstructural features of friction stir welds in various materials*. (). Great Abington, UK: The Welding Institute. Retrieved from <https://www.twi-global.com/pdfs/Industrial-Member-Reports/mr693.pdf>

Vasudévan, A. K., & Doherty, R. D. (1987). Grain boundary ductile fracture in precipitation hardened aluminum alloys. *Acta Metallurgica*, 35(6), 1193-1219. doi:10.1016/0001-6160(87)90001-0

Venkateswara Rao, R., & Senthil Kumar, M. (2020). Effect of pin geometry on material flow characteristics of friction stir welded dissimilar AA6061/AA2014 alloys. *Australian Journal of Mechanical Engineering*, , 1-15. doi:10.1080/14484846.2020.1723864

Verma, S., Gupta, M., & Mishra, J. P. (2016). Friction stir welding of aerospace materials: A state of art review. In B. Katalinic (Ed.), *DAAAM international scientific book* (pp. 135-150). Vienna, Austria: DAAAM International. doi:10.2507/daaam.scibook.2016.13

- Verma, S., & Misra, J. P. (2021). Experimental investigation on friction stir welding of dissimilar aluminium alloys. *Proceedings of the Institution of Mechanical Engineers. Part E, Journal of Process Mechanical Engineering*, 235(5), 1545-1554. doi:10.1177/09544089211008694
- Vidal, C., Infante, V., & Vilaça, P. (2010). Assessment of improvement techniques effect on fatigue behaviour of friction stir welded aerospace aluminium alloys. *Procedia Engineering; Fatigue 2010*, 2(1), 1605-1616.
doi:<https://doi.org/10.1016/j.proeng.2010.03.173>
- Vigraman, T., Krishna, M. V., & Kumar, M. V. S. P. (2021). Fine grain formation during phase transformation of a thermo-mechanically treated AA8090. *Materials Today : Proceedings*, 43, 844-850. doi:10.1016/j.matpr.2020.06.556
- Wang, X., Pan, Y., & Lados, D. A. (2018). Friction stir welding of dissimilar al/al and al/non-al alloys: A review. *Metallurgical and Materials Transactions.B, Process Metallurgy and Materials Processing Science*, 49(4), 2097-2117. doi:10.1007/s11663-018-1290-z
- Wanhill, R. J. H. (1994). Status and prospects for aluminium-lithium alloys in aircraft structures. *International Journal of Fatigue*, 16(1), 3-20. doi:[https://doi.org/10.1016/0142-1123\(94\)90441-3](https://doi.org/10.1016/0142-1123(94)90441-3)
- Wanhill, R. J. H., Symonds, N., Merati, A., Pasang, T., & Lynch, S. P. (2013). Five helicopter accidents with evidence of material and/or design deficiencies. *Engineering Failure Analysis*, 35, 133-146. doi:10.1016/j.engfailanal.2012.12.002
- Westland. (2018). *Westland helicopter process specification (W.H.P.S.) 439 hardness and electrical conductivity testing of metallic materials*
- Wilson Aero Metals Alliance. (2016). *Certificate of conformity R00174695*. Cambridgeshire, England: Wilson Aero Metals Alliance.

- Wong, J. (2020). Linear regression explained: A high-level overview of linear regression analysis. Retrieved from <https://towardsdatascience.com/linear-regression-explained-1b36f97b7572>
- Wu, H. (2017). *Systematic analysis of the advantages of stationary shoulder friction stir welding in joining high strength aluminium alloy AA7050-T7651*
- Wu, H., Chen, Y., Strong, D., & Prangnell, P. (2015). Stationary shoulder FSW for joining high strength aluminum alloys. *Journal of Materials Processing Technology*, 221, 187-196. doi:<https://doi.org/10.1016/j.jmatprotec.2015.02.015>
- Wu, P., Deng, Y., Fan, S., Ji, H., & Zhang, X. (2018). A study on dissimilar friction stir welded between the al-li-cu and the al-zn-mg-cu alloys. *Materials; Materials (Basel)*, 11(7), 1132. doi:10.3390/ma11071132
- Wu, T., Zhao, F., Luo, H., Wang, H., & Li, Y. (2019). Temperature monitoring and material flow characteristics of friction stir welded 2A14-t6 aerospace aluminum alloy. *Materials*, 12(20), 3387. doi:10.3390/ma12203387
- Xue, P., Ni, D. R., Wang, D., Xiao, B. L., & Ma, Z. Y. (2011). Effect of friction stir welding parameters on the microstructure and mechanical properties of the dissimilar Al–Cu joints. *Materials Science & Engineering.A, Structural Materials : Properties, Microstructure and Processing*, 528(13), 4683-4689. doi:10.1016/j.msea.2011.02.067
- Yang, H., Zhao, H., Xu, X., Zhou, L., Zhao, H., & Liu, H. (2021). Effect of stirring pin rotation speed on microstructure and mechanical properties of 2A14-T4 alloy T-joints produced by stationary shoulder friction stir welding. *Materials; Materials (Basel)*, 14(8), 1938. doi:10.3390/ma14081938

- You, J., Zhao, Y., Dong, C., Wang, C., Miao, S., Yi, Y., & Su, Y. (2020). Microstructure characteristics and mechanical properties of stationary shoulder friction stir welded 2219-T6 aluminium alloy at high rotation speeds. *International Journal of Advanced Manufacturing Technology*, 108(4), 987-996. doi:10.1007/s00170-019-04594-1
- Yue, Y., Wang, G., Yang, K., Wu, B., & Yan, D. (2018). Friction stir butt welding thin aluminum alloy sheets. *International Journal of Advanced Manufacturing Technology*, 96(9), 3139-3147. doi:10.1007/s00170-018-1798-z
- Zapata, J., Toro, M., & López, D. (2016). Residual stresses in friction stir dissimilar welding of aluminum alloys. *Journal of Materials Processing Technology*, 229, 121-127. doi:10.1016/j.jmatprotec.2015.08.026
- Zettler, R., Vugrin, T., & Schmucker, M. (2010). Effects and defects of friction stir welds. In D. Lohwasser, & Z. Chen (Eds.), *Friction stir welding: From basics to applications* (pp. 245-276). Cambridge, UK: Woodhead Publishing Limited.
- Zhang, H., Wang, M., Zhou, W., Zhang, X., Zhu, Z., Yu, T., & Yang, G. (2015). Microstructure–property characteristics of a novel non-weld-thinning friction stir welding process of aluminum alloys. *Materials & Design*, 86, 379-387. doi:10.1016/j.matdes.2015.06.106
- Zhang, L., & Wang, X. (2018). Microstructure evolution and properties of friction stir welding joint for 6082-T6 aluminum alloy. *Materials Research (São Carlos, São Paulo, Brazil); Mat.Res*, 21(6) doi:10.1590/1980-5373-mr-2018-0285
- Zhang, T., He, Y., Shao, Q., Zhang, H., & Wu, L. Comparative study on fatigue properties of friction stir welding joint and lap joint. Paper presented at the *13th International Conference on Fracture 2013*, 1604-1613.

- Zhang, Z., Xiao, B., Wang, D., & Ma, Z. Y. (2011). Effect of alclad layer on material flow and defect formation in friction-stir-welded 2024 aluminum alloy. *Metallurgical and Materials Transactions A. Physical Metallurgy and Materials Science*, 42A(6), 1717-1726.
doi:10.1007/s11661-010-0545-3
- Zhao, Y., Lin, S., Wu, L., & Qu, F. (2005). The influence of pin geometry on bonding and mechanical properties in friction stir weld 2014 al alloy. *Materials Letters*, 59(23), 2948-2952. doi:10.1016/j.matlet.2005.04.048
- Zhou, N., Song, D., Qi, W., Li, X., Zou, J., & Attallah, M. M. (2018). Influence of the kissing bond on the mechanical properties and fracture behaviour of AA5083-H112 friction stir welds. *Materials Science & Engineering.A, Structural Materials : Properties, Microstructure and Processing*, 719, 12-20. doi:10.1016/j.msea.2018.02.011
- Zolghadr, P., Akbari, M., & Asadi, P. (2019). Formation of thermo-mechanically affected zone in friction stir welding. *Materials Research Express; Mater.Res.Express*, 6(8), 86558.
doi:10.1088/2053-1591/ab1d25